

# DESIGNING BIOMOLECULAR HYDROGEL SCAFFOLDS FOR HEALTHCARE APPLICATIONS

VIJAY KUMAR PAL

*A thesis submitted for the partial fulfillment of  
the degree of Doctor of Philosophy*



Institute of Nano Science and Technology, Knowledge city, Sector 81, SAS Nagar,  
Manauli PO, Mohali 140306, Punjab, India.

Indian Institute of Science Education and Research Mohali  
Knowledge city, Sector 81, SAS Nagar, Manauli PO, Mohali 140306, Punjab, India.

May 2022



*Dedicated to my beloved  
parents and teachers*



## **Declaration**

The work presented in this thesis has been carried out by me under the guidance of Dr. Sangita Roy at the Institute of Nano Science and Technology, Mohali. This work has not been submitted in part or in full for a degree, a diploma, or a fellowship to any other university or institute. Whenever contributions of others are involved, every effort is made to indicate this clearly, with due acknowledgement of collaborative research and discussions. This thesis is a bona fide record of original work done by me and all sources listed within have been detailed in the bibliography.

VIJAY KUMAR PAL

In my capacity as the supervisor of the candidate's thesis work, I certify that the above statements by the candidate are true to the best of my knowledge.

Dr. SANGITA ROY



## Acknowledgments

I would like to acknowledge and give my heartfelt thanks to all those who have contributed in the completion of this thesis work and also made the journey joyful with wonderful memories.

First of all, I would like to thank my supervisor, Dr. Sangita Roy, for her continuous guidance, inspiration, patience, and unconditional support throughout this journey. Her constant encouragement and motivation have led to the completion of this thesis on time. I consider it an excellent opportunity to pursue this degree under her supervision and learn from her research experience. I would like to thank her for guiding me during these years and developing an excellent understanding of peptide supramolecule chemistry.

I would also like to thank my deepest gratitude to my doctoral committee members: Prof. P. Neelakandan and Dr. Sharmistha Sinha, for their regular comments and constructive suggestions and encouragement.

I would also like to thank Prof. Kamalakannan Kailasam, Dr. Debabrata Patra, Dr. Shyam Lal for their timely guidance and motivation.

I would like to extend my sincere gratitude to Prof. Amitava Patra, Director INST, for the facility, infrastructure, and support. I am grateful to the Former Director, Prof. Hirendra Nath Ghosh for his support and also to the Founding Director, Prof. A.K. Ganguli, for his support and guidance in this journey.

I am obliged to the INST family for providing me with a safe and productive work environment. Thank you for creating a comfortable lab atmosphere and making research facilities available to us. I would also like to express my gratitude to IISER Mohali and NABI Mohali for providing the necessary infrastructure during this time period.

I would like to thank all the administrative and non-administrative staff for always being there to help and support. I would also like to thank DST, India, for providing the regular institutional fellowship throughout this journey.

I would like to express my deepest gratitude to my wonderful labmates who made this journey exceptional. I would like to thank my seniors Dr. Nidhi Patel, Dr. Rashmi Jain, Dr. Harsimran Kaur and Pooja Sharma for being there and always being a helping hand. I would also like to thank my other lab members, Sourav Sen, Archita Sharma, Shambhavi, Japleen, Rakesh, and Sweta for their help and support. During my tenure, I have also come

across some of the intern students with whom I have good memories. My special thanks to Mamta, Vinupriya, Priyanka, Akhilesh, and Pratap for cherishing good moments.

Working in an interdisciplinary area requires expertise in many fields and in an institute where people of different background and different expertise work together, share their thoughts and suggestions. During my tenure, I have met several of such peoples and exchanged thoughts on the field. The list is long, but still, I want to mention few names: Dr. Swati, Dr. Naimat, Dr. Rajender, Dr. Ashmeet, Dr. Atul, Dr. Arpit, Dr. Anup, Dr. Sunaina, Nandan, Neha, Jijo, Anjana, Preeti, Rohit, Sonika, Shefali, Aashish, Aakriti, Aditi and many more. I would like to thank all of them for their support and help whenever needed.

Friends deserve special appreciation as they are the ones who stand by your side in the ups and downs in this journey. My heartiest regards to Namrata, Harsimran, Pooja, Avinash, Ravi, and Radhika, who always supported me in the tough times.

Finally, I would like to thank my family members, my parents, brother, and sister-in-law, who encouraged and guided me in every moment of this journey and longed to see this achievement come true. I would also like to thank God, for letting me through all the difficulties I have experienced and the guidance on a daily basis, and also the blessings.

Vijay Kumar Pal

## Abbreviations

ECM	Extracellular matrix
DNA	Deoxyribonucleic acid
GAGs	Glycosaminoglycans
HA	Hyaluronan
CS	Chondroitin sulphate
KS	Keratan sulphate
DS	Dermatan sulphate
HS	Heparan sulphate
Fmoc	Fluorenyl methoxycarbonyl
Nap	Naphthoxy acetic acid
ACN	Acetonitrile
DMF	Dimethylformamide
HFIP	Hexafluoro-2-propanol
DMSO	Dimethyl sulfoxide
NFC	Nanofibrillar cellulose
CMP	Collagen mimetic peptide
CIP	Collagen inspired peptide
DIC	<i>N,N'</i> diisopropylcarbodiimide
EDT	1,2-ethanedithiol
TFA	Trifluoroacetic acid
DCM	Dichloromethane
PBS	Phosphate buffered saline
FBS	Fatal bovine serum
MTT	3-(4,5-Dimethyl-2-thiazolyl)-2,5-diphenyltetrazolium bromide
FDA	Fluoresceine diacetate
PI	Propidium iodide
TBA	Thiobarbituric acid
TCA	Trichloroacetic acid
DCFH-DA	Dichlorodihydro-fluorescein diacetate
Cbz	Carbobenzoxy

SPPS	Solid phase peptide synthesis
RP-HPLC	Reverse phase high performance liquid chromatography
DLS	Dynamic light scattering
CD	Circular dichroism
FTIR	Fourier transform infrared
SEM	Scanning electron microscopy
TEM	Transmission electron microscopy
AFM	Atomic force microscopy
CLSM	Confocal laser scanning microscopy
ThT	Thioflavin T
XRD	X-Ray diffraction
SAXS	Small angle X-Ray scattering
DMEM	Dulbecco modified eagle medium
G'	Loss modulus
G''	Storage modulus
MGC	Minimum gelation oncentration
BSA	Bivine serum alibhi
FACS	Fluorescence activated cell sorting
ALP	Alkaline phosphatase
SAED	Selected area electron diffraction
CSI	Cell shape index
NCPs	Non-collagenous protein
ELR	Elastin like recombinants
EDX	Energy dispersive X-ray analysis
LVE	Linear viscoelastic
PFT	Peak force tapping
ROS	Reactive oxygen species
MIC	Minimum inhibitory concentration
TEMPO	2,2,6,6-tetramethylpiperidine-1-oxyl

## ABSTRACT

Natural biomolecular assemblies commonly involve non-covalent interactions among the specific building blocks, which can also be replicated in an artificial setup to fabricate the next-generation materials. In this direction, self-assembly of short peptides into a well-ordered supramolecular structure has gained immense interest for developing advanced materials at the nano dimension. In particular, differential supramolecular assemblies by modulating the self-assembling pathways can be achieved from a single type of building block, which responds differentially towards different cell types. In this context, we have designed oppositely charged collagen inspired shortest bioactive pentapeptide sequence as a minimalistic building block for development of next-generation biomaterials. Our rational design involves synthesis of two pentapeptides, where the fundamental molecular motif of collagen, that is Gly-X-Y has been mutated at the central position with positively charged, lysine, and negatively charged, aspartate residues, respectively to create ionic complementary peptides. Interestingly, simple mixing of the two peptides was found to induce the co-assembly of these designed peptides, which drives the formation of self-supporting hydrogel at physiological pH and thus enhanced the potential of exploring these peptides for biomedical applications. Furthermore, our approach was focused on mimicking the diverse biomolecular entities present in the native extracellular matrix (ECM) to create a closer mimic of the similar domain. In this direction, we have developed a conjugated hydrogel consisting of nanocellulose and collagen inspired complementary ionic peptides. Further, these biomolecular hydrogel constructs were explored towards cellular studies in order to develop a superior biomaterial, which represents an ideal replica of native ECM. Interestingly, these combined scaffolds supported cellular behaviour of both fibroblast as well as neural cells, highlighting the diversities of these conjugate hydrogels. Furthermore, we have attempted to overcome the limitations of negatively charged collagen inspired peptide to self-assemble at physiological pH along with the decreased cellular viability owing to the surface charge of the peptide by introducing the metal ions in the ensemble state. In this direction, we have explored the cooperative effect of the divalent metal ions to promote hydrogelation in the short collagen inspired peptide for developing advanced biomaterials. The presence of metal ions showed a distinct shift

in its equilibrium point of gelation and demonstrated the conversion from sol to gel at physiological pH and thus enabling the scope of fabricating an advanced biomaterial for controlling cellular behaviour. In similar direction, we have demonstrated the process of biomineralization in collagen inspired peptide and growth of Ca/P crystals on the peptide fiber. Furthermore, the peptide hydrogel scaffold exhibited good biocompatibility and supported adhesion of osteoblast cells. To this end, we have also quantified the biochemical marker (ALP) for determining the characteristic features of osteoblast cells. In this context, we have utilized the positively charged collagen inspired peptide to construct the spherical nanoparticles encapsulating an antimicrobial agent, ferulic acid. Interestingly, the nanoparticles demonstrated a dynamic shape transition into nanofibers when exposed to the basic environment of chronic wound, hence releasing the encapsulated ferulic acid. Furthermore, the collagen functionality induced biocompatibility and fast growth of the fibroblast cells on the surface. Thus, the bio-nano construct provided a dual functionality and environmental tunability, and offering advancement in the wound healing applications.

## SYNOPSIS

Bioinspired nanoarchitecture has lately gained attention as a versatile method for bridging the gap between fundamental biology and nanotechnology. Amidst several of these biomolecular entities, peptides are one of the essential components of proteins, which have emerged as the versatile candidate for the creating these nanomaterials. The utilization of short peptides as a building block has received a lot of interest because of their unique physical, chemical, and biocompatible attributes, which can be used in a variety of biomedical and nanotechnological applications related to biomedicine. Peptides have the unique advantage of offering variations in their sequence through variable side chains, which allows further modifications for necessary attachment of other biomolecular functionalities. This unique feature can lead to the variable molecular packing of these peptide monomers at the nanoscale, and thus resulting in a diverse range of hierarchical supramolecular structures. Ultrashort peptides are an important group of building blocks, which can manufacture and regulate the de novo design of self-assembled materials in a modular manner because of their diversity, flexibility, and ease of synthesis. These bioinspired short peptides follow a fascinating bottom-up approach called molecular self-assembly to produce these hydrogel scaffolds. Furthermore, the peptide hydrogels produced by simple non-covalent interactions are distinctive from the polymeric cross-linked hydrogels in terms of their inherent stimuli responsive nature under simple environmental changes. In particular, these biomaterials are extremely responsive towards external stimuli, which provides the unique property of displaying stimuli responsiveness to harness differential supramolecular structures based on a single gelator molecular structure. In this thesis, we have attempted to mimic one of the most abundant proteins of extracellular matrix (ECM), i.e., collagen and studied the effect of differential stimuli in producing diverse nanostructures from our minimalist peptide design that can control biochemical properties of the designer bioinspired scaffolds for fabrication of next generation biomaterials.

In particular, a single building block can attain differential supramolecular nanostructures by modulating their assembling pathways, which responds differentially towards different cell types. These peptide-based nanostructures offer extensive advantages in field of

biomedicine owing to their biocompatible nature and easy synthetic strategies. Further, we were interested in developing a bioactive peptide scaffold as a synthetic mimic of the natural extracellular matrix. Several of the macromolecules are responsible for regulating the functional processes of the ECM, out of which, collagen has been represented as the most abundant protein that plays a crucial role in cellular adhesion and proliferation. Recent developments in collagen inspired peptides were inclined toward the minimalist approach, which focusses on production of self-assembling short peptides capable of mimicking complex higher order structures with tunable mechanical properties. We have designed oppositely charged collagen inspired shortest bioactive pentapeptide sequences, as a minimalistic building block for the development of next-generation biomaterials. In particular we have rationally designed two collagen inspired short peptides with the oppositely charged amino acids such as lysine and aspartic acid. Depending on their overall surface charge, these individual peptides showed high propensity to form self-supporting hydrogel either at acidic or basic pH, which limits their biomedical applications. The differential surface charge of these peptide offers specific site for salt bridge interactions to induce the self-assembly within these peptides at the physiological pH. Such coulombic interactions further trigger the formation of the self-assembled hydrogels at physiological pH, which allows the possibility to explore these peptidic nanostructures towards biomedical applications. Very interestingly, a simple and facile strategy was utilized to maximize this attractive interaction by simply mixing the two components at a certain ratio and switching the pH of the medium to the physiological pH. The self-supporting co-assembled hydrogel enhanced the potential of exploring these peptides for biomedical purposes. This co-assembly of ionic peptides was further accompanied by the enhancement in the mechanical stiffness of the gels and reduction in overall zeta potential of the combined hydrogel, which provides the evidence for additional electrostatic interactions during salt-bridge formation other than  $\pi$ - $\pi$  interactions and hydrogen bonding at the nanoscale. Furthermore, the thixotropic nature of these gels offers an additional advantage of exploring these designer biomaterials as injectable gels. The nanofibers of co-assembled hydrogel were found to be highly biocompatible to the fibroblast cells compared to the individual peptides, which was evident from their cytotoxicity studies. We anticipate that our rational design of ECM protein mimics in the form of short bioactive peptides will

contribute significantly to the development of novel biomaterials and may open up a new avenue in the field of tissue engineering and regenerative medicines.

In this context, it is worth mentioning that the native ECM is composed of several macromolecules like, adhesion proteins, enzymes, minerals along with carbohydrate, glycosaminoglycans etc. that provide structural support and biochemical signalling for cellular adhesion and migration. Hence, it will be very interesting to see the effect of conjugating a sugar moiety to these collagen inspired peptides, which will provide the extra structural stability to the synthetic scaffold and will represent a closer mimic of the native ECM. To this end, protein and polysaccharides-based hydrogels have gained tremendous impetus in the field of tissue regeneration and other healthcare applications. Since, these novel biomaterials present a more realistic model for biological environment in the cellular neighbourhood, we have developed a new class of conjugated hydrogel based on carbohydrate polymer, that has been fabricated from biomass derived nanocellulose and collagen inspired complementary ionic peptides. Interestingly, these conjugate hydrogels were constructed via simple non-covalent interactions. The synthetic strategy utilized TEMPO oxidized cellulose nanofibers, which presented the anionic surface charge, and thus offer the scope of electrostatic interactions with the oppositely charged moieties of ionic peptides. Conjugate hydrogels developed from nanofibrillar cellulose and collagen inspired peptides showed enhanced mechanical strength as compared to the native peptide hydrogel. Further, these biomolecular hydrogel constructs were explored towards cellular studies in order to develop a superior replica of native extracellular matrix. Interestingly, differential cellular response could be induced in such novel biopolymeric matrix by judicious tuning of the intermolecular interactions to fabricate suitable matrix with variable physical properties, like, porosity, mechanical stiffness etc. Tunable porous network of these conjugated biopolymeric hydrogels stabilized by combination of CH/ $\pi$ , as well as hydrogen bonding interactions along with electrostatic interactions between the cellulose and collagen inspired peptides present a scaffold that successfully mimic the merits of the native extracellular matrix by combining peptide and sugar leading to significant cellular adhesion, growth, and proliferation. Interestingly, these combined scaffolds supported cellular behaviour of both fibroblast as well as neural cells, highlighting the diversities of these conjugate hydrogel.

Further in this direction, it is worth mentioning that several metal ions play crucial role in cellular functions. In order to mimic these metal coordinated biological nanostructures, the short peptide gelator was explored to show their differential interaction in presence of metal ions, which promote the hydrogelation in the short collagen inspired self-assembling peptides for developing advanced biomaterials. Introduction of the biologically relevant metal ions ( $\text{Ca}^{2+}/\text{Mg}^{2+}$ ) to the negatively charged peptide surpasses its limitation to self-assemble into a multi-scale structure at physiological pH. In particular, the negatively charged peptide NapFFGDO has demonstrated its ability to self-assemble at pH 5.0 but failed to self-assemble at physiological pH and remained as solution. Interestingly, the negatively charged moiety present at the surface of these nanofibers offers an additional advantage to undergo metal ion interaction to induce the hydrogelation among these short peptides. In presence of metal ions, the negatively charged peptide showed a distinct shift in its equilibrium point of gelation and demonstrated conversion from sol to gel at the physiological pH and thus enabling the scope of fabricating an advanced biomaterial for controlling cellular behaviour. Thus, with the addition of divalent metal salts to the NapFFGDO peptide, a threefold advantage has been achieved at the molecular domain that includes: 1) successful gelation at physiological pH as well as 2) lowering of the minimum gelation concentration, and thus facilitating the self-assembly of the peptide monomers and 3) an improvement in the physical properties like mechanical strength was achieved with an exceptional improvement biological response. More importantly, the metal coordinated peptide hydrogels were found to overcome the limitations of the negatively charged peptides and promoted biocompatibility and cellular proliferation at physiological pH. Thus, this study emphasizes the importance of incorporating metal ions as a simplistic approach for fine tuning of the structural and functional property of the synthetic matrix. Such an approach of cooperative self-assembly enhances the scope of these biomaterials, which can be applied in developing extracellular matrix mimics for futuristic applications. Further, as these peptide amphiphiles are known to attain diverse nanostructures when exposed to differential external stimuli or environmental conditions. We were keen to explore their potential for other therapeutic applications. In this direction, we have developed peptide-based nanoparticles, which encapsulate ferulic acid for its applications as efficient antimicrobial. Peptide-based supramolecular nano-assemblies have received

much attention due to their importance in drug delivery, therapeutics, and tissue regeneration owing to their stimuli responsive behaviour and biological relevance. Recent developments in dynamic self-assembly have shifted the emphasis towards producing novel nanostructures with stimuli-responsive assembly behaviour. We have developed a bio-nano construct with dual functionality and environmental tunability, offering advancements in the wound healing applications. In particular, we have utilized a collagen inspired peptide amphiphile to fabricate spherical nanoparticles via nanoprecipitation, and explored its unique intrinsic stimuli-responsive self-assembling property to encapsulate and release the hydrophobic drug, ferulic acid. The peptide-based spherical nanoparticles demonstrated a dynamic behaviour and a shape transition into nanofibers when exposed to the basic environment of a chronic wound, and triggering the release of the encapsulated ferulic acid. The structural transformation of the nanoparticles into the nanofibers provided an advanced synthetic scaffold for wound regeneration while the released ferulic acid provided assistance in combating microbial infection to offer a dual advantage of the nano-construct. Interestingly, the novel nanocarrier demonstrated an enhanced efficacy in the bactericidal effect offered by ferulic acid. Such transmorphic behaviour of the peptide could be used for constructing stimuli-responsive nano-assemblies for overcoming the limitations of the hydrophobic drugs in therapeutics.

We further explored the mineralization capability of these collagen inspired peptides to grow hydroxyapatite crystals on these peptide nanofibers. Collagen plays a crucial role in mineralizing several of the bone tissues while working with some of the non-collagenous proteins. These non-collagenous proteins are rich in acidic amino acid, which in principle, provide the nucleation sites for the hydroxyapatite growth. Inspired from this natural phenomenon, we have demonstrated the nucleation and growth of the hydroxyapatite crystals on these short collagen inspired peptide derived nanofibers. AFM studies revealed the slow growth of the hydroxyapatite crystal on these peptide fibers. Interestingly, these mineralized fibers have demonstrated enhancement in the young's modulus value of the individual fiber via peak force quantitative nano-mechanics. Furthermore, the mineralized collagen fibers have showed compatibility with the osteoblast cells up to 15 days of incubation. Upregulation of ALP expression and increased calcium content in the osteoblast cells showed the effectiveness of the mineralized peptide. These results

suggested that these short bioactive peptides can be exploited for a range of biomedical strategies in developing grafts for bone tissue regeneration.

Thus, the work in this thesis demonstrated the importance of external stimuli or environmental conditions in developing differential nanostructures with differential functions from a single peptide monomer. The research findings represent the electrostatic interactions among the oppositely charged peptides inspired from the single tripeptide unit of collagen molecule to develop a more biocompatible co-assembled system. The studies further demonstrated the benefits of conjugating carbohydrate polymer into these short peptides in developing a tunable synthetic scaffold. Furthermore, the thesis also demonstrates the cooperative effect of adding simple metal ions to promote hydrogelation and access superior physical properties and enhanced cellular compatibility. The studies further highlight the stimuli responsive shape transformable behaviour of these peptide nanostructures to encapsulate and release the hydrophobic drug molecules, serving a dual function of antibacterial agents and providing synthetic scaffold for the wound site. This thesis also demonstrated the controlled growth of hydroxyapatite crystals on these collagen fibers, which may display potential applications in bone tissue regeneration. Furthermore, by controlling the suitable parameters a single gelator molecule can lead to the fabrication of diverse nanostructures, which may serve significant potential in differential biomedical and tissue engineering applications. The non-conventional approach utilized for generating the diverse nanostructures from a collagen inspired peptide to develop synthetic scaffold holds great potential to create advanced nanomaterials for future biomedicine.

#### List of publications

##### Included in Thesis

1. Vijay Kumar Pal, Rashmi Jain, and Sangita Roy, Tuning the supramolecular structure and function of collagen mimetic ionic complementary peptides via electrostatic interactions. *Langmuir*, 2019, 36(4), 1003-1013.
2. Vijay Kumar Pal, Rashmi Jain, Sourav Sen, Kamalakannan Kailasam, and Sangita Roy, Designing nanofibrillar cellulose peptide conjugated polymeric hydrogel scaffold for controlling cellular behaviour. *Cellulose*, 2021, 28, 10335-10357.

3. Vijay Kumar Pal and Sangita Roy, Cooperative metal ion coordination to the short self-assembling peptide promotes hydrogelation and cellular proliferation. *Macromol. Biosci.*, 2022, 2100462.
4. Vijay Kumar Pal and Sangita Roy, Designing pH triggered smart shape transformable dynamic bioactive peptide nano-assemblies for antibacterial therapy. *ACS Appl. Nano Mater.* 2022, 5(8), 12019-12034.
5. Vijay Kumar Pal and Sangita Roy, Cooperative calcium phosphate deposition on collagen-based peptide nanofibers for application in bone tissue engineering. (Under review).

Not included in Thesis

1. Rashmi Jain, Vijay Kumar Pal, and Sangita Roy, Triggering supramolecular hydrogelation using a protein-peptide co-assembly approach. *Biomacromolecules*, 2020, 21(10), 4180-4193.
2. Harsimran Kaur, Pooja Sharma, Nidhi Patel, Vijay Kumar Pal, and Sangita Roy, Accessing highly tunable nanostructured hydrogels in a short ionic complementary peptide sequence via pH trigger. *Langmuir*, 2020, 36(41), 12107-12120.
3. Pooja Sharma, Vijay Kumar Pal, and Sangita Roy, An overview of latest advances in exploring bioactive peptide hydrogels for neural tissue engineering. *Biomater. Sci.* 2021, 9, 3911-3938.
4. Pooja Sharma, Vijay Kumar Pal, Harsimran Kaur, and Sangita Roy, Exploring the TEMPO-Oxidized Nanofibrillar Cellulose and Short Ionic-Complementary Peptide Composite Hydrogel as Biofunctional Cellular Scaffolds. *Biomacromolecules* 2021, 9, 3911-3938.



## Table of contents

	Page No.
<b>Declaration</b>	i
<b>Acknowledgment</b>	iii
<b>Abbreviation</b>	v
<b>Abstract</b>	vii
<b>Synopsis</b>	ix
<b>Table of Contents</b>	xvii
<b>List of Figures</b>	xxv
<b>List of Tables</b>	xlvi
<b>Chapter 1: Introduction</b>	1-44
1. Introduction	3
1.1 Molecular self-assembly	5
1.2 Native extracellular matrix-an inspiration for advanced material	7
1.3 Peptide based self-assembled system- A minimalistic approach to mimic natural macromolecules	9
1.3.1 Non-covalent interactions	10
1.3.1.1 Hydrogen bonding	10
1.3.1.2 Hydrophobic interactions	11
1.3.1.3 $\pi$ - $\pi$ interactions	11
1.3.1.4 Electrostatic interactions	12
1.3.1.5 van der Waal interactions	13
1.3.2 Peptide amphiphiles	14
1.3.3 Aromatic peptide amphiphiles	16
1.3.4 Ionic complementary peptides	17
1.4 Stimuli responsive peptide self-assembly as controlled by self-assembly pathway	17
1.4.1 pH triggered hydrogelation	18
1.4.2 Metal induced hydrogelation	19
1.4.3 Biocatalytic self-assembly	20

1.4.4 Light triggered self-assembly	21
1.4.5 Temperature induced hydrogelation	22
1.4.6 Self-assembly induced by molecular recognition	23
1.4.7 Solvent induced hydrogelation	24
1.5 Differential secondary structures formed by designer peptide	25
1.5.1 $\alpha$ -helix	25
1.5.2 $\beta$ -sheet	25
1.5.3 $\beta$ -hairpin	26
1.6 Peptide polymer bioconjugate	27
1.7 Recent advances in fabrication of collagen inspired peptide hydrogel	28
1.8 Aims and objective	32
1.9 References	33
<b>Chapter 2: Materials and methods</b>	<b>45-94</b>
2.1 Introduction	47
2.2 Materials	47
2.3 Design and synthesis of peptide amphiphile	48
2.3.1 Solid phase peptide synthesis	49
2.3.2 Reverse phase high pressure liquid chromatography	50
2.3.3 Mass spectroscopy	51
2.3.4 Self-assembly of the designer peptides	52
2.3.5 TEMPO oxidation of microfibrillar cellulose	54
2.3.5.1 Electric conductometric titration	55
2.3.5.2 Method of hydrogelation	55
2.3.5.3 Surface hydrophobicity measurement	56
2.3.6 Zeta potential measurement	56
2.3.7 Dynamic light scattering	56
2.4 Spectroscopic and microscopic characterization of self-assembled nanostructures	57
2.4.1 Circular dichroism	58
2.4.2 Fourier transform infrared spectroscopy	59

2.4.3	Fluorescence spectroscopy	60
2.4.4	Thioflavin T fluorescence assay	62
2.4.5	Congo Red Binding assay	62
2.4.6	Powder X-ray diffraction	63
2.4.7	Small angle X-ray scattering	64
2.4.8	Confocal laser scanning microscopy	65
2.4.9	Atomic force microscopy	66
2.4.10	Scanning electron microscopy	67
2.4.11	Transmission electron microscopy	69
2.4.12	Rheological analysis of peptide hydrogels	71
2.4.12.1	Assessment of mechanical strength	71
2.4.12.2	Thixotropic measurements	72
2.4.12.3	Dynamic compressive strain study	73
2.4.13	Mechanical stiffness via peak force quantitative nano-mechanics	73
2.5	Assessment of biological response towards the developed matrix and their therapeutic application	75
2.5.1	Cell lines and maintenance of cells	75
2.5.2	Biocompatibility studies	77
2.5.3	2D culture	78
2.5.4	Live dead staining	79
2.5.5	Cellular proliferation assay	79
2.5.6	Immunofluorescence staining	80
2.5.7	F-actin staining	81
2.5.8	Alizarin Red S staining	81
2.5.9	Scratch assay	82
2.5.10	Quantitative assessment of cellular population via fluorescence activated cell sorting (FACS)	83
2.5.11	ALP estimation	85
2.5.12	Assessment of antimicrobial activity	85
2.5.13	Evaluation of reactive oxygen species generation	87

2.5.14 Malondialdehyde assay	88
2.5.15 Statistics analysis	89
2.6 References	89
<b>Chapter 3: Modulating the supramolecular structure and function of self-assembling collagen inspired ionic complementary peptides via electrostatic interactions</b>	<b>95-126</b>
3.1 Introduction	97
3.2 Results and discussions	101
3.2.1 Design and self-assembly of collagen-inspired peptides	101
3.2.2 Morphological analysis	106
3.2.3 Nucleation and growth mechanism of peptide self-assembly	108
3.2.4 Spectroscopic characterization	109
3.2.5 Mechanical property	113
3.2.6 Evaluation of thixotropic behaviour	114
3.2.7 Cytotoxicity studies	118
3.3 Conclusions	119
3.4 References	120
<b>Chapter 4: Metal ion complexation promotes self-assembly within a short collagen inspired peptide domain and leads to fabrication of an advanced scaffold with enhanced cellular proliferation</b>	<b>127-170</b>
4.1 Introduction	129
4.2 Results and discussions	132
4.2.1 Design and gelation of collagen inspired self-assembling peptide	132
4.2.2 Spectroscopic characterization	136
4.2.3 Morphological analysis	141
4.2.4 Mechanical strength assessment	144
4.2.5 Cell culture studies	148
4.2.5.1 Evaluation of cellular cytotoxicity	148

4.2.5.2 Cellular adhesion	150
4.2.5.3 Assessment of cellular proliferation	153
4.2.5.4 F-actin staining (Rhodamine phalloidin)	154
4.2.5.5 Immunostaining for $\beta$ -III tubulin	156
4.2.5.6 Cellular migration assay	159
4.2.5.7 Flow cytometry for quantitative analysis of cellular behaviour	161
4.3 Conclusion	163
4.4 References	164
<b>Chapter 5: Cooperative calcium phosphate deposition on collagen- based peptide nanofibers for application in bone tissue engineering</b>	<b>171-198</b>
5.1 Introduction	173
5.2 Results and discussions	176
5.2.1 Design and mineralization of peptide nanofiber	176
5.2.2 Microscopic evidence of mineralized nanofibers	178
5.2.3 Spectroscopic analysis	182
5.2.3.1 Small Angle X-Ray Scattering analysis	185
5.2.4 Mechanical strength analysis	186
5.2.4.1 Rheological analysis	187
5.2.4.2 Peak force quantitative nano-mechanics via AFM	188
5.2.5 Structural analysis of the mineralized fibers	188
5.2.6 Cell studies	190
5.2.6.1 Biocompatibility studies of the mineralized peptide nanofibers	190
5.2.6.2 Cellular adhesion (2D cell culture)	192
5.2.6.3 Assessment of cellular proliferation	194
5.2.6.4 Cytoskeleton (F-actin) staining	195
5.2.6.5 Alkaline phosphatase (ALP) estimation	198
5.2.6.6 Calcium content estimation	199
5.3 Conclusion	200

5.4 References	201
<b>Chapter 6: Exploring non-covalent interactions among nanofibrillar cellulose-peptide conjugate polymeric hydrogels for developing advanced synthetic scaffolds</b>	<b>207-240</b>
6.1 Introduction	209
6.2 Results and discussions	213
6.2.1 TEMPO mediated oxidation of cellulose	213
6.2.2 Preparation of peptide cellulose conjugate hydrogel	214
6.2.3 Microscopic characterization of conjugate hydrogels	216
6.2.4 Small Angle X-Ray Scattering (SAXS) analysis	218
6.2.5 Mechanical property of conjugate hydrogel	221
6.2.6 Biocompatibility assessment of the conjugate hydrogel	222
6.2.7 2D cell culture on conjugate hydrogel	223
6.2.8 Cellular proliferation assay on conjugate hydrogels	226
6.2.9 Cytoskeletal staining	227
6.2.10 Immunostaining	229
6.2.11 Cellular migration assay	231
6.2.12 Quantitative analysis of cellular interaction via FACS	234
6.3 Conclusions	235
6.4 References	236
<b>Chapter 7: Designing pH responsive smart shape transformable dynamic nano-vehicle based on bioactive peptide nano-assemblies for antibacterial therapy and wound healing</b>	<b>241-270</b>
7.1 Introduction	243
7.2 Results and discussions	247
7.2.1 Synthesis and characterization of nanoparticles	247
7.2.2 Transmorphic behaviour of nanoparticles	251
7.2.3 Equivalence point and H-bonding	253

7.2.4 Drug encapsulation efficiency	254
7.2.5 Exploration of this peptide based novel nanomaterial as an advanced biomaterial for application in antibacterial therapy	256
7.2.5.1 Determination of antimicrobial property	256
7.2.5.2 Assays for antimicrobial mechanism	260
7.2.5.3 Microscopic examination of damaged cell membrane	261
7.2.5.4 Biocompatibility of these nanostructures to the mammalian cells	262
7.2.5.5 Cellular migration assay (wound closure)	264
7.3 Conclusions	265
7.4 References	266
<b>Chapter 8: Conclusions and future perspectives</b>	<b>271-280</b>
8.1 Summary	273
8.2 Future perspectives	276
Appendix I	281-285



## List of Figures

<b>Figure no.</b>	<b>Caption</b>	<b>Page no.</b>
<b>Figure 1.1</b>	World of peptide amphiphile with their potential applications in the field of biomedicine and healthcare	5
<b>Figure 1.2</b>	Schematic representation of extracellular matrix with various component required for cellular attachment and growth	8
<b>Figure 1.3</b>	Structural representation of 20 amino acids with variable side chain and schematic representation of the peptide bond formation among them	9
<b>Figure 1.4</b>	Schematic representation of hydrogen bonding in amino acids, resulting in the formation of peptide bond	10
<b>Figure 1.5</b>	Schematic representation of $\pi$ - $\pi$ interaction among the aromatic moieties stabilizing the peptide nanostructures	12
<b>Figure 1.6</b>	Schematic representation of electrostatic interaction among the oppositely charge amino acids stabilizing the self-assembled nano-structure	13
<b>Figure 1.7</b>	Schematic representation of peptide amphiphile with polar head and hydrophobic tail	15
<b>Figure 1.8</b>	Schematic representation of self-assembly via different physicochemical stimuli	19
<b>Figure 1.9</b>	Schematic representation of secondary structures attained by the short peptide amphiphiles	26
<b>Figure 2.1</b>	Schematic representation of the simple dipeptide synthesis via solid phase method	49
<b>Figure 2.2</b>	Schematic representation of the working principle and instrumental setup of the reverse phase high performance liquid chromatography	51
<b>Figure 2.3</b>	Schematic representation of pH switch gelation method: for ionic peptides positively charged at physiological pH repel the	53

adjacent peptide owing to similar charge repulsion, while at the pKa point the peptide tend to self-assemble into nanostructure owing to the charge neutralization

<b>Figure 2.4</b>	Schematic representation of conversion of hardwood cellulose into nanofibrous cellulose via TEMPO oxidation	54
<b>Figure 2.5</b>	Schematic representation of contact angle measurement through drop shape analyser	56
<b>Figure 2.6</b>	Schematic representation of the working principle of Dynamic Light Scattering (DLS)	57
<b>Figure 2.7</b>	Schematic representation of working principle of circular dichroism (CD)	58
<b>Figure 2.8</b>	Schematic representation of the working principle of Fourier Transform InfraRed (FTIR) spectroscopy	59
<b>Figure 2.9</b>	Jablonski diagram showing the possible electronic transition giving rise to absorption and emission	61
<b>Figure 2.10</b>	Schematic representation of working principle of powder X-Ray diffraction (XRD)	63
<b>Figure 2.11</b>	Schematic representation of work flow of small angle X-ray scattering (SAXS)	65
<b>Figure 2.12</b>	Schematic representation of working principle of Atomic Force Microscopy (AFM)	67
<b>Figure 2.13</b>	Schematic representation of the working principle of Scanning Electron Microscopy (SEM)	68
<b>Figure 2.14</b>	Schematic representation of the working principle of Transmission Electron Microscope (TEM)	70
<b>Figure 2.15</b>	Schematic representation of oscillatory rheology setup with cone plate above the sample	71
<b>Figure 2.16</b>	Schematic representation of the (a) interaction forces for Hertz model (with area normalized) and (b) force-distance curve, displaying the different contact regime between the tip and the surface as both the bodies approaches	74

<b>Figure 2.17</b>	Schematic representation of the diverse nanostructure achieved by short peptide amphiphiles and their applications in biomedical field	77
<b>Figure 2.18</b>	Schematic representation of the peptide hydrogels working as 2D scaffolds for the cellular adhesion and growth	78
<b>Figure 2.19</b>	Schematic representation of the scratch assay, showing the cellular migration over time	82
<b>Figure 2.20</b>	Schematic representation of the working principle of fluorescent activated cell sorting (FACS)	84
<b>Figure 2.21</b>	Schematic representation of amino acids as building block for development of differential nanostructures capable of giving antimicrobial properties	86
<b>Figure 2.22</b>	Schematic representation of ROS generation leading to cell wall rupture and bacterial cell death and estimation via DCFH-DA	87
<b>Figure 3.1</b>	Chemical structure of the designed collagen inspired peptides (a) NapFFGKO (positively charged peptide) and (b) NapFFGDO (negatively charged peptide).	101
<b>Figure 3.2</b>	Reverse phase HPLC and Mass spectra of the collagen inspired peptides (a,b) NapFFGKO and (c,d) NapFFGDO, respectively	102
<b>Figure 3.3</b>	Schematic representation of the self-assembly of peptide amphiphiles in their respective environment leading to hydrogel formation at different pH through counter ion stabilization; (a) NapFFGKO and (b) NapFFGDO. Upon mixing them together i.e. NapFFGKO:NapFFGDO 1.1:1, they showed gelation at physiological pH due to electrostatic	103
<b>Figure 3.4</b>	Acid-base titration curve of collagen inspired peptides showing the protonation and deprotonation states of amino and carboxyl groups of the respective amino acid residues in acidic and basic environment respectively	104
<b>Figure 3.5</b>	(a) Zeta potential graph showing the overall surface charge of individual peptides and combined peptides at different ratios. (b)	105

	Table showing the values of surface charge density of the individual peptides and co-assembled peptides	
<b>Figure 3.6</b>	AFM images of co-assembled hydrogels of ionic complementary peptides at different ratios of NapFFGKO:NapFFGDO respectively (a)1:1, (b)2:1, (c)1.5:1 and (d)1.1:1 at physiological pH. Scale bar 500nm	106
<b>Figure 3.7</b>	Morphological analysis of nanostructures present in the hydrogels. TEM and AFM images of nanostructures formed by hydrogelators (a, d) NapFFGKO, (b, e) NapFFGDO and (c, f) NapFFGKO+NapFFGDO (1.1:1) at their MGC	107
<b>Figure 3.8</b>	Morphological analysis of nucleation and growth mechanism of collagen inspired peptide hydrogels at different time points; (a) NapFFGKO, (b) NapFFGDO and (c) NapFFGKO+NapFFGDO (1.1:1 at their MGC)	109
<b>Figure 3.9</b>	Spectroscopic characterization of collagen inspired peptide hydrogels. (a) CD spectra of the individual hydrogelators and the combined peptides in their self-assembled state. (b) CD spectra of NapFFGKO at different pH (c) CD spectra of NapFFGDO at different pH and (d) FTIR spectra of hydrogels to determine the secondary structure	110
<b>Figure 3.10</b>	Thioflavin T binding assay showing the different extent of binding to the different supramolecular structures in the gel state and corresponding fluorescence microscopic imaging of the ThT bound hydrogels: (a, d) NapFFGKO (b, e) NapFFGDO (c, f) NapFFGKO + NapFFGDO	111
<b>Figure 3.11</b>	(a) Representative fluorescence emission spectra of peptide amphiphiles in sol and gel state, indicating the formation of the self-assembled nanostructure as evident from the quenched monomeric emission of the naphthoxy group in the gel state. (b)	112

Comparison of the intensity of the monomeric emission at wavelength 340nm.

<b>Figure 3.12</b>	Strain sweep analysis of collagen mimetic peptide hydrogels; (a) NapFFGKO, (b) NapFFGDO and (c) NapFFGKO+NapFFGDO	114
<b>Figure 3.13</b>	Rheology and thixotropic analysis of collagen inspired peptide hydrogels. (a) Mechanical strength analysis, through frequency sweep study of the individual hydrogelator and the co-assembled hydrogels. Graphical representation of thixotropic measurement of (b) NapFFGKO, (c) NapFFGDO and (d) co-assembled hydrogels (NapFFGKO+NapFFGDO) showing the recovery percentage of five repeat strain sweeps from 0.1 to 100% with 200 sec recovery period in between each sweep for all of the hydrogels	115
<b>Figure 3.14</b>	Comparison of percentage recovery in thixotropy measurement, showing the recovery percentage of five repeat strain sweep from 0.1 to 100% with 200 second recovery period in between each sweep for all of the hydrogels	115
<b>Figure 3.15</b>	AFM analysis of NapFFGKO at different time points of thixotropy study (a) before strain, (b) at 100% strain and (c) after recovery following the removal of the strain. Scale bar 500nm	116
<b>Figure 3.16</b>	AFM analysis of NapFFGDO at different time points of thixotropy study (a) before strain, (b) at 100% strain and (c) after recovery following the removal of the strain. Scale bar 500nm	116
<b>Figure 3.17</b>	AFM analysis of co-assembled system NapFFGKO+NapFFGDO at different time points of thixotropy study (a) before strain, (b) at 100% strain and (c) after recovery following the removal of the strain. Scale bar 500nm	117
<b>Figure 3.18</b>	Dynamic compressive strain study of the combined hydrogel NapFFGKO+NapFFGDO through 18G needle from a 2.5 cc syringe at an injection rate of 50 $\mu$ L/s. Data is represented as	117

force vs time and the inset image shows the custom-made setup to examine the force required for extrusion

- Figure 3.19** (a) Cytotoxicity studies comparing the effect of different collagen mimetic peptides on L929 cells at a concentration ranging from 100 $\mu$ g/ml to 1000 $\mu$ g/ml after incubation of 48hrs. (b) Bright field images of L929 cells after 48hrs of incubation with the individual peptides and their co-assembly. Scale bar 100 $\mu$ m 118
- Figure 4.1** (a) Schematic representation of hydrogelation induced in collagen inspired self-assembling peptide in the presence of metal ions at physiological pH, (b) Metal complexation induces hydrogelation in the peptide nanofibers, which further leads to enhancement in cell viability and proliferation 133
- Figure 4.2** Morphological analysis of (a) NapFFGDO (15mM) solution at physiological pH 7.0 via atomic force microscopy and (b) Morphological variation in peptide fiber after instant addition of metal salts (without incubation). Scale bar 500nm 135
- Figure 4.3** Spectroscopic characterization of metal ion complexed collagen inspired self-assembling peptide hydrogel. (a) CD spectra of peptide and metal ion complexed peptide at physiological pH, representing the  $\beta$  sheet-like structure. (b) FTIR spectra show the presence of  $\beta$ -sheet-like structure in metal ion complexed peptide hydrogels 137
- Figure 4.4** FTIR spectra after area normalization in the region of 1350-1480  $\text{cm}^{-1}$ , showing the variation in term of intensity upon interaction with the metal ion complexation (a) 5 mM and 10 mM of  $\text{CaCl}_2$  and (b) 5 mM and 10 mM of  $\text{MgSO}_4$  137
- Figure 4.5** (a) An increment in the fluorescence intensity of the Thioflavin T upon binding to the hydrophobic patches of the peptide hydrogels depicts the presence of  $\beta$ -sheet-like structure. (b) Redshift in Congo red absorption maximum upon binding the 138

- hydrophobic patches of the peptide hydrogel confirms the presence of  $\beta$  sheet-like structure
- Figure 4.6** Fluorescence microscopic images of Thioflavin T binding to the hydrophobic patches of peptide fibers, corresponds to the  $\beta$ -sheet like structure: (a) Blank ThT, (b) NapFFGDO, (c) NapFFGDO+CaCl<sub>2</sub> (5mM), (d) NapFFGDO+CaCl<sub>2</sub> (10mM), (e) NapFFGDO+MgSO<sub>4</sub> (5mM), and (f) NapFFGDO+MgSO<sub>4</sub> (10mM). Scale bar 200 $\mu$ m 139
- Figure 4.7** Fluorescence emission spectra of peptide amphiphiles in sol state showed the monomeric emission of naphthoxy group at 340nm, which showed extensive quenching in gel state upon self-assembly of the peptides 140
- Figure 4.8** Morphological evaluation of metal ion complexed peptide hydrogel through Atomic Force Microscopy (AFM). (a) NapFFGDO with 5 mM Ca<sup>2+</sup> ion and its sectional analysis view of metal complexation in (a.1), (b) NapFFGDO with 10 mM Ca<sup>2+</sup> ion and its sectional analysis view of metal complexation in (b.1). (c) Self-assembled nanofibrillar structure of NapFFGDO with 5 mM Mg<sup>2+</sup> ion, and (d) Self-assembled nanofibrillar structure of NapFFGDO with 10 mM Mg<sup>2+</sup> ion 141
- Figure 4.9** Morphological analysis of nucleation and growth of the self-assembled nanostructures of NapFFGDO and metal coordinated NapFFGDO hydrogels at different time points; (a-e) NapFFGDO, (f-j) NapFFGDO+CaCl<sub>2</sub> (5mM), (k-o) NapFFGDO+CaCl<sub>2</sub> (10mM), (p-t) NapFFGDO+MgSO<sub>4</sub> (5mM), and (u-y) NapFFGDO+MgSO<sub>4</sub> (10mM). Scale bar 500nm 143
- Figure 4.10** Comparative analyses of the mechanical strength of the collagen inspired self-assembling peptide NapFFGDO (30mM) at pH 5.0 and metal ion complexed peptide hydrogels at pH 7.0. (a) Storage moduli (G') of peptide hydrogels show improvement in mechanical strength variation after metal complexation. (b) Bar 144

graph representing the increment in the mechanical strength of the metal ion complexed hydrogels

- Figure 4.11** Rheological analysis revealed the thixotropic nature of the metal coordinated peptide hydrogels: (a) NapFFGDO+CaCl<sub>2</sub> (5mM), (b) NapFFGDO+CaCl<sub>2</sub> (10mM), (c) NapFFGDO+MgSO<sub>4</sub> (5mM), and (d) NapFFGDO+MgSO<sub>4</sub> (10mM) 146
- Figure 4.12** AFM analysis of metal coordinated peptide hydrogels at different point of thixotropic study: before strain, 100% strain, and after recovery (a-c) NapFFGDO+CaCl<sub>2</sub> (5mM), (d-f) NapFFGDO+CaCl<sub>2</sub> (10mM), (g-i) NapFFGDO+MgSO<sub>4</sub> (5mM), and (j-l) NapFFGDO+MgSO<sub>4</sub> (10mM). Scale bar 500nm 147
- Figure 4.13** Assessment of the comparative effect of negatively charged peptide and metal coordinated peptide hydrogel on cellular viability of (a) fibroblast (L929) and (b) glioma (C6) cells while treated with peptide nanofibers of variable concentrations ranging from 100 to 1000 µg/mL via MTT assay 148
- Figure 4.14** Bright field images of fibroblast cells (L929) after incubation of 48 hours with ion complexed peptides at concentration of 500 µg/mL. Scale bar 100 µm 149
- Figure 4.15** Bright field images of glioma cells (C6) after incubation of 48 hours with ion complexed peptides at concentration of 500 µg/mL. Scale bar 100 µm 150
- Figure 4.16** Assessment of cellular adhesion on 2D matrix of peptide hydrogel with fibroblast cells (L929) via Live/Dead staining. Fluorescence images of cells stained with FDA (live) and PI (dead) for different time interval of 48, 72, and 120 hours; (a-c) control, (d-f) NapFFGDO, (g-i) NapFFGDO + Ca5mM, (j-l) NapFFGDO + Ca10mM, (m-o) NapFFGDO + Mg5mM, (p-r) NapFFGDO + Mg10mM. Scale bar 50µm 151
- Figure 4.17** Assessment of cellular adhesion on 2D matrix of peptide hydrogel with glioma cells (C6) via Live/Dead staining. 152

Fluorescence images of cells stained with FDA (live) and PI (dead) for different time interval of 48, 72, and 120 hours; (a-c) control, (d-f) NapFFGDO, (g-i) NapFFGDO + Ca5mM, (j-l) NapFFGDO + Ca10mM, (m-o) NapFFGDO + Mg5mM, (p-r) NapFFGDO + Mg10mM. Scale bar 50 $\mu$ m

- Figure 4.18** Cellular proliferation of (a) fibroblast cells, L929 and (b) Glioma cells, C6 on metal ion complexed peptide hydrogels using Alamar blue assay at a different time point of 48, 72, and 120 hours. Represented data are mean of three different experiments, and asterisk representing the P-value was calculated using two-way ANOVA, Bonferroni's multiple comparison test. (\*\*\*\* represents P-value  $\leq 0.0001$ ) 153
- Figure 4.19** F-actin staining of fibroblast cell line (L929) with Rhodamine phalloidin adhered on (a-c) control, (d-f) NapFFGDO, (g-i) NapFFGDO + Ca5mM, (j-l) NapFFGDO + Ca10mM, (m-o) NapFFGDO + Mg5mM, (p-r) NapFFGDO + Mg10mM at different time point of 48, 72, 120 hours. Scale bar 10 $\mu$ m 154
- Figure 4.20** Assessment of (a) spread area and (b) cell shape index (CSI) of fibroblast cells on hydrogel coated cover slips of phalloidin staining 156
- Figure 4.21** Immunofluorescence staining of neural marker  $\beta$ -III tubulin in C6 cell line adhered on (a-c) control coverslips, (d-f) NapFFGDO, (g-i) NapFFGDO+Ca5mM, (j-l) NapFFGDO + Ca10mM, (m-o) NapFFGDO + Mg5mM, and (p-r) NapFFGDO + Mg10mM at different time point 48 hrs, 72 hrs, and 120 hrs of cell culture, respectively. Scale bar is 10 $\mu$ m 157
- Figure 4.22** Assessment of (a) spread area and (b) cell shape index (CSI) of glioma cells on hydrogel coated cover slips of  $\beta$ -III tubulin staining 158
- Figure 4.23** Cellular migration assay to study the effect of metal coordinated peptide on cellular migration in fibroblast cells (L929). Bright 159

field images of cellular migration at different time point of 0 hr, 12 hrs, and 24 hrs in presence of peptide hydrogel, scale bar 400 $\mu$ m

- Figure 4.24** Cellular migration assay to study the effect of metal coordinated peptide on cellular migration in glioma cells (C6). (a) Bright field images of cellular migration at different time point of 0 hr, 12 hrs, and 24 hrs in presence of peptide hydrogel, scale bar 400 $\mu$ m 160
- Figure 4.25** Quantitative analysis of the cellular migration assay of metal coordinated peptide on (a) fibroblast cells (L929) and (b) glioma cells (C6) 160
- Figure 4.26** Quantitative analysis of the cellular interaction with the hydrogel matrix via flow cytometry. Live and dead cells of fibroblast (L929) were stained and quantified by FDA and PI respectively; (a) Control, (b) NapFFGDO, (c) NapFFGDO + CaCl<sub>2</sub> 5mM, (d) NapFFGDO + CaCl<sub>2</sub> 10mM, (e) NapFFGDO + MgSO<sub>4</sub> 5mM, and (f) NapFFGDO + MgSO<sub>4</sub> 10mM. Q1 quadrant represents live cells, Q3 represents dead cells, and Q2, Q4 represents double-stained and unstained populations 161
- Figure 4.27** Quantitative analysis of the cellular interaction with the hydrogel matrix via flow cytometry. Live and dead cells of glioma (C6) were stained and quantified by FDA and PI respectively; (a) Control, (b) NapFFGDO, (c) NapFFGDO + CaCl<sub>2</sub> 5mM, (d) NapFFGDO + CaCl<sub>2</sub> 10mM, (e) NapFFGDO + MgSO<sub>4</sub> 5mM, and (f) NapFFGDO + MgSO<sub>4</sub> 10mM. Q1 quadrant represents live cells, Q3 represents dead cells, and Q2, Q4 represents double-stained and unstained populations 162
- Figure 5.1** Schematic representation of the mineralization induced by negatively charged collagen inspired peptide and the AFM image showing the fibers getting precipitated upon interaction 177
- Figure 5.2** Atomic Force Microscopy (AFM) of the peptide amphiphile (a) NapFFGKO and (b-d) time dependent growth of the 179

hydroxyapatite crystals on the peptide fibers (2, 12, and 24 hour). Arrow indicates the deposition of calcium phosphate nodules on the peptide fibers. Scale bar 500 nm

- Figure 5.3** Field Emission Scanning Electron Microscopy (FE-SEM) of the peptide amphiphile (a) NapFFGKO and (b) NapFFGKO+Glu+Ca+P (mineralized peptide) after 10 days of incubation. Arrow indicates the peptide nanofibers and crystalline growth of the hydroxyapatite all over the peptide surface. Scale bar 100nm 179
- Figure 5.4** Transmission Electron Microscopy (TEM) images of peptide amphiphile (a) NapFFGKO and (b) NapFFGKO+Glu+Ca+P (mineralized peptide). Scale bar 200 nm 180
- Figure 5.5** Microscopic examination of the mineralized peptide fibers (a) mineralized NapFFGKO after 7 days, (b) HR-TEM images of the mineralized peptide showing different lattice fringes, (c) Selected Area Electron Diffraction (SAED) pattern of the mineralized peptide matches with the preliminary hydroxyapatite crystals, and (d) Energy Dispersive X-ray Analysis (EDX) of the mineralized peptide showed the presence of metal ions deposited on the peptide fibers and the ratio of calcium to phosphorous has been determined, and the value is  $\sim 1.7$  181
- Figure 5.6** Elemental mapping of the mineralized fibers using energy dispersive X-Ray spectroscopy showing the percentage ratio of the calcium and phosphorous in the mineralized fibers. (a) Mineralized peptide fibers, (b) elemental mapping for the calcium present in the selected area (c) Elemental mapping of the phosphorus, present in the mineralized fiber and (d) is the merged channel of the calcium and phosphate 182
- Figure 5.7** Spectroscopic analyses of the mineralized peptide: (a) FTIR spectra, (b) Raman spectra, (c) XRD pattern, (d) X-Ray 183

photoelectron spectrum showing the preliminary growth of the hydroxyapatite crystals on the peptide fibers, (e) Photoelectron spectra of the Ca2p of the mineralized fibers, and (f) a deconvoluted peak of phosphorous showing both the transition state at binding energy 132.07 and 133.32 eV

- Figure 5.8** Deconvoluted XPS spectra for the control peptide and mineralized peptide nanofibers: (a & b) spectral difference in the N1s among control and mineralized peptide. (c & d) intensity difference in the C1s spectra between the control peptide and mineralized peptide. 185
- Figure 5.9** (a) The intensity profile of the control peptide and the mineralized peptide was obtained via small angle X-ray scattering (SAXS) analysis. (b) Rheological analyses of the mineralized peptide: Frequency sweep analysis of the oscillatory rheological investigation of the hydrogel (Image inset) digital image of the lyophilized hydrogel with intact integrity due to the mineralization. (c) Nitrogen adsorption-desorption isotherm to determine the structural nature of the mineralized hydrogels, and (d) Thermogravimetric analysis of the dried sample of control and mineralized peptide fibers. 187
- Figure 5.10** AFM image of the (a) peptide nanofiber and the (c) mineralized fiber in contact mode and their respective FD curve (b & d). The loading force was set to make indent into the sample and thus give realistic elastic modulus and deformation response 190
- Figure 5.11** Cytocompatibility assay of the peptide nanofibers (alone and mineralized) with osteoblast cells (a) 7F2 and (b) Saos-2 cells treated with peptide concentration ranging from 100 to 1000  $\mu\text{g mL}^{-1}$  via MTT assay 191
- Figure 5.12** Bright field images of the 7F2 osteoblast cells after incubation with the mineralized peptide fibers at their respective days 3, 5, 191

	and 7 days. (a-c) control, (d-f) peptide alone, and (g-i) mineralized peptide. Scale bar 100 $\mu$ m	
<b>Figure 5.13</b>	Bright field images of the Saos-2 osteoblast cells after incubation with the mineralized peptide fibers at their respective days 3, 5, and 7 days. (a-c) control, (d-f) peptide alone, and (g-i) mineralized peptide. Scale bar 100 $\mu$ m	192
<b>Figure 5.14</b>	Assessment of cellular adhesion ability on 2D matrix of peptide nanofibers with osteoblast cells (7F2) via Live-Dead staining. CLSM images with live cells stained with FDA and dead cells with PI at different time intervals of 24, 72, 120, and 168 hours, (a-d) control, (e-h) NapFFGKO peptide alone, and (i-l) mineralized NapFFGKO peptide. Scale bar 50 $\mu$ m	193
<b>Figure 5.15</b>	Assessment of cellular adhesion ability on 2D matrix of peptide nanofibers with osteoblast cells (Saos-2) via Live-Dead staining. CLSM images with live cells stained with FDA and dead cells with PI at different time intervals of 24, 72, 120, and 168 hours, (a-d) control, (e-h) NapFFGKO peptide alone, and (i-l) mineralized NapFFGKO peptide. Scale bar 50 $\mu$ m	195
<b>Figure 5.16</b>	Cellular proliferation of osteoblasts (a) 7F2 cells and (b) Saos-2 cells, on mineralized peptide fibers using Alamar Blue assay at three different time points of 72, 120, and 168 hours	189
<b>Figure 5.17</b>	F-actin staining of 7F2 osteoblast cells with Rhodamine phalloidin, (a & d) control, (b & e) NapFFGKO peptide alone, and (c & f) mineralized NapFFGKO peptide. Scale bar 10 $\mu$ m	196
<b>Figure 5.18</b>	Quantitative assessment of (a) spread area and (b) cell shape index (CSI) of osteoblast cells (7F2) on adhered on the peptide coated cover slips of phalloidin staining	196
<b>Figure 5.19</b>	F-actin staining of Saos-2 osteoblast cells with Rhodamine phalloidin, (a & d) control, (b & e) NapFFGKO peptide alone, and (c & f) mineralized NapFFGKO peptide. Scale bar 10 $\mu$ m	197

<b>Figure 5.20</b>	Quantitative assessment of (a) spread area and (b) cell shape index (CSI) of osteoblast cells (Saos-2) on adhered on the peptide coated cover slips of phalloidin staining	192
<b>Figure 5.21</b>	Alkaline phosphatase activity to confirm the osteogenic differentiation capabilities. ALP activity of osteoblasts after 120 and 168 hours	199
<b>Figure 5.22</b>	Alizarin Red S staining to demonstrate the calcium deposits: (a-c) Microscopic examination of 7F2 cells at three different time points 72, 120, 168 hours, (d-f) Microscopic examination of Saos-2 cells at three different time points 72, 120, 168 hours. Quantitative analysis of calcium deposits on the mineralized cells (g) 7F2 cells and (h) Saos-2 cells. Scale bar 200 $\mu\text{m}$	200
<b>Figure 6.1</b>	Schematic representation showing the different nano-structural morphologies of nanofibrillar cellulose (a) and its conjugate with collagen inspired ionic complementary peptides as associated via non-covalent interactions (b) the conjugate hydrogel scaffold can serve as superior matrix to promote cellular adhesion reflecting the higher cell population	212
<b>Figure 6.2</b>	Schematic representation of chemical conversion and functionalization of hardwood cellulose into nanofibrous cellulose via TEMPO oxidation	213
<b>Figure 6.3</b>	Characterization of nanofibrillar cellulose (NFC); (a) Assessment of carboxylate content of the nanofibrillar cellulose prepared from the TEMPO mediated oxidation. (b) FTIR spectra of TEMPO oxidized cellulose and (c) Atomic Force Microscopy (AFM) images showed fibers like structure. Scale bar 2 $\mu\text{m}$	214
<b>Figure 6.4</b>	Schematic representation of the stepwise hydrogelation methodology of cellulose peptide conjugate hydrogels	215
<b>Figure 6.5</b>	Scanning electron micrograph images of NFC (a) and 5:1 cellulose peptide conjugate hydrogel (b & c) showing the porous nature of material. Scale bar 50 $\mu\text{m}$ . Image inset shows the	217

contact angle measurement. Histogram developed from the pore distribution in the (d) NFC, (e) NFC + NapFFGKO, and (f) NFC + (NapFFGKO + NapFFGDO) hydrogels, representing the amount of pore distributed in the samples

- Figure 6.6** Small angle x-ray scattering profile of cellulose peptide conjugate hydrogels; (a) SAXS data profile displaying double logarithmic intensity versus Q plot for NFC (black) and NFC-peptide conjugate (red and blue) hydrogels. (b) Pair-distance distribution function (PDDF) plot for NFC and NFC-peptide conjugate hydrogel obtained through IFT 218
- Figure 6.7** Guinier plot analysis for (a) NFC, (b)NFC+NapFFGKO and (c) NFC +(NapFFGKO+NapFFGDO) 220
- Figure 6.8** In-silico modelling of the cellulose peptide conjugate hydrogels (a) Scattering shape of NFC hydrogels restored from dummy atom modelling (DAMMIF). SAXS envelop of NFC and their overlay with the conjugated models, (b)NFC+NapFFGKO and (c)NFC+ (NapFFGKO+NapFFGDO). 221
- Figure 6.9** Mechanical strength analysis: (a) frequency sweep performed for the cellulose peptide conjugate hydrogels at different mixing ratios. (b) Comparison of mechanical strength of conjugate hydrogels at different ratio 222
- Figure 6.10** Biocompatibility studies of cellulose-peptide conjugate hydrogels on (a) fibroblast cells (L929) and (c) neural cells (SH-SY5Y) at concentration ranging from 100µg/ml to 1000 µg/ml. Bright field images of (b) L929 and (d) SH-SY5Y cells respectively after 48hrs of incubation with the NFC and NFC peptide conjugate hydrogels at 500 µg/ml concentration along with the control. Scale bar 100 µm 223
- Figure 6.11** Cellular adhesion (2D) study of L929 cells on cellulose-peptide conjugate hydrogels. Assessment of cellular adhesion and proliferation on conjugate hydrogels by Live/Dead staining. 224

Images of cells after fluorescence staining showing cellular adhesion on (a to c) NFC, (d to f) NFC+NapFFGKO, (g to i) NFC+ (NapFFGKO+NapFFGDO) after 48 hrs, 72 hrs and 120 hrs respectively. Scale bar 100  $\mu$ m

**Figure 6.12** Cellular adhesion (2D) study of SH-SY5Y cells on cellulose- 225

peptide conjugate hydrogels. Assessment of cellular adhesion and proliferation on conjugate hydrogels by Live/Dead staining. Images of cells after fluorescence staining showing cellular adhesion on (a to c) NFC, (d to f) NFC+NapFFGKO, (g to i) NFC+ (NapFFGKO+NapFFGDO) after 48 hrs, 72 hrs and 120 hrs respectively. Scale bar 100  $\mu$ m

**Figure 6.13** Evaluation of cellular viability and proliferation via Alamar 226

assay on (a) fibroblast cells (L929) and (b) neural cells (SH-SY5Y) with conjugate hydrogels at 5:1 (NFC:peptide) concentration at different time point. All data presented as mean  $\pm$  SD. \* represents P-value  $\leq$  0.05 \*\* P-value  $\leq$  0.01, \*\*\* P-value  $\leq$  0.001 and \*\*\*\* P-value  $\leq$  0.0001 (Two-way ANOVA, Bonferroni's multiple comparisons tests)

**Figure 6.14** Cytoskeletal analysis in L929 cells in 2D cell culture on NFC 228

and peptide conjugated NFC. Staining of F-actin microfilaments with Rhodamine Phalloidin in L929 cells cultured on control coverslips (a-c), (d-f) Nanofibrillar cellulose, (g-i) NFC + NapFFGKO, and (j-l) NFC + (NapFFGKO+NapFFGDO) at different time point 48 hrs, 72 hrs, and 120 hrs of cell culture, respectively. Scale bar is 10 $\mu$ m

**Figure 6.15** Quantification of (a) cell spreading area and (b) cell shape index 228

of fibroblast (L929) cells on uncoated control and hydrogel coated coverslips

**Figure 6.16** Expression of neural marker  $\beta$ -III tubulin in SH-SY5Y cells in 230

2D cell culture. Immunofluorescent staining of  $\beta$ -III tubulin in SH-SY5Y cells cultured on control coverslips (a-c), (d-f)

	Nanofibrillar cellulose, (g-i) NFC + NapFFGKO, and (j-l) NFC + (NapFFGKO+NapFFGDO) at different time point 48 hrs, 72 hrs, and 120 hrs of cell culture, respectively. Scale bar is 10 $\mu$ m	
<b>Figure 6.17</b>	Quantification of (a) cell spreading area and (b) cell shape index of neural (SH-SY5Y) cells on uncoated control and hydrogel coated coverslips	230
<b>Figure 6.18</b>	Scratch assay to analyze the cellular migration of L929 cells in presence of nanofibrillar cellulose and peptide conjugated cellulose. (a) Scratch closure with the treatment of all the hydrogels as well as the untreated control at different time point; 0 hrs, 12 hrs, and 24 hrs. Scale bar is 400 $\mu$ m. (b) Quantification of the wound closure with time i.e., after 12 hrs and 24 hrs	232
<b>Figure 6.19</b>	Scratch assay to analyze the cellular migration of SH-SY5Y cells in presence of nanofibrillar cellulose and peptide conjugated cellulose. (a) Scratch closure with the treatment of all the hydrogels as well as the untreated control at different time point; 0 hrs, 12 hrs, and 24 hrs. Scale bar is 400 $\mu$ m. (b) Quantification of the wound closure with time i.e., after 12 hrs and 24 hrs	233
<b>Figure 6.20</b>	FACS analysis of L929 (a-d) and SH-SY5Y (e-h) cell lines. Live-dead population were identified by staining the cells with FDA and PI. Quadrant Q1 and Q3 indicates the percentage of live and dead cells respectively	234
<b>Figure 7.1</b>	Schematic representation of the encapsulated peptide nanoparticle synthesis via nanoprecipitation and structural transition of the peptide nanoparticles via pH switch from pH 7.0 to 8.5, leading to the transformation of nanosphere to nanofibers, releasing the FA	245
<b>Figure 7.2</b>	Collagen inspired peptide, NapFFGKO at physiological pH showed the formation of sheet like structure at sub micromolar concentration (200 $\mu$ M) as depicted by AFM studies	247

<b>Figure 7.3</b>	Schematic representation of the synthesis methodology of peptide-based nanoparticle via nanoprecipitation for the encapsulation of hydrophobic drug molecules (ferulic acid)	248
<b>Figure 7.4</b>	Characterization of the ferulic acid encapsulated peptide nanoparticles (FA-NPs): (a) DLS study of the nanoparticles at physiological pH, (b) Hydrodynamic radii and polydispersity index of the synthesized nanoparticles confirmed the stability over a time period of 36 hours. Stability assessment of nanoparticles in presence of culture medium (c) nutrient broth for bacterial culture, (d) DMEM for mammalian cell culture studies	249
<b>Figure 7.5</b>	(a) Surface charge of the peptide nanoparticles via zeta potential ( $\zeta$ ) measurement showing the positive charge on the surface of the nanoparticles at physiological pH. (b) AFM image of the nanoparticles showing the particle size in the range of 40-50 nm. Scale bar 1.0 $\mu$ m	250
<b>Figure 7.6</b>	Structural transition of the nanoparticles: (a) nanoparticle size distribution at physiological pH 7.0 and at slightly basic pH, 8.5, showed the drastic change in the size of the nanoparticles, (b) time dependent size analysis at a due course of 6 hours, (c) AFM of the peptide nanofibers as converted from spherical nanoparticles under pH stimuli (at pH 8.5) after 6 hours. Scale bar 1.0 $\mu$ m	251
<b>Figure 7.7</b>	Time dependent structural transition of the nanoparticles upon switching the pH of the aqueous medium from neutral (7.0) to basic (pH 8.5) via AFM studies. Scale bar 500 nm	252
<b>Figure 7.8</b>	(a) Acid-base titration curve to determine the equivalence point and the pKa value of the positively charged collagen inspired peptide, (b) FTIR spectra of the nanoparticles and peptide nanofibers	254

- Figure 7.9** Absorbance of nanoparticles: (a) UV-Vis spectra of the nanoparticles at pH 7.0 (black) and at pH 8.5 (red), respectively. The spectra at pH8.5 shows the presence of the characteristic peaks of ferulic acid, indicating the release of the encapsulated ferulic acid at pH 8.5. (b) UV-Vis spectra of the ferulic acid at different concentrations to make standard curve for the determination of the encapsulation efficiency. (c) Standard curve drawn from the respective absorbance obtained at 215 nm for determining the loading capacity of the peptide nanoparticles. (d) Cumulative release percentage of ferulic acid from the nanoparticles at weakly basic pH (8.5) 255
- Figure 7.10** Antimicrobial assay: (a) Determination of minimum inhibition concentration (MIC) against *E. coli* (gram -ve) and *S. aureus* (gram +ve) strains and (b) the respective colony forming unit (cfu) of both bacterial strains and their microscopic views at different concentrations of released FA, i.e., 750 µg/mL and 900 µg/mL. Scale bar 50 µm 257
- Figure 7.11** Live-Dead assay via CLSM, panel 1: live cells (stained with SYTO 9), panel 2: dead cells (stained with PI). Panel 3: merged population (stained with SYTO 9/PI). (a-c) control *E. coli* cells (untreated), (d-f) cells exposed to FA-NPs at 750 µg/mL, (g-i) cells exposed to FA-NPs at 900 µg/mL. (j-l) control *S. aureus* cells (untreated), (m-o) cells exposed to FA-NPs at 750 µg/mL, (p-r) cells exposed to FA-NPs at 900 µg/mL. Scale bar 10 µm 258
- Figure 7.12** Live-Dead assay via FACS (Quadrant 1: live cells, Quadrant 2: doubled stained cells, Quadrant 3: dead cells, Quadrant 4: unstained cells): (a-c) *E. coli* cells exposed to the different concentrations of nanoparticles with control cells. (d-f) *S. aureus* 259

cells exposed to the different concentrations of the nanoparticles with control cells i.e., 750  $\mu\text{g}/\text{mL}$  and 900  $\mu\text{g}/\text{mL}$

- Figure 7.13** Mechanism of antimicrobial property: (a) DCFH-DA assay to determine the ROS production via relative fluorescence intensity. (b) Malondialdehyde assay to determine the lipid peroxidation leading to the cell membrane disruption 260
- Figure 7.14** Field Emission Scanning Electron Microscopic (FE-SEM) images of the control bacteria cells (a, d) showing intact cellular membrane. Bacterial cells at 750  $\mu\text{g mL}^{-1}$  treatment showed stressed population (b, e) and at 900  $\mu\text{g mL}^{-1}$  FA-NPs showed damaged cell membrane (c, f). Scale bar 1  $\mu\text{m}$  262
- Figure 7.15** Cellular viability of the nanoparticles with fibroblast cells; (a) Biocompatibility studies to compare the effect of FA-NPs and released ferulic acid. (b) Bright field images of L929 cells with FA-NPs and (c) Bright field images of L929 cells with released ferulic acid at 900  $\mu\text{g}/\text{mL}$ . Scale bar 100  $\mu\text{m}$  263
- Figure 7.16** Scratch wound assay to analyze the migration ability of the fibroblast cells in presence of peptide nanofibers; (a) Scratch closure with the treatment at different time points. Scale bar 400  $\mu\text{m}$ . (b) Quantification of the wound closure with time i.e., after 12 hours and 24 hours 264

## List of Tables

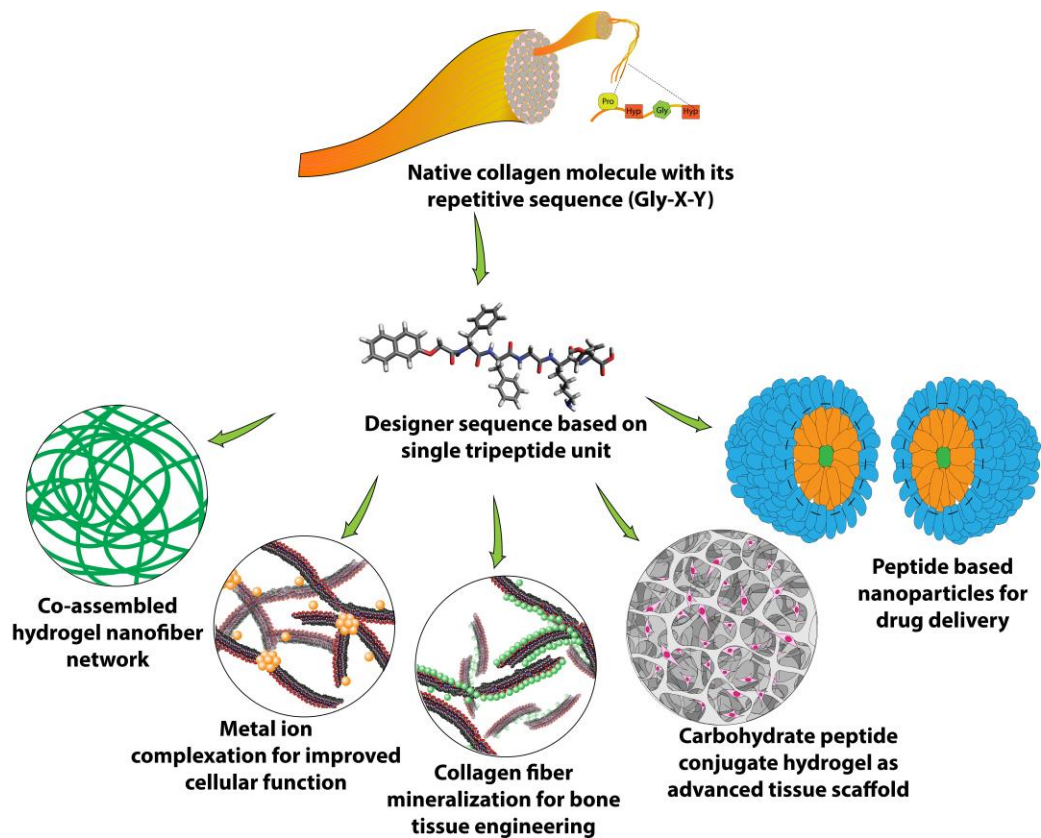
<b>Table no.</b>	<b>Caption</b>	<b>Page no.</b>
<b>Table 2.1</b>	Description of cell lines with their culture medium and source of origin.	76
<b>Table 3.1</b>	Minimum gelation concentration (MGC) of the collagen inspired peptides	105
<b>Table 3.2</b>	Fiber dimensions of collagen mimetic peptide hydrogels observed by Transmission electron microscopy (TEM) and Atomic Force Microscopy (AFM), were calculated by ImageJ software	107
<b>Table 4.1</b>	Optical images of peptide hydrogels formed in presence of metal ions, Ca <sup>2+</sup> and Mg <sup>2+</sup>	134
<b>Table 4.2</b>	The values of cell shape index (CSI) and area covered by fibroblast cells on control peptide scaffold as well as metal ions coordinated peptide scaffold as determined by F-actin staining (after 72 hours of incubation)	155
<b>Table 4.3</b>	The values of cell shape index (CSI) and area covered by glioma cells on control peptide scaffold as well as metal ion coordinated peptide scaffold as determined by $\beta$ -III tubulin staining (after 72 hours of incubation)	157
<b>Table 5.1</b>	Investigation of the biophysical properties of the control peptide and mineralized peptide scaffolds calculated via model dependent and model independent methods to obtain the Rg value	186
<b>Table 5.2</b>	Structural analysis (pore diameter, pore volume, surface area) of the mineralized nanofibers obtained using BET isotherm	189
<b>Table 5.3</b>	The value of CSI and area covered by the 7F2 and Saos-2 cells in control and in the mineralized peptide after F-actin staining	198
<b>Table 6.1</b>	Contact angle measurement of nanocellulose (NFC) and peptide conjugated nanocellulose hydrogels	217

<b>Table 6.2</b>	Biophysical properties of NFC and NFC-peptide conjugated hydrogels; both model dependent and model independent methods were used to calculate $R_g$	219
<b>Table 6.3</b>	Maximum particle dimensions used for IFT techniques for NFC and NFC peptide conjugate gels	219
<b>Table 6.4</b>	Table on CSI plot and area covered by fibroblast cells in F-actin staining	229
<b>Table 6.5</b>	Table on CSI plot and area covered by neuronal cells in $\beta$ -III tubulin staining	231

# **Chapter 1**

## **Introduction**





**Designing novel short self-assembling peptide amphiphiles inspired from native ECM derived collagen triple helix to fabricate diverse nanoscale structure to access diverse functions for wide range of biomedical applications, like drug delivery, antimicrobials as well as advanced tissue scaffolds.**



## 1. Introduction

*“I would like to describe a field, in which little has been done, but in which an enormous amount can be done in principle. This field is not quite the same as the others in that it will not tell us much of fundamental physics, but it is more like solid-state physics in the sense that it might tell us much of great interest about the strange phenomena that occur in complex situations.”*

*-Richard Feynman*

In 1959, Richard Feynman gave a classic talk entitled “*There is Plenty of Room at the bottom*” in an Annual meeting of American Physical Society at Caltech and the transcript was published in Caltech’s Engineering and Science.

Over the last two decades, the world has witnessed a tremendous advancement in the nanotechnology brings hope for the improvement in the field of healthcare and medicines.<sup>1,2</sup> The current healthcare system is facing a huge challenge in the form of tissue injuries and degenerative disorders. The development of innovative functional treatments that may effectively repair and functionally regenerate tissue after injury or degeneration is becoming increasingly important.<sup>3, 4</sup> Tissue grafts (autografts, allografts, and xenografts) are commonly employed in this approach and are usually regarded the gold standard in clinical research.<sup>5</sup> However, their restricted availability, negative immunological responses, poor biological response, and insufficient stability have long cast doubt on their suitability for sophisticated biomedical applications. These limitations have initiated the new discoveries that paved the way for the evolution of the contemporary study of "Biomaterials Science." The area of biomaterials research has progressed from the early 1970s, with the usage of "inert" and non-interactive materials to the current concept of producing cell instructive scaffolds that may drive live tissue regeneration by modifying cellular pathways at the molecular level.<sup>6, 7</sup> A wide range of materials have been invented towards the creation of sophisticated tissue mimics in this unique branch of science. Because of their inherent abundance in the native extracellular matrix (ECM), peptides and sugars are receiving emerging attention as they offer of attractive prospects in the field of biomaterial creation. They also fit perfectly into the contemporary frontier of biomaterial design, which is founded on the revolutionary idea of biomimicry. Advancement in field of tissue engineering inspires the use of close mimic of biological macromolecules to produce highly complex

extracellular matrix composition and architecture similar to that of native ECM.<sup>8-10</sup> The success of these synthetic biomaterials relies on the fact that it should match the necessary requirements of providing bioactive signals to modify cellular activity and aid tissue regeneration. It is also well documented that mechanical properties, such as matrix stiffness, topography, and porosity can significantly influence important cellular processes like adhesion, growth, proliferation, migration, and differentiation through sending necessary biophysical cues to the cells. Thus, effective repair and regeneration need a recapitulation of the native tissue's biophysical features. Because of the biocompatibility, biodegradability, and flexibility to achieve desired tunable modifications, the construction of cell instructive scaffolds from these bioactive peptides inspired from the natural ECM might be an attractive approach to develop advanced strategy in tissue regeneration. Furthermore, peptide possess inherent bio-functionality, which results in more biocompatibility in comparison to the synthetic polymeric scaffolds.<sup>11-14</sup> The peptide-based biomaterials can therefore offer important biological signals to control cellular destiny and functions and thus represents themselves as more appropriate biomaterial. These bioactive peptides with functional epitopes may self-assemble at physiological pH to produce a variety of supramolecular structures to stimulate several important biological pathways that govern cellular activity. Furthermore, a diverse functionality of the amino acids constituting the peptide backbone allows the production of a wide range of physicochemical responsive materials in order to manufacture ECM-mimetic hierarchically structured complex biomaterials from these monomeric units.<sup>15, 16</sup> Furthermore, exploration of bio-inspired sugar-peptide interactions to produce biomolecular scaffolds is another emerging method in this field, which has a lot of potential in the creation of next-generation biomaterials. Such multiscale assembly is expected to fabricate advanced functional material to solve various healthcare issues.

In this thesis, we have tried to explore molecular self-assembly of a collagen inspired pentapeptide to produce differential nanostructures that offer different biomedical applications. In principle, the newly developed biomaterials work by exploring the minimalistic design principle along with the bioinspired approach towards mimicking the complexity of the native ECM, which may offer significant translational potential in future.

## 1.1 Molecular self-assembly

Molecular self-assembly is the spontaneous arrangement of molecules into stable, structurally well-defined aggregates through non-covalent bonding and under equilibrium conditions.<sup>17</sup> The field of molecular self-assembly has captured tremendous attention in the broad area of material science as a bottom up approach as it provides the facile production of materials from simple building blocks with tailored properties and performances.<sup>18, 19</sup> A multitude of diverse functional nanostructures generated by this elegant molecular self-assembly strategy are common in nature.<sup>20, 21</sup> The relevance of molecular complementarity and compatibility in the construction of these spontaneous self-assembled structures is also reflected in the development of suitable functional biomaterial. Over the years of molecular selection and evolution, Nature has mastered the skill of selecting chemically compatible and structurally sustainable ingredients for molecule self-assembly.<sup>22-24</sup> These self-assembled structures are necessary for life because they ensure the precise operational activities of each and every live cell in biology.

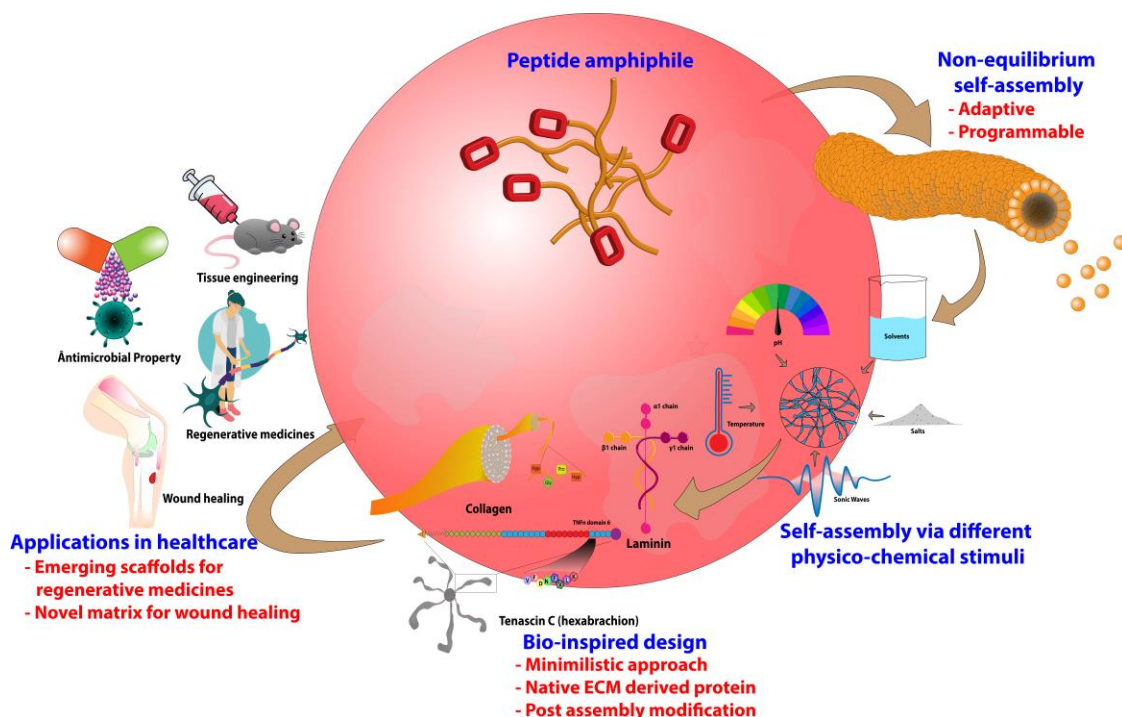


**Figure 1.1** World of peptide amphiphile with their potential applications in the field of biomedicine and healthcare.

Complex structures created by molecular self-assembly include lipid bilayers and vesicles as barriers or containers for subcellular organelles, highly organized polymeric

nucleic acids (DNA) as genetic information carriers, 3D polypeptides and proteins as ion pumps, cytoskeleton, and action executors.<sup>25, 26</sup> The functions of these macromolecules are determined by the arrangement of their primary building blocks at nanometer scale. Through these unique architectural wonders of biological world, Nature inspires us to design, produce, and manufacture superior and useful biomaterials by employing the fundamental knowledge acquired from its native molecular structural arrangements.

As described, molecular self-assembly is inherent in biological world and can be seen in several of the biological processes: microtubule formation, cytoplasmic membrane, DNA double helix formation, multicomponent protein molecule.<sup>27, 28</sup> All these macromolecules are in their self-assembled state, where in case of microtubule formation, polymerization of two globular proteins (alpha and beta tubulin) occurs to form protofilament leading to the formation of hollow tube-like structure called microtubule.<sup>29</sup> Similarly, well-ordered arrangement of the polar head molecules in the phospholipid bilayer and the nonpolar ends of the fatty acid chains leads to the formation of plasma membrane. Its stability is mostly due to the hydrophobic contact. This membrane is stable enough to act as a barrier to the transit of water-soluble ions ( $\text{Na}^+$ ,  $\text{K}^+$ , and  $\text{Ca}^{2+}$ ) and molecules to carry out crucial life processes. More importantly, DNA is another important self-assembled structure. This configuration of the building blocks induces non-covalent interactions such as hydrogen bonding and  $\pi$ - $\pi$  interactions between its nucleotide base pairs.<sup>30, 31</sup> The nucleotide is a monomeric unit of DNA that consists of a 5-carbon sugar (deoxyribose), and nitrogen-containing base (adenine (A), cytosine (C), guanine (G), and thymine (T), and a phosphate group connected to the sugar. To this direction, proteins present a classic illustration of the unique creation of the self-assembly process with utmost precision through specific spatiotemporal control. Protein folding, a self-assembly process that includes noncovalent interactions in the peptide sequence of proteins in water solution, produces the final protein structure in its native form.<sup>32, 33</sup> The main structure of a protein is a polypeptide sequence (primary structure) made up of 20 amino acids that connect via hydrogen bonding to generate secondary structure, such as  $\alpha$ -helices or  $\beta$ -sheets. Secondary structures further interact through H-bonding, hydrophobic interactions to develop tertiary structure and further hierarchical arrangement of the subunits leads to the formation of quaternary structure of protein molecule. Since last two decades, many research group focused on

the design and development of synthetic biomaterials using these small building blocks, inspired from natural biomacromolecules.

## **1.2 Native extracellular matrix- an inspiration for advanced material**

The extracellular matrix (ECM) functions as a natural biological framework, providing numerous structural and biochemical signals to the cells for optimal organ function.<sup>34</sup> The ECM is known to play important role in cell adhesion, proliferation, differentiation, morphogenesis, and tissue regeneration following damage.<sup>35, 36</sup> ECM interacts with cells through a variety of proteins and glycosaminoglycans, and these interactions are very important for maintaining the tissue's normal physiological condition.<sup>37-39</sup> Native ECM is made up of structural proteins (collagen, elastin), functional proteins (laminin, fibronectin, tenascins), glycoproteins, proteoglycans, and glycosaminoglycans, and different glycoproteins, proteoglycans, and glycosaminoglycans etc.<sup>36, 40-42</sup> Furthermore, depending on the physiological requirements of the organ, the composition and mechanical characteristics of the ECM vary dramatically across the body.<sup>40</sup> Native ECM also serves as a reservoir for the growth factors and signaling molecules, preserving their bioactivity while effectively displaying these functional cues to cell surface receptors for synergistic binding.<sup>43, 44</sup> Importantly, collagen has been identified as the most prevalent structural protein in the ECM, and it gives the tissue tensile strength, governs cell adhesion, and regulates migration.<sup>40, 42</sup> Stromal fibroblasts produce the majority of interstitial collagen.<sup>45</sup>

Collagens self-assemble into unique supramolecular structures in vivo, which are responsible for extracellular matrix' structure and function.<sup>46</sup> The collagen triple helix, which has a repeating unit (Gly-X-Y)<sub>n</sub> structure with X and Y being proline and hydroxyproline respectively, distinguishes the domains of the collagen molecule.<sup>47, 48</sup> Collagen is well recognized as the most abundant protein in ECM, which provides tensile strength in vertebrate tissues including tendon, cartilage, bone, and skin, where it is found as elongated fibrils.<sup>49</sup> Collagen also acts as a biochemical cue towards influencing morphogenesis and tissue development in vivo by regulating cellular adhesion, proliferation, chemotaxis, and migration.<sup>50</sup> Collagen has traditionally been a popular biomaterial for the production of tissue scaffolds since it is an essential component of the ECM in terms of its role in maintaining the structure and function. To this direction, another protein, elastin has also received attention as it was found to

be an integral part of the extracellular matrix and found in soft elastic tissues, such as skin, lungs, ligament, and blood vessels.<sup>51</sup> Other crucial members of natural ECM protein family constitutes fibronectin, proteoglycans, glycosaminoglycans (GAGs), hyaluronan (HA) etc.<sup>52-54</sup>

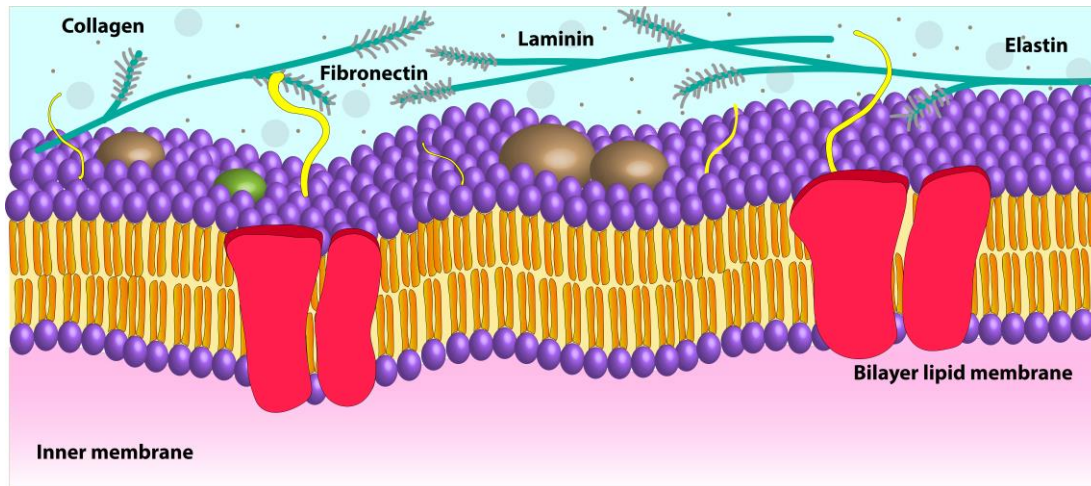


**Figure 1.2** Schematic representation of extracellular matrix with various component required for cellular attachment and growth.

Fibronectins are known to interact with high molecular weight proteins to provide structural and functional integrity to modulate cellular adhesion, growth, and proliferation.<sup>55, 56</sup> Several of the proteoglycans act as biological glue for maintaining the interaction among different macromolecules.<sup>57</sup> They are also known to have a function in morphogen gradient production during developmental processes including morphogenesis and tissue regeneration.<sup>42</sup> Dermatan and chondroitin sulfate-containing proteoglycans are predominant in the extracellular matrix, where they are involved in providing viscoelastic characteristics, water retention, and maintaining osmotic pressure.<sup>58</sup> Complex ECMs of cartilage, intervertebral discs, brain, tendons, and corneas include these proteoglycans as important structural elements. GAGs are negatively charged polysaccharides that are linear and sulfated. They are split into two types: sulfated GAGs, which include chondroitin sulphate (CS), dermatan sulphate (DS), keratan sulphate (KS), heparin, and heparan sulphate (HS), and non-sulfated GAGs, which include hyaluronan.<sup>58</sup> All these biomacromolecules have been extensively studied for their ability to function as synthetic scaffold for tissue regeneration.<sup>59-61</sup>

### 1.3 Peptide-based self-assembled systems- A minimalistic approach to mimic natural macromolecules

Peptides-based self-assembled systems offer a number of benefits over other physiologically relevant counter components, which makes them a good candidate for acting as building blocks for fabrication of ordered nanomaterials targeted for biomedical and nanotechnological applications.<sup>62, 63</sup> Amino acids are the fundamental building blocks of peptides. Interestingly, a wide variation in property can be attained in the new biomaterials via chemical diversity of the peptide chains, biomolecular chirality, and ionization ability of the building blocks (amino acids). In particular, 20 natural amino acids provide the necessary chemical diversity to the peptide chain while the stereoisomers provide the required chirality to the peptide chain and further, the charged amino acids (Asp, Glu, Lys, Arg, Ser, Cys) provide the ionizable functionality to the peptide chain. Peptide self-assembled systems are mainly stabilized via non-covalent interactions, which make them easy to fabricate and also tunable.

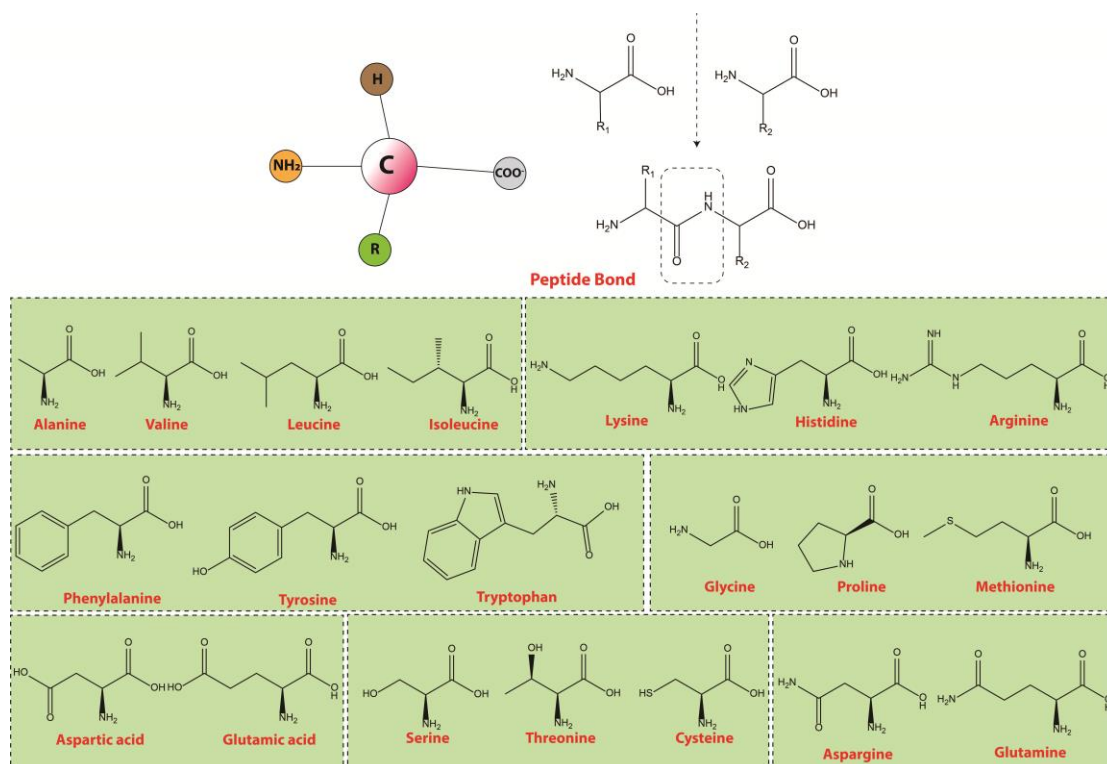


**Figure 1.3** Structural representation of 20 amino acids with variable side chain and schematic representation of the peptide bond formation among them.

These benefits have made them appealing candidates for drug delivery, tissue engineering, diagnostics, biosensing, and drug development applications.<sup>64-66</sup> Short bioactive peptides have been discovered to self-assemble into ordered nanostructures such as nanospheres, nanotubes, nanosheets, micelles, and fibrillar gels in recent years, making this field even more active and exciting.<sup>67-70</sup>

### 1.3.1 Non-covalent interactions driving the peptide self-assembly

The development of ordered nanostructures is aided by the synergistic impact of non-covalent interactions between the designed molecules during the self-assembly process.<sup>21</sup> These non-covalent interactions serve an important role in determining the structure that is thermodynamically stable. To comprehend and manage peptide self-assembly, we must first understand the several types of non-covalent interactions involved in the process, such as H-bond,  $\pi$ - $\pi$  stacking, electrostatic, hydrophobic, and van der Waals interactions.

#### 1.3.1.1 Hydrogen bonding

Hydrogen bond involves the interaction between a donor oxygen atom and an acceptor hydrogen molecule, which is weaker than ionic or covalent bond but stronger than van der Waals forces.<sup>71</sup> The approximate strength of a hydrogen bond is around 10-40 kJ mol<sup>-1</sup> at room temperature.<sup>72</sup> In case of peptide, hydrogen bond occurs between the amide of one peptide chain with the amine or carboxyl group of the adjacent peptide chain.

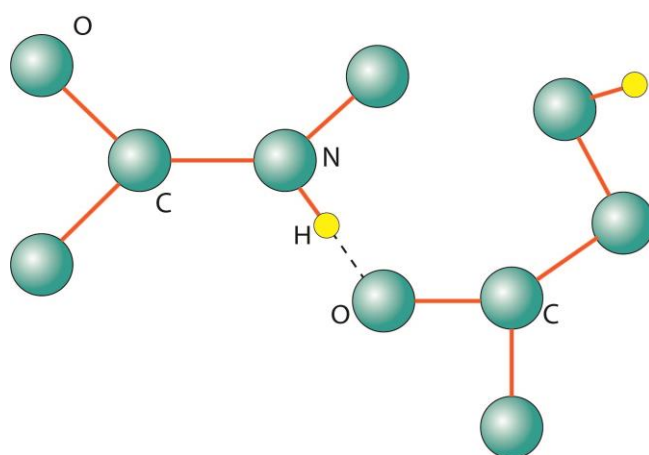


**Figure 1.4** Schematic representation of hydrogen bonding in amino acids, resulting in the formation of peptide bond.

Hydrogen bond is an important driving force for the production of peptide architectures, and plays a crucial role in the folding and stabilization process of the peptide's secondary structure.<sup>72</sup> The interaction is totally dependent on the geometry and the distance between the interacting molecule in stabilizing the secondary structures of the proteins/short peptides, which provides the directionality and structural support in the formation of peptide nanostructures.<sup>73</sup> The H-bond interaction is different among the different secondary structures of the proteins and the interactions among the amino acids are the major forces driving the formation of different secondary structures. Moreover, the selectivity and directionality govern the conversion of short peptide into 1D, 2D, and 3D nanostructures.<sup>74, 75</sup>

### ***1.3.1.2 Hydrophobic interactions***

Hydrophobic interactions are the well-established driving force in the peptide self-assembled systems. A dominant hydrophobic interaction among the short peptide monomers leads to the formation of micellar like structures, while the dominant hydrogen bonding leads to the aggregated amyloid like structures.<sup>76</sup> The monomeric units of peptide amphiphiles are unable to interact constructively with water molecules at lower concentration.<sup>77</sup> However, as the amphiphile concentration increases, the hydrophobic part of the molecule undergoes aggregation to minimize the contact with water molecule and exposed hydrophilic moieties at the surface.<sup>78</sup> The hydrophobic interactions in peptide amphiphiles can be modulated by incorporating aryl or acyl group in the peptide chain. In the well-known amyloidogenic diphenylalanine (Fmoc-FF) sequence the aromatic moieties play a crucial role through hydrophobic or  $\pi$ - $\pi$  interactions in stabilizing the peptide nanostructure.<sup>79</sup> Hydrophobic interactions generally lead to the disordered organization of the peptide amphiphiles, while  $\pi$ - $\pi$  interaction or cation- $\pi$  interactions lead to the formation of well-ordered and organized structures.<sup>80, 81</sup>

### ***1.3.1.3 $\pi$ - $\pi$ interactions***

The directional peptide growth induced via ordered  $\pi$ - $\pi$  stacking among the aromatic amino acids (phenylalanine or tyrosine) drives the self-assembly among short peptides.<sup>82</sup> Due to the robust nature of  $\pi$ - $\pi$  stacking, limited solubility and degradability was observed in aqueous environment. The strong nature of  $\pi$ - $\pi$  interaction induces the directional growth of the self-assembled structure.<sup>83</sup> The  $\pi$ - $\pi$  interaction among the

aromatic moieties originate from the quadrupole-quadrupole interactions between delocalized electrons in the p-orbitals.<sup>84</sup> Nowadays, the significance of these interactions can be seen in the case of aromatic group capped peptide amphiphiles, where  $\pi$ - $\pi$  stacking interactions, in conjunction with H-bonding interactions, drive the self-assembly of these minimalist peptide building blocks to produce a variety of supramolecular structures.<sup>85</sup> Furthermore, adding a cationic residue at the N-terminus and an aromatic residue at the C-terminus to a collagen-related peptide can cause "head-to-tail" assembly.<sup>86,87</sup> Similar to  $\pi$ - $\pi$  interactions in peptide self-assembly, such cation- $\pi$  interactions can promote the self-assembly of collagen triple helices into higher-order structures.<sup>88, 89</sup> Furthermore, the strength of the aforementioned non-covalent interactions is extremely sensitive to the self-environmental assembly's conditions. For example, the strength of ionic interactions is affected by the solvent's dielectric constant and the presence of a counter ion.<sup>90,91</sup>

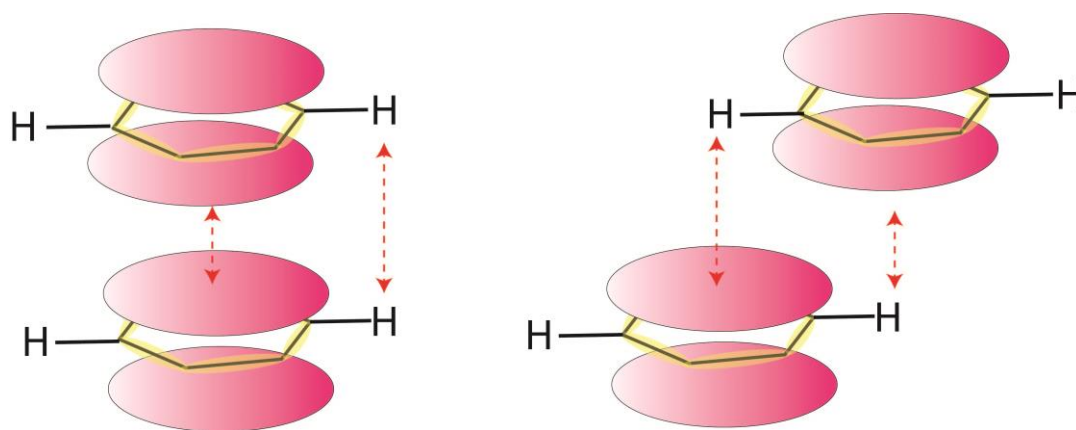


**Figure 1.5** Schematic representation of  $\pi$ - $\pi$  interaction among the aromatic moieties stabilizing the peptide nanostructures.

#### **1.3.1.4 Electrostatic interactions**

Another prevalent intermolecular interaction presents in the peptide self-assembly is the electrostatic interactions, which is one of the key players towards stabilizing the nanoscale architecture. Electrostatic interactions are coulombic interactions between oppositely charged ions that result in the formation of ion pairs. The dielectric solvent and the presence of mobile ions influence the strength of an ionic bond. The strength of an ionic bond lies in the range of  $500 \text{ kJ mol}^{-1}$  comparatively much higher than H-bond.<sup>92</sup> The stronger ionic interaction also have longer range than hydrogen bond, but the ionic interaction at longer range are weaker than hydrogen bond.<sup>93</sup> These

interactions are strongly dependent on the dielectric constant of the solvent.<sup>83</sup> In contrast to hydrogen bonding and hydrophobic interactions, these interactions play an important role in providing structural specificity to charged peptides.<sup>72</sup> pH responsive biomaterial can be generated by employing the ionic interaction among charged peptide monomers. The significance of various electrostatic interactions in the formation of peptide nanostructures has been critically examined.<sup>93, 94</sup> Ionic interactions have been studied widely in peptide self-assembly, which leads to the formation of hierarchical structure of the native protein molecule. O'Leary et.al., designed two charge complementary peptides that form salt-bridge hydrogen bond between lysine and aspartate to stabilize the triple helix in a sticky ended assembly of collagen mimetic peptide.<sup>95</sup> The salt bridge interaction among charged peptides transformed into nanofibers with characteristic triple helical packing, which later combined to form hydrogel.<sup>95</sup> Recently, our group has reported a short ionic complementary sequence, which can self-assemble at wide pH range.<sup>96</sup> The short ionic complementary peptides generates tunable hydrogels with differential biological activities.

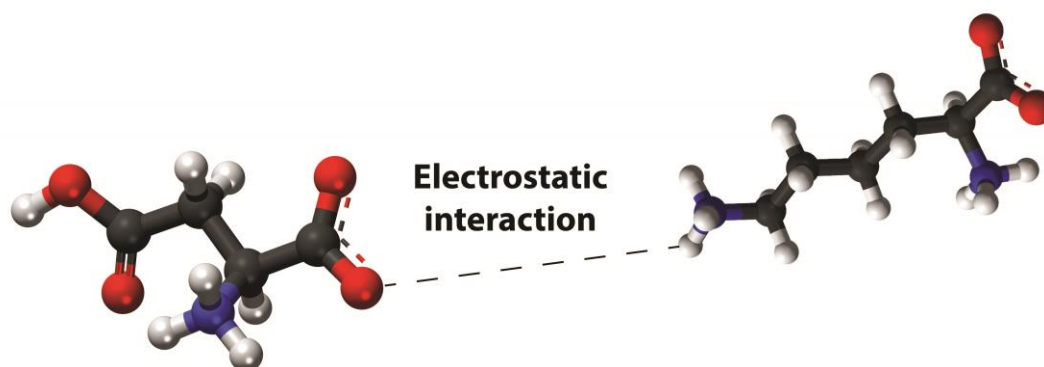


**Figure 1.6** Schematic representation of electrostatic interaction among the oppositely charge amino acids stabilizing the self-assembled nano-structure.

#### ***1.3.1.5 van der Waal interactions***

van der Waal interaction is non-selective, non-directional, non-additive and is also of comparable strength to hydrogen bond (5kJ).<sup>93</sup> In a peptide based self-assembled system, van der Waal force represents the main contributing force between the aliphatic chain of the peptide amphiphiles.<sup>97</sup> These interactions are caused by fluctuations in the electron distributions of the two closely spaced molecules and are classified as instantaneous electrostatic interactions. There are only few reports in the literature,

suggesting van der Waal as the major force for stabilization of the self-assembled structures.<sup>98, 99</sup>

Moreover, the bond strength of this particular non-covalent interaction is extremely sensitive to the environmental conditions during self-assembly. For example, hydrophobic interaction gets enhanced at higher temperature whereas H-bond get weakened at higher temperature.<sup>100</sup> H-bond and  $\pi$ - $\pi$  interactions show their maximum strength in aqueous environment as compared to the organic environment. Similarly, the ionic bond strength is dependent on the dielectric constant of the solvent, presence of counter ion and also show the sensitivity towards the pH of the solution. So, by tuning the environmental conditions from increasing the solubility of peptide amphiphile (disfavoring self-assembly) to decreasing the solubility (favoring self-assembly), this variation in the strength of non-covalent interactions at different environmental conditions can be used to trigger self-assembly of peptides.<sup>101</sup> Furthermore, the overall hydrophathy index of the peptide plays a significant role in determining the peptide's proclivity to self-assemble. A highly hydrophobic peptide will precipitate in water, whereas a highly hydrophilic peptide will dissolve completely, reducing the intermolecular interaction required for self-assembly. As a result, it is critical to rationally design peptide building blocks by balancing both the hydrophobic and hydrophilic nature of the final hydrogelator, which renders most of the gelator design as amphiphilic. As previously stated, environmental conditions can also play a significant role in tuning the self-assembling proclivity of peptides by directly influencing non-covalent interactions at the molecular level, this strategy of modulating nanostructure formation by exploring different self-assembly pathways is now widely used to fabricate diverse supramolecular structures within a single gelator domain. This strategy drives the formation of the nanoscale structure that are away from equilibrium. This pathway dependent self-assembly strategy is discussed in more detail in the following section.

### **1.3.2 Peptide amphiphiles**

Self-assembling peptide amphiphiles have proven their tremendous application in the field of scaffold development for tissue engineering.<sup>102-106</sup> A peptide amphiphile is generally composed of a polar amino acid head and a non-polar hydrophobic tail, which have the ability to form  $\beta$ -sheet like structure.<sup>107</sup> The charged amino acid sequences

provide the solubility to the peptide and the hydrophobic moiety stabilizes the core of the nanostructure.<sup>108</sup> Various bioactive sequences generated from ECM proteins can also be covalently linked to the charged residues to provide bioactivity to these scaffolds. The hydrophobic interactions among the alkyl chains, as well as the development of  $\beta$ -sheet like structures, induce the self-assembly of peptide amphiphiles, resulting in the formation of high aspect ratio long nanofibers.<sup>109</sup> In a peptide amphiphile, the bio-functional motifs are present on the surface of the peptide nanofibers, which are accessible to cells for adherence and proliferation.

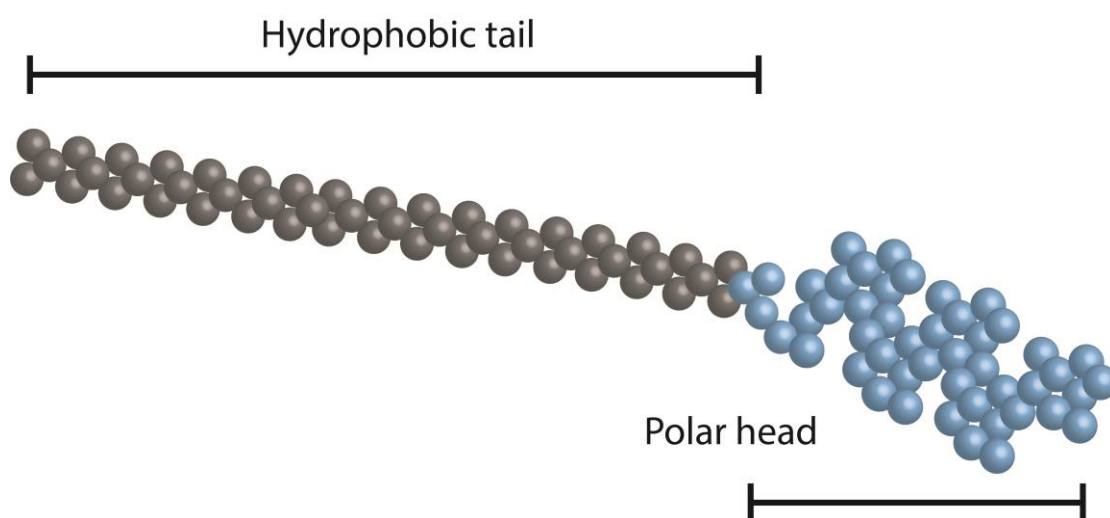


**Figure 1.7** Schematic representation of peptide amphiphile with polar head and hydrophobic tail.

These nanostructures are useful for a variety of biological applications because they have a high density of bio-functional epitopes on their surface that cells can perceive and respond to the biological signals.<sup>110,111</sup> Furthermore, these designer sequences were shown to be biocompatible and biodegradable.<sup>112,113</sup> Stupp and coworkers provided the first example of a peptide amphiphile molecule in 2001, when they used nanofibers to nucleate apatite crystals and produce hydroxyapatite.<sup>114</sup> Following this seminal work, the stupp laboratory has continued to investigate these nanostructures for a variety of biomedical applications.<sup>114,115</sup> These peptide amphiphiles were found to self-assemble into a range of nanostructures, including ribbons, twisted structures or aggregates, cylinders, and several other structures at the nanoscale. The impact of changing their molecular structure, such as alkyl chain length or  $\beta$ -sheet character was investigated to understand structure-function relationship in terms of the surface chemistry, as well as morphology, and bioactivity.<sup>116,117</sup> These peptide amphiphiles are now being explored

for their diverse applications in the field of wound healing, cancer therapy, antiangiogenic properties, drug delivery, tissue engineering etc.<sup>118-120</sup>

### **1.3.3 Aromatic peptide amphiphiles**

With the increasing demand for the fabrication of short peptide design to develop advanced tissue mimics, a new class of aromatic peptide has been evolved as a potential candidate.<sup>121</sup> These short peptide amphiphiles are composed of aromatic group attached to the N-terminal, which provides necessary hydrophobicity to the peptide for the self-assembly.<sup>122</sup> Fluorenyl methoxycarbonyl (Fmoc), naphthalene, and naphthoxyacetic acid are some of the examples which are used as the peptide modifier, which are termed as structure directing unit.<sup>123</sup> The most challenging factor of a short peptide amphiphile mimicking the nature protein is achieving the hierarchical assembly of the macromolecules. Short peptide amphiphiles fail to attain the similar structural property to the native macromolecular assemblies and could not form a stable highly complex nanoscale structure.<sup>124</sup> This might be owing to their shorter sequence length, which results in the lack of sufficient intermolecular interactions necessary for higher order structure leading to the sustained gel formation. In this context, the conjugation of hydrophobic moieties to the short bioactive peptide induces hydrogelation in the non-gelator peptides. These N-terminal modifications generally leads to the  $\pi$ - $\pi$  interactions among the aromatic groups, which further enhances the intermolecular interaction among the peptides and hence, induces the hydrogelation at physiological conditions.<sup>125</sup> These peptide hydrogels have been widely used for numerous cell culture applications because of the presence of bioactive motifs on the peptide nanofibrous structures. The capacity of aromatic group capped peptide amphiphiles to assist cellular adhesion, growth, and proliferation has been proven in the literature by several research groups.<sup>126</sup> An example of Fmoc based self-assembling peptide was reported with laminin and fibronectin sequence targeting the neural tissue engineering applications. The proposed peptide amphiphile formed hydrogel at physiological pH and were used to promote the adhesion and proliferation of neural progenitor cells at the injury site. The hydrogels were shown to be extremely biocompatible, allowing for cellular survival and tissue restoration. The relevance of developing tissue-specific bioactive scaffolds for directing cellular behaviour was clearly demonstrated by these findings. Recently, our group has reported laminin and cadherin derived bioactive sequences, which upon conjugating with the hydrophobic moiety mimics the structural and functional benefits of native

molecules.<sup>127, 128</sup> Therefore, introduction of hydrophobic moieties at the N-terminal of a bioactive peptide amphiphile produces a superior class of biomaterials with tunable physiochemical characteristics, resulting in the development of varied supramolecular structures for various applications in regenerative medicine.

### **1.3.4 Ionic complementary peptides**

Electrostatic interactions are one of the most common interactions that exists in biological systems, such as DNA-protein binding, ligand-substrate interactions etc. and are primarily responsible for providing the structural stability to the interacting molecules.<sup>129</sup> Various peptide inspired from natural proteins were designed and developed with potential ionic interacting groups. The first reported ionic peptide was inspired from Z-DNA binding protein i.e., EAK-16, which was known to undergo  $\beta$ -sheet conformation.<sup>130</sup> In a similar line, a well-known and extensively studied ionic peptide sequence RADA-16 has structural similarity with the EAK-16 peptide and forms peptide hydrogels.<sup>131</sup> The RADA-16 hydrogels have shown its neuronal attachment and differentiation ability. The ionic sequence has also been used as a carrier for anticancer drug in several studies.<sup>132</sup> Similarly, various other ionic complementary peptides (IEIK<sub>13</sub>, KLD<sub>12</sub>, FEFK) were reported to promote and enhance the cellular proliferation. They share a common structural aspect of alternating positively and negatively charged amino acid residues, which are flanked by a short spacer amino acid. These sequences may undergo spontaneous electrostatic interactions to construct hierarchical structure leading to gel formation. However, though all these ionic sequences are containing the repetitive unit of ionic complementary amino acids throughout the peptide backbone inducing stable salt bridge formation, but all of them are longer sequences, which may face synthetic challenges in large scale production. Hence, minimalistic peptides nanotechnology is an alternative approach to overcome this limitation, owing to its various advantages like ease of synthesis and purification process, which further enhances the scope of its application.

### **1.4 Stimuli responsive peptide self-assembly as controlled by self-assembly pathways**

As mentioned in the previous section, non-covalent interactions play a crucial role in the peptides self-assembly, which leads to the formation of multiscale hierarchical nano-structure. There are several reports where different environmental stimuli have

been used to modulate these non-covalent interactions and induce the self-assembly among these short peptides.<sup>21, 133, 134</sup> The proper amphiphilicity or the balance of hydrophobic and hydrophilic moieties of the peptide is required in order to induce the self-assembly among peptides to form the hydrogel. Here we attempted to discuss use of some of the most commonly used stimuli to induce hydrogelation among these short peptide amphiphiles: pH switch, metal coordination, solvent-switch, temperature, enzyme, light, sonication etc.

#### **1.4.1 pH triggered hydrogelation**

pH switch is among the most commonly used method of hydrogelation of peptide amphiphiles as this versatile methodology provide the ability to peptide to exist in different ionic forms at different pH, which induces differential solubility to the peptide at different pH.<sup>135</sup> In this method, particularly the designed peptide bearing ionizable functionality is first solubilized by gradually increasing the pH, and then the pH has been gradually decreased to achieve optimum hydrophobic-hydrophilic balance, and thus triggering self-association of the peptide molecules to form self-assembled nanostructures. As the pH rises, the carboxyl group at the C-terminus or the acidic or basic groups in the side chains of the amino acids gets deprotonated, allowing the peptide molecule to dissolve. A decrease in pH causes deprotonation, which reduces the solubility of the peptide monomers, resulting in a greater degree of intermolecular association. Using this methodology, several groups have reported the formation of self-supporting gels.<sup>135</sup> Xu and coworkers utilized this classical method to induce the self-assembly of various naphthyl conjugate short peptide amphiphiles.<sup>136</sup> Ulijn lab has also investigated pH-based gelation of various Fmoc-conjugated short peptide amphiphiles and formed self-supporting hydrogels for 3-D cell culture applications.<sup>85</sup> We have also utilized this similar approach towards fabricating supramolecular hydrogels. In particular, we have used pH-induced hydrogelation of collagen-inspired bioactive peptides. It was indeed evident that the advantages offered by this simple and elegant strategy to tune the ionic state of the peptides, make this methodology of gelation as the preferred strategy for inducing self-assembly of ionic peptides. Because the pH switch employs mineral acids and necessitates frequent vortexing and sonication to achieve uniform pH, and these physical factors are also known to have a significant impact on hydrogel properties. To this end, Adams and coworkers developed a more reliable method by utilizing the hydrolysis of glucono-d-lactone (GdL) to gluconic acid.

GdL dissolves quickly in water, with hydrolysis taking place over a longer timescale, allowing minimization of any detrimental effect from vortexing and mixing. The resulting hydrogels demonstrated improved and reproducible mechanical properties.<sup>137</sup>

#### 1.4.2 Metal ion induced hydrogelation

Recently, it was observed that the self-assembling pathway of peptide building blocks can be modulated by the addition of simple metal salts.<sup>135</sup> Metal salts are essential in a variety of physiological and pathophysiological conditions. They can interact with various functional groups on peptides, either inhibiting or accelerating the formation of supramolecular structures by controlling non-covalent interactions.<sup>138</sup> Furthermore, certain amino acids with ionizable groups in their side chains, such as aspartic acid, glutamic acid, histidine, and others, can interact with different cations and form different structures in the presence of metal salts. In particular, in the case of acidic amino acids, the presence of metal salts has been shown to significantly alter the gelation pH. In this thesis, we report the formation of differential supramolecular structures at physiological pH in the presence of divalent metal ions.<sup>139</sup>

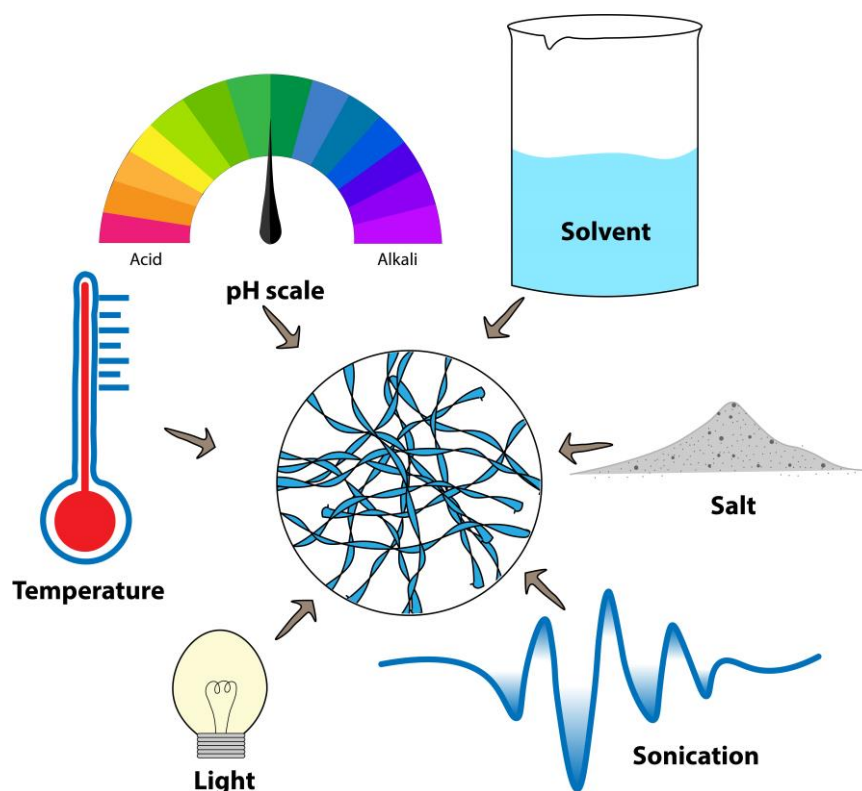


**Figure 1.8** Schematic representation of self-assembly via different physicochemical stimuli.

Furthermore, several short peptides have also been reported based on the natural metalloptides, which can interact with metal ions through their surface functionality. Our group has recently demonstrated a unique strategy for the controlled self-assembly pathway to create supramolecular hydrogel from a single dipeptide gelator by modulating the specific anions and transition metal salts.<sup>140</sup> Furthermore, Adams and co-workers demonstrated the structural transition from worm-like micellar structure of a functional dipeptide molecule upon adding calcium salt, which triggered the phase transition from sol to gel-like material.<sup>141, 142</sup> Additionally, another report by Parmar et al. explored the metal-binding site of the collagen triple helix to stabilize the CMP molecule. Both homo and heterotrimeric structures were stabilized by the addition of zinc (II) and other metal ions.<sup>143</sup> Another report demonstrated metal ion-assisted micro-collagen assembly, in which the heterotrimeric triple helix structure of collagen mimetic can be stabilized in the presence of metal ions.<sup>144</sup> Traditional approaches would make it impossible to obtain such unprecedented control over construction of supramolecular structure.

### **1.4.3 Biocatalytic self-assembly**

The approaches discussed so far, for inducing self-assembly have been classified as bulk environmental stimuli. These stimuli induce self-assembly by triggering changes in the bulk conditions around the peptide amphiphiles.<sup>67</sup> Another set of stimuli, on the other hand, operates under constant ambient circumstances but directly targets the peptide amphiphile to cause self-assembly. When paired with the specificity and selectivity of the enzyme catalyzed processes, this latter technique allows improved spatial and temporal control over self-assembly.<sup>145</sup> The generation of self-assembling building blocks from a non-assembling precursor is referred to as enzyme-triggered self-assembly.<sup>146</sup> This method of directing the synthesis of self-assembled nanostructures has a wide range of applications in biomedicine, including biosensing, controlled release, and the development of 3-D scaffolds, etc. Hydrolases, namely protease, phosphatase, esterase, and other enzymes have been used to create enzyme sensitive peptide amphiphiles.<sup>147-149</sup> Protease, phosphatase, esterase, and other enzymes have been used to develop enzyme responsive peptide amphiphiles.<sup>145</sup> Using enzyme catalyzed self-assembly to create enzyme responsive biomaterials necessitates specific components within a single precursor molecule: 1) an enzyme-sensitive component, 2) a self-assembly directing component, and 3) a molecular switch component that only

allows self-assembly when enzyme activation is initiated. All of these structural functionalities should be present in a single system without impacting the functionality each of these structural units.<sup>145</sup> The first example of enzyme-assisted self-assembly was reported by Xu and colleagues, where they used a phosphatase/kinase combination to de-phosphorylate Fmoc-tyrosine to induce gelation.<sup>150</sup> They went on to show that by altering the enzyme dosage, the final rheological features of the hydrogels can be easily modified.<sup>151</sup> This method of producing variations in the physical characteristics of the hydrogel within a single gelator domain is also recommended for building various scaffolds to influence stem-cell behaviour.<sup>145</sup> Furthermore, Xu and colleagues have demonstrated various examples of how his concept might be applied in biology. They have discovered a gelator, which showed a unique feature. For example, the peptide derivative when activated by enzymes, forms a hydrogel inside malignant cells, causing cell death.<sup>152</sup> Other studies of this research group also demonstrated that this method may be used to prevent bacterial colonization by employing an enzyme that is overexpressed in bacteria as a switch to produce nanofibers inside the bacterium, resulting in cell death.<sup>153</sup> Ulijn and co-workers have shown another pioneering example in this area of exploring enzyme assisted self-assembly of peptides. This classical study used this strategy to control supramolecular structure formation and accessed kinetically trapped structures that would otherwise be difficult to form using other synthetic pathways.<sup>154</sup> Biocatalytic self-assembly has now been used for a variety of applications, including wound healing, antibacterial drug synthesis, and molecular imaging, due to the improved control over structure evolution and selectivity.<sup>145, 153, 155, 156</sup>

#### **1.4.4 Light triggered self-assembly**

Another localized stimulus commonly employed to either activate or control the self-assembly of peptide-based supramolecular structures is light.<sup>157</sup> It interacts directly with the substance rather than physically perturbing the solution.<sup>157</sup> Various photo-responsive groups change their conformation and hence their optical characteristics in reaction to a specific wavelength of light, which may cause changes in their intermolecular interactions, resulting in differential self-assembling behaviour. Photo cleavable groups, such as nitro benzyl, and conformational changeable groups, such as azobenzene, are representing two types of these photo-responsive groups.<sup>158</sup> Ionization or isomerization occurs when these groups are irradiated with light of a certain

wavelength, changing the polarity and hydrophilicity of the molecule. To produce photo-responsive control over the material properties of the peptide hydrogels, these groups are rationally inserted into the peptide amphiphile design. Stupp's group first reported light-triggered self-assembly in seminal research in which they demonstrated the hydrogel production of a peptide amphiphile bearing a photocleavable group, i.e., nitro-benzyl group, in response to light stimulation.<sup>159</sup> By irradiating the gel with UV light, Adams and coworkers were able to modulate the material quality of the coumarin-based peptide hydrogelator after gelation.<sup>160</sup> In the presence of a photoacid generator, Raeburn et al. demonstrated UV light-induced gelation of a sequence of aromatic peptide compounds.<sup>161</sup> Similarly, Huang et al. demonstrated the photo-responsive behaviour of azobenzene conjugated short peptide sequence hydrogels. The sol to gel transition arises from the conformational shift of the azobenzene when exposed to UV radiation, which is appropriate for a variety of applications.<sup>162</sup> Lim and colleagues created an IR-responsive hybrid material made up of self-assembling peptides and carbon nanotubes.<sup>163</sup> This biomaterial was also used to stimulate the regeneration of functioning brain tissue.<sup>163</sup>

#### **1.4.5 Temperature induced hydrogelation**

In the case of short peptide amphiphiles, modulation of the temperature is also a popular way of gelation. The solution is heated first to solubilize the gelator molecules, then cooled to stimulate self-assembly.<sup>164</sup> Because of the presence of weak connections that can develop and break as a function of temperature, supramolecular hydrogels are predicted to be thermos-reversible.<sup>165</sup> Heating, in particular, improves the solubility of peptide amphiphiles by reducing hydrogen bonding connections between them. Following that, in the cooling phase, when the temperature drops, the solubility of the peptides in the solvent decreases, locking them into a self-assembled configuration at a certain temperature and attain either kinetically trapped structure or thermodynamically stable configuration.<sup>166</sup> The absolute duration and temperature of heating and cooling are significant factors that determine the material characteristics of the hydrogels.<sup>167</sup> Our laboratory has also recently documented the differential construction of supramolecular structures from a short aromatic peptide amphiphile using sonication and the heat cool technique.<sup>168</sup> In comparison to short twisted ribbons created using simply sonication, hydrogels formed using the heat-cool approach indicated the existence of a dense nanofibrous network. The rationale in this strategy relies on the

differential energy input into the system that drives the self-assembly in differential states. The shape of the nanostructures varied, which resulted in various biological responses.<sup>168</sup> Ulijn and co-workers have proved the importance of temperature in driving the nanostructures assemblies from peptide amphiphiles by meticulously managing the balance between hydrogen bonding and  $\pi$ - $\pi$  interactions.<sup>169</sup> Further they demonstrated the generation of differential supramolecular structures with varied gel strength and degradability from a single gelator molecule by merely varying the thermal history of the gelation.<sup>169</sup>

#### **1.4.6 Self-assembly induced by molecular recognition**

A unique relationship between molecules that display molecular complementarity based on their size, shape, or intermolecular interactions is termed as molecular recognition.<sup>170</sup> Molecular recognition is one of the fundamental strategy adopted in biological systems because it regulates the particular connections between biomolecules that allow them to perform desired activities like enzyme catalysis and DNA replication.<sup>171</sup> This interaction acts as a local stimulus and has been proven to influence and guide supramolecular structure formation.<sup>172-175</sup> This method has recently been used to create a variety of supramolecular structures using peptide-based building components.<sup>173-175</sup> Joseph et. al., demonstrated the host-guest interaction between the coumarin-conjugated peptide and  $\beta$ -cyclodextrin resulted in the structural transformation of peptide nanoparticles to 2-D sheet-like structures.<sup>172</sup> By manipulating the host-guest interactions, they were able to achieve great control over the shape and size of the nanostructures generated by peptide amphiphiles.<sup>176, 177</sup> In a similar line, it was shown that in the presence of light, host-guest chemistry between  $\beta$ -cyclodextrin and azobenzene coupled to a cationic peptide controlled the shape and surface charge of the nanostructures generated.<sup>172</sup> This variant was also used to illustrate the differential antibacterial activity. Another classical study by Mata and colleagues, demonstrated the use of host-guest interactions between adamantane and  $\beta$ -cyclodextrin to create non-covalently crosslinked nanofibrous networks with highly adjustable mechanical characteristics and degradation profiles, while maintaining the scaffold's biocompatibility.<sup>174</sup> Molecular recognition can thus be used as an emergent technique for fabricating sophisticated biomaterials with dynamic spatiotemporal activity.

### 1.4.7 Solvent induced hydrogelation

Short peptide amphiphiles' self-assembly is strongly reliant on the hydrophilic-lipophilic balance in their structure, which further balances numerous non-covalent interactions required for the formation of organized nanostructures.<sup>84</sup> Similarly, changing the solvent environment surrounding the gelator molecules may change the solvent-gelator and gelator-gelator interactions, which provide direct control over the viscoelastic behaviour and mechanical characteristics of the final gel phase material.<sup>178</sup> Because of the changing solvent-gelator interactions, peptide amphiphiles have varying solubility in different solvents and co-solvent systems, which might be used as a non-conventional technique to create distinct supramolecular structures from a single kind of gelator.<sup>179</sup> To use the solvent switch approach to promote self-assembly, the hydrophobic gelator molecules are first solubilized in an organic solvent (DMSO, ACN, methanol, DMF, acetone, HFIP, etc.) that is less polar than water.<sup>180-182</sup> In addition, water is added to the soluble gelator in an organic solvent, causing the gelator's solubility to change from highly soluble to weakly soluble.<sup>179</sup> During the switch, the intermolecular interactions between the gelator molecules are enhanced, resulting in the creation of supramolecular structures. Several studies in the literature have looked at the role of solvent-mediated gelation in influencing the material properties and shape of peptide nanostructures.<sup>180-182</sup> A hydrogel with differential microstructure, gel strength and their extent of recovery under shear stress from Fmoc-FF hydrogelator by merely varying the solvent type had been obtained.<sup>181</sup> This study also demonstrated that the organic solvents may be removed via a solvent exchange process, allowing these hydrogels to be used for a variety of biomedical purposes.<sup>181</sup> Verma and colleagues demonstrated that the shape of nanostructures generated by a peptide conjugate, which range from spheres to nanofibers, is determined by solvent interactions.<sup>180</sup> Our laboratory has also conducted a systematic investigation to modify the gelation behaviour of ECM derived laminin mimetic short peptides in the presence of various cosolvents to access diverse nanoscale structure. Interestingly, changing the solvent polarity from aqueous-organic combination to simply water resulted in substantial differences in the nanofibrous shape and gel stiffness of the proposed peptides.<sup>179</sup> This elegant approach is also intended to provide information on how to use solvents prudently when fabricating soft nano-biomaterials with regulated physiochemical characteristics. All these differential approaches of self-assembly leads to the formation

of peptide nanostructures, which relate to the secondary confirmation of protein molecule.

## **1.5 Differential secondary structures formed by designer peptides**

Peptides have been found to self-assemble into a variety of secondary structures depending on the size of the peptide chain and their organization, which will undergo intermolecular interactions to create differential secondary structures of the peptides at the nanoscale: These structures include 1)  $\alpha$ -helix or coiled coil, 2)  $\beta$ -sheet, and 3)  $\beta$ -hairpins, which are the examples of secondary structures that have been studied extensively in the field of peptide self-assembly.

### **1.5.1 $\alpha$ -helix or coiled coil**

The  $\alpha$ -helix is a typical secondary structural motif in proteins, consisting of a right-handed helix with a 3.6-amino-acid repetition per helical turn. Pauling, Corey, and Crick were the first to characterize the  $\alpha$ -helix structure of protein molecule.<sup>183</sup> Every two turns of a helix have seven residues labelled "a" through "g." The *i*th residue's carbonyl forms a hydrogen bond with the amide of the *i* + 4 in the helix (Figure 1.9). Heptad repetitions of hydrophobic and charged amino acid residues are seen in coiled-coils. The Woolfson group used "sticky end" assembly to present an extensively researched design of a fibrous coiled-coil based system.<sup>184, 185</sup> A non-covalently exchange of one structural domain of a peptide with another develops a new method to make fibrous structures. The structure can be designed in a way so that the third helix is not absorbed into the coiled-coil and creates a "sticky end," preventing the formation of the three-helix bundle.<sup>183</sup> A helix from another peptide must be added to reassemble the three helices bundle, allowing for the development of dimeric structures or fibers. Coiled coils allow for the creation of peptide-based nanofibrous structures that follow a set of well-established design criteria drawn from natural systems.<sup>183</sup> "Sticky-ends" and domain switching provide you a lot of control over supramolecular behaviour, whereas rational amino acid inclusion gives researchers the predictable structural alterations.<sup>183</sup>

### **1.5.2 $\beta$ -sheet**

$\beta$ -sheets are the most common and well-studied self-assembling domains in proteins and peptides.  $\beta$ -sheets are made up of alternating hydrophobic and hydrophilic amino

acid sequences. Each peptide sequence is referred to as  $\beta$ -strand.<sup>186</sup> The alignment of the strands determines whether the sheets are parallel or anti-parallel.<sup>187</sup> In parallel  $\beta$ -sheets, all the  $\beta$ -strands are oriented in the same way, such as N- to C- terminal and when the strands are organized in the opposite direction, it leads to the formation of antiparallel  $\beta$ -sheets.<sup>187</sup> The  $\beta$ -sheet structures are also known to be stabilized via electrostatic interactions between the alternating charged residues on the two strands.<sup>188</sup> Zhang et al. gave the first proof of synthetic peptides' ability to build nanofibrous structures containing  $\beta$ -sheets secondary structures.<sup>130, 188</sup> They created a library of oligopeptides with alternating hydrophobic and hydrophilic amino acid residues that self-assemble to generate  $\beta$ -sheet rich nanofibers in aqueous environment. The peptide sequence AEK-16 is made up of complimentary ionic residues that have a high inclination to interact with one another and create  $\beta$ -sheet-like structures.<sup>130</sup> Importantly, the peptide-based hydrogels made from these ionic-complementary peptides were shown to be extremely biocompatible, allowing mammalian cells to adhere, proliferate, migrate, and differentiate.<sup>189</sup>

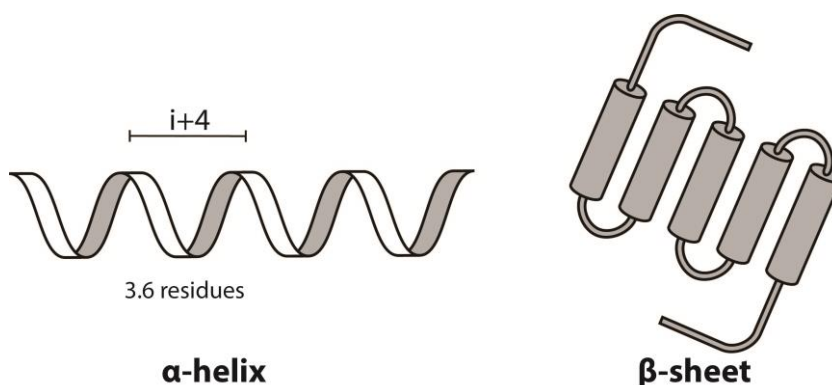


**Figure 1.9** Schematic representation of secondary structures attained by the short peptide amphiphiles.

### 1.5.3 $\beta$ -hairpin

$\beta$ -hairpins are a kind of peptide secondary structure made up of two strands of  $\beta$ -sheets that are orientated in opposing directions and joined by 2-4 amino acids.  $\beta$ -turns are the connecting loops between two strands.<sup>121</sup> Since, the structure resembles a hairpin and is made up of  $\beta$ -strands, they are termed as  $\beta$ -hairpins. The self-assembly of  $\beta$ -hairpin forming peptides has been widely explored by Pochan and Schneider.<sup>190-192</sup> They originally discovered the MAX1 peptide in 2002, which had repeating units of valine (V) and lysine (K) residues as well as intermittent tetrapeptides (-V<sup>D</sup>PPT-). This

designer sequence has been demonstrated to create type II-turns, with <sup>D</sup>P denoting the D isomer of proline.<sup>193</sup> When dissolved in water, this peptide tends to form random coils, but when present in Dulbecco's modified Eagle's medium (DMEM), a cell culture medium, it folds into a  $\beta$ -hairpin structure. Salts or a higher pH diminish electrostatic repulsion between lysine residues, allowing intermolecular hydrogen bonds between the two peptide arms to form more easily.<sup>194</sup> Since then, several additional MAX1 variations have been discovered, demonstrating the impact of hydrophobic and hydrophilic residue substitution on the self-assembly of these proteins.<sup>195</sup> MAX8, for example, is designed by replacing one lysine residue with glutamate, and it self-assembles quicker at lower pH than MAX1 peptides due to fewer repulsive positive charges.<sup>195</sup> Both MAX1 and MAX8 peptides have the ability to create hydrogels in the presence of cell culture medium, suggesting that they may offer potential applications in biomedicine.<sup>196</sup>

### **1.6 Peptide polymer bioconjugate- A better structural and bio-functional mimic of the native ECM**

As previously stated, tissue-specific scaffold design and manufacturing are incredibly valuable in regenerative medicine.<sup>197</sup> To offer appropriate biochemical, mechanical, and topographical signals to the cells for their growth and proliferation, the scaffold should match the structural and functional hierarchy of the ECM.<sup>198</sup> In this context, fabricating a scaffold with all of the desirable properties using only a single component of the native ECM is extremely difficult; for example, proteins and peptides represent only a single class of molecules present in the native ECM; thus, replicating the complete biochemical and biophysical microenvironment of the ECM using only peptide-based biomaterials is extremely difficult and far from an ideal mimic.<sup>199</sup> Multicomponent self-assembly is getting a lot of impetus in this approach for the construction of improved tissue scaffolds for tissue engineering.<sup>199, 200</sup> The most difficult aspect of building these scaffolds, however, is combining the adaptability of biologically sophisticated architecture with precise functionality in a system that is simple, safe, cost-effective, resilient, and reproducible. Exploring simple mixing of complex biomolecular building blocks of life to explore the possibility of biomolecular interactions to generate an ECM-mimetic composite biomaterial might be an emerging technique for synthetic scaffold development.<sup>9</sup> To this direction, sugar and peptide molecules make up the majority of the mammalian ECM, and they play an important

role in the biological signaling pathways that regulate cellular behaviour. Hence, developing a composite matrix bearing both the essential components of native ECM would be an elegant and facile approach, which may offer versatility in terms of its potential application in biomedicine. Furthermore, glycosylation of proteins and peptides is common in nature, where it is required for precise protein targeting. ECM-derived biomaterials have been proven to give crucial biochemical functionality to cells; nevertheless, these biomaterials are subject to batch-to-batch variance due to their animal origin and non-standardized extraction techniques.<sup>201</sup> Furthermore, controlling their physicochemical characteristics to accomplish desired function is difficult. Few synthetic systems have been constructed in the literature to study sugar-peptide interactions in order to generate improved biomaterials.<sup>202</sup> In this respect, it has been shown that polymer peptide-based hydrogels have better thermostability, biostability, and cellular adhesion than their peptide equivalent.<sup>203</sup> Furthermore, it was revealed that simple non-covalent interactions between a sugar and a designer ionic complimentary peptide exhibited improved physicochemical and biological features.<sup>204</sup> Following that, we have reported a new class of biomaterial by non-covalently conjugating a collagen-inspired short peptide to nanofibrillar cellulose (NFC).<sup>205</sup> When compared to NFC alone, the non-covalently connected sugar-peptide combination has shown improved cell proliferation over a longer period of incubation.<sup>205</sup> Recently, a multicomponent system made up of peptides, carbohydrates, vitamins, and proteins has been invented that mimicked the compositional complexity of the natural ECM.<sup>199</sup> In order to fabricate innovative biomaterials with improved physical and biological characteristics, interactions between biopolymers and proteins have been extensively studied in the literature.<sup>206</sup> However, very few report on the short peptide-polymer interaction have been explored to design the functional mimic of native ECM. The proposed synthetic scaffolds containing the polymer peptide conjugates are expected to solve challenges faced by the current biomaterials and also offers a better way for producing bioactive scaffolds with minimal synthetic challenges for tissue engineering applications.

### **1.7 Recent advances in fabrication of collagen inspired peptide hydrogels**

Collagen is the most abundantly found protein in the extracellular matrix (ECM) with more than 28 types and comprises of about ~30% of whole-body protein in humans.<sup>207</sup> Among different types of collagen, type I, II, and III are the most prevalent forms as they are mainly present in ECM while other collagens are mostly involved in making

network like structure as part of the basal membrane.<sup>208</sup> Role and architecture of these different types of collagen vary widely, still all of them share a common tertiary structure of triple helix. The structure of triple helix collagen comprises of three different left-handed polyproline-II-type helices, twisted in a manner with one residue staggered to form a right-handed helix.<sup>209</sup> Latest analysis of human genome has introduced numerous new types of collagens collectively known as fibril-associated collagen with interrupted triple helix (FACIT).<sup>210</sup> These newly identified collagens are known to attach to the surface of fibrous collagen (type II) in some specific tissue instead of assembling into higher ordered structures. These FACIT collagen alter the surface properties and assembly of fibrils, and are known to influence the fibrillar interaction between themselves and with other macromolecules.<sup>211</sup> Because of its structural and functional characteristics that offer extensive biocompatibility, high porosity, ability to conjugate with other materials, collagen has gained immense attention of scientists and fascinated them to explore this protein in supramolecular chemistry, polymer chemistry, tissue engineering and regenerative medicine through understanding in depth structure-function relationship.<sup>212, 213</sup> However, the structure and function of these collagen molecules vary widely in extracellular matrix, still all collagen molecules share a basic repeating sequence of Gly-X-Y (X=Proline and Y=Hydroxyproline) and display substantial post-translational modification (glycosylation and primary hydroxylation).<sup>214, 215</sup> Characteristic domain of Gly-X-Y polypeptide can be recognized with two unique features: (i) Presence of Gly at every third position in the tripeptide sequence,<sup>216, 217</sup> (ii) A high proportion of proline and hydroxyproline in the tripeptide sequence, where more than 50% of the total amino acid content of collagen was found to consist of hydroxyproline.<sup>218, 219</sup>

The secondary structure of collagen ( $\alpha$ -helix) is formed by the repetitive units of tripeptide linked together. Initiation of triple helix starts at the C-terminus and regulation of primary fibrils are involved at the N-terminus, while the non-helical domains are present at the end of  $\alpha$ -chains.<sup>220, 221</sup> All trimeric strand irrespective of collagen type fold into right-handed triple helix, which represents the hallmark of secondary structure of collagen.<sup>222</sup> Triple helix of collagen type I is usually formed of heterotrimer of two identical  $\alpha 1$  and one  $\alpha 2$  chains containing about 1000 amino acids, which is of approximately 300 nm in length and 1.5 nm in diameter.<sup>223</sup> Individually these  $\alpha$ -chains form left-handed rod-like helix, where the glycine residue is localized

around the central axis, while the other two amino acids covers the outer positions.<sup>224-</sup>  
<sup>226</sup> The right-handed triple helix of collagen molecules are formed via interstrand H-bonding between the  $\alpha$ -chains. Side chain residues of amino acids present at X and Y positions are distributed along the strand and are accessible for the extra binding sites. Hydrophobic interactions induced by aromatic residues and electrostatic interactions between oppositely charged groups plays a major role in stabilizing the triple helix and during the linear and lateral alignment of collagen fiber.<sup>227-229</sup>

Three similar  $\alpha$ -chains forming a triple helix are referred to as a homotrimer, while three different  $\alpha$ -chains form heterotrimers. All known 28 types of collagens can form homotrimeric (AAA) or heterotrimeric (AAB and ABC) compositions. Some of them can only form AAB heterotrimer, while some form both AAB and ABC heterotrimers.<sup>230</sup> The control that native collagen has on helix composition and its patterning has been a subject of research for a decade by mimicking the collagen molecule and studying their helix formation as homotrimers as well as heterotrimers.<sup>231,</sup>  
<sup>232</sup> Many different strategies have been used by the researchers for understanding these different compositional packing and staggering of collagen fibrils.<sup>223</sup> While majority of the research are focused on the homotrimeric species of collagen mimetic peptide, which has greatly enriched the knowledge of homotrimeric structure of collagen protein.<sup>233-235</sup> But for the last decade the interest has been shifted towards the heterotrimeric structure of collagen as many of the collagen types I, IV, and VIII plays a crucial role in maintaining the extracellular integrity.<sup>236</sup> Attempts have included engineering of the peptide motifs using the structure of native collagen molecule to form triple helix, which assemble into homotrimers. Several reports show the homotrimeric arrangement of collagen mimetic peptides to mimic the collagen molecule.<sup>207, 237-239</sup> Referring to the basic structure of collagen higher ordered assemblies have been observed using the POG triad, suggesting the specific role of proline and hydroxyproline for the association of collagen triple helices into higher order fibers. In a study by Brodsky group, understanding the structure, stability, conformation, and dynamics of collagen triple helix.<sup>215, 217, 240</sup> The sequence (GPO)<sub>10</sub> is found to be the most stabilizing and common triplet in collagen, which leads to the formation of fibril like structure similar to the native collagen, while (PPG)<sub>10</sub> was reported to undergo amorphous aggregation or form precipitation under the similar condition.<sup>241</sup> Such observation suggests the specific role of proline oxidation for

stabilizing the higher ordered structure of collagen triple helices. Various contradictory studies have been reported regarding the change in melting point of GPO peptide by varying the chain length of the triple helices. The biologically common structural design of heterotrimers is more complicated and only recently have gathered attention to design and synthesize the more complex part. The fundamental challenge is the large number of competing species for forming AAB, ABB or ABC.<sup>235</sup> Furthermore, the steric limitation at the glycine site compels each strand to have a single amino acid offset. As a result, each heterotrimer composition has numerous unique register; depending on whether B is the leading, middle, or following position, A2B can assemble as BAA, ABA, or AAB. The number of competing species grows from 8 to 27 when three peptides are combined.<sup>242</sup> Proline and hydroxyproline plays a crucial role in organizing the peptide backbone to form the triple helix conformation. The stereoelectronic effect causes the preorganization of helices and substitution of proline and hydroxyproline with any natural amino acid, this in turn reduces the organization and destabilizes the triple helix when compared to the canonical (POG)<sub>n</sub> repeats. Non-canonical registrations constitute a further complication in the heterotrimer construction where the peptides are offset by more than one amino acid. To comply with such steric limitations, each cross-section of the triple helix must include at least one glycine. Because of lacking the inter-strand H-bond and van der Waals interactions, the non-canonical type melt at much lower temperature than their canonical counterparts and lose their stability.<sup>243</sup> The highly cross-linked structure of collagen and its heterogenous existence makes it a topic of study. Hence, these structural and functional features inspire to design the artificial collagen in a regulated and controlled manner, which can mimic the hierarchical structural of natural collagen molecule. This thesis is focused on the design of the synthetic collagen inspired peptides (CIPs) to understand the hierarchical assembly of the native protein and modifications in the peptide sequence to attain the structural similarity at the nanoscale, with an emphasis on recent breakthroughs in the field of biomaterials, nanotechnology, and tissue engineering. To this end, literature reports reinforce the significance of the potential of structural mimics of natural collagen (CMPs or CIPs) developed by short peptide amphiphiles that can display huge applications in diverse field of biomedicine. These short bioactive peptide motifs inspired from collagen may have the capability to mimic the native ECM for the fabrication of advanced tissue mimics. We anticipate that these

scaffolds can provide the necessary biochemical and biomechanical cues to control the cellular behaviour.

### **1.8 Aims and objectives**

In this thesis, our aim is to adapt a minimalistic approach design and develop penta-peptide sequences inspired from the basic repetitive unit of a collagen triple helix. Keeping in mind the importance of charge pair interactions, which further lead to the hierarchical organization, we have designed ionic complementary peptide sequences. The aim of this thesis is to demonstrate the importance of external stimuli or environmental conditions in developing differential nanostructures to access differential functions from a single peptide monomer. The research work was carried out with following specific objectives:

- 1.** Exploring the electrostatic interactions among the oppositely charged peptides inspired from the single tripeptide unit of collagen molecule to develop a more biocompatible co-assembled system.
- 2.** The cooperative effect of adding simple divalent metal ions to promote hydrogelation and access superior physical properties and promote favourable cellular interactions with the designer matrix.
- 3.** Controlled growth of hydroxyapatite crystals on the collagen inspired peptide fibers with potential applications in bone tissue regeneration.
- 4.** Benefits of conjugating carbohydrate polymer into short collagen inspired peptides in developing a tunable synthetic scaffold for fabricating a better structural and bio-functional mimic of the native ECM.
- 5.** Exploring the stimuli responsive dynamic shape transformable behaviour of these peptide nanostructures to encapsulate and release the hydrophobic drug molecules, serving a dual function as nano-vehicle to transport antibacterial agents and providing an advanced synthetic scaffold for the wound site.

Furthermore, a single gelator molecule may be used to fabricate a variety of nanostructures by adjusting the appropriate parameters, which has considerable promise in biomedical and tissue engineering applications. The non-conventional approach used to build different nanostructures from a collagen-inspired peptide in

order to develop a synthetic scaffold has a lot of promise for developing advanced nanomaterials for future biomedicine.

## 1.9 References

1. Patil, M.; Mehta, D. S.; Guvva, S., Future impact of nanotechnology on medicine and dentistry. *J Indian Soc Periodontol* **2008**, *12* (2), 34-40.
2. Shi, J.; Votruba, A. R.; Farokhzad, O. C.; Langer, R., Nanotechnology in drug delivery and tissue engineering: from discovery to applications. *Nano Lett.* **2010**, *10* (9), 3223-3230.
3. Mahla, R. S., Stem Cells Applications in Regenerative Medicine and Disease Therapeutics. *Int J Cell Biol* **2016**, *2016*, 6940283-6940283.
4. Mao, A. S.; Mooney, D. J., Regenerative medicine: Current therapies and future directions. *Proc Natl Acad Sci U S A* **2015**, *112* (47), 14452-14459.
5. Roberts, T. T.; Rosenbaum, A. J., Bone grafts, bone substitutes and orthobiologics: the bridge between basic science and clinical advancements in fracture healing. *Organogenesis* **2012**, *8* (4), 114-124.
6. Amini, A. R.; Laurencin, C. T.; Nukavarapu, S. P., Bone tissue engineering: recent advances and challenges. *Crit Rev Biomed Eng* **2012**, *40* (5), 363-408.
7. Henkel, J.; Woodruff, M. A.; Epari, D. R.; Steck, R.; Glatt, V.; Dickinson, I. C.; Choong, P. F. M.; Schuetz, M. A.; Huttmacher, D. W., Bone Regeneration Based on Tissue Engineering Conceptions — A 21st Century Perspective. *Bone Research* **2013**, *1* (1), 216-248.
8. Cen, L.; Liu, W.; Cui, L.; Zhang, W.; Cao, Y., Collagen Tissue Engineering: Development of Novel Biomaterials and Applications. *Pediatric Research* **2008**, *63* (5), 492-496.
9. Chen, F.-M.; Liu, X., Advancing biomaterials of human origin for tissue engineering. *Prog. Polym. Sci.* **2016**, *53*, 86-168.
10. Kyburz, K. A.; Anseth, K. S., Synthetic mimics of the extracellular matrix: how simple is complex enough? *Annals of biomedical engineering* **2015**, *43* (3), 489-500.
11. Boni, R.; Ali, A.; Shavandi, A.; Clarkson, A. N., Current and novel polymeric biomaterials for neural tissue engineering. *Journal of Biomedical Science* **2018**, *25* (1), 90.
12. Grøndahl, L.; Jack, K. S.; Goonasekera, C. S., 5 - Composite materials for bone repair. In *Biomedical Composites (Second Edition)*, Ambrosio, L., Ed. Woodhead Publishing: 2017; pp 83-110.
13. Jung, K.; Corrigan, N.; Wong, E. H. H.; Boyer, C., Bioactive Synthetic Polymers. **2022**, *34* (2), 2105063.
14. Song, R.; Murphy, M.; Li, C.; Ting, K.; Soo, C.; Zheng, Z., Current development of biodegradable polymeric materials for biomedical applications. *Drug Des Devel Ther* **2018**, *12*, 3117-3145.
15. Quintanilla-Sierra, L.; García-Arévalo, C.; Rodríguez-Cabello, J. C., Self-assembly in elastin-like recombinamers: a mechanism to mimic natural complexity. *Materials Today Bio* **2019**, *2*, 100007.
16. Werten, M. W. T.; Eggink, G.; Cohen Stuart, M. A.; de Wolf, F. A., Production of protein-based polymers in *Pichia pastoris*. *Biotechnol. Adv.* **2019**, *37* (5), 642-666.
17. Pochan, D.; Scherman, O., Introduction: Molecular Self-Assembly. *Chem. Rev.* **2021**, *121* (22), 13699-13700.
18. Ariga, K.; Nishikawa, M.; Mori, T.; Takeya, J.; Shrestha, L. K.; Hill, J. P., Self-assembly as a key player for materials nanoarchitectonics. *Sci Technol Adv Mater* **2019**, *20* (1), 51-95.
19. Xu, H.; Chen, D.; Wang, S.; Zhou, Y.; Sun, J.; Zhang, W.; Zhang, X., Macromolecular self-assembly and nanotechnology in China. **2013**, *371* (2000), 20120305.
20. Wang, H.; Feng, Z.; Xu, B., Bioinspired assembly of small molecules in cell milieu. *Chem. Soc. Rev.* **2017**, *46* (9), 2421-2436.
21. Yadav, S.; Sharma, A. K.; Kumar, P., Nanoscale Self-Assembly for Therapeutic Delivery. *Frontiers in Bioengineering and Biotechnology* **2020**, *8*.

22. Chakrabarty, R.; Mukherjee, P. S.; Stang, P. J., Supramolecular coordination: self-assembly of finite two- and three-dimensional ensembles. *Chem. Rev.* **2011**, *111* (11), 6810-6918.
23. Grigalunas, M.; Brakmann, S.; Waldmann, H., Chemical Evolution of Natural Product Structure. *J. Am. Chem. Soc.* **2022**, *144* (8), 3314-3329.
24. Liu, B.; Pappas, C. G.; Ottel , J.; Schaeffer, G.; Jurissek, C.; Pieters, P. F.; Altay, M.; Mari , I.; Stuart, M. C. A.; Otto, S., Spontaneous Emergence of Self-Replicating Molecules Containing Nucleobases and Amino Acids. *J. Am. Chem. Soc.* **2020**, *142* (9), 4184-4192.
25. Berger, O.; Gazit, E., Molecular self-assembly using peptide nucleic acids. *Biopolymers* **2017**, *108* (1), 10.1002/bip.22930.
26. Fan, T.; Yu, X.; Shen, B.; Sun, L., Peptide Self-Assembled Nanostructures for Drug Delivery Applications. *Journal of Nanomaterials* **2017**, *2017*, 4562474.
27. Stephanopoulos, N., Hybrid Nanostructures from the Self-Assembly of Proteins and DNA. *Chem* **2020**, *6* (2), 364-405.
28. Whitesides, G. M.; Mathias, J. P.; Seto, C. T., Molecular self-assembly and nanochemistry: a chemical strategy for the synthesis of nanostructures. *Science* **1991**, *254* (5036), 1312-9.
29. Eshun-Wilson, L.; Zhang, R.; Portran, D.; Nachury, M. V.; Toso, D. B.; L hr, T.; Vendruscolo, M.; Bonomi, M.; Fraser, J. S.; Nogales, E., Effects of  $\alpha$ -tubulin acetylation on microtubule structure and stability. **2019**, *116* (21), 10366-10371.
30. Sharma, A.; Vaghasiya, K.; Verma, R. K.; Yadav, A. B., Chapter 3 - DNA nanostructures: chemistry, self-assembly, and applications. In *Emerging Applications of Nanoparticles and Architecture Nanostructures*, Barhoum, A.; Makhlouf, A. S. H., Eds. Elsevier: 2018; pp 71-94.
31. Yan, X.; Huang, S.; Wang, Y.; Tang, Y.; Tian, Y., Bottom-Up Self-Assembly Based on DNA Nanotechnology. *Nanomaterials (Basel, Switzerland)* **2020**, *10* (10), 2047.
32. McManus, J. J.; Charbonneau, P.; Zaccarelli, E.; Asherie, N., The physics of protein self-assembly. *Curr. Opin. Colloid Interface Sci.* **2016**, *22*, 73-79.
33. Solomonov, A.; Shimanovich, U., Self-Assembly in Protein-Based Bionanomaterials. **2020**, *60* (12), 1152-1170.
34. Urbanczyk, M.; Layland, S. L.; Schenke-Layland, K., The role of extracellular matrix in biomechanics and its impact on bioengineering of cells and 3D tissues. *Matrix Biol.* **2020**, *85-86*, 1-14.
35. Goodman, S. R., Chapter 7 - Cell Adhesion and the Extracellular Matrix. In *Goodman's Medical Cell Biology (Fourth Edition)*, Goodman, S. R., Ed. Academic Press: 2021; pp 203-247.
36. Winkler, J.; Abisoye-Ogunniyan, A.; Metcalf, K. J.; Werb, Z., Concepts of extracellular matrix remodelling in tumour progression and metastasis. *Nat. Commun.* **2020**, *11* (1), 5120.
37. Bhattacharjee, O.; Ayyangar, U.; Kurbet, A. S.; Ashok, D.; Raghavan, S., Unraveling the ECM-Immune Cell Crosstalk in Skin Diseases. *Frontiers in Cell Developmental Biology* **2019**, *7*.
38. Kular, J. K.; Basu, S.; Sharma, R. I., The extracellular matrix: Structure, composition, age-related differences, tools for analysis and applications for tissue engineering. **2014**, *5*, 2041731414557112.
39. Tracy, L. E.; Minasian, R. A.; Caterson, E. J., Extracellular Matrix and Dermal Fibroblast Function in the Healing Wound. *Adv Wound Care (New Rochelle)* **2016**, *5* (3), 119-136.
40. Frantz, C.; Stewart, K. M.; Weaver, V. M., The extracellular matrix at a glance. *J. Cell Sci.* **2010**, *123* (Pt 24), 4195-4200.
41. Karamanos, N. K.; Theocharis, A. D.; Piperigkou, Z.; Manou, D.; Passi, A.; Skandalis, S. S.; Vynios, D. H.; Orian-Rousseau, V.; Ricard-Blum, S.; Schmelzer, C. E. H.; Duca, L.; Durbeej, M.; Afratis, N. A.; Troeberg, L.; Franchi, M.; Masola, V.; Onisto, M., A guide to the composition and functions of the extracellular matrix. **2021**, *288* (24), 6850-6912.

42. Yue, B., Biology of the extracellular matrix: an overview. *J Glaucoma* **2014**, *23* (8 Suppl 1), S20-S23.
43. Brown, B. N.; Badylak, S. F., Extracellular matrix as an inductive scaffold for functional tissue reconstruction. *Transl Res* **2014**, *163* (4), 268-285.
44. Schultz, G. S.; Wysocki, A., Interactions between extracellular matrix and growth factors in wound healing. *Wound repair and regeneration : official publication of the Wound Healing Society [and] the European Tissue Repair Society* **2009**, *17* (2), 153-62.
45. Bhowmick, N. A.; Neilson, E. G.; Moses, H. L., Stromal fibroblasts in cancer initiation and progression. *Nature* **2004**, *432* (7015), 332-337.
46. Mouw, J. K.; Ou, G.; Weaver, V. M., Extracellular matrix assembly: a multiscale deconstruction. *Nat Rev Mol Cell Biol* **2014**, *15* (12), 771-785.
47. Ruiz-Rodriguez, L.; Loche, P.; Hansen, L. T.; Netz, R. R.; Fratzl, P.; Schneck, E.; Blank, K. G.; Bertinetti, L., Sequence-specific response of collagen-mimetic peptides to osmotic pressure. *MRS Bull.* **2021**, *46* (10), 889-901.
48. Shoulders, M. D.; Raines, R. T., Collagen structure and stability. *Annu. Rev. Biochem* **2009**, *78*, 929-958.
49. Muiznieks, L. D.; Keeley, F. W., Molecular assembly and mechanical properties of the extracellular matrix: A fibrous protein perspective. *Biochimica et Biophysica Acta (BBA) - Molecular Basis of Disease* **2013**, *1832* (7), 866-875.
50. Bonnans, C.; Chou, J.; Werb, Z., Remodelling the extracellular matrix in development and disease. *Nat Rev Mol Cell Biol* **2014**, *15* (12), 786-801.
51. Mecham, R. P., Elastin in lung development and disease pathogenesis. *Matrix biology : journal of the International Society for Matrix Biology* **2018**, *73*, 6-20.
52. Gao, Y.; Liu, S.; Huang, J.; Guo, W.; Chen, J.; Zhang, L.; Zhao, B.; Peng, J.; Wang, A.; Wang, Y.; Xu, W.; Lu, S.; Yuan, M.; Guo, Q., The ECM-Cell Interaction of Cartilage Extracellular Matrix on Chondrocytes. *BioMed research international* **2014**, *2014*, 648459.
53. Silva, A. C.; Pereira, C.; Fonseca, A. C. R. G.; Pinto-do-Ó, P.; Nascimento, D. S., Bearing My Heart: The Role of Extracellular Matrix on Cardiac Development, Homeostasis, and Injury Response. **2021**, *8*, 621644.
54. Wu, Y. J.; La Pierre, D. P.; Wu, J.; Yee, A. J.; Yang, B. B., The interaction of versican with its binding partners. *Cell research* **2005**, *15* (7), 483-94.
55. Parisi, L.; Toffoli, A.; Ghezzi, B.; Mozzoni, B.; Lumetti, S.; Macaluso, G. M., A glance on the role of fibronectin in controlling cell response at biomaterial interface. *Jpn Dent Sci Rev* **2020**, *56* (1), 50-55.
56. Speziale, P.; Arciola, C. R.; Pietrocola, G., Fibronectin and Its Role in Human Infective Diseases. *Cells* **2019**, *8* (12), 1516.
57. Walimbe, T.; Panitch, A., Proteoglycans in Biomedicine: Resurgence of an Underexploited Class of ECM Molecules. **2020**, *10*, 1661.
58. Mattson, J. M.; Turcotte, R.; Zhang, Y., Glycosaminoglycans contribute to extracellular matrix fiber recruitment and arterial wall mechanics. *Biomech Model Mechanobiol* **2017**, *16* (1), 213-225.
59. BaoLin, G.; Ma, P. X., Synthetic biodegradable functional polymers for tissue engineering: a brief review. *Sci China Chem* **2014**, *57* (4), 490-500.
60. Kaliva, M.; Chatzinikolaidou, M.; Vamvakaki, M., CHAPTER 1 Applications of Smart Multifunctional Tissue Engineering Scaffolds. In *Smart Materials for Tissue Engineering: Applications*, The Royal Society of Chemistry: 2017; pp 1-38.
61. Zhu, J.; Marchant, R. E., Design properties of hydrogel tissue-engineering scaffolds. *Expert Rev Med Devices* **2011**, *8* (5), 607-626.
62. Abudula, T.; Bhatt, K.; Eggermont, L. J.; O'Hare, N.; Memic, A.; Bencherif, S. A., Supramolecular Self-Assembled Peptide-Based Vaccines: Current State and Future Perspectives. *Front. in Chem.* **2020**, *8*, 598160.
63. Zheng, M.; Pan, M.; Zhang, W.; Lin, H.; Wu, S.; Lu, C.; Tang, S.; Liu, D.; Cai, J., Poly( $\alpha$ -1-lysine)-based nanomaterials for versatile biomedical applications: Current advances and perspectives. *Bioact. Mater.* **2021**, *6* (7), 1878-1909.

64. Er, S.; Laraib, U.; Arshad, R.; Sargazi, S.; Rahdar, A.; Pandey, S.; Thakur, V. K.; Díez-Pascual, A. M., Amino Acids, Peptides, and Proteins: Implications for Nanotechnological Applications in Biosensing and Drug/Gene Delivery. *Nanomaterials (Basel, Switzerland)* **2021**, *11* (11), 3002.
65. La Manna, S.; Di Natale, C.; Onesto, V.; Marasco, D., Self-Assembling Peptides: From Design to Biomedical Applications. *International journal of molecular sciences* **2021**, *22* (23), 12662.
66. Shah, A.; Malik, M. S.; Khan, G. S.; Nosheen, E.; Iftikhar, F. J.; Khan, F. A.; Shukla, S. S.; Akhter, M. S.; Kraatz, H.-B.; Aminabhavi, T. M., Stimuli-responsive peptide-based biomaterials as drug delivery systems. *Chem. Eng. J.* **2018**, *353*, 559-583.
67. Du, Z.; Fan, B.; Dai, Q.; Wang, L.; Guo, J.; Ye, Z.; Cui, N.; Chen, J.; Tan, K.; Li, R.; Tang, W., Supramolecular peptide nanostructures: Self-assembly and biomedical applications. *Giant* **2022**, *9*, 100082.
68. Feyzizarnagh, H.; Yoon, D.-Y.; Goltz, M.; Kim, D.-S., Peptide nanostructures in biomedical technology. **2016**, *8* (5), 730-743.
69. Hamley, I. W.; Castelletto, V., Self-Assembly of Peptide Bioconjugates: Selected Recent Research Highlights. *Bioconjug Chem.* **2017**, *28* (3), 731-739.
70. Wang, Y.; Zhang, X.; Wan, K.; Zhou, N.; Wei, G.; Su, Z., Supramolecular peptide nano-assemblies for cancer diagnosis and therapy: from molecular design to material synthesis and function-specific applications. *Journal of Nanobiotechnology* **2021**, *19* (1), 253.
71. Mason, T. O.; Buell, A. K., The Kinetics, Thermodynamics and Mechanisms of Short Aromatic Peptide Self-Assembly. *Advances in experimental medicine and biology* **2019**, *1174*, 61-112.
72. Wang, J.; Liu, K.; Xing, R.; Yan, X., Peptide self-assembly: thermodynamics and kinetics. *Chem. Soc. Rev.* **2016**, *45* (20), 5589-5604.
73. Madhusudan Makwana, K.; Mahalakshmi, R., Implications of aromatic-aromatic interactions: From protein structures to peptide models. *Protein science : a publication of the Protein Society* **2015**, *24* (12), 1920-1933.
74. Kim, J.; Han, T. H.; Kim, Y. I.; Park, J. S.; Choi, J.; Churchill, D. G.; Kim, S. O.; Ihee, H., Role of water in directing diphenylalanine assembly into nanotubes and nanowires. *Adv. Mater.* **2010**, *22* (5), 583-7.
75. Paramonov, S. E.; Jun, H. W.; Hartgerink, J. D., Self-assembly of peptide-amphiphile nanofibers: the roles of hydrogen bonding and amphiphilic packing. *J. Am. Chem. Soc.* **2006**, *128* (22), 7291-8.
76. Tsonchev, S.; Niece, K. L.; Schatz, G. C.; Ratner, M. A.; Stupp, S. I., Phase Diagram for Assembly of Biologically-Active Peptide Amphiphiles. *J. Phys. Chem. B* **2008**, *112* (2), 441-447.
77. Sjögren, H.; Ericsson, C. A.; Evenäs, J.; Ulvenlund, S., Interactions between charged polypeptides and nonionic surfactants. *Biophys. J.* **2005**, *89* (6), 4219-4233.
78. Israelachvili, J. N., 19 - Thermodynamic Principles of Self-Assembly. In *Intermolecular and Surface Forces (Third Edition)*, Israelachvili, J. N., Ed. Academic Press: San Diego, 2011; pp 503-534.
79. Lee, J.; Ju, M.; Cho, O. H.; Kim, Y.; Nam, K. T., Tyrosine-Rich Peptides as a Platform for Assembly and Material Synthesis. *Adv Sci (Weinh)* **2018**, *6* (4), 1801255-1801255.
80. Lampel, A., Biology-Inspired Supramolecular Peptide Systems. *Chem* **2020**, *6* (6), 1222-1236.
81. Lombardo, D.; Kiselev, M. A.; Magazù, S.; Calandra, P., Amphiphiles Self-Assembly: Basic Concepts and Future Perspectives of Supramolecular Approaches. *Advances in Condensed Matter Physics* **2015**, *2015*, 151683.
82. Zhu, P.; Yan, X.; Su, Y.; Yang, Y.; Li, J., Solvent-induced structural transition of self-assembled dipeptide: from organogels to microcrystals. *Chemistry (Weinheim an der Bergstrasse, Germany)* **2010**, *16* (10), 3176-83.
83. Hu, X.; Liao, M.; Gong, H.; Zhang, L.; Cox, H.; Waigh, T. A.; Lu, J. R., Recent advances in short peptide self-assembly: from rational design to novel applications. *Curr. Opin. Colloid Interface Sci.* **2020**, *45*, 1-13.

84. Li, Y.; Cao, Y., The Physical Chemistry for the Self-assembly of Peptide Hydrogels. *Chin. J. Polym. Sci.* **2018**, *36* (3), 366-378.
85. Smith, A. M.; Williams, R. J.; Tang, C.; Coppo, P.; Collins, R. F.; Turner, M. L.; Saiani, A.; Ulijn, R. V., Fmoc-Diphenylalanine Self Assembles to a Hydrogel via a Novel Architecture Based on  $\pi$ - $\pi$  Interlocked  $\beta$ -Sheets. *Adv. Mater.* **2008**, *20* (1), 37-41.
86. Banerjee, J.; Azevedo, H. S., Crafting of functional biomaterials by directed molecular self-assembly of triple helical peptide building blocks. *Interface Focus* **2017**, *7* (6), 20160138-20160138.
87. Cejas, M. A.; Kinney, W. A.; Chen, C.; Leo, G. C.; Tounge, B. A.; Vinter, J. G.; Joshi, P. P.; Maryanoff, B. E., Collagen-Related Peptides: Self-Assembly of Short, Single Strands into a Functional Biomaterial of Micrometer Scale. *J. Am. Chem. Soc.* **2007**, *129* (8), 2202-2203.
88. Chen, C. C.; Hsu, W.; Kao, T. C.; Horng, J. C., Self-assembly of short collagen-related peptides into fibrils via cation- $\pi$  interactions. *Biochemistry* **2011**, *50* (13), 2381-3.
89. Yao, L.; He, M.; Li, D.; Tian, J.; Liu, H.; Xiao, J., Terminal aspartic acids promote the self-assembly of collagen mimic peptides into nanospheres. *RSC Adv.* **2018**, *8* (5), 2404-2409.
90. Ristroph, K. D.; Prud'homme, R. K., Hydrophobic ion pairing: encapsulating small molecules, peptides, and proteins into nanocarriers. *Nanoscale Advances* **2019**, *1* (11), 4207-4237.
91. Smiatek, J., Theoretical and Computational Insight into Solvent and Specific Ion Effects for Polyelectrolytes: The Importance of Local Molecular Interactions. *Molecules* **2020**, *25* (7), 1661.
92. Meot-Ner, M., The Ionic Hydrogen Bond. *Chem. Rev.* **2005**, *105* (1), 213-284.
93. Faul, C. F. J.; Antonietti, M., Ionic Self-Assembly: Facile Synthesis of Supramolecular Materials. *Adv. Mater.* **2003**, *15* (9), 673-683.
94. Rehm, T. H.; Schmuck, C., Ion-pair induced self-assembly in aqueous solvents. *Chem. Soc. Rev.* **2010**, *39* (10), 3597-3611.
95. O'Leary, L. E.; Fallas, J. A.; Bakota, E. L.; Kang, M. K.; Hartgerink, J. D., Multi-hierarchical self-assembly of a collagen mimetic peptide from triple helix to nanofibre and hydrogel. *Nat Chem* **2011**, *3* (10), 821-8.
96. Kaur, H.; Sharma, P.; Patel, N.; Pal, V. K.; Roy, S., Accessing Highly Tunable Nanostructured Hydrogels in a Short Ionic Complementary Peptide Sequence via pH Trigger. *Langmuir* **2020**, *36* (41), 12107-12120.
97. Caplan, M. R.; Moore, P. N.; Zhang, S.; Kamm, R. D.; Lauffenburger, D. A., Self-assembly of a beta-sheet protein governed by relief of electrostatic repulsion relative to van der Waals attraction. *Biomacromolecules* **2000**, *1* (4), 627-31.
98. 1 - The concept of self-assembling and the interactions involved. In *Controlled Drug Delivery*, Mateescu, M. A.; Ispas-Szabo, P.; Assaad, E., Eds. Woodhead Publishing: 2015; pp 1-20.
99. Xu, L.; Miao, X.; Ying, X.; Deng, W., Two-Dimensional Self-Assembled Molecular Structures Formed by the Competition of van der Waals Forces and Dipole-Dipole Interactions. *The Journal of Physical Chemistry C* **2012**, *116* (1), 1061-1069.
100. Mallamace, D.; Fazio, E.; Mallamace, F.; Corsaro, C., The Role of Hydrogen Bonding in the Folding/Unfolding Process of Hydrated Lysozyme: A Review of Recent NMR and FTIR Results. *International journal of molecular sciences* **2018**, *19* (12), 3825.
101. Liu, Y.; Zhang, L.; Wei, W., Effect of noncovalent interaction on the self-assembly of a designed peptide and its potential use as a carrier for controlled bFGF release. *International journal of nanomedicine* **2017**, *12*, 659-670.
102. Gelain, F.; Luo, Z.; Rioult, M.; Zhang, S., Self-assembling peptide scaffolds in the clinic. *npj Regenerative Medicine* **2021**, *6* (1), 9.
103. Hartgerink, J. D.; Beniash, E.; Stupp, S. I., Peptide-amphiphile nanofibers: A versatile scaffold for the preparation of self-assembling materials. **2002**, *99* (8), 5133-5138.

104. He, B.; Yuan, X.; Zhou, A.; Zhang, H.; Jiang, D., Designer functionalised self-assembling peptide nanofibre scaffolds for cartilage tissue engineering. *Expert Reviews in Molecular Medicine* **2014**, *16*, e12.
105. Moore, A. N.; Hartgerink, J. D., Self-Assembling Multidomain Peptide Nanofibers for Delivery of Bioactive Molecules and Tissue Regeneration. *Acc. Chem. Res.* **2017**, *50* (4), 714-722.
106. Najafi, H.; Jafari, M.; Farahavar, G.; Abolmaali, S. S.; Azarpira, N.; Borandeh, S.; Ravanfar, R., Recent advances in design and applications of biomimetic self-assembled peptide hydrogels for hard tissue regeneration. *Bio-Design and Manufacturing* **2021**, *4* (4), 735-756.
107. Qiu, F.; Chen, Y.; Tang, C.; Zhao, X., Amphiphilic peptides as novel nanomaterials: design, self-assembly and application. *International journal of nanomedicine* **2018**, *13*, 5003-5022.
108. Chan, K. H.; Xue, B.; Robinson, R. C.; Hauser, C. A. E., Systematic Moiety Variations of Ultrashort Peptides Produce Profound Effects on Self-Assembly, Nanostructure Formation, Hydrogelation, and Phase Transition. *Scientific Reports* **2017**, *7* (1), 12897.
109. Cui, H.; Webber, M. J.; Stupp, S. I., Self-assembly of peptide amphiphiles: from molecules to nanostructures to biomaterials. *Biopolymers* **2010**, *94* (1), 1-18.
110. Goldberg, M.; Langer, R.; Jia, X., Nanostructured materials for applications in drug delivery and tissue engineering. *J Biomater Sci Polym Ed* **2007**, *18* (3), 241-268.
111. Malhotra, B. D.; Ali, M. A., Nanomaterials in Biosensors: Fundamentals and Applications. *Nanomaterials for Biosensors* **2018**, 1-74.
112. Guimard, N. K. E.; Sessler, J. L.; Schmidt, C. E., Towards a Biocompatible, Biodegradable Copolymer Incorporating Electroactive Oligothiophene Units. *Macromolecules* **2009**, *42* (2), 502-511.
113. Tanaka, M.; Sato, K.; Kitakami, E.; Kobayashi, S.; Hoshiba, T.; Fukushima, K., Design of biocompatible and biodegradable polymers based on intermediate water concept. *Polym. J.* **2015**, *47* (2), 114-121.
114. Hendricks, M. P.; Sato, K.; Palmer, L. C.; Stupp, S. I., Supramolecular Assembly of Peptide Amphiphiles. *Acc. Chem. Res.* **2017**, *50* (10), 2440-2448.
115. Hartgerink, J. D.; Beniash, E.; Stupp, S. I., Self-assembly and mineralization of peptide-amphiphile nanofibers. *Science* **2001**, *294* (5547), 1684-8.
116. Bilardo, R.; Traldi, F.; Vdovchenko, A.; Resmini, M., Influence of surface chemistry and morphology of nanoparticles on protein corona formation. *Wiley Interdiscip. Rev. Nanomed. Nanobiotechnol.* **2022**, e1788.
117. Han, S.; Kim, D.; Han, S.-h.; Kim, N. H.; Kim, S. H.; Lim, Y.-b., Structural and Conformational Dynamics of Self-Assembling Bioactive  $\beta$ -Sheet Peptide Nanostructures Decorated with Multivalent RNA-Binding Peptides. *J. Am. Chem. Soc.* **2012**, *134* (38), 16047-16053.
118. Gao, D.; Guo, X.; Zhang, X.; Chen, S.; Wang, Y.; Chen, T.; Huang, G.; Gao, Y.; Tian, Z.; Yang, Z., Multifunctional phototheranostic nanomedicine for cancer imaging and treatment. *Materials Today Bio* **2020**, *5*, 100035.
119. Senapati, S.; Mahanta, A. K.; Kumar, S.; Maiti, P., Controlled drug delivery vehicles for cancer treatment and their performance. *Signal Transduct Target Ther* **2018**, *3*, 7-7.
120. Soukasene, S.; Toft, D. J.; Moyer, T. J.; Lu, H.; Lee, H.-K.; Standley, S. M.; Cryns, V. L.; Stupp, S. I., Antitumor activity of peptide amphiphile nanofiber-encapsulated camptothecin. *ACS nano* **2011**, *5* (11), 9113-9121.
121. Habibi, N.; Kamaly, N.; Memic, A.; Shafiee, H., Self-assembled peptide-based nanostructures: Smart nanomaterials toward targeted drug delivery. *Nano Today* **2016**, *11* (1), 41-60.
122. Dehsorkhi, A.; Castelletto, V.; Hamley, I. W., Self-assembling amphiphilic peptides. *Journal of peptide science : an official publication of the European Peptide Society* **2014**, *20* (7), 453-467.
123. Stüber, W.; Knolle, J.; Breipohl, G., Synthesis of peptide amides by Fmoc-solid-phase peptide synthesis and acid labile anchor groups. *Int. J. Pept. Protein Res.* **1989**, *34* (3), 215-21.

124. Singh, N.; Kumar, M.; Miravet, J. F.; Ulijn, R. V.; Escuder, B., Peptide-Based Molecular Hydrogels as Supramolecular Protein Mimics. *2017*, *23* (5), 981-993.
125. Li, L.; Xie, L.; Zheng, R.; Sun, R., Self-Assembly Dipeptide Hydrogel: The Structures and Properties. *Front Chem* **2021**, *9*, 739791-739791.
126. Acar, H.; Srivastava, S.; Chung, E. J.; Schnorenberg, M. R.; Barrett, J. C.; LaBelle, J. L.; Tirrell, M., Self-assembling peptide-based building blocks in medical applications. *Adv Drug Deliv Rev* **2017**, *110-111*, 65-79.
127. Jain, R.; Roy, S., Designing a bioactive scaffold from coassembled collagen–laminin short peptide hydrogels for controlling cell behaviour. *RSC Adv.* **2019**, *9* (66), 38745-38759.
128. Kaur, H.; Roy, S., Designing aromatic N-cadherin mimetic short-peptide-based bioactive scaffolds for controlling cellular behaviour. *J. Mater. Chem. B* **2021**, *9* (29), 5898-5913.
129. Zhou, H.-X.; Pang, X., Electrostatic Interactions in Protein Structure, Folding, Binding, and Condensation. *Chem. Rev.* **2018**, *118* (4), 1691-1741.
130. Zhang, S.; Lockshin, C.; Cook, R.; Rich, A., Unusually stable beta-sheet formation in an ionic self-complementary oligopeptide. *Biopolymers* **1994**, *34* (5), 663-72.
131. Sun, Y.; Li, W.; Wu, X.; Zhang, N.; Zhang, Y.; Ouyang, S.; Song, X.; Fang, X.; Seeram, R.; Xue, W.; He, L.; Wu, W., Functional Self-Assembling Peptide Nanofiber Hydrogels Designed for Nerve Degeneration. *ACS Appl. Mater. Interfaces* **2016**, *8* (3), 2348-2359.
132. Karavasili, C.; Panteris, E.; Vizirianakis, I. S.; Koutsopoulos, S.; Fatouros, D. G., Chemotherapeutic Delivery from a Self-Assembling Peptide Nanofiber Hydrogel for the Management of Glioblastoma. *Pharm. Res.* **2018**, *35* (8), 166.
133. Chagri, S.; Ng, D. Y. W.; Weil, T., Designing bioresponsive nanomaterials for intracellular self-assembly. *Nat. Rev. Chem.* **2022**, *6*(5), 320-338.
134. Chen, J.; Zou, X., Self-assemble peptide biomaterials and their biomedical applications. *Bioact. Mater.* **2019**, *4*, 120-131.
135. Lee, S.; Trinh, T. H. T.; Yoo, M.; Shin, J.; Lee, H.; Kim, J.; Hwang, E.; Lim, Y.-B.; Ryou, C., Self-Assembling Peptides and Their Application in the Treatment of Diseases. *International journal of molecular sciences* **2019**, *20* (23), 5850.
136. Yang, Z.; Liang, G.; Ma, M.; Gao, Y.; Xu, B., Conjugates of naphthalene and dipeptides produce molecular hydrogelators with high efficiency of hydrogelation and superhelical nanofibers. *J. Mater. Chem.* **2007**, *17* (9), 850-854.
137. Adams, D. J.; Butler, M. F.; Frith, W. J.; Kirkland, M.; Mullen, L.; Sanderson, P., A new method for maintaining homogeneity during liquid–hydrogel transitions using low molecular weight hydrogelators. *Soft Matter* **2009**, *5* (9), 1856-1862.
138. Lim, J. Y. C.; Lin, Q.; Xue, K.; Loh, X. J., Recent advances in supramolecular hydrogels for biomedical applications. *Materials Today Advances* **2019**, *3*, 100021.
139. Pal, V. K.; Roy, S., Cooperative Metal Ion Coordination to the Short Self-Assembling Peptide Promotes Hydrogelation and Cellular Proliferation. *Macromolecular Bioscience* **2022**, 2100462.
140. Sharma, P.; Kaur, H.; Roy, S., Inducing Differential Self-Assembling Behavior in Ultrashort Peptide Hydrogelators Using Simple Metal Salts. *Biomacromolecules* **2019**, *20* (7), 2610-2624.
141. Cardoso, A. Z.; Mears, L. L. E.; Cattoz, B. N.; Griffiths, P. C.; Schweins, R.; Adams, D. J., Linking micellar structures to hydrogelation for salt-triggered dipeptide gelators. *Soft Matter* **2016**, *12* (15), 3612-3621.
142. Chen, L.; McDonald, T. O.; Adams, D. J., Salt-induced hydrogels from functionalised-dipeptides. *RSC Adv.* **2013**, *3* (23), 8714-8720.
143. Parmar, A. S.; Xu, F.; Pike, D. H.; Belure, S. V.; Hasan, N. F.; Drzewiecki, K. E.; Shreiber, D. I.; Nanda, V., Metal Stabilization of Collagen and de Novo Designed Mimetic Peptides. *Biochemistry* **2015**, *54* (32), 4987-4997.
144. Toksoz, S.; Mammadov, R.; Tekinay, A. B.; Guler, M. O., Electrostatic effects on nanofiber formation of self-assembling peptide amphiphiles. *J. Colloid Interface Sci.* **2011**, *356* (1), 131-7.

145. Williams, R. J.; Mart, R. J.; Ulijn, R. V., Exploiting biocatalysis in peptide self-assembly. *Biopolymers* **2010**, *94* (1), 107-117.
146. Ulijn, R. V., Enzyme-responsive materials: a new class of smart biomaterials. *J. Mater. Chem.* **2006**, *16* (23), 2217-2225.
147. Adler-Abramovich, L.; Perry, R.; Sagi, A.; Gazit, E.; Shabat, D., Controlled assembly of peptide nanotubes triggered by enzymatic activation of self-immolative dendrimers. *Chembiochem : a European journal of chemical biology* **2007**, *8* (8), 859-62.
148. Yang, Z.; Liang, G.; Xu, B., Enzymatic Hydrogelation of Small Molecules. *Acc. Chem. Res.* **2008**, *41* (2), 315-326.
149. Yang, Z.; Xu, B., A simple visual assay based on small molecule hydrogels for detecting inhibitors of enzymes. *Chem. Commun.* **2004**, (21), 2424-2425.
150. Yang, Z.; Gu, H.; Fu, D.; Gao, P.; Lam, J. K.; Xu, B., Enzymatic Formation of Supramolecular Hydrogels. *Adv. Mater.* **2004**, *16* (16), 1440-1444.
151. Yang, Z.; Liang, G.; Ma, M.; Gao, Y.; Xu, B., In vitro and in vivo enzymatic formation of supramolecular hydrogels based on self-assembled nanofibers of a beta-amino acid derivative. *Small (Weinheim an der Bergstrasse, Germany)* **2007**, *3* (4), 558-62.
152. Zhou, J.; Xu, B., Enzyme-Instructioned Self-Assembly: A Multistep Process for Potential Cancer Therapy. *Bioconjug Chem.* **2015**, *26* (6), 987-999.
153. Yang, Z.; Liang, G.; Guo, Z.; Guo, Z.; Xu, B., Intracellular Hydrogelation of Small Molecules Inhibits Bacterial Growth. *Angew. Chem. Int. Ed.* **2007**, *46* (43), 8216-8219.
154. Hirst, A. R.; Roy, S.; Arora, M.; Das, A. K.; Hodson, N.; Murray, P.; Marshall, S.; Javid, N.; Sefcik, J.; Boekhoven, J.; van Esch, J. H.; Santabarbara, S.; Hunt, N. T.; Ulijn, R. V., Biocatalytic induction of supramolecular order. *Nat Chem* **2010**, *2* (12), 1089-94.
155. Gao, Y.; Shi, J.; Yuan, D.; Xu, B., Imaging enzyme-triggered self-assembly of small molecules inside live cells. *Nat. Commun.* **2012**, *3* (1), 1033.
156. Hsu, J. Y.; McKeon, R.; Goussev, S.; Werb, Z.; Lee, J. U.; Trivedi, A.; Noble-Haeusslein, L. J., Matrix metalloproteinase-2 facilitates wound healing events that promote functional recovery after spinal cord injury. *J. Neurosci.* **2006**, *26* (39), 9841-50.
157. Li, T.; Lu, X.-M.; Zhang, M.-R.; Hu, K.; Li, Z., Peptide-based nanomaterials: Self-assembly, properties and applications. *Bioact. Mater.* **2022**, *11*, 268-282.
158. Wang, G.; Zhang, J., Photoresponsive molecular switches for biotechnology. *Journal of Photochemistry and Photobiology C: Photochemistry Reviews* **2012**, *13* (4), 299-309.
159. Muraoka, T.; Koh, C. Y.; Cui, H.; Stupp, S. I., Light-triggered bioactivity in three dimensions. *Angew. Chem. Int. Ed. Engl.* **2009**, *48* (32), 5946-9.
160. Draper, E. R.; McDonald, T. O.; Adams, D. J., Photodimerisation of a coumarin-dipeptide gelator. *Chem. Commun.* **2015**, *51* (64), 12827-12830.
161. Raeburn, J.; McDonald, T. O.; Adams, D. J., Dipeptide hydrogelation triggered via ultraviolet light. *Chem. Commun.* **2012**, *48* (75), 9355-9357.
162. Huang, Y.; Qiu, Z.; Xu, Y.; Shi, J.; Lin, H.; Zhang, Y., Supramolecular hydrogels based on short peptides linked with conformational switch. *Org. Biomol. Chem.* **2011**, *9* (7), 2149-2155.
163. Kim, H. W.; Yang, K.; Jeong, W. J.; Choi, S. J.; Lee, J. S.; Cho, A. N.; Chang, G. E.; Cheong, E.; Cho, S. W.; Lim, Y. B., Photoactivation of Noncovalently Assembled Peptide Ligands on Carbon Nanotubes Enables the Dynamic Regulation of Stem Cell Differentiation. *ACS Appl Mater Interfaces* **2016**, *8* (40), 26470-26481.
164. Draper, E. R.; Adams, D. J., Low-Molecular-Weight Gels: The State of the Art. *Chem* **2017**, *3* (3), 390-410.
165. Bernhard, S.; Tibbitt, M. W., Supramolecular engineering of hydrogels for drug delivery. *Adv Drug Deliv Rev* **2021**, *171*, 240-256.
166. Sarma, R.; Wong, K.-Y.; Lynch, G. C.; Pettitt, B. M., Peptide Solubility Limits: Backbone and Side-Chain Interactions. *The journal of physical chemistry. B* **2018**, *122* (13), 3528-3539.
167. Karoyo, A. H.; Wilson, L. D., A Review on the Design and Hydration Properties of Natural Polymer-Based Hydrogels. *Materials (Basel)* **2021**, *14* (5), 1095.

168. Kaur, H.; Jain, R.; Roy, S., Pathway-Dependent Preferential Selection and Amplification of Variable Self-Assembled Peptide Nanostructures and Their Biological Activities. *ACS Appl. Mater. Interfaces* **2020**, *12* (47), 52445-52456.
169. Debnath, S.; Roy, S.; Abul-Haija, Y. M.; Frederix, P. W. J. M.; Ramalheite, S. M.; Hirst, A. R.; Javid, N.; Hunt, N. T.; Kelly, S. M.; Angulo, J.; Khimyak, Y. Z.; Ulijn, R. V., Tunable Supramolecular Gel Properties by Varying Thermal History. *Chem. Eur. J.* **2019**, *25* (33), 7881-7887.
170. Ciferri, A., Molecular recognition mechanisms directing the self-assembly of biological structures. *Soft Matter* **2020**, *16* (39), 8985-8995.
171. Chung, W. J.; Sena, M.; Merzlyak, A.; Lee, S. W., 2.206 - Phages as Tools for Functional Nanomaterials Development. In *Comprehensive Biomaterials*, Ducheyne, P., Ed. Elsevier: Oxford, 2011; pp 95-111.
172. Joseph, J. P.; Singh, A.; Gupta, D.; Miglani, C.; Pal, A., Tandem Interplay of the Host-Guest Interaction and Photoresponsive Supramolecular Polymerization to 1D and 2D Functional Peptide Materials. *ACS Appl. Mater. Interfaces* **2019**, *11* (31), 28213-28220.
173. Redondo-Gómez, C.; Abdouni, Y.; Becer, C. R.; Mata, A., Self-Assembling Hydrogels Based on a Complementary Host-Guest Peptide Amphiphile Pair. *Biomacromolecules* **2019**, *20* (6), 2276-2285.
174. Redondo-Gómez, C.; Padilla-Lopátegui, S.; Mata, A.; Azevedo, H. S., Peptide Amphiphile Hydrogels Based on Homoternary Cucurbit[8]uril Host-Guest Complexes. *Bioconj Chem* **2022**, *33* (1), 111-120.
175. Xie, X.; Gao, B.; Ma, Z.; Liu, J.; Zhang, J.; Liang, J.; Chen, Z.; Wu, L.; Li, W., Host-Guest Interaction Driven Peptide Assembly into Photoresponsive Two-Dimensional Nanosheets with Switchable Antibacterial Activity. *Chinese Chemical Society Chemistry* **2021**, *3* (7), 1949-1962.
176. Ma, X.; Zhao, Y., Biomedical Applications of Supramolecular Systems Based on Host-Guest Interactions. *Chem. Rev.* **2015**, *115* (15), 7794-7839.
177. Zhu, H.; Wang, H.; Shi, B.; Shangguan, L.; Tong, W.; Yu, G.; Mao, Z.; Huang, F., Supramolecular peptide constructed by molecular Lego allowing programmable self-assembly for photodynamic therapy. *Nat. Commun.* **2019**, *10* (1), 2412.
178. Chen, L.; Raeburn, J.; Sutton, S.; Spiller, D. G.; Williams, J.; Sharp, J. S.; Griffiths, P. C.; Heenan, R. K.; King, S. M.; Paul, A.; Fuzeland, S.; Atkins, D.; Adams, D. J., Tuneable mechanical properties in low molecular weight gels. *Soft Matter* **2011**, *7* (20), 9721-9727.
179. Jain, R.; Roy, S., Tuning the gelation behavior of short laminin derived peptides via solvent mediated self-assembly. *Materials Science and Engineering: C* **2020**, *108*, 110483.
180. Ghosh, S.; Verma, S., Solvent-mediated morphological transformations in peptide-based soft structures. *Tetrahedron* **2008**, *64* (27), 6202-6208.
181. Raeburn, J.; Mendoza-Cuenca, C.; Cattoz, B. N.; Little, M. A.; Terry, A. E.; Zamith Cardoso, A.; Griffiths, P. C.; Adams, D. J., The effect of solvent choice on the gelation and final hydrogel properties of Fmoc-diphenylalanine. *Soft Matter* **2015**, *11* (5), 927-935.
182. Raeburn, J.; Pont, G.; Chen, L.; Cesbron, Y.; Lévy, R.; Adams, D. J., Fmoc-diphenylalanine hydrogels: understanding the variability in reported mechanical properties. *Soft Matter* **2012**, *8* (4), 1168-1174.
183. Ulijn, R. V.; Smith, A. M., Designing peptide based nanomaterials. *Chem. Soc. Rev.* **2008**, *37* (4), 664-675.
184. Papapostolou, D.; Smith, A. M.; Atkins, E. D. T.; Oliver, S. J.; Ryadnov, M. G.; Serpell, L. C.; Woolfson, D. N., Engineering nanoscale order into a designed protein fiber. *Proc Natl Acad Sci U S A* **2007**, *104* (26), 10853-10858.
185. Walshaw, J.; Woolfson, D. N., Open-and-shut cases in coiled-coil assembly: alpha-sheets and alpha-cylinders. *Protein Sci.* **2001**, *10* (3), 668-73.
186. Pauling, L.; Corey, R. B., Configurations of Polypeptide Chains With Favored Orientations Around Single Bonds: Two New Pleated Sheets. *Proc Natl Acad Sci U S A* **1951**, *37* (11), 729-740.
187. Khakshoor, O.; Nowick, J. S., Artificial beta-sheets: chemical models of beta-sheets. *Curr. Opin. Chem. Biol.* **2008**, *12* (6), 722-9.

188. Zhang, S.; Holmes, T.; Lockshin, C.; Rich, A., Spontaneous assembly of a self-complementary oligopeptide to form a stable macroscopic membrane. *Proc Natl Acad Sci U S A* **1993**, *90* (8), 3334-3338.
189. Zhang, S., Fabrication of novel biomaterials through molecular self-assembly. *Nat. Biotechnol.* **2003**, *21* (10), 1171-1178.
190. Chan, K. H.; Lee, W. H.; Ni, M.; Loo, Y.; Hauser, C. A. E., C-Terminal Residue of Ultrashort Peptides Impacts on Molecular Self-Assembly, Hydrogelation, and Interaction with Small-Molecule Drugs. *Scientific Reports* **2018**, *8* (1), 17127.
191. Rughani, R. V.; Schneider, J. P., Molecular Design of beta-Hairpin Peptides for Material Construction. *MRS Bull.* **2008**, *33* (5), 530-535.
192. Worthington, P.; Langhans, S.; Pochan, D.,  $\beta$ -hairpin peptide hydrogels for package delivery. *Adv Drug Deliv Rev* **2017**, *110-111*, 127-136.
193. Schneider, J. P.; Pochan, D. J.; Ozbas, B.; Rajagopal, K.; Pakstis, L.; Kretsinger, J., Responsive Hydrogels from the Intramolecular Folding and Self-Assembly of a Designed Peptide. *J. Am. Chem. Soc.* **2002**, *124* (50), 15030-15037.
194. Ozbas, B.; Kretsinger, J.; Rajagopal, K.; Schneider, J. P.; Pochan, D. J., Salt-Triggered Peptide Folding and Consequent Self-Assembly into Hydrogels with Tunable Modulus. *Macromolecules* **2004**, *37* (19), 7331-7337.
195. Lindsey, S.; Piatt, J. H.; Worthington, P.; Sönmez, C.; Satheye, S.; Schneider, J. P.; Pochan, D. J.; Langhans, S. A., Beta Hairpin Peptide Hydrogels as an Injectable Solid Vehicle for Neurotrophic Growth Factor Delivery. *Biomacromolecules* **2015**, *16* (9), 2672-83.
196. Haines-Butterick, L.; Rajagopal, K.; Branco, M.; Salick, D.; Rughani, R.; Pilarz, M.; Lamm, M. S.; Pochan, D. J.; Schneider, J. P., Controlling hydrogelation kinetics by peptide design for three-dimensional encapsulation and injectable delivery of cells. *Proc Natl Acad Sci U S A* **2007**, *104* (19), 7791-7796.
197. Chan, B. P.; Leong, K. W., Scaffolding in tissue engineering: general approaches and tissue-specific considerations. *Eur Spine J* **2008**, *17 Suppl 4* (Suppl 4), 467-479.
198. Shigemitsu, H.; Hamachi, I., Design Strategies of Stimuli-Responsive Supramolecular Hydrogels Relying on Structural Analyses and Cell-Mimicking Approaches. *Acc. Chem. Res.* **2017**, *50* (4), 740-750.
199. Falcone, N.; Shao, T.; Andoy, N. M. O.; Rashid, R.; Sullan, R. M. A.; Sun, X.; Kraatz, H.-B., Multi-component peptide hydrogels – a systematic study incorporating biomolecules for the exploration of diverse, tuneable biomaterials. *Biomater. Sci.* **2020**, *8* (20), 5601-5614.
200. Okesola, B. O.; Mata, A., Multicomponent self-assembly as a tool to harness new properties from peptides and proteins in material design. *Chem. Soc. Rev.* **2018**, *47* (10), 3721-3736.
201. Liao, S. W.; Yu, T.-B.; Guan, Z., De Novo Design of Saccharide–Peptide Hydrogels as Synthetic Scaffolds for Tailored Cell Responses. *J. Am. Chem. Soc.* **2009**, *131* (48), 17638-17646.
202. Ehrbar, M.; Rizzi, S. C.; Schoenmakers, R. G.; Miguel, B. S.; Hubbell, J. A.; Weber, F. E.; Lutolf, M. P., Biomolecular hydrogels formed and degraded via site-specific enzymatic reactions. *Biomacromolecules* **2007**, *8* (10), 3000-7.
203. Liu, J.; Sun, Z.; Yuan, Y.; Tian, X.; Liu, X.; Duan, G.; Yang, Y.; Yuan, L.; Lin, H.-C.; Li, X., Peptide Glycosylation Generates Supramolecular Assemblies from Glycopeptides as Biomimetic Scaffolds for Cell Adhesion and Proliferation. *ACS Appl. Mater. Interfaces* **2016**, *8* (11), 6917-6924.
204. Fernández-Muñoz, T.; Recha-Sancho, L.; López-Chicón, P.; Castells-Sala, C.; Mata, A.; Semino, C. E., Bimolecular based heparin and self-assembling hydrogel for tissue engineering applications. *Acta Biomater* **2015**, *16*, 35-48.
205. Pal, V. K.; Jain, R.; Sen, S.; Kailasam, K.; Roy, S., Designing nanofibrillar cellulose peptide conjugated polymeric hydrogel scaffold for controlling cellular behaviour. *Cellulose* **2021**, *28* (16), 10335-10357.
206. Wilk, S.; Benko, A., Advances in Fabricating the Electrospun Biopolymer-Based Biomaterials. *J Funct Biomater* **2021**, *12* (2), 26.

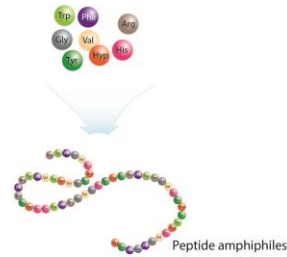
207. Yu, S. M.; Li, Y.; Kim, D., Collagen Mimetic Peptides: Progress Towards Functional Applications. *Soft matter* **2011**, 7 (18), 7927-7938.
208. Luo, T.; Kiick, K. L., Collagen-Like Peptide Bioconjugates. *Bioconjug Chem.* **2017**, 28 (3), 816-827.
209. Shoulders, M. D.; Raines, R. T., Collagen Structure and Stability. **2009**, 78 (1), 929-958.
210. Koch, M.; Foley, J. E.; Hahn, R.; Zhou, P.; Burgeson, R. E.; Gerecke, D. R.; Gordon, M. K., alpha 1(Xx) collagen, a new member of the collagen subfamily, fibril-associated collagens with interrupted triple helices. *J. Biol. Chem.* **2001**, 276 (25), 23120-6.
211. Robertson, A. M.; Watton, P. N., Chapter 8 - Mechanobiology of the Arterial Wall. In *Transport in Biological Media*, Becker, S. M.; Kuznetsov, A. V., Eds. Elsevier: Boston, 2013; pp 275-347.
212. Blum, K. M.; Novak, T.; Watkins, L.; Neu, C. P.; Wallace, J. M.; Bart, Z. R.; Voytik-Harbin, S. L., Acellular and cellular high-density, collagen-fibril constructs with suprafibrillar organization. *Biomater. Sci.* **2016**, 4 (4), 711-723.
213. Strauss, K.; Chmielewski, J., Advances in the design and higher-order assembly of collagen mimetic peptides for regenerative medicine. *Curr. Opin. Biotechnol.* **2017**, 46, 34-41.
214. Berisio, R.; Vitagliano, L.; Mazzarella, L.; Zagari, A., Crystal structure of the collagen triple helix model [(Pro-Pro-Gly)(10)](3). *Protein Sci.* **2002**, 11 (2), 262-70.
215. Ramshaw, J. A.; Shah, N. K.; Brodsky, B., Gly-X-Y tripeptide frequencies in collagen: a context for host-guest triple-helical peptides. *J Struct Biol* **1998**, 122 (1-2), 86-91.
216. Jones, E. Y.; Miller, A., Analysis of structural design features in collagen. *J. Mol. Biol.* **1991**, 218 (1), 209-19.
217. Persikov, A. V.; Ramshaw, J. A. M.; Brodsky, B., Collagen model peptides: Sequence dependence of triple-helix stability. **2000**, 55 (6), 436-450.
218. Rich, A.; Crick, F. H., The molecular structure of collagen. *J. Mol. Biol.* **1961**, 3, 483-506.
219. Thiagarajan, G.; Li, Y.; Mohs, A.; Strafacci, C.; Popiel, M.; Baum, J.; Brodsky, B., Common Interruptions in the Repeating Tripeptide Sequence of Non-fibrillar Collagens: Sequence Analysis and Structural Studies on Triple-helix Peptide Models. *J. Mol. Biol.* **2008**, 376 (3), 736-748.
220. Bhowmick, M.; Fields, G. B., Stabilization of collagen-model, triple-helical peptides for in vitro and in vivo applications. *Methods in molecular biology (Clifton, N.J.)* **2013**, 1081, 167-94.
221. Mouw, J. K.; Ou, G.; Weaver, V. M., Extracellular matrix assembly: a multiscale deconstruction. *Nature Reviews Molecular Cell Biology* **2014**, 15 (12), 771-785.
222. Fidler, A. L.; Boudko, S. P.; Rokas, A.; Hudson, B. G., The triple helix of collagens – an ancient protein structure that enabled animal multicellularity and tissue evolution. **2018**, 131 (7), jcs203950.
223. Gautieri, A.; Vesentini, S.; Redaelli, A.; Buehler, M. J., Hierarchical structure and nanomechanics of collagen microfibrils from the atomistic scale up. *Nano Lett.* **2011**, 11 (2), 757-66.
224. Chow, W. Y.; Forman, C. J.; Bihan, D.; Puzskarska, A. M.; Rajan, R.; Reid, D. G.; Slatter, D. A.; Colwell, L. J.; Wales, D. J.; Farndale, R. W.; Duer, M. J., Proline provides site-specific flexibility for in vivo collagen. *Scientific Reports* **2018**, 8 (1), 13809.
225. Krane, S. M., The importance of proline residues in the structure, stability and susceptibility to proteolytic degradation of collagens. *Amino Acids* **2008**, 35 (4), 703.
226. Melton, S. D.; Brackhahn, E. A. E.; Orlin, S. J.; Jin, P.; Chenoweth, D. M., Rules for the design of aza-glycine stabilized triple-helical collagen peptides. *Chem. Sci.* **2020**, 11 (39), 10638-10646.
227. Cowan, P. M.; McGavin, S.; North, A. C., The polypeptide chain configuration of collagen. *Nature* **1955**, 176 (4492), 1062-4.
228. Ramachandran, G. N.; Kartha, G., Structure of Collagen. *Nature* **1955**, 176 (4482), 593-595.
229. Rich, A.; Crick, F. H., The structure of collagen. *Nature* **1955**, 176 (4489), 915-6.

230. Russell, L. E.; Fallas, J. A.; Hartgerink, J. D., Selective assembly of a high stability AAB collagen heterotrimer. *J. Am. Chem. Soc.* **2010**, *132* (10), 3242-3.
231. Bhowmick, M.; Fields, G. B., Stabilization of collagen-model, triple-helical peptides for in vitro and in vivo applications. *Methods in molecular biology (Clifton, N.J.)* **2013**, *1081*, 167-194.
232. Tanrikulu, I. C.; Westler, W. M.; Ellison, A. J.; Markley, J. L.; Raines, R. T., Templated Collagen “Double Helices” Maintain Their Structure. *J. Am. Chem. Soc.* **2020**, *142* (3), 1137-1141.
233. Chen, E. A.; Lin, Y.-S., Using synthetic peptides and recombinant collagen to understand DDR–collagen interactions. *Biochimica et Biophysica Acta (BBA) - Molecular Cell Research* **2019**, *1866* (11), 118458.
234. Li, Y.; Mo, X.; Kim, D.; Yu, S. M., Template-tethered collagen mimetic peptides for studying heterotrimeric triple-helical interactions. *Biopolymers* **2011**, *95* (2), 94-104.
235. O’Leary, L. E. R.; Fallas, J. A.; Hartgerink, J. D., Positive and Negative Design Leads to Compositional Control in AAB Collagen Heterotrimers. *J. Am. Chem. Soc.* **2011**, *133* (14), 5432-5443.
236. Gelse, K.; Pöschl, E.; Aigner, T., Collagens--structure, function, and biosynthesis. *Adv Drug Deliv Rev* **2003**, *55* (12), 1531-46.
237. Fallas, J. A.; O’Leary, L. E. R.; Hartgerink, J. D., Synthetic collagen mimics: self-assembly of homotrimers, heterotrimers and higher order structures. *Chem. Soc. Rev.* **2010**, *39* (9), 3510-3527.
238. Li, Y.; Foss, C. A.; Summerfield, D. D.; Doyle, J. J.; Torok, C. M.; Dietz, H. C.; Pomper, M. G.; Yu, S. M., Targeting collagen strands by photo-triggered triple-helix hybridization. **2012**, *109* (37), 14767-14772.
239. Wang, A. Y.; Mo, X.; Chen, C. S.; Yu, S. M., Facile Modification of Collagen Directed by Collagen Mimetic Peptides. *J. Am. Chem. Soc.* **2005**, *127* (12), 4130-4131.
240. Persikov, A. V.; Ramshaw, J. A. M.; Brodsky, B., Prediction of Collagen Stability from Amino Acid Sequence\*. *J. Biol. Chem.* **2005**, *280* (19), 19343-19349.
241. Fawzi, N. L.; Yap, E.-H.; Okabe, Y.; Kohlstedt, K. L.; Brown, S. P.; Head-Gordon, T., Contrasting disease and nondisease protein aggregation by molecular simulation. *Acc. Chem. Res.* **2008**, *41* (8), 1037-1047.
242. Walker, D. R.; Hulan, S. A. H.; Peterson, C. M.; Li, I. C.; Gonzalez, K. J.; Hartgerink, J. D., Predicting the stability of homotrimeric and heterotrimeric collagen helices. *Nat Chem* **2021**, *13* (3), 260-269.
243. Jalan, A. A.; Jochim, K. A.; Hartgerink, J. D., Rational Design of a Non-canonical “Sticky-Ended” Collagen Triple Helix. *J. Am. Chem. Soc.* **2014**, *136* (21), 7535-7538.

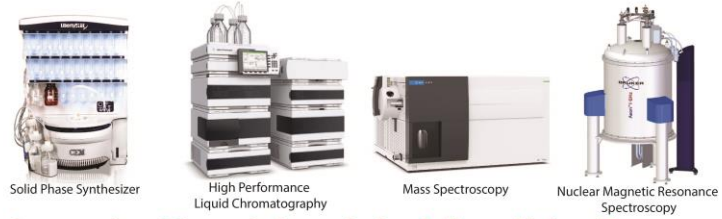
# **Chapter 2**

## **Materials and methodology**





**Design, synthesis and purification of peptide**



**Spectroscopic and Microscopic characterization of self-assembled peptide nanostructures**



**Synthetic scaffolds for controlling cellular behaviour**





## 2.1 Introduction

In this chapter, we aim to provide the detailed list of chemicals required for the synthesis of the peptide and their multiscale self-assembly, instrumentation techniques required to characterize the self-assembled nanostructures and protocols used to carry out the experiments as discussed in the thesis. The experimental work that flows in all the projects follows a similar pattern, which can be divided as mentioned below:

1. Design, synthesis and characterization of the bioinspired peptide building block.
2. Self-assembly of peptide monomers in presence of external stimuli.
3. Multiscale self-assembly strategy to create peptide-peptide or sugar-peptide conjugate based functional nanostructures.
4. Spectroscopic and microscopic characterization of the self-assembled peptide hydrogels and their biomolecular conjugates.
5. Assessment of biological response towards the developed matrix and their therapeutic applications.

All the experiments and assays involve different instrumentations. This chapter also covers the basic principle of these instruments and the protocols used in order to characterize the structural and functional features of the developed biomaterial.

## 2.2 Materials

All the chemicals used in this research work are of high purity (>99% or more). All the chemicals required for solid phase peptide synthesis, that include Fmoc-protected amino acids, oxyma base, diisopropylcarbodiimide (DIC), Rink amide MBHA resin, piperazine, anisole, 1,2-ethanedithiol (EDT), thioanisole were purchased from Sigma-Aldrich. Trifluoroacetic acid (TFA), dichloromethane (DCM), dimethylformamide (DMF), diethyl ether, sodium hypochlorite (14%) was purchased from Merck. Sodium hydroxide pellets, Magnesium sulphate ( $\text{MgSO}_4 \cdot 7\text{H}_2\text{O}$ ), Calcium chloride ( $\text{CaCl}_2 \cdot 2\text{H}_2\text{O}$ ), Sodium phosphate dibasic ( $\text{Na}_2\text{HPO}_4$ ) were purchased from HiMedia. The soft wood cellulose pulp was procured from a sanitary napkin making private company (Asian Agencies [Bestie] Pvt. Ltd. Bangalore, INDIA). All the cell culture medium used for culturing different types of cells, Fatal Bovine Serum (FBS), Trypsin-EDTA solution, Pen-Strep antibiotic solution, Dimethyl sulphoxide (cell culture grade),

1X phosphate buffered saline, formaldehyde, MTT (3-(4,5-Dimethyl-2-thiazolyl)-2,5-diphenyltetrazolium bromide), Thioflavin T, Congo Red, Alamar Blue, DAPI (4',6-diamidino-2-phenylindole), FDA (fluorescein diacetate), PI (propidium iodide), DiOC<sub>18</sub>(3) (3,3-dipropylloxycarbocyanine iodide) were purchased from HiMedia. Live-Dead BacLight bacterial viability kit (L13152, Thermo fisher scientific), rabbit monoclonal primary antibody against  $\beta$ -III tubulin and anti-rabbit Alexa fluor 555 conjugates were purchased from cell signaling technology (CST). AFM tip was procured from Newgen Technologies and TEM grid (200 mesh, Cu) was procured from Ted Pella, Inc. Thiobarbituric acid (TBA), trichloroacetic acid (TCA), and 2,7 dichlorodihydro-fluorescein diacetate (DFH-DA) were purchased from Sigma-Aldrich. The bacterial strains, Escherichia coli (MTCC Accession number 1610T) and Staphylococcus aureus (MTCC Accession number 1430T) were procured from Microbial Type Culture Collection (MTCC) Chandigarh, India. Mouse fibroblast cell line (L929), Glioma cells (C6) and neural cells (SH-SY5Y) were procured from the cell repository of National Centre for Cell Science (NCCS), Pune, India and osteoblasts 7F2 (mouse bone marrow) and Saos-2 (human osteosarcoma) were procured from ATCC (American Type Culture Collection).

### **2.3 Design and synthesis of peptide amphiphile**

In the beginning of third millennium, peptide therapeutics market crosses the multi-billion-dollar level.<sup>1</sup> With more than 400 peptides in clinical studies, chemical synthesis of peptide has gained utmost interest due to their rapid, efficient, reliable methodology.<sup>1</sup> For nearly a century, the sequential construction of peptides from amino acid precursors has been reported. The idea is simple: peptide elongation is accomplished through a coupling process between amino acids, followed by the removal of a reversible protecting group. Fischer and Fourneau reported the first peptide synthesis and are also responsible for giving the term “peptide”.<sup>2</sup> Carbobenzoxy (cbz), the first reversible N<sup>α</sup>-protecting group was created by Bergmann and Zervas.<sup>3</sup> Conventional approach of peptide synthesis or solution-phase method has a long and elegant history.<sup>4</sup> Peptide synthesis in presence of a solid support linked to a resin turn out to be revolutionary in peptide chemistry as it simplifies the tedious purification steps and automatic synthetic procedure, which saves the time.<sup>4</sup> In this thesis, we have used solid phase peptide synthesis for synthesizing the ionic complementary collagen inspired peptides. Our approach for the peptide design was focused on developing short length collagen

inspired peptide, which showed the property to self-assemble in three dimensional nanofibrous structure. Our simplistic design was focused on incorporating the classical amyloid fragment, diphenylalanine molecule to the N-terminal of the tripeptide (Gly-X-Y), which was inspired from the basic repetitive unit of native collagen protein. The middle position of proline was further modified by two differently charged amino acids which would further induce interactions between the ionic complementary charge on the residues to create complex hierarchical structure leading to the formation of diverse gels.<sup>5</sup> The acidic and basic surface charge of the individual pentapeptides resulted in the formation of self-assembled structure at different pH by stabilization through charge neutralization of the counter ions present in the solution microenvironment.

### 2.3.1 Solid phase peptide synthesis (SPPS)

Following the emergence of solid-phase technique, peptide synthesis has become a more realistic aspect of modern scientific research as it reduces the tedious and challenging purification steps involved in the liquid phase synthesis.<sup>6-8</sup>

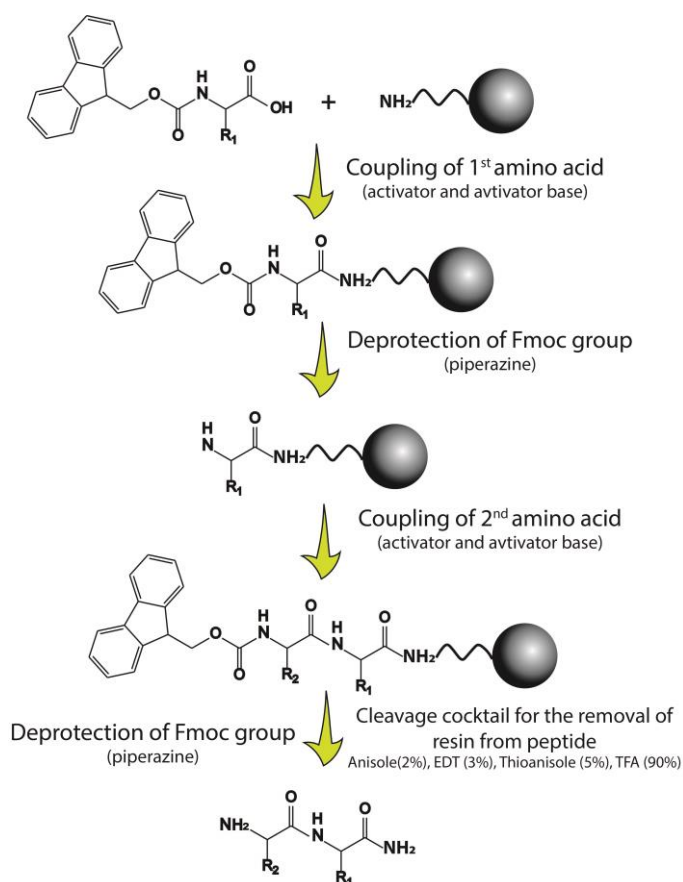


**Figure 2.1** Schematic representation of the simple dipeptide synthesis via solid phase method.

In this methodology, the peptide synthesis involves the use of a solid support over which numerous couplings and deprotection steps were performed to synthesize the desired peptide. The SPPS strategy involves two different approaches for the peptide synthesis according to the presence of protecting groups at N-terminal as well as in the side chains of the corresponding amino acids within the desired sequence. The protecting groups include: (i) Boc/Bzl and (ii) Fmoc/tBu.<sup>4</sup> Boc is acid labile while Fmoc is base labile and their side chain protecting groups were removed using TFA and the same cocktail solution was used to remove the peptide from resin. Each amino acid of the designed peptide was coupled sequentially from C-terminal to N-terminal through a solid support (resin) (Figure 2.1). Initially, the Fmoc-protected amino acid binds to the amine group of the resin and form amide linkage at the C-terminal. To further accommodate the upcoming amino acid, Fmoc from the first amino acid was removed using 10% piperazine and the next amino acid binds to the linked amino acid via same amide linkage, where 0.5 M *N,N*-diisopropylcarbodiimide (DIC) act as the activator and 1M Oxyma act as an activator base. The same process was followed on to add several numbers of amino acid to synthesize a long peptide chain via SPPS. Peptide sequences in this thesis were synthesized using a microwave-assisted solid phase peptide synthesizer (Liberty Blue CEM, Mathews, NC, USA). After complete synthesis, the peptide was detached from the solid support (resin) using the cleavage cocktail (Anisole 2%, EDT 3%, Thioanisole 5%, TFA 90%). During the removal of resin, the side chain protection also gets cleaved from the peptide. The cleaved solution was filtered and precipitated drop-wise in chilled ether. The synthesized peptides were further analysed for their purity and were characterized through mass spectrometry.

### **2.3.2 Reverse Phase-High Pressure Liquid Chromatography (RP-HPLC)**

In peptide chemistry, HPLC has emerged as an important tool because of its exquisite sensitivity, speed and resolution.<sup>9</sup> RP-HPLC can be used to check the purity control, quantitative analyses of the synthesized peptide, and it has become the analytical technique of choice for peptide study.<sup>10, 11</sup> HPLC, like other chromatographic methods, requires the use of a stationary phase (column) and a mobile phase (liquid). The injected sample was passed through the stationary phase with the use of a pump. The reverse phase high performance liquid chromatography (HPLC) system from Waters equipped with a photodiode array detector (Water 2998) was used to analyze the purity of the synthesized peptide.

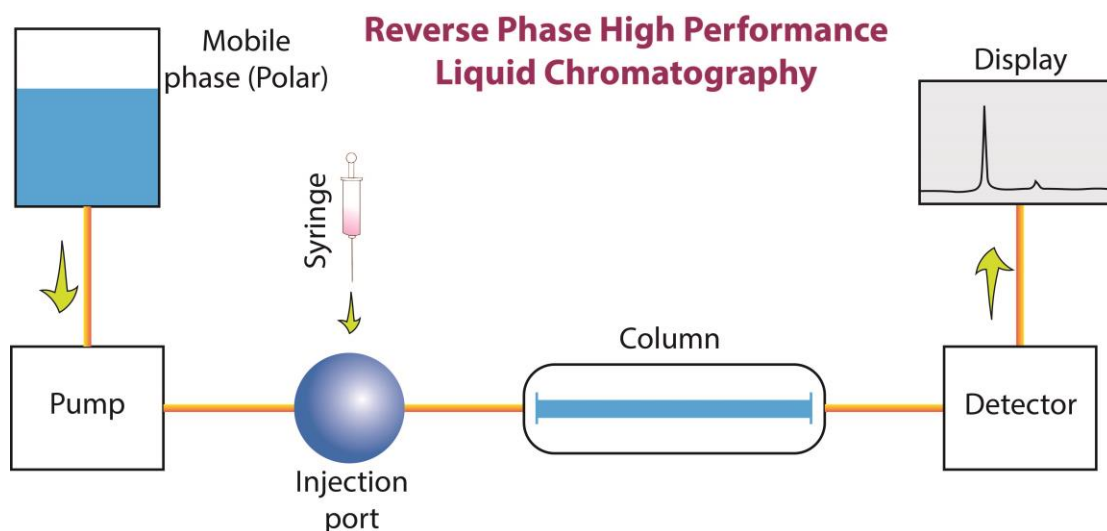


**Figure 2.2** Schematic representation of the working principle and instrumental setup of the reverse phase high performance liquid chromatography.

The affinities of the sample with the mobile and stationary phases determine how each molecular components within the sample are separated, which is controlled by the polarity of each of the components. When a component has a stronger affinity for the mobile phase, it will reach the detector first, rather than the component with a higher affinity for the stationary phase. The individual component's affinity for the stationary phase or the mobile phase determines the component's retention duration, which can be utilised to separate the components. In RP-HPLC, C-18 column is used as stationary phase and due to their non-polar nature, the non-polar component with the highest hydrophobicity has the longest retention time. Reverse phase HPLC system from Waters equipped with a photodiode array detector (Waters 2998) was used to analyse the purity of the synthesized peptides. 30  $\mu\text{L}$  of the sample was injected into waters C-18 spherisorb (4.6 x 250 mm) column having 5  $\mu\text{m}$  fused silica particles at a flow rate of 1 mL/min. A linear gradient of acetonitrile and water was used to elute the sample for a run time of 30 minutes. The sample was prepared by dissolving the requisite quantity of peptide in 1 mL of acetonitrile-water (50:50 mixture). The intensity of the peak was identified at 212 nm and 310 nm by a photodiode array detector.

### 2.3.3 Mass Spectroscopy (MS)

Mass spectroscopy is a technique for analysing the organic molecules present in samples qualitatively.<sup>12</sup> In general, it's used to determine the molecular weight of the biomolecule is in a sample. The molecule is converted into ions using an ionisation

method, with or without fragmentation.<sup>13</sup> The ions were characterised by their mass to charge ratios and relative abundance under magnetic field after ionisation, and then focussed on the detector or photographic plate according to their mass and charge. Electrospray ionisation was utilised to ionise the peptides.<sup>13</sup> The MS is frequently used in conjunction with HPLC, allowing the evaluation of the molecular mass of chemicals separated by HPLC. LC-MS analysis was carried out by using Acquity QDa mass detector equipped with RP-HPLC system (**Chapter 3**).

#### **2.3.4 Self-assembly of the designer peptides (pH-switch method)**

The synthesized ionic complementary collagen inspired peptides were studied for their gelation behaviour via pH switch method. As discussed in the previous chapter, the hydrophobic and hydrophilic balance within the monomeric molecular domain stabilizes the self-assembled structure to construct the nanostructures through hierarchical assembly, which holds the water molecule to form hydrogel. pH switch is the most widely used and studied method for triggering the hydrogelation among peptide amphiphiles.<sup>14, 15</sup> Change in the pH of the medium allows the ionization of the peptide, which further leads to the dissolution of peptide in aqueous environment. Both the ionic complementary peptides were prepared via dissolution and the induction of the gelation was attempted near to their respective pKa values of the functional amino acids (aspartate and lysine). The requisite amount of the peptides (30mM) was dissolved in water in a screw-capped vial with an internal diameter of 10mm and this was followed by varying the pH of the solution, gelation was achieved. NapFFGKO, was dissolved in ultrapure water (pH 7.0), then gradually NaOH (0.1M) was added to increase the pH to 9.0, which resulted in gelation. In contrast, to dissolve NapFFGDO, pH of the solution was raised to 9.0 and after its dissolution, 0.1M HCl was used to lower down the pH slowly to 5.0, where it showed gelation. To prepare the combined gel, both peptides were dissolved and the pH was adjusted to their gelation condition and then mixed in the calculated ratio. The gels were used for further characterization after the incubation of 24hrs (**discussed in chapter 3**). To further evaluate the equivalence point of the ionic peptide, we carried out the acid-base titration.<sup>16, 17</sup> The titration curve for both the collagen inspired peptides were performed on a benchtop pH meter (Oakton pH 550 benchtop). NapFFGKO (1mM) was dissolved in water and the pH was brought to 2.69 by adding 5 $\mu$ l of 1N HCl. Then, the solution was titrated with 0.1N NaOH until the solution pH reaches 12.

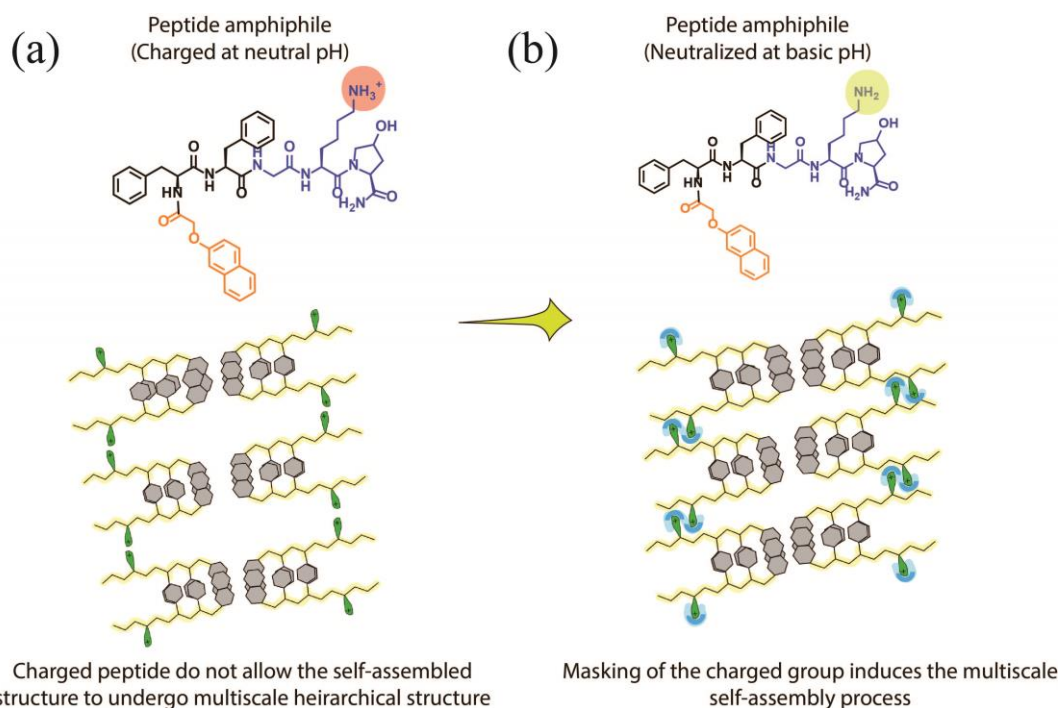


**Figure 2.3** Schematic representation of pH switch gelation method: for ionic peptides positively charged at physiological pH repel the adjacent peptide owing to similar charge repulsion, while at the pKa point the peptide tend to self-assemble into nanostructure owing to the charge neutralization.

As NapFFGDO is not soluble in water, 1mM of NapFFGDO was dissolved by adding 10 $\mu$ l of 2N NaOH resulting in final pH of the solution nearly 12. Further, 0.1N HCl was added gradually to decrease the pH to 2.7. The points where sudden change in pH was observed were marked as point of protonation and deprotonation. For the metal ion coordinated self-assembly, the negatively charged collagen inspired peptide remained in the sol state at physiological pH at its minimum gelation concentration (MGC) of 30 mM. However, the addition of the divalent metal ( $\text{Ca}^{2+}/\text{Mg}^{2+}$ ) ions to the system promotes the hydrogelation at much lower concentration. The MGC value has been reduced to 15mM in presence of salts as compared to the peptide monomer itself, which was found to be 30mM, which has been mentioned in chapter 3 and 4, respectively.<sup>5</sup> In this strategy, the requisite amount of the peptide (15 mM) was dissolved by increasing the pH to 10.0 using 1N NaOH in a screw-capped vial with an internal diameter of 10 mm. The dissolved peptide was brought to neutral pH slowly via the addition of 1N HCl and kept for incubation of 6 hours before adding salts into it. The instant addition of metal ions to the system leads to aggregation and precipitation of the peptide. The aging of 6 hours ensured the formation of short fibers, which upon interaction with

divalent metal ions leads to hydrogelation at physiological pH. Metal coordinated hydrogels were prepared by adding different concentrations of metal salts (5 mM and 10 mM) from the stock solution of salts. All stock solutions of the salts ( $\text{CaCl}_2 \cdot 2\text{H}_2\text{O}$  and  $\text{MgSO}_4 \cdot 7\text{H}_2\text{O}$ ) were prepared in Milli-Q water (18.2 M $\Omega$ ) at a concentration of 250 mM. In relevance to the media composition, we have utilized the same salts as additives as the preferred choice to check their effect on hydrogelation resulting from differential intermolecular interactions leading to differential cellular response.

### 2.3.5 TEMPO-oxidation of microfibrillar cellulose

TEMPO oxidation is a method to oxidize the polysaccharide and functionalize the polymer with carboxylate anionic functionality on the surface along with sodium counter ions. TEMPO mediated oxidation of cellulose is the most promising, efficient and energy-saving process to convert the microfibrillar cellulose into nanofibrillar cellulose with functionalized carboxyl groups.<sup>18</sup>

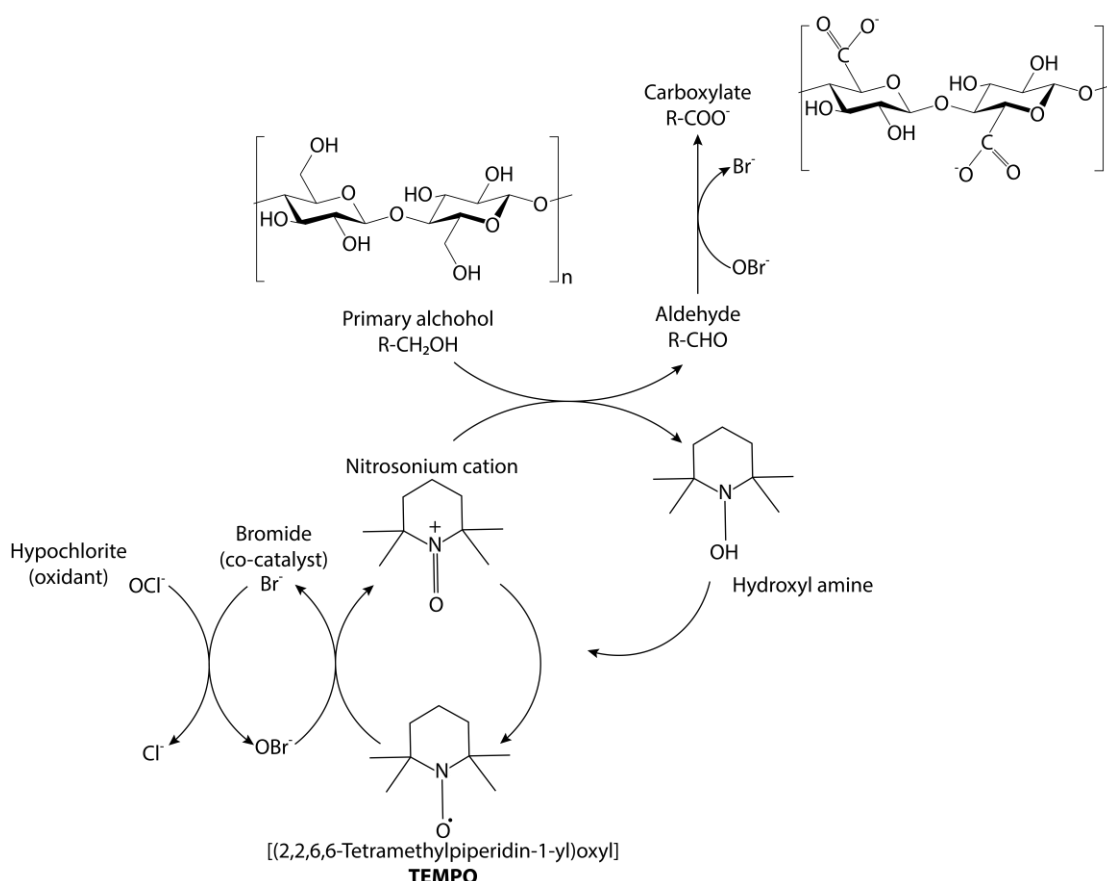


**Figure 2.4** Schematic representation of conversion of hardwood cellulose into nanofibrous cellulose via TEMPO oxidation

In this thesis, we have used softwood cellulose pulp (5g), dispersed in water (500 ml) containing TEMPO (80mg, 0.1mM) and sodium bromide (500mg, 1mM). The pH of NaOCl (10-14%) solution was adjusted to achieve pH 10 by adding 0.1N HCl. 5mmol NaOCl per gram of cellulose was used to start the TEMPO mediated oxidation of cellulose, and the reaction was stirred continuously at room temperature for 10 days.<sup>19</sup> The pH of the mixture was maintained at 10 using 1N NaOH and was continuously added in short intervals until no consumption of NaOH was observed. The TEMPO-oxidized nanofibrillar cellulose was washed thoroughly several times with distilled water by centrifugation at 5000 rpm for 10 min for the complete removal of remaining chemicals. Washed nanofibrillar cellulose was then lyophilized to obtain the dried cellulose, which was further used in all the experiments.

#### **2.3.5.1 Electric conductometric titration to calculate carboxylate content after the oxidation reaction**

It was essential to calculate the percentage conversion of the hydroxy group into carboxylate group after the TEMPO oxidation. The amount of conversion to carboxylate ions of the oxidized cellulose was determined by the classical method measuring electrical conductivity.<sup>19, 20</sup> Lyophilized samples of cellulose (0.3g) were added in 50ml distilled water with 5ml of 0.01M NaCl. The solutions were kept for stirring to synthesize a well-dispersed slurry-like material. The pH of the mixture was brought to pH 2.5 with the addition of 0.1N HCl. To this solution, a 0.05N NaOH solution was further added maintaining a constant rate of 100 $\mu$ l/min till the pH of the solution attained a final pH of pH 11 as indicated by a pH meter. A plot was generated with conductivity and pH to determine the extent of conversion of carboxyl group.

#### **2.3.5.2 Method of hydrogelation to construct nanofibrillar cellulose peptide conjugate**

Hydrogelation of the nanofibrillar cellulose and peptide was further attempted by preparing the aqueous suspension of nanofibrillar cellulose (NFC) and keeping it at 4°C for 2hrs to allow the swelling of cellulose fibers. For dissolution of cellulose, 20mg NaOH was used (per 100mg of cellulose), which was kept for stirring for 5-6hrs at 4°C followed by keeping it at -2°C for overnight. The peptide hydrogel was added to the dissolved cellulose just before keeping it at -2°C for overnight. The prepared hydrogel was allowed to thaw at ambient condition for few minutes and then it was washed with

the distilled water via diffusion or solvent exchange methodologies for several times to remove the excess NaOH present in the hydrogel. In this process, the final pH of the system was maintained at physiological pH.<sup>21</sup>

### 2.3.5.3 Surface hydrophobicity measurement via drop shape analyser

The surface hydrophobicity of the cellulose and cellulose-peptide conjugates were measured through contact angle using Drop shape analyser (DSA25E, Kruss). Measurements were performed in the absence of the solvent. A thin film of cellulose gels was made on the top of a glass slide and kept for air drying. A water drop was dropped on the surface of the dried sample and the angle between surface and water droplet was measured via drop shape analyser.<sup>22</sup> Similarly, the conjugate gels were also investigated to analyze the extent of modifications in surface hydrophobicity.

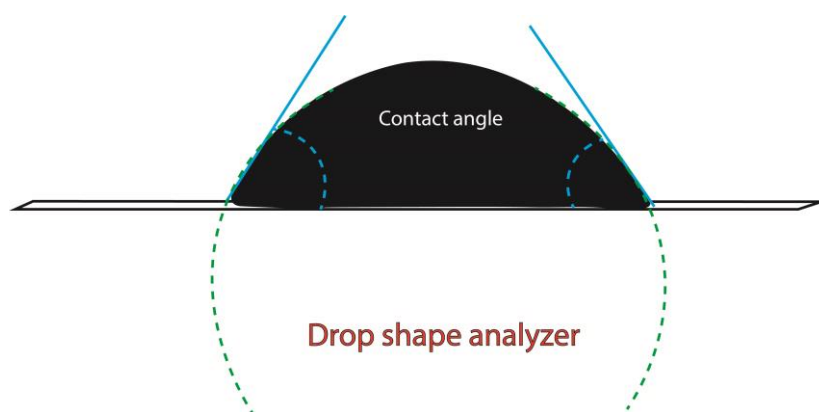


**Figure 2.5** Schematic representation of contact angle measurement through drop shape analyser.

### 2.3.6 Zeta potential measurement

Peptide solutions at 10mM concentrations were used for measurement of zeta potential using Malvern Zeta Sizer Nano (ZSP). Both the ionic complementary peptides were titrated against each other to attain the neutral charge, which gives the calculated value by mixing both the peptides (**chapter 3**).<sup>23</sup> Zeta potential of the peptide nanoparticles were also monitored via same protocol and instrument (**chapter 7**).

### 2.3.7 Dynamic Light Scattering

Dynamic Light Scattering (DLS) follows the Brownian motion of the dispersed particle in liquid. The particles in liquid move in all directions and collide each other, which causes the production of energy and further induces the particle movement.<sup>24</sup> As the

transferred energy is not constant, smaller particles tend to move faster than bigger particles.<sup>24</sup> The speed of the particle movement and other parameters like viscosity, temperature, Boltzmann constant can be used to calculate the hydrodynamic radii of the particle.

$$D_h = \frac{k_B T}{3\pi\eta D_T} \dots\dots\dots(\text{Eq. 2.1})$$

*(Stokes-Einstein equation)*

Where, D is translational diffusion coefficient (m<sup>2</sup>/s), k<sub>B</sub> is Boltzmann constant, T is temperature (K), η is viscosity (Pa.s), R<sub>H</sub> is hydrodynamic radius (m).

The particle size, i.e., the hydrodynamic radius, polydispersity index (PDI) was measured from ZetaSizer Nano ZSP (Malvern Instruments).<sup>25</sup> According to their electrophoretic mobility, prepared samples were subjected to equilibrate for 120 seconds prior to the examination. The prepared nanoparticles were added to the bacterial and mammalian cell culture media to check their stability over 36 hours via dynamic light scattering (**chapter 7**).

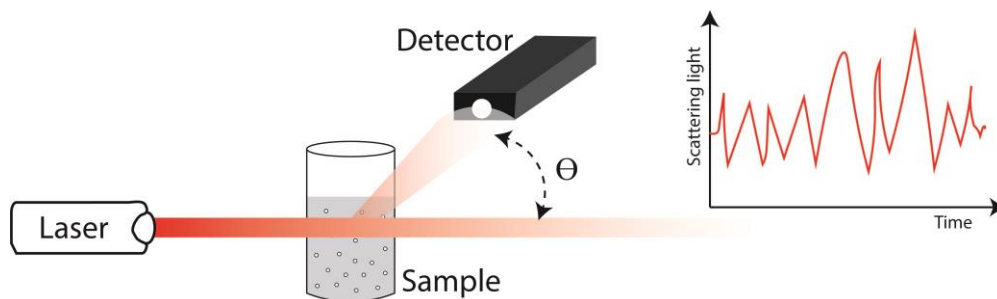


**Figure 2.6** Schematic representation of the working principle of Dynamic Light Scattering (DLS).

## 2.4 Spectroscopic and microscopic characterization of self-assembled nanostructures

Non-covalent interactions between peptide molecules lead to their self-assembly into highly organized and well-defined supramolecular structures, which are then entangled to form a 3D fibrous network that effectively entraps water. Various spectroscopic techniques are used to investigate non-covalent interactions and structure development, which are covered in the next section.

### 2.4.1 Circular Dichroism (CD) spectroscopy

Circular Dichroism is the most common technique to determine the secondary structure of peptide and proteins in solution.<sup>26</sup> CD spectroscopy is based on the absorption deflection of circularly polarized left and right light of an optically active molecule. CD is widely used to discriminate the secondary structures of proteins i.e., ( $\alpha$ -helix,  $\beta$ -sheet, random coils etc.). Protein secondary structures are characterized by far UV, where the peptide bond serve as a chromophore and near UV gives the insight into protein's tertiary structure.<sup>27</sup> Spectral region of 160-240nm falls under far UV range, and this range is of particular interest because singlet electronic transition in the backbone peptide bond of a protein occurs at 190 and 220 nm (N-C=O).<sup>28</sup> The transition at 220 nm is from the lone pair on oxygen to a  $\pi$  antibonding orbital ( $n\pi^*$  transition) and the transition at 190 nm is from a non-bonding  $\pi$  orbital to the  $\pi$  orbital ( $\pi\pi^*$  transition).<sup>29</sup> These two transitions mix in the chiral environment of a protein and result in distinct spectra for each secondary structural element present within the protein. Exciton splitting of the  $\pi\pi^*$  transition gives rise to the positive peak at 190 nm and the negative peak at 208 nm in the CD spectrum for an  $\alpha$ -helix alongside a negative peak at 220 nm due to the  $n\pi^*$  transition.<sup>29</sup> The electronic transitions at 208 and 190 nm are polarized, parallel, and perpendicular, respectively, to the helix axis in  $\alpha$ -helical structures.<sup>29</sup> Characteristic CD spectra for other secondary structural motifs are also observed: a  $\beta$ -sheet has a positive peak around 195 nm and a negative peak around 215 nm and a protein with no dominant secondary structure (a random coil) has a negative peak around 200 nm. In case of aromatic group capped short peptide sequence, CD spectra gives important insights into the structural arrangement of designed peptide amphiphiles after self-assembly.

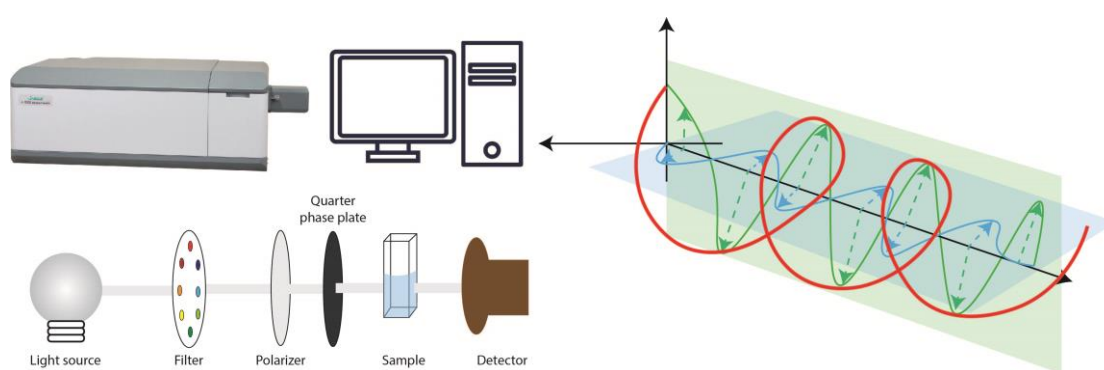


**Figure 2.7** Schematic representation of working principle of circular dichroism (CD).

CD measurements of the peptide hydrogels were performed using Jasco J-1500 CD spectrophotometer. Spectra for all the hydrogels were obtained between a wavelength of 195-320 nm with 1 s integrations with a step size of 1 nm and a single acquisition with a slit width of 1 nm. A 0.1 mm quartz cuvette was used in which three repeat scans were compiled to generate the average spectra. The results were analysed using the Jasco Spectra Manager. HT voltage curve was recorded to demonstrate the noise-free data.

#### 2.4.2 Fourier Transform InfraRed (FTIR) spectroscopy

Fourier Transform InfraRed spectroscopy is also a common technique to study the secondary structure of peptide and proteins.<sup>30</sup> Peptides are made up of a chain of amino acids linked by an amide bond. The change in the amide bond's vibration frequency caused by differing hydrogen bonding interactions among the amino acids can provide useful information about the protein's secondary structure.<sup>31</sup> Amide vibrations involve C=O, C-N and N-H groups of an amide bond, resulting in characteristic spectral features of proteins. Theoretical and experimental studies have revealed the presence of nine IR bands, which are termed amide A, amide B and amides I–VII.<sup>32</sup> The amide I band was discovered to be the most intense and effective for analysing the secondary structure of proteins out of all the amide bands, which represents primarily the C=O (70-85%) stretching vibration of the amide groups and occurs in the region 1600–1700  $\text{cm}^{-1}$ .<sup>33</sup>

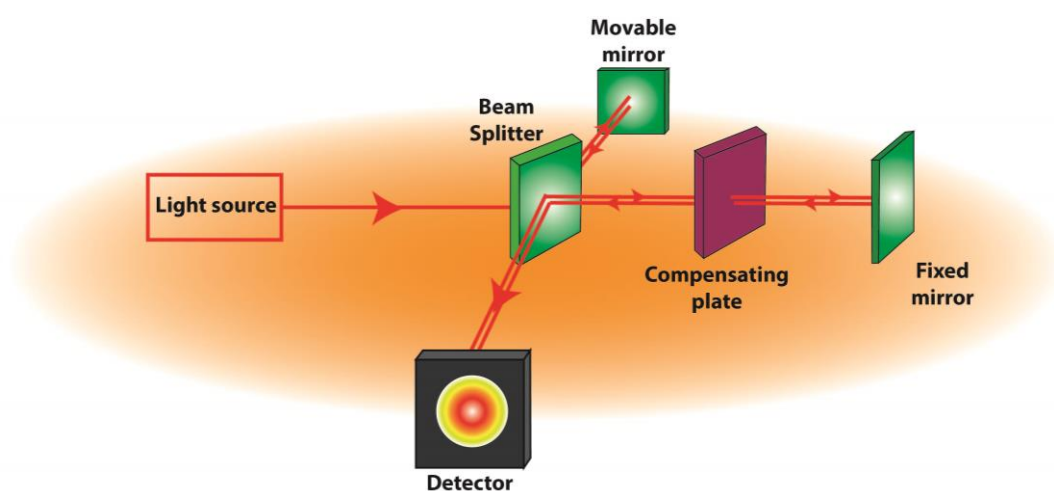


**Figure 2.8** Schematic representation of the working principle of Fourier Transform InfraRed (FTIR) spectroscopy.

In addition to this amide II band, there has been significant contribution from the bending vibrations of the N–H (40- 60%), and from the C-N stretching vibrations (18-40%), which occur at 1510 and 1580  $\text{cm}^{-1}$  region. Hydrogen bonding and the coupling between transition dipoles are among the most important factors governing conformational sensitivity of the amide bands.<sup>34</sup> The amide I band position for the  $\alpha$ -helical conformation is located at 1650-1655  $\text{cm}^{-1}$ . The  $\beta$ -sheet band frequency is located at 1620  $\text{cm}^{-1}$  and a weaker band associated with high-frequency vibration of antiparallel  $\beta$ -sheet structure is reported at 1680  $\text{cm}^{-1}$ .

In this thesis, Agilent Cary 620 FTIR spectrophotometer (**chapter 3**) and Bruker Vertex 70 ATR spectrophotometer (**chapter 4, 5, 6, 7**) were used for the sample analysis. All the peptide hydrogels and peptide nanostructures were freeze-dried to record their FTIR spectra. The spectra was obtained across the wavelength of 400 to 4000  $\text{cm}^{-1}$  at a resolution of 2  $\text{cm}^{-1}$ . The obtained spectra were background subtracted and processed. The difference in the spectral intensity after metal ion complexation was simply area normalized in the frequency region of 1390-1460  $\text{cm}^{-1}$  via origin software.

### 2.4.3 Fluorescence spectroscopy

Fluorescence spectroscopy is a frequently used analytical tool for studying a compound's fluorescence properties in order to gain insight into the physical and chemical behaviour of macromolecules and their interactions.<sup>35</sup> High sensitivity of this method is the key advantage as the sample amount is usually used in very low, and small traces of fluorescent species can be detected quantitatively.<sup>36</sup> The capacity of some functional groups to absorb light at a given wavelength and then emit light of a larger wavelength after a short period of time is known as fluorescence.<sup>37</sup> The classical Jablonski diagram is used to depict the processes that occur between light absorption and emission.<sup>38</sup> In a Jablonski diagram (Figure 2.9) S0, S1, and S2 represent the singlet ground, first, and second electronic states, respectively. Frank-Condon principle states that a fluorophore can exist in a variety of vibrational energy levels at each of these electronic energy levels, as shown by the numbers 0, 1, 2, and so on. To demonstrate the instantaneous nature of light absorption, transitions between phases are portrayed as vertical lines. Transitions take roughly 10–15 seconds, which is too short for considerable nuclei movement. Typically, a fluorophore is stimulated to a higher vibrational level of S1 or S2. The excited molecule quickly relaxes to the S1 vibrational

level, which is the lowest vibrational level. Internal conversion is the term for this procedure, which takes 10–12 seconds or less. Since fluorescence lifetimes are typically near 10<sup>-8</sup> s, internal conversion is generally complete prior to emission. As a result, fluorescence emission is usually caused by S1's lowest energy vibrational state. Molecules in the S1 state can convert to the first triplet state T1 through spin conversion.

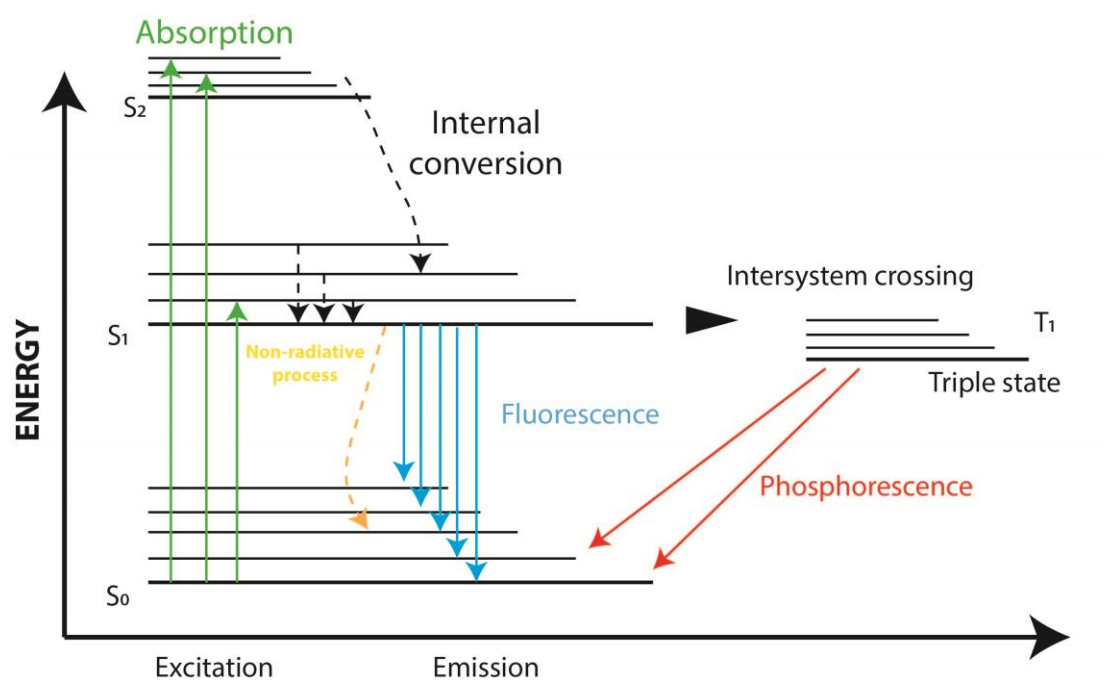


**Figure 2.9** Jablonski diagram showing the possible electronic transition giving rise to absorption and emission.

Another phenomenon, phosphorescence is generally shifted to longer wavelength (lower energy) relative to fluorescence. Intersystem crossover is the process of converting S1 to T1. Because the transition from T1 to the singlet ground state is restricted, triplet emission rate constants are several orders of magnitude lower than fluorescence rate constants. The fluorescence of the molecules is affected by a variety of parameters, including temperature, pH, local polarity, aggregation, and the presence of nearby molecules that can quench the energy of the molecules under study.<sup>39</sup> In this thesis, all the fluorescence studies are performed in a steady state spectrofluorometer (FS5) from Edinburg Instruments. The variation in the fluorescence of the aromatic group present at the N-terminal was assessed via spectrofluorometer. The peptide amphiphile at physiological pH 7.0 in monomeric state (0.25mM) and gel state (15mM) (after addition of salt) was transferred to a quartz cuvette (10 X 4mm). The samples

were excited at 240 nm corresponding to the absorption maxima of naphthoxy moiety, and emission spectra were acquired in the 260-510 nm range both in monomeric and gel state with data pitch of 1nm and bandwidth of 3 nm.

#### **2.4.4 Thioflavin T fluorescence assay**

We have further used the fluorescence spectrophotometer to determine the binding capacity of a fluorescent dye Thioflavin T. ThT recognizes and binds to the beta rich peptide structures, which commonly adopts the “cross- $\beta$ ” structures, an extended  $\beta$ -conformation running perpendicular to the long axis leading to the multiple  $\beta$ -sheets.<sup>40</sup> The ThT binds to these cross-strand ladder consists of repeating side chain interactions across the  $\beta$ -sheet layers.<sup>41</sup> However, ThT interaction is specific to the structural motif in the fibrils, which is basically the hydrophobic patches of the  $\beta$ -sheet structures and it has an affinity towards it. ThT stock solution (8mg in 10 ml MQ water) was freshly prepared and filtered through 0.2  $\mu$ m syringe filters. The working solution was prepared by diluting stock solution (1ml to 50ml) with water. The fluorescence intensity was measured for 1ml of working solution by excitation at 440nm (slitwidth 1nm) and emission at 482nm (slitwidth 1nm) with an average intensity of 5 accumulations. For measuring the fluorescence intensity of peptide hydrogels, 1ml of the working solution was titrated with 20 $\mu$ l of peptide hydrogels/solutions. For each sample, the spectra were recorded from 450 to 600nm at room temperature. The final intensity for each sample was plotted after subtracting the ThT spectrum in water.

#### **2.4.5 Congo Red (CR) Binding Assay**

Congo red is an amyloidogenic dye that is commonly used to stain amyloid fibrils in tissues.<sup>42</sup> When this dye interacts with amyloids, it exhibits dramatic changes in spectrophotometric characteristics. Its absorption spectra in aqueous solution exhibits a maximum absorption at 490 nm.<sup>43</sup> When bound to  $\beta$ -sheet-rich amyloid fibrils, the CR molecules adopt a specific orientation (i.e., with the long axis of the CR molecules lying parallel to the fibril axis) and become torsionally restricted.<sup>44</sup> This induces a characteristic increase in absorption and a red shift in the absorption maximum from 490 to 540 nm. We have used congo red binding assay to confirm the presence of cross- $\beta$  sheet like structures into the hydrogels (**Chapter 4**). Briefly, the stock solution was freshly prepared by dissolving 2.5 mg of Congo red (CR) dye in 10 mL of MilliQ water containing 10% ethanol, and the solution was filtered through a 0.2-micron filter to

remove the undissolved dye. Metal coordinated peptide hydrogels prepared at 15 mM concentrations were diluted 10 times. These diluted samples were further incubated with 10  $\mu\text{L}$  of the Congo red stock solution for 30 minutes in the dark. Absorption spectra of the Congo red containing hydrogels were collected on a UV-Vis spectrophotometer (UV-2600 Shimadzu) using a quartz cuvette (1 cm path length) in the range of 200-700 nm.

#### 2.4.6 Powder X-ray diffraction (XRD)

Another useful tool for determining the molecular packing of short peptide amphiphiles in the gel state is XRD.<sup>45</sup> An X-ray beam is incident on a crystalline sample in XRD, and it is diffracted in many different directions. The angles and intensities of these diffracted beams are measured to provide a three-dimensional representation of the electron density within the crystal.<sup>46</sup> This electron density shows the atom's average positions in the crystal, their chemical bonds, crystallographic disorder, and other details.

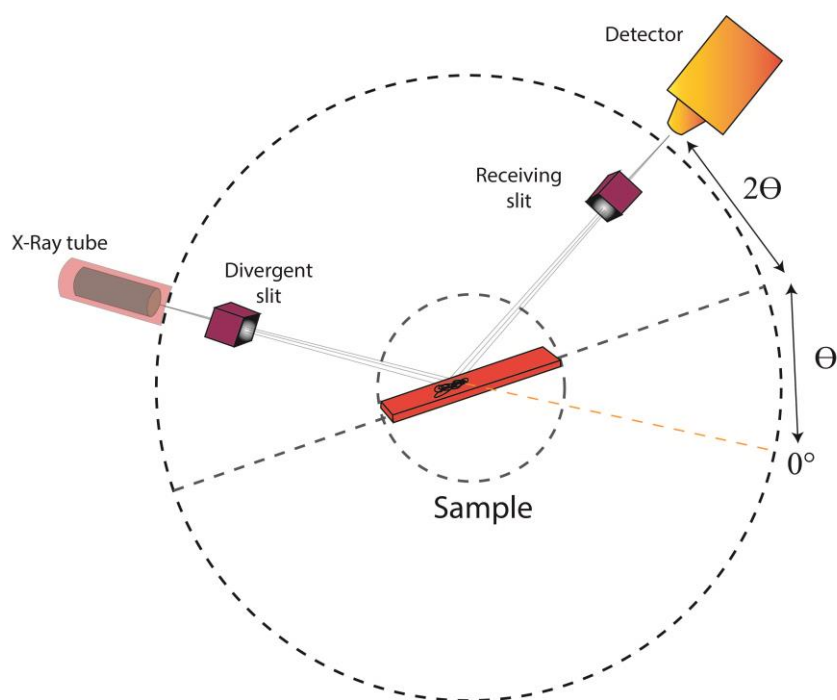


**Figure 2.10** Schematic representation of working principle of powder X-Ray diffraction (XRD).

After self-assembly, amorphous peptides can form crystalline structures that diffract x-rays and produce distinct peaks. The diffraction of x-rays was explained as ‘reflections’

from different planes of crystals, firstly by W.L. Bragg.<sup>47</sup> These reflections satisfy the following equation, known as Bragg's equation:

$$n(\lambda) = 2d \sin \theta \quad \dots\dots\dots(\text{Eq. 2.2})$$

Here,  $n$  is a positive integer (1,2, 3,  $n$ ),  $\lambda$  is the wavelength,  $d$  is the distance between the atomic planes, and  $\theta$  is the angle of incidence of the X-ray beams.

In this thesis, Bruker D8 Advance X-ray diffractometer instrument equipped with Cu  $K\alpha$  radiation source ( $\lambda = 1.541 \text{ \AA}$ ) was used under the accelerating voltage of 40 kV and 25 mA. The  $2\theta$  range used for recording the XRD pattern of peptide assemblies was  $5^\circ$  to  $80^\circ$ . The lyophilized hydrogel samples were used for XRD analysis. XRD has provided the information regarding the presence of preliminary growth of the hydroxyapatite crystals on the peptide nanofiber (discussed in **chapter 5**).

#### **2.4.7 Small Angle X-Ray Scattering (SAXS)**

Small-angle scattering (SAS, angle  $0$ - $2^\circ$ ) has proven a strong method for understanding biomaterial structure. SAS is a scattering method based on the slight deflection of collimated radiation away from the straight path when it interacts with obstacles larger than the radiation's wavelength.<sup>48</sup> The "angle" in SAS refers to the deflection angle of radiation. The shape and size of structures in a sample can be determined using SAS approaches.<sup>49</sup> A monochromatic beam of X-rays is directed at a sample in a SAXS apparatus, and some of the X-rays scatter while the majority pass through the material without interfering with it. The scattered X-rays form a scattering pattern, which is then detected at a detector which is typically a 2-dimensional flat X-ray detector situated behind the sample perpendicular to the direction of the primary beam that initially hit the sample. The scattering pattern contains the information on the structure of the sample. In this thesis, SAXS experiments were carried out on SAXSess mc<sup>2</sup> instrument procured from Anton-Paar with line-collimation system using a Cu  $K\alpha$  source with wavelength of  $1.54 \text{ \AA}$ . Perkin Elmer cyclone plate recorder was used to record the data. SAXSQuant 2D software was used to reduce the dimensional data to one dimensional, Intensity (I) vs scattering vector (q) plot. SAXS intensity profiles were fitted in shape-independent category and examined by two different models; Debye (1947) model, which was implemented in SasView as mono\_gauss\_coil model and an extension of Debye's original scattering law, Schulz-Zimm model having an extra parameter (polydispersity of the polymer ( $M_w/M_n$ )), as poly\_gauss\_coil model. The fitting was

carried out using SasView 5.0 software. The effective structure factor,  $S_{\text{eff}}(q)$ , was also calculated for each molecule.

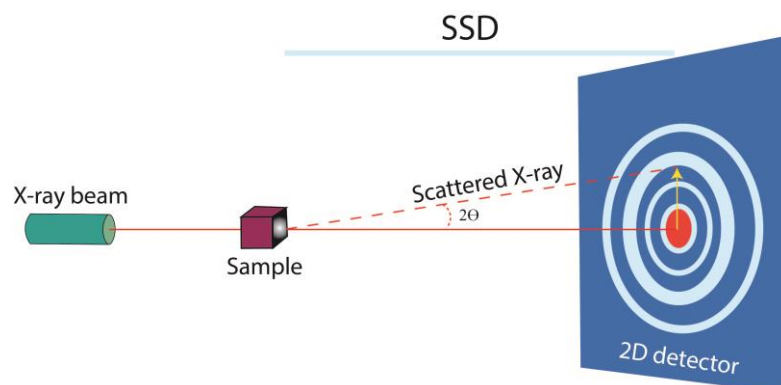


**Figure 2.11** Schematic representation of work flow of small angle X-ray scattering (SAXS).

Ten separate models were made for every dataset using DAMMIF program, which were further superimposed, an averaging was done using DAMAVER program. This was followed by further optimization using DAMMIN program. Superimposition of nanofibrillar cellulose and peptide modelled structures were achieved using ATSAS plugin and all representations were drawn using PyMol program.

#### **2.4.8. Confocal Laser Scanning Microscopy (CLSM)**

Confocal Laser Scanning Microscopy (CLSM) is a commonly used technique for imaging fluorescent sample, as well as real time imaging and 3D screening.<sup>50</sup> The working principle of the instrument is based on point-by-point illumination of the sample and elimination of out-of-focus light.<sup>51</sup> The light source (laser system) emits coherent light, which passes through a pinhole aperture on a confocal plane with an objective near the specimen and another pinhole aperture in front of the photomultiplier detector.<sup>51</sup> The laser, which is reflected by a dichroic mirror, falls over the sample in a set focal plane, causing secondary fluorescence to be emitted from certain places on the specimen (in the same focal plane). The light is reflected back via the dichroic mirror and focused on the detector pinhole aperture. The placement of spatial pinholes to block out-of-focus light in image generation gives confocal imaging the advantage of high resolution and contrast.<sup>50, 51</sup> However, the greater resolution produced by blocking light at the pinhole came at the expense of diminished signal strength, necessitating extended exposure times to minimise the signal to noise ratio.<sup>52</sup> The confocal microscope used

in this thesis is from Carl Zeiss, LSM880 for live-dead staining for bacterial as well as mammalian cells and also for F-actin and immunofluorescence staining ( $\beta$ -III tubulin).

#### 2.4.9 Atomic Force Microscopy (AFM)

Atomic force microscopy is a strong tool for assessment of biomaterial shape and mechanical characteristics with nanoscale spatial resolution.<sup>53</sup> It is commonly used in biology to define the morphological characteristics of fiber-forming proteins and peptides.<sup>54</sup> The technique involves moving a sharp probe tip across a sample surface using piezoelectricity, which creates deflections in the probe's cantilever.<sup>55</sup> These deflections are then used to create a topographical map for each x,y pixel on the scanned area. An optical detecting system is used in the most popular AFM setup. The probe tip, which is mounted on the end of a cantilever, is illuminated by a laser. This laser reflects onto a position-sensitive photodiode with four quadrants. The photodiode signal from the laser point in each quadrant will change as the cantilever deflects due to the probe's interaction with the surface. The controller keeps track of this change. The change in voltage of the photodiode is used to compute the cantilever's movement. The cantilever or the surface itself can be moved with accuracy by a piezo scanner in 3D. The forces obtained during scanning are rebuilt computationally, resulting in the development of an image. Probe, a microfabricated sharp spike attached on the end of the cantilever, is one of the most important requirements of AFM.

The resolving power of an instrument is usually determined by the tip's sharpness. Silicon or silicon nitride is used for the cantilever-tip assembly. We have used AFM in tapping mode to visualize the morphological features of the nanostructures present in the hydrogel state (**in chapter 3,4,5,6,7**).<sup>56</sup> For AFM analysis, the hydrogels were diluted and drop cast on the surface of fresh silicon wafer. The sample was air-dried. The atomic force microscopy (AFM) images were obtained by scanning the silicon wafer surface in air under ambient conditions using Bruker Multimode 8 scanning probe microscope operated in tapping mode with Nanoscope V controller and a J-scanner. The Tapping mode tips were used with silicon cantilever for standard tapping in air obtained from Budget sensors (Tap150Al-G) with resonant frequency, 150 kHz and force constant  $5 \text{ Nm}^{-1}$ .

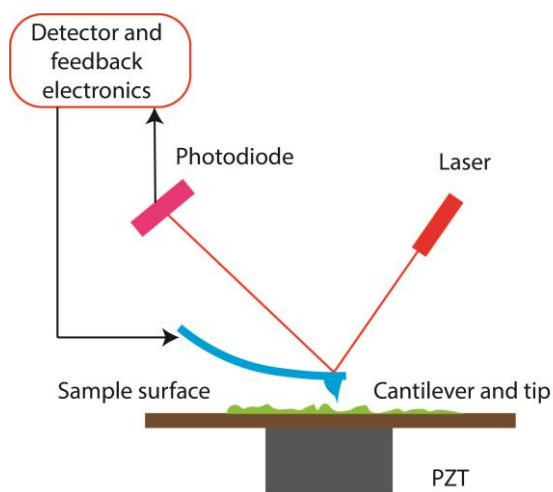


**Figure 2.12** Schematic representation of working principle of Atomic Force Microscopy (AFM).

#### 2.4.10 Scanning Electron Microscopy (SEM)

The scanning electron microscope (SEM) is a tool for visualising and analysing sample surfaces. The imaging of samples in a SEM is mostly conducted with secondary electrons.<sup>57</sup> When compared to the energy of primary electrons, these electrons have a very low energy (about 50 eV) (up to 30 keV). Because of their low energy, these electrons can only escape from the specimen's surface area, providing information about the surface topography. It was also discovered that backscattered electrons are widely employed for imaging with a backscatter detector located accordingly. The number of electrons backscattered from a specific place on the specimen is determined by the specimen's local elemental density.<sup>58</sup> As a result, backscattered electrons offer a "density image" as well as information on the elemental composition. Due to their great energy, backscattered electrons are likewise more resistant to charge. The morphology and surface topology of cellulose peptide conjugate hydrogels were determined by Scanning Electron Microscope procured from JEOL, USA (JSM-IT300). The experimental parameters were set to acquire the data at 15kV, while the probe current was fixed at 30 $\mu$ A. The cellulose peptide conjugate hydrogel was casted onto the silicon wafer before gelation and then kept at -2 °C for gelation. After gelation, the silicon wafer containing the sample was washed for several times and allowed to dry in the desiccator under vacuum. Samples were sputtered with gold for 60s prior to imaging. The distribution of the pore size throughout the samples was quantified by SEM images. In particular, the pore size and the distribution were calculated using ImageJ software.

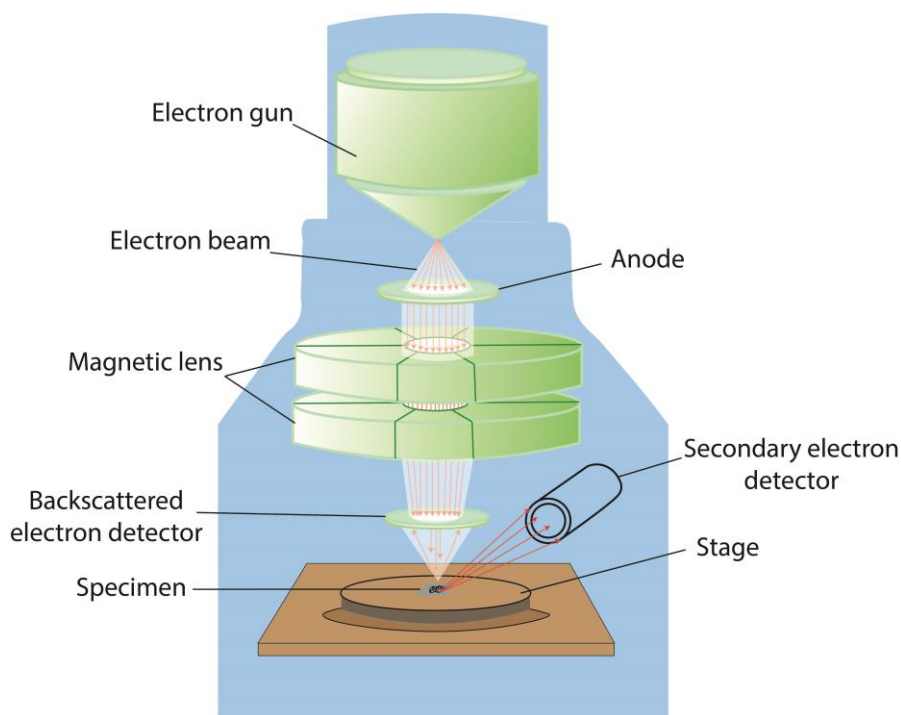


**Figure 2.13** Schematic representation of the working principle of Scanning Electron Microscopy (SEM).

In **chapter 7**, the bacterial cells were observed for the damaged cellular membrane via field emission scanning electron microscopy (FE-SEM). Bacterial cells in the log phase were harvested and washed with normal saline, which was followed by incubation with the nanoparticles for 6 hours. After incubation, both the nanoparticle treated and the non-treated cells were washed several times to remove the nanoparticles and resuspended in normal saline for the sample preparation. Glass coverslips were cleaned and coated with poly-L-lysine for 5 minutes in a 24 well plate and kept for air dry in oven (60°C). The bacterial cells were fixed by 4% formaldehyde solution for 15 minutes followed by washing with normal saline. Formaldehyde is used to crosslink the bacterial protein to stabilize the ultrastructure of the bacterial cells. The cells were post fixed in 1% tannic acid solution for 15 minutes to fix the bilipid membrane preventing the extraction of lipid during gradual dehydration. The washed cells were then drop cast onto the poly-L-lysine coated coverslips and incubated for 1 hour at 4°C. After the complete binding of cells on coverslips, the samples were subjected for dehydration by immersing the coverslips in a gradient ethanol solution (30-100 %). The dehydrated samples were kept in a vacuum container to avoid the moisture gain. The samples were then gold coated for 60 seconds before imaging through a JSM-7610F Schottky Field Emission Scanning Electron Microscopy with an accelerating voltage of 5 kV. The

images were captured at a working distance of 8.14 mm in standard mode with secondary electron detector.

#### **2.4.11 Transmission Electron Microscopy (TEM)**

The interaction of an electron wave with the matter provides information about the microstructural organization of the specimen in an electron microscope. Images from transmission electron microscopy may be obtained on a fluorescent screen with a magnification of approximately 1,000,000x and a resolution of better than 1 Å.<sup>59</sup> Furthermore, by studying the X-ray produced by the interaction of the accelerated electrons with the sample, the elemental composition of a sample may be determined with high spatial resolution.<sup>60</sup> Typically, a thermionic cannon is used to generate high-speed electrons that are focused onto the specimen by various electromagnetic lenses. For an average accelerating voltage of 100 kV in TEM, the specimen should be around 70 nm thick. The specimen is put on copper grids, which are then placed in a holder and vacuum-sealed before being injected into the goniometer of the TEM. The goniometer allows for extremely precise and steady specimen holder control while imaging. TEM is comprised of two types of interactions between primary electron and atom of the specimen: (i) Elastic scattering and (ii) In-elastic scattering.<sup>61</sup> Heavy metals can be added to the biological samples or soft materials to optimize the ratio between elastic and inelastic scattering. Staining with heavy metal fixes the sample shape, enhance contrast and also protect the sample against radiation damage.

Due to the presence of light elements such as C, H, O, N, S, P, and others, peptide-based nanostructures are commonly thought of as soft materials. As a result, these materials are generally electron transparent and must be stained with heavy metal-containing substances such as uranyl acetate or phosphotungstic acid, which are electron dense and offer the necessary image contrast for peptide nanostructure visualization. Because of the presence of diverse functional groups, these heavy metals can either interact with the nanomaterial or just stain the backdrop of the sample, depending on whether the staining is positive or negative. Metals that stick to certain sections of the sample are added to get a positive heavy metal staining. Furthermore, a small portion of the sample is exposed to very powerful electrons in TEM, which may cause damage to the sample. In this case, optimal heavy metal staining also protects the material from radiation damage. A negative stain is a fine-grained metal solution that

creates a contrast by covering and surrounding the material. The detector is the final component of the electron microscope that has a significant impact on image quality.

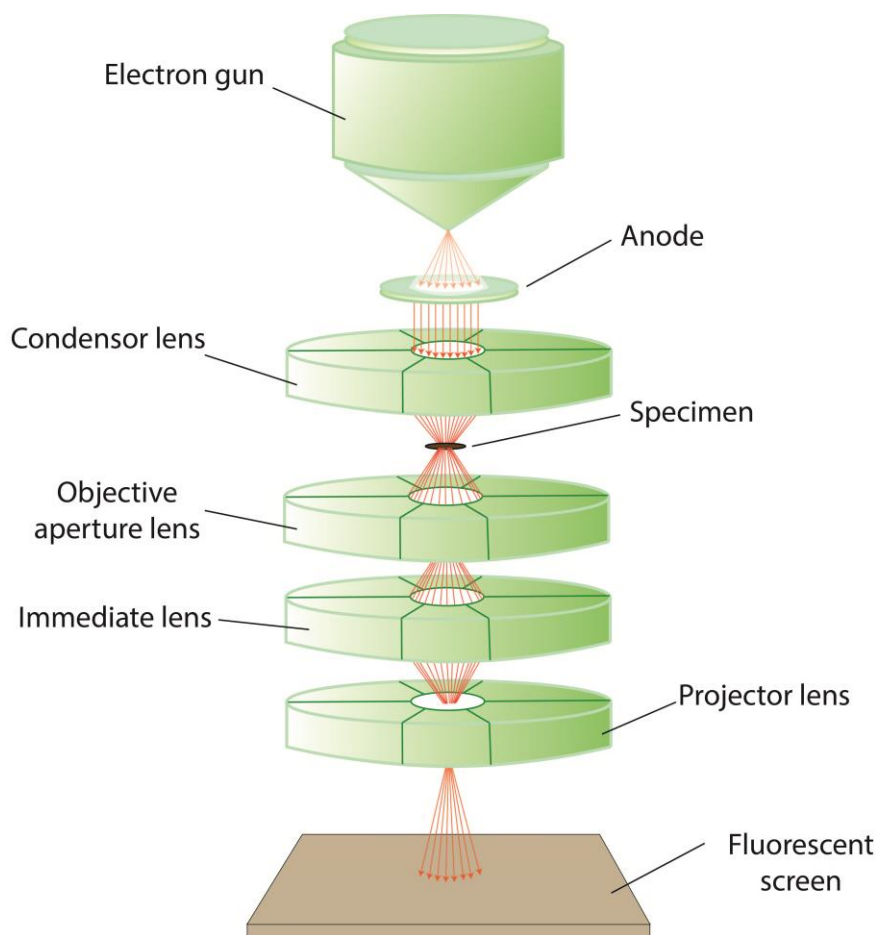


**Figure 2.14** Schematic representation of the working principle of Transmission Electron Microscope (TEM).

By translating electrons into photons in a scintillator layer, a CCD camera records the electrons. Direct detection devices (DDD) are now widely employed in the field of structural biology. DDD cameras can detect electrons directly, minimizing blurring and increasing recording speed. The chip is also thinner, which reduces the amount of backscattering of electrons in the chip. To examine the peptide nanostructure in TEM, the peptide gels were allowed to adsorb for 4 min on the carbon coated TEM grid. Excess sample was wicked off with the filter paper. It was followed by the addition of 2% (w/v) Uranyl Nitrate with an incubation time of 3-5 minutes and wicking off the excess stain, same procedure of staining was repeated thrice. Samples were then kept in the desiccator under vacuum. TEM micro-graphs were recorded with a JEOL JEM 2100 with a tungsten filament at an accelerating voltage of 200 kV.

## 2.4.12 Rheological analysis of peptide hydrogels

### 2.4.12.1 Assessment of mechanical strength

Supramolecular hydrogels are soft, viscoelastic polymers that are physically crosslinked. Their mechanical characteristics control a variety of technical applications, including drug delivery, biomaterial construction, and biosensor design etc.<sup>62, 63</sup> The mechanical strength and viscoelastic properties of the supramolecular hydrogel are mostly determined by the gelation process as well as the peptide building block concentration.<sup>64</sup> To characterize their static and dynamic viscoelastic behaviour, rheology is the method of choice.<sup>65, 66</sup> The gelation kinetics and stiffness of a gel are disclosed in rheology by applying shear and measuring the strain, or vice versa. In a sinusoidal oscillation, a deformation is introduced as shear strain or stress on the hydrogels. The shear stress or strain is calculated using the sine wave phase shift as a function of the applied angular frequency. Rheology is a great way to track changes in gel structures as they transition from sol to gel (assembly formation) and vice versa (breaking of assemblies).<sup>67</sup> The shear storage modulus ( $G'$ ; energy stored in deformation), shear loss modulus ( $G''$ ; energy released in deformation), and the loss factor ( $\tan\delta = G''/G'$ ) are all measured in a hydrogel rheological characteristics.

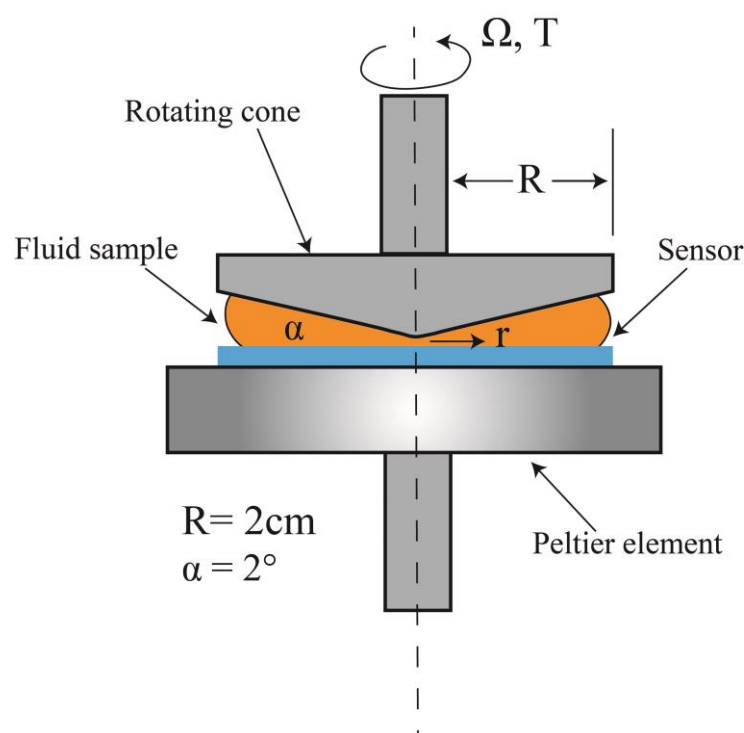


**Figure 2.15** Schematic representation of oscillatory rheology setup with cone plate above the sample.

A viscoelastic property of a hydrogel can be explained by its parameter of measurement duration, frequency, and strain.  $G'' > G'$  ( $\tan \delta > 1$ ) implies a viscous–liquid driven hydrogel, whereas  $G' > G''$  ( $\tan \delta < 1$ ) indicates an elastic solid governed hydrogel. The storage modulus,  $G'$ , and loss modulus,  $G''$ , are the most common parameters evaluated for a hydrogel in a common oscillatory rheological experiment.  $G'$  (Pa) and  $G''$  (Pa) are commonly measured as functions of time, angular frequency, and oscillatory strain. A linear viscoelastic regime (LVR) of a material can be determined by monitoring the moduli versus strain curve.<sup>68</sup> Initially strain sweep was carried out to evaluate the LVR. The peptide hydrogels were then subjected to dynamic frequency sweep rheological analysis on Anton Parr MCR302 rheometer using a 50 mm parallel plate geometry. Peptide hydrogels were incubated for 24 hours before measurement. The storage modulus ( $G'$ ) and loss modulus ( $G''$ ) of the hydrogels were recorded as a function of frequency between 1 to 100 Hz while maintaining the temperature 25 °C throughout the experiment. A time-dependent strain was applied to access the thixotropic behaviour of peptide hydrogels at a frequency of 0.1% to 100% to monitor gel to sol transition and vice versa. Both the frequency sweep and thixotropic studies were repeated thrice to ensure the reproducibility of the produced data.

#### **2.4.12.2 Thixotropic measurements**

The storage modulus evolution of a hydrogel immediately after it has been subjected to steady-state shear of considerable amplitude by the upper plate of a bench-top rheometer is a regularly used methodology for measurement of investigating the shear-thinning and self-healing behaviour of physical hydrogels. Following shearing, such a measurement frequently reveals a considerable fall in the storage modulus value, followed by slow storage modulus evolution post-shear cessation. To examine the under shear and post-shear behaviour, solid injectable hydrogels are shear treated with a rheometer. The thixotropic nature of the hydrogels developed from collagen inspired peptides were explored by applying step strain cycle with maximum deformation of 100% for 600 seconds followed by 1% strain for 200 seconds at 1Hz. The thixotropic behaviour of the hydrogels was monitored up to 5 cycles and to check the change in the fiber morphology, AFM samples were made at different strain points. Further to check the injectability and printability of the peptide hydrogels, we performed dynamic compression test to calculate the force required to extrude the hydrogel from a syringe with needle of gauge size 30.

### 2.4.12.3 Dynamic compressive strain study

The injectability and printability nature of the peptide hydrogels were examined via dynamic compressive strain study using axial compression tester, BiSS, India. The prepared hydrogel was transferred into a 2.5 cc syringe with 18G needle and the extrusion was made at a rate of 50  $\mu\text{L/s}$ , which calculates the force required for the extrusion of the peptide hydrogel.

### 2.4.13 Mechanical stiffness via peak force quantitative nano-mechanics

Atomic Force Microscopy (AFM) is a well-known scanning probe microscopy technique for investigating materials topology, which have the ability of sense the surface of a sample via electrically and magnetically.<sup>69, 70</sup> SPM provides nanometre resolution and non-destructive interaction with samples, which makes it very useful tool for biologist.<sup>71</sup> Apart from the topographical information, AFM can also be used to detect the intermolecular forces with a spatial resolution. It can be used to provide *in situ* imaging of an indentation point and can calculate the Young's modulus (E) of the material.<sup>72-74</sup> Contact angle ( $A_c$ ) between the AFM probe and sample surface can only be measured via the nanometric contact. Contact mechanic models have been reported to examine the AFM picoindentation data: (i) Hertz model, (ii) JKR model (Johnson, Kendall and Roberts), and (iii) DMT model (Derjaguin, Muller and Toporov). In this thesis, we have used Hertz model to calculate the Young's modulus of the peptide nanofibers and hydroxyapatite mineralized peptide nanofibers in **chapter 5**.

In 1981, a German physicist developed the model Henrich-Hertz, where both the tip and the sample are considered as two spheres of radius  $R_1$  and  $R_2$ . This model does not calculate the interpenetration of the materials nor the acting force ( $F_a$ ) between the surface and the AFM tip, it only assumes elastic deformation of the material. The contact between the sample and the tip gives a flat and circular contact, which is given by this equation:

$$A_c = \pi \left[ \frac{RF}{K} \right]^{2/3} \dots\dots\dots(\text{Eq. 2.3})$$

Where, R represents combined curvature radius and K is the combined elastic modulus of the material.

$$K = \frac{4}{3} \left[ \frac{1-\nu_i^2}{E_i} + \frac{1-\nu^2}{E} \right]^{-1} \dots\dots\dots(\text{Eq. 2.4})$$

E represents Young’s modulus of the material and  $\nu$  represents the Poisson ratio of the indenter.

Calculating the Young’s modulus of peptide nanofibers follows four basic steps: (i) tip sensitivity, (ii) spring constant, (iii) indenting the sample, and (iv) fitting the curve and calculating the Young’s modulus. **Tip sensitivity:** This is an experimental value, correlating the tip deflection and photodetector voltage. To obtain the tip sensitivity, an undeformable surface is required (blank silicon wafer used in this study). The experiment was performed in contact mode with a setpoint of 0.5V and deflection of 100 nm. Select the “*ramp*” button and set force distance to 500 nm in the master panel and press *continuous* scan. A force distance curve appears and to overcome the piezo drift the continuous scan was left to run for 5-10 minutes. After that, perform a single scan and check whether the blue and red lines are on top of each other. Select the deformation area as shown in (Figure 2.16b) and click on *calculate the deflection sensitivity* in the master panel, the value should be between 30-100 nm/V.

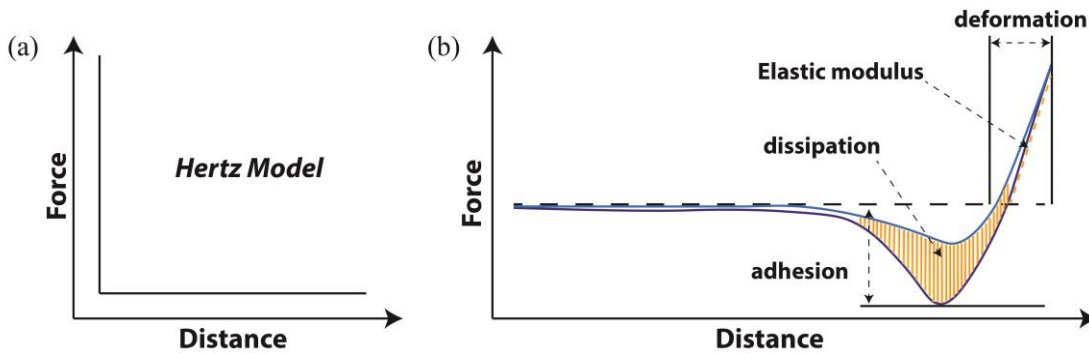


**Figure 2.16** Schematic representation of the (a) interaction forces for Hertz model (with area normalized) and (b) force-distance curve, displaying the different contact regime between the tip and the surface as both the bodies approaches.

After this, we have calculated the **spring constant** by using thermal tuning. Withdraw the tip to a certain distance and perform thermal tuning, the microscope will now complete the cantilever tuning and record 50 spectrum. Click “*fit*” and calculate the spring contact, the spring constant of a tip lies between 50-200 pN/nm. Now, the silicon wafer containing peptide nanofiber was mounted and the image was taken in contact

mode and from the image 50-100 points were chosen and analysed via “*point and shoot*”. A number of force-distance curve was obtained from different region of the sample, to get statistically relevant data. For fitting the curve, open the force curve in analyses window and fit the curve in axis 1 by keeping force in y axis and steps or distance in x axis. For calculating the Young’s modulus apply Hertz model equation;

$$F = \left[ \frac{3}{4} E_{\text{eff}} \sqrt{R} \right] h_e^{3/2} \dots\dots\dots(\text{Eq. 2.5})$$

Where,  $F$  is the applied force and  $E_{\text{eff}}$  is the elastic modulus, which can be calculated from the below equation.

$$\frac{1}{E_{\text{eff}}} = \left[ \frac{1-\nu^2}{E} + \frac{1-\nu_i^2}{E_i} \right] \dots\dots\dots(\text{Eq. 2.6})$$

Where  $\nu$  represents the Poisson ration and  $i$  corresponds to the substrate mechanical property ( $\text{SiO}_2$   $E_i= 76$  GPa and  $\nu_i = 0.17$ ).

$$\text{Slope} = \left[ \frac{3}{4} E_{\text{eff}} \sqrt{R} \right] \dots\dots\dots(\text{Eq. 2.7})$$

To further plot the force versus distance or separation curve, calculate the slope of contact region and extract the Young’s modulus from the below equation, where  $R$  corresponds to tip radius and  $h_e$  is the separation.<sup>69, 70</sup>

## **2.5 Assessment of biological response towards the developed matrix and their therapeutic applications**

### **2.5.1 Cell lines and maintenance of cells**

As indicated in the aims and objectives, we have explored the differential properties of the collagen inspired peptide, which varies from developing a synthetic scaffold or serving as a template for bone mineralization or towards development of polymer peptide conjugates etc. we have used cell lines from different tissues of origin to check

the biological response of the designed peptide hydrogels. In this thesis, we have used fibroblast cells (L929), as it is one of the major cells producing collagen for the structural support for the tissue and we have used osteoblast cells 7F2 and Saos-2 for studying the effect of mineralized peptide fibers.<sup>75</sup> We have also utilized neural (SH-SY5Y) and glioma cells (C6) to check the comparative effect of the peptide fibers on the soft tissue cells to assess the diversity of the developed matrices. The cell lines were procured from National Centre for Cell Science (NCCS), Cell repository, Pune, India and American Type Culture Collection, USA.

Fibroblast (L929), osteoblast (7F2) and glioma (C6) cells were cultured in Dulbecco's Modified Eagle Medium (DMEM), supplemented with 10% fetal bovine serum and 1% pen-strep solution. Neural cells were grown in Ham's F-12 medium with high glutamate and 10% fetal bovine serum and 1% pre-strep solution. Osteoblast cells (Saos-2) were cultured in McCoy's 5A supplemented with 20% fetal bovine serum and 1% Pen-Strep antibiotic solution. All the cells were cultured at 37°C in a humidified incubator, with 5% CO<sub>2</sub>. For long term studies, the medium was changed after every 48 hours of incubation and the cells were trypsinized at 70% of their confluency with 1X trypsin-EDTA solution.

**Table 2.1** Description of cell lines with their culture medium and source of origin.

Cell line	Source	Media
<b>L929 cell line</b>	Mouse fibroblast	DMEM + 10% FBS +1% Antibiotic
<b>C6 cell line</b>	Rat glioma	DMEM + 10% FBS +1% Antibiotic
<b>SH-SY5Y cell line</b>	Human Neuroblastoma	Ham's F-12 + 10% FBS + 1% Antibiotic
<b>7F2 cell line</b>	Mouse Bone Marrow	DMEM + 10% FBS +1% Antibiotic
<b>Saos-2 cell line</b>	Human Osteosarcoma	McCoy's 5A + 10% FBS + 1% Antibiotic

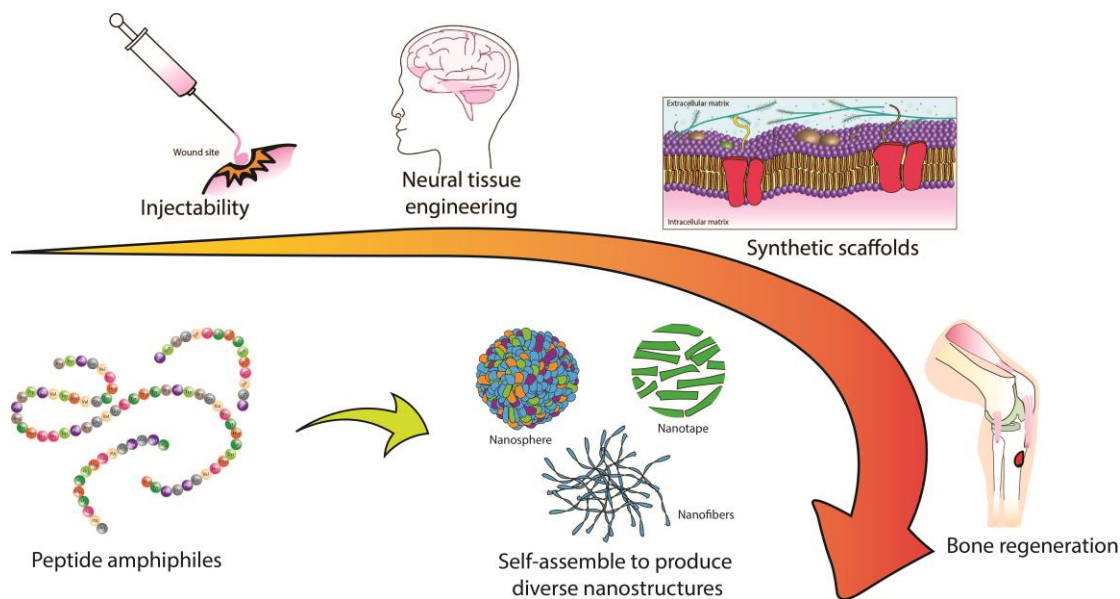


**Figure 2.17** Schematic representation of the diverse nanostructure achieved by short peptide amphiphiles and their applications in biomedical field.

### 2.5.2 Biocompatibility studies

The biocompatible behaviour of the designed peptides were estimated by a most widely used method, MTT [3- (4, 5-Dimethylthiazol)-2, 5-Diphenyltetrazolium bromide] assay.<sup>76</sup> MTT is a pale yellow coloured compound, which readily penetrates into the live mammalian cells. The tetrazolium dye gets reduced in the presence of several oxidoreductases and dehydrogenases enzyme to convert into the formazon product. The produced formazon product accumulates inside the cells in insoluble form and get solubalized in presence of DMSO.<sup>5, 77</sup> The method has been used to assess the cytotoxicity of the proposed peptides in its monomeric form and also in its self-assembled form for the different cell lines used in this thesis. The cells with density 5000 per well were seeded and incubated before the treatment of peptide at a concentration range of 100 to 1000  $\mu\text{g}/\text{mL}$ . In particular, cells were incubated with the peptide samples at variable concentrations for 24 and 48 hours respectively to monitor the changes in morphology. The cytotoxicity was evaluated by incubating the cells further with MTT for 4 hours. MTT dye was reduced by live population of the cells and resulted in formazan, which is readily soluble in DMSO.<sup>78</sup> The quantity of solubilized formazan produced was measured at 595 nm. This value is directly proportional to the

cellular viability. All experiments were repeated three times in triplicates, and the data are represented as mean  $\pm$ SD.

### 2.5.3 2D cell culture

A conventional approach was followed towards developing the synthetic scaffold that involves securing, nourishing and growing cell cultures on a flat bottom of tissue culture flask or petridish.<sup>79</sup> They are the foundation for practically all contemporary routine assays and have a large body of literature to back them up.<sup>80</sup> 2D cell culture is a traditional method to assess the cellular adhesion and proliferation ability of the synthetic scaffold casted on a flat bottom.<sup>81</sup> 2D culture of the cells for assessment of biocompatibility and the evaluation of the potential of the collagen inspired peptide hydrogels towards supporting cellular growth and survival were determined on a 2D matrix formed by the hydrogel.<sup>82, 83</sup> A thin layer of peptide fibers were coated on the surface of the sterilized coverslip and placed in cell culture dishes. The thin layer of the nanofibers and the hydrogel were sterilized under UV in a biosafety cabinet, followed by overnight incubation with DMEM for media exchange in the hydrogel matrix. The hydrogel-coated coverslips were assessed for their stability upon incubation in a cell culture medium for media exchange and long-term media perfusion. Perfused media was exchanged with the media containing  $5 \times 10^4$  cells and incubated for different periods before examining for the live and dead population. A time-dependent study was carried out to assess the exposure effect of peptide environment for different types of cells.

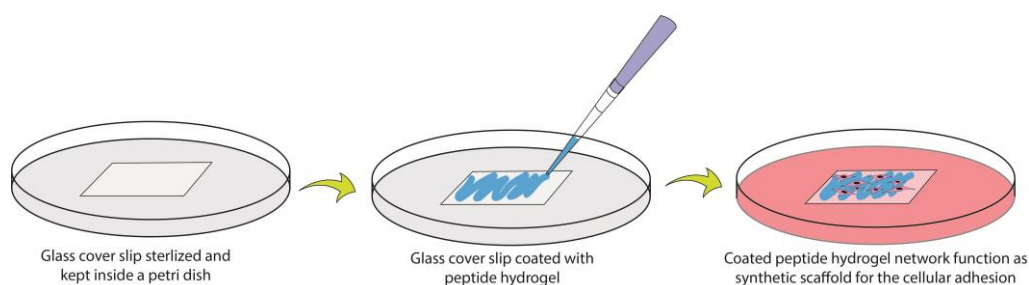


**Figure 2.18** Schematic representation of the peptide hydrogels working as 2D scaffolds for the cellular adhesion and growth.

The adhered cells were monitored in a confocal laser scanning microscope (CLSM) using live-dead staining, as described in the next section.

#### 2.5.4 Live-Dead Staining

To differentiate the live and dead population in a 2D culture, the cells were differentially labelled (fluorescently) and observed under confocal microscope. We have used DiOC<sub>18</sub>(3) and PI for staining live and dead population in **chapter 6**. DiOC<sub>18</sub>(3) is a lipophilic dye, which stain the membrane and gives green fluorescence. In **chapter 4 and 5**, live cells were stained with fluoresceine diacetate (FDA) and similarly dead cells were stained with propidium iodide (PI). DiOC<sub>18</sub>(3) is a lipophilic carbocyanine green fluorescent dye, which gives high fluorescent intensity when incorporated into the membrane.<sup>84, 85</sup> It can stain both types of cells live as well as dead, whereas fluoresceine diacetate is a cell permeable esterase dye that serve as a viability probe for measuring the enzymatic activity of the cells. The green fluorescent produced upon hydrolysis by the intracellular esterase to highly fluorescet fluoresceine and can only stain the live cells.<sup>86, 87</sup> The working solution of FDA was prepared by adding 4  $\mu$ L of stock per 1 mL of PBS from 3.5 mM stock solution prepared in DMSO. Similarly, a stock solution of Propidium iodide (PI) was prepared in PBS (3.75 mM) 2  $\mu$ L of this stock solution was diluted in 1 mL of PBS to prepare the working solution of PI. Both the dyes were filtered before use to remove the undissolved crystals of the dye. Cells were incubated with FDA for 15 minutes, followed by washing with 1X PBS three times. Further, cells were incubated with PI for 20 minutes, followed by washing with 1X PBS three times. The cells adhered onto the hydrogel matrix were visualized using a confocal laser scanning microscope (Zeiss LSM880 confocal microscope, Carl Zeiss) and the images were captured with 10x magnification.

#### 2.5.5 Cellular proliferation assay

The relative rate of cell division within a target tissue can be assessed by using an immunohistochemistry staining technique.<sup>88, 89</sup> A cell proliferation assay provides a direct and accurate measurement of the number of live-dead cells in a population. In this thesis, we have used Alamar Blue assay to quantitate the cellular proliferation in **chapter 4,5 and 6**. Alamar Blue is a fluorescence indicator used to quantify cellular viability and proliferation at different time points. Thin layer of peptide fibers, mineralized peptide and conjugate hydrogels were coated on the surface of 96 well-plate. Coated samples were sterilized via UV in a biosafety cabinet, followed by the addition of respective medium to perfuse into the hydrogel matrix, and were kept for

overnight incubation. Perfused media was replaced with the media containing 1000 cells/well and examined for the proliferation at different time points of 48 hrs, 72 hrs, and 120 hrs respectively, using Alamar blue assay. 10% of Alamar blue in respective medium was prepared and incubated with treated cells for 8 hours. The incubated samples were further monitored in a microplate reader (Tecan Infinite M Plex) to study the reduction of Alamar blue solution using an excitation and emission wavelength of 560nm and 590nm, respectively. Experiments were repeated three times, and data were represented as mean  $\pm$  SD.

### **2.5.6 Immunofluorescence staining**

Cells of neuronal origin have shown the most abundant class III  $\beta$ -tubulin isotype, but its widespread distribution in tumors has also demonstrated neuronal differentiation.<sup>90</sup> Morphological changes in the neuronal cells are linked to the reorganization of the actin cytoskeleton, which further is controlled by the expression of the  $\beta$ -III tubulin.<sup>91, 92</sup> To assess the morphological changes that occurred in the glioma and neuronal cells at different time points of peptide treatment, we have monitored the microtubule formation via immunofluorescence staining technique.<sup>93</sup> Peptide hydrogel-coated coverslips containing cells adhered on top of the surface were observed for the  $\beta$ -III tubulin expression and monitored for the different period time of 48 hrs, 72 hrs, and 120 hrs, respectively. *Glioma* (C6) and *neural* cells (SH-SY5Y) were studied for the expression of  $\beta$ -III tubulin. In this experiment,  $5 \times 10^4$  cells were seeded and cultured on coverslips coated with peptide hydrogel for three different time points 48 hrs, 72 hrs, and 120 hrs respectively. The cultured cells for the respective days of study were fixed for 15 minutes in 4% solution of formaldehyde. After fixing, samples were washed thrice with 1X PBS to remove the excess formaldehyde from the dish and further permeabilized with 0.5% TritonX-100 at room temperature for 15 minutes. Again, the cells were washed thrice and kept in 5% BSA solution for an hour for blocking. After blocking, cells were washed using 1X PBS followed by incubating it with rabbit monoclonal primary antibody against  $\beta$ -III tubulin (1:500 dilution) (D71G9, CST) at 4°C for overnight. After primary antibody binding, cells were washed with dilution buffer (1% BSA, 0.1 % TritonX-100 in 1X PBS) followed by incubation with anti-rabbit Alexa Fluor 555 conjugate (1:1000 dilution) (4413S, CST) for 2 h. Cell nuclei were stained with DAPI (1 $\mu$ g/mL) (TC229, HiMedia) after completing the immunostaining. The coverslips were mounted and visualized via confocal laser

scanning microscope (Zeiss LSM880 confocal microscope, Carl Zeiss), and the images were captured under high magnification (63x).

### **2.5.7 F-actin staining**

In order to visualize and quantitate the change in morphology of the cells in the presence of peptide, cells were stained with Rhodamine Phalloidin for F-actin, which binds to the actin filament of the cytoplasm, and to stain the nuclei of the cells, DAPI has been utilized.<sup>94</sup> The morphological analysis of phalloidin staining can be judiciously correlated with the cellular viability and adhesion assays.<sup>94</sup> Fibroblast and osteoblast cells were used to stain F-actin in **chapter 4,5 and 6** to show the spread morphology of the cells and change in shape upon differential treatments. F-actin staining of fibroblast cells provides the change in cell shape upon peptide treatment. In each experiments 50,000 cells were seeded and cultured on coverslips coated with peptide hydrogels for three different periods 48 hrs, 72hrs, and 120hrs, respectively. The cultured cells for the respective days of study were fixed for 15 minutes in 4% solution of formaldehyde. After fixing, samples were washed thrice with 1X PBS to remove the excess formaldehyde from the dish and further permeabilized with 0.5% TritonX-100 at room temperature for 15 minutes. Again, the cells were washed thrice and kept in 5% BSA solution for an hour for blocking. After blocking, cells were further incubated with Rhodamine Phalloidin (1:250 dilution) (Invitrogen R415) in PBS with 1.5% w/v BSA at room temperature for 30 minutes. Cell nuclei were stained with DAPI (1µg/ml) after completing the Phalloidin staining. The coverslips were mounted and visualized by confocal laser scanning microscope (Zeiss LSM880 confocal microscope, Carl Zeiss), and the images were captured at higher magnification (63x).

### **2.5.8 Alizarin Red staining**

Alizarin Red S (3,4-Dihydroxy-9,10-dioxo-9,10-dihydroanthracene-2-sufonic acid) is a water-soluble sodium salt.<sup>95</sup> Alizarin Red S is broadly used for staining calcium deposits in tissue. The dye known to bind the calcium species in the cells and gives pink or red colour under bright field microscope.<sup>42</sup> In chapter 5 we have allowed the cells to grow on the mineralized peptide matrix and further harvested at different time points of 3, 5 and 7 days, respectively. After removing the residual media, the cells were washed with 1X PBS. The treated cells were fixed with 4% para-formaldehyde solution for 15 minutes followed by washing with PBS thrice. The fixed cells were then stained

with 2% Alizarin red stain (pH 4.1 - 4.3) for 5 minutes. The pH of the Alizarin red solution was adjusted by 0.5M sodium hydroxide solution. The stained cells were then washed for several times with milli-Q and observed under bright field microscope. To further quantitate the amount of calcium deposits in the mineralized cells, the stained dyes, was resubstituted in the 20% acetic acid solution for 20 minutes followed by neutralization in ammonia. The absorbance of the dissolved stain was quantitated in the spectrophotometer at 405nm, which is the absorption maxima of the dye.

### 2.5.9 Scratch assay

Cellular migration plays a crucial role in the development and maintenance of multicellular organism. Cellular migration can be divided into two types: (1) a single migration and (2) collective cell migration. Collective cell migration involves cell-cell adhesion, cell polarization, chemical and mechanical cues, which allows the cells to migrate collectively. *In vitro* scratch assay provide an easy, low cost and well developed method to determine the migration property of cells. A monolayer of cells were scratched by creating a clean surface for the cells to migrate.

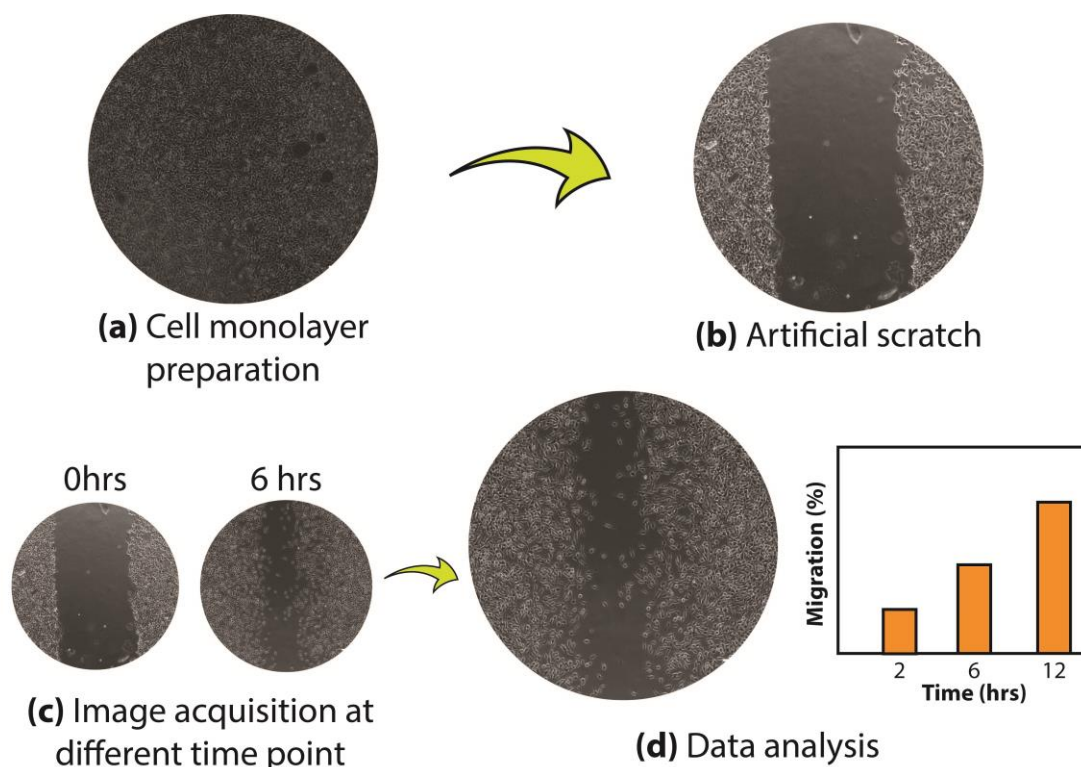


**Figure 2.19** Schematic representation of the scratch assay, showing the cellular migration over time.

A time point observation under microscope helps to quantify the rate of migration of cells. This assay is used to understand the molecular mechanism affecting the cellular migration and the effect of synthetic biomolecules on modulating the cellular migration for several therapies. To study the cellular migration or wound healing property of the reported material in this thesis, we have performed scartch assay and the similar protocol has been followed in **chapter 4,6 and 7**. Promotion of cellular migration or wound closure capability by the peptide hydrogelator was assessed by performing in vitro scratch assay. The cells were seeded at a density of  $10^5$  cells per well in 24 well plate and allowed to form a monolayer. A scratch was made with the help of 1mL tip into each of the wells containing a monolayer of cells. The pre-formed gels were UV sterilized and then diluted with cell culture media to make the solution concentration of 1000  $\mu\text{g/ml}$ , further added to the cells. The plate was placed in an incubator and imaged at different time points (0 h, 12 hrs, 24 hrs) using an upright Olympus microscope at 10X magnification. The quantification of the area covered by cellular migration in the wound site was done by ImageJ software.

#### **2.5.10 Quantitative assessment of cellular population via Fluorescence Activated Cell Sorting (FACS)**

Fluorecence-activated cell sorting (FACS) is a specialized technique to sort the heterogenous mixture of biological cells based on their differential phenotype.<sup>96</sup> Through this elegant technique, investigation of a single cell population can be performed without influencing other cells. The workin principle uses specific light scattering and fluorecent characteristic of each cells.<sup>97, 98</sup> A cell suspension used for separation are allowed to enter into a narrow, rapidly flowing stream of liquid and the stream flow was managed in a way to maintain a sufficient separation between cells relative to their diameter.<sup>99</sup> Further, the stream was modulated to form small droplets via vibrating mechanism and the system is adjusted in a way that only one cell can enter in a single droplet. This droplet was further passed from a fluorescence measuring station, which identify and separate the cells according to the fluorescent character of the cells. We have used FACS for quantification of live dead population of mammalian cells in the peptide treated samples and also in the bacterial population in **chapter 4, 6 and 7**, respectively. In case of mammalian cells, a fixed population was treated with peptide hydrogels, and then the live/dead population of the cells was quantified with fluorescein diacetate (FDA)/PI stain.

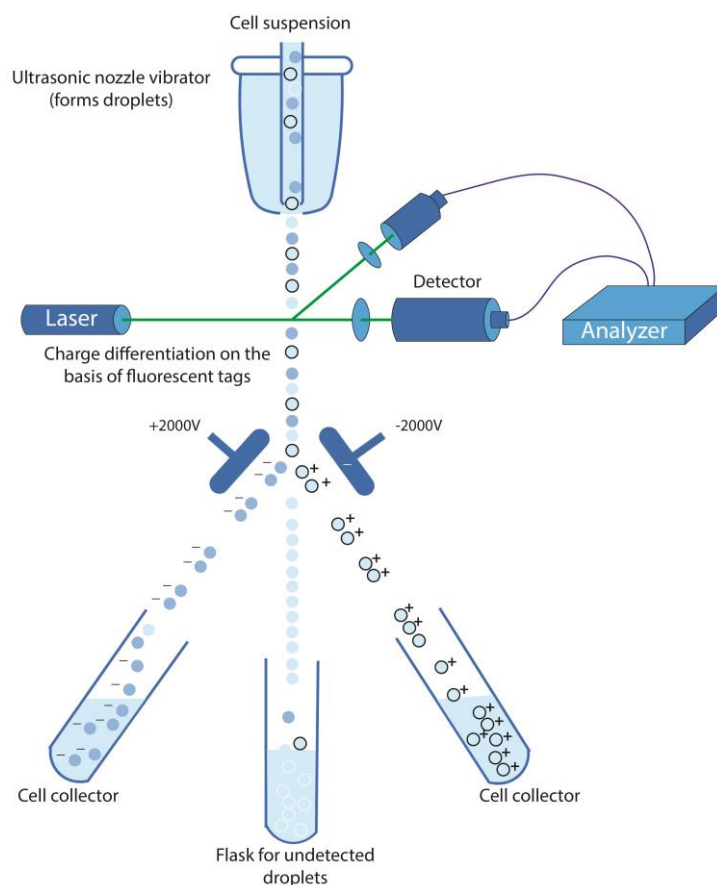


**Figure 2.20** Schematic representation of the working principle of fluorescent activated cell sorting (FACS).

In this experiment, fibroblast (L929), glioma (C6) and neural (SH-SY5Y) cells were seeded at a density of  $5 \times 10^5$  cells in culture dishes and incubated for 24 hours prior to the treatment with the hydrogels. After that, DMEM containing  $1000 \mu\text{g/mL}$  of peptide both in the presence and absence of metal salts were used as a treatment for the cells, which were kept for incubation. After the incubation of 48 hours, cells were trypsinized and transferred to microcentrifuge tubes. Cells were pelleted down via centrifugation (3000 rpm; 5 min) and washed three times using 1X PBS. The cells were then stained with FDA and PI for 15 minutes and washed subsequently with 1X PBS. Further, the stained cells were resubstituted in  $500 \mu\text{L}$  PBS and proceeded for the analysis. Percentage of viable and dead cells were analyzed via FACS Aria flow cytometer (BD Biosciences, San Jose, CA, USA). The fluorescence of FDA and PI were collected in FITC and PI channels, respectively. A total of 10,000 events from each sample were acquired to ensure adequate data, and FlowJo software was used to represent the data using pseudocolor. Detailed description of sample preparation for bacterial population via FACS has been discussed in section 2.5.12 (Live-Dead assay).

### 2.5.11 ALP estimation (enzymatic mineralization)

Alkaline phosphatase (ALP) plays a crucial role in the remodelling of bone and its resorption and mineralization of carbonated apatite.<sup>100</sup> The enzyme directed deposition of carbonated apatite hydrolysis of organic phosphoesters increases the local concentration of inorganic phosphate groups. ALP directs the hydrolysis of organic phosphoesters leading to the increased production of inorganic phosphate group in the surrounding environment, which results into deposition of carbonated apatite.<sup>101, 102</sup> Moreover, ALP is also known to decrease the pyrophosphate concentration, which generally inhibit the growth of apatite crystals. ALP also regulate the process of calcification, which suggests its role in the early stage of mineralization. In order to analyse the *in vitro* ALP activity, cell lysate was collected at day 3, 5 and 7. The media was removed and cells were washed with 1X PBS, the cells were then harvested by trypsinization and resuspended in milli-Q water. The cells were sonicated for 20 minutes and the supernatant was collected in a different microcentrifuge tube and further frozen at -20°C. In order to estimate the ALP activity, 100 µL of the supernatant of cells were added to the 100 µL of working reagent consisted of (0.5M 2S-amino-2 methyl-l-propenyl), 5mM p-nitro-phenol phosphate, 5mM magnesium chloride (1:1:1). Equal volume of sodium hydroxide was used to stop the reaction and the final absorbance was measured at 405nm in a plate reader.

### 2.5.12 Assessment of antimicrobial activity

Protein/peptide based self-assembled systems have been widely used in developing antimicrobial therapeutics because of their structural versatility and functional benefits.<sup>103, 104</sup> Such intrinsic property has shifted the interest in constructing an array of well-defined versatile nanostructures with diverse antimicrobial functions.<sup>105, 106</sup> Peptide nanostructures may play different roles to showcase efficient antimicrobial activity: 1) charged peptide surface induce antimicrobial activity or 2) it may act as efficient nanocarrier to transport the antimicrobial agents in a facile manner. In this thesis, antimicrobial property of ferulic acid encapsulated in the peptide-based nanoparticle (FA-NPs) were examined in **chapter 7**. As the nanoparticle showed structural transition at slightly basic pH of 8.5 and to study the antibacterial effect of the released ferulic acid on bacterial population, the bacterial culture was grown in a modified medium of pH 8.5. This modified medium will also provide the necessary

environment for the nanoparticle to undergo structural transition to release the encapsulated ferulic acid.

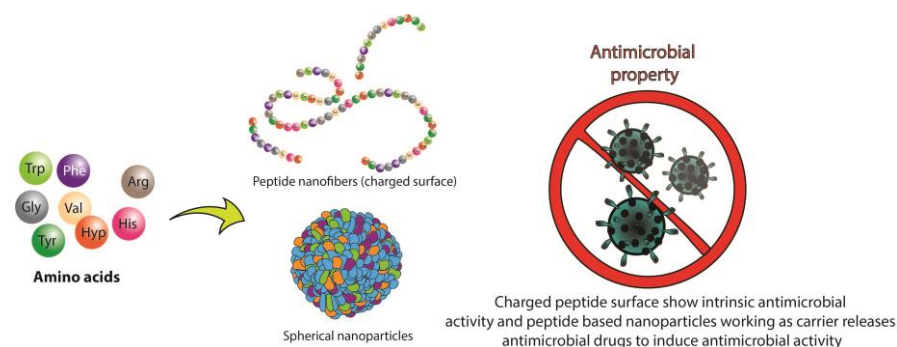


**Figure 2.21** Schematic representation of amino acids as building block for development of differential nanostructures capable of giving antimicrobial properties.

For determining the MIC values, both the bacterial cultures (*E. coli* and *S. aureus*) were grown to their log phase. The bacterial populations were further diluted with the liquid medium containing different concentrations of ferulic acid nanoparticles (0 - 1000 [FA]  $\mu\text{g mL}^{-1}$ ) to obtain a final cell density of  $10^8$  cfu  $\text{mL}^{-1}$ . The 12-well plate (polystyrene flat bottom) containing bacterial culture was incubated with nanoparticles at 37 °C for 6 hours. The growth percentage was calculated by measuring the OD at 600 nm against a blank (without cells) after the incubation. To further confirm the inhibitory activity of the nanoparticles, 100  $\mu\text{L}$  of the same incubated sample was plated onto the nutrient agar plate and further incubated for 12 hours at 37 °C to observe any growth. The differential colony-forming ability of the treated samples can be observed in the incubated agar plates.<sup>107</sup>

*Live-Dead Assay.* The bactericidal activity of the FA-NPs was analyzed by monitoring the change in the cellular population via CLSM and FACS studies at the sub-MIC concentrations (750 and 900 [FA]  $\mu\text{g mL}^{-1}$ ). The overnight grown bacterial culture of *E. coli* cells ( $2 \times 10^8$ ) and *S. aureus* cells ( $2 \times 10^7$ ) were harvested by centrifuging the bacterial suspension for 10 minutes at 6000 rpm, and at 4°C. The obtained pellet of bacterial culture was washed with normal saline (0.85% NaCl) to remove the excess media, preventing the further division of the bacterial cells. The pellets were resuspended in the normal saline containing the FA-NPs at their desired minimum inhibitory concentrations. The cells exposed to the nanoparticles were incubated for 6 hours to see the interactive effect of the nanoparticles on the bacterial cells. The exposed cells were again centrifuged and resuspended in the normal saline to reach the cell

density of  $2 \times 10^6$  cfu mL<sup>-1</sup>. The cell suspensions were stained with Syto9 (9  $\mu$ M) and PI (30  $\mu$ M) using LIVE/DEAD Backlight Bacterial Kit for 20 minutes under dark conditions.<sup>108</sup> 5  $\mu$ L of the stained bacterial suspension was trapped between an 18 mm square coverslip and a glass slide, which was further monitored under a confocal microscope. For the FACS-based quantification, a similar sample preparation process was followed, and the stained cells were diluted (1:50) in normal saline. The samples were analyzed on a FACS Aria Fusion instrument (BD Sciences, San Jose, CA, USA) using a blue laser (488 nm) and yellow-green laser (561 nm) for the excitation of Syto 9 and PI, respectively. A total of 10,000 events from each sample were acquired to ensure adequate data and represented in a pseudocolor plot using FlowJo software.

### 2.5.13 Evaluation of Reactive Oxygen Species (ROS) generation

It has been reported in the literature that the mechanism of antimicrobial activity relies on the irreversible change in the membrane integrity (local rupture and pore formation) of the bacterial cells through hydrophobicity changes and decline in negative surface charge leads to the leakage of essential intracellular constituents.<sup>109, 110</sup> These are the well-known pathways for the bactericidal activity of ferulic acid as discussed in **chapter 7**.<sup>107, 111</sup> In this direction, the extent of reactive oxygen species (ROS) generation and membrane damage in both bacterial cultures were determined. Freshly cultured cells of both strains were harvested by centrifugation (6000 rpm, 10 minutes, at 4°C), followed by washing thrice with normal saline, and further resuspended in the same medium.

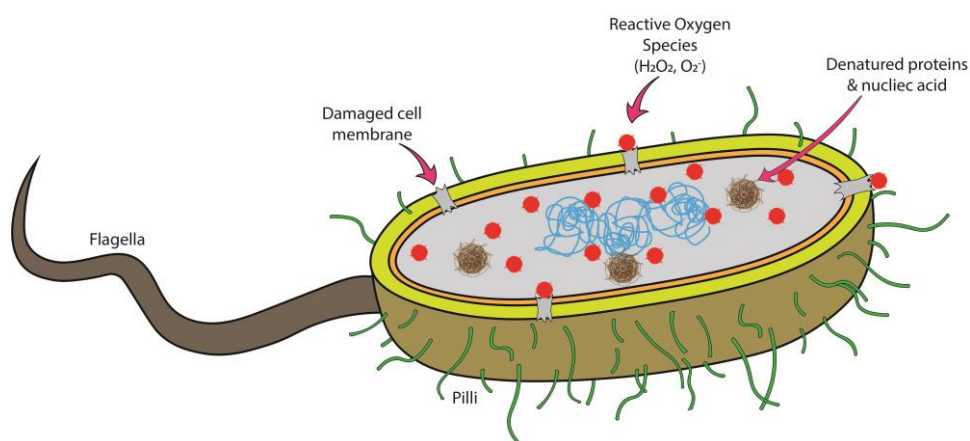


**Figure 2.22** Schematic representation of ROS generation leading to cell wall rupture and bacterial cell death and estimation via DCFH-DA.

An oxidation-sensitive fluorescent dye, DCFH-DA (2,7-dichlorodihydro-fluorescein diacetate) was used for the ROS generation assay.<sup>112</sup> The bacterial cells were stained with DCFH-DA (10  $\mu\text{M}$ ) for 1 hour in the dark (150 rpm, 37°C) before exposing the cells to the nanoparticles. The dye penetrates within the bacterial cells, where the diacetate was cleaved by the esterase enzyme, resulting in unstable DCFH. Upon treatment with the nanoparticles, bacterial cells generate reactive oxygen species, which react with the unstable DCFH and convert it into a fluorescent DCF. The DCFH-DA loaded cells were centrifuged and washed twice with normal saline to remove the free dye molecule. Furthermore, the stained cells were exposed to the nanoparticles and kept for incubation for 6 hours in dark conditions. The fluorescence intensity of the released DCF, was recorded in a microplate reader (Tecan Infinite M Plex) using an excitation and emission wavelength of 485 and 535 nm, respectively. Cells without DCFH-DA were used as a negative control, and nanoparticles dispersion (500  $\mu\text{g mL}^{-1}$ ) with 2 mM  $\text{H}_2\text{O}_2$  was employed as a positive control.<sup>113</sup>

#### **2.5.14 Malondialdehyde Assay (MDA)**

Malondialdehyde (MDA) is among the most commonly used biomarker to determine lipid peroxidation.<sup>114</sup> Oxidative degradation of fatty acids, glycolipids, phospholipids are the major factors responsible for lipid peroxidation, which leads to membrane disruption of bacterial cells. Lipid peroxidation leads to the damaged membrane, which can be further assessed by colorimetric measurement of the extent of malondialdehyde (MDA) in cells.<sup>114</sup> Extent of lipids peroxidation was estimated in **chapter 7**, where peptide based nanoparticles encapsulating ferulic acid showed antibacterial property. Nanoparticle exposed cells were resuspended in 1 mL 2.5% (w/w) freshly prepared trichloroacetic acid, which was further followed by centrifugation at high speed (12000 rpm, 20 minutes, 4°C). The supernatant was mixed with 0.5% (w/v) thiobarbituric acid and 20% (w/v) trichloroacetic acid in an equal volume. The mixture was further heated in a water bath for 30 minutes at 90°C, followed by centrifugation (12000 rpm, 20 minutes, 4°C). The absorbance of the MDA-TBA adduct was measured at 532 nm using a UV-Vis spectrophotometer, and the MDA content was expressed as picomoles per mg of protein.

### 2.5.15 Statistical analysis

The data were averaged and presented as mean SD. Cellular proliferation, migration results over the collagen inspired peptide scaffold and conjugate scaffolds as well as biological assays for evaluation of antimicrobial mechanism of ferulic acid were statistically analyzed using a two-way ANOVA (95% confidence interval) followed by Bonferroni's multiple comparison test with a triplicate sample size in GraphPad Prism 8.0 software. Asterisk symbols on the graph depict \*( $p \leq 0.05$ ), \*\*( $p \leq 0.01$ ), \*\*\*( $p \leq 0.001$ ), and \*\*\*\*( $p \leq 0.0001$ ) where P value less than or equal to 0.05 was considered to be statistically significant.

### 2.6 References

1. Saladin, P. M.; Zhang, B. D.; Reichert, J. M., Current trends in the clinical development of peptide therapeutics. *IDrugs : the investigational drugs journal* **2009**, *12* (12), 779-84.
2. Fischer E, F. E. U. e., Über einige Derivate des Glykocolls. *Ber. Dtsch. Chem. Ges.* **1901**, *34*, 2868-2877.
3. Bergmann M, Z. L., Über ein allgemeines Verfahren der Peptid-synthese. *Ber. Dtsch. Chem. Ges.* **1932**, *65* (7), 1192-1201.
4. Fields, G. B., Introduction to peptide synthesis. *Current protocols in protein science* **2002**, *Chapter 18*, Unit-18.1.
5. Pal, V. K.; Jain, R.; Roy, S., Tuning the Supramolecular Structure and Function of Collagen Mimetic Ionic Complementary Peptides via Electrostatic Interactions. *Langmuir* **2020**, *36* (4), 1003-1013.
6. Amblard, M.; Fehrentz, J. A.; Martinez, J.; Subra, G., Methods and protocols of modern solid phase Peptide synthesis. *Molecular biotechnology* **2006**, *33* (3), 239-54.
7. Merrifield, R. B., Solid Phase Peptide Synthesis. I. The Synthesis of a Tetrapeptide. *J. Am. Chem. Soc.* **1963**, *85* (14), 2149-2154.
8. Mueller, L. K.; Baumruck, A. C.; Zhdanova, H.; Tietze, A. A., Challenges and Perspectives in Chemical Synthesis of Highly Hydrophobic Peptides. **2020**, *8*.
9. Mant, C. T.; Chen, Y.; Yan, Z.; Popa, T. V.; Kovacs, J. M.; Mills, J. B.; Tripet, B. P.; Hodges, R. S., HPLC analysis and purification of peptides. *Methods in molecular biology (Clifton, N.J.)* **2007**, *386*, 3-55.
10. Boysen, R. I.; Hearn, M. T., HPLC of peptides and proteins. *Current protocols in protein science* **2001**, *Chapter 8*, Unit8.7.
11. Engstrom, R. C., Quantitative chemical analysis; second edition (Harris, Daniel C.). *J. Chem. Educ.* **1988**, *65* (5), A140.
12. Xu, W.; Jimenez, R. B.; Mowery, R.; Luo, H.; Cao, M.; Agarwal, N.; Ramos, I.; Wang, X.; Wang, J., A Quadrupole Dalton-based multi-attribute method for product characterization, process development, and quality control of therapeutic proteins. *mAbs* **2017**, *9* (7), 1186-1196.
13. Banerjee, S.; Mazumdar, S., Electrospray Ionization Mass Spectrometry: A Technique to Access the Information beyond the Molecular Weight of the Analyte. *International Journal of Analytical Chemistry* **2012**, *2012*, 282574.
14. Draper, E. R.; Adams, D. J., Controlling the Assembly and Properties of Low-Molecular-Weight Hydrogelators. *Langmuir* **2019**, *35* (20), 6506-6521.

15. Raeburn, J.; Zamith Cardoso, A.; Adams, D. J., The importance of the self-assembly process to control mechanical properties of low molecular weight hydrogels. *Chem. Soc. Rev.* **2013**, *42* (12), 5143-5156.
16. Jin, H.; Ding, Y.-H.; Wang, M.; Song, Y.; Liao, Z.; Newcomb, C. J.; Wu, X.; Tang, X.-Q.; Li, Z.; Lin, Y.; Yan, F.; Jian, T.; Mu, P.; Chen, C.-L., Designable and dynamic single-walled stiff nanotubes assembled from sequence-defined peptoids. *Nat. Commun.* **2018**, *9* (1), 270.
17. Nam, K. T.; Shelby, S. A.; Choi, P. H.; Marciel, A. B.; Chen, R.; Tan, L.; Chu, T. K.; Mesch, R. A.; Lee, B.-C.; Connolly, M. D.; Kisielowski, C.; Zuckermann, R. N., Free-floating ultrathin two-dimensional crystals from sequence-specific peptoid polymers. *Nature materials* **2010**, *9* (5), 454-460.
18. Isogai, A.; Saito, T.; Fukuzumi, H., TEMPO-oxidized cellulose nanofibers. *Nanoscale* **2011**, *3* (1), 71-85.
19. Saito, T.; Isogai, A., TEMPO-Mediated Oxidation of Native Cellulose. The Effect of Oxidation Conditions on Chemical and Crystal Structures of the Water-Insoluble Fractions. *Biomacromolecules* **2004**, *5* (5), 1983-1989.
20. Saito, T.; Kimura, S.; Nishiyama, Y.; Isogai, A., Cellulose Nanofibers Prepared by TEMPO-Mediated Oxidation of Native Cellulose. *Biomacromolecules* **2007**, *8* (8), 2485-2491.
21. Wan, C.; Li, J., Facile Synthesis of Well-Dispersed Superparamagnetic  $\gamma$ -Fe<sub>2</sub>O<sub>3</sub> Nanoparticles Encapsulated in Three-Dimensional Architectures of Cellulose Aerogels and Their Applications for Cr(VI) Removal from Contaminated Water. *ACS Sustainable Chemistry & Engineering* **2015**, *3* (9), 2142-2152.
22. Wan, Z.; Wang, L.; Ma, L.; Sun, Y.; Yang, X., Controlled Hydrophobic Biosurface of Bacterial Cellulose Nanofibers through Self-Assembly of Natural Zein Protein. *ACS Biomater. Sci. Eng.* **2017**, *3* (8), 1595-1604.
23. Rasmussen, M. K.; Pedersen, J. N.; Marie, R., Size and surface charge characterization of nanoparticles with a salt gradient. *Nat. Commun.* **2020**, *11* (1), 2337.
24. Ashizawa, K., [Nanosize Particle Analysis by Dynamic Light Scattering (DLS)]. *Yakugaku zasshi : Journal of the Pharmaceutical Society of Japan* **2019**, *139* (2), 237-248.
25. Ramos, A. P., 4 - Dynamic Light Scattering Applied to Nanoparticle Characterization. In *Nanocharacterization Techniques*, Da Róz, A. L.; Ferreira, M.; de Lima Leite, F.; Oliveira, O. N., Eds. William Andrew Publishing: 2017; pp 99-110.
26. Rogers, D. M.; Jasim, S. B.; Dyer, N. T.; Auvray, F.; Réfrégiers, M.; Hirst, J. D., Electronic Circular Dichroism Spectroscopy of Proteins. *Chem* **2019**, *5* (11), 2751-2774.
27. Gopal, R.; Park, J. S.; Seo, C. H.; Park, Y., Applications of circular dichroism for structural analysis of gelatin and antimicrobial peptides. *International journal of molecular sciences* **2012**, *13* (3), 3229-44.
28. Jiang, J.; Abramavicius, D.; Bulheller, B. M.; Hirst, J. D.; Mukamel, S., Ultraviolet spectroscopy of protein backbone transitions in aqueous solution: combined QM and MM simulations. *The journal of physical chemistry. B* **2010**, *114* (24), 8270-8277.
29. Laverty, G.; McCloskey, A. P.; Gilmore, B. F.; Jones, D. S.; Zhou, J.; Xu, B., Ultrashort Cationic Naphthalene-Derived Self-Assembled Peptides as Antimicrobial Nanomaterials. *Biomacromolecules* **2014**, *15* (9), 3429-3439.
30. Fabian, H.; Mäntele, W., Infrared Spectroscopy of Proteins. In *Handbook of Vibrational Spectroscopy*, 2001.
31. Haris, P. I.; Chapman, D., The conformational analysis of peptides using Fourier transform IR spectroscopy. *Biopolymers* **1995**, *37* (4), 251-63.
32. Yang, H.; Yang, S.; Kong, J.; Dong, A.; Yu, S., Obtaining information about protein secondary structures in aqueous solution using Fourier transform IR spectroscopy. *Nat. Protoc.* **2015**, *10* (3), 382-396.
33. Nevskaya, N. A.; Chirgadze, Y. N., Infrared spectra and resonance interactions of amide-I and II vibration of alpha-helix. *Biopolymers* **1976**, *15* (4), 637-48.
34. Cunha, A. V.; Salamatova, E.; Bloem, R.; Roeters, S. J.; Woutersen, S.; Pshenichnikov, M. S.; Jansen, T. L. C., Interplay between Hydrogen Bonding and Vibrational

- Coupling in Liquid N-Methylacetamide. *The Journal of Physical Chemistry Letters* **2017**, *8* (11), 2438-2444.
35. Lakowicz, J. R., Instrumentation for Fluorescence Spectroscopy. In *Principles of Fluorescence Spectroscopy*, Lakowicz, J. R., Ed. Springer US: Boston, MA, 2006; pp 27-61.
  36. Ishikawa-Ankerhold, H. C.; Ankerhold, R.; Drummen, G. P. C., Advanced fluorescence microscopy techniques--FRAP, FLIP, FLAP, FRET and FLIM. *Molecules* **2012**, *17* (4), 4047-4132.
  37. Itagaki, H., Chapter 3 - Fluorescence Spectroscopy. In *Experimental Methods in Polymer Science*, Tanaka, T., Ed. Academic Press: Boston, 2000; pp 155-260.
  38. Berezin, M. Y.; Achilefu, S., Fluorescence lifetime measurements and biological imaging. *Chem. Rev.* **2010**, *110* (5), 2641-2684.
  39. Hall, M. D.; Yasgar, A.; Peryea, T.; Braisted, J. C.; Jadhav, A.; Simeonov, A.; Coussens, N. P., Fluorescence polarization assays in high-throughput screening and drug discovery: a review. *Methods Appl Fluoresc* **2016**, *4* (2), 022001-022001.
  40. Biancalana, M.; Koide, S., Molecular mechanism of Thioflavin-T binding to amyloid fibrils. *Biochim. Biophys. Acta* **2010**, *1804* (7), 1405-12.
  41. Raeburn, J.; Chen, L.; Awhida, S.; Deller, R. C.; Vatish, M.; Gibson, M. I.; Adams, D. J., Using molecular rotors to probe gelation. *Soft Matter* **2015**, *11* (18), 3706-3713.
  42. Yakupova, E. I.; Bobyleva, L. G.; Vikhlyantsev, I. M.; Bobylev, A. G., Congo Red and amyloids: history and relationship. *Biosci. Rep.* **2019**, *39* (1), BSR20181415.
  43. Wu, C.; Scott, J.; Shea, J.-E., Binding of Congo red to amyloid protofibrils of the Alzheimer A $\beta$ (9-40) peptide probed by molecular dynamics simulations. *Biophys. J.* **2012**, *103* (3), 550-557.
  44. Jacob, R. S.; Ghosh, D.; Singh, P. K.; Basu, S. K.; Jha, N. N.; Das, S.; Sukul, P. K.; Patil, S.; Sathaye, S.; Kumar, A.; Chowdhury, A.; Malik, S.; Sen, S.; Maji, S. K., Self healing hydrogels composed of amyloid nano fibrils for cell culture and stem cell differentiation. *Biomaterials* **2015**, *54*, 97-105.
  45. Dehsorkhi, A.; Castelletto, V.; Hamley, I. W., Self-assembling amphiphilic peptides. *Journal of peptide science : an official publication of the European Peptide Society* **2014**, *20* (7), 453-467.
  46. Holder, C. F.; Schaak, R. E., Tutorial on Powder X-ray Diffraction for Characterizing Nanoscale Materials. *ACS Nano* **2019**, *13* (7), 7359-7365.
  47. Pope, C. G., X-Ray Diffraction and the Bragg Equation. *J. Chem. Educ.* **1997**, *74* (1), 129.
  48. Hyland, L. L.; Taraban, M. B.; Yu, Y. B., Using small-angle scattering techniques to understand mechanical properties of biopolymer-based biomaterials. *Soft Matter* **2013**, *9* (43), 10218-10228.
  49. Guilbaud, J.-B.; Saiani, A., Using small angle scattering (SAS) to structurally characterise peptide and protein self-assembled materials. *Chem. Soc. Rev.* **2011**, *40* (3), 1200-1210.
  50. Denis, S.; Eric, R. W., Confocal Microscopy. In *Encyclopedia of Biomaterials and Biomedical Engineering, Second Edition*, CRC Press: 2008.
  51. Vesely, P., Handbook of Biological Confocal Microscopy, 3rd ed. By James B. Pawley, Editor. Springer Science + Business Media, LLC, New York (2006). ISBN 10: 0-387-25921-X; ISBN 13: 987-0387-25921-5; hardback; 28 + 985 pages. **2007**, *29* (3), 91-91.
  52. Sanderson, M. J.; Smith, I.; Parker, I.; Bootman, M. D., Fluorescence microscopy. *Cold Spring Harb Protoc* **2014**, *2014* (10), pdb.top071795-pdb.top071795.
  53. Marrese, M.; Guarino, V.; Ambrosio, L., Atomic Force Microscopy: A Powerful Tool to Address Scaffold Design in Tissue Engineering. *J Funct Biomater* **2017**, *8* (1), 7.
  54. Chen, G.-f.; Xu, T.-h.; Yan, Y.; Zhou, Y.-r.; Jiang, Y.; Melcher, K.; Xu, H. E., Amyloid beta: structure, biology and structure-based therapeutic development. *Acta Pharmacologica Sinica* **2017**, *38* (9), 1205-1235.
  55. Li, M.; Xi, N.; Wang, Y.; Liu, L., Nanoscale Multiparametric Imaging of Peptide-Assembled Nanofibrillar Hydrogels by Atomic Force Microscopy. *IEEE Transactions on Nanotechnology* **2019**, *18*, 315-328.

56. Bagrov, D.; Gazizova, Y.; Podgorsky, V.; Udovichenko, I.; Danilkovich, A.; Prusakov, K.; Klinov, D., Morphology and aggregation of RADA-16-I peptide Studied by AFM, NMR and molecular dynamics simulations. *Biopolymers* **2016**, *106* (1), 72-81.
57. Vernon-Parry, K. D., Scanning electron microscopy: an introduction. *III-Vs Review* **2000**, *13* (4), 40-44.
58. Nguyen, J. N. T.; Harbison, A. M., Scanning Electron Microscopy Sample Preparation and Imaging. *Methods in molecular biology (Clifton, N.J.)* **2017**, *1606*, 71-84.
59. Goodhew, P., General Introduction to Transmission Electron Microscopy (TEM). In *Aberration-Corrected Analytical Transmission Electron Microscopy*, 2011; pp 1-19.
60. Franken, L. E.; Grünewald, K.; Boekema, E. J.; Stuart, M. C. A., A Technical Introduction to Transmission Electron Microscopy for Soft-Matter: Imaging, Possibilities, Choices, and Technical Developments. **2020**, *16* (14), 1906198.
61. Lupini, A. R.; de Jonge, N., The three-dimensional point spread function of aberration-corrected scanning transmission electron microscopy. *Microscopy and microanalysis : the official journal of Microscopy Society of America, Microbeam Analysis Society, Microscopical Society of Canada* **2011**, *17* (5), 817-826.
62. Aswathy, S. H.; Narendrakumar, U.; Manjubala, I., Commercial hydrogels for biomedical applications. *Heliyon* **2020**, *6* (4), e03719.
63. Du, X.; Zhou, J.; Shi, J.; Xu, B., Supramolecular Hydrogelators and Hydrogels: From Soft Matter to Molecular Biomaterials. *Chem. Rev.* **2015**, *115* (24), 13165-13307.
64. Sathaye, S.; Mbi, A.; Sonmez, C.; Chen, Y.; Blair, D. L.; Schneider, J. P.; Pochan, D. J., Rheology of peptide- and protein-based physical hydrogels: Are everyday measurements just scratching the surface? **2015**, *7* (1), 34-68.
65. Mackiewicz, P.; Szydło, A., Viscoelastic Parameters of Asphalt Mixtures Identified in Static and Dynamic Tests. *Materials (Basel)* **2019**, *12* (13), 2084.
66. Mrokowska, M. M.; Krztoń-Maziopa, A., Viscoelastic and shear-thinning effects of aqueous exopolymer solution on disk and sphere settling. *Scientific Reports* **2019**, *9* (1), 7897.
67. Lee, C. H.; Lu, Y.; Shen, A. Q., Evaporation induced self assembly and rheology change during sol-gel coating. **2006**, *18* (5), 052105.
68. Qian, Y.; Ma, S.; Kawashima, S.; De Schutter, G. J. T.; Mechanics, A. F., Rheological characterization of the viscoelastic solid-like properties of fresh cement pastes with nanoclay addition. **2019**, *103*, 102262.
69. Garcia-Manyes, S.; Oncins, G.; Sanz, F., Effect of Ion-Binding and Chemical Phospholipid Structure on the Nanomechanics of Lipid Bilayers Studied by Force Spectroscopy. *Biophys. J.* **2005**, *89* (3), 1812-1826.
70. Jyoti, A.; Prokop, R. M.; Li, J.; Vollhardt, D.; Kwok, D. Y.; Miller, R.; Möhwald, H.; Neumann, A. W., An investigation of the compression rate dependence on the surface pressure-surface area isotherm for a dipalmitoyl phosphatidylcholine monolayer at the air/water interface. *Colloids and Surfaces A: Physicochemical and Engineering Aspects* **1996**, *116* (1), 173-180.
71. Stigter, D.; Mingins, J.; Dill, K. A., Phospholipid interactions in model membrane systems. II. Theory. *Biophys. J.* **1992**, *61* (6), 1616-29.
72. Bhushan, B.; Kasai, T., A surface topography-independent friction measurement technique using torsional resonance mode in an AFM. *Nanotechnology* **2004**, *15* (8), 923-935.
73. Bhushan, B.; Qi, J., Phase contrast imaging of nanocomposites and molecularly thick lubricant films in magnetic media. *Nanotechnology* **2003**, *14* (8), 886-895.
74. Gählin, R.; Jacobson, S., A novel method to map and quantify wear on a micro-scale. *Wear* **1998**, *222* (2), 93-102.
75. Wang, J.; Liu, J.; Guo, Y., Cell Growth Stimulation, Cell Cycle Alternation, and Anti-Apoptosis Effects of Bovine Bone Collagen Hydrolysates Derived Peptides on MC3T3-E1 Cells Ex Vivo. *Molecules* **2020**, *25* (10), 2305.
76. van Meerloo, J.; Kaspers, G. J.; Cloos, J., Cell sensitivity assays: the MTT assay. *Methods in molecular biology (Clifton, N.J.)* **2011**, *731*, 237-45.

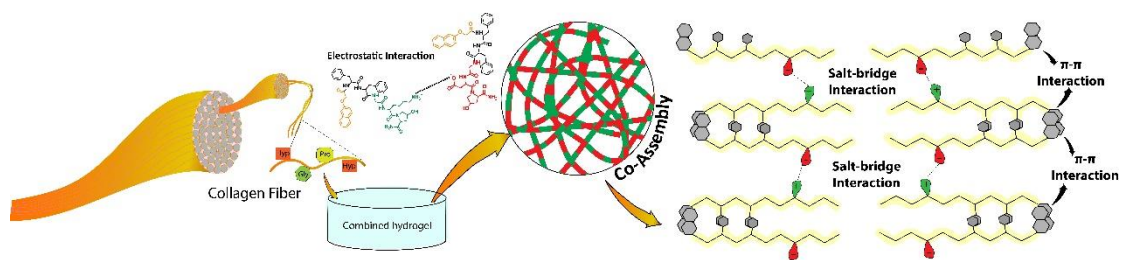
77. Mosmann, T., Rapid colorimetric assay for cellular growth and survival: Application to proliferation and cytotoxicity assays. *Journal of Immunological Methods* **1983**, *65* (1), 55-63.
78. Kamiloglu, S.; Sari, G.; Ozdal, T.; Capanoglu, E., Guidelines for cell viability assays. **2020**, *1* (3), 332-349.
79. Kapałczyńska, M.; Kolenda, T.; Przybyła, W.; Zajączkowska, M.; Teresiak, A.; Filas, V.; Ibbs, M.; Bliźniak, R.; Łuczewski, Ł.; Lamperska, K., 2D and 3D cell cultures - a comparison of different types of cancer cell cultures. *Arch Med Sci* **2018**, *14* (4), 910-919.
80. Edmondson, R.; Broglie, J. J.; Adcock, A. F.; Yang, L., Three-dimensional cell culture systems and their applications in drug discovery and cell-based biosensors. *Assay Drug Dev Technol* **2014**, *12* (4), 207-218.
81. Jain, R.; Roy, S., Designing a bioactive scaffold from coassembled collagen–laminin short peptide hydrogels for controlling cell behaviour. *RSC Adv.* **2019**, *9* (66), 38745-38759.
82. Worthington, P.; Pochan, D. J.; Langhans, S. A., Peptide Hydrogels - Versatile Matrices for 3D Cell Culture in Cancer Medicine. *Front Oncol* **2015**, *5*, 92-92.
83. Zimoch, J.; Padiál, J. S.; Klar, A. S.; Vallmajo-Martin, Q.; Meuli, M.; Biedermann, T.; Wilson, C. J.; Rowan, A.; Reichmann, E., Polyisocyanopeptide hydrogels: A novel thermo-responsive hydrogel supporting pre-vascularization and the development of organotypic structures. *Acta biomater.* **2018**, *70*, 129-139.
84. Höppner, M.; Luhm, J.; Schlenke, P.; Koritke, P.; Frohn, C., A flow-cytometry based cytotoxicity assay using stained effector cells in combination with native target cells. *J Immunol Methods* **2002**, *267* (2), 157-63.
85. Majewska, A.; Yiu, G.; Yuste, R., A custom-made two-photon microscope and deconvolution system. *Pflugers Archiv : European journal of physiology* **2000**, *441* (2-3), 398-408.
86. Jenner, N. K.; Ostrander, G. K.; Kavanagh, T. J.; Livesey, J. C.; Shen, M. W.; Kim, S. C.; Holmes, E. H., A flow cytometric comparison of DNA content and glutathione levels in hepatocytes of English sole (*Parophrys vetulus*) from areas of differing water quality. *Arch. Environ. Contam. Toxicol.* **1990**, *19* (6), 807-15.
87. Proffitt, R. T.; Tran, J. V.; Reynolds, C. P., A fluorescence digital image microscopy system for quantifying relative cell numbers in tissue culture plates. *Cytometry* **1996**, *24* (3), 204-13.
88. Fedchenko, N.; Reifenrath, J., Different approaches for interpretation and reporting of immunohistochemistry analysis results in the bone tissue - a review. *Diagn Pathol* **2014**, *9*, 221-221.
89. Hawes, D.; Shi, S.-R.; Dabbs, D. J.; Taylor, C. R.; Cote, R. J., Immunohistochemistry. *Modern Surgical Pathology* **2009**, 48-70.
90. Katsetos, C. D.; Del Valle, L.; Legido, A.; de Chadarévian, J. P.; Perentes, E.; Mörk, S. J., On the neuronal/neuroblastic nature of medulloblastomas: a tribute to Pio del Rio Hortega and Moises Polak. *Acta neuropathologica* **2003**, *105* (1), 1-13.
91. Katsetos, C. D.; Herman, M. M.; Mörk, S. J., Class III beta-tubulin in human development and cancer. *Cell motility and the cytoskeleton* **2003**, *55* (2), 77-96.
92. Pal, V. K.; Jain, R.; Sen, S.; Kailasam, K.; Roy, S., Designing nanofibrillar cellulose peptide conjugated polymeric hydrogel scaffold for controlling cellular behaviour. *Cellulose* **2021**, *28* (16), 10335-10357.
93. Mattern, R.-H.; Read, S. B.; Pierschbacher, M. D.; Sze, C.-I.; Eliceiri, B. P.; Kruse, C. A., Glioma cell integrin expression and their interactions with integrin antagonists: Research Article. *Cancer Ther* **2005**, *3A*, 325-340.
94. Kaur, H.; Roy, S., Designing aromatic N-cadherin mimetic short-peptide-based bioactive scaffolds for controlling cellular behaviour. *J. Mater. Chem. B* **2021**, *9* (29), 5898-5913.
95. Shanker, U.; Jassal, V.; Rani, M., Catalytic removal of organic colorants from water using some transition metal oxide nanoparticles synthesized under sunlight. *RSC Adv.* **2016**, *6* (97), 94989-94999.

96. Fei, C.; Nie, L.; Zhang, J.; Chen, J., Potential Applications of Fluorescence-Activated Cell Sorting (FACS) and Droplet-Based Microfluidics in Promoting the Discovery of Specific Antibodies for Characterizations of Fish Immune Cells. *Front Immunol* **2021**, *12*, 771231-771231.
97. Collier, J. L., FLOW CYTOMETRY AND THE SINGLE CELL IN PHYCOLOGY. *Journal of phycology* **2000**, *36* (4), 628-644.
98. Koch, C.; Harnisch, F.; Schröder, U.; Müller, S., Cytometric fingerprints: evaluation of new tools for analyzing microbial community dynamics. **2014**, *5*.
99. Nath, B.; Raza, A.; Sethi, V.; Dalal, A.; Ghosh, S. S.; Biswas, G., Understanding flow dynamics, viability and metastatic potency of cervical cancer (HeLa) cells through constricted microchannel. *Scientific Reports* **2018**, *8* (1), 17357.
100. Golub, E. E.; Boesze-Battaglia, K., The role of alkaline phosphatase in mineralization. *Curr. Opin. Orthop.* **2007**, *18* (5), 444-448.
101. Orimo, H., The mechanism of mineralization and the role of alkaline phosphatase in health and disease. *J Nippon Med Sch* **2010**, *77* (1), 4-12.
102. Warnes, T. W., Alkaline phosphatase. *Gut* **1972**, *13* (11), 926-37.
103. Guo, Z.; Wang, Y.; Tan, T.; Ji, Y.; Hu, J.; Zhang, Y., Antimicrobial d-Peptide Hydrogels. *ACS Biomater. Sci. Eng.* **2021**, *7* (4), 1703-1712.
104. Schnaider, L.; Brahmachari, S.; Schmidt, N. W.; Mensa, B.; Shaham-Niv, S.; Bychenko, D.; Adler-Abramovich, L.; Shimon, L. J. W.; Kolusheva, S.; DeGrado, W. F.; Gazit, E., Self-assembling dipeptide antibacterial nanostructures with membrane disrupting activity. *Nat. Commun.* **2017**, *8* (1), 1365.
105. Sis, M. J.; Webber, M. J., Drug Delivery with Designed Peptide Assemblies. *Trends in Pharmacological Sciences* **2019**, *40* (10), 747-762.
106. Yang, J.; An, H.-W.; Wang, H., Self-Assembled Peptide Drug Delivery Systems. *ACS Appl. Bio Mater.* **2021**, *4* (1), 24-46.
107. Borges, A.; Ferreira, C.; Saavedra, M. J.; Simões, M., Antibacterial activity and mode of action of ferulic and gallic acids against pathogenic bacteria. *Microbial drug resistance (Larchmont, N.Y.)* **2013**, *19* (4), 256-65.
108. Bhargava, A.; Pareek, V.; Roy Choudhury, S.; Panwar, J.; Karmakar, S., Superior Bactericidal Efficacy of Fucose-Functionalized Silver Nanoparticles against *Pseudomonas aeruginosa* PAO1 and Prevention of Its Colonization on Urinary Catheters. *ACS Appl. Mater. Interfaces* **2018**, *10* (35), 29325-29337.
109. Li, J.; Koh, J.-J.; Liu, S.; Lakshminarayanan, R.; Verma, C. S.; Beuerman, R. W., Membrane Active Antimicrobial Peptides: Translating Mechanistic Insights to Design. *Front Neurosci* **2017**, *11*, 73-73.
110. Wang, L.; Hu, C.; Shao, L., The antimicrobial activity of nanoparticles: present situation and prospects for the future. *International journal of nanomedicine* **2017**, *12*, 1227-1249.
111. Shi, C.; Zhang, X.; Sun, Y.; Yang, M.; Song, K.; Zheng, Z.; Chen, Y.; Liu, X.; Jia, Z.; Dong, R.; Cui, L.; Xia, X., Antimicrobial Activity of Ferulic Acid Against *Cronobacter sakazakii* and Possible Mechanism of Action. *Foodborne pathogens and disease* **2016**, *13* (4), 196-204.
112. Wang, H.; Joseph, J. A., Quantifying cellular oxidative stress by dichlorofluorescein assay using microplate reader. *Free radical biology & medicine* **1999**, *27* (5-6), 612-6.
113. Castro-Alferez, M.; Polo-López, M. I.; Fernández-Ibáñez, P., Intracellular mechanisms of solar water disinfection. *Scientific reports* **2016**, *6*, 38145-38145.
114. Khoubnasabjafari, M.; Ansarin, K.; Jouyban, A., Reliability of malondialdehyde as a biomarker of oxidative stress in psychological disorders. *Bioimpacts* **2015**, *5* (3), 123-127.

# Chapter 3

Modulating the supramolecular structure and function of self-assembling collagen inspired ionic complementary peptides via electrostatic interactions





**A minimalistic approach of peptide self-assembly has been adapted that includes judicious choice of molecular components with oppositely charged amino acid residues within collagen inspired shortest bioactive pentapeptide domain for the development of next-generation biomaterials.**



### 3.1 Introduction

As discussed in chapter 1, molecular self-assembly is one of the most important approaches to form complex functional biomolecular structures in natural system.<sup>1-11</sup> The process of self-assembly and disassembly of biomolecules in nature leads to the formation of bio-functional macromolecular organization with great complexity, which helps to perform *in vivo* functions and keep the organisms alive.<sup>12-15</sup> The concept of utilizing the molecular self-assembly approach by designing simple building blocks that shows propensities to undergo extensive intermolecular interactions was inspired from natural system of organizing macromolecules. This bottom up fabrication is an effective strategy to construct extracellular (ECM) mimics, which can be widely used as functional materials for tissue engineering and regenerative medicines.<sup>16-22</sup> Apart from structural roles, ECM also plays vital role in complex biological processes such as cell adhesion, cell-to-cell communication and differentiation, which in turn regulates tissue development, wound healing, immune response and other physiological functions.<sup>23, 24</sup> It is believed that certain bioactive molecules are responsible for regulating the functional processes of the ECM, which includes fibronectins, laminin, elastin, collagen etc.<sup>25, 26</sup> Therefore, it is an interesting approach to design the self-assembling molecules mimicking such bioactive molecules to create complex nanoscale structures that may find suitable biomedical applications.

Collagen, the most abundant protein of native ECM, have captured huge interest, owing to its structural and functional characteristics, which can be explored in tissue engineering and other biomedical applications.<sup>27-29</sup> The excellent self-assembling properties and biodegradability of natural collagen have translated it as a material of choice for various biomedical purposes such as drug delivery, hemostatic agent, wound dressing and scaffold for tissue regeneration, etc.<sup>30</sup> However, certain limitations like difficulty in introducing sequence-specific modification, thermal stability and possible contamination with pathogenic substances restrict the use of natural collagen.<sup>27, 31, 32</sup> In spite of a wide variety of architectures (fibrous, facit, short chain, membrane and others) and functions (rigidity, strength and structural support), collagen is marked with a distinct triple helical domain consisting of a regular repetitive unit of Gly-X-Y sequence in the primary protein structure (where X is usually proline and Y is hydroxyproline).<sup>33, 34</sup> Glycine is located at every third position of the polypeptide chain and being the smallest amino acid with no alkyl/aryl or other side chain functionality enables the close

packing of the whole molecule.<sup>35</sup> The amide proton of glycine participates in H-bonding with the carbonyl group of nearby X-residue. The post-translational modification of Y-position from proline to hydroxyproline further stabilizes the collagen structure by additional H-bonding between OH-group of hydroxyproline residue and water.<sup>36,37</sup> The reports by B. Brodsky's group provide the detailed explanations about the effect of amino acid sequence alterations on the triple helical structure of collagen and further describe how these structural modulations can lead to molecular defects to trigger collagen based diseases.<sup>38</sup> The detailed studies of collagen structure provide evidences for the X- and Y- alternations, which retain their fibrillary structure.<sup>39</sup>

Moreover, the increasing demand and detailed molecular-level understanding of collagen structure motivated the use of synthetic collagen and collagen mimetic peptides (CMPs).<sup>40, 41</sup> More commonly, the peptides containing 15-40 amino acid residues are reported to form such supramolecular structures of collagen, both homotrimer and heterotrimers.<sup>42, 43</sup> It is very difficult to mimic all the steps of the complex organization of native collagen self-assembly. In this context, there are reports, which successfully achieved the 3D nanostructure from a synthetic collagen inspired peptide (CIP), but lack the hierarchical organization that may lead to gelation.<sup>36,44</sup> There are only limited reports on collagen inspired peptide design, where gelation was observed, but they lack the nanofibrous or helical structure similar to native collagen.<sup>32</sup> In this context, it is crucial to achieve gelation in such small molecular domain to induce higher order self-assembled complex architecture to mimic the structure and functions of native ECM protein. This would further open up a new avenue for development of collagen inspired biomaterials to solve many problems of biology.

A variety of analogs of the basic Gly-X-Y sequence has been observed in nature, in different species.<sup>45</sup> In the absence of proline and hydroxyproline, the bacterial collagen compensates for their structural stability through charged amino acid residues like aspartate, glutamate, lysine, and arginine.<sup>42</sup> In a similar line, Chaikof and co-workers demonstrated the zwitterionic peptide assembly, using the 36 amino acid containing CMP to demonstrate the similar structural integrity, as that of natural collagen.<sup>46</sup> Later, a classical report by Hartegrink's group replicated the complex multi-hierarchical self-assembly of collagen by designing a CMP of 36-mer and demonstrated self-assembly of a triple helix to nanofibers and gel formation.<sup>32</sup> Their CMP design involves salt

bridged hydrogen bonds to stabilize the hierarchical structure of the molecule. A recent report by Conticello group, clearly demonstrates the design of protomers based on positively and negatively charged collagen mimetic peptides of 36-mer amino acid residue, where the self-assembly can be directed towards the formation of multilayer structures like nanosheets.<sup>47</sup> Therefore, the above reports clearly suggested that in addition to hydrogen bonding and hydrophobic interactions, which may be further coupled with complementary ionic interactions and thus can lead to a more effective intermolecular association to trigger the formation of a stable hydrogel.<sup>47</sup> It is clearly evident from the earlier reports that along with the basic backbone structure of the collagen inspired peptides, side-chain interactions between the non-imino acid residues (at X and Y positions) of the peptides also plays a pivotal role in determining the secondary structure and its stability.<sup>48</sup>

Furthermore, the literature reports clearly demonstrated that the self-assembly of an important class of peptides, like, ionic complementary peptides which generally show higher mechanical strength in physiological condition. However, surprisingly, their pivotal role in the field of tissue engineering is been less explored.<sup>12</sup> Self-assembling short peptides with alternating charged residues can induce strong electrostatic interactions, which may further lead to the hierarchical organization in these short peptides.<sup>49-55</sup> Zhang and co-workers discussed the importance of alternating ionic complementary peptide for tissue repair, alternating sequence of arginine and aspartate with alanine as spacer (RADA)<sub>16</sub> form hydrogel, in which chondrocyte cells were encapsulated and used for cartilage repair.<sup>56, 57</sup> Pochan and Schneider illustrated a 20 amino acid long peptide of alternating charged residues, which self-assemble into  $\beta$ -hairpin structure and promotes the NIH 3T3 fibroblast proliferation.<sup>58</sup>

It was further interesting to note that, only a few attempts were focused on designing short length collagen inspired peptides, which showed the property to self-assemble in three dimensional nanofibrous structure. One of the classical reports by Yang et. al., reported a library of 6 octa-peptides (based on the repeating sequence of Gly-X-Y).<sup>29</sup> The peptides were modified at X position with different amino acids accessing diverse range of intermolecular interactions to form random coils. These peptides showed favorable interactions with fibroblast, 3T3 cells. In a similar line, another example by Tekinay and co-worker showed the design of octapeptide amphiphile as a collagen presenting scaffold. The amphiphile sequence was based on Pro-Hyp-Gly (POG)

functional motif that formed  $\beta$ -sheet structure and showed their potential application for the prevention of progressive IVD (intra vertebral disc) degeneration.<sup>59</sup> However, the later reports also showed self-assembly of mixed peptide sequences, using similar design principles that rely on modulating the intermolecular interaction to direct and fabricate novel nanostructures based on the bioactive sequences.<sup>59</sup>

Keeping in mind the importance of charge-pair interactions, we used this unique strategy of designing two ionic complementary peptide sequences based on the native collagen motif. These peptides are expected to undergo strong electrostatic interactions which may further lead to hierarchical organization. Our specific design included aromatic modification followed by the classical diphenylalanine sequence bearing two Phenylalanine (Phe) moieties at N-terminal to promote self-assembly via  $\pi$ - $\pi$  interactions.<sup>60</sup> The Phe- residues in native collagen are known to confer rigidity and stability to the flexible structures.<sup>61</sup> Interestingly, our simplistic design was focused on connecting this self-assembly promoting classical amyloid fragment to the single chain of basic structural unit of collagen i.e. Gly-X-Y, where the middle position of proline was further modified by two differently charged amino acids, which would further induce interactions between the ionic complementary amino acids to create complex hierarchical structure leading to the formation of diverse gels. The acidic and basic surface charge of the individual pentapeptides resulted in the formation of self-assembled structure at different pH by stabilization through charge neutralization of the counter ions present in the solution microenvironment. Interestingly, simple mixing of the two CIPs with opposite charge at near equivalent amount resulted in complete charge neutralization and thus shifting sol to gel equilibrium to physiological pH. To the best of our knowledge, this is the first report on the shortest collagen inspired peptide, which is easy to synthesize and have the propensity to self-assemble into a three-dimensional nanofibrous structure at ambient condition and is stabilized by non-covalent aromatic  $\pi$ - $\pi$  interactions, H-bonding and charge pair interactions. However, due to the shorter length of the sequence, the alpha-helical structures are not stabilized and the resulting materials predominantly showed the properties of the amyloid-like peptide. This fact is also supported by the report by Muller *et. al.*, which says that the self-assembly properties of the amphiphilic peptides are dependent on the sequence and size of the non-polar amino acid residues.<sup>62</sup> These short collagen inspired peptides displaying amyloid-like properties can serve as models for understanding the role of

collagen in amyloid-based diseases.<sup>41</sup> Furthermore, these short self-assembling peptide hydrogels and their co-assembly created biocompatible scaffold, which can further enhances their scope to be explored as effective bioactive scaffold. We envisage that these biomimetic hydrogels scaffolds developed from short collagen inspired peptides displaying similar fibrillar architectures as collagen exhibits in native ECM may open up new opportunities for targeted applications in the biomedical arena.

## 3.2 Results and discussions

### 3.2.1 Design and self-assembly of collagen-inspired peptides.

In this study, we have designed the short amphiphilic CIP's (NapFFGKO and NapFFGDO), based on the basic repeating unit of collagen molecule, Gly-X-Y (X=Proline, Y=Hydroxyproline) (Figure 3.1). In the molecular design, proline was replaced with two oppositely charged amino acids (lysine and aspartic acid), which is expected to display differential surface charge depending on the pH of the medium. An aromatic dipeptide sequence, naphthoxy acetyl capped classical diphenylalanine residue was incorporated in the design at the N-terminal to increase the hydrophobic interactions between the peptides, which would further enable the CIPs to form gel.

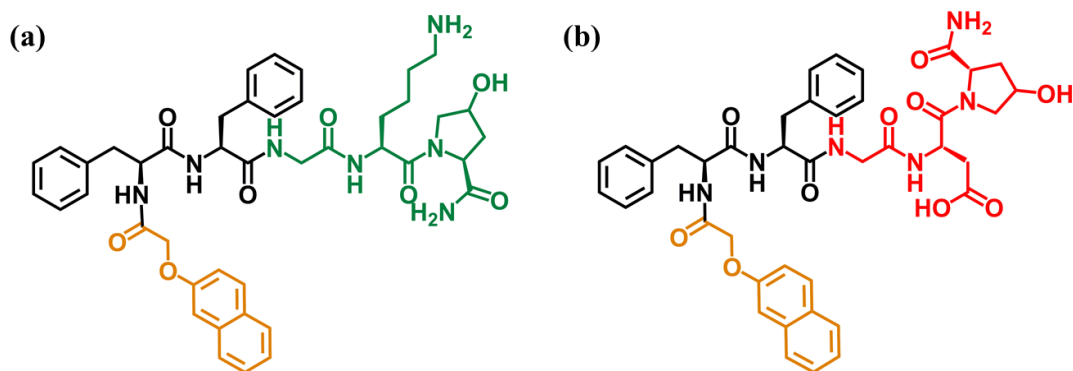


**Figure 3.1** Chemical structure of the designed collagen inspired peptides (a) NapFFGKO (positively charged peptide) and (b) NapFFGDO (negatively charged peptide).

The hydroxyl group of hydroxyproline may also participate in intermolecular H-bonding, which imparts reasonable hydrophilicity within the molecule and hence is likely to be responsible for the water solubilization of the peptides.<sup>63</sup> The peptides were synthesized via solid phase peptide chemistry and the purity of the dried products was further quantified by reverse-phase high-performance liquid chromatography (Waters)

using a mobile phase gradient of acetonitrile from 5% to 95% in water (each with 0.1% trifluoroacetic acid) (Figure 3.2). The newly designed peptides were characterized by mass spectroscopy.

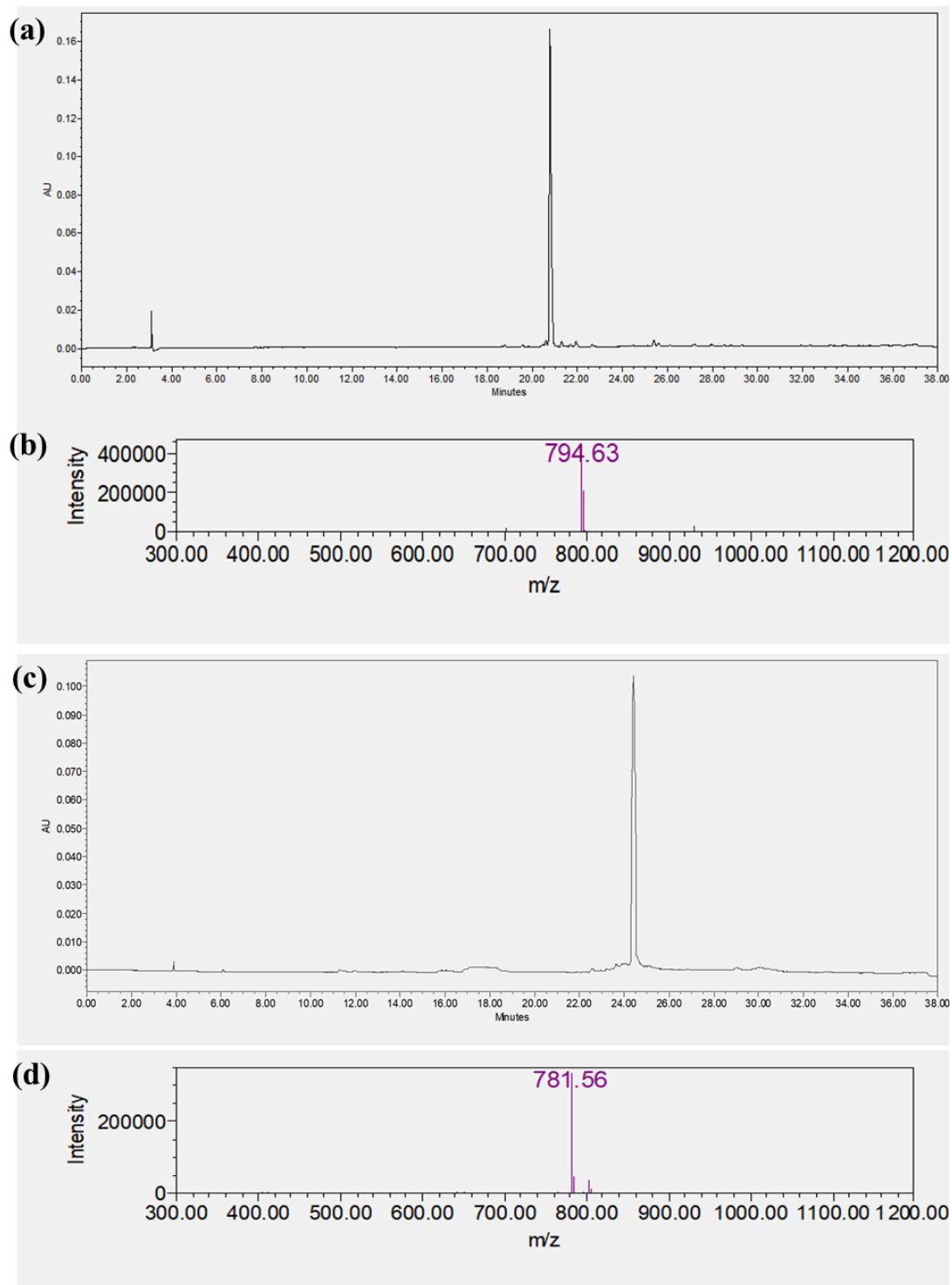


**Figure 3.2** Reverse phase HPLC and Mass spectra of the collagen inspired peptides (a,b) NapFFGKO and (c,d) NapFFGDO, respectively.

Gelation was carried out via pH switch method at minimum gelation concentration (MGC) of 30mM for both the peptides. Very interestingly, these peptides showed a pH responsive sol to gel transition, depending on their logP values and the surface charge present in both the peptides. The positively charged peptide NapFFGKO with a logP value of 1.03, failed to form gel at physiological pH owing to the ionization of the peptide leading to the charge repulsion between the positively charged lysine residues (Figure 3.3). However, the neutralization of amine groups by counter ions at slightly basic pH, i.e., pH 9 can induce gelation to form a self-supporting hydrogel.

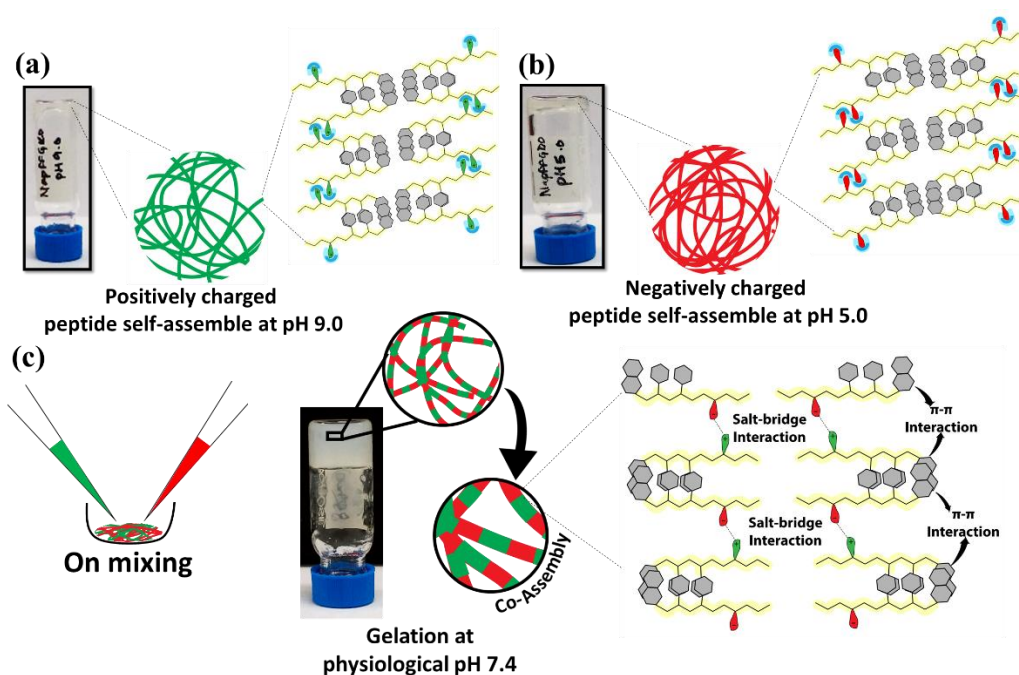


**Figure 3.3** Schematic representation of the self-assembly of peptide amphiphiles in their respective environment leading to hydrogel formation at different pH through counter ion stabilization; (a) NapFFGKO and (b) NapFFGDO. Upon mixing them together i.e. NapFFGKO:NapFFGDO 1.1:1, they showed gelation at physiological pH due to electrostatic interaction among the charged peptides (c) NapFFGKO + NapFFGDO.

In contrast, NapFFGDO displayed a logP value of 3.28, with aspartic acid residue being negatively charged at physiological pH was unable to undergo intermolecular association to induce further gelation. The interaction of deprotonated aspartic acid residue with counter ions, at acidic pH (~5) resulted into gelation. (Figure 3.3). The charged state of amino and carboxyl groups was further evaluated by acid base titration of individual peptides.<sup>64, 65</sup> For NapFFGKO, the region below pH 3.65 showed the fully

protonated state of amino group, while increase in pH from 3.65 to 9.14 showed neutralization of protonated amine group. Similarly, for NapFFGDO, the region above pH 9.91 represents the completely deprotonated state of carboxyl group of aspartic acid and the further decrease of pH leads to the charge neutralization (Figure 3.4).

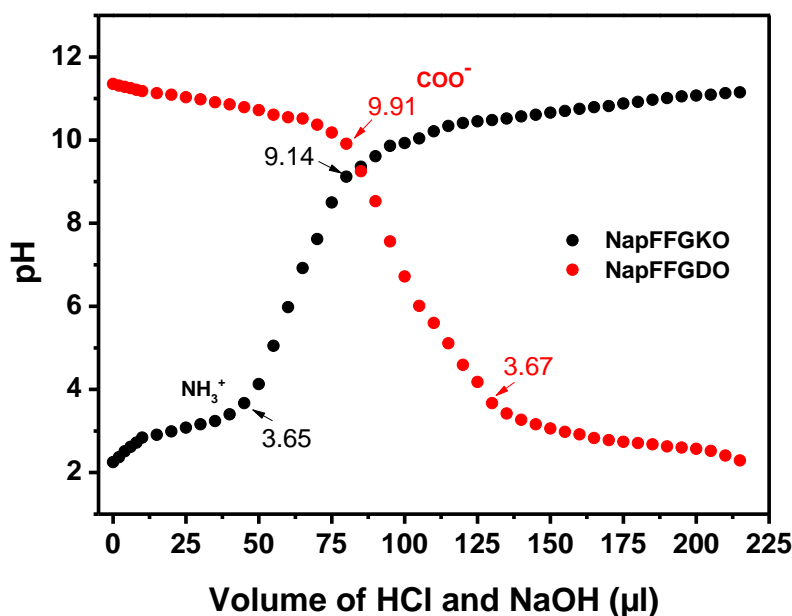


**Figure 3.4** Acid-base titration curve of collagen inspired peptides showing the protonation and deprotonation states of amino and carboxyl groups of the respective amino acid residues in acidic and basic environment respectively.

This provides the evidence of gelation of NapFFGKO at pH 9 and NapFFGDO at pH 5. In individual peptides, the aromatic Nap-moiety and diphenylalanine induces aromatic  $\pi$ - $\pi$  interaction, while carboxyl groups and amine groups in the peptide backbone formed H-bonding, which are responsible for their self-assembly.<sup>66</sup> Most importantly, the rationale for designing these peptides was focused to trigger their gelation at physiological pH which, in turn, can control the biological applications of the peptides. Upon simple mixing, the electrostatic interaction neutralize the oppositely charged residues and thus enhances the hydrogen bond interaction between them.<sup>67</sup> Initiation of electrostatic interactions between the positively and negatively charged peptide along with aromatic  $\pi$ - $\pi$  interactions leads to the stronger self-assembly at physiological pH, at a significantly lower concentration of the individual peptides, which is reflected in the reduction of MGC value. The MGC value for the co-assembled

gel has been found to be 15mM, which was 30mM for the individual peptide (Table 3.1).

**Table 3.1** Minimum gelation concentration (MGC) of the collagen inspired peptides.

Peptide	MGC (mM)
NapFFGKO	30
NapFFGDO	30
NapFFGKO + NapFFGDO	15

The ratio of both the peptides was optimized by monitoring the change in zeta potential by simply titrating both the peptides against each other. As predicted, at the physiological pH, NapFFGKO showed overall positive surface charge of +49.5mV whereas NapFFGDO showed a negative surface charge of -48.7mV, which was expected due to the presence of lysine and aspartic acid residues in the respective peptides (Figure 3.5). At this point it was crucial to evaluate the optimized ratio of both the positively charged peptide NapFFGKO and negatively charged peptide NapFFGDO, which could create a micro environment of neutral charge through maximization of the electrostatic interactions. To this direction, titration was carried out between the two peptides to achieve the neutral charge point at pH 7.4. The ratio utilized included NapFFGKO against NapFFGDO were 1:1, 2:1, 1.5:1, 1.1:1. The co-assembled peptides with the ratio of 1.1:1 showed near charge neutralization point of around +3.7mV (Figure 3.5).

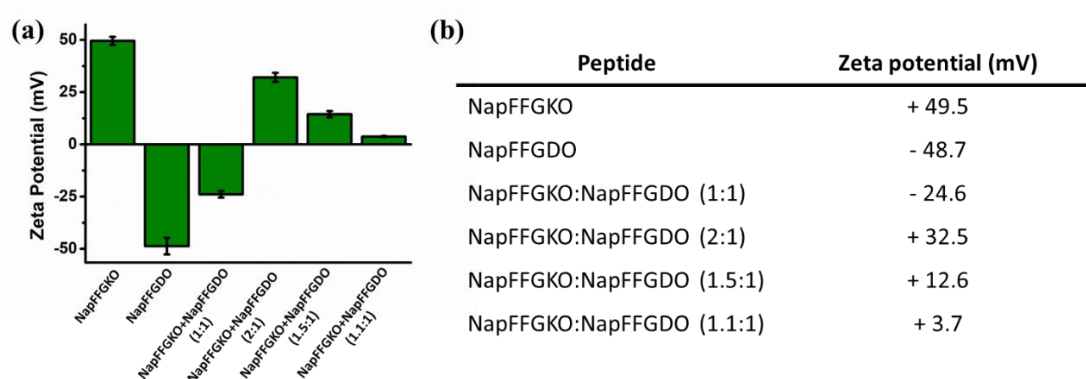


**Figure 3.5** (a) Zeta potential graph showing the overall surface charge of individual peptides and combined peptides at different ratios. (b) Table showing the values of surface charge density of the individual peptides and co-assembled peptides.

This finding clearly depicts that combining both the peptides in nearly equivalent amounts can neutralize the overall surface charge in the combined hydrogel which is highly crucial to support adhesion and growth of different types of cells. Furthermore, it was clearly evident from AFM studies that, an enhanced amount of NapFFGKO showed formation of spherical aggregates (Figure 3.6b), which tends to associate in presence of NapFFGDO and further growth was found to take place to shorter nanofibers in 1.5:1 ratio of NapFFGKO and NapFFGDO (Figure 3.6c). Upon further increasing the extent of NapFFGDO, entangled nanofibers were observed at 1.1:1 ratio of NapFFGKO and NapFFGDO respectively. (Figure 3.6d)

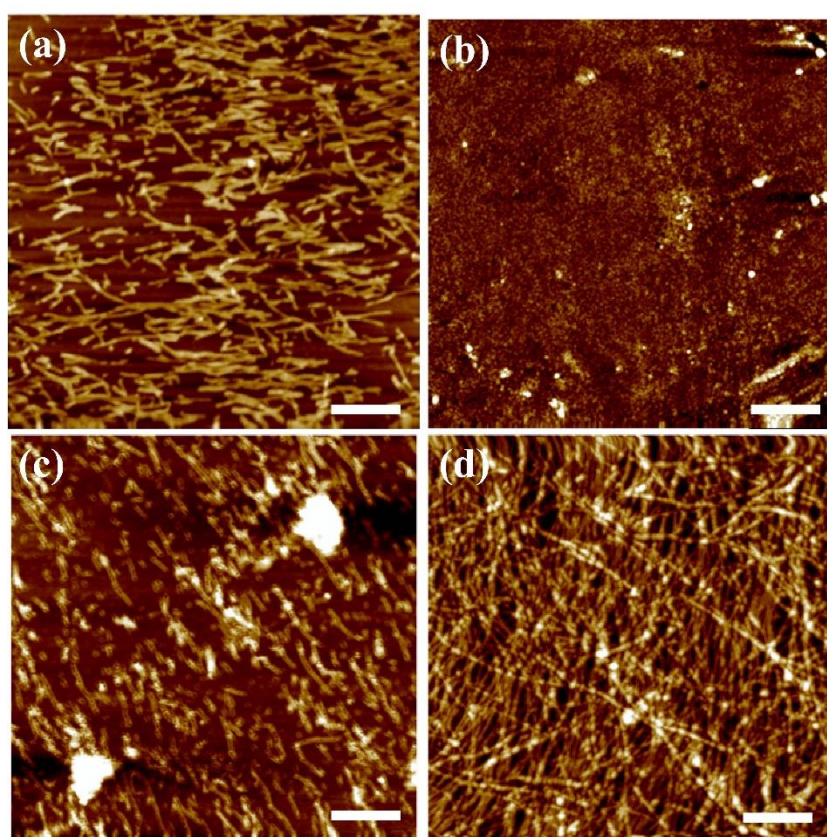


**Figure 3.6** AFM images of co-assembled hydrogels of ionic complementary peptides at different ratios of NapFFGKO:NapFFGDO respectively (a)1:1, (b)2:1, (c)1.5:1 and (d)1.1:1 at physiological pH. Scale bar 500nm.

**3.2.2 Morphological Analysis.** To further understand the nanostructures present in the self-assembled system of both the collagen inspired peptides and the combined hydrogel, Atomic Force Microscopy (AFM) and Transmission Electron Microscopy (TEM) were carried out. TEM is a classical tool used to get an insight into the morphology of the nanostructures formed in the self-assembled system. TEM images

revealed the formation of nanofiber networks with variable fiber diameter (Figure 3.7a,b,c). As observed in the TEM, fibers diameter varied from 7-10nm (Table 3.2) and length varied up to several micrometers and no significant difference in morphology, as well as diameter, was observed after co-assembly. Tapping mode AFM images of both the peptides and combined gel at MGC further confirmed the nanofiber formation with a fiber dimension ranging from 23-32nm. (Figure 3.7d,e,f).

**Table 3.2** Fiber dimensions of collagen mimetic peptide hydrogels observed by Transmission electron microscopy (TEM) and Atomic Force Microscopy (AFM), were calculated by ImageJ software.

Peptide	Fiber Dimension from TEM (nm)	Fiber Dimension from AFM (nm)
NapFFGKO	9.55±1.1	28.4±2.8
NapFFGDO	7.34±1.0	23.1±4.1
NapFFGKO+NapFFGDO	10.67±1.1	32.5±3.5

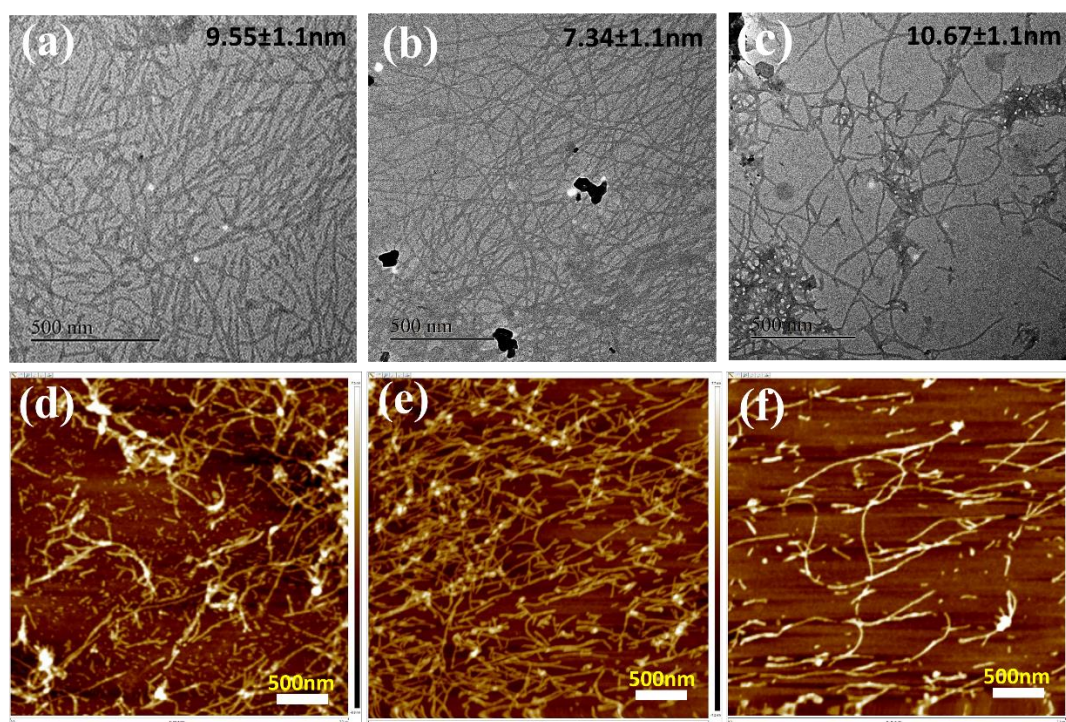


**Figure 3.7** Morphological analysis of nanostructures present in the hydrogels. TEM and AFM images of nanostructures formed by hydrogelators (a, d) NapFFGKO, (b, e) NapFFGDO and (c, f) NapFFGKO+NapFFGDO (1.1:1) at their MGC.

Hence, these morphological analyses of the hydrogels suggest that the peptides self-assemble into higher order fibrillar nanostructures through various intermolecular interactions (hydrogen bonding,  $\pi$ - $\pi$  interaction and electrostatic interactions). Both TEM and AFM revealed a denser and thinner network structure for individual peptide whereas, more flat and thicker fibers were captured in the co-assembled based gels.

**3.2.3 Nucleation and growth mechanism of peptide self-assembly.** The multi-scale hierarchical self-assembly of peptides is governed by synergistic interplay of kinetic and thermodynamic factors. The thermodynamic parameters include molecular design while the kinetic parameters include concentration, ionic strength, pH, solvent, temperature, etc.<sup>68</sup> The peptide self-assembly is mainly driven by non-covalent interactions. It is believed that directional H-bonds guide the fibrillation process for the formation of nanofibers, while the van der Waals or hydrophobic interactions, play important role in further fiber-fiber interactions.<sup>68</sup> However, the self-assembly pathways are determined by the solute-solute and solvent-solute interactions. Depending upon stability of the resulting nanostructures, the shape of the energy landscapes is determined.<sup>69</sup> The supramolecular nanofibril formation is driven by nucleation dependent polymerization, which includes initial nucleation event followed by the growth events towards higher order structures.<sup>69</sup> To demonstrate the nucleation and growth of peptide self-assembly, we conducted morphological analysis at different time points, through AFM (Figure 3.8). At the initial stage, up to 15 minutes, small spherical aggregates were observed. However, after 30 minutes, the density of nanostructures formed was much higher in co-assembled peptides in comparison to individual peptides. This might be due to the reason that nucleation phase was dominant in co-assembled gels, due to electrostatic interactions, resulting in large number of nucleation sites for further growth.<sup>70</sup> While in individual peptides, the residual charged moiety might reduce the nucleation sites and thus proceeded by faster growth events i.e., after 30 minutes. After 24 hrs, the density of the nanofibers has significantly increased resulting into dense fibrous networks. Interestingly, the presence of irregular aggregated structures was observed, along with the fibers, even after 24 and 48 hrs. Similar appearance of the irregular aggregated structures were also evident in TEM images as shown in figure (3.7b and c). The phenomenon of dynamic nanostructures at different time points can be clearly explained on the basis of kinetically trapped structures. The initial fast nucleation occurred due to increased local concentration of

peptides, after dissolution. The solvophobic effects of the primary assemblies exclude water from the surface and leads to entropy maximization.<sup>70</sup> The energy changes resulted into more stable higher order assemblies induced by the parallel alignment of oriented organization.<sup>68</sup> The molecular self-assemblies tend to achieve thermodynamically stable structures via various kinetically controlled structures.<sup>68</sup>

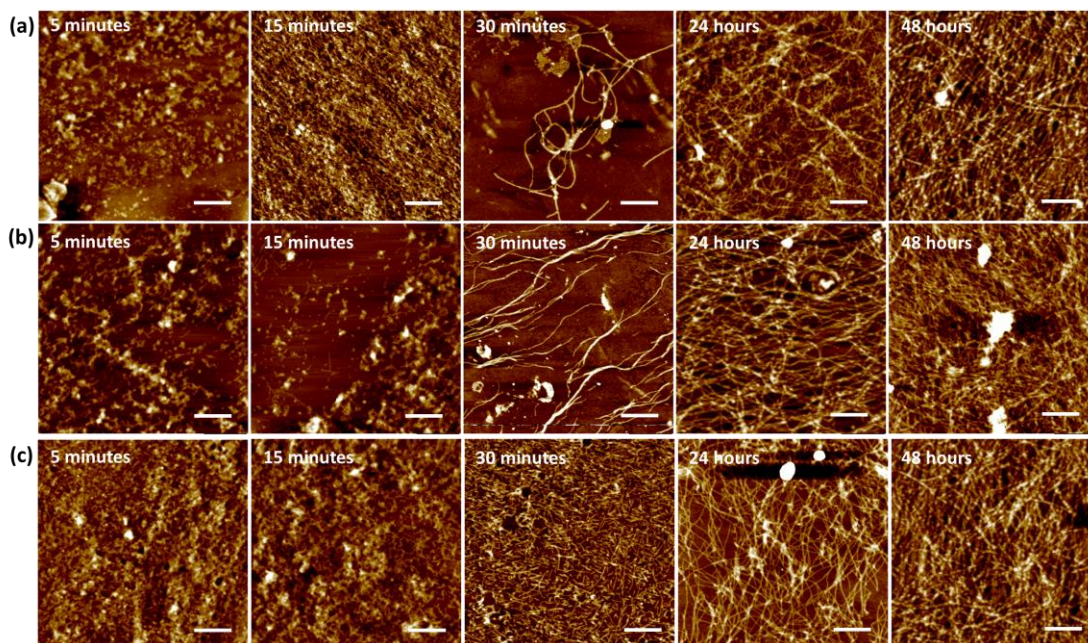


**Figure 3.8** Morphological analysis of nucleation and growth mechanism of collagen inspired peptide hydrogels at different time points; (a) NapFFGKO, (b) NapFFGDO and (c) NapFFGKO+NapFFGDO (1.1:1 at their MGC).

### 3.2.4 Spectroscopic characterization

To get an insight into the molecular interactions present in the self-assembled peptide gels several spectroscopic studies, like, Circular Dichroism (CD), Fourier Transform Infrared (FTIR) and Fluorescence spectroscopy were performed. CD spectra of both peptides showed the characteristic CD signals as positive ellipticity at 195nm and a negative ellipticity at 220nm indicating the presence of  $\beta$ -sheet like structures<sup>71</sup> (Figure 3.9a). Whereas, in the combined hydrogel, the  $\beta$ -sheet signals were found to be red shifted to 240nm, which signifies the formation of more ordered structures due to the involvement of electrostatic interactions between the oppositely charged peptides (Figure 3.9a). The results corroborate with S. Xu's report, which explains that self-assembly driven by electrostatic interactions leads to aggregation of linear chains which matures into more ordered  $\beta$ -sheets.<sup>72</sup> Recently, Hamachi's group studied the real-time

self-sorting behavior within peptide nanofibers, where different types of nanofibers, each composed of distinct building units are making a multicomponent system. A simple sum of CD spectra was obtained for self-sorted fibers whereas altered CD pattern displayed by co-assembled fibers. CD study clearly identified the self-sorted fibers over co-assembled system.<sup>73</sup> Through these findings, we can corroborate that the co-assembly phenomenon is evident in our combined peptides, as it displayed an altered CD spectra with a red shift indicating twisted structure (Figure 3.9a). CD spectra of both the peptides was investigated at different pH to check the order of nanostructures forming at that stage.

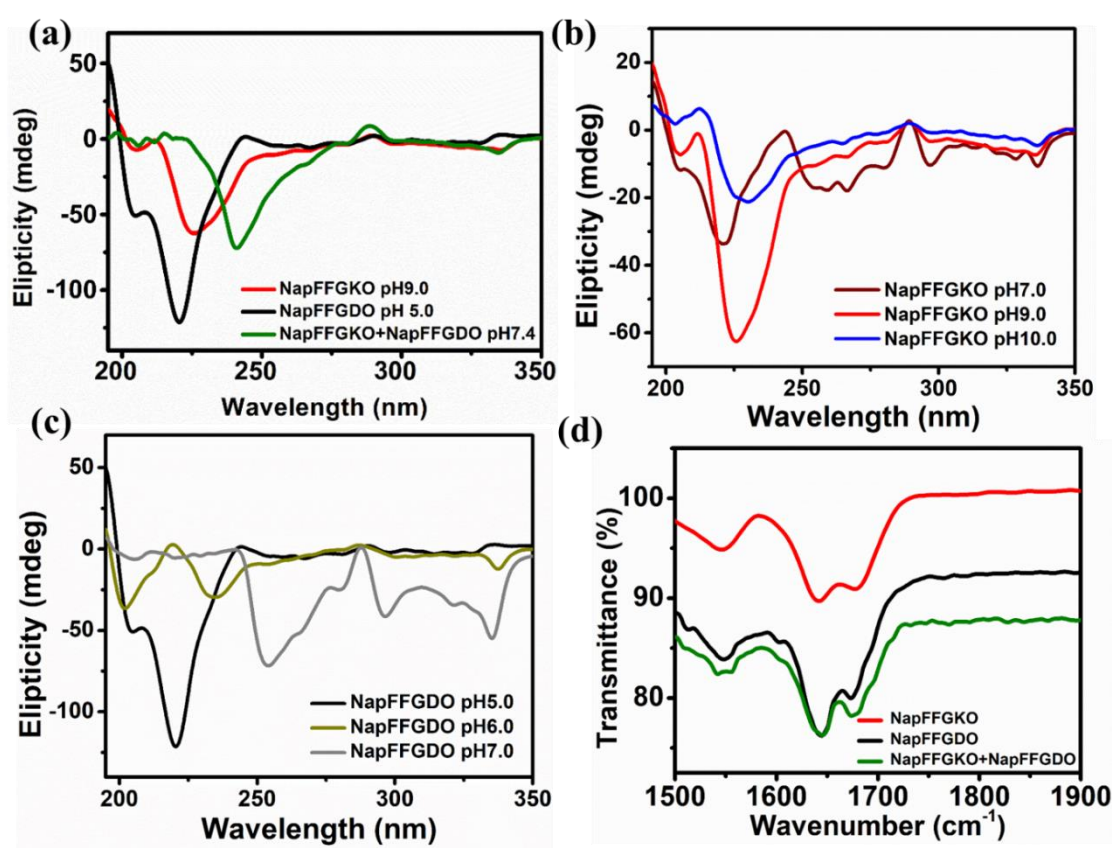


**Figure 3.9** Spectroscopic characterization of collagen inspired peptide hydrogels. (a) CD spectra of the individual hydrogelators and the combined peptides in their self-assembled state. (b) CD spectra of NapFFGKO at different pH (c) CD spectra of NapFFGDO at different pH and (d) FTIR spectra of hydrogels to determine the secondary structure.

It was quite interesting to note that at gelation pH of NapFFGKO i.e., at pH 9.0 a significant CD signal was observed indicating the presence of  $\beta$ -sheet conformation, however the signal intensity was reduced at pH 7 and 10, indicating the disruption of

the nanostructure (Figure 3.9b). A reverse pattern was observed for NapFFGDO, which showed a distinct  $\beta$ -sheet signal at acidic pH i.e., 5, at which it formed gel. Interestingly, the nanostructures dissolved up on further increase in pH of the solution, which was evident from the disappearance of the respective CD signal (Figure 3.9c). To further investigate the formation of peptide secondary structures, we studied the characteristic amide I and amide II bands of peptides in the  $1600\text{ cm}^{-1}$  to  $1700\text{ cm}^{-1}$  region using FTIR spectroscopy. Amide I band corresponds to stretching vibration of C=O bond and Amide II band corresponds to bending vibration of N-H bond.<sup>74</sup> The FTIR spectra of both individual peptide hydrogels and the combined hydrogels showed a significant peak around  $1640\text{ cm}^{-1}$  corresponding to  $\beta$ -sheet and peak at  $1670\text{ cm}^{-1}$  is due to the presence of carbonyl group present at the N-terminal end of the peptide<sup>75</sup> (Figure 3.9d).

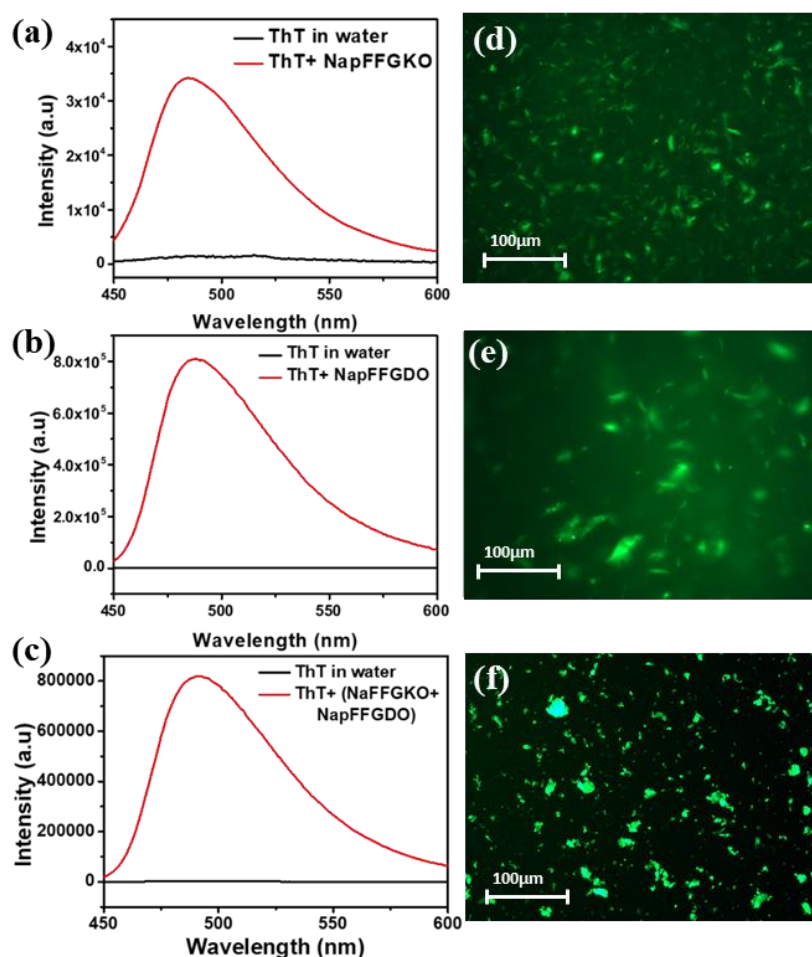


**Figure 3.10** Thioflavin T binding assay showing the different extent of binding to the different supramolecular structures in the gel state and corresponding fluorescence microscopic imaging of the ThT bound hydrogels: (a, d) NapFFGKO (b, e) NapFFGDO (c, f) NapFFGKO + NapFFGDO.

FTIR peak around  $1560\text{ cm}^{-1}$  in both the peptides is assigned for the deprotonated  $\text{COO}^-$  and shift of this peak towards a lower wavenumber for the combined gel is indicating the presence of more ordered structures with the possible electrostatic interactions in the co-assembled system.<sup>76, 77</sup> It is evident from both the above spectroscopic analysis (CD and FTIR) that the synthesized peptides are self-assembling to give  $\beta$ -sheets like structures. To further confirm the formation of  $\beta$ -sheet-like structures, Thioflavin T binding assay was performed. ThT is a benzothiazole dye and is known to give enhanced fluorescence when bound to any hydrophobic patches present in the gel.<sup>78</sup> An interesting change was visible when the hydrogelator molecule was incubated with ThT and further excited at 440nm. An enhanced emission peak at 485nm was evident in comparison to the negligible fluorescence intensity of ThT alone (without hydrogelator molecule) (Figure 3.10a,b,c). The enhancement in the relative intensity of ThT with both the peptides and combined peptides clearly suggested the binding of ThT to a self-assembled nanostructure, rich in  $\beta$ -sheet-like structures and thus further supports the CD and FTIR results. The fluorescence microscopic evaluation further reinforced the spectroscopic results. In this study, the peptide hydrogels were incubated with the ThT stock in 1:1 ratio for 10-15 minutes before investigation. The dye bound to the hydrophobic patches of the supramolecular structures showed fluorescence, which can be clearly observed in the microscope.

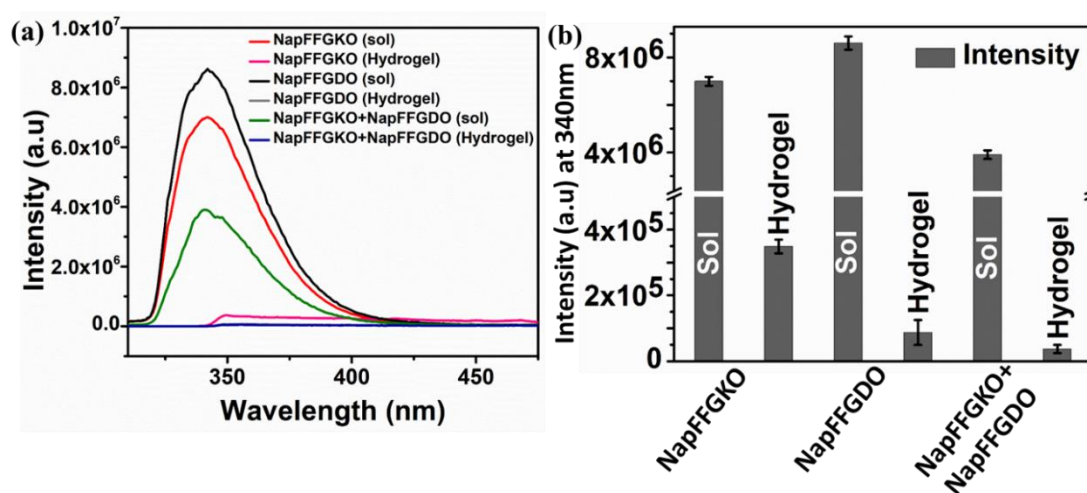


**Figure 3.11** (a) Representative fluorescence emission spectra of peptide amphiphiles in sol and gel state, indicating the formation of the self-assembled nanostructure as evident from the quenched monomeric emission of the naphthoxy group in the gel state. (b) Comparison of the intensity of the monomeric emission at wavelength 340nm.

The more intense patches with co-assembled peptide hydrogels indicate the presence of stronger/intense self-assembled nanostructure due to the involvement of electrostatic interactions (Figure 3.10d,e,f). Apart from hydrogen bonding and hydrophobic interactions between the amino acid backbones,  $\pi$ - $\pi$  interaction between the aromatic groups plays a crucial role in the formation of peptide-based supramolecular structures.<sup>79</sup> Fluorescence emission spectra of this aromatic moiety differ greatly in sol and gel phase. In the gel phase, aromatic groups self-assemble via  $\pi$ - $\pi$  stacking which leads to the decrease in fluorescence intensity. This is clearly evident from the quenching of characteristic naphthyl emission peak at 340nm upon excitation at 270nm which is due to  $\pi$ - $\pi$  interaction between the molecules during self-assembly (Figure 3.11a). On comparing the relative intensities of both the peptides and combined peptides, the monomeric peak of combined hydrogel showed relatively low intensity than the individual hydrogels (Figure 3.11b). The probable reason for this observation could be the closer packing of aromatic naphthyl moiety due to instant electrostatic interactions, which makes naphthyl monomers unavailable for excitation.

**3.2.5 Mechanical Property.** Assessment of mechanical strength of the gels is highly crucial for their futuristic applications.<sup>80</sup> To determine the mechanical property of the hydrogels, oscillatory amplitude sweep and dynamic frequency sweep were carried out. Oscillatory amplitude sweep gives the linear viscoelastic range (LVE) and the dynamic frequency sweep determines the storage ( $G'$ ) (elastic component) and loss modulus ( $G''$ ) (viscous component). The LVE range from amplitude sweep was calculated to be around 0.1 to 1.0% for all the three hydrogels (Figure 3.12). The storage moduli in gels exceeded loss moduli, indicating solid like behavior of the material.<sup>81</sup> Both the peptide hydrogels showed the storage modulus of around 3-4kPa at 30mM (Figure 3.13) whereas the combined gel showed the storage modulus of 6-7kPa which is about double in comparison to the individual gels, suggesting the strong interaction between the peptide chain. In the similar context, it is worth mentioning the report by Joyner et al., demonstrated the role of electrostatic interactions in improving the mechanical strength of the peptides.<sup>82</sup> The authors showed that complementary ionic peptides having more ionic pairs results into higher strength (2 times higher) than the peptides having lower number of ionic pairs. Another report by Jian et al., showed ~5fold increase in mechanical strength of Fmoc-YD/Fmoc-YK co-assembled gels in comparison to individual Fmoc-peptide.<sup>66</sup> Our results were found to be corroborated with the reports

available in literature and thus provide evidence for the improved mechanical strength due to the additional electrostatic attraction-enhanced hydrogen bonding between two oppositely charged peptides.

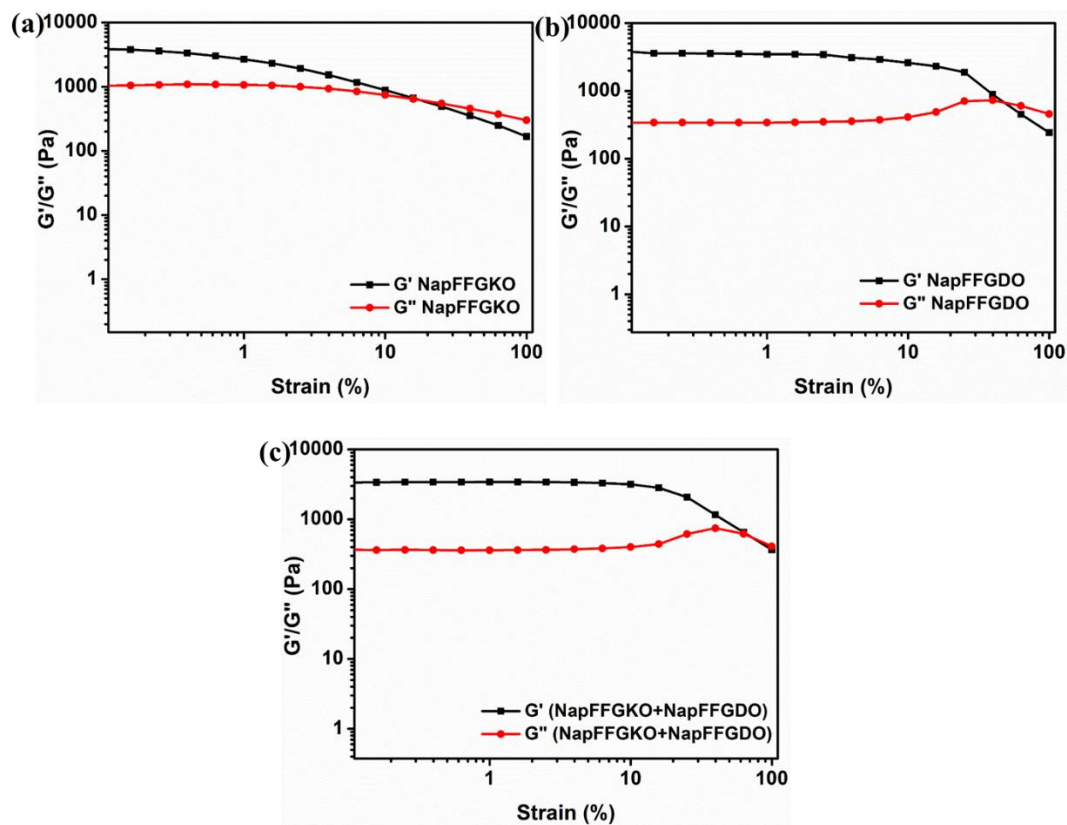


**Figure 3.12** Strain sweep analysis of collagen mimetic peptide hydrogels; (a) NapFFGKO, (b) NapFFGDO and (c) NapFFGKO+NapFFGDO.

**3.2.6 Evaluation of thixotropic behavior.** In order to develop a biomaterial to be used in biomedicines, it would be highly desirable to investigate its self-healing behavior. Peptide hydrogels should withstand the mechanical deformation from the strain exerted onto the bulk hydrogel as well as forces applied by the cells present in the local environment. In order to characterize the self-healing behavior, the gels were subjected to a series of step strain rheology experiment.<sup>83</sup> Interestingly, all the three hydrogels demonstrated the thixotropic behavior (Figure 3.13b,c,d) since they do not lose any mechanical integrity and showed rapid recovery in strength after removal of 100% strain. All the three hydrogels showed almost 100% recovery (Figure 3.14) hence, suggesting their self-healing capability.

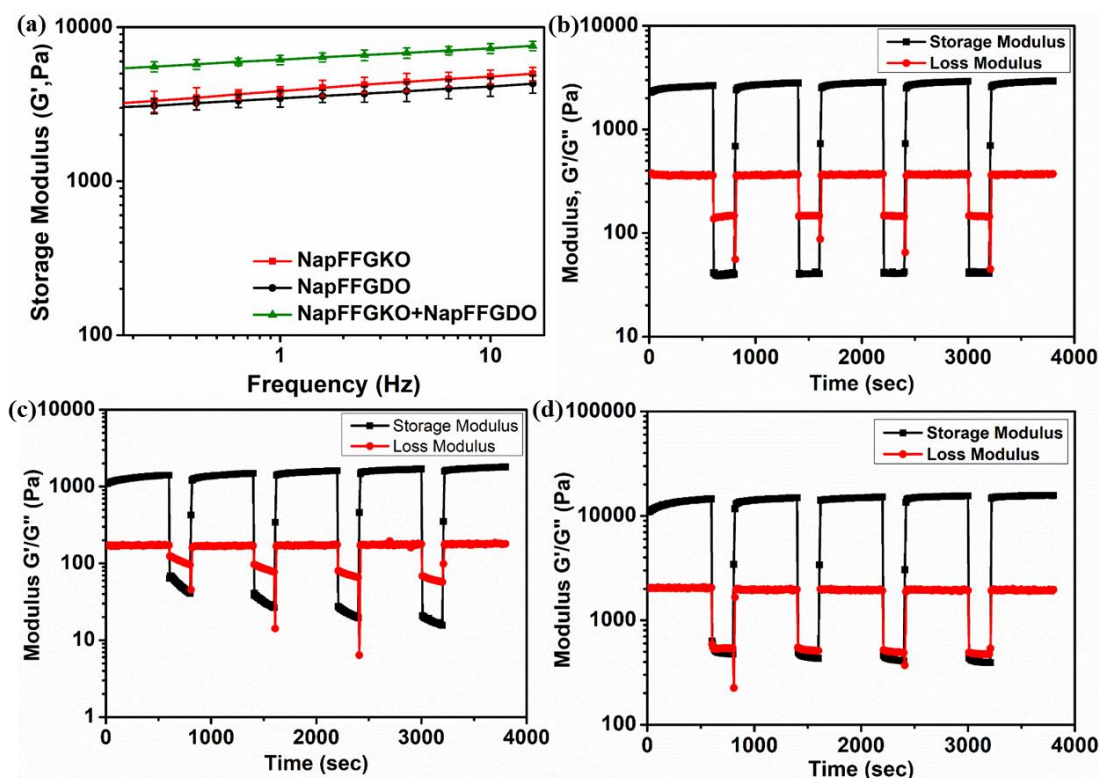


**Figure 3.13** Rheology and thixotropic analysis of collagen inspired peptide hydrogels. (a) Mechanical strength analysis, through frequency sweep study of the individual hydrogelator and the co-assembled hydrogels. Graphical representation of thixotropic measurement of (b) NapFFGKO, (c) NapFFGDO and (d) co-assembled hydrogels (NapFFGKO+NapFFGDO) showing the recovery percentage of five repeat strain sweeps from 0.1 to 100% with 200 sec recovery period in between each sweep for all of the hydrogels.

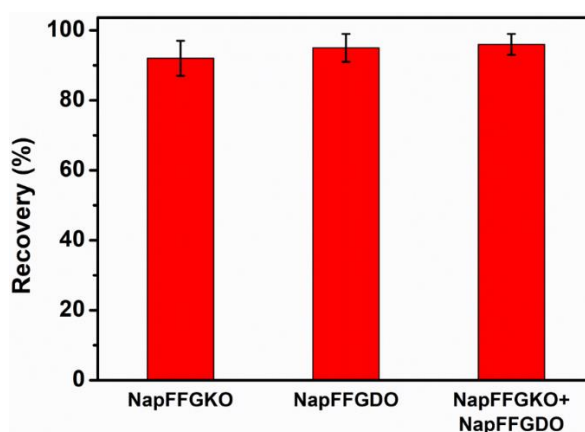


**Figure 3.14** Comparison of percentage recovery in thixotropy measurement, showing the recovery percentage of five repeat strain sweep from 0.1 to 100% with 200 second recovery period in between each sweep for all of the hydrogels.

Whereas in case of combined hydrogel, the storage modulus and loss modulus were very close at 100% strain. This behaviour suggested that even at 100% strain, the hydrogel did not deform completely or converted to sol, this behavior suggests the presence of higher order structure with possible electrostatic interaction in the combined peptides (Figure 3.13d). These results helped to conclude that hydrogels obtained from short collagen inspired peptide have the potential to serve as injectable matrix for encapsulating cells. AFM studies were performed to get an insight into the changes in the nano-architecture during the deformation cycles. Long and dense fibers in the gel phase were changed into short fibers upon applying the deforming strain of 100% and after removal of strain most of the fibers were able to regain their structure in all the three gels (Figure 3.15, 3.16, 3.17).

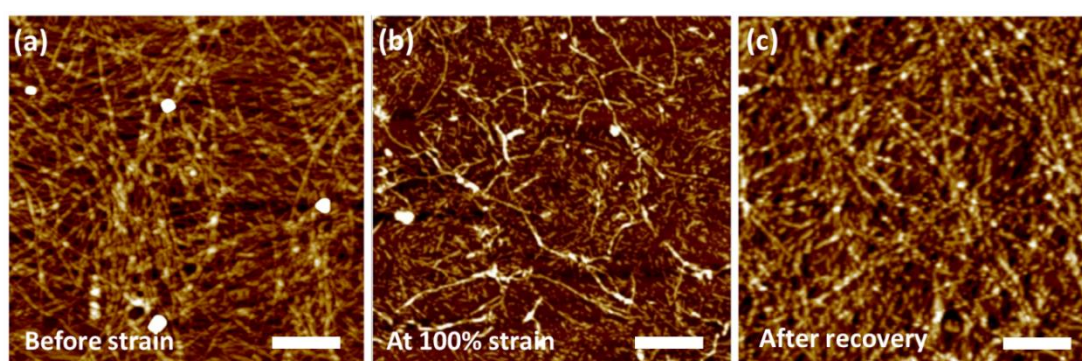


**Figure 3.15** AFM analysis of NapFFGKO at different time points of thixotropy study (a) before strain, (b) at 100% strain and (c) after recovery following the removal of the strain. Scale bar 500nm.

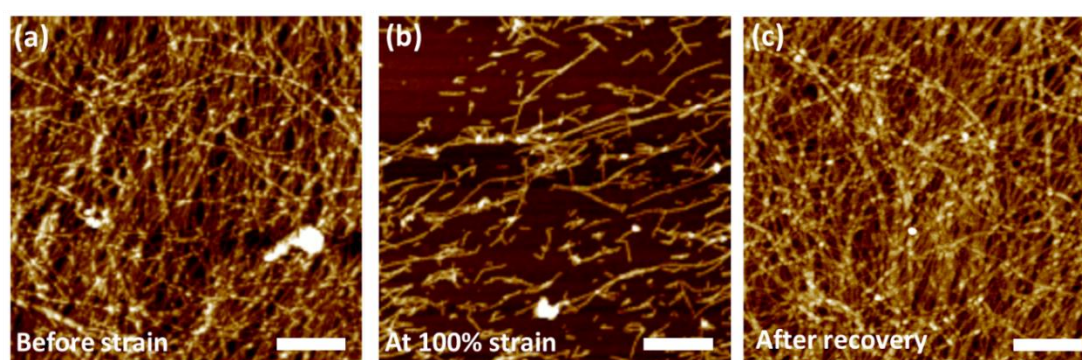


**Figure 3.16** AFM analysis of NapFFGDO at different time points of thixotropy study (a) before strain, (b) at 100% strain and (c) after recovery following the removal of the strain. Scale bar 500nm.

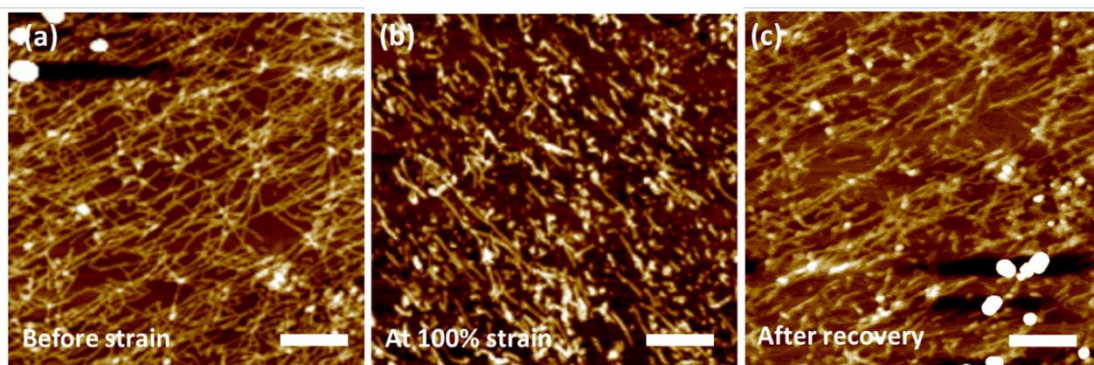


**Figure 3.17** AFM analysis of co-assembled system NapFFGKO+NapFFGDO at different time points of thixotropy study (a) before strain, (b) at 100% strain and (c) after recovery following the removal of the strain. Scale bar 500nm.

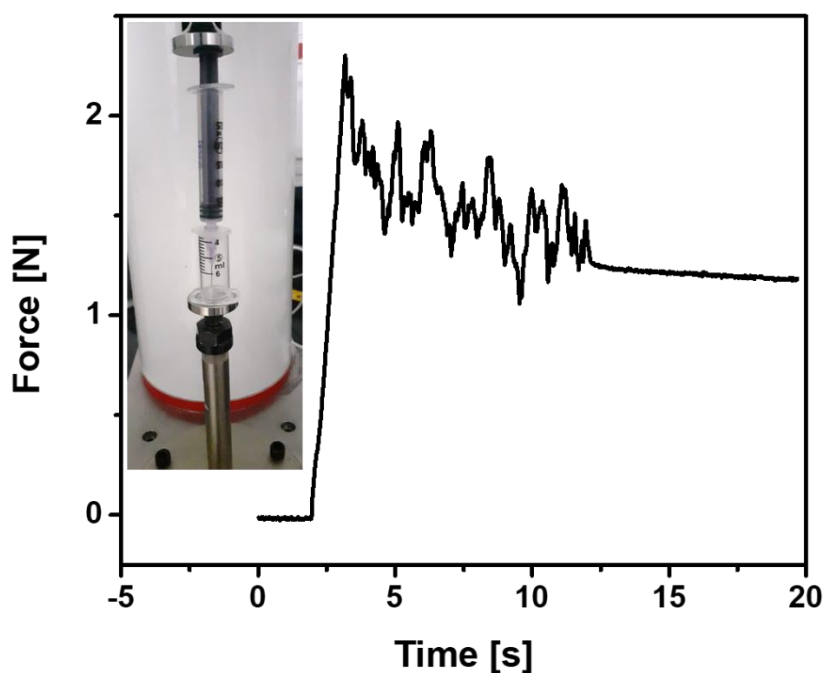


**Figure 3.18** Dynamic compressive strain study of the combined hydrogel NapFFGKO+NapFFGDO through 18G needle from a 2.5 cc syringe at an injection rate of 50  $\mu\text{L/s}$ . Data is represented as force vs time and the inset image shows the custom-made setup to examine the force required for extrusion.

To further determine the injectability or printability of the presented peptide hydrogels, we have performed dynamic compressive strain study.<sup>84</sup> The hydrogel was placed in a 2.5 cc syringe with 18 G needle attached to it. The force was applied to extrude the hydrogel at a rate of 50  $\mu\text{L/s}$  and the force required to extrude the hydrogel was

calculated using the axial compression tester (BiSS, India). We have used the combined hydrogel (NapFFGKO+NapFFGDO) for this study at a concentration of 40mM to check its printability, as it has the neutralized surface charge and also better mechanical strength. As observed from the dynamic compressive study, the force required to extrude the combined hydrogel was 2.24 N. The extruded sample can be used to make guided structures and hence have the futuristic applications in 3D bioprinting.<sup>85, 86</sup>

**3.2.7 Cytotoxicity studies.** Hydrogels with varying polarity and stiffness are being used as a scaffold for different cell types.<sup>87</sup> In order to explore the potential of the successful construct for mimicking extracellular matrix, cytocompatibility of the peptides should be assessed. Cytotoxicity assay of fibroblast cells (mouse fibroblast cell line L929) in presence of NapFFGKO, NapFFGDO and the combined peptides were evaluated by 3-(4, 5-dimethylthiazol-2-yl)-2, 5-diphenyltetrazolium bromide (MTT) reduction assay. Cell viability was assessed after incubating the fibroblast cells with different concentrations of peptides for 48hrs.

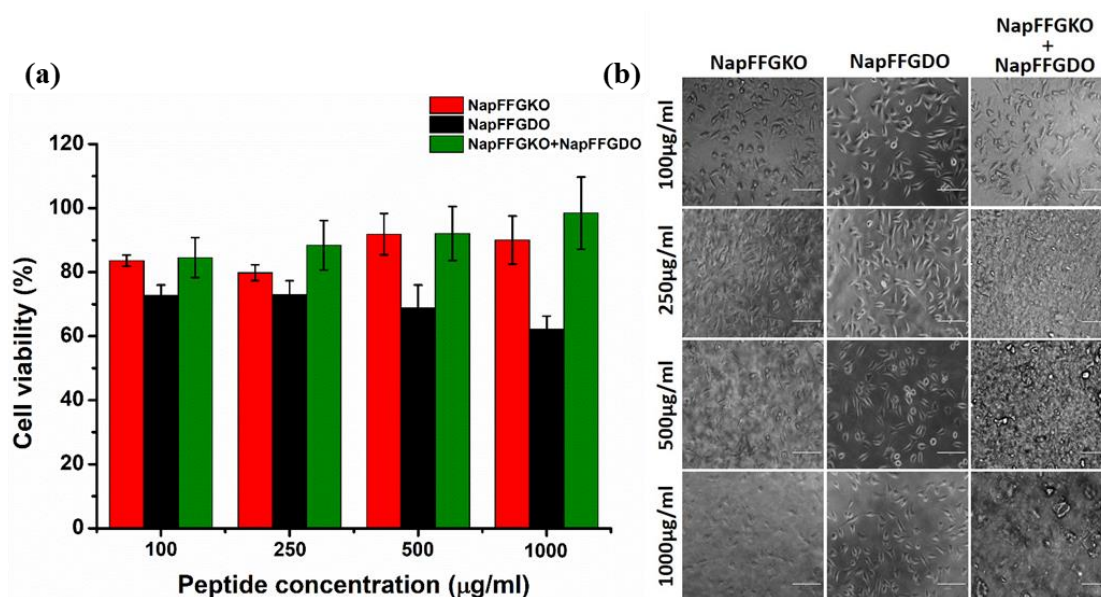


**Figure 3.19** (a) Cytotoxicity studies comparing the effect of different collagen mimetic peptides on L929 cells at a concentration ranging from 100µg/ml to 1000µg/ml after incubation of 48hrs. (b) Bright field images of L929 cells after 48hrs of incubation with the individual peptides and their co-assembly. Scale bar 100µm.

However, to support the cell growth, the peptide solutions were used at physiological pH, which is crucial for their survival. In this context, it is worth mentioning that a clear evidence was observed through CD spectroscopic studies, that individual peptides

formed random coiled structures at physiological pH (~7). The less ordered random coil structures of the individual peptide were found to be less supportive matrix towards the cells, while co-assembled fibrillary nanostructures were found to present highly compatible interface for the cells. It has been already reported that, in addition to surface functionality, the morphology and mechanical strength of the nanostructures play a significant role in determining its interaction with the cells.<sup>19</sup> It was observed that, NapFFGKO showed 80-90% biocompatibility, while NapFFGDO showed 60-70% biocompatibility in the concentration range of 100-1000 $\mu$ g/ml. The probable reason for lower cell viability could be because of the less ordered random coil nanostructures present at physiological pH. It was noteworthy that, an overall surface charge on the positively charged NapFFGKO and overall negative surface charge on NapFFGDO were found to be detrimental to the cells.<sup>19</sup> Interestingly, this limitation has been successfully overcome in the combined peptides due to surface charge neutralization at physiological conditions. Hence, the nanofibers produced in the combined hydrogel were found to support the cell growth by providing effective bioactive scaffold to the cells for adherence. This biocompatible nature of the combined gel nanofibers showed almost 100% cell viability against fibroblast cells indicating highly biocompatible nature of the scaffold (Figure 3.18a). Shape and number of the adhered cells in treated samples were similar to that of the control, which was maintained even up to 1000  $\mu$ g/ml, demonstrating the significant compatibility of the designed peptides towards the cells (Figure 3.18b). The higher biocompatibility of co-assembled complementary ionic peptides can be supported by enhancing the complexity of the matrix through post assembly modification design of several synthetic cell interacting peptides like, RADA, MAX, Q11, EAK, which were based on alternating oppositely charged residues.<sup>88, 89</sup> Thus the biological activity of the charge neutralized hydrogel highlighted this excellent potential to be developed as a superior biomimetic scaffold.

### **3.3 Conclusion**

In summary, we report for the first time, the crucial molecular design of oppositely charged collagen inspired shortest bioactive pentapeptide sequences, as a minimalistic building block for development of next-generation biomaterials. The peptide features the repeating unit of collagen molecule (Gly-Pro-Hyp), where proline has been replaced with two oppositely charged amino acids, lysine and aspartate in two ionic

complementary sequences. The designed sequences showed effective self-assembly either at acidic/basic pH depending up on their overall surface charge. However, such phenomenon limits their bio-applications. Surprisingly, simple mixing of the two peptides were found to induce the co-assembly of these designed peptide, which drives the formation of self-supporting hydrogel at physiological pH and thus enhanced the potential of exploring these peptides for biomedical purposes. Initiation of the electrostatic interaction was found to have profound effect on gelation behavior of the short bioactive peptides. The minimum gelation concentration of the individual peptides has been reduced with an increase in their mechanical strength at physiological pH for their co-assembled state. Such interesting feature enhanced the scope of these designed gels to be explored as smart biomaterial to support their biological functions. Interestingly, these bioinspired peptide sequences showed excellent biocompatibility with the fibroblast cells, which provides the evidence for developing such functional materials for biomedical applications.

#### Note:

The permission has been granted by authors and corresponding author of the published paper prior to its adoption in the present thesis. The publication associated with this work is:

Vijay Kumar Pal, Rashmi Jain, and Sangita Roy, Tuning the Supramolecular Structure and Function of Collagen Mimetic Ionic Complementary Peptides via Electrostatic Interactions. *Langmuir*, **2019**, *36*(4), 1003-1013

### 3.4 References

1. Hartgerink, J. D.; Beniash, E.; Stupp, S. I., Self-Assembly and Mineralization of Peptide-Amphiphile Nanofibers. *Science* **2001**, *294* (5547), 1684-1688.
2. Draper, E. R.; Eden, E. G.; McDonald, T. O.; Adams, D. J., Spatially resolved multicomponent gels. *Nat Chem* **2015**, *7* (10), 848-52.
3. Webber, M. J.; Appel, E. A.; Meijer, E. W.; Langer, R., Supramolecular biomaterials. *Nature materials* **2016**, *15* (1), 13-26.
4. Du, X.; Zhou, J.; Shi, J.; Xu, B., Supramolecular Hydrogelators and Hydrogels: From Soft Matter to Molecular Biomaterials. *Chem. Rev.* **2015**, *115* (24), 13165-307.
5. Ji, W.; Yuan, C.; Zilberzweig-Tal, S.; Xing, R.; Chakraborty, P.; Tao, K.; Gilead, S.; Yan, X.; Gazit, E., Metal-Ion Modulated Structural Transformation of Amyloid-Like Dipeptide Supramolecular Self-Assembly. *ACS Nano* **2019**, *13* (6), 7300-7309.

6. Sharma, P.; Kaur, H.; Roy, S., Inducing Differential Self-Assembling Behavior in Ultrashort Peptide Hydrogelators Using Simple Metal Salts. *Biomacromolecules* **2019**, *20* (7), 2610-2624.
7. Shang, Y.; Zhi, D.; Feng, G.; Wang, Z.; Mao, D.; Guo, S.; Liu, R.; Liu, L.; Zhang, S.; Sun, S.; Wang, K.; Kong, D.; Gao, J.; Yang, Z., Supramolecular Nanofibers with Superior Bioactivity to Insulin-Like Growth Factor-I. *Nano Lett.* **2019**, *19* (3), 1560-1569.
8. Raymond, D. M.; Nilsson, B. L., Multicomponent peptide assemblies. *Chem. Soc. Rev.* **2018**, *47* (10), 3659-3720.
9. Guo, Z.; Zhang, X.; Wang, Y.; Li, Z., Supramolecular Self-Assembly of Perylene Bisimide Derivatives Assisted by Various Groups. *Langmuir* **2019**, *35* (2), 342-358.
10. Singh, N.; Kumar, M.; Miravet, J. F.; Ulijn, R. V.; Escuder, B., Peptide-Based Molecular Hydrogels as Supramolecular Protein Mimics. *Chem. Eur. J.* **2017**, *23* (5), 981-993.
11. Stupp, S. I., Self-Assembly and Biomaterials. *Nano Lett.* **2010**, *10* (12), 4783-4786.
12. Zhang, W.; Yu, X.; Li, Y.; Su, Z.; Jandt, K. D.; Wei, G., Protein-mimetic peptide nanofibers: Motif design, self-assembly synthesis, and sequence-specific biomedical applications. *Prog. Polym. Sci.* **2018**, *80*, 94-124.
13. Li, J.; Xing, R.; Bai, S.; Yan, X., Recent advances of self-assembling peptide-based hydrogels for biomedical applications. *Soft Matter* **2019**, *15* (8), 1704-1715.
14. Xu, T.; Cai, Y.; Zhong, X.; Zhang, L.; Zheng, D.; Gao, Z.; Pan, X.; Wang, F.; Chen, M.; Yang, Z.,  $\beta$ -Galactosidase instructed supramolecular hydrogelation for selective identification and removal of senescent cells. *Chem. Commun.* **2019**, *55* (50), 7175-7178.
15. Liyanage, W.; Vats, K.; Rajbhandary, A.; Benoit, D. S. W.; Nilsson, B. L., Multicomponent dipeptide hydrogels as extracellular matrix-mimetic scaffolds for cell culture applications. *Chem. Commun.* **2015**, *51* (56), 11260-11263.
16. Reches, M.; Gazit, E., Casting Metal Nanowires Within Discrete Self-Assembled Peptide Nanotubes. *Science* **2003**, *300* (5619), 625-627.
17. Ulijn, R. V.; Smith, A. M., Designing peptide based nanomaterials. *Chem. Soc. Rev.* **2008**, *37* (4), 664-75.
18. Todd, S. J.; Farrar, D.; Gough, J. E.; Ulijn, R. V., Enzyme-triggered cell attachment to hydrogel surfaces. *Soft Matter* **2007**, *3* (5), 547.
19. Jayawarna, V.; Richardson, S. M.; Hirst, A. R.; Hodson, N. W.; Saiani, A.; Gough, J. E.; Ulijn, R. V., Introducing chemical functionality in Fmoc-peptide gels for cell culture. *Acta Biomater* **2009**, *5* (3), 934-43.
20. Alakpa, Enateri V.; Jayawarna, V.; Lampel, A.; Burgess, Karl V.; West, Christopher C.; Bakker, Sanne C. J.; Roy, S.; Javid, N.; Fleming, S.; Lamprou, Dimitris A.; Yang, J.; Miller, A.; Urquhart, Andrew J.; Frederix, Pim W. J. M.; Hunt, Neil T.; Péault, B.; Ulijn, Rein V.; Dalby, Matthew J., Tunable Supramolecular Hydrogels for Selection of Lineage-Guiding Metabolites in Stem Cell Cultures. *Chem* **2016**, *1* (2), 298-319.
21. Li, S.; Xing, R.; Chang, R.; Zou, Q.; Yan, X., Nanodrugs based on peptide-modulated self-assembly: Design, delivery and tumor therapy. *Curr. Opin. Colloid Interface Sci.* **2018**, *35*, 17-25.
22. Yamada, Y.; Patel, N. L.; Kalen, J. D.; Schneider, J. P., Design of a Peptide-Based Electronegative Hydrogel for the Direct Encapsulation, 3D Culturing, in Vivo Syringe-Based Delivery, and Long-Term Tissue Engraftment of Cells. *ACS Appl. Mater. Interfaces* **2019**.
23. Luo, T.; Kiick, K. L., Collagen-like peptides and peptide-polymer conjugates in the design of assembled materials. *Eur. Polym. J.* **2013**, *49* (10), 2998-3009.
24. Wan, Y.; Liu, L.; Yuan, S.; Sun, J.; Li, Z., pH-Responsive Peptide Supramolecular Hydrogels with Antibacterial Activity. *Langmuir* **2017**, *33* (13), 3234-3240.
25. Patterson, J.; Martino, M. M.; Hubbell, J. A., Biomimetic materials in tissue engineering. *Mater. Today* **2010**, *13* (1), 14-22.
26. Kyburz, K. A.; Anseth, K. S., Synthetic mimics of the extracellular matrix: how simple is complex enough? *Annals of biomedical engineering* **2015**, *43* (3), 489-500.
27. He, L.; Theato, P., Collagen and collagen mimetic peptide conjugates in polymer science. *Eur. Polym. J.* **2013**, *49* (10), 2986-2997.

28. Kotch, F. W.; Raines, R. T., Self-assembly of synthetic collagen triple helices. *Proc Natl Acad Sci U S A* **2006**, *103* (9), 3028-33.
29. Hu, Y.; Wang, H.; Wang, J.; Wang, S.; Liao, W.; Yang, Y.; Zhang, Y.; Kong, D.; Yang, Z., Supramolecular hydrogels inspired by collagen for tissue engineering. *Org Biomol Chem* **2010**, *8* (14), 3267-71.
30. Toksoz, S.; Mammadov, R.; Tekinay, A. B.; Guler, M. O., Electrostatic effects on nanofiber formation of self-assembling peptide amphiphiles. *J. Colloid Interface Sci.* **2011**, *356* (1), 131-7.
31. Chiang, C. H.; Fu, Y. H.; Horng, J. C., Formation of AAB-Type Collagen Heterotrimers from Designed Cationic and Aromatic Collagen-Mimetic Peptides: Evaluation of the C-Terminal Cation- $\pi$  Interactions. *Biomacromolecules* **2017**, *18* (3), 985-993.
32. O'Leary, L. E.; Fallas, J. A.; Bakota, E. L.; Kang, M. K.; Hartgerink, J. D., Multi-hierarchical self-assembly of a collagen mimetic peptide from triple helix to nanofibre and hydrogel. *Nat Chem* **2011**, *3* (10), 821-8.
33. Shi, Y.; Wang, S.; Wang, X.-M.; Cai, Q.; Cui, F.-Z.; Li, H.-D., Hierarchical self-assembly of a collagen mimetic peptide (PKG)<sub>n</sub> (POG)<sub>2n</sub> (DOG)<sub>n</sub> via electrostatic interactions. *Front. Mater. Sci.* **2011**, *5* (3), 293-300.
34. Luo, J.; Tong, Y. W., Self-Assembly of Collagen-Mimetic Peptide Amphiphiles into Biofunctional Nanofiber. *ACS Nano* **2011**, *5* (10), 7739-7747.
35. Yu, S. M.; Li, Y.; Kim, D., Collagen Mimetic Peptides: Progress Towards Functional Applications. *Soft Matter* **2011**, *7* (18), 7927-7938.
36. Kar, K.; Ibrar, S.; Nanda, V.; Getz, T. M.; Kunapuli, S. P.; Brodsky, B., Aromatic interactions promote self-association of collagen triple-helical peptides to higher-order structures. *Biochemistry* **2009**, *48* (33), 7959-68.
37. Babu, I. R.; Ganesh, K. N., Enhanced Triple Helix Stability of Collagen Peptides with 4R-Aminopropyl (Amp) Residues: Relative Roles of Electrostatic and Hydrogen Bonding Effects. *J. Am. Chem. Soc.* **2001**, *123* (9), 2079-2080.
38. Parmar, A. S.; Nunes, A. M.; Baum, J.; Brodsky, B., A peptide study of the relationship between the collagen triple-helix and amyloid. *Biopolymers* **2012**, *97* (10), 795-806.
39. Goldberga, I.; Li, R.; Duer, M. J., Collagen Structure–Function Relationships from Solid-State NMR Spectroscopy. *Acc. Chem. Res.* **2018**, *51* (7), 1621-1629.
40. Lee, H. J.; Lee, J. S.; Chansakul, T.; Yu, C.; Elisseff, J. H.; Yu, S. M., Collagen mimetic peptide-conjugated photopolymerizable PEG hydrogel. *Biomaterials* **2006**, *27* (30), 5268-76.
41. Cejas, M. A.; Kinney, W. A.; Chen, C.; Vinter, J. G.; Almond, H. R., Jr.; Balss, K. M.; Maryanoff, C. A.; Schmidt, U.; Breslav, M.; Mahan, A.; Lacy, E.; Maryanoff, B. E., Thrombogenic collagen-mimetic peptides: Self-assembly of triple helix-based fibrils driven by hydrophobic interactions. *Proc Natl Acad Sci U S A* **2008**, *105* (25), 8513-8.
42. Jalan, A. A.; Demeler, B.; Hartgerink, J. D., Hydroxyproline-Free Single Composition ABC Collagen Heterotrimer. *J. Am. Chem. Soc.* **2013**, *135* (16), 6014-6017.
43. Jalan, A. A.; Hartgerink, J. D., Pairwise interactions in collagen and the design of heterotrimeric helices. *Curr. Opin. Chem. Biol.* **2013**, *17* (6), 960-7.
44. Krishna, O. D.; Kiick, K. L., Supramolecular Assembly of Electrostatically Stabilized, Hydroxyproline-Lacking Collagen-Mimetic Peptides. *Biomacromolecules* **2009**, *10* (9), 2626-2631.
45. Shoulders, M. D.; Raines, R. T., Collagen structure and stability. *Annu. Rev. Biochem* **2009**, *78*, 929-958.
46. Rele, S.; Song, Y.; Apkarian, R. P.; Qu, Z.; Conticello, V. P.; Chaikof, E. L., D-Periodic Collagen-Mimetic Microfibers. *J. Am. Chem. Soc.* **2007**, *129* (47), 14780-14787.
47. Jiang, T.; Xu, C.; Liu, Y.; Liu, Z.; Wall, J. S.; Zuo, X.; Lian, T.; Salaita, K.; Ni, C.; Pochan, D.; Conticello, V. P., Structurally defined nanoscale sheets from self-assembly of collagen-mimetic peptides. *J. Am. Chem. Soc.* **2014**, *136* (11), 4300-8.
48. Spassov, V. Z.; Yan, L.; Flook, P. K., The dominant role of side-chain backbone interactions in structural realization of amino acid code. ChiRotor: a side-chain prediction

algorithm based on side-chain backbone interactions. *Protein science : a publication of the Protein Society* **2007**, *16* (3), 494-506.

49. Gao, J.; Tang, C.; Elsayy, M. A.; Smith, A. M.; Miller, A. F.; Saiani, A., Controlling Self-Assembling Peptide Hydrogel Properties through Network Topology. *Biomacromolecules* **2017**, *18* (3), 826-834.

50. Lee, N. R.; Bowerman, C. J.; Nilsson, B. L., Effects of Varied Sequence Pattern on the Self-Assembly of Amphipathic Peptides. *Biomacromolecules* **2013**, *14* (9), 3267-3277.

51. Wan, Y.; Wang, Z.; Sun, J.; Li, Z., Extremely Stable Supramolecular Hydrogels Assembled from Nonionic Peptide Amphiphiles. *Langmuir* **2016**, *32* (30), 7512-7518.

52. Berdugo, C.; Nalluri, S. K. M.; Javid, N.; Escuder, B.; Miravet, J. F.; Ulijn, R. V., Dynamic Peptide Library for the Discovery of Charge Transfer Hydrogels. *ACS Appl. Mater. Interfaces* **2015**, *7* (46), 25946-25954.

53. Elsayy, M. A.; Smith, A. M.; Hodson, N.; Squires, A.; Miller, A. F.; Saiani, A., Modification of  $\beta$ -Sheet Forming Peptide Hydrophobic Face: Effect on Self-Assembly and Gelation. *Langmuir* **2016**, *32* (19), 4917-4923.

54. Zhang, S.; Holmes, T.; Lockshin, C.; Rich, A., Spontaneous assembly of a self-complementary oligopeptide to form a stable macroscopic membrane. *Proc. Nat. Acad. Sci.* **1993**, *90* (8), 3334-3338.

55. Zhang, S.; Lockshin, C.; Cook, R.; Rich, A., Unusually stable  $\beta$ -sheet formation in an ionic self-complementary oligopeptide. *Biopolymers* **1994**, *34* (5), 663-672.

56. Holmes, T. C.; de Lacalle, S.; Su, X.; Liu, G.; Rich, A.; Zhang, S., Extensive neurite outgrowth and active synapse formation on self-assembling peptide scaffolds. *Proc. Nat. Acad. Sci.* **2000**, *97* (12), 6728-6733.

57. Kisiday, J.; Jin, M.; Kurz, B.; Hung, H.; Semino, C.; Zhang, S.; Grodzinsky, A. J., Self-assembling peptide hydrogel fosters chondrocyte extracellular matrix production and cell division: Implications for cartilage tissue repair. *Proc. Nat. Acad. Sci.* **2002**, *99* (15), 9996-10001.

58. Kretsinger, J. K.; Haines, L. A.; Ozbas, B.; Pochan, D. J.; Schneider, J. P., Cytocompatibility of self-assembled  $\beta$ -hairpin peptide hydrogel surfaces. *Biomaterials* **2005**, *26* (25), 5177-5186.

59. Uysal, O.; Arslan, E.; Gulseren, G.; Kilinc, M. C.; Dogan, I.; Ozalp, H.; Caglar, Y. S.; Guler, M. O.; Tekinay, A. B., Collagen Peptide Presenting Nanofibrous Scaffold for Intervertebral Disc Regeneration. *ACS Appl. Bio Mater.* **2019**, *2* (4), 1686-1695.

60. Liyanage, W.; Nilsson, B. L., Substituent Effects on the Self-Assembly/Coassembly and Hydrogelation of Phenylalanine Derivatives. *Langmuir* **2016**, *32* (3), 787-799.

61. Kar, K.; Ibrar, S.; Nanda, V.; Getz, T. M.; Kunapuli, S. P.; Brodsky, B., Aromatic Interactions Promote Self-Association of Collagen Triple-Helical Peptides to Higher-Order Structures. *Biochemistry* **2009**, *48* (33), 7959-7968.

62. Wang, K.; Keasling, J. D.; Muller, S. J., Effects of the sequence and size of non-polar residues on self-assembly of amphiphilic peptides. *Int. J. Biol. Macromol.* **2005**, *36* (4), 232-40.

63. Radmer, R. J.; Klein, T. E., Triple helical structure and stabilization of collagen-like molecules with 4(R)-hydroxyproline in the Xaa position. *Biophys. J.* **2006**, *90* (2), 578-588.

64. Jin, H.; Ding, Y.-H.; Wang, M.; Song, Y.; Liao, Z.; Newcomb, C. J.; Wu, X.; Tang, X.-Q.; Li, Z.; Lin, Y.; Yan, F.; Jian, T.; Mu, P.; Chen, C.-L., Designable and dynamic single-walled stiff nanotubes assembled from sequence-defined peptoids. *Nat. Commun.* **2018**, *9* (1), 270.

65. Nam, K. T.; Shelby, S. A.; Choi, P. H.; Marciel, A. B.; Chen, R.; Tan, L.; Chu, T. K.; Mesch, R. A.; Lee, B.-C.; Connolly, M. D.; Kisielowski, C.; Zuckermann, R. N., Free-floating ultrathin two-dimensional crystals from sequence-specific peptoid polymers. *Nature materials* **2010**, *9* (5), 454-460.

66. Jian, H.; Wang, M.; Dong, Q.; Li, J.; Wang, A.; Li, X.; Ren, P.; Bai, S., Dipeptide Self-Assembled Hydrogels with Tunable Mechanical Properties and Degradability for 3D Bioprinting. *ACS Appl. Mater. Interfaces* **2019**.

67. Liu, K.; Kang, Y.; Ma, G.; Möhwald, H.; Yan, X., Molecular and mesoscale mechanism for hierarchical self-assembly of dipeptide and porphyrin light-harvesting system. *PCCP* **2016**, *18* (25), 16738-16747.
68. Yuan, C.; Levin, A.; Chen, W.; Xing, R.; Zou, Q.; Herling, T. W.; Challa, P. K.; Knowles, T. P. J.; Yan, X., Nucleation and Growth of Amino Acid and Peptide Supramolecular Polymers through Liquid–Liquid Phase Separation. *Angew. Chem. Int. Ed.* **2019**, *58* (50), 18116-18123.
69. Ji, W.; Yuan, C.; Chakraborty, P.; Gilead, S.; Yan, X.; Gazit, E., Stoichiometry-controlled secondary structure transition of amyloid-derived supramolecular dipeptide co-assemblies. *Commun. Chem.* **2019**, *2* (1), 65.
70. Yuan, C.; Ji, W.; Xing, R.; Li, J.; Gazit, E.; Yan, X., Hierarchically oriented organization in supramolecular peptide crystals. *Nat. Rev. Chem.* **2019**, *3* (10), 567-588.
71. Li, J.; Du, X.; Hashim, S.; Shy, A.; Xu, B., Aromatic–Aromatic Interactions Enable  $\alpha$ -Helix to  $\beta$ -Sheet Transition of Peptides to Form Supramolecular Hydrogels. *J. Am. Chem. Soc.* **2017**, *139* (1), 71-74.
72. Xu, S., Cross- $\beta$ -Sheet Structure in Amyloid Fiber Formation. *J. Phys. Chem. B* **2009**, *113* (37), 12447-12455.
73. Onogi, S.; Shigemitsu, H.; Yoshii, T.; Tanida, T.; Ikeda, M.; Kubota, R.; Hamachi, I., In situ real-time imaging of self-sorted supramolecular nanofibres. *Nat. Chem.* **2016**, *8*.
74. Byler, D. M.; Susi, H., Examination of the secondary structure of proteins by deconvolved FTIR spectra. *Biopolymers* **1986**, *25* (3), 469-487.
75. Jain, R.; Khandelwal, G.; Roy, S., Unraveling the Design Rules in Ultrashort Amyloid-Based Peptide Assemblies toward Shape-Controlled Synthesis of Gold Nanoparticles. *Langmuir* **2019**, *35* (17), 5878-5889.
76. Abul-Haija, Y. M.; Scott, G. G.; Sahoo, J. K.; Tuttle, T.; Ulijn, R. V., Cooperative, ion-sensitive co-assembly of tripeptide hydrogels. *Chem. Commun.* **2017**, *53* (69), 9562-9565.
77. Scott, G. G.; McKnight, P. J.; Tuttle, T.; Ulijn, R. V., Tripeptide Emulsifiers. *Adv. Mater.* **2016**, *28* (7), 1381-1386.
78. Krebs, M. R. H.; Bromley, E. H. C.; Donald, A. M., The binding of thioflavin-T to amyloid fibrils: localisation and implications. *J. Struct. Biol.* **2005**, *149* (1), 30-37.
79. Smith, A. M.; Williams, R. J.; Tang, C.; Coppo, P.; Collins, R. F.; Turner, M. L.; Saiani, A.; Ulijn, R. V., Fmoc-Diphenylalanine Self Assembles to a Hydrogel via a Novel Architecture Based on  $\pi$ - $\pi$  Interlocked  $\beta$ -Sheets. *Adv. Mater.* **2008**, *20* (1), 37-41.
80. Ahmed, E. M., Hydrogel: Preparation, characterization, and applications: A review. *J. Adv. Res.* **2015**, *6* (2), 105-121.
81. Feig, V. R.; Tran, H.; Lee, M.; Bao, Z., Mechanically tunable conductive interpenetrating network hydrogels that mimic the elastic moduli of biological tissue. *Nat. Commun.* **2018**, *9* (1), 2740.
82. Joyner, K.; Taraban, M. B.; Feng, Y.; Yu, Y. B., An interplay between electrostatic and polar interactions in peptide hydrogels. *Biopolymers* **2013**, *100* (2), 174-83.
83. Clarke, D. E.; Pashuck, E. T.; Bertazzo, S.; Weaver, J. V. M.; Stevens, M. M., Self-Healing, Self-Assembled  $\beta$ -Sheet Peptide–Poly( $\gamma$ -glutamic acid) Hybrid Hydrogels. *J. Am. Chem. Soc.* **2017**, *139* (21), 7250-7255.
84. Thomas, J.; Chopra, V.; Sharma, A.; Panwar, V.; Kaushik, S.; Rajput, S.; Mittal, M.; Guha, R.; Chattopadhyay, N.; Ghosh, D., An injectable hydrogel having proteoglycan-like hierarchical structure supports chondrocytes delivery and chondrogenesis. *Int. J. Biol. Macromol.* **2021**, *190*, 474-486.
85. Li, J.; Wu, C.; Chu, P. K.; Gelinsky, M., 3D printing of hydrogels: Rational design strategies and emerging biomedical applications. *Materials Science and Engineering: R: Reports* **2020**, *140*, 100543.
86. Advincula, R. C.; Dizon, J. R. C.; Caldon, E. B.; Viers, R. A.; Siacor, F. D. C.; Maalihan, R. D.; Espera, A. H., On the progress of 3D-printed hydrogels for tissue engineering. *MRS Communications* **2021**, *11* (5), 539-553.
87. El-Sherbiny, I. M.; Yacoub, M. H., Hydrogel scaffolds for tissue engineering: Progress and challenges. *Glob Cardiol Sci Pract* **2013**, *2013* (3), 316-342.

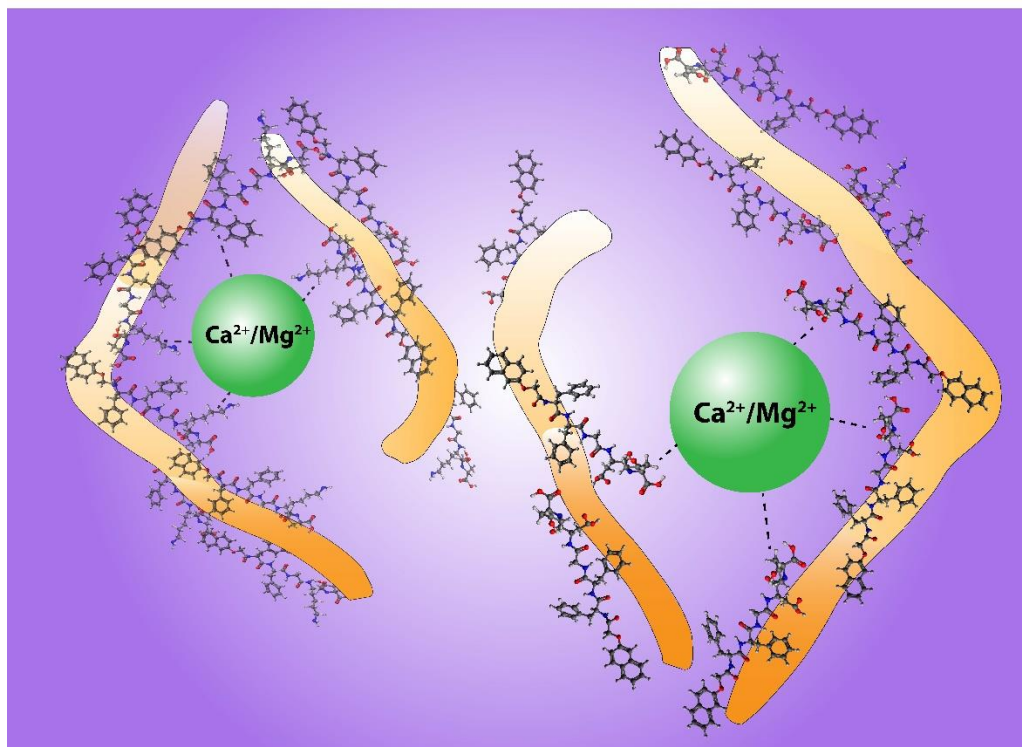
88. Rad-Malekshahi, M.; Lempsink, L.; Amidi, M.; Hennink, W. E.; Mastrobattista, E., Biomedical Applications of Self-Assembling Peptides. *Bioconjug Chem* **2016**, 27 (1), 3-18.
89. Wu, E. C.; Zhang, S.; Hauser, C. A. E., Self-Assembling Peptides as Cell-Interactive Scaffolds. *Adv. Funct. Mater.* **2012**, 22 (3), 456-468.



# Chapter 4

Metal ion complexation promotes self-assembly within a short collagen inspired peptide domain and leads to fabrication of an advanced scaffold with enhanced cellular proliferation





**Cooperative effect of metal ion coordination in the bioactive peptide scaffold inspired from native collagen protein was found to promote the hydrogelation at physiological conditions leading to enhanced cellular proliferation.**



## 4.1 Introduction

As discussed in the previous chapter, non-covalent interactions among short peptides and proteins led to their molecular self-assembly into supramolecular packaging, which provides the fundamental basis of life. In nature, most of the complex biological processes are governed by supramolecular association among the biomolecules, where non-covalent interactions play a significant role.<sup>1-3</sup> Over the past few years, supramolecular chemistry has been evolved to enlighten numerous interdisciplinary areas at the interface of biology, chemistry, and physics.<sup>4-6</sup> Various complex biological phenomena, such as enzyme-substrate complex, protein-protein interactions, intricate packing and replication of DNA molecule etc., are some of the well-known examples of the cooperative non-covalent interactions.<sup>7,8</sup> To this direction, the literature has well documented that many of the natural proteins and enzymes require metal ions, which contribute to their structural integrity and functional property.<sup>9</sup> Several metal cations were identified to be involved in various biophysical and biochemical processes.<sup>10</sup> In particular, few metal ions, like,  $\text{Ca}^{2+}$ ,  $\text{Mg}^{2+}$ , and  $\text{Cu}^{2+}$  were reported to increase the protein stability, while other ions, like,  $\text{K}^+$ ,  $\text{Na}^+$  were identified for their role in regulating cell processes.<sup>11</sup> There were several reports that indicated the participation of metal ions, like,  $\text{Co}^{2+}$ ,  $\text{Ni}^{2+}$ ,  $\text{Zn}^{2+}$  in enzyme catalysis.<sup>12-14</sup> Hence, mimicking the interaction of protein and peptide with metal ions under *in vitro* conditions, can be a useful strategy to create bioinspired functional materials.<sup>15-20</sup> In this context, significant literature reports were available, which indicated that protein and peptides display variable functional groups exposed at the surface. These active functional groups can initiate the interactions with different metal ions.<sup>21-24</sup>

In this context, supramolecular self-assembly has gained immense attention, which was focused on fabrication of complex functional biomolecular structures.<sup>25-28</sup> Structural and functional mimic of native tissue is the key component for designing the next-generation biomaterial that may solve the problems associated with healthcare. Hence, the emerging paradigm relies on designing an array of well-defined nanostructures with diverse functionality and biocompatibility that can be achieved via the self-assembly of peptides.<sup>29</sup> This strategy has been widely explored for biomedical applications in recent years.<sup>30-33</sup> Self-assembling peptide amphiphiles were further designed for hydrogelation using specific triggers that include both environmental trigger as well as locally applied stimuli in particular, pH, temperature, salt, enzyme etc., which

eventually give rise to hierarchical organization leading to supramolecular hydrogels.<sup>34</sup> <sup>35</sup> In this direction, metal-ligand interactions are emerging as a new design paradigm in supramolecular chemistry leading to the fabrication of supramolecular nanostructures with variable nanoscale structures and functions.<sup>36</sup> Literature reports indicated that several biophysical and biochemical phenomena are regulated by specific ion and protein interactions.<sup>37</sup> Metal ions can interact with protein and peptides primarily through electrostatic interactions, which may alter the structures and functions of the macromolecules.<sup>38-40</sup> In particular, metal cations are known to interact with the amide (CONH) backbone, functional side chain, or carboxylic acid group of protein/peptide and thus can alter their folding and aggregation pattern in the solution phase.<sup>41</sup> Hence, it can be envisioned that the peptide sequences with a side chain functionality that primarily comprising of a carboxylic acid moiety may show the propensity to self-assemble in the presence of divalent or trivalent metal ions.

Furthermore, several short peptides have also been reported based on the natural metalloptides, which can interact with metal ions through their surface functionality. In this context, Wei Ji et al. reported a structural transformation of the amyloid-like dipeptide in the presence of a series of metal ions.<sup>42</sup> This classical work demonstrated the inhibition of the disease-associated amyloid-like  $\beta$ -sheet aggregation and controlled structural transformation of these aggregates into a super helix,  $\beta$ -sheets, and random coils in the presence of monovalent ( $\text{Na}^+/\text{K}^+$ ), divalent ( $\text{Zn}^{2+}/\text{Cu}^{2+}$ ), and trivalent ( $\text{Fe}^{3+}/\text{Al}^{3+}$ ) ions, respectively.<sup>42</sup> Another study by Sharma et al. demonstrated a unique strategy for the controlled self-assembly pathway to create supramolecular hydrogel from a single dipeptide gelator by modulating the specific anions and transition metal salts.<sup>39</sup> Furthermore, Adams and co-workers demonstrated the structural transition from worm-like micellar structure of a functional dipeptide molecule upon adding calcium salt, which triggered the phase transition from sol to gel-like material and led to the formation of nanofibrillar network.<sup>43,44</sup> This important study further reinforced the fact that the introduction of metal ions can also drastically enhance the mechanical strength and thermal stability of the amphiphilic peptide hydrogel.<sup>45</sup> A recent report by A. Fortunato et al. demonstrated the metal ion triggered hydrogelation of pyrene peptide conjugate. This study reported the use of multivalent cations to demonstrate metal-ligand interactions between metal ion and glutamic acid side chain, which further displayed variation in mechanical and morphological property of the hydrogels.<sup>46</sup>

Additionally, another report by Parmar et al. explored the metal-binding site of the collagen triple helix to stabilize the CMP molecule. Both homo and heterotrimeric structures were stabilized by the addition of zinc (II) and other metal ions.<sup>47</sup> Another report demonstrated the metal ion-assisted assembly of micro-collagen, where in combination with metal ion, heterotrimeric triple helix structure of collagen mimetic peptide can be stabilized.<sup>48</sup>

In this context, it is worth mentioning that collagen is the most abundant structural and functional protein of the extracellular matrix that plays a crucial role in regulating functional processes, like, cell adhesion, cell to cell communication, and differentiation.<sup>49</sup> Natural collagen's exceptional self-assembling capabilities and biodegradability have put up the appeal to consider it as a preferred material for fabricating the next-generation scaffold targeted for biomedical applications, such as tissue engineering, drug delivery etc.<sup>50</sup> To this end, it was increasingly recognized that a useful approach can be adapted to identify and design a small molecular domain from the native protein, which can attain the similar complex architecture and bio-functional properties of the native collagen.<sup>51</sup> In order to fabricate an ideal mimic of natural collagen protein, extensive attempts have been devoted towards designing the specific motifs inspired from this natural protein.<sup>52-54</sup> To this direction, we have explored the hydrogelation of a negatively charged collagen inspired peptide at physiological pH in the presence of biologically relevant metal ions ( $\text{Ca}^{2+}/\text{Mg}^{2+}$ ) to construct a biomaterial suitable for biomedical applications. It has been interesting to note that the designed short pentapeptide sequence (2-Naphthoxy acetic acid-Phe-Phe-Gly-Asp-Hyp) has demonstrated its ability to self-assemble at pH 5.0 but failed to self-assemble into higher order fiber like structure at physiological pH and hence it remained as solution. Surprisingly, the overall negative surface charge due to the exposed carboxyl group of aspartate moiety offers the researcher an additional advantage to explore it as an ideal candidate for inducing hydrogelation in the presence of metal ions at physiological conditions. It is expected that the metal ions will interact electrostatically with the oxygen atom of the carboxylate functionality and therefore will mask the negative charge on the surface of the nanofiber, which will lead to the reduction in repulsive force between the negatively charged carboxylate ion. In nature, especially four metal cations; Sodium ( $\text{Na}^+$ ), Potassium ( $\text{K}^+$ ), Calcium ( $\text{Ca}^{2+}$ ), and Magnesium ( $\text{Mg}^{2+}$ ), are preferentially bound to oxygen molecules electrostatically and play a crucial role in

triggering cellular responses.<sup>55</sup> Alkali metal ions i.e., Na<sup>+</sup> and K<sup>+</sup> demonstrated various ionic radii and hydration energy that hardly form complexes.<sup>56</sup> Whereas, Ca<sup>2+</sup> and Mg<sup>2+</sup> ions have gained reasonable interest due to their relative importance in cellular growth and their multiplication, as they impart crucial impact on the macromolecular synthesis and metabolic parameters in the cultured cells.<sup>57</sup> Interestingly, the negatively charged collagen inspired self-assembling peptide, which remained in sol form at physiological pH, demonstrated a shift in its equilibrium point of hydrogelation in the presence of divalent metal ions (Ca<sup>2+</sup>/Mg<sup>2+</sup>) at physiological pH. We observed an instant conversion of sol to gel in the presence of the metal ions. Furthermore, a significant enhancement in the mechanical strength of the metal coordinated hydrogels was achieved over control peptide hydrogels at pH 5.0, which was otherwise a non-gelator at physiological pH. FTIR studies further confirmed the metal binding capacity of the peptide, and AFM studies confirmed metal complexation between the short peptide fibers leading to a dense nanofibrous matrix. Thus, with the addition of divalent metal salts to the NapFFGDO peptide, a threefold advantage has been achieved at the molecular domain that includes: 1) successful gelation at physiological pH as well as 2) lowering of the minimum gelation concentration, and thus facilitating the self-assembly of the peptide monomers and 3) an improvement in the physical properties was achieved like mechanical strength etc. More importantly, the metal coordinated peptide hydrogels were found to overcome the limitations of the negatively charged peptides and promoted biocompatibility and cellular proliferation at physiological pH. This study emphasizes the importance of incorporating metal ions as a simplistic approach for fine-tuning of the structural and functional properties of the synthetic matrix. Such an approach for developing biomimetic scaffolds via metal coordination overcomes the limitations of individual peptide and unveil the new opportunities for developing an advanced biomaterial for biomedical applications.

## **4.2 Result and discussion**

**4.2.1 Design and gelation of collagen inspired self-assembling peptide.** In this work, our focus was to explore the biologically relevant metal ions towards controlling the self-assembling behaviour of a biologically inspired peptide in order to develop a simplistic and facile methodology. As indicated, upon coordination with metal ions, peptides can instigate conformational changes in their self-assembly, which may lead to diverse nanoscale structure leading to variable manifestation of the functional

properties of the peptides.<sup>58</sup> Furthermore, the role of negatively charged peptide moieties has already been discussed in terms of its coordination ability with the metal ions, like,  $\text{Na}^+$ ,  $\text{K}^+$ ,  $\text{Ca}^{2+}$ , and  $\text{Mg}^{2+}$  in the biological system.<sup>59</sup> Herein we attempted to induce differential self-assembly within a negatively charged collagen inspired self-assembling peptide (NapFFGDO) in the presence of metal ions at physiological pH (Figure 4.1).

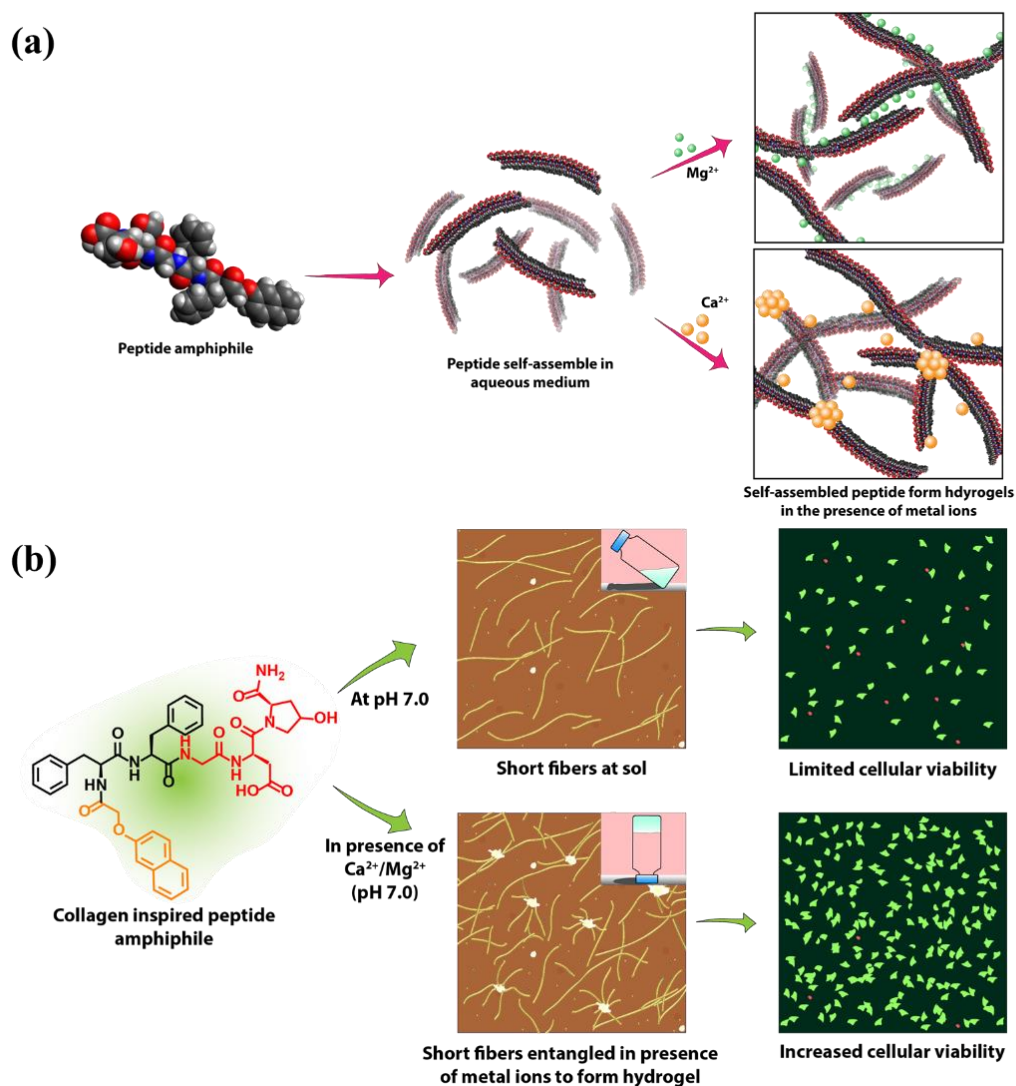


**Figure 4.1** (a) Schematic representation of hydrogelation induced in collagen inspired self-assembling peptide in the presence of metal ions at physiological pH, (b) Metal complexation induces hydrogelation in the peptide nanofibers, which further leads to enhancement in cell viability and proliferation.

Our earlier study on NapFFGDO revealed that the designer sequence failed to form a self-supporting hydrogel at physiological pH owing to the charge repulsion imparted

by the negatively charged aspartic acid residue on the peptide surface, which restricted the peptide monomers to assemble into hydrogel. However, the peptide was found to induce gelation at 30 mM concentration only when the pH was lowered to pH 5, owing to the protonation of carboxylic acid residues of aspartic acids. In this way, it overcomes the repulsive force and established stable intermolecular association.<sup>60</sup> However, the gelation at acidic pH restricts its applications in healthcare. It would be interesting to mask the negative charge at the physiological pH together with enhancement in intermolecular association, which may be induced by cross-linking with biologically relevant metal ions. As these gels were fabricated to further apply in solving the problem of biological issues, the salts were taken in accordance to the ionic supplements of the biological medium that supports cellular growth.<sup>61</sup>

**Table 4.1** Optical images of peptide hydrogels formed in presence of metal ions, Ca<sup>2+</sup> and Mg<sup>2+</sup>.

Peptide	Salts	Optical images (sol/gel)
NapFFGDO (15mM, pH 7.0)	NA	
NapFFGDO (15mM, pH 7.0)	5 mM CaCl <sub>2</sub> .2H <sub>2</sub> O	
NapFFGDO (15mM, pH 7.0)	10 mM CaCl <sub>2</sub> .2H <sub>2</sub> O	
NapFFGDO (15mM, pH 7.0)	5 mM MgSO <sub>4</sub> .7H <sub>2</sub> O	
NapFFGDO (15mM, pH 7.0)	10 mM MgSO <sub>4</sub> .7H <sub>2</sub> O	

Hence, we specifically aim to induce a stable self-association of this collagen inspired self-assembling peptide monomers outweighing the repulsive force between the peptide

chains to fabricate a stable hydrogel at physiological pH, which may find significant potential in promoting cellular adhesion and proliferation.

In particular, 15mM of the NapFFGDO was dissolved at a higher pH (12.0) by adding 1N NaOH. Then pH of the medium was slowly lowered down to physiological pH via the addition of 1N HCl. The resulting solution of NapFFGDO remained sol after 24-hour incubation (Table 4.1). As revealed by the AFM study, the peptide sol contains the mixture of short and long fibers (Figure 4.2a), which upon further incubation grow longer but were unable to induce higher order entanglement to form hydrogel due to the charge repulsion between the ionized group of aspartic acid exposed at the surface at physiological pH. We were keen to explore metal ion coordination at this phase since short peptides were known to interact with divalent metal ions ( $\text{Ca}^{2+}/\text{Mg}^{2+}$ ) through the carboxyl group of aspartate molecules purely via electrostatic interaction.<sup>62</sup> A metal ion bonded or coordinated to a ligand or surrounding molecules may form a coordination complex.<sup>56</sup> In particular, calcium and magnesium ions were employed, which show high coordination.<sup>56</sup> In general, magnesium show 6 (octahedral coordination) while calcium can attain a variety of coordination, i.e. 7 to 9.<sup>56</sup> Calcium and magnesium prefer coordination with the carboxylate oxygen of aspartate and glutamate, showing the major site of interaction in the protein molecule.<sup>63</sup>

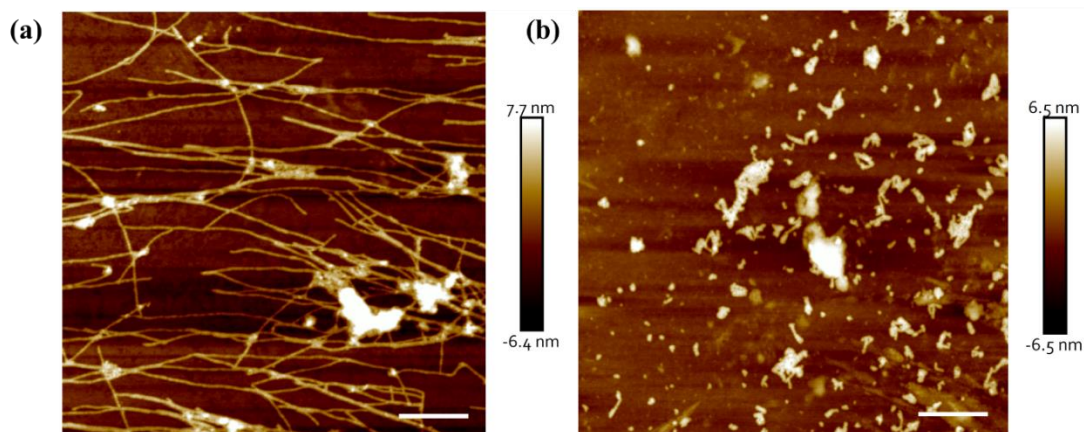


**Figure 4.2** Morphological analysis of (a) NapFFGDO (15mM) solution at physiological pH 7.0 via atomic force microscopy and (b) Morphological variation in peptide fiber after instant addition of metal salts (without incubation). Scale bar 500nm

Calcium ion being larger can attain octahedral configuration via interacting with ligands in a bidentate manner, whereas magnesium ion can only interact with the carboxylate group in a monodentate fashion.<sup>56</sup> It has been reported that calcium and magnesium

ions can bind on an average to four carboxylic oxygen, however, calcium ions, can accommodate the entry of one more carbonyl group to the coordination sphere.<sup>64</sup> Literature reports revealed that calcium ion shows more tendency for binding with carbonyl or carboxyl groups in its available space, while magnesium ion displays preferred affinity for water molecules. This has been evident in the dense and opaque hydrogel network of metal ion coordinated peptide hydrogel. Most importantly, the peptide molecules showed stable hydrogelation in the presence of metal salts at much lower concentration, which is half of the concentration that has been reported earlier for the same peptide at pH 5. The metal complexation displayed an MGC value of 15 mM, which was reported as 30 mM for the peptide alone.<sup>60</sup> As monovalent or divalent metal cations are generally known to bind the carbonyl group of the amide group (CONH), which further interferes with hydrogen bonding interaction in the solution phase.<sup>8</sup> This interference leads to aggregation of the peptide nanofibers due to the stronger interaction among nucleation phase of peptide nanostructures (Figure 4.2b). The divalent metal ions interact to short nucleating centers of the peptide nanostructures and turns the solution in aggregates. To avoid this aggregation, the metal salts were added to the aged sol of peptide-containing short fiber, which upon interaction resulted in the hydrogel.<sup>65</sup>

#### 4.2.2 Spectroscopic Characterization

Various spectroscopic studies were performed to get an insight into the major non-covalent interactions driving the self-assembled peptide structures. CD spectroscopy was utilized to analyze the secondary structure of the peptide amphiphiles in the self-assembled state. CD spectra of negatively charged peptide showed the characteristic peak at ~240nm corresponding to the  $\pi$ - $\pi^*$  transition due to the aromatic phenyl alanine moieties indicative of the presence of  $\beta$  sheet-like structures. It has been observed that upon binding with the metal ions, there has been a moderate shift in the position of the signal (Figure 4.3a). A small peak was predominantly present in all the hydrogels at 295 nm corresponding to the  $n$ - $\pi^*$  transition of naphthoxy aromatic group.<sup>66</sup> It was evident that the peptide fiber at physiological pH self-assemble via non-covalent interactions, which remains stable after coordinating with the metal ions and hence showed a similar CD pattern. In order to get a better understanding of the secondary structures, FTIR spectroscopy was employed to determine the intermolecular H-bond interactions between the peptide backbone. A strong transmittance peak at ~1630  $\text{cm}^{-1}$

in the amide I region is indicative of possible  $\beta$ -sheet like structures, and a weaker peak around  $\sim 1670\text{ cm}^{-1}$  generally signifies the antiparallel arrangement of these  $\beta$ -sheets.<sup>66</sup>

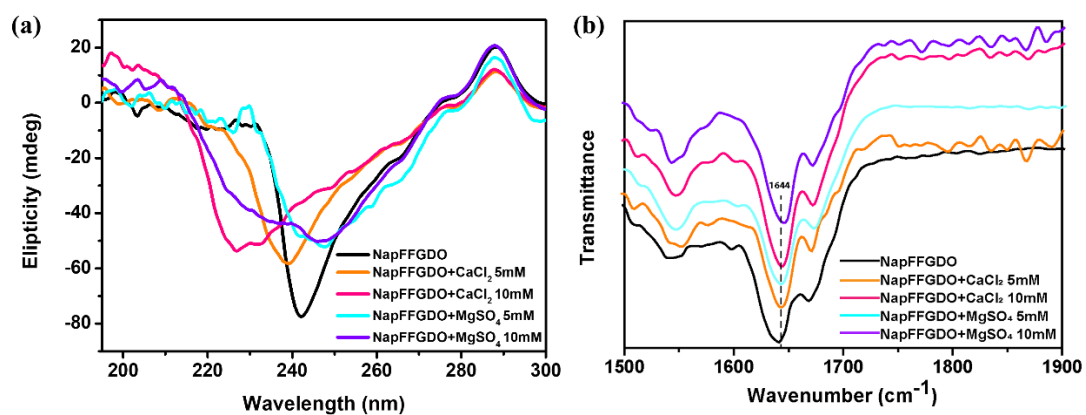


**Figure 4.3** Spectroscopic characterization of metal ion complexed collagen inspired self-assembling peptide hydrogel. (a) CD spectra of peptide and metal ion complexed peptide at physiological pH, representing the  $\beta$  sheet-like structure. (b) FTIR spectra show the presence of  $\beta$ -sheet-like structure in metal ion complexed peptide hydrogels.

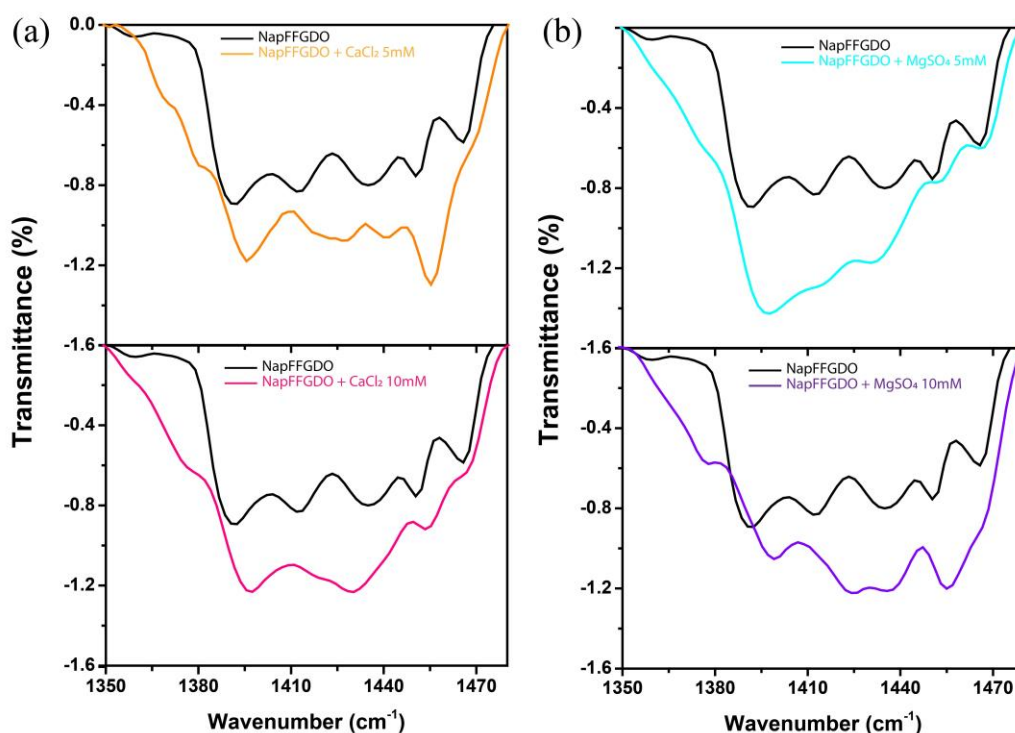


**Figure 4.4** FTIR spectra after area normalization in the region of  $1350\text{-}1480\text{ cm}^{-1}$ , showing the variation in term of intensity upon interaction with the metal ion complexation (a) 5 mM and 10 mM of  $\text{CaCl}_2$  and (b) 5 mM and 10 mM of  $\text{MgSO}_4$ .

All the samples showed an intense peak of carbonyl stretching at  $1640\text{ cm}^{-1}$ , suggesting the presence of  $\beta$  sheet-like structures (Figure 4.3b). In addition, the frequency region of  $1390\text{-}1480\text{ cm}^{-1}$  were simply area normalized, and the peptide hydrogel showed the spectral change (in terms of intensity) due to the presence of divalent cations (Figure 4.4).<sup>41</sup> Specifically, the amide-II region at  $1540\text{ cm}^{-1}$  and the broad band at  $1440\text{ cm}^{-1}$  showed an enhancement in their intensities upon coordination with the metal ions, which can be correlated with the report by Zhao et.al.<sup>41</sup> The study clearly indicated the fact that C-N stretching and N-H bending (in-plane) are primarily evident in the amide-II region, and relatively broadened and an enhancement in the intensity around  $1440\text{ cm}^{-1}$  in the peptide hydrogels were observed, which suggested the presence of metal-ion complexation. As the spectra were normalized in the region  $1350\text{-}1480\text{ cm}^{-1}$ , the difference spectra showed a spectral shift in the presence of divalent metal ions from  $1390\text{ cm}^{-1}$  to  $1397\text{ cm}^{-1}$ . Both CD and FTIR showed clear evidence for the presence of  $\beta$ -sheet-like structures in the nanoscale regime. To further confirm the presence of the  $\beta$ -sheet-like secondary structure, Thioflavin T binding assay was performed.<sup>67</sup> ThT recognizes and binds to the beta rich peptide structures, which commonly adopts the “cross- $\beta$ ” structures, an extended  $\beta$ -conformation running perpendicular to the long axis leading to the multiple  $\beta$ -sheets.<sup>68</sup> The ThT binds to these cross-strand ladder consists of repeating side chain interactions across the  $\beta$ -sheet layers.

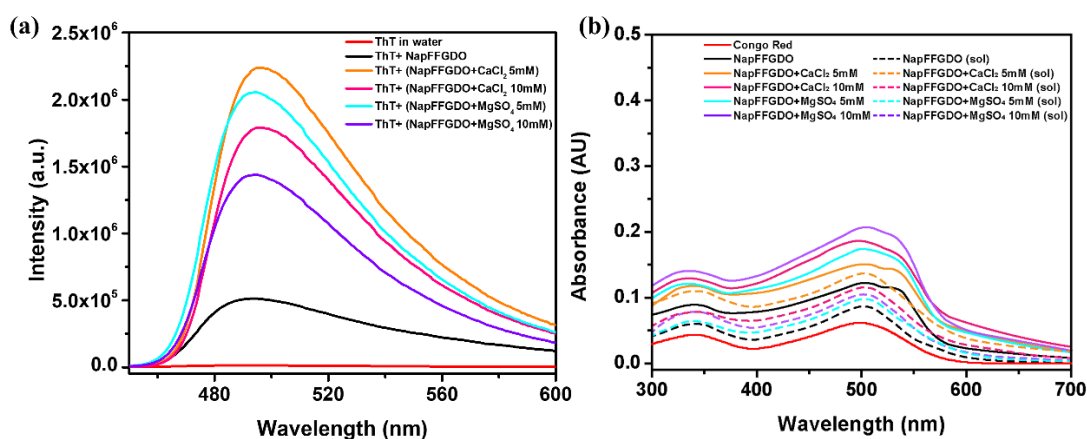


**Figure 4.5** (a) An increment in the fluorescence intensity of the Thioflavin T upon binding to the hydrophobic patches of the peptide hydrogels depicts the presence of  $\beta$ -sheet-like structure. (b) Redshift in Congo red absorption maximum upon binding the hydrophobic patches of the peptide hydrogel confirms the presence of  $\beta$  sheet-like structure.

However, ThT interaction is specific to the structural motif in the fibrils, which is basically the hydrophobic patches of the  $\beta$ -sheet structures and it has an affinity towards it.<sup>69</sup> Increased fluorescence intensity at 488 nm was observed when the ThT solution was allowed to incubate with the nanofibrillar network of the peptide followed by its excitation at 440 nm (Figure 4.5a).

Interestingly, NapFFGDO alone showed a moderate enhancement in the fluorescence intensity and, upon coordinating with the metal ions, showed significant enhancement in the intensity, suggesting the formation of a more ordered structure. Hence an increase in the hydrophobic patches was evident in the metal coordinated hydrogels. Fluorescence microscopy was performed to further confirm the spectroscopic results of ThT binding. The peptide hydrogel incubated with ThT solution showed the binding of the dye to the hydrophobic patches with enhanced fluorescence emission under a microscope (Figure 4.6).

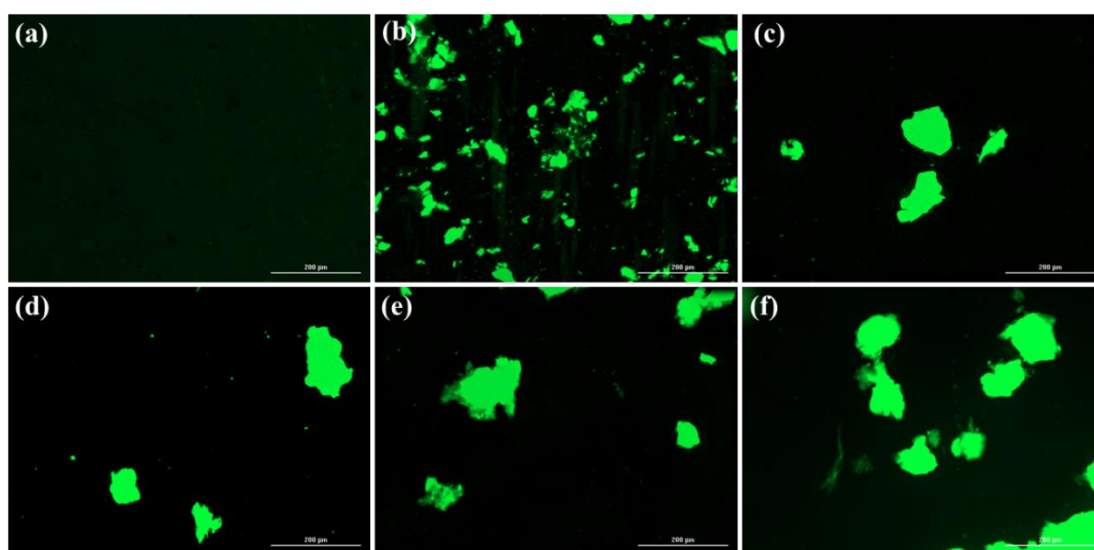


**Figure 4.6** Fluorescence microscopic images of Thioflavin T binding to the hydrophobic patches of peptide fibers, corresponds to the  $\beta$ -sheet like structure: (a) Blank ThT, (b) NapFFGDO, (c) NapFFGDO+CaCl<sub>2</sub> (5mM), (d) NapFFGDO+CaCl<sub>2</sub> (10mM), (e) NapFFGDO+MgSO<sub>4</sub> (5mM), and (f) NapFFGDO+MgSO<sub>4</sub> (10mM). Scale bar 200 $\mu$ m

The presence of  $\beta$ -sheet-like structures was further confirmed via Congo red binding assay, a classical approach to assess the formation of amyloid-like aggregated structures.<sup>70</sup> Literature reports have indicated that amyloid peptide form twisted  $\beta$ -sheet-like structures. It was evident that CR dye shows a shift in its absorption

maximum upon binding with the amyloid-like structures.<sup>67</sup> The CR dye shows its intrinsic absorption at 498 nm, which on binding with the amyloid-like structures, shows a shift in the absorption maxima to 520-540 nm.<sup>67</sup> In this direction, all the hydrogel samples showed redshifts in the absorption maxima of the CR dye from 500 nm to 530-540 nm, which further indicated the formation of  $\beta$ -sheet structures, leading to the amyloid-like fibrils (Figure 4.5b). Furthermore, earlier literature has demonstrated that the interactions among the aromatic moieties of the peptides also play a crucial role in the formation of peptide self-assembled structure.<sup>71</sup> Aromatic groups trigger the self-assembly via  $\pi$ - $\pi$  stacking interaction, which can be differentiated based on their intrinsic fluorescence emission of the fluorophore spectra in monomeric and gel state. The naphthoxyl group has an intrinsic fluorescence, which upon excitation at 270 nm gives rise to monomeric emission at 340 nm. Our results have indicated that the intensity of the monomeric emission of the peptide building blocks at physiological pH showed extensive quenching up on coordination with the metal ions, leading to the transition to the gel state.

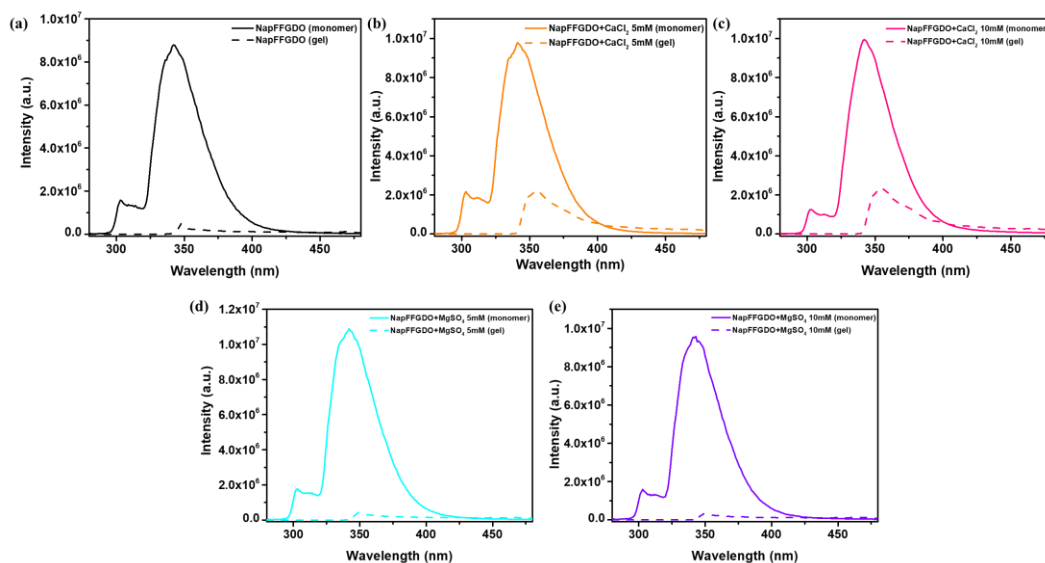


**Figure 4.7** Fluorescence emission spectra of peptide amphiphiles in sol state showed the monomeric emission of naphthoxy group at 340nm, which showed extensive quenching in gel state upon self-assembly of the peptides.

Such extensive quenching of the emission intensity may be attributed to the reduced availability of the naphthoxyl monomer, which may remain buried in the hydrophobic core of the self-assembled nanostructures. Such phenomenon is originated from the

interactions of the naphthoxyl group with the other aromatic moiety via  $\pi$ - $\pi$  interaction in the self-assembled structure in the respective gel state (Figure 4.7).

**4.2.3 Morphological analysis.** It was crucial to understand the morphological changes that occurred in the metal ion coordinated system, as differential topological interactions were expected to induce gelation in the collagen inspired self-assembling peptide at physiological pH. We envisioned that the nucleation and growth of the self-assembled structure may follow a different pathway in the presence of metal ions. Atomic force microscopy (AFM) was used to understand the structural variation in the collagen inspired self-assembling peptide fibers in the presence of divalent metal ions ( $\text{Ca}^{2+}/\text{Mg}^{2+}$ ). As reported in our earlier study, negatively charged collagen inspired self-assembling peptide (NapFFGDO) showed long nanofibers at acidic pH, i.e. pH 5.0 with fiber dimension 25-30nm.<sup>60</sup>

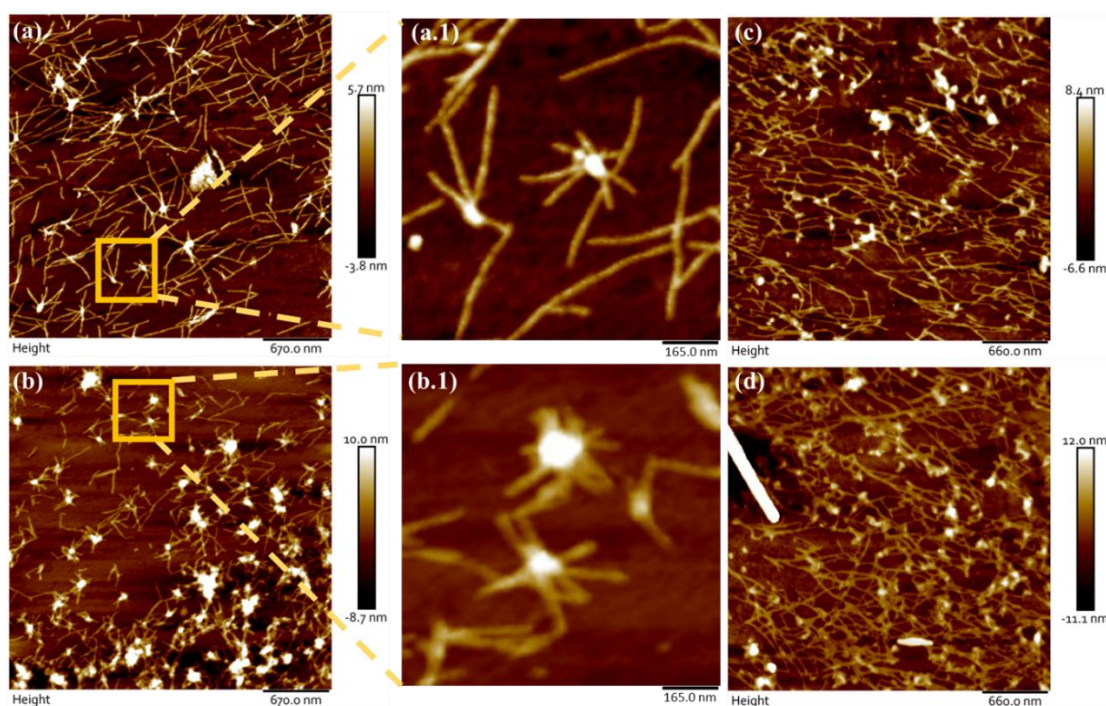


**Figure 4.8** Morphological evaluation of metal ion complexed peptide hydrogel through Atomic Force Microscopy (AFM). (a) NapFFGDO with 5 mM  $\text{Ca}^{2+}$  ion and its sectional analysis view of metal complexation in (a.1), (b) NapFFGDO with 10 mM  $\text{Ca}^{2+}$  ion and its sectional analysis view of metal complexation in (b.1). (c) Self-assembled nanofibrillar structure of NapFFGDO with 5 mM  $\text{Mg}^{2+}$  ion, and (d) Self-assembled nanofibrillar structure of NapFFGDO with 10 mM  $\text{Mg}^{2+}$  ion.

When divalent metal salts ( $\text{Ca}^{2+}/\text{Mg}^{2+}$ ) were added into these aged negatively charged peptide nanofibers, gelation was induced, and a change in the morphology of the peptide nanoarchitecture was observed. Calcium ion with bigger radii usually formed a centric core to which the short fibers were attached, which was also evident in the AFM images (Figure 4.8a & b). Peptide hydrogels with calcium salts of concentrations 5mM and 10mM, respectively showed similar kinds of peptide nanoscale structures. It was observed that the fibers were nucleated from the calcium ion core through electrostatic attraction leading to the binding of the peptide nanostructure through ionic cross-linking, and thus creating highly ordered structures as probed in the sectional analysis of AFM studies (Figure 4.8a.1 & b.1). However, electrostatic interactions among peptides and magnesium ions lead to the formation of cross-linked fibers at both the concentrations of 5mM and 10mM, respectively (Figure 4.8c & d). It has been evident in recent years that the cooperative association of kinetic and thermodynamic variables governs the stable multi-scale self-assembly of the peptide. Thermodynamic variables include molecular design, while kinetic variables rely on parameters like concentration, ionic strength, pH, temperature as the triggers for the self-assembly.<sup>72</sup>

It was clearly evident from the spectroscopic studies that the nanofiber formation of the collagen inspired self-assembling peptide at physiological pH are mainly driven by the non-covalent interactions, like  $\pi$ - $\pi$  interaction, hydrophobic interaction, and H-bond that stabilize the nanoscale structure. The nucleation and growth mechanism of the supramolecular nanofibril formation can demonstrate the dynamics of the hydrogelation of collagen inspired self-assembling peptide in the presence of divalent metal ions ( $\text{Ca}^{2+}/\text{Mg}^{2+}$ ).<sup>73</sup>

To this direction, we have performed time-dependent morphological analysis through AFM at different time points i.e., 5 minutes, 30 minutes, 1 hour, 12 hours, and 24 hours. AFM analysis revealed the nucleation and growth mechanism of NapFFGDO at physiological pH at different time points of the self-assembly process in the presence of metal ions (Figure 4.9 a-e). The short fiber-like structure was observed just after 30 minutes, which further nucleated and formed mesh of short and long fibers in 24 hours. The metal salts were added to the peptide sol after incubating them for 6 hours to ensure the aged sample must have short fibers that can further interact through the cooperative effect of metal salts. Calcium ion coordinated hydrogelation showed short fiber

interacting with the metal ion and resulted in the interlinked network-like structure, which grows over time (Figure 4.9 f-j).

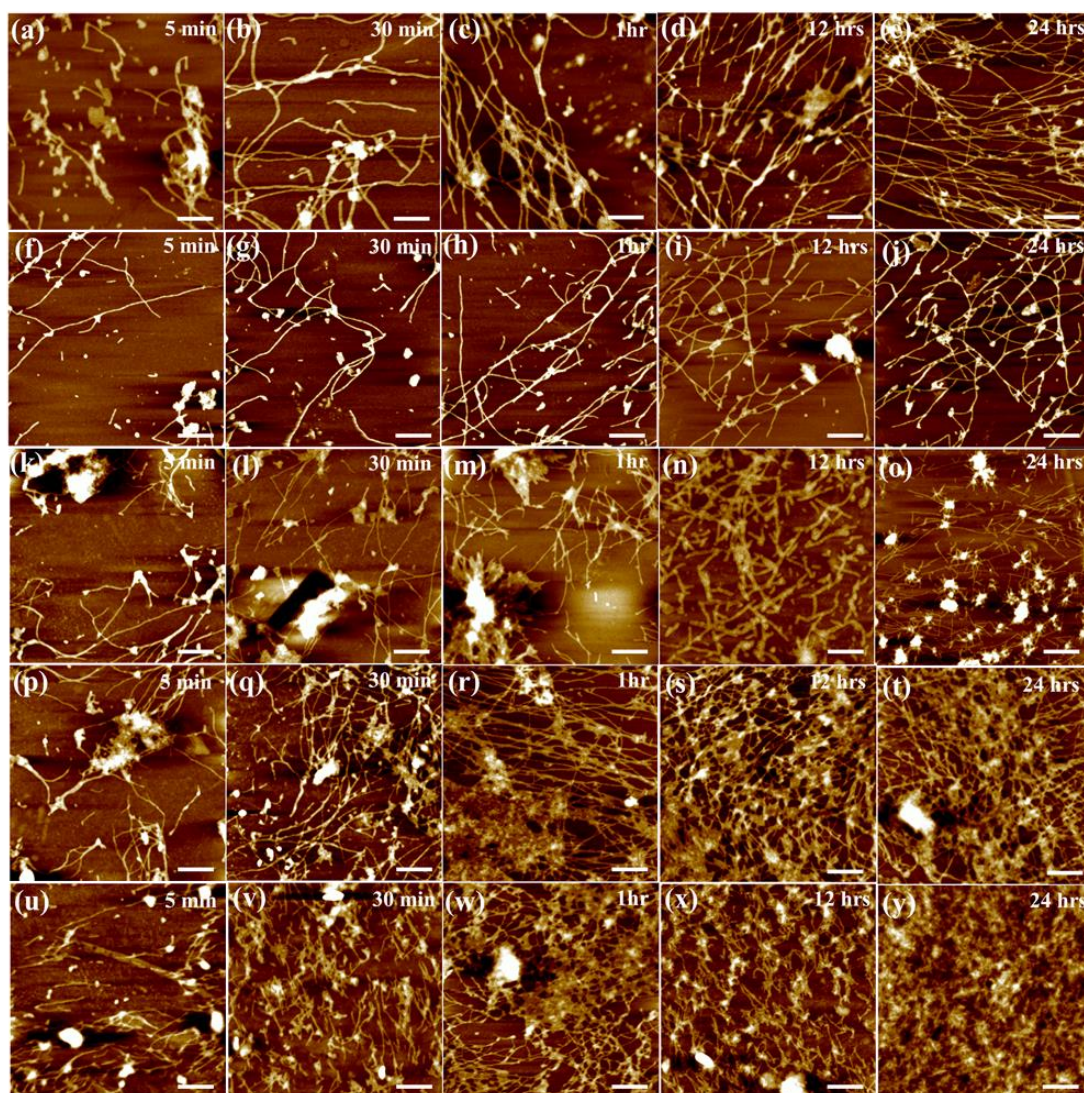


**Figure 4.9** Morphological analysis of nucleation and growth of the self-assembled nanostructures of NapFFGDO and metal coordinated NapFFGDO hydrogels at different time points; (a-e) NapFFGDO, (f-j) NapFFGDO+CaCl<sub>2</sub> (5mM), (k-o) NapFFGDO+CaCl<sub>2</sub> (10mM), (p-t) NapFFGDO+MgSO<sub>4</sub> (5mM), and (u-y) NapFFGDO+MgSO<sub>4</sub> (10mM). Scale bar 500nm.

It is interesting to note that the hydrogel samples with calcium salt concentration (i.e., 10 mM) showed a similar pattern but with a dense network showing the presence of more calcium sites where fibers can be seen nucleating from the central core of metal ions and remained bound to the ions (Figure 4.9 k-o). Hydrogelation induced in the presence of magnesium ion at concentration of 5mM (Figure 4.9 p-t) and 10mM (Figure

4.9 u-y) demonstrated growth of nanofibers via cross-linking between metal coordinated fibers. However, enhanced fiber density over time resulted in the formation of a dense peptide network.

**4.2.4 Mechanical strength assessment.** Over the years, it has been established that the physical properties of these synthetic scaffolds have a great impact on controlling cellular fate and behaviour.<sup>74</sup> In order to determine the mechanical stiffness of the proposed metal coordinated peptide hydrogel, amplitude and frequency sweep was carried out. Dynamic frequency sweep was carried out to calculate storage ( $G'$ ) and loss ( $G''$ ) modulus of the material depicting elastic and viscous components of the hydrogels. In this study, all the hydrogel samples showed higher value of storage modulus as compared to that of the loss modulus, indicating the solid (gel) like behaviour of the material.<sup>75</sup> The previously reported negatively charged peptide (NapFFGDO) at higher concentration, i.e., 30mM (MGC of the peptide alone at pH 5.0), has been included as a reference point to show the improvement in the mechanical strength of the material after coordination with divalent metal ions, which triggered the gelation at physiological pH.<sup>76</sup>

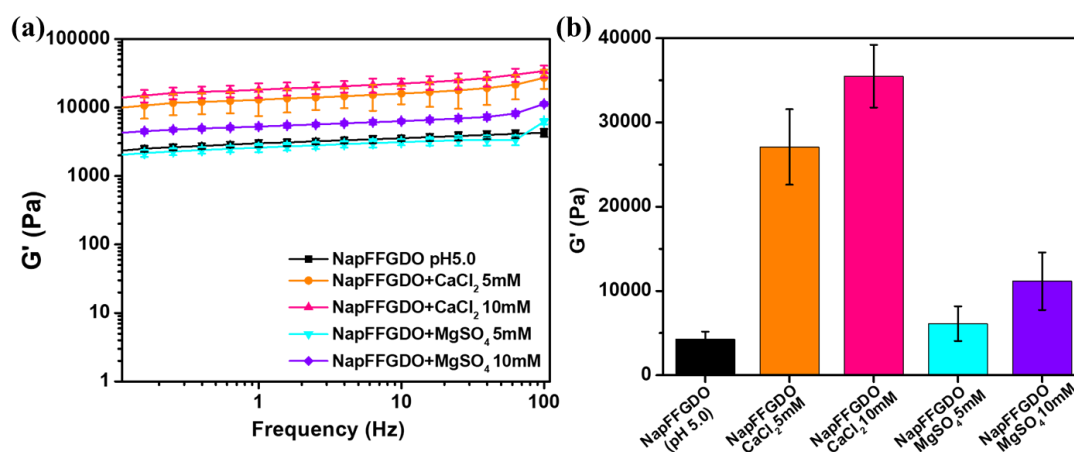


**Figure 4.10** Comparative analyses of the mechanical strength of the collagen inspired self-assembling peptide NapFFGDO (30mM) at pH 5.0 and metal ion complexed peptide hydrogels at pH 7.0. (a) Storage moduli ( $G'$ ) of peptide hydrogels show improvement in mechanical strength variation after metal complexation. (b) Bar graph representing the increment in the mechanical strength of the metal ion complexed hydrogels.

However, the peptide at 15mM concentration remained as a solution and hence cannot be included for a comparative assessment. As described earlier, peptide hydrogel formed at 30mM concentration at pH 5.0 showed a storage modulus of around 3-4 kPa.<sup>60</sup> Importantly, the metal coordinated peptide hydrogels, which triggered gelation at physiological pH, showed significant enhancement in the mechanical strength even at a much lower concentration i.e., 15mM concentration (at pH 7.0). Interestingly, the addition of  $\text{Ca}^{2+}$  ion to the solution showed a remarkable improvement in the mechanical strength of NapFFGDO. The respective values of storage modulus were found to be 25-28 kPa and 33-35 kPa in the presence of 5mM and 10mM of calcium salt, respectively, while the gelator concentration was only 15mM. As expected, a similar effect was observed in the presence of  $\text{Mg}^{2+}$  ion; however, the increase in mechanical strength was moderate, the value has been increased up to a of 5-6 kPa and 8-10 kPa in the presence of 5mM and 10mM of magnesium salt respectively (Figure 4.10a). Calcium ( $\text{Ca}^{2+}$ ) and Magnesium ( $\text{Mg}^{2+}$ ) ions were mainly coordinated with oxygen atoms of carboxylate ion of aspartic acid, and the interactions were purely electrostatic. Calcium ion prefers higher coordination than that of magnesium ion, and calcium ion is more likely to interact with carboxylate ion in a bidentate manner, whereas magnesium ion always interacts in a monodentate way.<sup>56</sup> Since the calcium ion is larger, it tends to attain octahedral configuration of bidentate coordination of calcium ion with the carboxyl group of aspartic acid resulting in hydrogelation with higher strength. On the other hand, magnesium ions interact with the carboxyl group in a monodentate way, can only entangle the fibers and enhance the mechanical strength to a moderate extent, as shown in the rheological analysis (Figure 4.10b). As shown in the AFM studies, the apparent presence of entangled fiber in magnesium ion coordinated peptide fibers, leads to hydrogelation with a reasonable enhancement in gel strength, while the presence of a centric core of a network of calcium ions attached to the maximum number of peptide fibers leads to the formation of stronger hydrogels.

*4.2.4.1. Evaluation of thixotropic behaviour.* Furthermore, thixotropic hydrogels have gained immense attention in the past few years owing to their possible formulation as injectable gels that may offer several applications in diverse areas of biomedicine.<sup>77</sup> Since the peptide hydrogels are evolving through dynamic non-covalent interactions, like hydrogen bonding, ionic bonding, and metal coordination, these interactions make them self-healing materials.<sup>78</sup> A recent study by the Yi Cao group demonstrated the

improvement in Young's modulus, break strength, and break strain of the peptide-metal ion coordinated hydrogels compared to the single ligand-metal ion bonds.<sup>79</sup> Non-covalent cross-linker with increased coordination site showed improved toughness and stretchability of the material.<sup>80</sup>

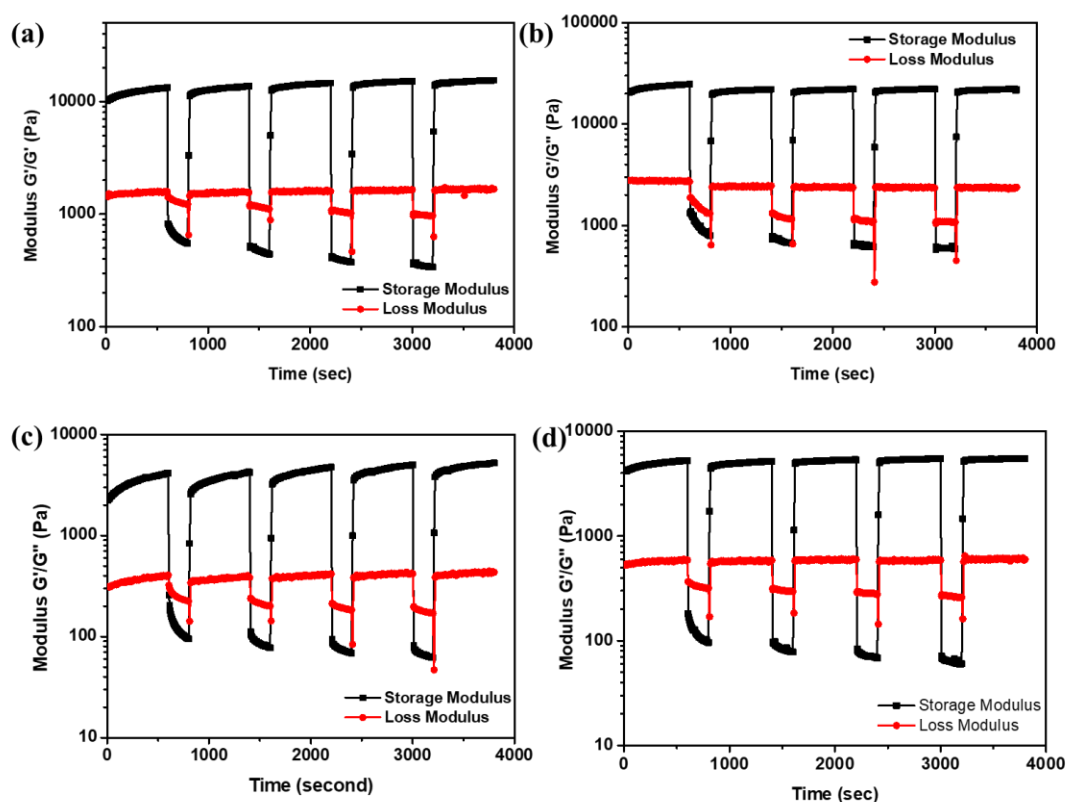


**Figure 4.11** Rheological analysis revealed the thixotropic nature of the metal coordinated peptide hydrogels: (a) NapFFGDO+CaCl<sub>2</sub> (5mM), (b) NapFFGDO+CaCl<sub>2</sub> (10mM), (c) NapFFGDO+MgSO<sub>4</sub> (5mM), and (d) NapFFGDO+MgSO<sub>4</sub> (10mM).

In order to assess the thixotropic behaviour of the metal coordinated peptide hydrogels, a step strain measurement was performed by oscillatory rheology. Interestingly, all four metal coordinated peptide hydrogels demonstrated thixotropic property (Figure 4.11) because a rapid recovery was observed after removing 100% strain without losing the mechanical integrity. Almost 100% recovery was observed in all the hydrogels irrespective of metal ions and their relative concentrations, suggesting the mechanoresponsive behaviour of the metal coordinated hydrogels. These results suggested that the hydrogels obtained from metal coordinated collagen inspired self-assembling peptide have the optimal physical property to serve as an injectable matrix.

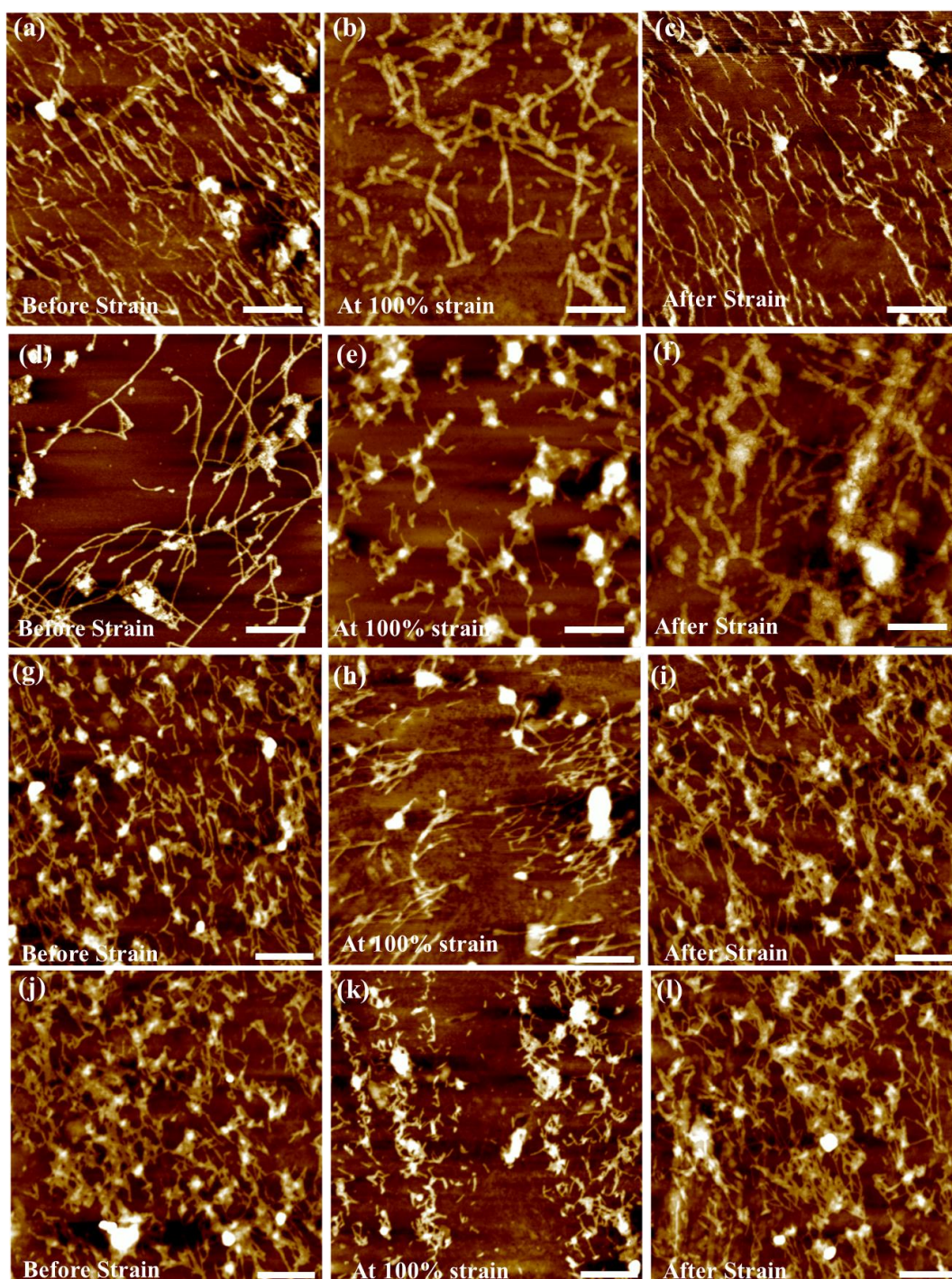


**Figure 4.12** AFM analysis of metal coordinated peptide hydrogels at different point of thixotropic study: before strain, 100% strain, and after recovery (a-c) NapFFGDO+CaCl<sub>2</sub> (5mM), (d-f) NapFFGDO+CaCl<sub>2</sub> (10mM), (g-i) NapFFGDO+MgSO<sub>4</sub> (5mM), and (j-l) NapFFGDO+MgSO<sub>4</sub> (10mM). Scale bar 500nm

Furthermore, to understand the variation in the nanoarchitecture that occurred in the peptide hydrogels during the step strain cycle, AFM studies were carried out. In the case of  $\text{Ca}^{2+}$  mediated self-assembled system, more interwind structures were observed in the gel phase (Figure 4.12a & 4.12d), which were converted into shorter fiber upon 100% strain (Figure 4.12b & 4.12e). However, short fibers were able to rejoin to form longer fibers upon removal of the strain (Figure 4.12c & 4.12f), showing the complete recovery of the mechanical property. Similar behaviour of conversion of longer fiber into shorter and regain in the fiber length after removal of strain was observed in case of  $\text{Mg}^{2+}$  coordinated peptide hydrogels (Figure 4.12g-i & j-l).

#### 4.2.5. Cell culture studies

*4.2.5.1 Evaluation of cellular cytotoxicity.* At this point, we were intrigued to find out whether the coordination with the metal ions to the negatively charged hydrogels can show improvement in their biocompatibility at physiological pH. In this direction, our study established the simple approach of coordinating metal ions to negatively charged peptides to overcome the limited biocompatibility of the peptide at physiological pH. In order to assess the potential of the metal coordinated biomolecular construct for mimicking the native ECM, cytocompatibility assay of the peptide scaffold with fibroblast (L929) and glioma (C6) cells was performed via MTT reduction assay.<sup>67</sup>

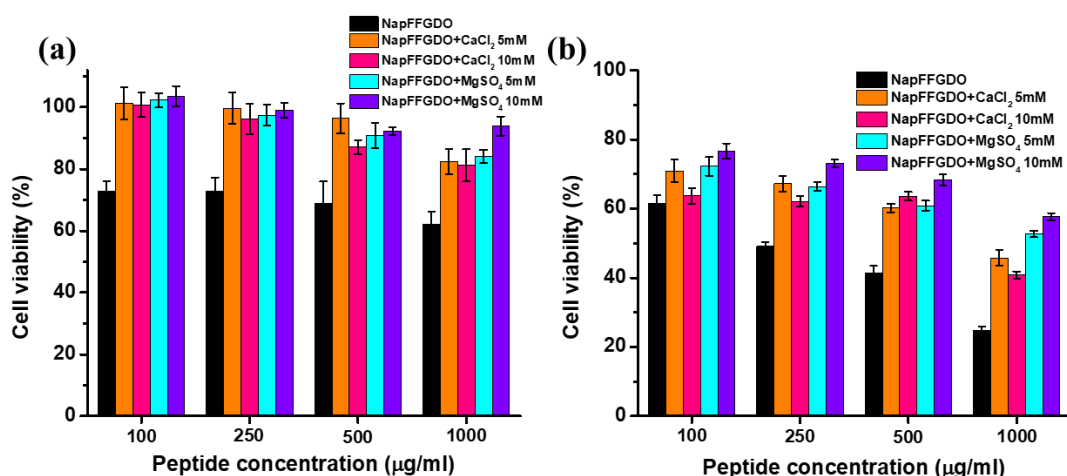


**Figure 4.13** Assessment of the comparative effect of negatively charged peptide and metal coordinated peptide hydrogel on cellular viability of (a) fibroblast (L929) and (b) glioma (C6) cells while treated with peptide nanofibers of variable concentrations ranging from 100 to 1000 µg/mL via MTT assay.

As reported in our previous study, negatively charged peptide (NapFFGDO) showed cellular viability of around 60-65% when incubated with fibroblast cells for 48 hours using different peptide concentrations.<sup>60</sup> Furthermore, the peptide demonstrated limited cellular viability of 60-30% with glioma cells using different concentrations of peptide (100-1000  $\mu\text{g}/\text{mL}$ ). The viability was found to decrease with subsequent increase in peptide concentration. Interestingly, significant enhancement in the cellular viability was observed in all the metal coordinated peptide hydrogels. An increase in the cellular viability of the fibroblast cells was observed in the presence of 5 mM  $\text{Ca}^{2+}$  ions, which is 80-100% with varying concentration of the metal coordinated peptide scaffold. A slightly reduced viability of 80-90% was observed at 10 mM, however, it was reasonably higher than the peptide itself. Our findings can be correlated to the earlier reports that depict that the increased concentration of calcium ions up to 10-15 mM leads to a slight decrease in cell viability and loss of morphology.<sup>81</sup> Whereas the presence of magnesium ions at a concentration of 5 mM and 10 mM coordinated to peptide scaffold showed cellular viability of 90-100% irrespective of the concentrations of peptide (Figure 4.13a). After 48 hours of incubation with negatively charged peptide, bright-field images of fibroblast cells showed the loss of appendages and increased nuclei size, leading to slow proliferation and detachment from the surface.

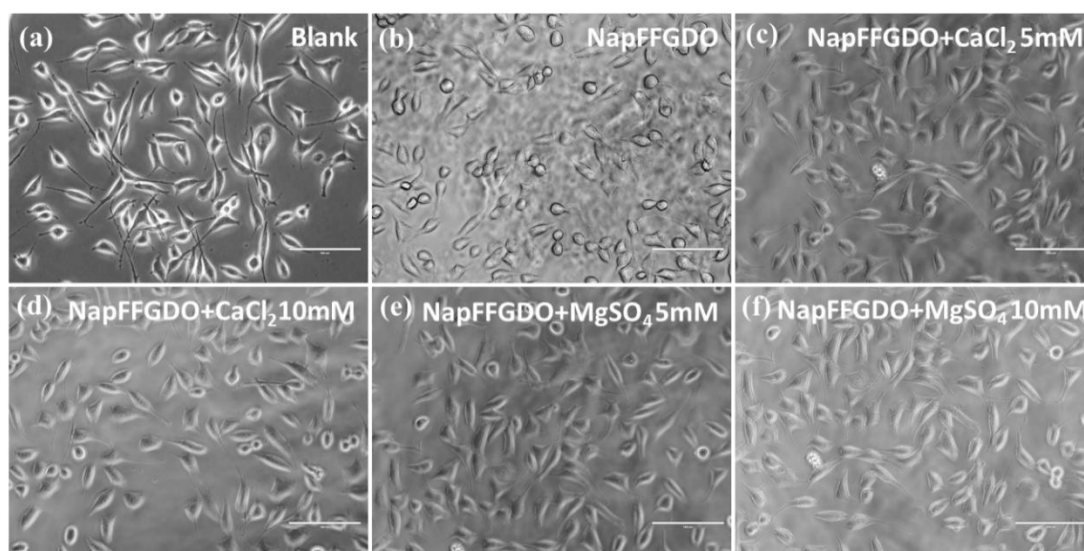


**Figure 4.14** Bright field images of fibroblast cells (L929) after incubation of 48 hours with ion complexed peptides at concentration of 500  $\mu\text{g}/\text{mL}$ . Scale bar 100  $\mu\text{m}$ .

Interestingly, cells with metal coordinated peptide treatment showed similar morphology compared to the control fibroblast cells (Figure 4.14). Cells were found to retain their morphology even after longer time of incubation with the metal coordinated peptide scaffold. Whereas, glioma cells upon treatment with metal coordinated peptide hydrogels showed increased viability at all the concentrations up to 60-70% compared to the control peptide. A significant difference in cellular viability at 1000  $\mu\text{g}/\text{mL}$  were observed in peptide with both the metal salts. Magnesium ions at both concentrations showed better cellular viability than the calcium ions (Figure 4.13b). The increased concentration of divalent metal salts after a certain threshold leads to show the detrimental effect on the cells. A similar change in cell morphology and increased live cell population was observed in the glioma cells as evident from the bright field images after 48 hours of incubation (Figure 4.15), which is well correlated with the MTT results.

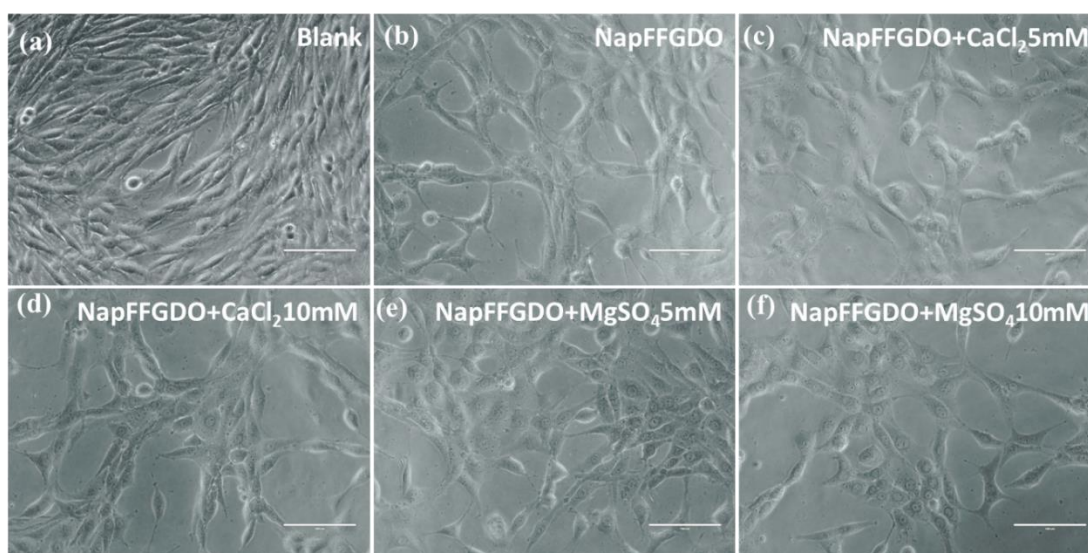


**Figure 4.15** Bright field images of glioma cells (C6) after incubation of 48 hours with ion complexed peptides at concentration of 500  $\mu\text{g}/\text{mL}$ . Scale bar 100  $\mu\text{m}$ .

**4.2.5.2 Cellular adhesion. 2D culture.** In order to develop biomaterial with enhanced cell survival and proliferation property, cells were assessed via 2D cell culture. Live dead staining of cells on 2D construct was carried out to evaluate the potential of the matrices for cellular growth and proliferation. In order to support the cellular adhesion and growth, the peptide should be capable of forming a nanofibrous peptide network, which provides the matrix for cellular adhesion. In this context, it has been reported that in addition to the chemical functionality, fiber morphology and mechanical strength

of the hydrogels play a crucial role in determining the cellular adhesion property.<sup>82</sup> In this direction, cells adhered to the hydrogel-coated coverslips were investigated for 5 days. Negatively charged peptide (NapFFGDO) at 15mM do not form hydrogel but showed the presence of peptide nanofiber in sol as observed in the AFM images (Figure 4.2). A thin layer of the peptide sol was coated and air-dried on the coverslip, which was further UV sterilized before adding cells to it. Interestingly, metal coordinated peptide hydrogels showed a clear difference in cellular proliferation compared to the negatively charged peptide (Figure 4.16 & 4.17). It was evident that a decreased cell population and significant change in the cellular morphology took place in the charged peptide. In this context, report by Jayawarna et. al. indicated that the peptide with uncharged residue possess more biocompatibility towards different types of cells in comparison to the exposed gel surfaces of positively and negatively charged residues.<sup>[74]</sup>

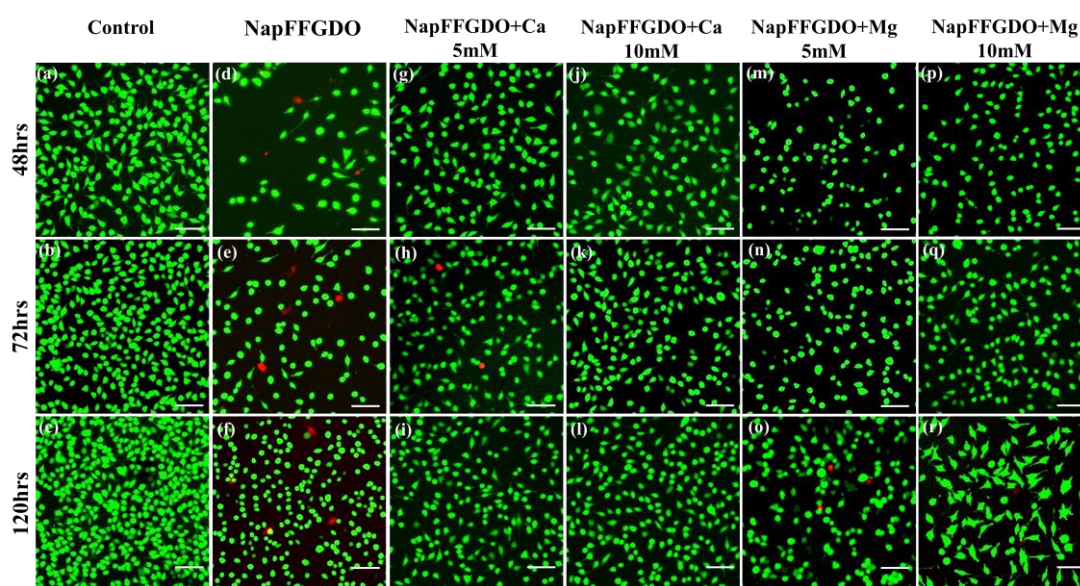


**Figure 4.16** Assessment of cellular adhesion on 2D matrix of peptide hydrogel with fibroblast cells (L929) via Live/Dead staining. Fluorescence images of cells stained with FDA (live) and PI (dead) for different time interval of 48, 72, and 120 hours; (a-c) control, (d-f) NapFFGDO, (g-i) NapFFGDO + Ca5mM, (j-l) NapFFGDO + Ca10mM, (m-o) NapFFGDO + Mg5mM, (p-r) NapFFGDO + Mg10mM. Scale bar 50 $\mu$ m.

It is noteworthy that the presence of positive or negative surface charge are found to be detrimental as it may interfere with the attachment of the cells to the surface and its

interactions with the cells. Hence, it may be expected that the masking of the charges by cross-linking with specific ions of biological origin may result in fabrication of an improved interface for the cells. Very interestingly, upon coordination with divalent metal ions, the hydrogel scaffolds showed an increment in cellular proliferation, and a spread morphology was achieved (Figure 4.16). Interestingly, cell density of the fibroblast cells was found to increase with time in all the metal coordinated hydrogels.

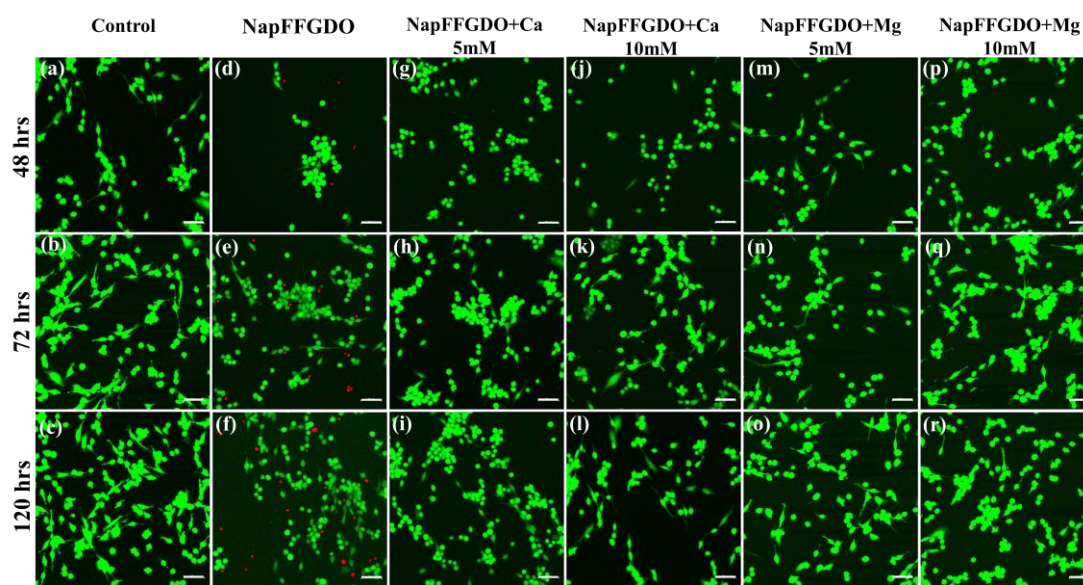


**Figure 4.17** Assessment of cellular adhesion on 2D matrix of peptide hydrogel with glioma cells (C6) via Live/Dead staining. Fluorescence images of cells stained with FDA (live) and PI (dead) for different time interval of 48, 72, and 120 hours; (a-c) control, (d-f) NapFFGDO, (g-i) NapFFGDO + Ca5mM, (j-l) NapFFGDO + Ca10mM, (m-o) NapFFGDO + Mg5mM, (p-r) NapFFGDO + Mg10mM. Scale bar 50 $\mu$ m.

At the same time, the control peptide showed similar cellular density throughout the incubation time, suggesting decreased proliferation rate of cells in the presence of the control peptide. Similar observations were made with glioma cells; the cellular toxicity was moderately higher in glioma cells. As the C6 cells were derived from rat glioma, a neural cell, it can be envisaged that peptide matrix developed were of higher mechanical strength, and hence may not be ideally suitable for the adherence and proliferation of the neural cells. Such observations further explained the reduced cellular adhesion and proliferation of glioma cells in the peptide hydrogels. More importantly, the presence of calcium ions triggered the instant hydrogelation, which resulted in higher enhanced mechanical strength. Such enhancement in the gel strength could be a probable reason for the decrease in cellular viability and proliferation of the glioma cells.<sup>83</sup> Thus, 2D

studies showed a similar pattern of cellular adhesion as observed in the cytocompatibility assay with the metal coordinated hydrogels.

**4.2.5.3 Assessment of cellular proliferation.** The cytotoxicity assay revealed the biocompatible nature of the derived scaffold, while the 2D cell culture studies demonstrated the cell-supportive nature of the metal ion coordinated peptide hydrogel scaffolds. To further determine the potential of these scaffolds to construct newly designed matrices, it will be extremely preferable to quantify the cellular viability and proliferation via Alamar blue assay. Alamar blue is a non-toxic, water-soluble dye that can be utilized to continuously monitor the cells for their proliferation.<sup>84</sup> It was evident from the proliferation study that the cells are viable and proliferating after 48 hours of cell seeding on the control sample (Figure 4.18). Significant differences in the rate of cellular proliferation were observed in control, negatively charged peptide, and metal ion coordinated peptide scaffolds after 48 hours of incubation. This difference in the cellular proliferation of fibroblast cells among different metal coordinated peptide scaffolds conferred the results observed in the cell viability and 2D assay. Moreover, cells demonstrated differential response over different metal ion coordinated hydrogels over 5 days (Figure 4.18a). The negatively charged peptide showed a lower extent of cellular proliferation than that of the control, which further showed a significant enhancement in the presence of metal ions.

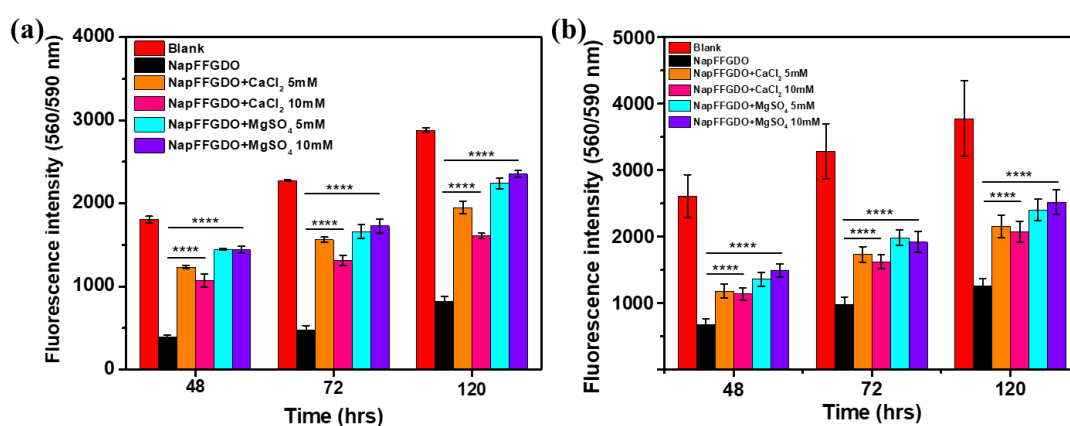


**Figure 4.18** Cellular proliferation of (a) fibroblast cells, L929 and (b) Glioma cells, C6 on metal ion complexed peptide hydrogels using Alamar blue assay at a different time point of 48, 72, and 120 hours. Represented data are mean of three different experiments, and asterisk representing the P-value was calculated using two-way ANOVA, Bonferroni's multiple comparison test. (\*\*\*\* represents P-value  $\leq 0.0001$ )

Similar observations were made in glioma cells, though the proliferation rate of C6 was slow in the presence of peptide hydrogels, but apparent differences between negatively charged peptide and metal coordinated peptide were visible (Figure 4.18b). Statistical analysis via two-way ANOVA showed a significant difference in the proliferation capability between negatively charged peptide and metal coordinated peptide by P-value  $\leq 0.0001$  in both the cell lines. Cellular viability and proliferation results suggested the importance of these metal ion coordinated constructs in developing advanced scaffolds for controlling and directing the cellular response. Furthermore, this simple strategy of hydrogelation and increased cellular proliferation can be solely employed to surpass the limitations associated with the charged bioactive peptides to represent a better mimic for extracellular matrix.

4.2.5.4 *F-actin staining (Rhodamine Phalloidin)*. 2D cell culture results of fibroblast cells with negatively charged peptides showed a slow proliferation rate and change in the morphology of the cells with the progression of time of incubation. Interestingly, all the metal coordinated peptide hydrogels demonstrated an increment in cellular adherence and proliferation.

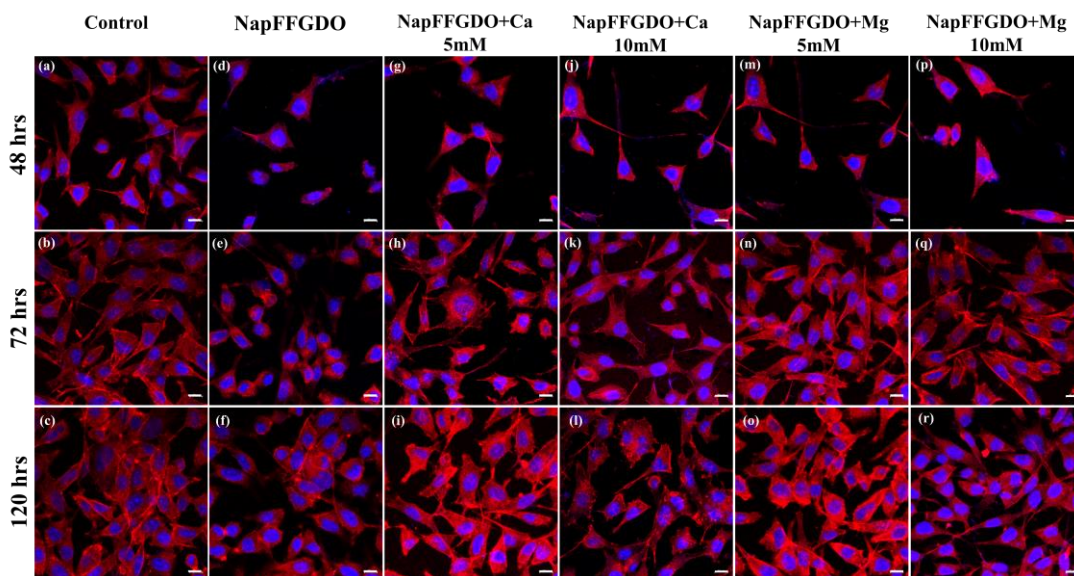


**Figure 4.19** F-actin staining of fibroblast cell line (L929) with Rhodamine phalloidin adhered on (a-c) control, (d-f) NapFFGDO, (g-i) NapFFGDO + Ca5mM, (j-l) NapFFGDO + Ca10mM, (m-o) NapFFGDO + Mg5mM, (p-r) NapFFGDO + Mg10mM at different time point of 48, 72, 120 hours. Scale bar 10 $\mu$ m.

In order to visualize and quantitate the change in morphology of the cells in the presence of peptide, cells were stained with Rhodamine Phalloidin for F-actin, which binds to the actin filament of the cytoplasm, and to stain the nuclei of the cells, DAPI has been utilized (Figure 4.19). The morphological analysis of phalloidin staining can be judiciously correlated with the cellular viability and adhesion assays.<sup>85</sup> Fibroblast cells adhered to the control peptide-coated surface showed slow proliferation of the cells, while the change in the morphology with decreased surface area and cell shape index was also calculated for the cells to quantitate the difference that occurred upon interacting with peptide (Figure 4.20). The cells can be seen to lose the morphology upon prolonged exposure with the control peptide hydrogels. Fluorescence images showed cells with increased nuclei size and rounded morphology of the fibroblast cells, with a spread area of  $220 \pm 20 \mu\text{m}^2$  and cell shape index of  $0.6 \pm 0.05$  (Table S2). The calculated value of CSI represents the cell shape and size parameter. The CSI value close to 1 represents the circular morphology of the cells, while the CSI value close to 0 represents elongated cells.<sup>86</sup> Interestingly, the metal coordinated peptide hydrogels showed better adhesion and elongated morphology of cells, while magnesium salts showed better adhesion and proliferation than the hydrogel stabilized via calcium ions.

**Table 4.2** The values of cell shape index (CSI) and area covered by fibroblast cells on control peptide scaffold as well as metal ions coordinated peptide scaffold as determined by F-actin staining (after 72 hours of incubation).

Sample	CSI values	Area covered ( $\mu\text{m}^2$ )
Control	$0.353 \pm 0.065$	$321.95 \pm 35.15$
NapFFGDO	$0.596 \pm 0.076$	$220.82 \pm 17.27$
NapFFGDO+CaCl <sub>2</sub> (5 mM)	$0.396 \pm 0.053$	$280.78 \pm 21.67$
NapFFGDO+CaCl <sub>2</sub> (10 mM)	$0.456 \pm 0.047$	$260.57 \pm 19.16$
NapFFGDO+MgSO <sub>4</sub> (5 mM)	$0.37 \pm 0.023$	$282.56 \pm 24.16$
NapFFGDO+ MgSO <sub>4</sub> (10 mM)	$0.365 \pm 0.065$	$295.57 \pm 14.16$

The cell spread area on calcium coordinated peptide hydrogel construct (5mM and 10mM) was found to be ( $280 \pm 21.7 \mu\text{m}^2$  and  $260 \pm 19.2 \mu\text{m}^2$  respectively), whereas magnesium ion construct with 5mM and 10mM salt concentration showed ( $284 \pm 20.7$

$\mu\text{m}^2$  and  $295 \pm 21.2 \mu\text{m}^2$  respectively) (Figure 4.20a). The CSI value of blank (control) showed a value of  $0.35 \pm 0.06$ , suggesting the elongated and spread morphology of the cells.

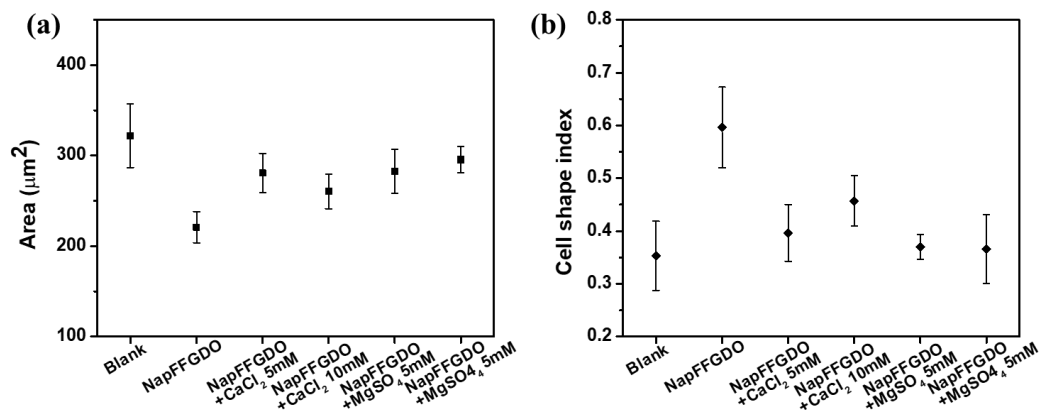


**Figure 4.20** Assessment of (a) spread area and (b) cell shape index (CSI) of fibroblast cells on hydrogel coated cover slips of phalloidin staining.

It was observed that the cells adhered on the metal coordinated construct showed the better spread area as compared to the control peptide, the peptide with calcium salt of 5mM and 10mM gives CSI value of  $0.40 \pm 0.05$  and  $0.45 \pm 0.04$  and peptide with magnesium salt of 5mM, and 10mM showed CSI value of  $0.37 \pm 0.02$  and  $0.36 \pm 0.06$  respectively (Figure 4.20b). Metal coordinated peptide construct showed the spread area and CSI value similar to the control, with a spread area and CSI value of  $321 \pm 25 \mu\text{m}^2$  and  $0.34 \pm 0.02$ , respectively.

**4.2.5.5 Immunostaining for  $\beta$ -III tubulin.** Cells of neuronal origin are known to show the most abundant class III  $\beta$ -tubulin isotype, but its widespread distribution in tumors has also demonstrated neuronal differentiation.<sup>87</sup> Morphological changes in the neuronal cells are linked to the reorganization of the actin cytoskeleton, which further is controlled by the expression of the  $\beta$ -III tubulin.<sup>88, 89</sup> To assess the morphological changes that occurred in the glioma cells at different time points of peptide treatment, we have monitored the microtubule formation via immunofluorescence staining technique. Peptide hydrogel-coated coverslips containing cells adhered on top of the surface were observed for the  $\beta$ -III tubulin expression and monitored for the different period time of 48 hrs, 72 hrs, and 120 hrs (**Figure 4.21**). It was evident from the microscopic examination that cell density increased over 5 days steadily and limited the correct visualization of the elongated morphology of the cells. Cells on the metal

coordinated peptide hydrogel coated coverslips showed a steady increase in population over time, with the elongated cells showed the microtubule formation, which was comparable to the blank sample (tissue culture plates).

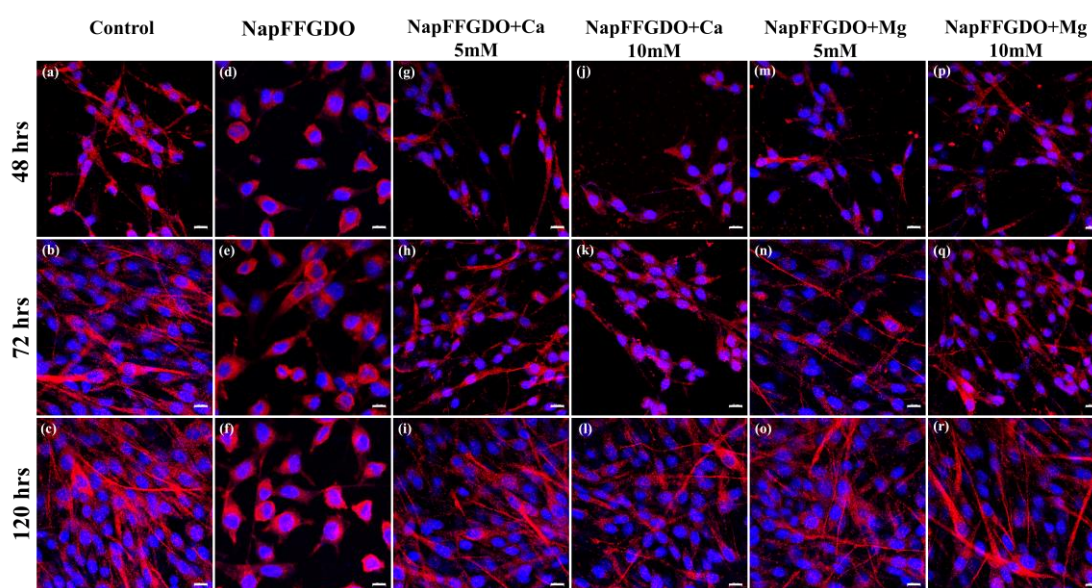


**Figure 4.21** Immunofluorescence staining of neural marker  $\beta$ -III tubulin in C6 cell line adhered on (a-c) control coverslips, (d-f) NapFFGDO, (g-i) NapFFGDO+Ca5mM, (j-l) NapFFGDO + Ca10mM, (m-o) NapFFGDO + Mg5mM, and (p-r) NapFFGDO + Mg10mM at different time point 48 hrs, 72 hrs, and 120 hrs of cell culture, respectively. Scale bar is 10 $\mu$ m.

**Table 4.3** The values of cell shape index (CSI) and area covered by glioma cells on control peptide scaffold as well as metal ion coordinated peptide scaffold as determined by  $\beta$ -III tubulin staining (after 72 hours of incubation).

Sample	CSI values	Area covered ( $\mu\text{m}^2$ )
Control	$0.163 \pm 0.024$	$225.01 \pm 9.63$
NapFFGDO	$0.474 \pm 0.060$	$149.77 \pm 5.79$
NapFFGDO+CaCl <sub>2</sub> (5 mM)	$0.256 \pm 0.055$	$199.45 \pm 12.73$
NapFFGDO+CaCl <sub>2</sub> (10 mM)	$0.377 \pm 0.047$	$192.41 \pm 9.41$
NapFFGDO+MgSO <sub>4</sub> (5 mM)	$0.298 \pm 0.031$	$207.71 \pm 6.64$
NapFFGDO+ MgSO <sub>4</sub> (10 mM)	$0.245 \pm 0.065$	$211.85 \pm 9.11$

At the same time, the sample containing negatively charged peptide hydrogel showed less population over time, and cells with round morphology suggested the slow proliferation and change in morphology of the glioma cells, respectively. The cells can be seen to lose the morphology upon prolonged exposure with the negatively charged peptide hydrogels. Fluorescence images showed cells with increased nuclei size and rounded morphology of the glioma cells, with a spread area of  $149 \pm 5.7 \mu\text{m}^2$  and cell shape index of  $0.48 \pm 0.06$  (Table 4.3). Interestingly, the metal coordinated peptide hydrogels showed better adhesion and elongated morphology of cells, while magnesium salts showed better adhesion and proliferation than the hydrogel stabilized via calcium ions. The cell spread area on calcium coordinated peptide hydrogel construct (5mM and 10mM) was found to be ( $199 \pm 12.7 \mu\text{m}^2$  and  $192 \pm 9.41 \mu\text{m}^2$  respectively), whereas magnesium ion construct with 5mM and 10mM salt concentration showed ( $207 \pm 6.64 \mu\text{m}^2$  and  $211 \pm 9.11 \mu\text{m}^2$  respectively) (Figure 4.22a). The CSI value of blank (control) showed a value of  $0.163 \pm 0.02$ , suggesting the elongated and spread morphology of the cells. It was observed that the cells adhered on the metal coordinated construct showed better spread area as compared to the control peptide. Cell cultured on the peptide with calcium salt of 5mM and 10mM exhibited a CSI value of  $0.25 \pm 0.05$  and  $0.37 \pm 0.03$ , and on peptide with magnesium salt of 5mM and 10mM, the cells showed CSI value of  $0.29 \pm 0.03$  and  $0.24 \pm 0.06$  respectively (Figure 4.22b).

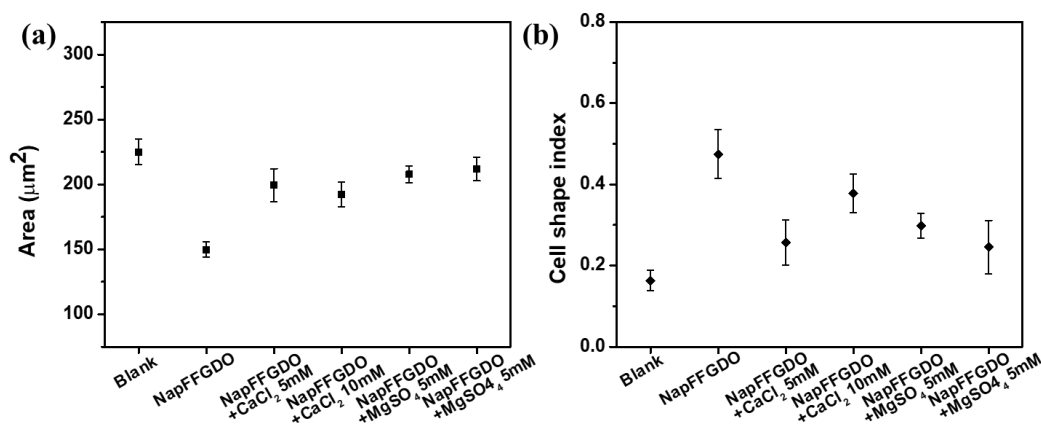


**Figure 4.22** Assessment of (a) spread area and (b) cell shape index (CSI) of glioma cells on hydrogel coated cover slips of  $\beta$ -III tubulin staining.

4.2.5.6 *Cellular migration assay.* Cell migration is a key component involved in many biological processes and wound recovery, where the cells should be able to migrate and cover the wound site.<sup>90</sup> For designing and developing a next-generation synthetic matrix, inherent cell migration property plays a crucial role in enhancing the scope of the biomaterial.<sup>90</sup> The ability of the synthetic construct to help cells adhere, migrate, and proliferate is the essential factor for wound closure. In this direction, collagen was identified as one of the most abundant proteins present in the matrix, which helps the cells to adhere and migrate.<sup>91</sup>

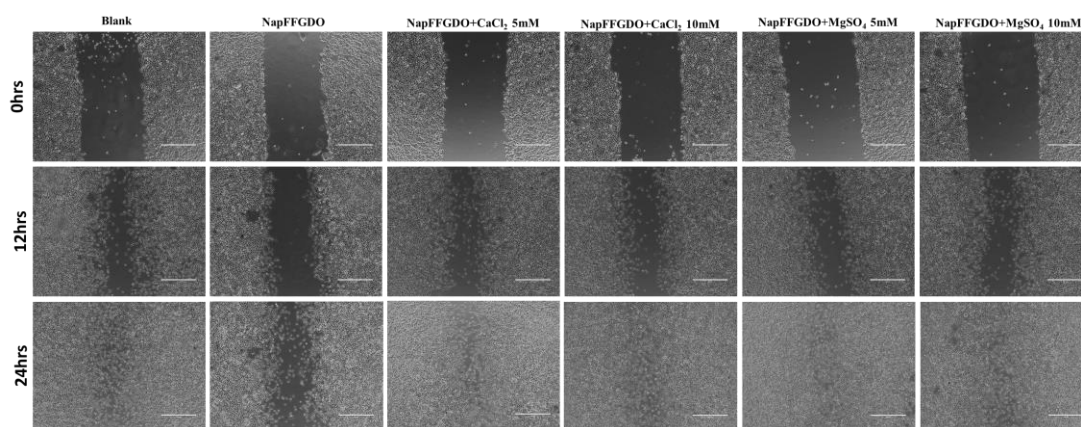


**Figure 4.23** Cellular migration assay to study the effect of metal coordinated peptide on cellular migration in fibroblast cells (L929). Bright field images of cellular migration at different time point of 0 hr, 12 hrs, and 24 hrs in presence of peptide hydrogel, scale bar 400 $\mu$ m

Hence, collagen inspired self-assembling peptides with metal coordination can also be explored to divulge their potential role in cellular migration. For the migration study, we applied a well-known method of the scratch assay<sup>90</sup> to evaluate the migration ability of the peptide hydrogels. Migration of fibroblast and glioma cells was monitored under a bright field microscope at different time point up to 24 hours in the presence of metal coordinated peptide treatment. From the scratch assay of fibroblast cells, it was evident that after 24 hours of incubation, almost 90% of the area was covered in control (Figure 4.23). In contrast, the negatively charged peptide showed only 50% of the migration in the scratched area. Interestingly, the metal coordinated peptide showed enhancement in the migration compared to that of control. On comparing the migration capability, it has been demonstrated that among the two divalent cations, magnesium ions showed an enhanced effect in the migration with fibroblast cells. To further quantitate the area

covered by the cells, we have calculated the area covered and plotted based on the percentage migration, which showed 72% and 67% of migration in calcium ion 5mM and 10mM respectively, 81% and 83% of migration in magnesium ion at 5mM and 10mM respectively at time points of 12 hours and 24 hours (Figure 4.25a). Similarly, bright field images of the glioma cells showed slow migration as compared to the fibroblast cells (Figure 4.24).

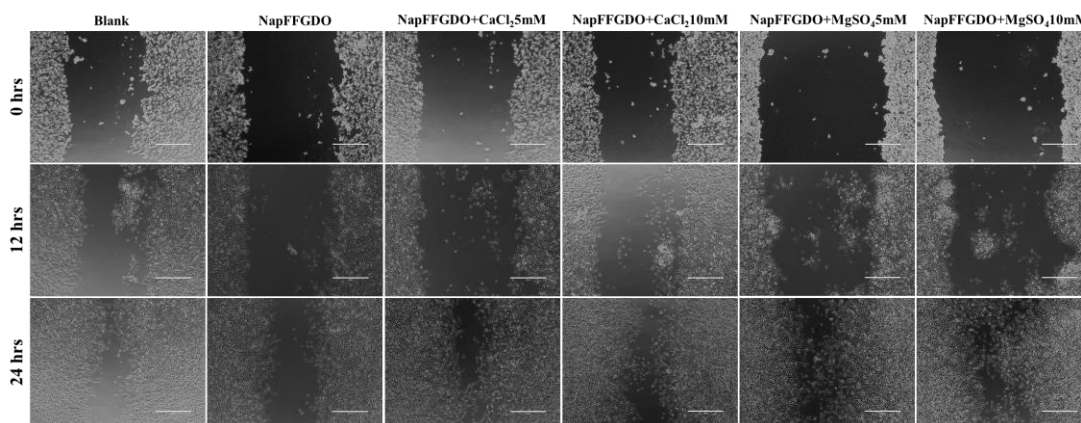


**Figure 4.24** Cellular migration assay to study the effect of metal coordinated peptide on cellular migration in glioma cells (C6). (a) Bright field images of cellular migration at different time point of 0 hr, 12 hrs, and 24 hrs in presence of peptide hydrogel, scale bar 400 $\mu$ m

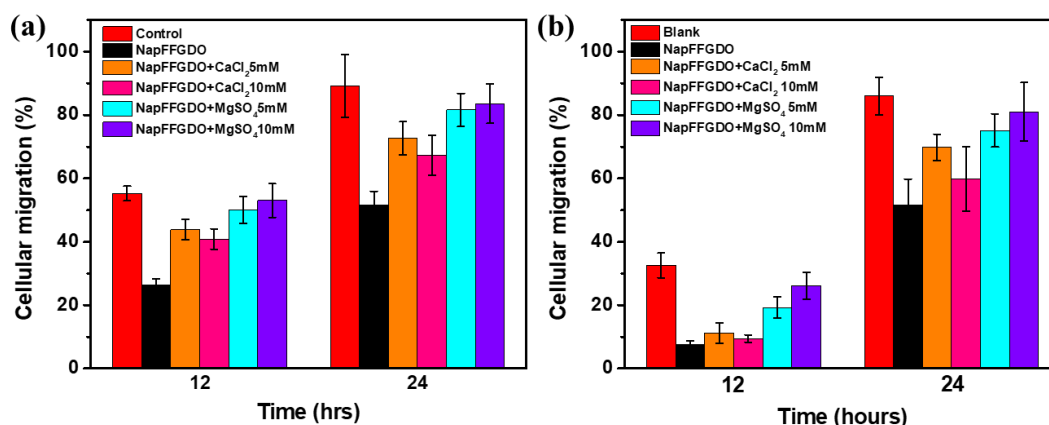


**Figure 4.25** Quantitative analysis of the cellular migration assay of metal coordinated peptide on (a) fibroblast cells (L929) and (b) glioma cells (C6).

Almost 85% of the area was covered in the control, while only 50% of the area was covered in the negatively charged peptide. After addition of the salts to the peptide hydrogels the migration capability was enhanced up to 69% and 59% in the presence

of calcium ions of concentration 5mM and 10mM respectively. The addition of magnesium ions showed migration of 72% and 76% at 5mM and 10mM salt concentrations, respectively at time points of 12 hours and 24 hours (Figure 4.25b). Metal ion coordinated peptide hydrogel showed enhanced cellular migration as compared to the control peptide, which again correlate with cellular cytotoxicity and adhesion studies.

*4.2.5.7 Flow cytometry for quantitative analysis of cellular behaviour.* Flow cytometry was performed to further support the effect of metal coordination to the collagen inspired self-assembling peptide hydrogel scaffolds on biocompatibility, adhesion, and proliferation of fibroblast and glioma cells. This study will provide the quantitative assessment for the live and dead cell population using live/dead staining assay, which could display the differential effect of metal ion coordination on the negatively charged peptide.<sup>92</sup>

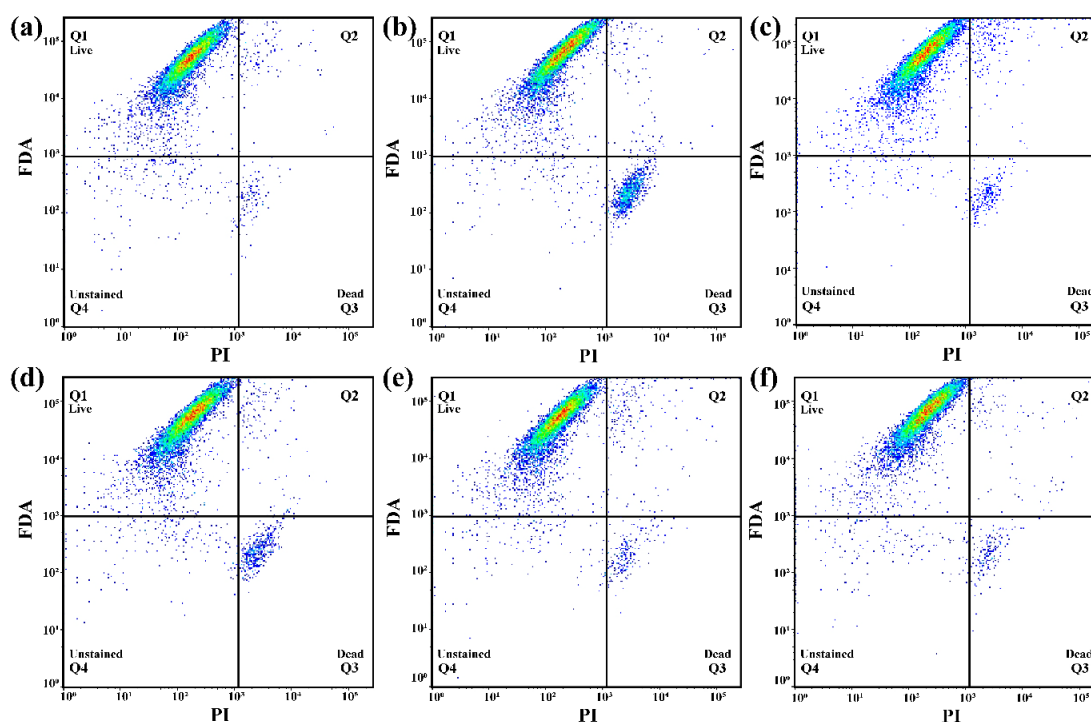


**Figure 4.26** Quantitative analysis of the cellular interaction with the hydrogel matrix via flow cytometry. Live and dead cells of fibroblast (L929) were stained and quantified by FDA and PI respectively; (a) Control, (b) NapFFGDO, (c) NapFFGDO + CaCl<sub>2</sub> 5mM, (d) NapFFGDO + CaCl<sub>2</sub> 10mM, (e) NapFFGDO + MgSO<sub>4</sub> 5mM, and (f) NapFFGDO + MgSO<sub>4</sub> 10mM. Q1 quadrant represents live cells, Q3 represents dead cells, and Q2, Q4 represents double-stained and unstained populations.

Treated cells and control cells were allowed to stain with FDA/PI for live and dead populations, respectively. Q1 region and Q4 region corresponds to live/dead populations respectively, while Q3 region indicates the unstained and Q2 region corresponds to the double-stained population in the pseudocolor plot of FACS analysis. L929 cells in the control experiment showed 96% live population, while a gradual decrease in the live cell population 79% were observed in the cells treated with negatively charged peptide alone. Interestingly, the live-cell population increases significantly after metal ion complexation with peptide hydrogels. The percentage of live cell population increases up to 94% for 5mM of calcium ion, which is very similar to that of the control. However, significant live cell population was also evident at 10mM of the calcium ion coordinated with peptide nanofibers the value is around 89%. The similar effect of decreased cellular viability was observed after a certain concentration of metal ions coordinated with the peptide nanofibers.

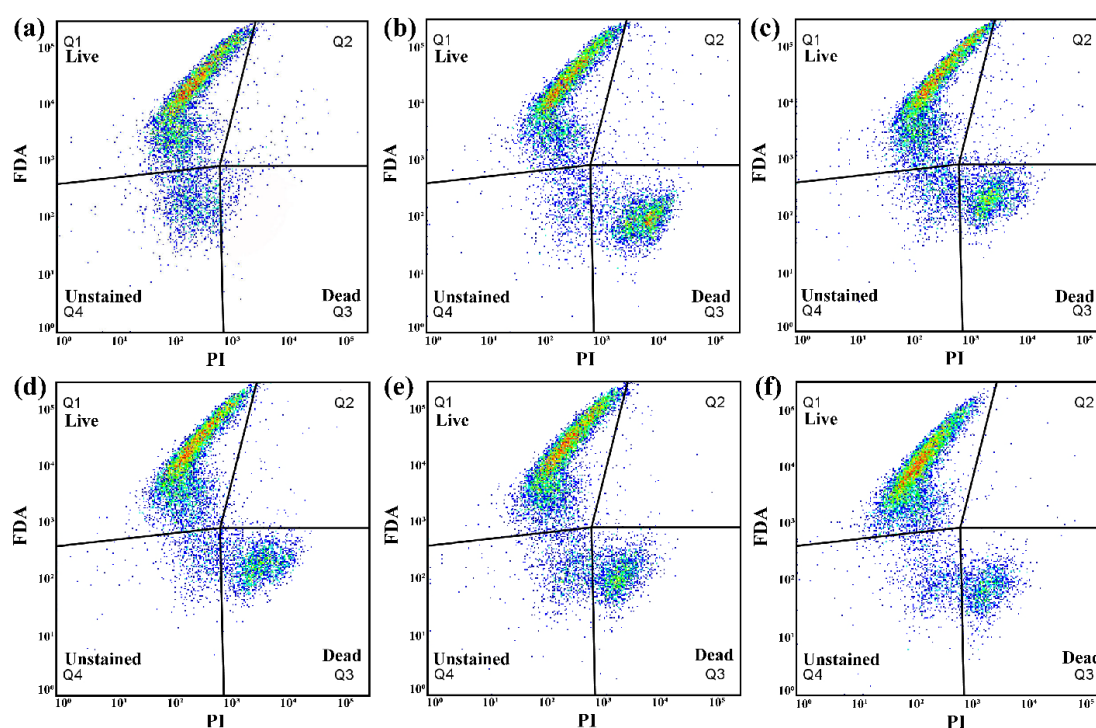


**Figure 4.27** Quantitative analysis of the cellular interaction with the hydrogel matrix via flow cytometry. Live and dead cells of glioma (C6) were stained and quantified by FDA and PI respectively; (a) Control, (b) NapFFGDO, (c) NapFFGDO + CaCl<sub>2</sub> 5mM, (d) NapFFGDO + CaCl<sub>2</sub> 10mM, (e) NapFFGDO + MgSO<sub>4</sub> 5mM, and (f) NapFFGDO + MgSO<sub>4</sub> 10mM. Q1 quadrant represents live cells, Q3 represents dead cells, and Q2, Q4 represents double-stained and unstained populations.

Whereas, a higher percentage of 93% and 95% live cell population were observed in the presence of magnesium ions with concentrations 5mM and 10mM, respectively (Figure 4.26). Thus, increased live cell population can be correlated with the beneficial effect of metal ion complexation, which mask the surface charge of the peptide nanofibers and provides the necessary adherent sites for the cells to attach and grow over time. The live dead population of the glioma cells (C6) corroborates the above finding of lesser biocompatibility, adhesion, proliferation. A variable percentage of live cell population was evident, for example, 94% in control, 57% in negatively charged peptide, 73% and 70% of 5mM and 10mM in case of  $\text{Ca}^{2+}$  ion coordinated peptide hydrogel scaffold, 78% and 82% for 5mM and 10mM of  $\text{Mg}^{2+}$  ion-containing peptide showed live population (Figure 4.27). The results revealed the enhanced cellular response of the metal coordinated peptide hydrogels compared to the control peptide.

### 4.3 Conclusion

In conclusion, we present the cooperative effect of biologically relevant metal ion coordination in a minimalist bioactive peptide molecular domain to promote hydrogelation at physiological pH. By simply adding metal ions, the detrimental effect of surface charge of the peptide can be minimized, which has direct implication in promoting cellular proliferation to develop next-generation biomaterial for tissue engineering applications. A designer sequence inspired from native collagen triple helical peptide sequence (Gly-Asp-Hyp) was designed that display negatively charged surface at physiological pH and thus self-assemble at pH 5.0. Since, the peptide monomer failed to self-assemble at an ambient condition, hence its application in biomedicine is limited. Interestingly, the negatively charged peptide shifted its equilibrium point of self-assembly and showed conversion from sol to gel in the presence of divalent metal ions ( $\text{Ca}^{2+}/\text{Mg}^{2+}$ ) at physiological pH. Moreover, highly tunable hydrogels with diverse mechanical strength can be developed by simply tuning specific metal ions of biological relevance and their relative concentrations in the solution. Thus, this simple methodology can be utilized as a powerful approach that can overcome the limitations of charged peptide construct. In this regard, we achieved diverse gels with higher mechanical strength at a much lower concentration, as reported earlier.<sup>60</sup> The changes in physical properties was found to bring in a difference in biological activities. The differential cellular response was observed in the new designer construct i.e., metal coordinated hydrogels. Cellular viability, adhesion, and

proliferation demonstrated the importance of metal ions in modulating the collagen inspired peptide assembly as a next-generation biomaterial. Furthermore, the new constructs with metal ions promoted cellular functions, as evident from the F-actin and  $\beta$ -III tubulin staining studies. Interestingly, significant enhancement in cellular viability, adhesion, and proliferation was evident in peptide hydrogels prepared with magnesium coordination compared to calcium ions, which may be attributed to their differential spatiotemporal arrangement in the self-assembled state, that may affect their physical cues to the specific cell types. Such interesting cooperative self-assembly enhances the scope of these biomaterials, which can be applied in developing extracellular matrix mimics for futuristic applications.

**Note:**

The permission has been granted by authors and corresponding author of the published paper prior to its adoption in the present thesis. The publication associated with this work is:

Vijay Kumar Pal, and Sangita Roy, Cooperative Metal Ion Coordination to the Short-Assembling Peptide Promotes Hydrogelation and Cellular Proliferation. *Macromol. Biosci.*, **2022**, 2100462.

#### 4.4 References

1. Cringoli, M. C.; Fornasiero, P.; Marchesan, S., Chapter 10 Minimalistic Peptide Self-assembly into Supramolecular Biomaterials. In *Soft Matter for Biomedical Applications*, The Royal Society of Chemistry: 2021; pp 236-263.
2. Davis, A. V.; Yeh, R. M.; Raymond, K. N., Supramolecular assembly dynamics. *Proc Natl Acad Sci U S A* **2002**, 99 (8), 4793-4796.
3. Mahadevi, A. S.; Sastry, G. N., Cooperativity in Noncovalent Interactions. *Chem. Rev.* **2016**, 116 (5), 2775-2825.
4. Du, X.; Zhou, J.; Shi, J.; Xu, B., Supramolecular Hydrogelators and Hydrogels: From Soft Matter to Molecular Biomaterials. *Chemical Reviews* **2015**, 115 (24), 13165-13307.
5. Fleming, S.; Ulijn, R. V., Design of nanostructures based on aromatic peptide amphiphiles. *Chemical Society Reviews* **2014**, 43 (23), 8150-8177.
6. Marchesan, S.; Waddington, L.; Easton, C. D.; Kushkaki, F.; McLean, K. M.; Forsythe, J. S.; Hartley, P. G., Tripeptide Self-Assembled Hydrogels: Soft Nanomaterials for Biological Applications. *BioNanoScience* **2013**, 3 (1), 21-29.
7. Huang, J.; Zhang, X.; Fu, K.; Wei, G.; Su, Z., Stimulus-responsive nanomaterials under physical regulation for biomedical applications. *J. Mater. Chem. B* **2021**, 9 (47), 9642-9657.
8. Zhou, H.-X.; Pang, X., Electrostatic Interactions in Protein Structure, Folding, Binding, and Condensation. *Chem. Rev.* **2018**, 118 (4), 1691-1741.
9. Zou, R.; Wang, Q.; Wu, J.; Wu, J.; Schmuck, C.; Tian, H., Peptide self-assembly triggered by metal ions. *Chem. Soc. Rev.* **2015**, 44 (15), 5200-5219.
10. Hwang, K.; Hosseinzadeh, P.; Lu, Y., Biochemical and Biophysical Understanding of Metal Ion Selectivity of DNazymes. *Inorg. Chim. Acta* **2016**, 452, 12-24.

11. Sissi, C.; Palumbo, M., Effects of magnesium and related divalent metal ions in topoisomerase structure and function. *Nucleic Acids Res.* **2009**, *37* (3), 702-711.
12. Castaneda, C. A.; Lopez, J. E.; Joseph, C. G.; Scholle, M. D.; Mrksich, M.; Fierke, C. A., Active Site Metal Identity Alters Histone Deacetylase 8 Substrate Selectivity: A Potential Novel Regulatory Mechanism. *Biochemistry* **2017**, *56* (42), 5663-5670.
13. Guo, Y.; Wang, S.; Du, H.; Chen, X.; Fei, H., Silver Ion-Histidine Interplay Switches Peptide Hydrogel from Antiparallel to Parallel  $\beta$ -Assembly and Enables Controlled Antibacterial Activity. *Biomacromolecules* **2019**, *20* (1), 558-565.
14. Xiao, J.; Zhu, Y.; Huddleston, S.; Li, P.; Xiao, B.; Farha, O. K.; Ameer, G. A., Copper Metal–Organic Framework Nanoparticles Stabilized with Folic Acid Improve Wound Healing in Diabetes. *ACS Nano* **2018**, *12* (2), 1023-1032.
15. Levin, A.; Hakala, T. A.; Schnaider, L.; Bernardes, G. J. L.; Gazit, E.; Knowles, T. P. J., Biomimetic peptide self-assembly for functional materials. *Nature Reviews Chemistry* **2020**, *4* (11), 615-634.
16. Lu, H.; Lutz, H.; Roeters, S. J.; Hood, M. A.; Schäfer, A.; Muñoz-Espí, R.; Berger, R.; Bonn, M.; Weidner, T., Calcium-Induced Molecular Rearrangement of Peptide Folds Enables Biomineralization of Vaterite Calcium Carbonate. *J. Am. Chem. Soc.* **2018**, *140* (8), 2793-2796.
17. Misra, R.; Rudnick-Glick, S.; Adler-Abramovich, L., From Folding to Assembly: Functional Supramolecular Architectures of Peptides Comprised of Non-Canonical Amino Acids. **2021**, *21* (8), 2100090.
18. Pelay-Gimeno, M.; Glas, A.; Koch, O.; Grossmann, T. N., Structure-Based Design of Inhibitors of Protein–Protein Interactions: Mimicking Peptide Binding Epitopes. **2015**, *54* (31), 8896-8927.
19. Radvar, E.; Azevedo, H. S., Supramolecular Peptide/Polymer Hybrid Hydrogels for Biomedical Applications. **2019**, *19* (1), 1800221.
20. Shen, Y.; Levin, A.; Kamada, A.; Toprakcioglu, Z.; Rodriguez-Garcia, M.; Xu, Y.; Knowles, T. P. J., From Protein Building Blocks to Functional Materials. *ACS Nano* **2021**, *15* (4), 5819-5837.
21. Hoque, J.; Sangaj, N.; Varghese, S., Stimuli-Responsive Supramolecular Hydrogels and Their Applications in Regenerative Medicine. **2019**, *19* (1), 1800259.
22. Knight, A. S.; Larsson, J.; Ren, J. M.; Bou Zerdan, R.; Seguin, S.; Vrahas, R.; Liu, J.; Ren, G.; Hawker, C. J., Control of Amphiphile Self-Assembly via Bioinspired Metal Ion Coordination. *J. Am. Chem. Soc.* **2018**, *140* (4), 1409-1414.
23. Nakai, T.; Hirakura, T.; Sakurai, Y.; Shimoboji, T.; Ishigai, M.; Akiyoshi, K., Injectable Hydrogel for Sustained Protein Release by Salt-Induced Association of Hyaluronic Acid Nanogel. **2012**, *12* (4), 475-483.
24. Zhao, F.; Ma, M. L.; Xu, B., Molecular hydrogels of therapeutic agents. *Chemical Society Reviews* **2009**, *38* (4), 883-891.
25. Fichman, G.; Gazit, E., Self-assembly of short peptides to form hydrogels: Design of building blocks, physical properties and technological applications. *Acta biomater.* **2014**, *10* (4), 1671-1682.
26. Marchesan, S.; Styan, K. E.; Easton, C. D.; Waddington, L.; Vargiu, A. V., Higher and lower supramolecular orders for the design of self-assembled heterochiral tripeptide hydrogel biomaterials. *J. Mater. Chem. B* **2015**, *3* (41), 8123-8132.
27. Ren, P.; Li, J.; Zhao, L.; Wang, A.; Wang, M.; Li, J.; Jian, H.; Li, X.; Yan, X.; Bai, S., Dipeptide Self-assembled Hydrogels with Shear-Thinning and Instantaneous Self-healing Properties Determined by Peptide Sequences. *ACS Appl. Mater. Interfaces* **2020**, *12* (19), 21433-21440.
28. Xu, F.; Liu, J.; Tian, J.; Gao, L.; Cheng, X.; Pan, Y.; Sun, Z.; Li, X., Supramolecular Self-Assemblies with Nanoscale RGD Clusters Promote Cell Growth and Intracellular Drug Delivery. *ACS Appl. Mater. Interfaces* **2016**, *8* (44), 29906-29914.
29. Stephanopoulos, N.; Ortony, J. H.; Stupp, S. I., Self-Assembly for the Synthesis of Functional Biomaterials. *Acta Mater.* **2013**, *61* (3), 912-930.

30. Habibi, N.; Kamaly, N.; Memic, A.; Shafiee, H., Self-assembled peptide-based nanostructures: Smart nanomaterials toward targeted drug delivery. *Nano Today* **2016**, *11* (1), 41-60.
31. Liu, J.; Sun, Z.; Yuan, Y.; Tian, X.; Liu, X.; Duan, G.; Yang, Y.; Yuan, L.; Lin, H.-C.; Li, X., Peptide Glycosylation Generates Supramolecular Assemblies from Glycopeptides as Biomimetic Scaffolds for Cell Adhesion and Proliferation. *ACS Appl. Mater. Interfaces* **2016**, *8* (11), 6917-6924.
32. Vargiu, A. V.; Iglesias, D.; Styan, K. E.; Waddington, L. J.; Easton, C. D.; Marchesan, S., Design of a hydrophobic tripeptide that self-assembles into amphiphilic superstructures forming a hydrogel biomaterial. *Chem. Commun.* **2016**, *52* (35), 5912-5915.
33. Zhan, J.; Cai, Y.; Ji, S.; He, S.; Cao, Y.; Ding, D.; Wang, L.; Yang, Z., Spatiotemporal Control of Supramolecular Self-Assembly and Function. *ACS Appl. Mater. Interfaces* **2017**, *9* (11), 10012-10018.
34. D'Souza, A.; Yoon, J. H.; Beaman, H.; Gosavi, P.; Lengyel-Zhand, Z.; Sternisha, A.; Centola, G.; Marshall, L. R.; Wehrman, M. D.; Schultz, K. M.; Monroe, M. B.; Makhlynets, O. V., Nine-Residue Peptide Self-Assembles in the Presence of Silver to Produce a Self-Healing, Cytocompatible, Antimicrobial Hydrogel. *ACS Appl. Mater. Interfaces* **2020**, *12* (14), 17091-17099.
35. Webber, M. J.; Appel, E. A.; Meijer, E. W.; Langer, R., Supramolecular biomaterials. *Nature materials* **2016**, *15* (1), 13-26.
36. Yi, X.; He, J.; Wang, X.; Zhang, Y.; Tan, G.; Zhou, Z.; Chen, J.; Chen, D.; Wang, R.; Tian, W.; Yu, P.; Zhou, L.; Ning, C., Tunable Mechanical, Antibacterial, and Cytocompatible Hydrogels Based on a Functionalized Dual Network of Metal Coordination Bonds and Covalent Crosslinking. *ACS Appl. Mater. Interfaces* **2018**, *10* (7), 6190-6198.
37. Roberts, D.; Keeling, R.; Tracka, M.; van der Walle, C. F.; Uddin, S.; Warwicker, J.; Curtis, R., Specific Ion and Buffer Effects on Protein-Protein Interactions of a Monoclonal Antibody. *Molecular Pharmaceutics* **2015**, *12* (1), 179-193.
38. Abul-Haija, Y. M.; Scott, G. G.; Sahoo, J. K.; Tuttle, T.; Ulijn, R. V., Cooperative, ion-sensitive co-assembly of tripeptide hydrogels. *Chem Commun (Camb)* **2017**, *53* (69), 9562-9565.
39. Sharma, P.; Kaur, H.; Roy, S., Inducing Differential Self-Assembling Behavior in Ultrashort Peptide Hydrogelators Using Simple Metal Salts. *Biomacromolecules* **2019**, *20* (7), 2610-2624.
40. Singh, N.; Kumar, M.; Miravet, J. F.; Ulijn, R. V.; Escuder, B., Peptide-Based Molecular Hydrogels as Supramolecular Protein Mimics. **2017**, *23* (5), 981-993.
41. Zhao, J.; Wang, J., Uncovering the Sensitivity of Amide-II Vibration to Peptide-Ion Interactions. *J. Phys. Chem. B* **2016**, *120* (36), 9590-9598.
42. Ji, W.; Yuan, C.; Zilberzwige-Tal, S.; Xing, R.; Chakraborty, P.; Tao, K.; Gilead, S.; Yan, X.; Gazit, E., Metal-Ion Modulated Structural Transformation of Amyloid-Like Dipeptide Supramolecular Self-Assembly. *ACS Nano* **2019**, *13* (6), 7300-7309.
43. Cardoso, A. Z.; Mears, L. L. E.; Cattoz, B. N.; Griffiths, P. C.; Schweins, R.; Adams, D. J., Linking micellar structures to hydrogelation for salt-triggered dipeptide gelators. *Soft Matter* **2016**, *12* (15), 3612-3621.
44. Chen, L.; McDonald, T. O.; Adams, D. J., Salt-induced hydrogels from functionalised-dipeptides. *RSC Adv.* **2013**, *3* (23), 8714-8720.
45. Basak, S.; Singh, I.; Banerjee, A.; Kraatz, H.-B., Amino acid-based amphiphilic hydrogels: metal ion induced tuning of mechanical and thermal stability. *RSC Adv.* **2017**, *7* (24), 14461-14465.
46. Fortunato, A.; Mba, M. J. G., Metal Cation Triggered Peptide Hydrogels and Their Application in Food Freshness Monitoring and Dye Adsorption. **2021**, *7*.
47. Parmar, A. S.; Xu, F.; Pike, D. H.; Belure, S. V.; Hasan, N. F.; Drzewiecki, K. E.; Shreiber, D. I.; Nanda, V., Metal Stabilization of Collagen and de Novo Designed Mimetic Peptides. *Biochemistry* **2015**, *54* (32), 4987-4997.
48. LeBruin, L. T.; Banerjee, S.; O'Rourke, B. D.; Case, M. A., Metal ion-assembled micro-collagen heterotrimers. **2011**, *95* (11), 792-800.

49. Frantz, C.; Stewart, K. M.; Weaver, V. M., The extracellular matrix at a glance. *J. Cell Sci.* **2010**, *123* (Pt 24), 4195-4200.
50. Toksoz, S.; Mammadov, R.; Tekinay, A. B.; Guler, M. O., Electrostatic effects on nanofiber formation of self-assembling peptide amphiphiles. *Journal of colloid and interface science* **2011**, *356* (1), 131-7.
51. Meyer, M., Processing of collagen based biomaterials and the resulting materials properties. *Biomed Eng Online* **2019**, *18* (1), 24-24.
52. Wang, Y.; Zhang, W.; Gong, C.; Liu, B.; Li, Y.; Wang, L.; Su, Z.; Wei, G., Recent advances in the fabrication, functionalization, and bioapplications of peptide hydrogels. *Soft Matter* **2020**, *16* (44), 10029-10045.
53. Wei, G.; Su, Z.; Reynolds, N. P.; Arosio, P.; Hamley, I. W.; Gazit, E.; Mezzenga, R., Self-assembling peptide and protein amyloids: from structure to tailored function in nanotechnology. *Chem. Soc. Rev.* **2017**, *46* (15), 4661-4708.
54. Zhang, W.; Yu, X.; Li, Y.; Su, Z.; Jandt, K. D.; Wei, G., Protein-mimetic peptide nanofibers: Motif design, self-assembly synthesis, and sequence-specific biomedical applications. *Progress in Polymer Science* **2018**, *80*, 94-124.
55. Korolev, N.; Lyubartsev, A. P.; Rupprecht, A.; Nordenskiöld, L., Competitive binding of Mg<sup>2+</sup>, Ca<sup>2+</sup>, Na<sup>+</sup>, and K<sup>+</sup> ions to DNA in oriented DNA fibers: experimental and Monte Carlo simulation results. *Biophys. J.* **1999**, *77* (5), 2736-49.
56. Katz, A. K.; Glusker, J. P.; Beebe, S. A.; Bock, C. W., Calcium Ion Coordination: A Comparison with That of Beryllium, Magnesium, and Zinc. *J. Am. Chem. Soc.* **1996**, *118* (24), 5752-5763.
57. McKeehan, W. L.; Ham, R. G., Calcium and magnesium ions and the regulation of multiplication in normal and transformed cells. *Nature* **1978**, *275* (5682), 756-758.
58. Roy, S.; Javid, N.; Sefcik, J.; Halling, P. J.; Ulijn, R. V., Salt-Induced Control of Supramolecular Order in Biocatalytic Hydrogelation. *Langmuir* **2012**, *28* (48), 16664-16670.
59. Yu, H.; Noskov, S. Y.; Roux, B., Two mechanisms of ion selectivity in protein binding sites. **2010**, *107* (47), 20329-20334.
60. Pal, V. K.; Jain, R.; Roy, S., Tuning the Supramolecular Structure and Function of Collagen Mimetic Ionic Complementary Peptides via Electrostatic Interactions. *Langmuir* **2020**, *36* (4), 1003-1013.
61. Dulbecco, R.; Freeman, G., Plaque production by the polyoma virus. *Virology* **1959**, *8* (3), 396-7.
62. André, I.; Kesvatera, T.; Jönsson, B.; Akerfeldt, K. S.; Linse, S., The role of electrostatic interactions in calmodulin-peptide complex formation. *Biophys. J.* **2004**, *87* (3), 1929-1938.
63. Einspahr, H.; Bugg, C. E. J. M. I. B. S., Crystal structure studies of calcium complexes and implications for biological systems. **1984**, *17*, 51-97.
64. Permyakov, E., *Metalloproteomics*. John Wiley & Sons: 2009; Vol. 2.
65. Okur, H. I.; Kherb, J.; Cremer, P. S., Cations Bind Only Weakly to Amides in Aqueous Solutions. *J. Am. Chem. Soc.* **2013**, *135* (13), 5062-5067.
66. Laverty, G.; McCloskey, A. P.; Gilmore, B. F.; Jones, D. S.; Zhou, J.; Xu, B., Ultrashort Cationic Naphthalene-Derived Self-Assembled Peptides as Antimicrobial Nanomaterials. *Biomacromolecules* **2014**, *15* (9), 3429-3439.
67. Sharma, P.; Kaur, H.; Roy, S. J. A. B. S.; Engineering, Designing a Tenascin-C-Inspired Short Bioactive Peptide Scaffold to Direct and Control Cellular Behavior. *ACS Biomater. Sci. Eng.* **2019**, *5* (12), 6497-6510.
68. Biancalana, M.; Makabe, K.; Koide, A.; Koide, S., Molecular mechanism of thioflavin-T binding to the surface of beta-rich peptide self-assemblies. *J. Mol. Biol.* **2009**, *385* (4), 1052-1063.
69. Sabaté, R.; Lascu, I.; Saupe, S. J., On the binding of Thioflavin-T to HET-s amyloid fibrils assembled at pH 2. *J Struct Biol* **2008**, *162* (3), 387-96.
70. Liang, G.; Xu, K.; Li, L.; Wang, L.; Kuang, Y.; Yang, Z.; Xu, B., Using Congo red to report intracellular hydrogelation resulted from self-assembly of small molecules. *Chem. Commun.* **2007**, (40), 4096-4098.

71. Mandal, D.; Nasrolahi Shirazi, A.; Parang, K., Self-assembly of peptides to nanostructures. *Org. Biomol. Chem.* **2014**, *12* (22), 3544-3561.
72. Yuan, C.; Ji, W.; Xing, R.; Li, J.; Gazit, E.; Yan, X., Hierarchically oriented organization in supramolecular peptide crystals. *Nature Reviews Chemistry* **2019**, *3* (10), 567-588.
73. Yuan, C.; Levin, A.; Chen, W.; Xing, R.; Zou, Q.; Herling, T. W.; Challa, P. K.; Knowles, T. P. J.; Yan, X., Nucleation and Growth of Amino Acid and Peptide Supramolecular Polymers through Liquid-Liquid Phase Separation. **2019**, *58* (50), 18116-18123.
74. Ghasemi-Mobarakeh, L.; Prabhakaran, M. P.; Tian, L.; Shamirzaei-Jeshvaghani, E.; Dehghani, L.; Ramakrishna, S., Structural properties of scaffolds: Crucial parameters towards stem cells differentiation. *World J Stem Cells* **2015**, *7* (4), 728-744.
75. Yan, C.; Pochan, D. J., Rheological properties of peptide-based hydrogels for biomedical and other applications. *Chem. Soc. Rev.* **2010**, *39* (9), 3528-3540.
76. Xing, Q.; Yates, K.; Vogt, C.; Qian, Z.; Frost, M. C.; Zhao, F., Increasing Mechanical Strength of Gelatin Hydrogels by Divalent Metal Ion Removal. *Scientific Reports* **2014**, *4* (1), 4706.
77. Jain, R.; Roy, S., Controlling Neuronal Cell Growth through Composite Laminin Supramolecular Hydrogels. *ACS Biomaterials Science & Engineering* **2020**, *6* (5), 2832-2846.
78. Sharma, P.; Pal, V. K.; Roy, S., An overview of latest advances in exploring bioactive peptide hydrogels for neural tissue engineering. *Biomaterials Science* **2021**, *9* (11), 3911-3938.
79. Zeng, L.; Song, M.; Gu, J.; Xu, Z.; Xue, B.; Li, Y.; Cao, Y., A Highly Stretchable, Tough, Fast Self-Healing Hydrogel Based on Peptide-Metal Ion Coordination. *Biomimetics (Basel)* **2019**, *4* (2), 36.
80. Lallemand, M.; Yu, L.; Cai, W.; Rischka, K.; Hartwig, A.; Haag, R.; Hugel, T.; Balzer, B. N., Multivalent non-covalent interactions lead to strongest polymer adhesion. *Nanoscale* **2022**, *14* (10), 3768-3776.
81. Zhang, W.; He, H.; Tian, Y.; Gan, Q.; Zhang, J.; Yuan, Y.; Liu, C., Calcium ion-induced formation of  $\beta$ -sheet/-turn structure leading to alteration of osteogenic activity of bone morphogenetic protein-2. *Scientific Reports* **2015**, *5* (1), 12694.
82. Jayawarna, V.; Richardson, S. M.; Hirst, A. R.; Hodson, N. W.; Saiani, A.; Gough, J. E.; Ulijn, R. V., Introducing chemical functionality in Fmoc-peptide gels for cell culture. *Acta Biomater* **2009**, *5* (3), 934-43.
83. Balion, Z.; Sipailaite, E.; Stasyte, G.; Vailionyte, A.; Mazetyte-Godiene, A.; Seskeviciute, I.; Bernotiene, R.; Phopase, J.; Jekabsone, A., Investigation of Cancer Cell Migration and Proliferation on Synthetic Extracellular Matrix Peptide Hydrogels. **2020**, *8*.
84. Kaur, H.; Sharma, P.; Patel, N.; Pal, V. K.; Roy, S., Accessing Highly Tunable Nanostructured Hydrogels in a Short Ionic Complementary Peptide Sequence via pH Trigger. *Langmuir* **2020**, *36* (41), 12107-12120.
85. Kaur, H.; Roy, S., Designing aromatic N-cadherin mimetic short-peptide-based bioactive scaffolds for controlling cellular behaviour. *J. Mater. Chem. B* **2021**, *9* (29), 5898-5913.
86. Versaevel, M.; Grevesse, T.; Gabriele, S., Spatial coordination between cell and nuclear shape within micropatterned endothelial cells. *Nat. Commun.* **2012**, *3* (1), 671.
87. Katsetos, C. D.; Del Valle, L.; Legido, A.; de Chadarevian, J. P.; Perentes, E.; Mörk, S. J., On the neuronal/neuroblastic nature of medulloblastomas: a tribute to Pio del Rio Hortega and Moises Polak. *Acta neuropathologica* **2003**, *105* (1), 1-13.
88. Katsetos, C. D.; Herman, M. M.; Mörk, S. J., Class III beta-tubulin in human development and cancer. *Cell motility and the cytoskeleton* **2003**, *55* (2), 77-96.
89. Pal, V. K.; Jain, R.; Sen, S.; Kailasam, K.; Roy, S., Designing nanofibrillar cellulose peptide conjugated polymeric hydrogel scaffold for controlling cellular behaviour. *Cellulose* **2021**, *28* (16), 10335-10357.
90. Liang, C.-C.; Park, A. Y.; Guan, J.-L., In vitro scratch assay: a convenient and inexpensive method for analysis of cell migration in vitro. *Nat. Protoc.* **2007**, *2* (2), 329-333.
91. Kotch, F. W.; Raines, R. T., Self-assembly of synthetic collagen triple helices. *Proc Natl Acad Sci U S A* **2006**, *103* (9), 3028-33.

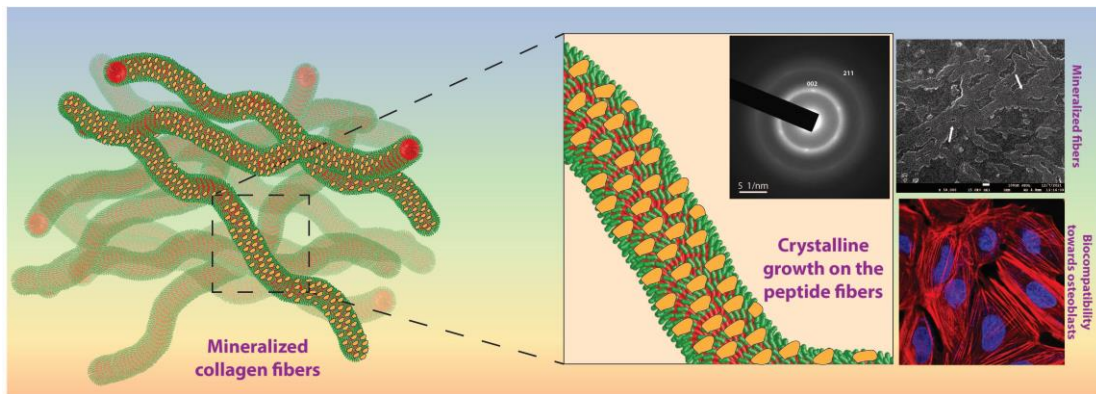
92. Kaur, H.; Jain, R.; Roy, S., Pathway-Dependent Preferential Selection and Amplification of Variable Self-Assembled Peptide Nanostructures and Their Biological Activities. *ACS Applied Materials & Interfaces* **2020**, *12* (47), 52445-52456.



# **Chapter 5**

Cooperative calcium phosphate deposition on collagen-based peptide nanofibers for application in bone tissue engineering





**Positively charged collagen inspired peptide has been fabricated, which served as template for the crystalline growth of hydroxyapatite crystals**



## 5.1 Introduction

Over the years, Nature has experienced a rigorous process of natural selection, which allowed organisms to develop the most facile and accessible routes for synthesizing functional materials, which has gained immense interest in the field of material chemistry and other related areas.<sup>1-8</sup> The advancements in this field not only provide insights into how mineral-rich tissues are being created *in-vivo* but also serve as a source of inspiration for the development of advanced materials based on similar principles.<sup>9-15</sup> Mineralized tissues, such as bone and teeth, have hierarchical structures, which upon damage or loss, require grafts to aid the healing process.<sup>16, 17</sup> Moreover, with significant disadvantages of limited supplies, discomfort at the harvest site, immunogenicity, and transmission of infectious diseases, there is a growing need for developing synthetic grafts for the treatment of damaged or diseases mineralized tissues.<sup>18, 19</sup> Because of the hierarchical complexity of these mineralized tissues, fabrication of ideal synthetic grafts that can fulfill the requirement is still a challenge for material scientists. Mimicking the biological process to construct these mineralized structures has gained attention in the recent years.<sup>20-24</sup> A close consideration of the structural composition of bone has revealed that a complex combination of calcium phosphate in the form of the mineral hydroxyapatite, as well as collagenous fibrous proteins, make up bone and teeth. Bone is a unique tissue with extraordinary mechanical and biological properties due to its intricate nanostructure.<sup>25, 26</sup> It has been realized that the extracellular matrix, particularly connective tissues with their collagen fibers, is crucial for force transmission and maintenance of the bone structure.<sup>27</sup> The natural process of mineralization is a complex phenomenon that takes place within the extracellular matrix that involves several intermolecular interactions.<sup>28</sup> In-depth studies have revealed that among other collagen types, type I collagen is the most prevalent matrix protein involved in the mineralization process.<sup>29-31</sup>

Collagen has been identified as the primary constituent of bone and represents more than 90% of the organic matrix.<sup>32, 33</sup> There are several shreds of evidence, which suggest that osteogenesis imperfecta is caused due to affected quality of the collagen protein.<sup>33, 34</sup> The collagen matrix in bone is very densely packed and is arranged in a trabecular and cortical array.<sup>35-37</sup> Extensive studies were carried out to reveal that acidic non-collagenous proteins (NCPs) found in the extracellular matrix, such as osteopontin, dentin, fetuin etc., that play a key role in mineralization by nucleating Hap

crystallization or modulating crystal growth.<sup>38</sup> Owing to the recognition of the crucial role of collagen protein in the mineralization of bone, collagen fibril mineralization has been effectively replicated *in vitro* utilizing the poly-aspartic acid (pAsp) as the replacement for NCPs.<sup>39, 40</sup> Nudelman et. al., demonstrated the replacement of non-collagenous protein with the use of pAsp in the *in vitro* mineralization model, which unfolds the fact that the highly negatively charged nanocluster binds preferentially to the highly positive charged a-band of collagen fibrils located at their gap zones.<sup>41, 42</sup>

Controlled deposition of calcium phosphate minerals in a synthetic system can be achieved by allowing intrafibrillar mineralization, which further provides guidance for the development of next-generation materials for promoting hard tissue regeneration.<sup>43,</sup>

<sup>44</sup> In several attempts, researchers have used self-assembling long peptides, peptide-polymers or protein-polymer conjugates to mimic the mineralization of collagen fibrils.<sup>39, 45-50</sup> In a report by Hartgerink et. al., a peptide amphiphile was allowed to self-assemble via pH switch method. The design of the peptide amphiphile allows it to cross-link with another fiber, which further allows the mineralization of hydroxyapatite to develop composite materials.<sup>51</sup> In a study by Yuping et. al., a self-assembling peptide based on elastin-like recombinants (ELRs) showed intrafibrillar mineralization.<sup>43</sup> The study has established that the spatial confinement formed by continuum  $\beta$ -spiral structure in an unperturbed fibrillar structure is critical to inducing intrafibrillar mineralization rather than electrostatic interactions or bioactive sequence in the recombiner composition.<sup>43</sup> In another report by Li et. al., a novel oligopeptide amphiphile was used to mineralize enamel, where the oligopeptides were allowed to self-assemble into the nanofibrous structure and immersed into the solution of calcium chloride and sodium hypophosphate to evaluate its tendency of mineralization.<sup>52</sup> In a similar line, a synergistic effect of BMP-7 derived peptide and cyclic RGD peptide for the mineralization and regulating the osteogenic differentiation was investigated.<sup>53</sup> Apart from short self-assembling peptides derived from different non-collagenous proteins, natural collagen has also been used to understand the mineralization process.<sup>54,</sup>  
<sup>55</sup> Hoyer et. al., presented the biomimetic mineralization of salmon-derived collagen, where the porous scaffold from mineralized salmon collagen was prepared by controlled freeze-drying and cross-linking, which can be used to induce adhesion of human mesenchymal stem cells (hMSCs) to show osteogenic differentiation.<sup>56</sup> Beniash group has shown the bioinspired synthesis of the mineralized collagen fibers, where

they showed the importance of non-collagenous protein in regulating the biomineralization of natural collagen molecules.<sup>39</sup> As a substitute for the non-collagenous proteins (NCPs), they have opted for pAsp, as an analog of the NCPs. The study further revealed that collagen alone does not affect the mineral formation, and it needs the NCPs to initiate the mineralization. This mechanism of collagen mineralization can lead to the development of novel bioinspired nanostructures materials.<sup>39</sup> Hence, it would be extremely intriguing if the synthetically designed short collagen-inspired peptide sequence could be explored to get an in-depth understanding of the mechanism of biomineralization.

To this end, it was increasingly recognized that a suitable approach might be applied to discover and develop a smaller molecular domain from the original protein, which can achieve the complex hierarchical structure and bio-functional properties of native collagen protein. Significant efforts have been made to develop the specific functional motifs inspired by this natural protein.<sup>57, 58</sup> In this direction, we have adapted a simplistic approach to designing the shortest collagen-inspired peptide sequence and explored its potential to induce a biomineralization process in order to fabricate next-generation biomaterial for bone tissue regeneration. The literature studies in this direction so far have revealed the fact that the peptide derivatives utilized in this direction were inspired by several proteins that include elastin, fibronectin, BMPs etc. However, collagen, which is an integral part of the native ECM was yet to be explored in this direction. Hence, we attempted to use our novel short collagen-inspired sequence towards biomineralization, which bears significant relevance to the native ECM protein. With this objective in mind, an interesting study by Gibson group has indicated the formation of small aggregates upon the addition of the calcium and phosphorous salts to the pAsp adsorbed collagen fiber.<sup>16</sup> A clear indication of physical entrapment of the calcium phosphate complex was observed, which led to the formation of globular mineral deposits. Taking advantage of the fundamental knowledge and prior investigation, we have used the positively charged peptide (NapFFGKO) to induce the mineralization. It has been interesting to note that the positively charged pentapeptide (2-Naphthoxyacetic acid-Phe-Phe-Gly-Lys-Hyp) has demonstrated its ability to get dissolved and propensity to self-assemble at physiological pH. The positively charged peptide nanofibers can facilitate the adsorption of the negatively charged amino acids onto the fiber surface through charge pair interactions, which can act as the nucleation

sites for the mineralization. Interestingly, the simultaneous addition of glutamic acid (Glu), calcium chloride ( $\text{CaCl}_2$ ), and disodium phosphate ( $\text{Na}_2\text{HPO}_4$ ) may allow the even adsorption of glutamic acid on the fiber surface, where the nucleation of calcium phosphate may be initiated. A time-dependent AFM analysis revealed the crystalline growth of hydroxyapatite on peptide fibers as crystal deposits. The extent of mineralization was found to increase with time and resulting in an increase in fiber width and also converting the transparent solution into an opaque solution. Upon incubation, the mineralized fibers led to the evolution of more stronger peptide fiber mesh, which resulted in the hierarchical self-assembly leading to hydrogelation of the solution. Thus, this finding signifies that all the companion substrates must interact in a synergistic manner in solution to mineralize the collagen fibers. Furthermore, the mineralized peptide amphiphile can further enhance its scope to be explored as an effective scaffold for inducing mineralization or osteogenic differentiation.

## **5.2 Results and discussions**

### **5.2.1 Design and mineralization of peptide nanofiber**

The positively charged collagen inspired peptide (NapFFGKO) was synthesized following a standard solid phase peptide synthesis method as described earlier in chapter 3. In this work, our focus was to explore the ability of these short collagen inspired peptide to induce mineralization, where the peptide fibers can serve as the substrate for the nucleation site for the hydroxyapatite growth. To this end, it is well known that the peptide/protein rich in carboxylate group facilitates the mineralization process to a significant extent.<sup>59</sup> It was evident from the literature studies that the acidic amino acids may induce the formation of intrafibrillar calcium carbonate, especially the poly(aspartic acid) has been shown to stimulate the calcium phosphate and calcium carbonate intrafibrillar deposition.<sup>60-62</sup> More specifically, it was observed that the collagen fibrils containing pAsp sites, showed prenucleation cluster of calcium phosphate mineralization.<sup>42</sup> Following the charge driver prenucleation process, we utilized the negatively charged collagen inspired peptide (NapFFGDO) for the mineralization process. The peptide was dissolved in water (physiological pH) and the mixture was kept for 12 hours to incubate, where the peptides tend to self-assemble and form peptide nanofibers. In order to check the mineralization capability, the incubated peptide solution was mixed with salt solutions of  $\text{CaCl}_2 \cdot 2\text{H}_2\text{O}$  (5mM) and  $\text{Na}_2\text{HPO}_4$

(2.5mM). After addition of salt solutions to this negatively charged peptide solution, instant precipitation was observed and small aggregated structures were observed in the AFM analyses (Figure 5.1a).

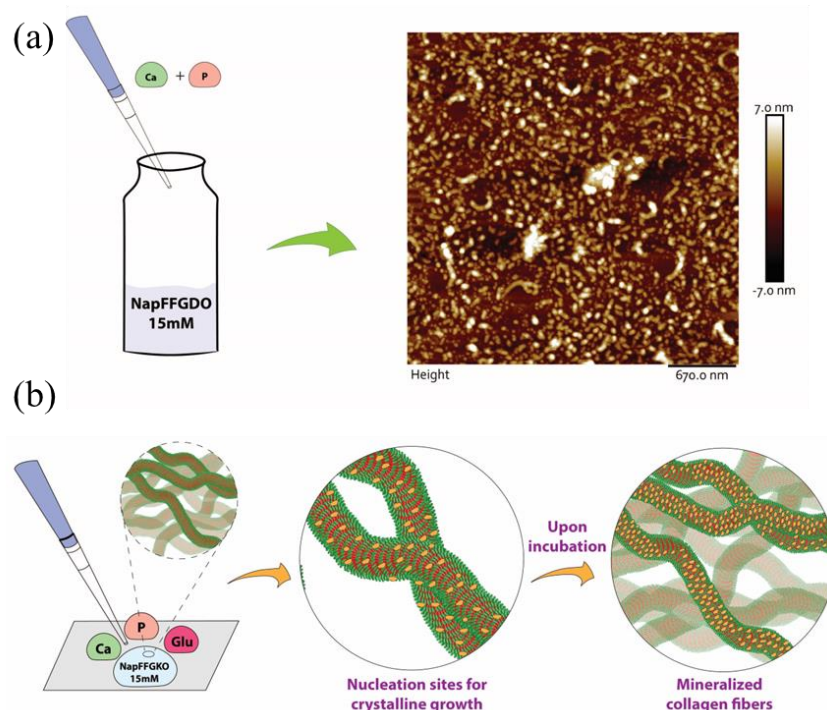


**Figure 5.1** Schematic representation of the mineralization induced by negatively charged collagen inspired peptide and the AFM image showing the fibers getting precipitated upon interaction.

The peptide fibers containing aspartate moieties embedded into the structure interacts with the calcium phosphate complex and develop a strong interaction, which results in the globular mineral deposits. This strong interaction among the aspartate and calcium phosphate disrupts the peptide fiber structure and results into precipitate (Figure 5.1). This pronounced difference in morphology produced with negatively charged peptide indicates that either the aspartate moiety trapped into the calcium phosphate complexation (physical interaction) or has been chemically interacted to the Ca/P complex.<sup>16</sup> To overcome this challenge, we have utilized an unique approach that involves the use of the oppositely charged collagen inspired peptide (NapFFGKO), which will display positive charge on the surface and thus making the exposed surface available for adsorption of the negatively charged amino acid peptide residue through

electrostatic interaction. Thus, this strategy of utilizing ionic complementary interactions can overcome the challenges faced by the negatively charged short collagen inspired peptide. The peptide was dissolved in water (physiological pH) and the mixture was kept for 12 hours to incubate, where the peptides tend to self-assemble and form peptide nanofibers. In order to check the mineralization capability, the incubated peptide solution was mixed with salt solutions of  $\text{CaCl}_2 \cdot 2\text{H}_2\text{O}$  (5mM),  $\text{Na}_2\text{HPO}_4$  (2.5mM) and Glutamic acid (Glu). The negatively charged amino acid (Glu) gets adsorbed on the peptide surface and provides the nucleation site for the binding of Ca/P mineralized crystals. The peptide solution (15mM) upon the addition of calcium and phosphorous salts with glutamic acid were kept to incubate to induce nucleation of hydroxyapatite crystals on the peptide fibers (Figure 5.1b). The crystalline growth of calcium phosphate on to the peptide fibers can be correlated with the peptide solution turning opaque with time and also with sol to gel conversion. Furthermore, these finding suggested the unique behaviour of the negatively charged amino acid (Glu) as it plays a crucial role in inducing the mineralization process. These results also suggested that  $\text{CaCl}_2$ ,  $\text{Na}_2\text{HPO}_4$ , and Glu should interact in solution phase and work cooperatively to nucleate the crystalline growth.

### **5.2.2 Microscopic evidence of mineralized nanofibers**

To further confirm the growth of hydroxyapatite crystals onto the peptide fibers, we carried out several microscopic investigations (AFM, SEM, and TEM) to visualize the peptide fibers with hydroxyapatite crystals deposited on the surface. We envisioned that the calcium phosphate deposition on peptide fibers would be initiated at the surface, which provides the nucleation site for crystalline growth. Atomic Force Microscopy (AFM) was used to understand the structural variation that occurred at the nanoscale after the addition of metal salts onto the Glu adsorbed peptide fibers. The collagen fiber (NapFFGKO) alone showed the formation of long peptide fibers after 12 hours of incubation (Figure 5.2a). After the addition of  $\text{CaCl}_2$ ,  $\text{Na}_2\text{HPO}_4$ , and Glu to this incubated solution, the samples for AFM were prepared at different time points to visualize the growth of hydroxyapatite crystals.

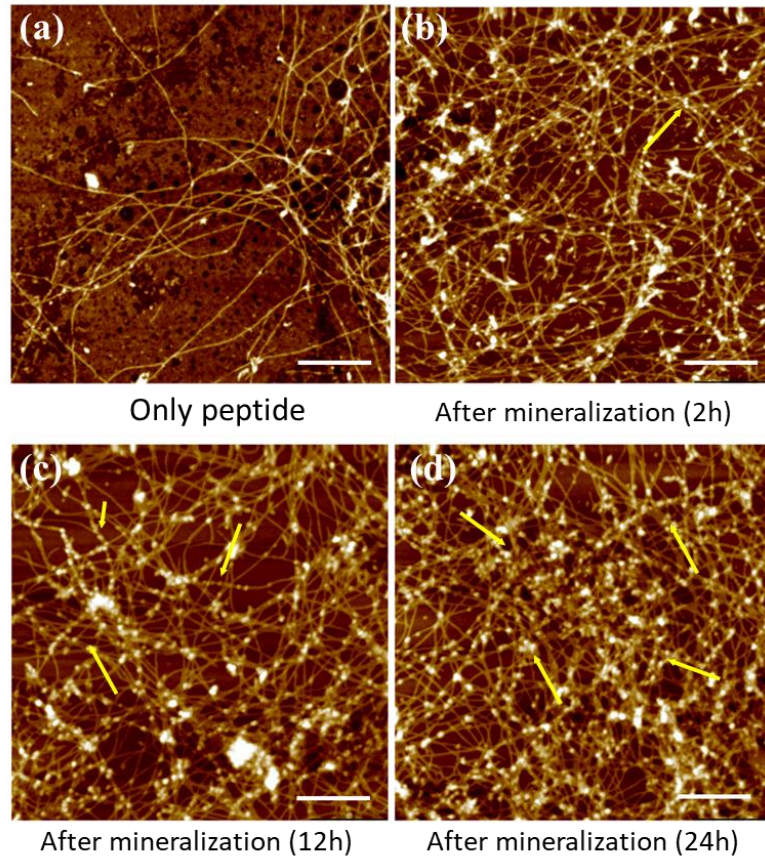


**Figure 5.2** Atomic Force Microscopy (AFM) of the peptide amphiphile (a) NapFFGKO and (b-d) time dependent growth of the hydroxyapatite crystals on the peptide fibers (2, 12, and 24 hour). Arrow indicates the deposition of calcium phosphate nodules on the peptide fibers. Scale bar 500 nm.

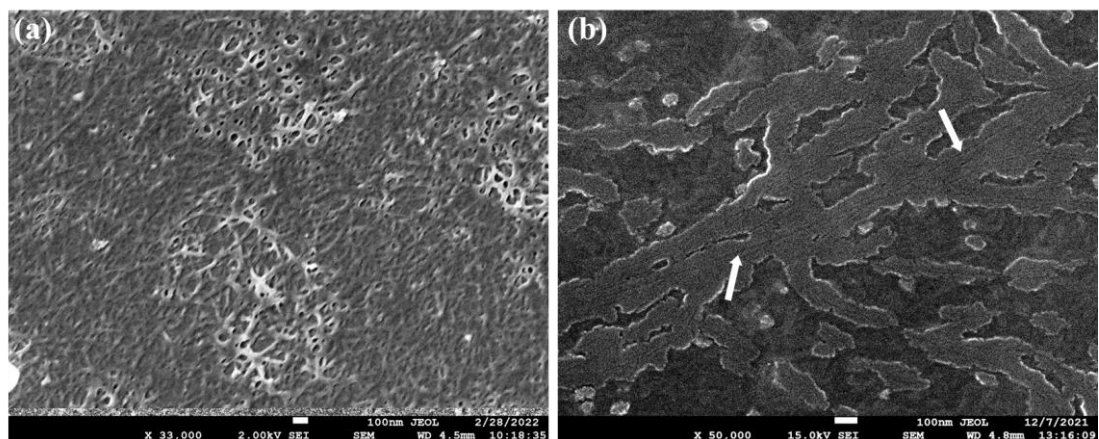


**Figure 5.3** Field Emission Scanning Electron Microscopy (FE-SEM) of the peptide amphiphile (a) NapFFGKO and (b) NapFFGKO+Glu+Ca+P (mineralized peptide) after 10 days of incubation. Arrow indicates the peptide nanofibers and crystalline growth of the hydroxyapatite all over the peptide surface. Scale bar 100nm

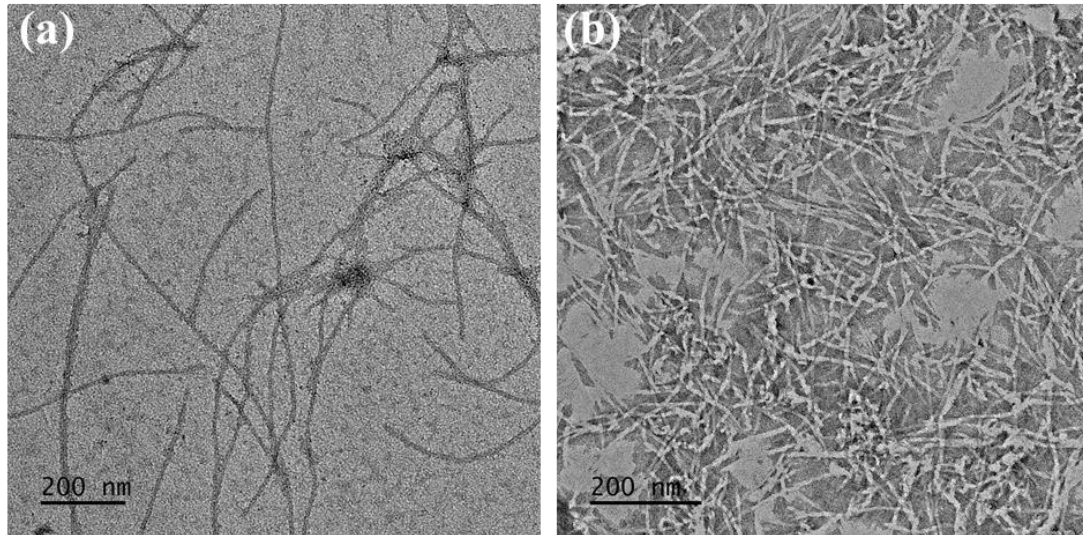


**Figure 5.4** Transmission Electron Microscopy (TEM) images of peptide amphiphile (a) NapFFGKO and (b) NapFFGKO+Glu+Ca+P (mineralized peptide). Scale bar 200 nm

It is evident from the AFM analysis that with increasing time from 2 hours, to 12 hours, and to 24 hours (Figure 5.2 b,c,d) the crystalline growth on the peptide fibers was enhanced and at the end of 24 hours, the whole surface of the peptide fibers was covered with the mineralized crystals (Figure 5.2d). This observation can be correlated with few other studies where growth of hydroxyapatite crystal has been demonstrated on the ionic peptide fibers (RADA16, MDG-1).<sup>63-65</sup> Further, the peptide fibers were monitored via Field Emission Scanning Electron Microscopy (FE-SEM), long fiber-like structure were observed. The peptide fiber of ~20nm width were observed in figure 5.3a and after mineralization the diameter of the peptide fiber increases, due to the deposition of hydroxyapatite crystals on the peptide fibers. Figure 5.3b showed the individual fibers with thick layer of crystalline growth of hydroxyapatite crystals on it after 10 days of incubation.

The arrows in the image indicates the peptide backbone and as observed in AFM study, most of the region of the exposed surface of peptide fibers were covered by the crystals after 24 hours of incubation. Even, after 10 days of incubation the crystalline growth carries on and results into a thick layer of hydroxyapatite crystals, which gives rise to 100-150 nm thick width. It is clearly evident from the AFM and FE-SEM study that the peptide fiber is serving as the template for the crystalline growth of the hydroxyapatite crystals. Similar results were observed in the Transmission Electron Microscopy

(TEM) images, which revealed that the clean peptide fibers were allowing the growth of the grow hydroxyapatite crystals on the peptide surface (Figure 5.4a,b).

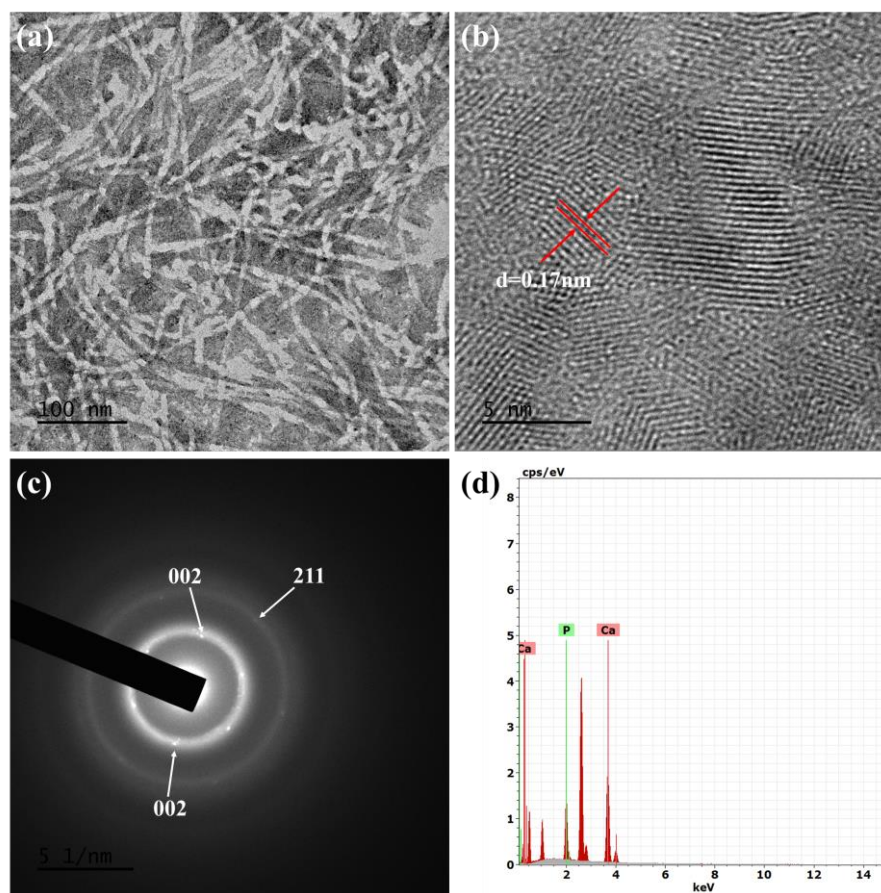


**Figure 5.5** Microscopic examination of the mineralized peptide fibers (a) mineralized NapFFGKO after 7 days, (b) HR-TEM images of the mineralized peptide showing different lattice fringes, (c) Selected Area Electron Diffraction (SAED) pattern of the mineralized peptide matches with the preliminary hydroxyapatite crystals, and (d) Energy Dispersive X-ray Analysis (EDX) of the mineralized peptide showed the presence of metal ions deposited on the peptide fibers and the ratio of calcium to phosphorous has been determined, and the value is  $\sim 1.7$ .

Interestingly, the (High-Resolution Transmission Electron Microscopy) HR-TEM and (Selected Area Electron Diffraction) SAED patterning of the mineralized fibers revealed a broad diffraction pattern, which indicates the mineral particles lack long-range crystallographic order, suggesting the amorphous nature of the material (Figure 5.5 c). The SAED pattern showed major fractions of the mineralized peptide fibers has a typical preliminary hydroxyapatite diffraction pattern with distinct (002), (211) reflections.

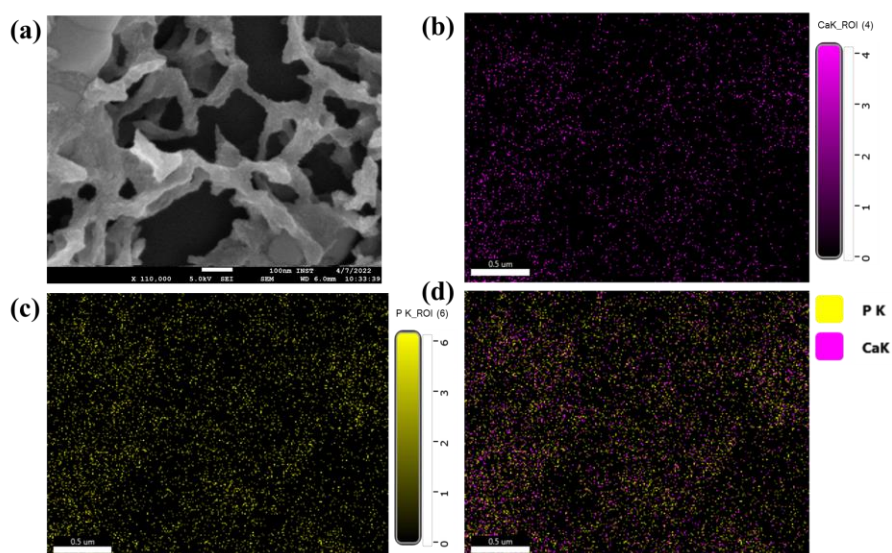


**Figure 5.6** Elemental mapping of the mineralized fibers using energy dispersive X-Ray spectroscopy showing the percentage ratio of the calcium and phosphorous in the mineralized fibers. (a) Mineralized peptide fibers, (b) elemental mapping for the calcium present in the selected area (c) Elemental mapping of the phosphorus, present in the mineralized fiber and (d) is the merged channel of the calcium and phosphate.

To further understand the deposition process of the mineralized phase of collagen fibers, we performed energy dispersive X-Ray analysis (EDX). The EDX data revealed the presence of Ca and P element in the sample (Figure 5.5d). The EDX data showed the molar ratio of  $\sim 1.7$  after 7 days of incubation in the mineralized fiber. The Ca/P ratio matches with the stoichiometric (1.67) for hydroxyapatite and suggests the peptide fibers are able to induce the growth of the crystalline structures of hydroxyapatite on the surface (Figure 5.6).

### 5.2.3 Spectroscopic analysis

To further confirm the presence of calcium phosphate crystals on the peptide fibers, we carried out several spectroscopic examinations. The FTIR spectrum showed the featured peak of amide-II at  $1640\text{ cm}^{-1}$ , suggesting the presence of beta-sheet-like structures in the peptide fibers. The major peaks of  $\text{PO}_4^{3-}$  moieties, including the bending modes<sup>66</sup> at  $610\text{ cm}^{-1}$  ( $\nu_4$ ) and asymmetric stretching vibrations at  $1022$  and  $1128\text{ cm}^{-1}$  ( $\nu_3$ ) (Figure 5.7a) were evident in the recorded FT-IR spectra. In this context, the peak at  $1424\text{ cm}^{-1}$  may be contributed to  $\text{CO}_3^{2-}$ .<sup>67</sup> Furthermore, Raman spectroscopy was utilized to evaluate the formation of hydroxyapatite crystals. Hydroxyapatite crystals have a characteristic peak in the Raman spectrum at  $472\text{ cm}^{-1}$  for  $\nu_2$  bending P-

O-P,  $\nu_4$  bending at 563 and 603  $\text{cm}^{-1}$ ,  $\nu_1$  stretching at 960  $\text{cm}^{-1}$ , and  $\nu_3$  stretching at 1035-1045  $\text{cm}^{-1}$ .<sup>68, 69</sup>

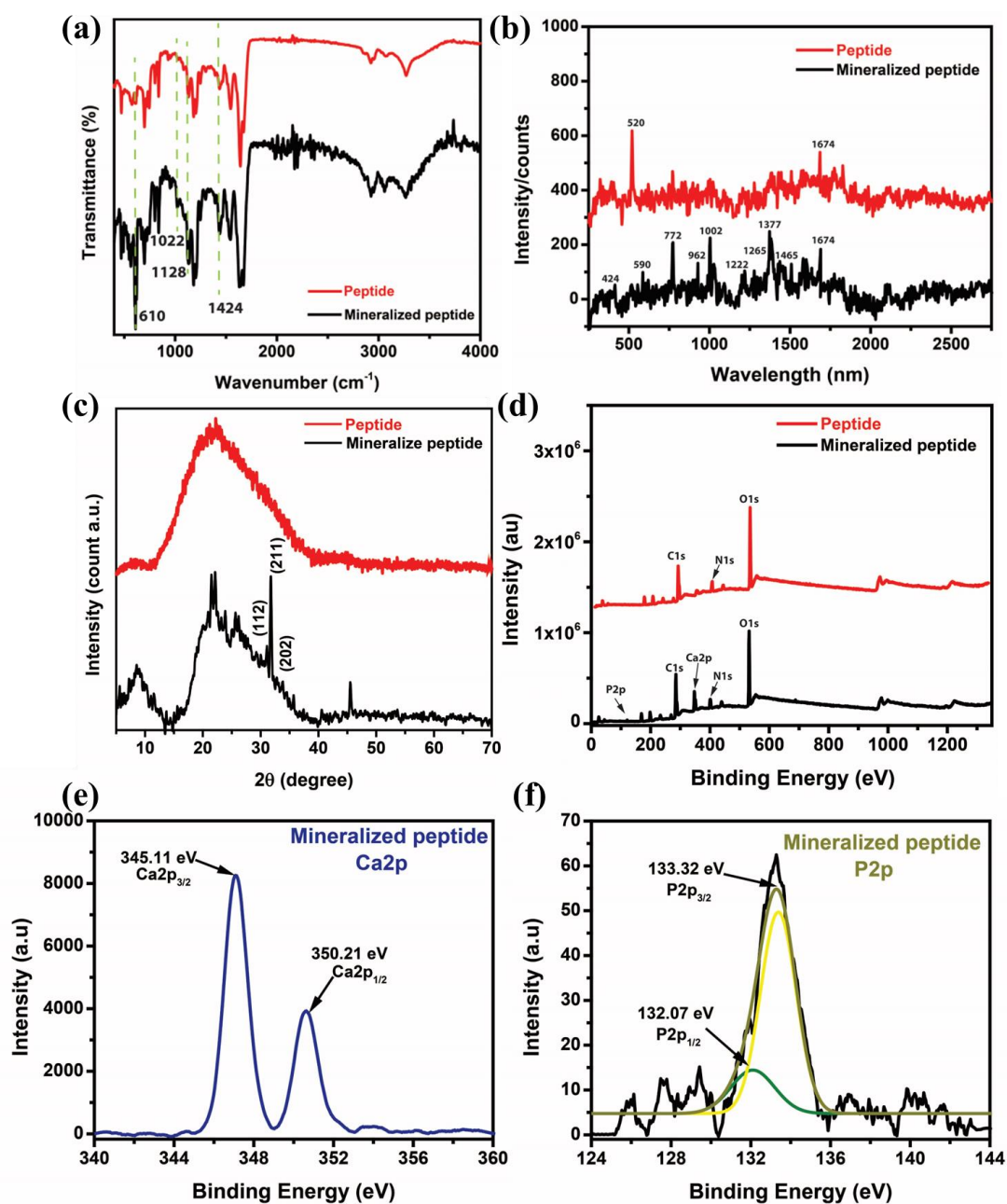


**Figure 5.7** Spectroscopic analyses of the mineralized peptide: (a) FTIR spectra, (b) Raman spectra, (c) XRD pattern, (d) X-Ray photoelectron spectrum showing the preliminary growth of the hydroxyapatite crystals on the peptide fibers, (e) Photoelectron spectra of the Ca2p of the mineralized fibers, and (f) a deconvoluted peak of phosphorous showing both the transition state at binding energy 132.07 and 133.32 eV.

Further, the peptide amphiphile showed its characteristic peak at  $\sim 1674\text{ cm}^{-1}$ , which is attributed to the presence of  $\beta$  sheet-like structures.<sup>70</sup> Furthermore, the mineralized fibers were analyzed to evaluate the presence of  $\text{PO}_4$  groups. Peaks at  $424\text{ cm}^{-1}$ ,  $590\text{ cm}^{-1}$ , and  $962\text{ cm}^{-1}$  correspond to the  $\nu_2$ ,  $\nu_4$ ,  $\nu_1$  stretching of the P-O-P groups, respectively (Figure 5.7b). Most of the signature peaks of the hydroxyapatite were found to be present in the mineralized collagen fibers, suggesting the successful crystalline deposition of hydroxyapatite on the collagen fibers. Furthermore, an X-ray diffraction study was used to investigate the effect of mineralization on the peptide fiber, which may be correlated to the finding from other spectroscopic analyses. The mineralized fiber was analyzed through XRD, and the diffraction pattern of the peptide and the mineralized peptide showed a broad peak ranging from  $15$  to  $30^\circ$ . Thus, the pattern revealed the amorphous nature of the peptide nanofibers (Figure 5.7c).

The XRD results are in accordance with the reference XRD pattern for the preliminary growth of the hydroxyapatite crystals, while most of the major peaks and minor peaks can probably be ascribed to the various substituted hydroxyapatites.<sup>54</sup> The diffraction peaks at  $2\theta = 31.1, 31.7, 33.8$  corresponds to the (112), (211), and (202) planes of hydroxyapatite, respectively. To further understand the structural features of the mineralized peptide fibers, we performed X-ray photoelectron spectroscopy, which identifies the core level shifts of the characteristic peaks of Ca, P, N, and C between the control and mineralized peptide fibers (Figure 5.7d). The presence of  $\text{Ca}2p_{1/2}$  at binding energy  $350.21\text{ eV}$  and  $\text{Ca}2p_{3/2}$  at binding energy  $345.11\text{ eV}$  in the photoelectron spectra of mineralized peptide fiber evidently demonstrate the presence of hydroxyapatite crystals (Figure 5.7e).<sup>71</sup> Whereas, a peak of phosphorous with relatively less intensity at  $133.32\text{ eV}$  was observed, which upon deconvolution showed the splitting into two spectral peaks of  $\text{P}2p_{1/2}$  ( $132.07\text{ eV}$ ) and  $\text{P}2p_{3/2}$  ( $133.32\text{ eV}$ ) (Figure 5.7f). Both the photoelectron spectra of calcium and phosphorus were found to significantly match with the inorganic component of bone tissue i.e., hydroxyapatite.<sup>72</sup> The increment in the  $\text{N}1s$  intensity at binding energy  $399.48\text{ eV}$  of the mineralized peptide is clear evidence of mineralization onto the peptide fibers. Furthermore, in figure S4a, the deconvoluted spectra of  $\text{N}1s$  showed the presence of two peaks, which upon mineralization, shows an enhancement in their intensities. In the  $\text{N}1s$  spectrum, the spectra peak at  $401.25\text{ eV}$  corresponds to the main signal ( $\text{N}_1$ ), whereas a small peak at  $399.48\text{ eV}$  corresponds to the unprotonated nitrogen of the peptide backbone.<sup>73</sup> The

increased intensity of the spectral peak of N1s at 399.48 eV is due to the protonated nitrogen of lysine (Figure 5.8b), which upon formation of the ionic bond with the carboxylate group of glutamate, displayed an enhancement in the intensity. Furthermore, C1s signal of the self-assembled peptide showed three distinct peaks upon deconvolution (Figure 5.8 c & d). In particular, C<sub>1</sub> peak at binding energy 284.39 eV was evident, which corresponds to C-C carbon of the amino acid side chains, while C<sub>2</sub> peak at binding energy 285.88 eV corresponds to the C-N carbon of the peptide chain, and C<sub>3</sub> peak at binding energy 288.16 eV indicates to N-C=O peptide bond carbons of the self-assembling peptide.<sup>73</sup>

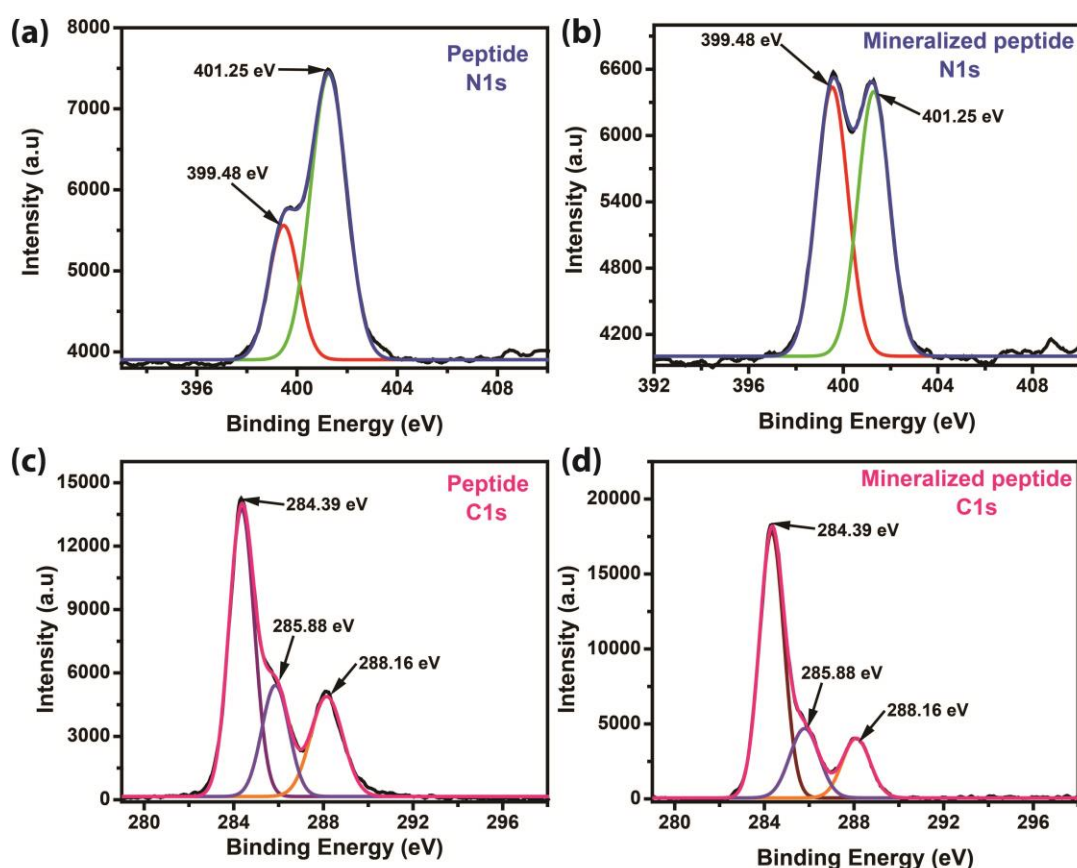


**Figure 5.8** Deconvoluted XPS spectra for the control peptide and mineralized peptide nanofibers: (a & b) spectral difference in the N1s among control and mineralized peptide. (c & d) intensity difference in the C1s spectra between the control peptide and mineralized peptide.

**5.2.3.1 Small angle X-Ray scattering analysis (SAXS).** Small angle scattering was performed to get further insight into the structural differences between the control peptide and mineralized peptide. SAXS is a well-known technique to determine the

structural variation within materials in the nanoscale regime.<sup>74, 75</sup> The electron microscopic analyses and the AFM study have clearly demonstrated the crystalline growth of hydroxyapatite crystals on the peptide fiber, which was evident in the respective images displaying enhanced diameter of the mineralized fibers. The SAXS intensity profile of the control peptide and the mineralized peptide also showed a distinct difference in their scattering profiles (Figure 5.9a). The scattering data were fitted by Debye model<sup>76</sup> and Schulz-Zimm model, which considers scattering from monodisperse and polydisperse Gaussian polymers, respectively.<sup>77</sup> Guinier approximation is usually applicable at a very low scattering angle, which allows the calculation of the radius of gyration ( $R_g$ ) and intensity at zero angles ( $q=0$ ).<sup>78</sup> The radius of gyration ( $R_g^2$ ) represents the average electron density-weighted square distance from the center of the object.<sup>79</sup> The  $R_g$  (radius of gyration) of the control peptide was found to be 9.23 nm from the shape-independent model fit, and for the mineralized peptide, it was found to be 14.41 nm. Hence, it was very interesting to draw the connection that the increased  $R_g$  value of the mineralized fiber has resulted in the clear deposition of hydroxyapatite on the peptide fiber, which further leads to the increased  $R_g$  value of the mineralized fibers (Table 5.1).

**Table 5.1** Investigation of the biophysical properties of the control peptide and mineralized peptide scaffolds calculated via model dependent and model independent methods to obtain the  $R_g$  value.

	$R_g$ (nm) (Guinier Model)	Model fit $R_g$ (nm) (Debye Model)	Radius (nm)
<b>NapFFGKO</b>	8.92 ±0.11	9.23±0.22	15.605
<b>Mineralized NapFFGKO</b>	14.03±0.14	14.41±0.13	29.035

#### 5.2.4 Mechanical strength analysis

Another interesting phenomenon was evident at the nanoscale owing to the deposition of hydroxyapatite crystals on the peptide fiber surface. It was evident that owing to crystalline growth on the peptide fiber surface, the peptide solution has been converted into hydrogel with time, which may be beneficial for cellular adhesion, growth, and

proliferation. Hence, it is crucial to investigate the mechanical strength of the mineralized fibers for the development of advanced scaffolds for biological applications.

#### 5.2.4.1 Rheological measurements

To this direction, the mechanical stiffness of the mineralized peptide fiber was investigated using a dynamic oscillatory rheology experiment.<sup>80</sup> The linear viscoelastic range (LVE) was calculated from the oscillatory amplitude sweep, which showed the gamma value of 0.1% with which frequency sweep was performed.

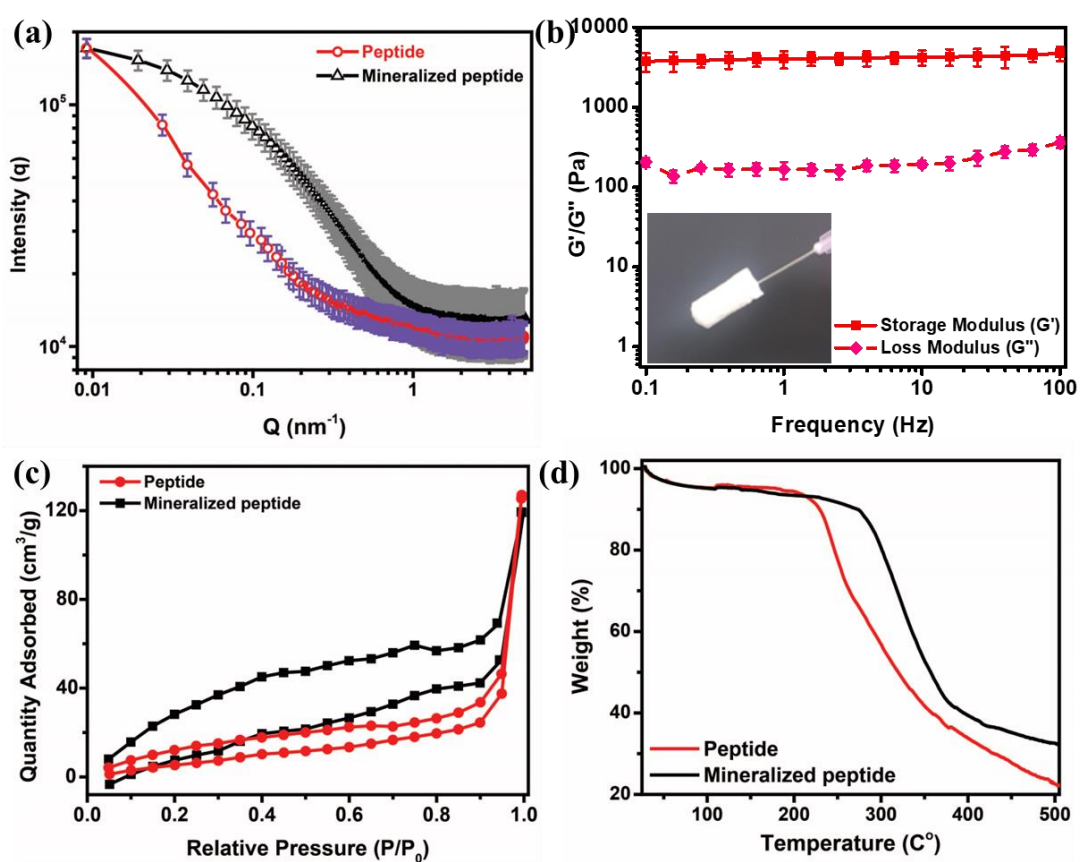


**Figure 5.9** (a) The intensity profile of the control peptide and the mineralized peptide was obtained via small angle X-ray scattering (SAXS) analysis. (b) Rheological analyses of the mineralized peptide: Frequency sweep analysis of the oscillatory rheological investigation of the hydrogel (Image inset) digital image of the lyophilized hydrogel with intact integrity due to the mineralization. (c) Nitrogen adsorption-desorption isotherm to determine the structural nature of the mineralized hydrogels, and

(d) Thermogravimetric analysis of the dried sample of control and mineralized peptide fibers.

An enhancement in storage moduli than loss moduli is indicative of the solid-like behaviour of the material.<sup>81</sup> The mineralized hydrogel contains 15mM of the peptide (NapFFGKO), which is significantly lower than the minimum gelation concentration (MGC) of the peptide itself that was reported to be 30 mM as indicated in our earlier studies.<sup>81</sup> The mineralized peptide showed a storage modulus of 3-4 KPa (Figure 5.9b), which is similar to the modulus of the peptide hydrogel at 30 mM concentration at basic pH (9.0).<sup>81</sup> However, at 15mM, the peptide itself remained in the solution state owing to the charge repulsion and lack of sufficient intermolecular interactions at this sub-gelation concentration at physiological pH. The addition of biologically relevant salts into the peptide solution was found to induce the hydrogelation, which resulted in the hydrogel of mechanical stiffness of 3-4 KPa, which is similar to the mechanical stiffness at 15 mM concentration of the peptide, as indicated in our another study.<sup>82</sup> This inspires us to calculate the individual stiffness of the peptide fibers with enhanced width and crystalline growth on the peptide fiber.

#### *5.2.4.2 Peak force quantitative nano-mechanics via AFM*

Recently, AFM has emerged as one of the most suitable advanced techniques measure the local elasticity quantitatively because of its ability to image and point out a single molecule.<sup>83</sup> The quantitative analysis of the mechanical stiffness of the peptide fibers was assessed via peak force tapping (PFT), which is a scanning technique where a force-distance curve was generated each time the probe touched the sample in a vertical motion. The loading force was set to make an indent into the sample and thus give a realistic elastic modulus and deformation response. The value of the Young's modulus of peptide nanofiber (NapFFGKO) was estimated to be in the order of  $1.2 \pm 0.1$  GPa. In contrast, Young's modulus of mineralized peptide fiber showed enhancement in the strength up to  $3.2 \pm 0.2$  GPa (Figure 5.10). The force-distance curve was used to calculate Young's modulus of the material at a specific point on the captured image. The enhancement in the mechanical stiffness after mineralization is a clear indication of the crystalline growth on the peptide fiber, which provides improved mechanical strength and also leads to the hydrogelation of the mineralized peptide fibers.

#### **5.2.5 Structural analysis of the mineralized peptide**

The hydrogel formed in the presence of the mineralized fibers showed improved structural integrity on freeze drying (image inset figure 5.9b), which motivated us to examine their structural parameter via Brunauer-Emmet-Teller (BET) and Thermogravimetric Analysis (TGA). The estimation of the porous nature of the mineralized peptide hydrogel was investigated from the nitrogen adsorption-desorption isotherm acquired using BET. The N<sub>2</sub> adsorption-desorption isotherm analysis of the mineralized peptide hydrogel suggests the presence of macroporous structures. Interestingly, a shift of the hysteresis loop towards a lower  $P/P_0$  value is indicative of a reduction in the pore size (Figure 5.9c). A decrease in the pore size of the mineralized peptide can be considered as evidence of the crystalline growth on the peptide fibers, which was further calculated from the BJH equation. The pore size was found to be 17.2 nm within peptide itself, which was reduced to 6.51 nm upon mineralization. Such decrease in pore size was further accompanied by enhancement in surface area of 42.5 m<sup>2</sup>/g for mineralized fibers in comparison to the peptide itself with 23.2 m<sup>2</sup>/g surface area. This difference in the pore size of the mineralized fibers also leads to the increased pore volume and surface area of the mineralized hydrogels (Table 5.2).

**Table 5.2** Structural analysis (pore diameter, pore volume, surface area) of the mineralized nanofibers obtained using BET isotherm.

	<b>Pore diameter (nm)</b>	<b>Pore volume (cc/g)</b>	<b>Surface area (m<sup>2</sup>/g)</b>
<b>NapFFGKO</b>	17.20	0.31	23.21
<b>Mineralized NapFFGKO</b>	6.51	0.43	42.53

The inclusion of mineralization among peptide fibers further aids in the enhancement in the structural support of the hydrogel. The dried mass of control peptide fiber and mineralized peptide fiber were assessed for their weight loss via TGA. The TGA graph of the control peptide fibers and mineralized peptide fiber showed a clear difference in the weight loss percentage (Figure 5.9d). At around 100 °C, a slight weight loss of ~10% was observed in both samples, which is suggestive of the loss of water molecule that was adsorbed onto the surface. Furthermore, the native peptide fibers showed a gradual decrease in the weight percentage starting at around 213 °C, which was

followed by a total weight loss of ~80% at 500 °C. Interestingly, the mineralized peptide showed a gradual decrease in weight percentage at around 280 °C, which was followed by a maximum weight loss of ~70 % at 500 °C. Hence, a relatively lesser extent of weight loss of the mineralized hydrogel as assessed quantitatively by TGA is suggestive of the incorporation of the inorganic composites (hydroxyapatite) on the peptide fibers, which provide the mechanical stiffness and sufficient integrity to the material with enhanced thermal stability.

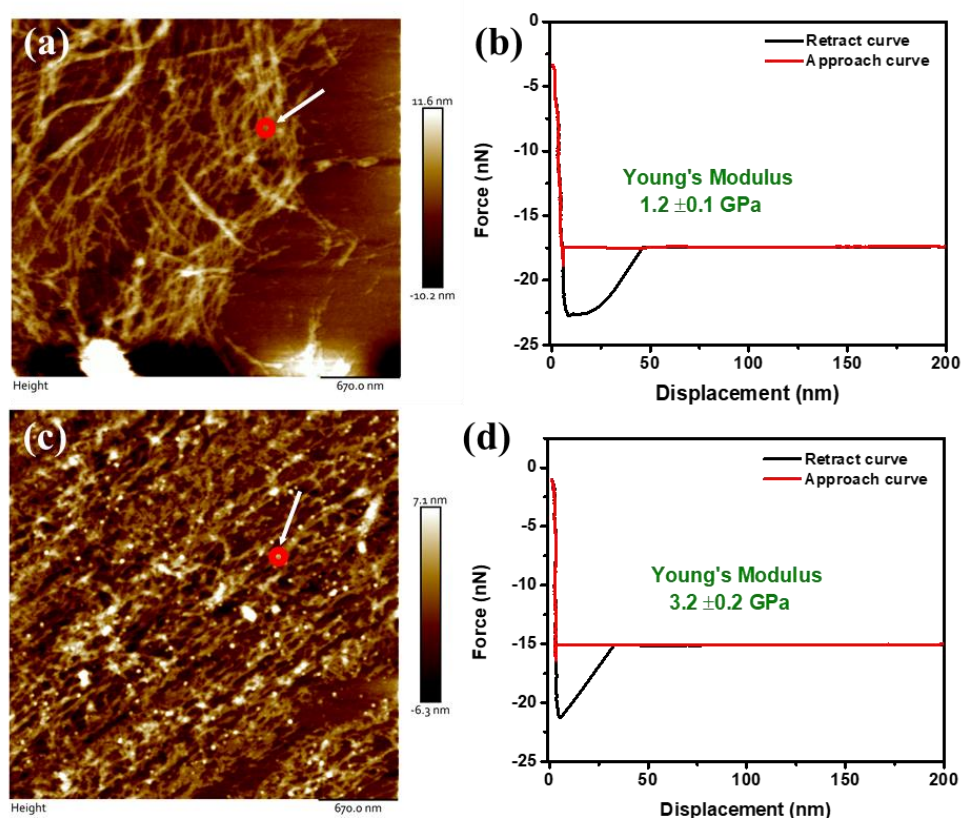


**Figure 5.10** AFM image of the (a) peptide nanofiber and the (c) mineralized fiber in contact mode and their respective FD curve (b & d). The loading force was set to make indent into the sample and thus give realistic elastic modulus and deformation response.

## 5.2.6 Cell studies

### 5.2.6.1 Biocompatibility studies of the mineralized peptide nanofibers

At this point, we were curious to check the biocompatible nature of the collagen inspired peptide and effect of mineralized peptide on two different osteoblast cell lines (7F2 and Saos-2). The biocompatible nature of the peptide alone and the mineralized peptide was assessed via MTT reduction assay. As reported in our earlier study, the

positively charged peptide showed compatible nature (~100%) with the fibroblast cells at different peptide concentrations.<sup>81</sup> Interestingly, the positively charged peptide showed similar compatible nature with osteoblast cells as well up to 7 days of incubation.

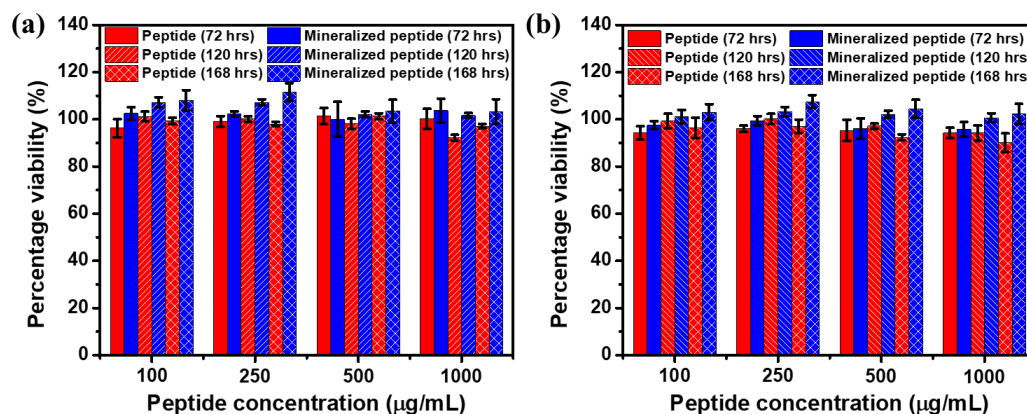


**Figure 5.11** Cytocompatibility assay of the peptide nanofibers (alone and mineralized) with osteoblast cells (a) 7F2 and (b) Saos-2 cells treated with peptide concentration ranging from 100 to 1000  $\mu\text{g mL}^{-1}$  via MTT assay.

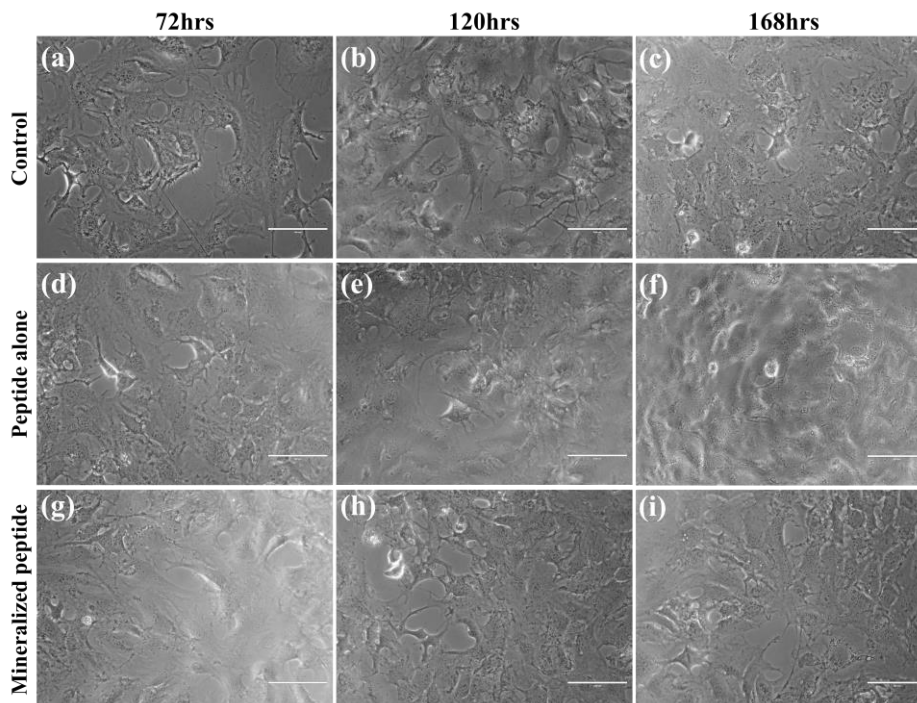


**Figure 5.12** Bright field images of the 7F2 osteoblast cells after incubation with the mineralized peptide fibers at their respective days 3, 5, and 7 days. (a-c) control, (d-f) peptide alone, and (g-i) mineralized peptide. Scale bar 100  $\mu\text{m}$

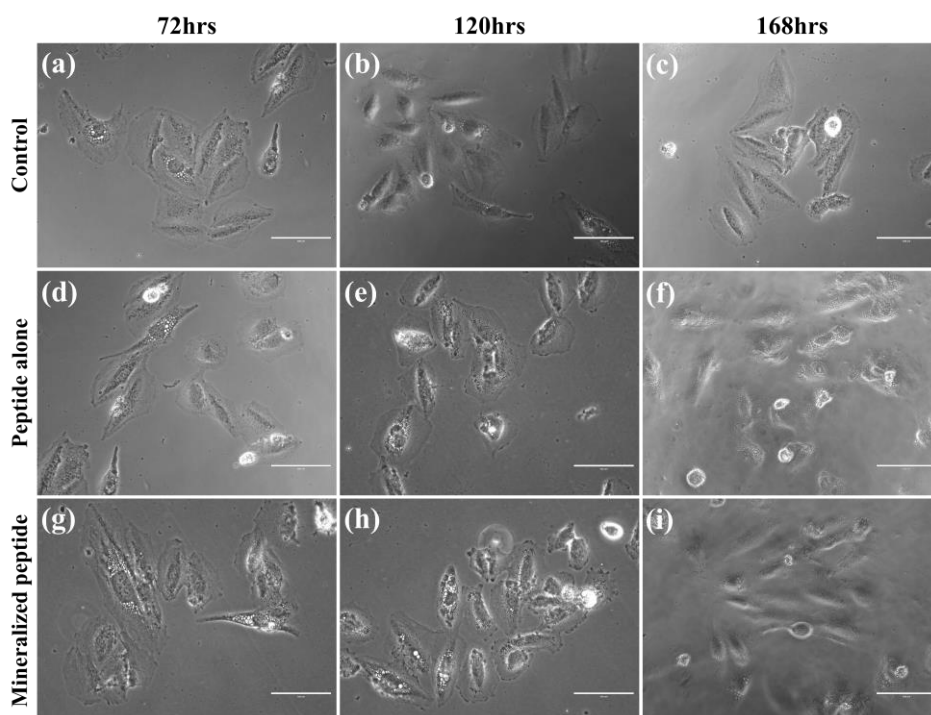


**Figure 5.13** Bright field images of the Saos-2 osteoblast cells after incubation with the mineralized peptide fibers at their respective days 3, 5, and 7 days. (a-c) control, (d-f) peptide alone, and (g-i) mineralized peptide. Scale bar 100  $\mu\text{m}$

The results further indicated that the mineralized peptide show a small enhancement in slight enhanced cellular viability in comparison to the peptide alone, suggesting the benefits of the crystalline growth of hydroxyapatite over the period of time (Figure 5.12). The mineralized peptide was found to be exceptionally compatible and up to 7 days of examination and the similar was observed in the bright field images of the treated cells (Figure 5.12 & 5.13).

#### 5.2.6.2 Cellular adhesion (2D cell culture)

In order to assess the potential of the developed biomaterial for promoting cellular studies, 2D culture was done and the cellular adhesion of the cells were assessed for live-dead assay via the 2D cell culture studies. Live-dead staining assay on 2D construct was carried out to evaluate the potential of the proposed construct for its adhesion ability towards cells. In order to support the cellular adhesion, the peptide should be able to provide the required peptide nanofibrous network, which helps in the adhesion and growth of the cells.

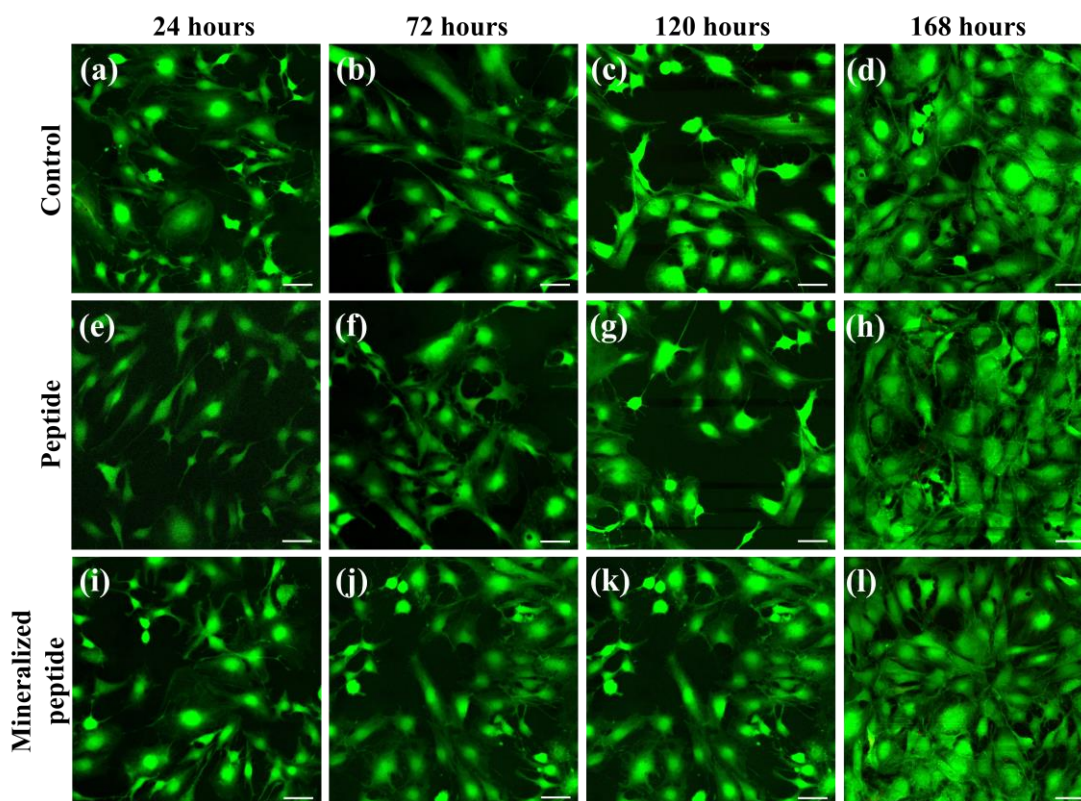


**Figure 5.14** Assessment of cellular adhesion ability on 2D matrix of peptide nanofibers with osteoblast cells (7F2) via Live-Dead staining. CLSM images with live cells stained with FDA and dead cells with PI at different time intervals of 24, 72, 120, and 168 hours, (a-d) control, (e-h) NapFFGKO peptide alone, and (i-l) mineralized NapFFGKO peptide. Scale bar 50  $\mu$ m.

In this regard, it has been revealed that, in addition to chemical functionality, the fiber shape and mechanical strength of peptide hydrogel network play an important role in developing cellular adhesion properties.<sup>84</sup> A thin layer of peptide nanofibers were coated and air-dried on the coverslip, which was further UV sterilized before seeding cells on the peptide fibers. An evident increase in the cell population of both the osteoblasts (7F2 and Saos-2) can be observed in the images showing the compatible nature of the matrix and the similar was observed up to 7 days of incubation. More importantly, the mineralized fibers were shown crystalline growth on the peptide fibers, which leads to the increased fiber dimension and also increases the density of the fiber network. This increased fiber density provides more stronger scaffold for the cells to adhere and grow, as observed at the end of 7<sup>th</sup> day in both the cells lines (Figure 5.14 & 5.15). Thus, 2D studies showed a similar pattern of cellular adhesion as observed in the biocompatibility assay of the mineralized peptide fibers.

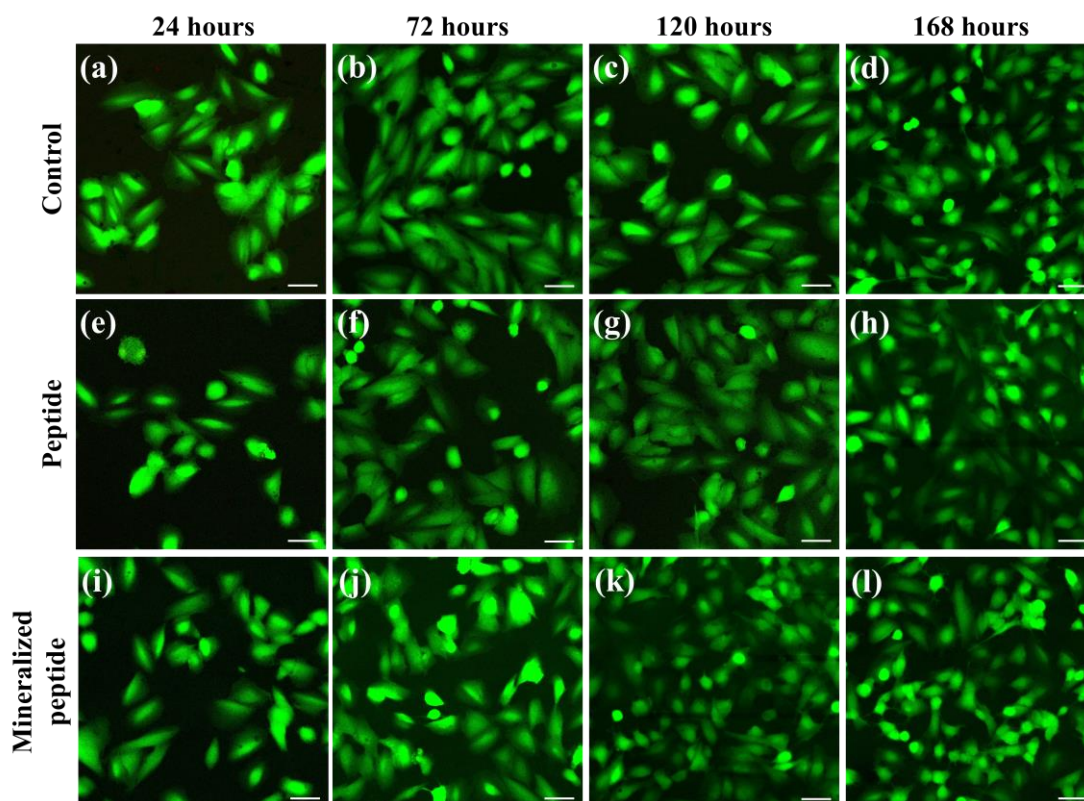


**Figure 5.15** Assessment of cellular adhesion ability on 2D matrix of peptide nanofibers with osteoblast cells (Saos-2) via Live-Dead staining. CLSM images with live cells stained with FDA and dead cells with PI at different time intervals of 24, 72, 120, and 168 hours, (a-d) control, (e-h) NapFFGKO peptide alone, and (i-l) mineralized NapFFGKO peptide. Scale bar 50  $\mu\text{m}$ .

### 5.2.6.3 Assessment of cellular proliferation

The cytotoxicity assay revealed the biocompatible nature of the positively charged peptide as shown earlier.<sup>81</sup> Further, the mineralized fibers showed a more appropriate microenvironment for the cells as indicated in the cytotoxicity assay. 2D culture studies also demonstrated the cell supportive nature of the mineralized fibers. To investigate the potential of the mineralized fibers to develop novel tailored matrix for inducing osteogenesis, we used Alamar Blue assay to quantify the cellular viability and proliferation ability. Alamar Blue is a nontoxic, water-soluble dye that can be used to monitor the cells over a long period of time for cellular proliferation. The proliferation study was carried out for 7 days and the cells were found to proliferate up to 7 days of incubation. Marginal difference was observed in the peptide alone and mineralized peptide proliferation rate in comparison to the blank well (Figure 5.16).

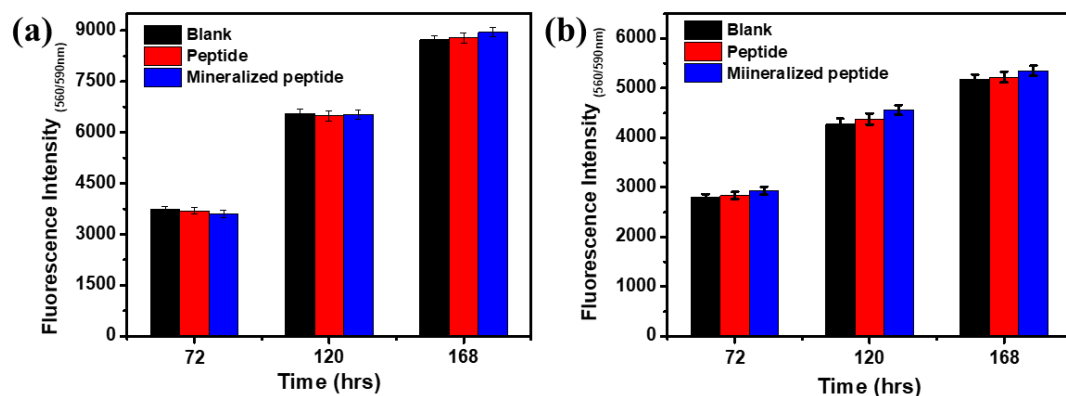


**Figure 5.16** Cellular proliferation of osteoblasts (a) 7F2 cells and (b) Saos-2 cells, on mineralized peptide fibers using Alamar Blue assay at three different time points of 72, 120, and 168 hours.

Moreover, an equivalent proliferation rate was observed in 7F2 cells up to 5 days, which on further incubation showed slight increased rate of proliferation for the mineralized peptide fibers and somewhat similar observations were made in the Saos-2 cells with increased proliferation rate for the mineralized peptide fibers. The cellular viability and proliferation assay revealed the importance of these mineralized peptide fibers in developing advanced scaffolds for controlling and directing the cellular growth.

#### 5.2.6.4 Cytoskeleton (F-actin) staining

The mineralized fibers were observed to be extremely biocompatible towards the osteoblast cells and thus supporting cellular adhesion, growth and proliferation over the time. In order to visualize and quantitate the cell morphology upon interaction with the mineralized fibers, the cells were stained with phalloidin (Rhodamine phalloidin) and DAPI for F-actin and nuclei, respectively. The phalloidin stained cells can be judiciously linked with the cellular viability and adhesion assays. The osteoblast cells adhered to the mineralized peptide surface showed spread morphology with increased surface area and cell shape index (CSI) value, suggesting the proliferation ability of the mineralized peptide fiber after 7 days of incubation. Fluorescence images showed the spread area of  $620.95 \mu\text{m}^2$  and CSI of 0.65 (Figure 5.17) for 7F2 cells and spread area of  $691.95 \mu\text{m}^2$  and CSI of 0.75 (Figure 5.19) for Saos-2 cells.

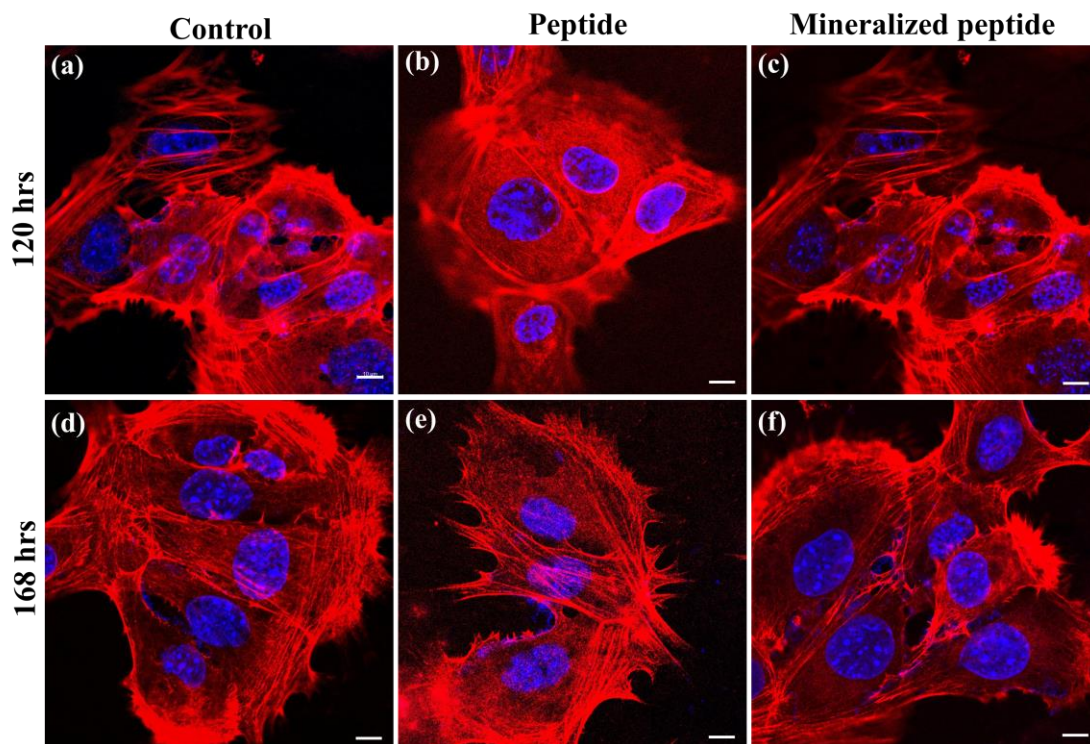


**Figure 5.17** F-actin staining of 7F2 osteoblast cells with Rhodamine phalloidin, (a & d) control, (b & e) NapFFGKO peptide alone, and (c & f) mineralized NapFFGKO peptide. Scale bar 10  $\mu\text{m}$ .

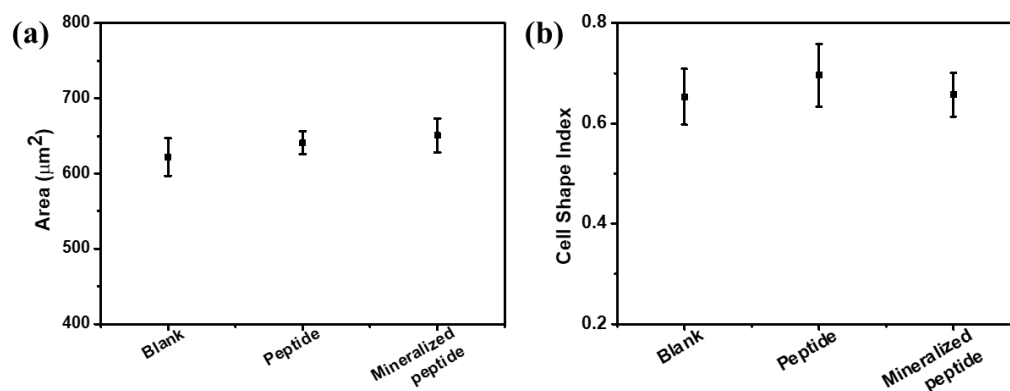


**Figure 5.18** Quantitative assessment of (a) spread area and (b) cell shape index (CSI) of osteoblast cells (7F2) on adhered on the peptide coated cover slips of phalloidin staining.

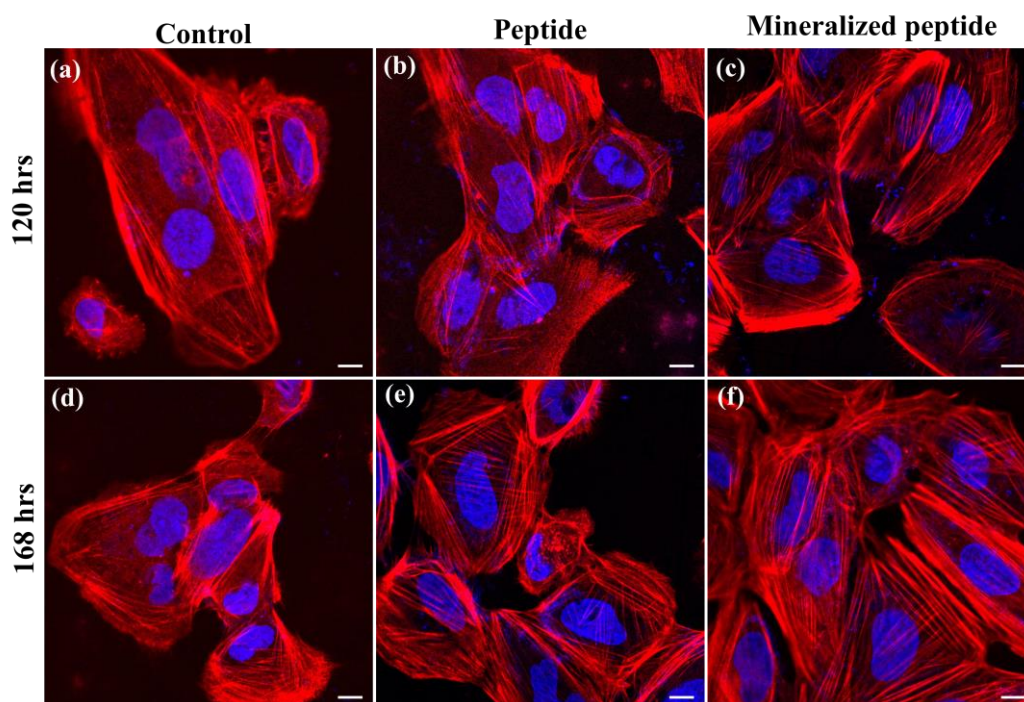


**Figure 5.19** F-actin staining of Saos-2 osteoblast cells with Rhodamine phalloidin, (a & d) control, (b & e) NapFFGKO peptide alone, and (c & f) mineralized NapFFGKO peptide. Scale bar 10  $\mu\text{m}$ .

The mineralized peptide showed the spread area of  $650.78 \mu\text{m}^2$  and the corresponding CSI value of 0.65 for 7F2 cells and  $700.78 \mu\text{m}^2$  spread area and 0.76 CSI value for Saos-2 cells.

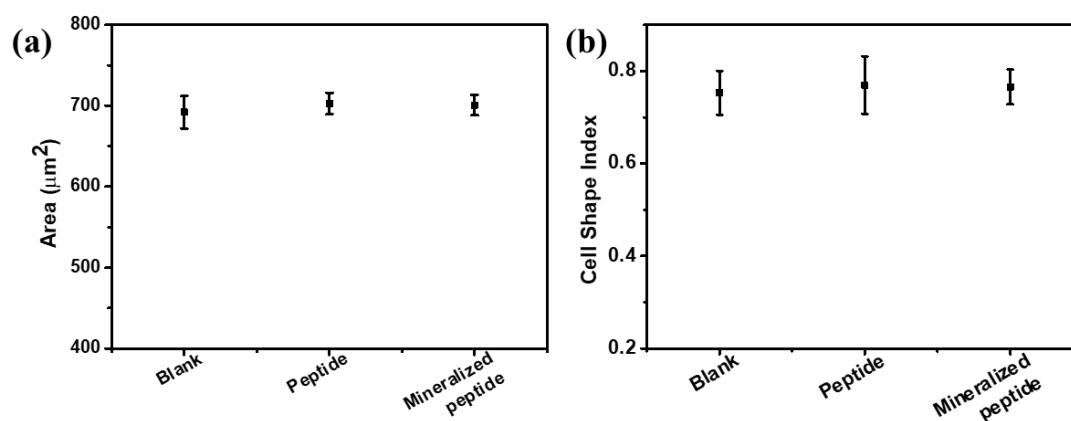


**Figure 5.20** Quantitative assessment of (a) spread area and (b) cell shape index (CSI) of osteoblast cells (Saos-2) on adhered on the peptide coated cover slips of phalloidin staining.

Suggesting the consistence morphology maintenance of cells adhered on the mineralized peptides. The calculated CSI value represents the cell shape parameter and the value close to 1 represents the circular morphology and value close to 0 represents the elongated morphology of the cells. Interestingly, the cells adhered on the mineralized peptide surface showed slightly better spread morphology upon prolonged incubation of 7 days. Both the osteoblast cells showed similar pattern of growth and proliferation with the mineralized peptides. It was observed that the cells adhered on the peptide alone showed spread area of  $640.82 \mu\text{m}^2$  and the corresponding CSI value of 0.69 for 7F2 cells and  $702.82 \mu\text{m}^2$  spread area and 0.76 CSI value for Saos-2 cells.

**Table 5.3** The value of CSI and area covered by the 7F2 and Saos-2 cells in control and in the mineralized peptide after F-actin staining.

Sample	CSI values	Area covered ( $\mu\text{m}^2$ )	CSI value	Area covered ( $\mu\text{m}^2$ )
	7F2		Saos-2	
Control	$0.653 \pm 0.055$	$621.95 \pm 25.1$	$0.753 \pm 0.047$	$691.45 \pm 20.12$
Peptide (NapFFGKO)	$0.696 \pm 0.062$	$640.82 \pm 15.22$	$0.769 \pm 0.062$	$702.52 \pm 13.02$
Mineralized peptide	$0.657 \pm 0.043$	$650.78 \pm 22.67$	$0.765 \pm 0.037$	$700.32 \pm 12.53$

Overall, these results suggested the cells are maintaining similar shape and morphology over the mineralized fibers. To further confirm the osteoinductive property of the mineralized fibers over the osteoblast cells, we carried out some of the important assays to quantitate the biomarkers for osteogenesis. We envisage that these studies would further establish the successful use of the biomineralized fibers derived from collagen protein towards bone tissue regeneration.

### 5.2.6.5 Alkaline phosphatase (ALP) estimation

Several biological characteristics altered significantly during the differentiation of MSCs into osteoblasts, including increased calcium deposition and increased alkaline phosphatase activity.<sup>85</sup> The enzyme directed deposition of carbonated apatite hydrolysis of organic phosphoesters increases the local concentration of inorganic phosphate groups.<sup>86</sup> ALP directs the hydrolysis of organic phosphoesters leading to the increased production of inorganic phosphate group in the surrounding, which results into deposition of carbonated apatite.<sup>87, 88</sup> Moreover, ALP is also known to decrease the pyrophosphate concentration, which generally inhibit the growth of apatite crystals.<sup>89</sup>

ALP also regulate the process of calcification, which suggests its role in the early stage of mineralization.<sup>90</sup> ALP is an early marker for the osteogenic differentiation. High level of ALP was measured when osteoblast cells (7F2 and Saos-2) were cultured on the mineralized peptide substrate. After 7 days of incubation, high amount ALP was detected in the cells cultured on the mineralized peptide in comparison to the control and peptide alone.

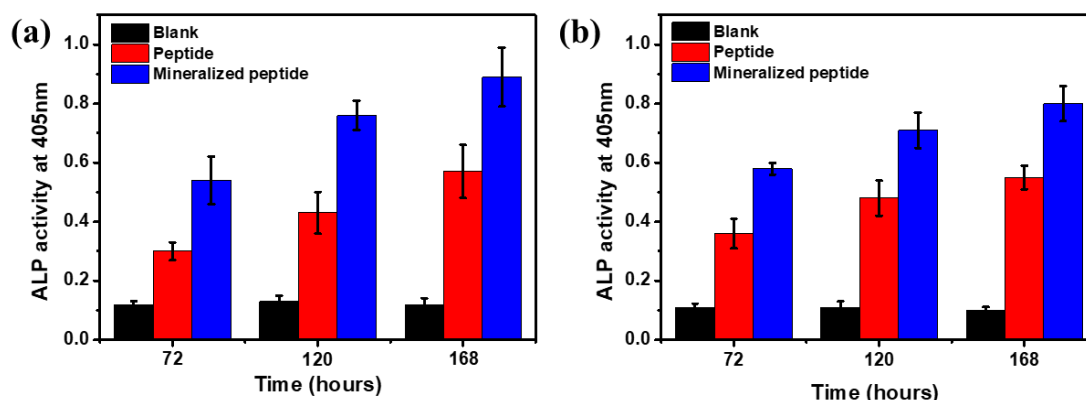


**Figure 5.21** Alkaline phosphatase activity to confirm the osteogenic differentiation capabilities. ALP activity of osteoblasts after 120 and 168 hours.

### 5.2.6.6 Calcium content estimation

Alizarin Red S staining is a commonly used procedure to examine the extracellular calcium deposition because of its efficient and preferential binding to the calcium ion.<sup>53</sup> The efficient binding of the two entities act as an indicator to demonstrate mesenchymal stem cells (MSCs) mineralization on various substrate.<sup>53, 91</sup> Meanwhile, mature osteoblasts are identified by their capacity to deposit minerals. The cells adhered onto the mineralized peptide showed distinct amount of calcium nodule development after 7 days of culturing, according to the Alizarin Red staining as shown in figure 5.21. As the incubation time increases, a large population of cells stained with Alizarin Red S were observed in the sample containing mineralized peptide fibers. The results indicated that the mineralized peptides could promote the bone formation to some extent, which can lead to the osteogenic differentiation. The calcium content was investigated by quantifying the deposited calcium nodules (Figure 5.21). The resubstituted amount of calcium deposits was quantitated at 405nm, which showed a

gradual increase with time. The mineralized peptide was known to enhance the deposition in both the osteoblast cells (7F2 and Saos-2).

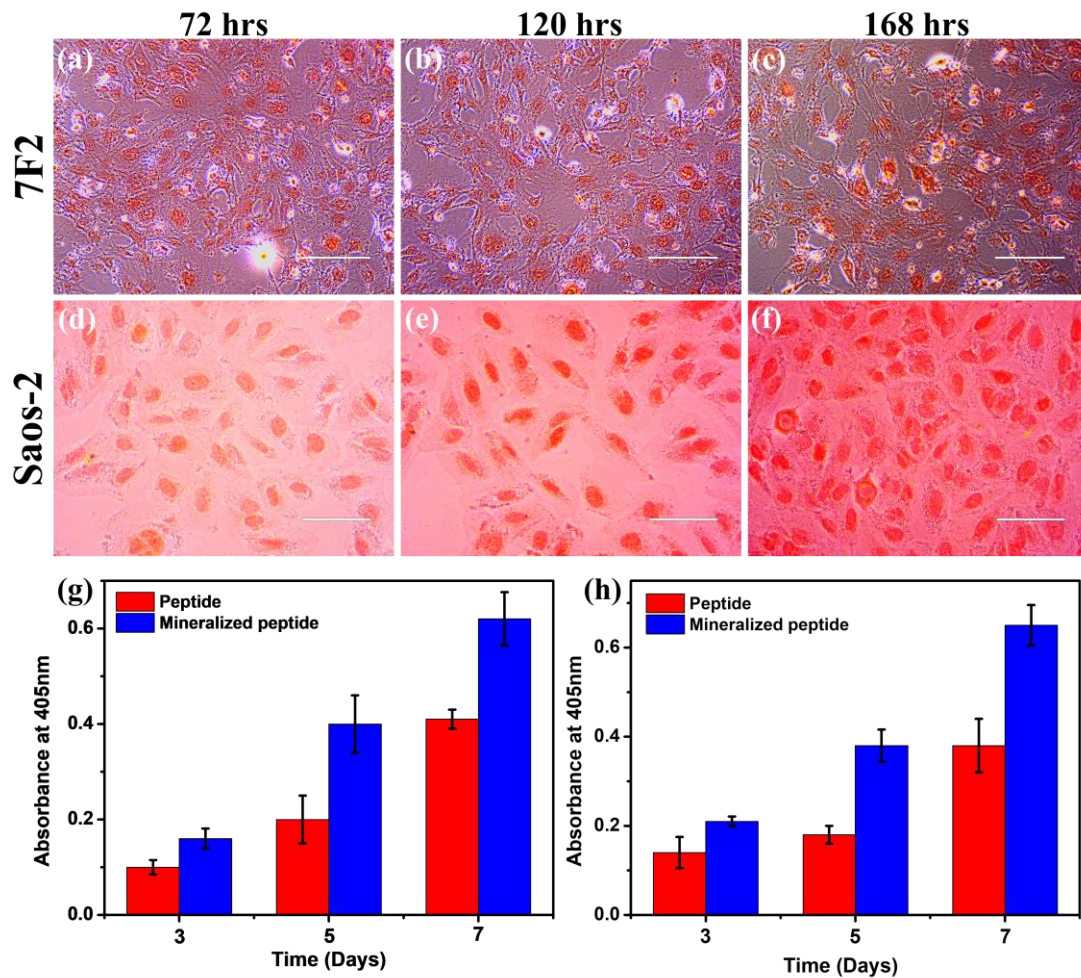


**Figure 5.22** Alizarin Red S staining to demonstrate the calcium deposits: (a-c) Microscopic examination of 7F2 cells at three different time points 72, 120, 168 hours, (d-f) Microscopic examination of Saos-2 cells at three different time points 72, 120, 168 hours. Quantitative analysis of calcium deposits on the mineralized cells (g) 7F2 cells and (h) Saos-2 cells. Scale bar 200  $\mu$ m

Hence, the increased ALP production and the deposition of calcium granules on the cells treated with mineralized peptide clearly demonstrate the osteoinductive property of the peptide fiber.

### 5.3 Conclusion

In conclusion, for the first time, we report the classical strategy of using the shortest collagen-inspired peptide to induce mineralization. This study provides critical insight

into the mechanism of mineralization of peptide fibers inspired by collagen with the preliminary growth of hydroxyapatite crystals. The overall mechanism involves the mutual and combined interactions of all the four components (peptide fiber, calcium chloride, disodium phosphate, and glutamic acid) to initiate the nucleation step of the mineralization. The simplistic strategy utilizes the glutamic acid that was adsorbed onto the peptide fiber surface, which interacts through the electrostatic interactions with the positively charged lysine moieties present on the fiber surface. This ionic complementarity in the intermolecular interactions leads to an optimum interaction for the growth of the minerals on the fiber surface, which enhances their stability and thus overcomes the challenges of clustering, leading to precipitation. It was evident that the area of calcium deposits, which were considered the site of nucleation, further grew to cover the entire peptide nanofiber. Microscopic and spectroscopic characterization revealed the deposition of hydroxyapatite crystal on the peptide fiber. Furthermore, mineralization of the peptide nanofiber enhanced the viscoelastic property of the solution leading to the hydrogelation with enhanced mechanical stiffness and improved thermal stability. These mineralized fibers were also found to be biocompatible with the osteoblast and further promote the cellular proliferation of both the cell lines 7F2 and Saos-2. Mechanistic insights have revealed that the mineralized peptide showed increased production of alkaline phosphatase (ALP) after 7 days of incubation, and a similar phenomenon was observed in Alizarin Red S staining. Thus, this novel approach demonstrated that the mineralized collagen peptide nanofiber network is capable of promoting osteogenesis and enhancing the mineralization ability of the collagen fibers. This strategy further reinforced the simplistic design and fabrication of short bioinspired peptide motifs and the potential application of these mineralized biomimetic collagen fibers towards effectively constructing the grafts for bone tissue engineering.

#### 5.4 References

1. Bell, E. L.; Finnigan, W.; France, S. P.; Green, A. P.; Hayes, M. A.; Hepworth, L. J.; Lovelock, S. L.; Niikura, H.; Osuna, S.; Romero, E.; Ryan, K. S.; Turner, N. J.; Flitsch, S. L., Biocatalysis. *Nat. Rev. Methods Primers* **2021**, *1* (1), 46.
2. Dias, D. A.; Urban, S.; Roessner, U., A historical overview of natural products in drug discovery. *Metabolites* **2012**, *2* (2), 303-336.
3. Newman, D. J.; Cragg, G. M., Natural Products as Sources of New Drugs over the Nearly Four Decades from 01/1981 to 09/2019. *J. Nat. Prod.* **2020**, *83* (3), 770-803.

4. Sharma, P.; Pal, V. K.; Roy, S., An overview of latest advances in exploring bioactive peptide hydrogels for neural tissue engineering. *Biomater. Sci.* **2021**, *9* (11), 3911-3938.
5. Yuan, C.; Ji, W.; Xing, R.; Li, J.; Gazit, E.; Yan, X., Hierarchically oriented organization in supramolecular peptide crystals. *Nat. Rev. Chem.* **2019**, *3* (10), 567-588.
6. Zhang, H.; Kang, L.; Zou, Q.; Xin, X.; Yan, X., Coordination-assembled supramolecular nanoplatforms: structural modulation and theranostic applications. *Curr. Opin. Biotechnol.* **2019**, *58*, 45-52.
7. Jonker, A. M.; Löwik, D. W. P. M.; van Hest, J. C. M., Peptide- and Protein-Based Hydrogels. *Chem. Mater.* **2012**, *24* (5), 759-773.
8. de Melo Pereira, D.; Habibovic, P., Biomineralization-Inspired Material Design for Bone Regeneration. *Adv. Healthc. Mater.* **2018**, *7* (22), 1800700.
9. Chen, F.-M.; Liu, X., Advancing biomaterials of human origin for tissue engineering. *Prog Polym Sci* **2016**, *53*, 86-168.
10. Pedde, R. D.; Mirani, B.; Navaei, A.; Styan, T.; Wong, S.; Mehrali, M.; Thakur, A.; Mohtaram, N. K.; Bayati, A.; Dolatshahi-Pirouz, A.; Nikkhah, M.; Willerth, S. M.; Akbari, M., Emerging Biofabrication Strategies for Engineering Complex Tissue Constructs. *Adv. Mater.* **2017**, *29* (19), 1606061.
11. Xie, J.; Ping, H.; Tan, T.; Lei, L.; Xie, H.; Yang, X.-Y.; Fu, Z., Bioprocess-inspired fabrication of materials with new structures and functions. *Prog. Mater. Sci.* **2019**, *105*, 100571.
12. Zhang, K.; Wang, S.; Zhou, C.; Cheng, L.; Gao, X.; Xie, X.; Sun, J.; Wang, H.; Weir, M. D.; Reynolds, M. A.; Zhang, N.; Bai, Y.; Xu, H. H. K., Advanced smart biomaterials and constructs for hard tissue engineering and regeneration. *Bone Res.* **2018**, *6* (1), 31.
13. Cantaert, B.; Beniash, E.; Meldrum, F. C., Nanoscale Confinement Controls the Crystallization of Calcium Phosphate: Relevance to Bone Formation. *Chem. Eur. J.* **2013**, *19* (44), 14918-14924.
14. Liu, L.; Shang, Y.; Li, C.; Jiao, Y.; Qiu, Y.; Wang, C.; Wu, Y.; Zhang, Q.; Wang, F.; Yang, Z.; Wang, L., Hierarchical Nanostructured Electrospun Membrane with Periosteum-Mimic Microenvironment for Enhanced Bone Regeneration. *Adv. Healthc. Mater.* **2021**, *10* (21), 2101195.
15. Wang, L.-N.; Meng, Y.-F.; Feng, Y.; Wang, H.-C.; Mao, L.-B.; Yu, S.-H.; Wang, Z.-L., Amorphous Precursor-Mediated Calcium Phosphate Coatings with Tunable Microstructures for Customized Bone Implants. *Adv. Healthc. Mater.* **2022**, 2201248.
16. Zeiger, D. N.; Miles, W. C.; Eidelman, N.; Lin-Gibson, S., Cooperative Calcium Phosphate Nucleation within Collagen Fibrils. *Langmuir* **2011**, *27* (13), 8263-8268.
17. Elsharkawy, S.; Mata, A., Hierarchical Biomineralization: from Nature's Designs to Synthetic Materials for Regenerative Medicine and Dentistry. *Adv. Healthc. Mater.* **2018**, *7* (18), 1800178.
18. Dimitriou, R.; Jones, E.; McGonagle, D.; Giannoudis, P. V., Bone regeneration: current concepts and future directions. *BMC Med.* **2011**, *9* (1), 66.
19. Oryan, A.; Alidadi, S.; Moshiri, A.; Maffulli, N., Bone regenerative medicine: classic options, novel strategies, and future directions. *J Orthop Surg Res* **2014**, *9* (1), 18-18.
20. Katiyar, N. K.; Goel, G.; Hawi, S.; Goel, S., Nature-inspired materials: Emerging trends and prospects. *NPG Asia Mater.* **2021**, *13* (1), 56.
21. Wu, S.; Chen, Y.; Guo, X.; Wu, Y., Collagen mineralization and its applications in hard tissue repair. *Mater. Chem. Front.* **2021**, *5* (19), 7071-7087.
22. Li, J.; Xing, R.; Bai, S.; Yan, X., Recent advances of self-assembling peptide-based hydrogels for biomedical applications. *Soft Mater* **2019**, *15* (8), 1704-1715.
23. Yang, C.; Yang, Z.; Gu, H.; Chang, C. K.; Gao, P.; Xu, B., Facet-Selective 2D Self-Assembly of TiO<sub>2</sub> Nanoleaves via Supramolecular Interactions. *Chem. Mater.* **2008**, *20* (24), 7514-7520.
24. Li, Z.; Lu, W. W.; Chiu, P. K. Y.; Lam, R. W. M.; Xu, B.; Cheung, K. M. C.; Leong, J. C. Y.; Luk, K. D. K., Strontium–calcium coadministration stimulates bone matrix osteogenic factor expression and new bone formation in a large animal model. *J. Orthop. Res.* **2009**, *27* (6), 758-762.

25. Kjaer, M., Role of extracellular matrix in adaptation of tendon and skeletal muscle to mechanical loading. *Physiol Rev* **2004**, *84* (2), 649-98.
26. Patel, A.; Zaky, S. H.; Schoedel, K.; Li, H.; Sant, V.; Beniash, E.; Sfeir, C.; Stolz, D. B.; Sant, S., Design and evaluation of collagen-inspired mineral-hydrogel nanocomposites for bone regeneration. *Acta Biomater* **2020**, *112*, 262-273.
27. Tzaphlidou, M., Bone architecture: collagen structure and calcium/phosphorus maps. *J Biol Phys* **2008**, *34* (1-2), 39-49.
28. Dahl, T.; Veis, A., Electrostatic interactions lead to the formation of asymmetric collagen-phosphoryn aggregates. *Connect Tissue Res* **2003**, *44 Suppl 1*, 206-13.
29. Midura, R. J.; Vasanji, A.; Su, X.; Wang, A.; Midura, S. B.; Gorski, J. P., Calcospherulites isolated from the mineralization front of bone induce the mineralization of type I collagen. *Bone* **2007**, *41* (6), 1005-16.
30. Paschalis, E. P.; Recker, R.; DiCarlo, E.; Doty, S. B.; Atti, E.; Boskey, A. L., Distribution of collagen cross-links in normal human trabecular bone. *J Bone Miner Res* **2003**, *18* (11), 1942-6.
31. Tzaphlidou, M., The role of collagen in bone structure: an image processing approach. *Micron (Oxford, England : 1993)* **2005**, *36* (7-8), 593-601.
32. Bailey, A. J.; Wotton, S. F.; Sims, T. J.; Thompson, P. W., Post-translational modifications in the collagen of human osteoporotic femoral head. *Biochem Biophys Res Commun* **1992**, *185* (3), 801-5.
33. Pace, J. M.; Atkinson, M.; Willing, M. C.; Wallis, G.; Byers, P. H., Deletions and duplications of Gly-Xaa-Yaa triplet repeats in the triple helical domains of type I collagen chains disrupt helix formation and result in several types of osteogenesis imperfecta. *Hum Mutat* **2001**, *18* (4), 319-26.
34. Bank, R. A.; Tekoppele, J. M.; Janus, G. J.; Wassen, M. H.; Puijls, H. E.; Van der Sluijs, H. A.; Sackers, R. J., Pyridinium cross-links in bone of patients with osteogenesis imperfecta: evidence of a normal intrafibrillar collagen packing. *J Bone Miner Res* **2000**, *15* (7), 1330-6.
35. Adachi, E.; Hopkinson, I.; Hayashi, T., Basement-membrane stromal relationships: interactions between collagen fibrils and the lamina densa. *Int Rev Cytol* **1997**, *173*, 73-156.
36. Kafantari, H.; Kounadi, E.; Fatouros, M.; Milonakis, M.; Tzaphlidou, M., Structural alterations in rat skin and bone collagen fibrils induced by ovariectomy. *Bone* **2000**, *26* (4), 349-53.
37. Kounadi, E.; Fountos, G.; Tzaphlidou, M., The influence of inflammation-mediated osteopenia (IMO) on the structure of rabbit bone and skin collagen fibrils. *Connect Tissue Res* **1998**, *37* (1-2), 69-76.
38. Stock, S. R., The Mineral-Collagen Interface in Bone. *Calcif. Tissue. Int.* **2015**, *97* (3), 262-280.
39. Deshpande, A. S.; Beniash, E., Bioinspired Synthesis of Mineralized Collagen Fibrils. *Cryst. Growth Des.* **2008**, *8* (8), 3084-3090.
40. Jee, S. S.; Kasinath, R. K.; DiMasi, E.; Kim, Y.-Y.; Gower, L., Oriented hydroxyapatite in turkey tendon mineralized via the polymer-induced liquid-precursor (PILP) process. *CrystEngComm* **2011**, *13* (6), 2077-2083.
41. Nudelman, F.; Lausch, A. J.; Sommerdijk, N. A.; Sone, E. D., In vitro models of collagen biomineralization. *J Struct Biol* **2013**, *183* (2), 258-69.
42. Nudelman, F.; Pieterse, K.; George, A.; Bomans, P. H.; Friedrich, H.; Brylka, L. J.; Hilbers, P. A.; de With, G.; Sommerdijk, N. A., The role of collagen in bone apatite formation in the presence of hydroxyapatite nucleation inhibitors. *Nature materials* **2010**, *9* (12), 1004-9.
43. Li, Y.; Rodriguez-Cabello, J. C.; Aparicio, C., Intrafibrillar mineralization of self-assembled elastin-like recombinamer fibrils. *ACS Appl. Mater. Interface* **2017**, *9* (7), 5838-5846.
44. Kim, S.; Lee, M., Rational Design of Hydrogels to Enhance Osteogenic Potential. *Chem. Mater.* **2020**, *32* (22), 9508-9530.

45. Gonen-Wadmany, M.; Oss-Ronen, L.; Seliktar, D., Protein-polymer conjugates for forming photopolymerizable biomimetic hydrogels for tissue engineering. *Biomaterials* **2007**, *28* (26), 3876-86.
46. He, G.; George, A., Dentin Matrix Protein 1 Immobilized on Type I Collagen Fibrils Facilitates Apatite Deposition in Vitro\*. *J. Biol. Chem.* **2004**, *279* (12), 11649-11656.
47. Oosterlaken, B. M.; Vena, M. P.; de With, G., In Vitro Mineralization of Collagen. *Adv. Mater.* **2021**, *33* (16), 2004418.
48. Tavafoghi, M.; Cerruti, M., The role of amino acids in hydroxyapatite mineralization. *J. R. Soc. Interface* **2016**, *13* (123), 20160462.
49. Rabatic, B. M.; Claussen, R. C.; Stupp, S. I., Templated Mineralization of Peptide-Based Unsymmetric Bolaamphiphiles. *Chem. Mater.* **2005**, *17* (24), 5877-5879.
50. Sone, E. D.; Stupp, S. I., Bioinspired Magnetite Mineralization of Peptide–Amphiphile Nanofibers. *Chem. Mater.* **2011**, *23* (8), 2005-2007.
51. Hartgerink, J. D.; Beniash, E.; Stupp, S. I., Self-Assembly and Mineralization of Peptide-Amphiphile Nanofibers. *Science* **2001**, *294* (5547), 1684-1688.
52. Li, Q.-L.; Ning, T.-Y.; Cao, Y.; Zhang, W.-b.; Mei, M. L.; Chu, C. H., A novel self-assembled oligopeptide amphiphile for biomimetic mineralization of enamel. *BMC Biotechnol.* **2014**, *14* (1), 32.
53. Yin, W.-N.; Cao, F.-Y.; Han, K.; Zeng, X.; Zhuo, R.-X.; Zhang, X.-Z., The synergistic effect of a BMP-7 derived peptide and cyclic RGD in regulating differentiation behaviours of mesenchymal stem cells. *J. Mater. Chem. B* **2014**, *2* (47), 8434-8440.
54. Qiu, Z.-Y.; Cui, Y.; Tao, C.-S.; Zhang, Z.-Q.; Tang, P.-F.; Mao, K.-Y.; Wang, X.-M.; Cui, F.-Z., Mineralized Collagen: Rationale, Current Status, and Clinical Applications. *Materials (Basel)* **2015**, *8* (8), 4733-4750.
55. Tomoaia, G.; Pasca, R.-D., On the Collagen Mineralization. A Review. *Clujul. Med.* **2015**, *88* (1), 15-22.
56. Hoyer, B.; Bernhardt, A.; Heinemann, S.; Stachel, I.; Meyer, M.; Gelinsky, M., Biomimetically mineralized salmon collagen scaffolds for application in bone tissue engineering. *Biomacromolecules* **2012**, *13* (4), 1059-66.
57. Wang, Y.; Zhang, W.; Gong, C.; Liu, B.; Li, Y.; Wang, L.; Su, Z.; Wei, G., Recent advances in the fabrication, functionalization, and bioapplications of peptide hydrogels. *Soft Mater* **2020**, *16* (44), 10029-10045.
58. Zhang, W.; Yu, X.; Li, Y.; Su, Z.; Jandt, K. D.; Wei, G., Protein-mimetic peptide nanofibers: Motif design, self-assembly synthesis, and sequence-specific biomedical applications. *Prog Polym Sci* **2018**, *80*, 94-124.
59. He, G.; Gajjeraman, S.; Schultz, D.; Cookson, D.; Qin, C.; Butler, W. T.; Hao, J.; George, A., Spatially and temporally controlled biomineralization is facilitated by interaction between self-assembled dentin matrix protein 1 and calcium phosphate nuclei in solution. *Biochemistry* **2005**, *44* (49), 16140-16148.
60. Olszta, M. J.; Odom, D. J.; Douglas, E. P.; Gower, L. B., A new paradigm for biomineral formation: mineralization via an amorphous liquid-phase precursor. *Connective tissue research* **2003**, *44 Suppl 1*, 326-34.
61. Deshpande, A. S.; Beniash, E., Bio-inspired Synthesis of Mineralized Collagen Fibrils. *Cryst. Growth Des.* **2008**, *8* (8), 3084-3090.
62. Olszta, M. J.; Douglas, E. P.; Gower, L. B., Scanning electron microscopic analysis of the mineralization of type I collagen via a polymer-induced liquid-precursor (PILP) process. *Calcified tissue international* **2003**, *72* (5), 583-91.
63. Li, K.; Zhang, Z.; Li, D.; Zhang, W.; Yu, X.; Liu, W.; Gong, C.; Wei, G.; Su, Z. J. A. F. M., Biomimetic ultralight, highly porous, shape-adjustable, and biocompatible 3D graphene minerals via incorporation of self-assembled peptide nanosheets. **2018**, *28* (29), 1801056.
64. Prajapati, S.; Tao, J.; Ruan, Q.; De Yoreo, J. J.; Moradian-Oldak, J., Matrix metalloproteinase-20 mediates dental enamel biomineralization by preventing protein occlusion inside apatite crystals. *Biomaterials* **2016**, *75*, 260-270.

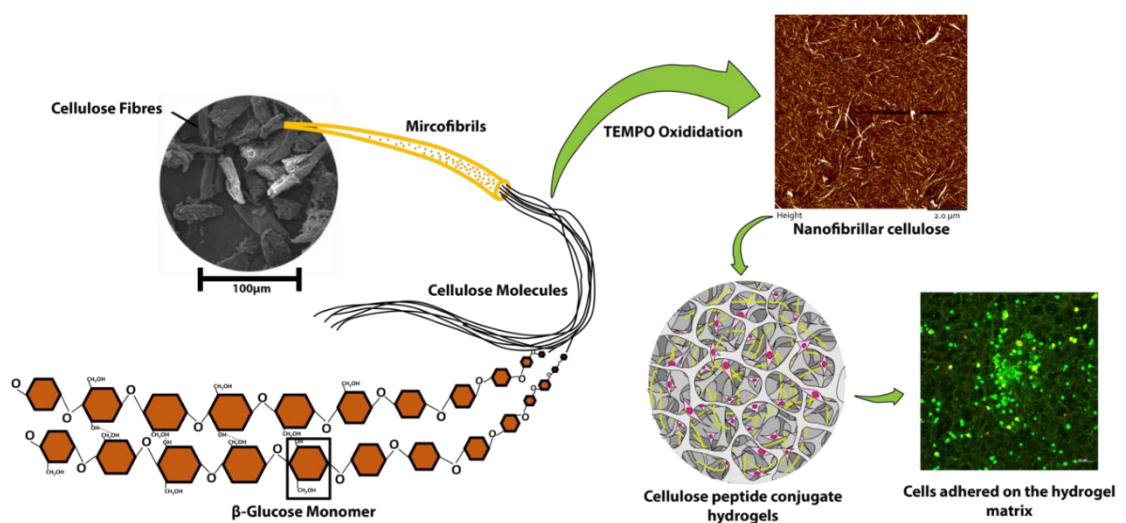
65. Rivas, M.; Del Valle, L. J.; Alemán, C.; Puiggalí, J., Peptide Self-Assembly into Hydrogels for Biomedical Applications Related to Hydroxyapatite. *Gels* **2019**, *5* (1), 14.
66. Zhong, C.; Chu, C. C., Biomimetic mineralization of acid polysaccharide-based hydrogels: towards porous 3-dimensional bone-like biocomposites. *J. Mater. Chem.* **2012**, *22* (13), 6080-6087.
67. Manoj, M.; Mangalaraj, D.; Ponpandian, N.; Viswanathan, C., Core-shell hydroxyapatite/Mg nanostructures: surfactant free facile synthesis, characterization and their in vitro cell viability studies against leukaemia cancer cells (K562). *RSC Adv.* **2015**, *5* (60), 48705-48711.
68. Cosmidis, J.; Benzerara, K.; Guyot, F.; Skouri-Panet, F.; Duprat, E.; Féraud, C.; Guigner, J.-M.; Babonneau, F.; Coelho, C., Calcium-Phosphate Biomineralization Induced by Alkaline Phosphatase Activity in *Escherichia coli*: Localization, Kinetics, and Potential Signatures in the Fossil Record. *Front. Earth Sci.* **2015**, *3*.
69. Stammeier, J. A.; Purgstaller, B.; Hippler, D.; Mavromatis, V.; Dietzel, M., In-situ Raman spectroscopy of amorphous calcium phosphate to crystalline hydroxyapatite transformation. *MethodsX* **2018**, *5*, 1241-1250.
70. Ronen, M.; Kalanoor, B. S.; Oren, Z.; Ron, I.; Tischler, Y. R.; Gerber, D., Characterization of peptides self-assembly by low frequency Raman spectroscopy. *RSC Adv.* **2018**, *8* (29), 16161-16170.
71. Gomes, G. C.; Borghi, F. F.; Ospina, R. O.; López, E. O.; Borges, F. O.; Mello, A., Nd:YAG (532nm) pulsed laser deposition produces crystalline hydroxyapatite thin coatings at room temperature. *Surf. Coat. Technol.* **2017**, *329*, 174-183.
72. Raikar, G. N.; Ong, J. L.; Lucas, L. C., Hydroxyapatite characterized by XPS. *J. Surf. Sci. Spectra* **1996**, *4* (1), 9-13.
73. Secchi, V.; Franchi, S.; Dettin, M.; Zamuner, A.; Beranová, K.; Vladescu, A.; Battocchio, C.; Graziani, V.; Tortora, L.; Iucci, G., Hydroxyapatite surfaces functionalized with a self-assembling peptide: XPS, raris and nexafs study. *J. Nanomater.* **2020**, *10* (6), 1151.
74. Pal, V. K.; Jain, R.; Sen, S.; Kailasam, K.; Roy, S., Designing nanofibrillar cellulose peptide conjugated polymeric hydrogel scaffold for controlling cellular behaviour. *Cellulose* **2021**, *28* (16), 10335-10357.
75. Sharma, P.; Pal, V. K.; Kaur, H.; Roy, S., Exploring the TEMPO-Oxidized Nanofibrillar Cellulose and Short Ionic-Complementary Peptide Composite Hydrogel as Biofunctional Cellular Scaffolds. *Biomacromolecules* **2022**, *23* (6), 2496-2511.
76. Debye, P., Molecular-weight determination by light scattering. *J The Journal of Physical Chemistry* **1947**, *51* (1), 18-32.
77. Tobita, H., Random Branching of Polymer Chains with Schulz-Zimm Distribution. 1. Bivariate Distribution and Related Formulae. *Macromol. Theory Simul.* **2020**, *29* (2), 1900056.
78. Svergun, D. I.; Koch, M. H., Small-angle scattering studies of biological macromolecules in solution. *J Reports on Progress in Physics* **2003**, *66* (10), 1735.
79. Jacques, D. A.; Trewhella, J., Small-angle scattering for structural biology—Expanding the frontier while avoiding the pitfalls. *J Protein science* **2010**, *19* (4), 642-657.
80. Jain, R.; Pal, V. K.; Roy, S., Triggering Supramolecular Hydrogelation Using a Protein-Peptide Coassembly Approach. *Biomacromolecules* **2020**, *21* (10), 4180-4193.
81. Pal, V. K.; Jain, R.; Roy, S., Tuning the Supramolecular Structure and Function of Collagen Mimetic Ionic Complementary Peptides via Electrostatic Interactions. *Langmuir* **2020**, *36* (4), 1003-1013.
82. Pal, V. K.; Roy, S., Cooperative Metal Ion Coordination to the Short Self-Assembling Peptide Promotes Hydrogelation and Cellular Proliferation. *Macromol. Biosci.* **2022**, *22* (5), 2100462.
83. Adamcik, J.; Berquand, A.; Mezzenga, R., Single-step direct measurement of amyloid fibrils stiffness by peak force quantitative nanomechanical atomic force microscopy. *Appl. Phys. Lett.* **2011**, *98* (19), 193701.
84. Jayawarna, V.; Richardson, S. M.; Hirst, A. R.; Hodson, N. W.; Saiani, A.; Gough, J. E.; Ulijn, R. V., Introducing chemical functionality in Fmoc-peptide gels for cell culture. *Acta Biomater* **2009**, *5* (3), 934-43.

85. Higuchi, A.; Ling, Q. D.; Hsu, S. T.; Umezawa, A., Biomimetic cell culture proteins as extracellular matrices for stem cell differentiation. *Chem. Rev.* **2012**, *112* (8), 4507-40.
86. Golub, E. E.; Boesze-Battaglia, K., The role of alkaline phosphatase in mineralization. **2007**, *18* (5), 444-448.
87. de Jonge, L. T.; Leeuwenburgh, S. C. G.; van den Beucken, J. J. J. P.; Wolke, J. G. C.; Jansen, J. A., Electro sprayed Enzyme Coatings as Bioinspired Alternatives to Bioceramic Coatings for Orthopedic and Oral Implants. **2009**, *19* (5), 755-762.
88. Orimo, H., The mechanism of mineralization and the role of alkaline phosphatase in health and disease. *J Nippon Med Sch* **2010**, *77* (1), 4-12.
89. Osathanon, T.; Giachelli, C. M.; Somerman, M. J., Immobilization of alkaline phosphatase on microporous nanofibrous fibrin scaffolds for bone tissue engineering. *Biomaterials* **2009**, *30* (27), 4513-21.
90. Warnes, T. W., Alkaline phosphatase. *Gut* **1972**, *13* (11), 926-937.
91. Sun, H.; Feng, K.; Hu, J.; Soker, S.; Atala, A.; Ma, P. X. J. B., Osteogenic differentiation of human amniotic fluid-derived stem cells induced by bone morphogenetic protein-7 and enhanced by nanofibrous scaffolds. **2010**, *31* (6), 1133-1139.

# Chapter 6

Exploring non-covalent interactions  
among nanofibrillar cellulose-peptide  
conjugate polymeric hydrogels for  
developing advanced synthetic scaffolds





**CH/ $\pi$  and H-bond stabilized nanofibrillar cellulose-peptide conjugate hydrogels were fabricated to achieve superior biochemical and structural properties at the nanoscale to promote cellular adhesion and proliferation.**



## 6.1 Introduction

As discussed in earlier chapters, extracellular matrix is composed of multicomponent system comprising of proteins, sugars, glycolipids and several other growth hormones. So, it will be very interesting to explore the effect of conjugating polymer to these peptide hydrogels as this will provide the essential mechanical integrity to the peptide hydrogels essential for its long-term stability. In this direction, cellulose being the most widely distributed and abundant natural polymer, has been extensively used due to its biodegradability, biocompatibility, and non-toxicity.<sup>1-4</sup> Cellulose and cellulose-based composites stand out as indispensable and versatile biomaterials for tissue engineering, tissue repair and wound healing applications.<sup>5-9</sup> However, the next generation cellulose-based products and their engineering applications are limited with traditional cellulosic materials.<sup>10</sup> In particular, the development in biomaterial fabrication utilizing this ancient biomolecule faces major challenges owing to its low solubility in aqueous as well as organic solvents due to its hydrogen bonded structure.<sup>11</sup> To this direction, extracting the cellulose at nanoscale leads to the fabrication of a new generation building block based on cellulose composite, which can further overcome the challenges associated with the hierarchical structure of the native cellulose.<sup>12-16</sup> Interestingly, diverse physicochemical properties at the cellulosic domain can be achieved either by chemical functionalization or by its transformation into nanocellulose via different methods, which are significantly important in determining their applications in tissue engineering and biotechnological purposes.<sup>17-19</sup> Among several methods, (2,2,6,6-tetramethylpiperidine-1-oxyl) TEMPO is one of the most widely used and efficient method for functionalizing cellulose under mild conditions, which results in the selective oxidation of alcoholic hydroxyl functionalities to aldehydes, ketones, and carboxyl functional groups.<sup>20</sup> Earlier reports have revealed that TEMPO mediated oxidation of hardwood may result in the formation of separated cellulose nanofibers of 3-4nm width.<sup>21</sup> Such transformation within the nanomaterials was accompanied by conversion of primary hydroxyl group to carboxyl group in the classic cellulosic domain.<sup>22</sup>

To this direction, nanofibrillar cellulose (NFC) possessing several advantages of biocompatibility, biodegradability, chemical modification, low density, and high mechanical strength has emerged as an excellent candidate for 3D hydrogel scaffold for several biomedical applications.<sup>23, 24</sup> G. Paul and co-workers reported the bacterial

cellulose based nanofibrous scaffold with enhanced adhesion of human vascular endothelial cells by functionalizing the nanofibrous cellulose with GRGDS oligopeptides via *endotransglucosylase* mediated coupling.<sup>25</sup> Furthermore, cationic modification of the nanocellulose to trimethyl ammonium beta hydroxy propyl cellulose was observed to enhance the cellular adhesion, proliferation, and promoting the formation of 3D network of neuroblastic and eosinophilic cells on this modified nanocellulose scaffolds.<sup>26</sup> To this end, P. Kallio and co-workers fabricated the nanocellulose with negative and positive charges using TEMPO and EPTMAC (2, 3-epoxy propyl trimethyl ammonium chloride). Furthermore, the effect of surface charge on these cellulosic biomaterials was reported towards controlling human dermal cell behavior.<sup>27</sup> Enhancement in cell adhesion and proliferation was observed on both the surfaces, however, anionic surface was found to be comparatively more effective in promoting cell proliferation.<sup>28</sup> Specific application of NFC, as substitute for ligament and tendon was reported by Mathew et al., where the NFC was dissolved in ionic liquid for different time intervals.<sup>29</sup> The dissolved NFC constituted the matrix while the undissolved part constructed the reinforcing phase, making an NFC nanocomposite with high mechanical strength, very similar to natural ligament and tendon. The resulting nanocomposite supported the adhesion and growth of ligament cells and endothelial cells, and thus proposing its application for artificial ligament and tendon.<sup>29</sup> These bio-composites could be used as implants for clinical applications as well as for wound dressing materials.<sup>30</sup>

Interestingly, these surface charge modifications or functionalization of nanofibrillar cellulose allow the covalent attachment of peptides, proteins, and other polymers to control and direct cell behavior. In this context, Y. Chau and group reported a polyvalent lytic peptide-polymer conjugate, which can overcome multidrug resistance.<sup>31</sup> In this report, the hexapeptide (KW)<sub>3</sub> was conjugated with carboxymethyl dextran through click chemistry.<sup>31</sup> To this direction, different covalent modification strategies have been explored to produce cellulose-peptide conjugates, such as, nitroxide-mediated polymerization, atom transfer radical polymerization, or reverse addition fragment chain transfer polymerization.<sup>32-34</sup> On the other hand, there were only few reports present in the literature, which showed the non-covalent interactions between polymer and peptide. A report by K. James and co-workers demonstrated the differential interaction of crystalline cellulose and cellulose nanowhiskers with a

heptapeptide (WHWTYYW), which involves the Y5 amino acid interacting through CH/ $\pi$  interaction and hydrogen bonding with the free hydroxyl group as well as six membered glucose rings of cellulose.<sup>35</sup> However, no reports were available in the literature on cellulose conjugates with specific proteins/peptides of biological relevance.

To this direction it is well known that collagen is the most abundant protein, and it plays a crucial role in cellular adhesion and proliferation in the extracellular matrix in addition to providing structural integrity to the cells.<sup>36</sup> Interestingly, recent reports have been extensively focused on the preparation of synthetic collagen and collagen like peptides to understand their molecular level arrangement and to mimic their complex architecture to attain the structural and functional attributes of native extracellular matrix (ECM).<sup>37-40</sup> As mentioned in chapter 3, we have recently reported two collagen inspired ionic complementary pentapeptides, which undergo strong electrostatic interaction to create complex hierarchical structure leading to the formation of diverse gels. The newly developed scaffolds have demonstrated excellent biocompatibility towards fibroblast cells.<sup>41</sup> To this direction, it is desirable to keep in mind the higher complexity of the native ECM, which consists of a combination of proteins, lipids, and polysaccharides.<sup>42</sup> So, in order to enhance the scope of the newly developed peptidic domain for wide range of cells, it would be extremely attractive to combine these bioactive peptides with the highly useful nano-cellulosic materials. Such strategy would integrate the mechanical rigidity and bioactivity of the cellulosic nanofibers and biochemical cues provided by the collagen inspired peptides (CIPs) to control and direct specific cell behaviour. Thus, the present study demonstrates the non-covalent conjugation of short CIPs<sup>41</sup> with the TEMPO oxidized nanocellulose fibers. We hypothesize that several non-covalent interactions are associated with these cellulose-peptide conjugates, such as CH/ $\pi$  interaction and H-bonding, which drive the self-assembly to create novel nanostructure. Furthermore, additional interactions are expected to take place between the charged amino acid residues and the carboxyl groups of cellulose, formed by TEMPO oxidation. Conjugate hydrogels developed from nanofibrillar cellulose and collagen inspired peptides are expected to show enhanced mechanical strength as compared to the native peptide hydrogel. A combination of these variable intermolecular interactions further dictated the morphology of the final hydrogel construct with variable pore size distribution. The differential pore

distribution presented on the exposed surface of the hydrogel matrix further controlled the cellular adhesion and proliferation. To the best of our knowledge, this designer composite hydrogel has been reported for the first time, which was fabricated from the shortest bioactive collagen inspired peptide and nano-fibrillated cellulose (Figure 6.1). Conjugate matrix containing the collagen inspired peptide as epitope could help the cells to adhere and proliferate, while the nanofibrous cellulose can create the similar architecture of the synthetic matrix. Thus, the presence of these two components may allow the conjugate hydrogel to function as a stable matrix with superior properties to promote adherence of the cells. The porous network of the nanofibrous cellulose will also allow the easy exchange of media to support cellular proliferation. Our study further indicated that these hydrogels can hold great potential for developing an advanced biomaterial by combining the properties of both bio-functional protein and carbohydrate polymer.<sup>43-50</sup>

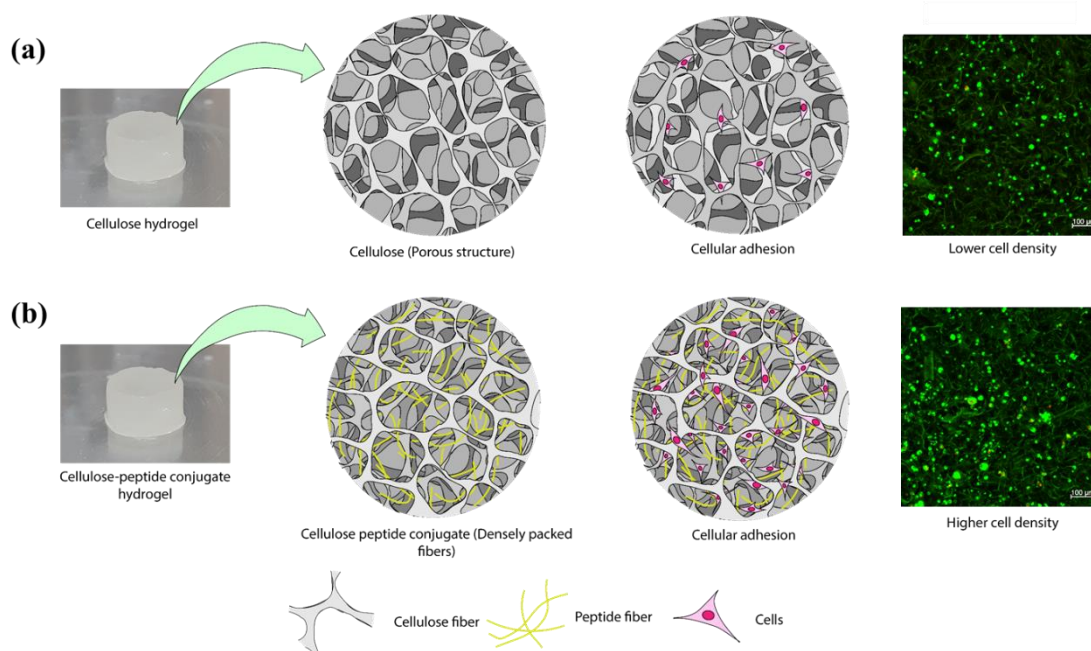


**Figure 6.1** Schematic representation showing the different nano-structural morphologies of nanofibrillar cellulose (a) and its conjugate with collagen inspired ionic complementary peptides as associated via non-covalent interactions (b) the conjugate hydrogel scaffold can serve as superior matrix to promote cellular adhesion reflecting the higher cell population.

## 6.2 Results and Discussion

### 6.2.1 TEMPO mediated oxidation of cellulose

In order to develop a novel synthetic extracellular matrix, we have chosen cellulose microfibrils, derived from natural biomass, which would essentially be cost-effective, abundant and biocompatible. Further, our strategy was focused on converting the microfibrillar cellulose into nanocellulose via TEMPO oxidation.<sup>20, 51</sup> TEMPO-mediated oxidation will introduce a significant amount of carboxylate groups into the native cellulose while maintaining their fibrous morphology and crystallinities (Figure 6.2).<sup>52, 53</sup>

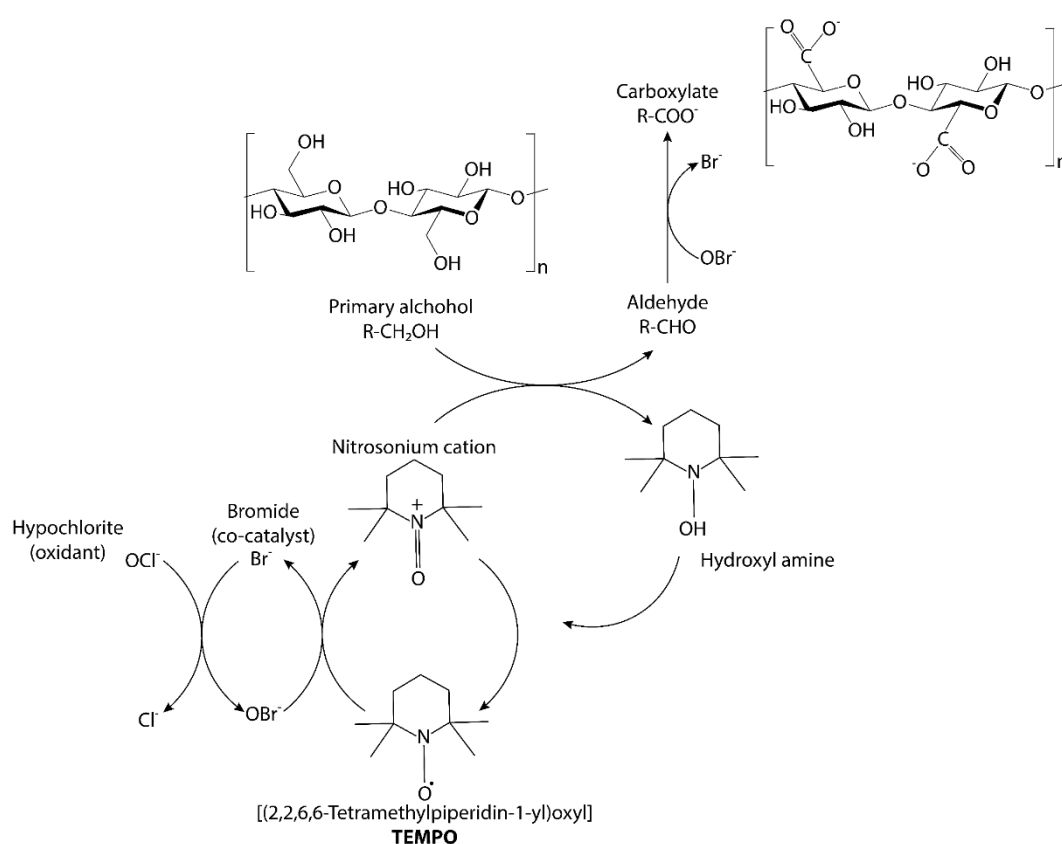


**Figure 6.2** Schematic representation of chemical conversion and functionalization of hardwood cellulose into nanofibrous cellulose via TEMPO oxidation.

At this point, it was crucial to understand the chemical modification at the molecular level. To this direction, carboxylate content as formed by the oxidation of the primary hydroxyl groups of cellulose with the addition of 5 mmol NaOCl was assessed by the electrical conductivity titration method.<sup>20</sup> The carboxylate content was found to increase with enhancement in time, up to 180 minutes. The saturation point was

achieved at 0.56 mmol/g, which further showed no marginal increment afterwards until 24 hours (Figure 6.3a). To further investigate the presence of carboxyl group, FTIR spectroscopy was utilized. The emergence of peak around  $1750\text{cm}^{-1}$  showed the presence of carboxyl group (Figure 6.3b). To confirm the formation of cellulosic fibers in the nanoscale regime, atomic force microscopy (AFM) was performed to study the morphology of nanofibrillar cellulose. The diameter of cellulose nanofibers in AFM was revealed as  $23\pm 2.5\text{ nm}$  (Figure 6.3c). The above results confirmed the conversion of nanofibrillar cellulose from microfibrillar cellulose following the conversion of hydroxyl group to carboxyl via TEMPO oxidation.

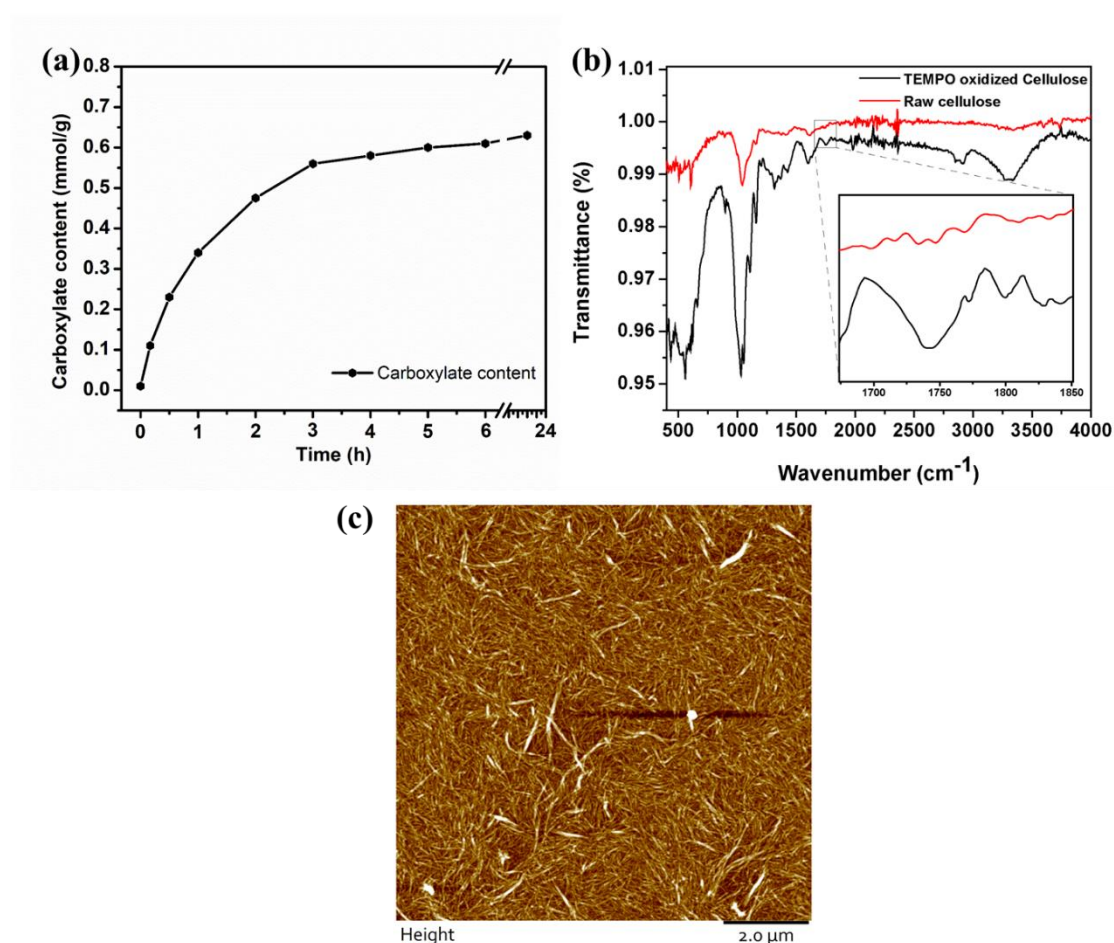


**Figure 6.3** Characterization of nanofibrillar cellulose (NFC); (a) Assessment of carboxylate content of the nanofibrillar cellulose prepared from the TEMPO mediated oxidation. (b) FTIR spectra of TEMPO oxidized cellulose and (c) Atomic Force Microscopy (AFM) images showed fibers like structure. Scale bar  $2\mu\text{m}$ .

**6.2.2 Preparation of peptide cellulose conjugate hydrogel.** After successful modification to the cellulose nanofibrils, we utilized a simple mixing strategy to

construct the composite sugar-peptide hydrogel. In this context, the shortest collagen inspired peptides, i.e., NapFFGKO and NapFFGDO were synthesized using a recently reported protocol.<sup>41</sup> In the previous work, as mentioned in chapter 3, we have reported that when these ionic complementary peptides were mixed at an optimum ratio, they tend to self-associate with each other through an effective salt-bridge formation leading to the fabrication of self-associated hydrogel at physiological pH.<sup>41</sup> Two different ratios (w/w) of nanofibrillar cellulose vs peptide were used to prepare the cellulose conjugate hydrogels (2:1 and 5:1). The dissolved solution of collagen inspired peptides was mixed in the dispersed cellulose suspension and the solutions were kept overnight at -2 °C for gelation. The detailed methodology has been described in the chapter 2 in this thesis. Gelation was followed by washing with water so as to get rid of excess base by diffusion or solvent exchange method to attain physiological pH (Figure 6.4).

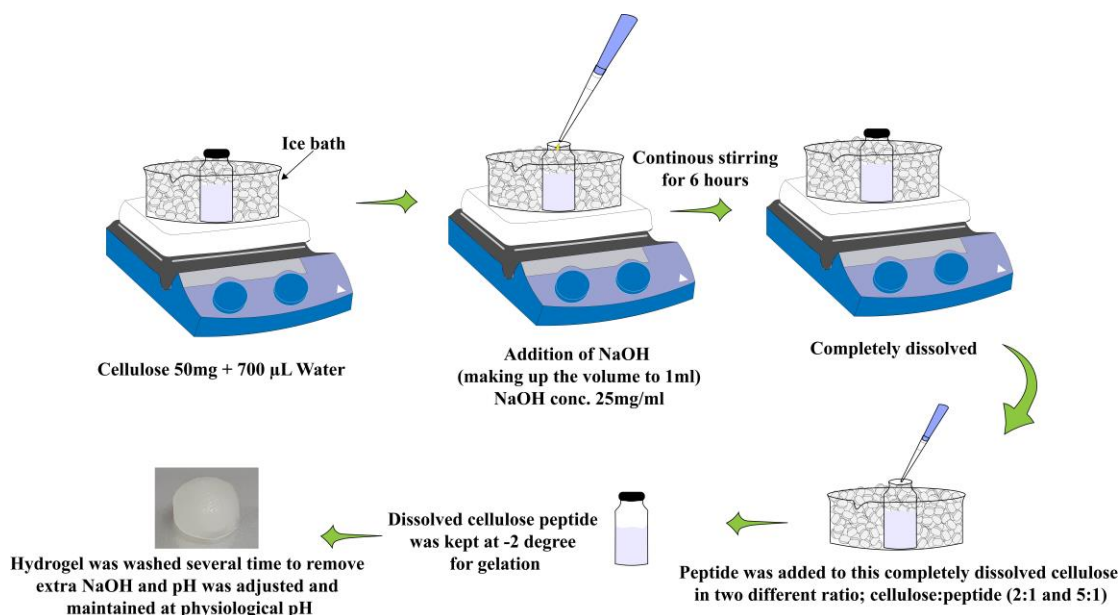


**Figure 6.4** Schematic representation of the stepwise hydrogelation methodology of cellulose peptide conjugate hydrogels.

However, the hydrogels formed by nanocellulose and peptide ratio of 2:1 showed mild structural disintegration while washing as compared to 5:1 ratio, which was further investigated through mechanical strength analysis. Interestingly, NapFFGKO was found to induce the formation of hydrogels with nanofiber cellulose at physiological pH; however, NapFFGDO failed to form the hydrogel. Such differential behavior of the two peptides in the cellulose matrix may have originated from the differential surface charge of the peptides at physiological pH.<sup>41</sup> As expected, it can be assumed

that the positively charged NapFFGKO may interact with the carboxyl group of cellulose nanofibers through salt-bridge interaction to induce the association of the peptide motif to the cellulose matrix. However, NapFFGDO will experience a charge repulsion from cellulose nanofiber and thus failed to form a stable gel with cellulose fibers. Charge repulsion between negatively charged peptide and carboxyl groups of modified cellulose nanofibers outweighs the possible CH/ $\pi$  and H-bonding to stabilize the co-assembly of two molecular components. Interestingly, when both the differentially charged peptides i.e., NapFFGKO and NapFFGDO were mixed with nanofibrous cellulose, the negatively charged moiety of aspartate is expected to be engaged in forming electrostatic interaction with the lysine residue of NapFFGKO and hence the composite peptide fiber will not display any negative surface charge for imparting the charge repulsion with cellulose nanofibers. Apart from the CH/ $\pi$  and H-bonding, the conjugate system was now also accommodating the electrostatically stabilized peptides, which enhanced the stability of the multi-component biomolecular system and thus making it a more stable self-supporting hydrogel-based biomaterial owing to the additional intermolecular interactions leading to induction of advanced properties.

**6.2.3 Microscopic characterization of conjugate hydrogels.** The morphological analyses of nanofibrillar cellulose and peptide conjugated cellulose hydrogels were carried out using a scanning electron microscope. The conjugate hydrogels showed well defined, interconnected, three-dimensional porous networks, similar to nanofibrillar cellulose (Figure 6.5). However, the pore size and distribution were different in cellulose and cellulose peptide conjugate gels (Figure 6.5d-f). Interestingly, the bioactive peptide motifs have marked a clear impact on the differential pore size distribution owing to the differential charge display at the exposed surface leading to differential structural overlap, as induced by variable intermolecular interaction. For all the hydrogels, pore size was found to be in the micron range, however, ionic complementary peptides i.e., NapFFGKO and NapFFGDO induced highly porous structure compared to other conjugate gels induced by cationic peptide, i.e., NapFFGKO (Figure 6.5c). The number of pores can be used to describe the surface roughness, as higher pore distribution depicts a more rough surface, whereas a surface with lesser pores appears smooth (Figure 6.5d-f).<sup>53</sup> The plausible reason for differential surface appearance might be due to the ionic interactions between positively charged

CIPs and the carboxyl group of cellulose that led to the increased fibril dimension and smooth surface. However, the mixed CIPs introduced salt bridge interactions leading to a greater extent of CH/ $\pi$  and H-bonding interaction resulting in a relatively more compact network with more roughness.

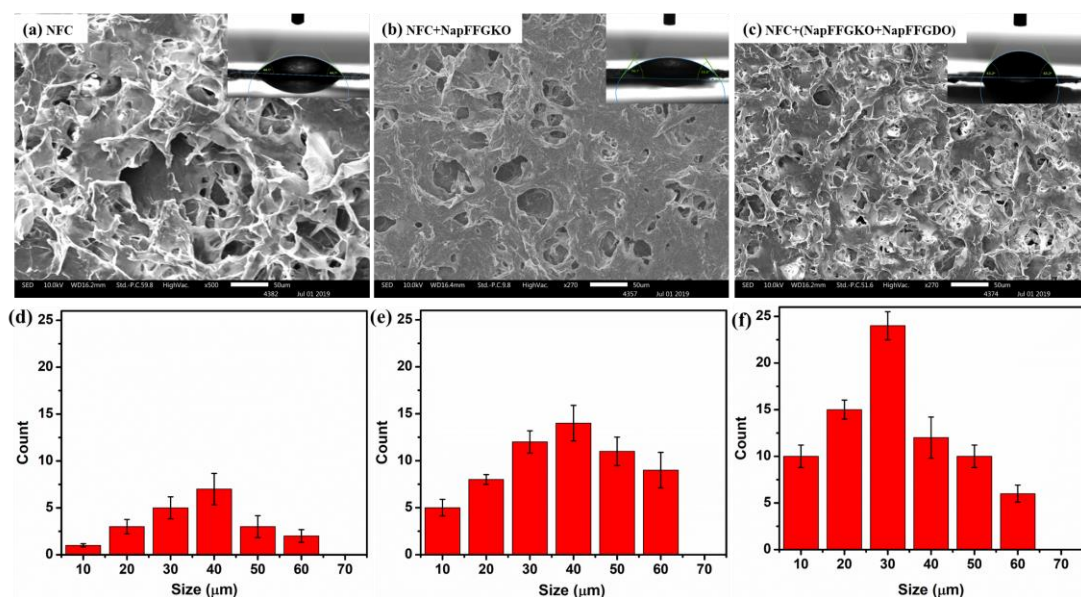


**Figure 6.5** Scanning electron micrograph images of NFC (a) and 5:1 cellulose peptide conjugate hydrogel (b & c) showing the porous nature of material. Scale bar 50μm. Image inset shows the contact angle measurement. Histogram developed from the pore distribution in the (d) NFC, (e) NFC + NapFFGKO, and (f) NFC + (NapFFGKO + NapFFGDO) hydrogels, representing the amount of pore distributed in the samples.

**Table 6.1** Contact angle measurement of nanocellulose (NFC) and peptide conjugated nanocellulose hydrogels.

	Contact angle
NFC	44.1°
NFC+NapFFGKO	55.0°
NFC+(NapFFGKO+NapFFGDO)	63.2°

To further confirm the surface roughness and hydrophobicity of the composite hydrogels, we measured contact angles.<sup>54</sup> Nanofibrillar cellulose showed a contact angle of 44.1° while the conjugate hydrogel with positively charged peptide showed a moderate increase in the contact angle of 55.0° and thus indicating a relatively

hydrophobic surface. Interestingly, the conjugate composite gels containing the ionic complementary peptides together with nanofibrillar cellulose showed a further increment in the contact angle to 63.2° (Table 6.1), suggesting an incremental enhancement in the hydrophobicity of the composite material, which was expected to be more favorable for improved cellular adhesion.

**6.2.4 Small Angle X-Ray Scattering (SAXS) analysis.** In an attempt to understand the mechanism behind the formation of different porous and surface topologies due to cellulose peptide interactions, the small-angle X-ray scattering (SAXS) technique was used. SAXS intensity  $I(Q)$  profiles were measured for NFC, NFC+NapFFGKO and NFC+(NapFFGKO+NapFFGDO) gels (Figure 6.6a). The SAXS data were fitted to the Debye model, which considers small-angle scattering from monodisperse Gaussian polymer<sup>55</sup> and the Schulz-Zimm model takes scattering from polydisperse Gaussian polymer. Guinier approximation was used at a very small scattering angle to assess the SAXS scattering data.<sup>56</sup>

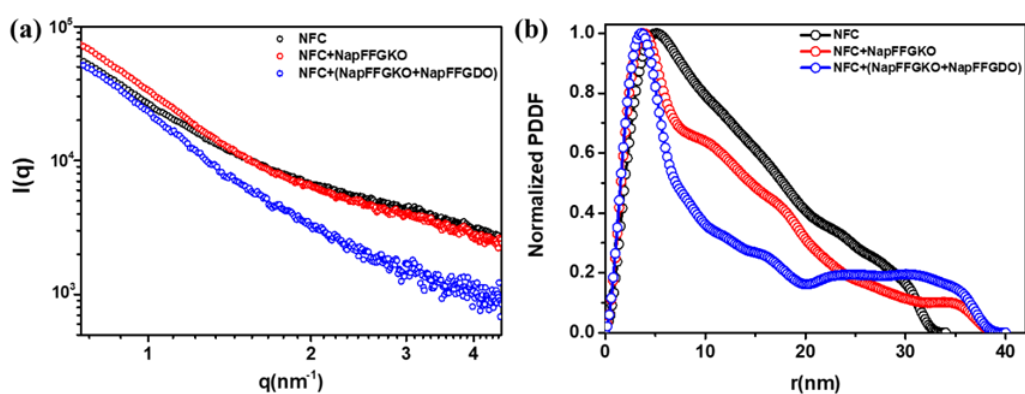


**Figure 6.6** Small angle x-ray scattering profile of cellulose peptide conjugate hydrogels; (a) SAXS data profile displaying double logarithmic intensity versus  $Q$  plot for NFC (black) and NFC-peptide conjugate (red and blue) hydrogels. (b) Pair-distance distribution function (PDDF) plot for NFC and NFC-peptide conjugate hydrogel obtained through IFT.

Guinier plot shows the scattering intensity  $I(q)$  vs square amplitude of scattering vector,  $q^2$  (Å<sup>-2</sup>),<sup>57</sup> which allows the calculation of radius of gyration and the intensity  $I(0)$  at zero angle scattering ( $q=0$ ). The radius of gyration ( $R_g^2$ ) is the average electron density-weighted squared distance of the scatters from the center of the object.<sup>58</sup> The zero-angle

scattering intensity and radius of gyration are used to calculate and generate molecular weight and valid structure of the molecule, respectively.<sup>59</sup>

**Table 6.2:** Biophysical properties of NFC and NFC-peptide conjugated hydrogels; both model dependent and model independent methods were used to calculate  $R_g$ .

	$R_g$ (nm) (Guinier Model)	Model fit $R_g$ (nm) (Debye Model)	Model fit $R_g$ (nm) (Schulz-Zimm Model)	Radius (nm)
NFC	....	5.52±0.12	5.58±0.45	7.803
NFC+NapFFGKO	4.53±0.09	6.71±0.03	6.87±0.03	9.488
NFC+ (NapFFGKO +NapFFGDO)	3.76±0.02	5.14±0.01	5.03±0.01	7.268

Guinier plot is shown with the line of best fit, which also provides the information about sample aggregation and interparticle interference according to the movement of slope of the plot. A linear Guinier plot suggests the sample is free from both aggregation and interparticle interference.<sup>60</sup> The  $R_g$  (radius of gyration) of the NFC from shape independent model fit was 5.52 nm, consistent with Guinier analysis (Figure 6.7). The  $R_g$  of NFC+NapFFGKO and NFC+(NapFFGKO+NapFFGDO) were 6.71 nm and 5.14 nm, respectively (Table 6.2). It was interesting to note that the  $R_g$  value obtained for NFC was slightly lower than the NFC+NapFFGKO, suggesting the complete overlap of the hydrodynamic volume of cellulose fibers while slightly higher  $R_g$  with NapFFGKO+NapFFGDO suggests a small overlap between the hydrodynamic volume of NFC and combined peptide and maximum part of the NFC were fairly exposed to the solvent and not covered by the peptide.<sup>56</sup>

**Table 6.3** Maximum particle dimensions used for IFT techniques for NFC and NFC peptide conjugate gels.

	Bayesian $D_{max}$	Glatter $D_{max}$
NFC	33.81	34.25
NFC+NapFFGKO	38.45	39.32
NFC+(NapFFGKO+NapFFGDO)	39.22	40.32

Additional information about the shape of the particle can be measured by calculating the pair distance distribution factor (PDDF) (Figure 6.6b). PDDF was calculated by two different techniques, Glatter's<sup>61</sup> technique and a tool that uses Bayesian statistics.<sup>62</sup> Both the methods produce the similar radii of gyration (Table 6.3). Higher  $D_m$  value of NFC peptide conjugates suggested the overlapping of peptide on the surface of cellulose fiber, which was less in the case of combined peptide (NapFFGKO+NaapFFGDO) while higher in the case of (NapFFGKO) mostly because of the greater extent of charge interactions.

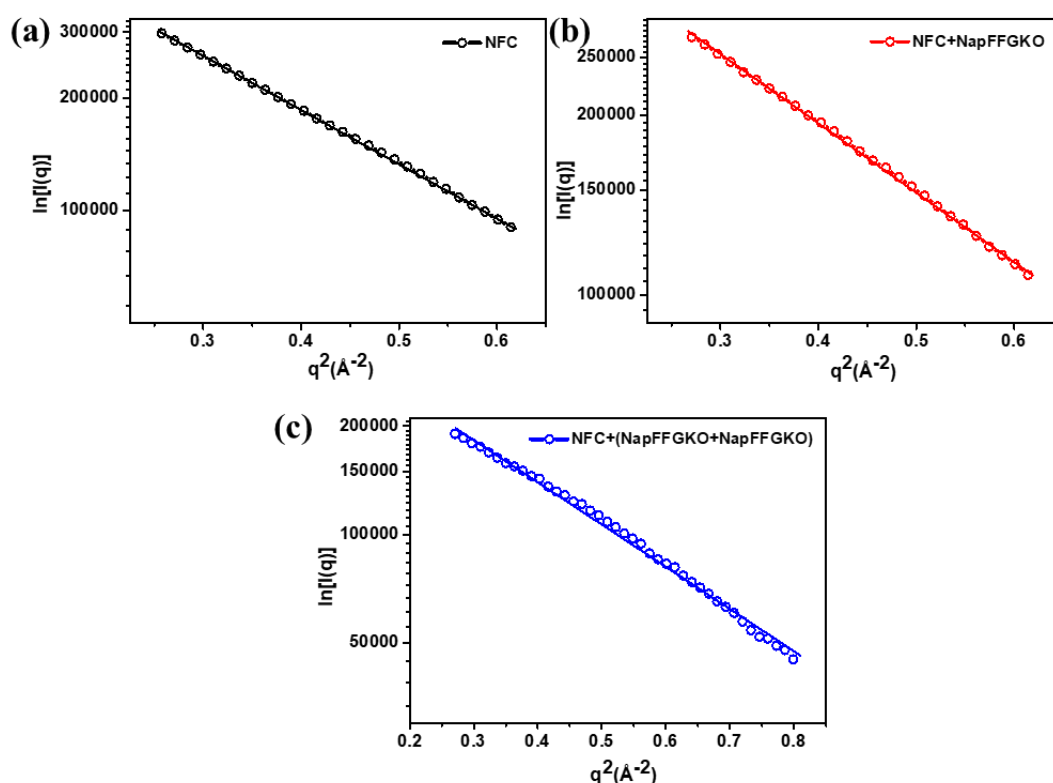


**Figure 6.7** Guinier plot analysis for (a) NFC, (b)NFC+NapFFGKO and (c) NFC +(NapFFGKO+NapFFGDO).

Using the SAXS  $I(Q)$  and  $P(r)$  profiles, scattering shape of NFC peptide conjugates under different conjugation and association state were computed and was compared with the unconjugated NFC to check the structural change in the cross section of NFC (Figure 6.8). Moreover, the resultant DAMMIF models<sup>63</sup> of peptide conjugates were superimposed with NFC by aligning their inertial axes, NFC+NapFFGKO model (Figure 6.8b) showed increased cross-sectional area in comparison to the unconjugated NFC, confirming the charge-based interaction.

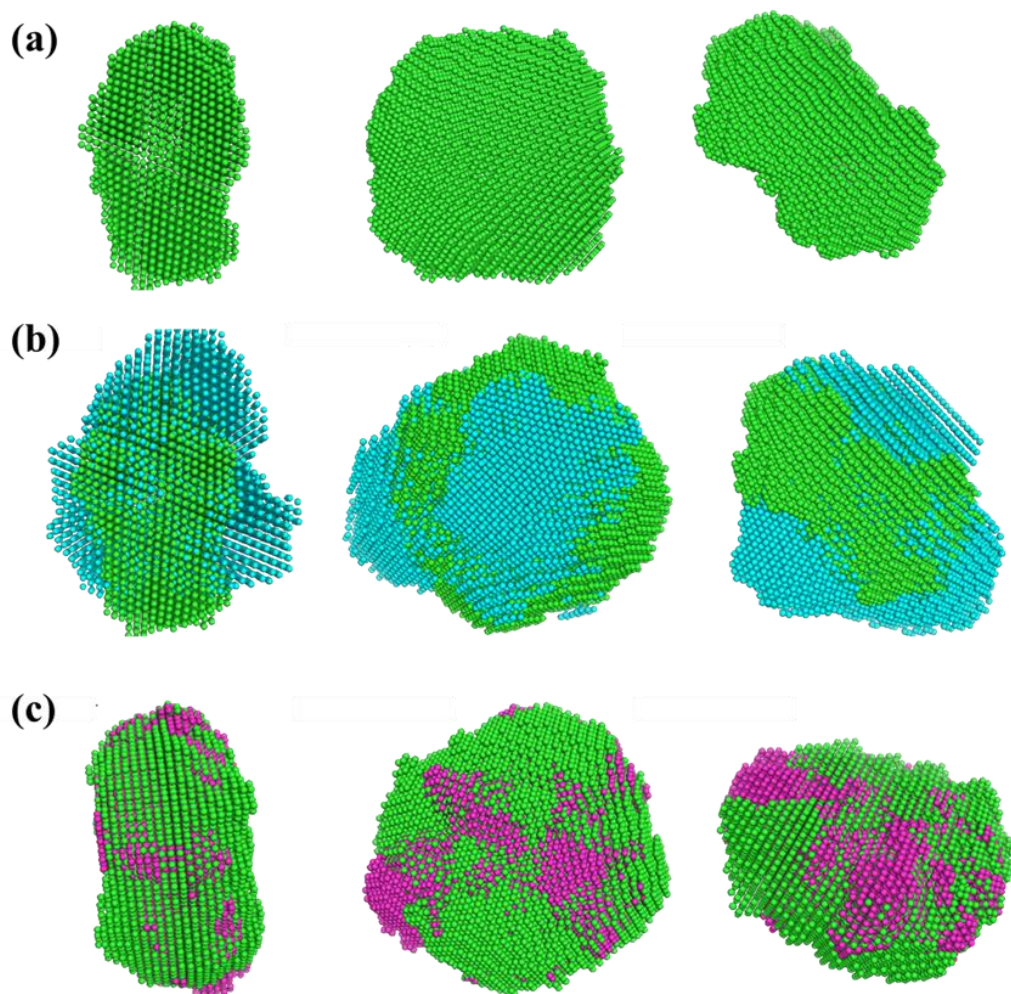


**Figure 6.8** In-silico modelling of the cellulose peptide conjugate hydrogels (a) Scattering shape of NFC hydrogels restored from dummy atom modelling (DAMMIF). SAXS envelop of NFC and their overlay with the conjugated models, (b)NFC+NapFFGKO and (c)NFC+ (NapFFGKO+NapFFGDO).

**6.2.5 Mechanical property of conjugate hydrogel.** It is crucial to understand the effect of peptide conjugation with the cellulose fiber on their mechanical strength as it plays a crucial role in controlling cellular behavior.<sup>64</sup> A moderate increment in storage modulus was evident in NFC+NapFFGKO, i.e. 7.5 KPa, compared to NFC, i.e. 6.5 KPa. Owing to the association of both components with additional electrostatic interactions, which has also been reflected in their contact angle enhancement studies. The individual peptide showed mechanical strength in the range of 3-4 KPa while the co-assembled peptide hydrogels showed mechanical strength in the range of 7-8 KPa. Furthermore, the incorporation of NFC matrix influenced the mechanical strength and structural rigidity of the matrix, which further enhances the scope of this biomaterial to

be used as scaffold for futuristic applications. However, the combination of the ionic complementary peptide in the cellulose matrix showed has a significant influence on the gel strength of the conjugate matrix. The value increased to 13.5 KPa and 17 KPa depending on the mixing ratio of cellulose and peptide components i.e., 2:1 and 5:1. (Figure 6.9), which was further evident from the highest contact angle values of the conjugate hydrogel, indicating the significant enhancement in the hydrophobicity.

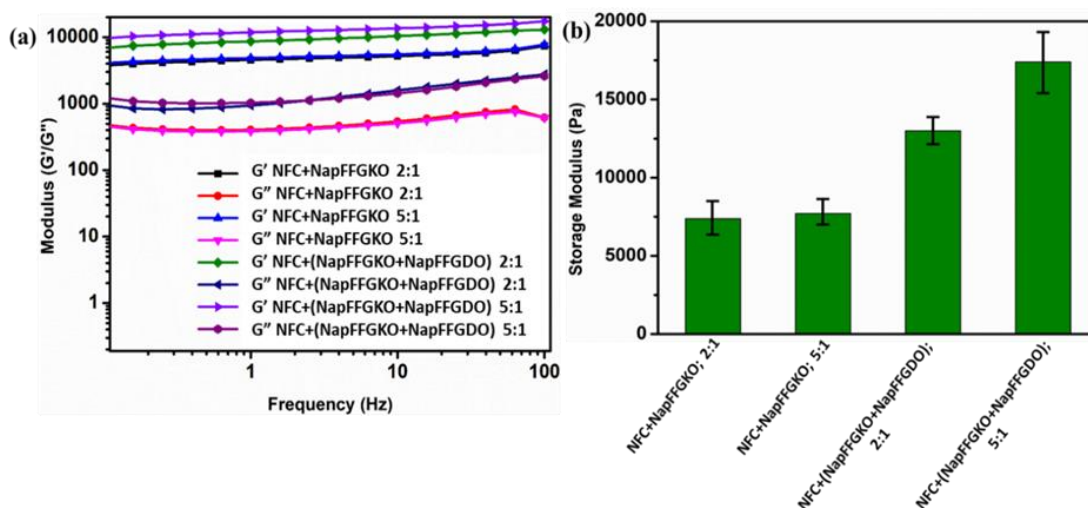


**Figure 6.9** Mechanical strength analysis: (a) frequency sweep performed for the cellulose peptide conjugate hydrogels at different mixing ratios. (b) Comparison of mechanical strength of conjugate hydrogels at different ratio.

As illustrated from the mechanical stiffness study, conjugate hydrogels with cellulose and peptide in 5:1 ratio were more stable and showed higher mechanical strength. Hence, all the experiments, including surface morphology, SAXS analysis, and cellular response, were performed, keeping the ratio of cellulose to peptide 5:1.

**6.2.6 Biocompatibility assessment of the conjugate hydrogel.** Since its inception, the design concept of combining bioactive peptide sequence within cellulose matrix was directed to fabricate the next-generation biomaterial, which could essentially mimic the microenvironment of native ECM. To this direction, cytotoxicity of the cellulose peptide conjugate material was evaluated by MTT assay.<sup>65</sup> The fibroblast (L929) cells and neural (SH-SY5Y) cells were incubated with cellulose-peptide conjugates at different concentrations for 48 hrs. For both the cell lines of different origin almost 100% viability was observed in unconjugated and conjugated hydrogels up to 1000  $\mu\text{g/ml}$  concentration, suggesting the highly biocompatible nature of these biomaterials

(Figure 6.10a-c). To obtain further supportive evidence for biocompatibility of these matrices, bright field images of the cells on the matrices were captured, which showed the elongated cells similar to control cells, suggesting no morphological changes in the metabolically active cells (Figure 6.10b-d).

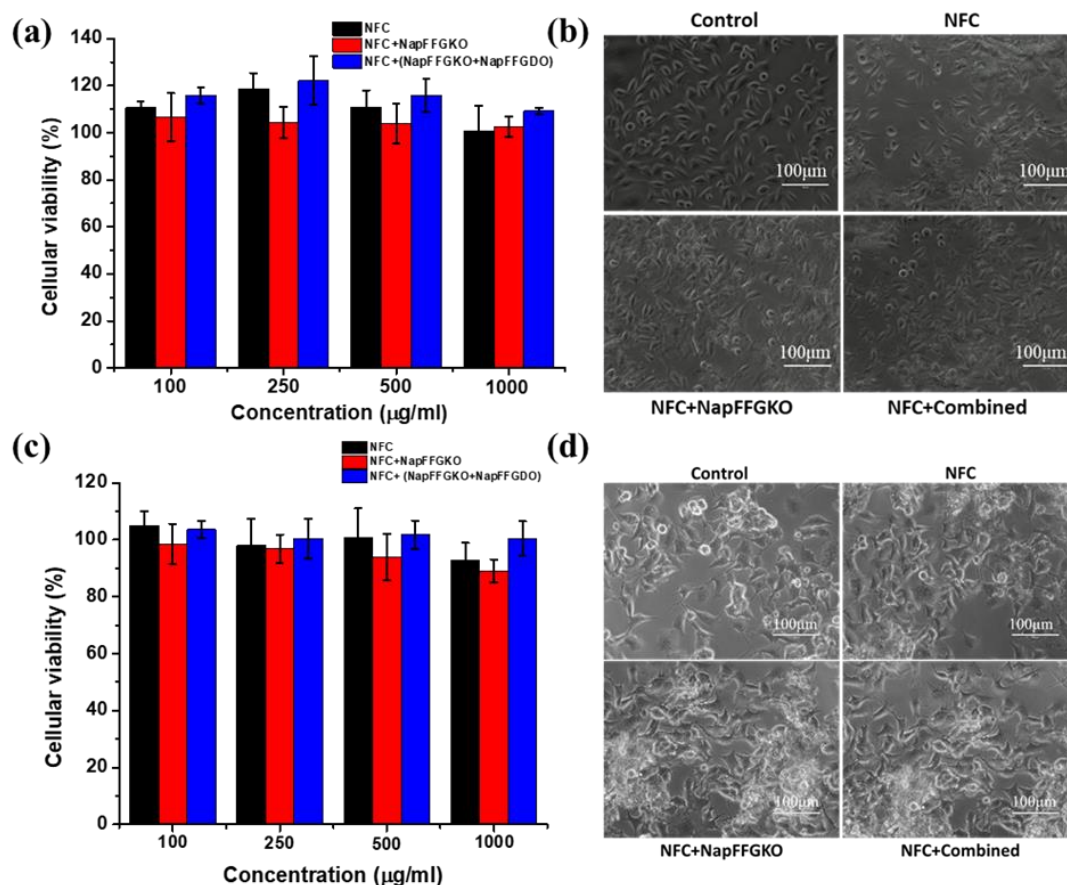


**Figure 6.10** Biocompatibility studies of cellulose-peptide conjugate hydrogels on (a) fibroblast cells (L929) and (c) neural cells (SH-SY5Y) at concentration ranging from 100µg/ml to 1000 µg/ml. Bright field images of (b) L929 and (d) SH-SY5Y cells respectively after 48hrs of incubation with the NFC and NFC peptide conjugate hydrogels at 500 µg/ml concentration along with the control. Scale bar 100 µm.

**6.2.7 2D cell culture on conjugate hydrogel.** Furthermore, we were quite curious to explore this new class of designer biomaterials towards the fabrication of the bioactive scaffolds, which can show immense potential for cellular growth and proliferation on these matrices.<sup>66, 67</sup> To this direction, live-dead staining was performed on these 2D constructs. In particular, a thin layer of conjugate hydrogel was set on a glass coverslip, which was further perfused with culture medium to check the gel layer stability over 24

hrs. Cell culture medium was replaced and both types of cells were seeded onto the surface of the prepared conjugate hydrogels. The adhesion of cells followed by proliferation were investigated on these biomaterials for 5 days (Figure 6.11 and 6.12).

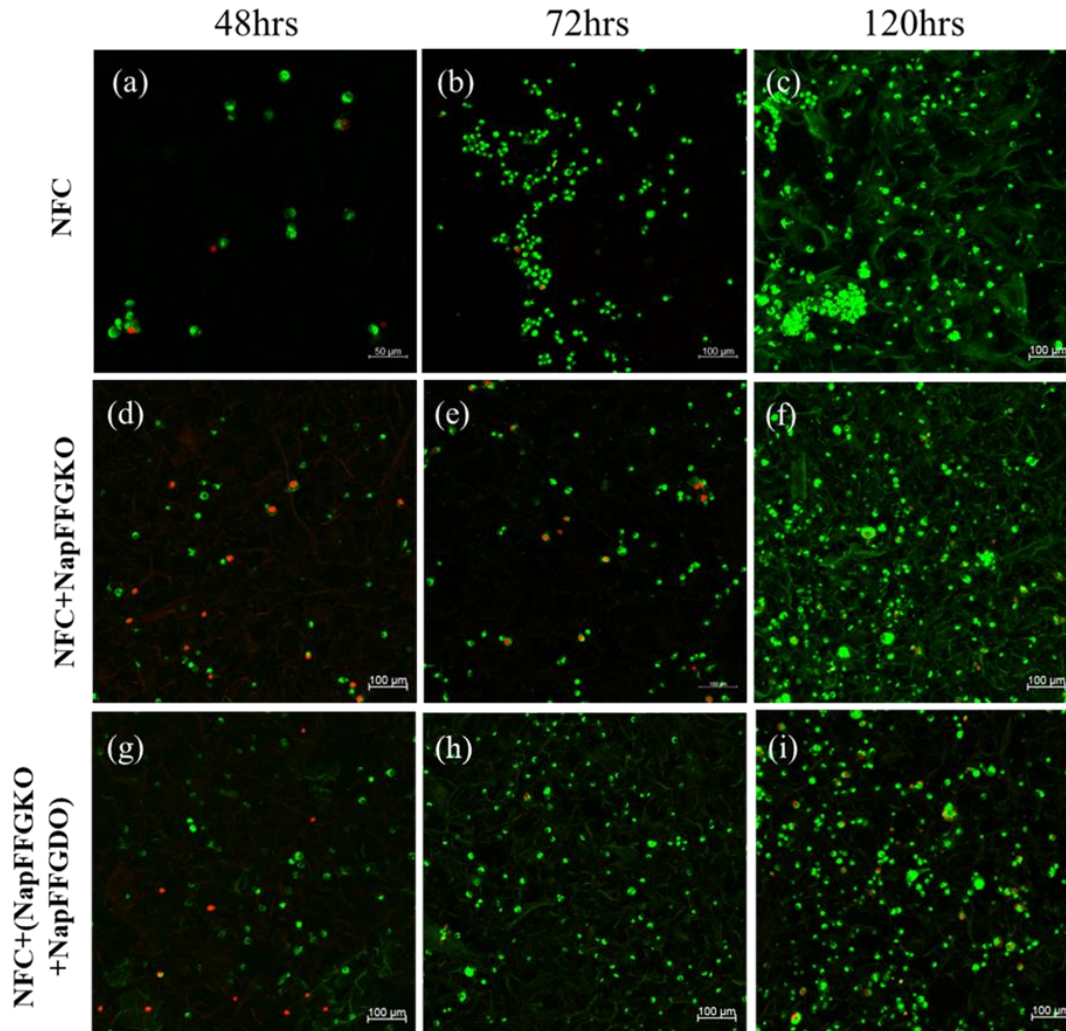


**Figure 6.11** Cellular adhesion (2D) study of L929 cells on cellulose-peptide conjugate hydrogels. Assessment of cellular adhesion and proliferation on conjugate hydrogels by Live/Dead staining. Images of cells after fluorescence staining showing cellular adhesion on (a to c) NFC, (d to f) NFC+NapFFGKO, (g to i) NFC+(NapFFGKO+NapFFGDO) after 48 hrs, 72 hrs and 120 hrs respectively. Scale bar 100 μm.

Interestingly, a clear difference was evident in cellular proliferation depending upon the surface functionality of these gels. It was quite interesting to note a significant enhancement in the cell density on these NFC and NFC-peptide conjugate gels over

time. The positively charged peptide NFC+NapFFGKO showed a slow progression in cellular growth and proliferation as compared to other conjugate gels.

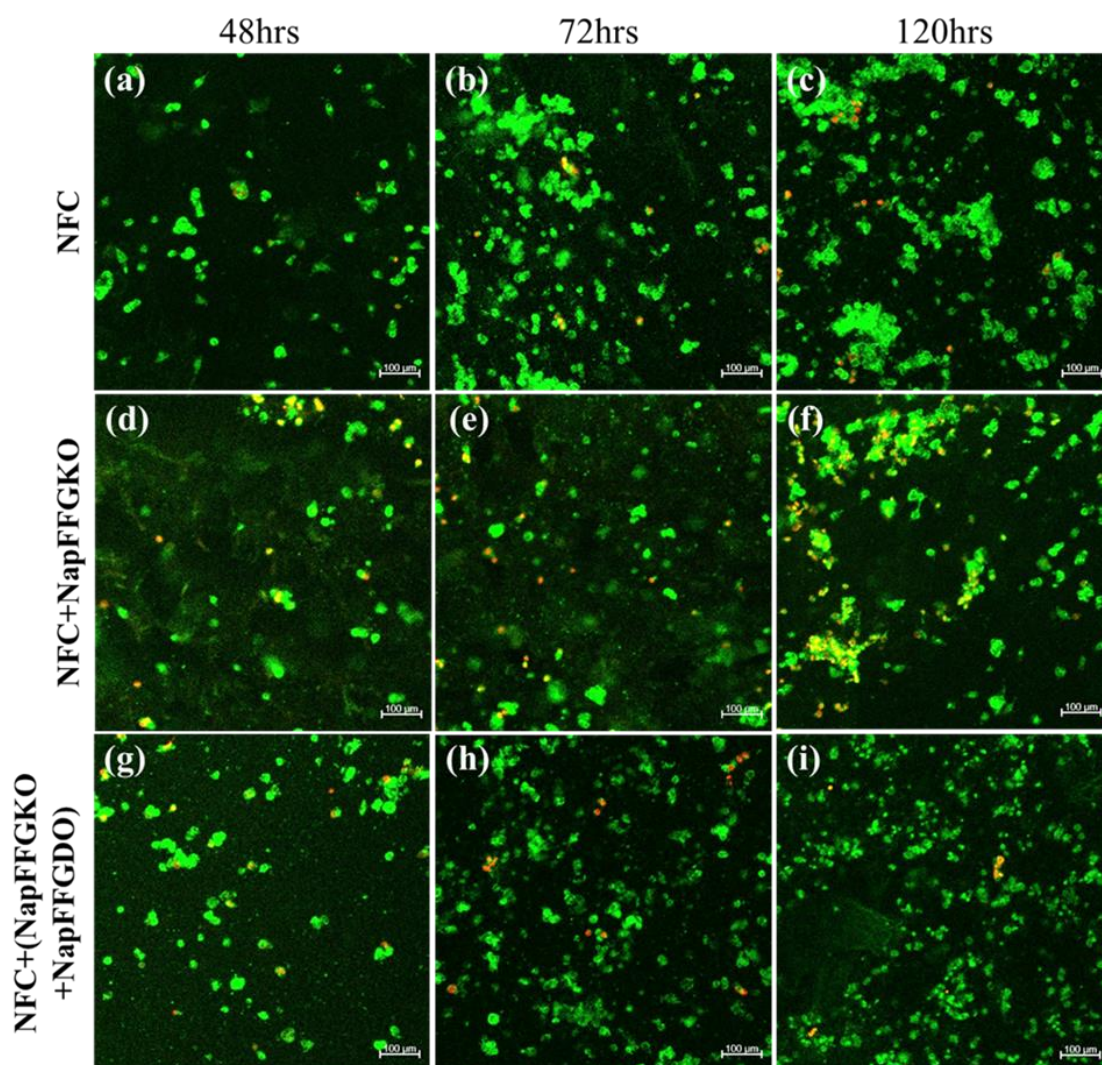


**Figure 6.12** Cellular adhesion (2D) study of SH-SY5Y cells on cellulose-peptide conjugate hydrogels. Assessment of cellular adhesion and proliferation on conjugate hydrogels by Live/Dead staining. Images of cells after fluorescence staining showing cellular adhesion on (a to c) NFC, (d to f) NFC+NapFFGKO, (g to i) NFC+(NapFFGKO+NapFFGDO) after 48 hrs, 72 hrs and 120 hrs respectively. Scale bar 100 μm.

The possible reason for this differential bioactivity could have been originated from their different surface topology. As smooth surface morphology of the NFC+ NapFFGKO conjugate hydrogel provides lesser surface area for cell adhesion and proliferation, in contrast to that of rough surfaces of the conjugate gels with ionic complementary peptides and cellulose nanofibers, which promotes the adhesion of cells

to the surface in the conjugate gels containing ionic complementary peptides.<sup>53</sup> The confocal microscopic images further confirmed that a more porous and rougher surface of NFC+ (NapFFGKO+NapFFGDO) promoted the proliferation of a greater number of live cells, suggesting a superior matrix for the adherence of fibroblast cells.

**6.2.8 Cellular proliferation assay on conjugate hydrogels.** The above studies have clearly demonstrated that the nanofibrous cellulose and peptide conjugated hydrogel scaffold were significantly biocompatible and supportive for the improved adhesion and growth of both the fibroblast and neural cells. In order to find out the versatility of these scaffolds, it will be highly desirable to quantify the total cellular viability and cellular proliferation of the cells on these newly designed matrices. Interestingly, Alamar blue assay was found to be an exclusive solution to this direction, as it was earlier shown to display a significant potential for quantification of cellular proliferation.<sup>68</sup>

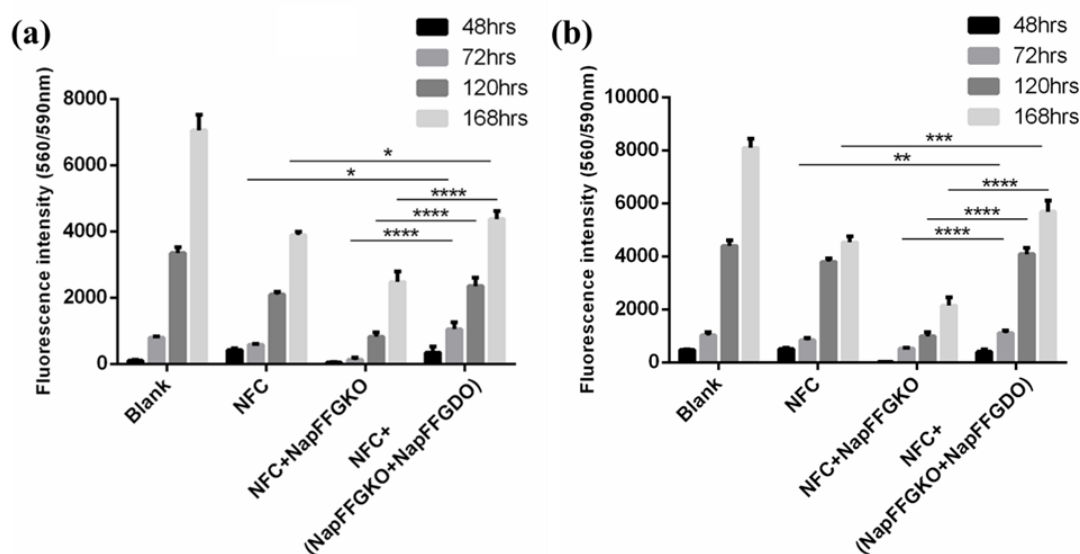


**Figure 6.13** Evaluation of cellular viability and proliferation via Alamar assay on (a) fibroblast cells (L929) and (b) neural cells (SH-SY5Y) with conjugate hydrogels at 5:1 (NFC:peptide) concentration at different time point. All data presented as mean  $\pm$  SD. \* represents P-value  $\leq$  0.05 \*\* P-value  $\leq$  0.01, \*\*\* P-value  $\leq$  0.001 and \*\*\*\* P-value  $\leq$  0.0001 (Two-way ANOVA, Bonferroni's multiple comparisons tests).

Very interestingly, similar cell counts were observed in conjugate gels as that of the control sample. Such observation was a clear indication of the cell supportive behavior of this conjugate matrix for both the cell lines. Over a longer period of time, i.e., 7 days,

NFC+NapFFGKO exhibited decreased cell population compared to that of the unconjugated NFC matrix. The anomalous behavior could be correlated with the presence of positively charged peptides on the surface of this hydrogel, which may lead to the formation of a smooth surface and thereby interfering with cellular adhesion and proliferation. However, the association of the two complementary ionic peptides in conjugate gels with NFC exhibited a significantly higher proliferation rate, which demonstrated a steady enhancement in the proliferation from 72 hrs gradually up to 7 days (Figure 6.13). Significant enhancement in cell population could be explained through the formation of a more porous and comparatively rough surface of the conjugate matrix, leading to increased cell density.<sup>53</sup>

**6.2.9 Cytoskeletal staining.** In 2D investigations, live-dead staining with fibroblast cells revealed that the matrix was biocompatible, which can support cellular viability and growth of cells on nanofibrillar cellulose and peptide conjugated nanofibrillar cellulose matrix. The conjugate system with co-assembled peptide showed similar adhesion and proliferation as that of the control. Whereas, the positively charged peptide (NapFFGKO) conjugate hydrogel showed slow progression in cellular growth and proliferation. In order to visualize the change in the cellular morphology, cells were stained with phalloidin (Rhodamine Phalloidin) and DAPI for F-actin and nuclei, respectively. After labeling the cells adhered to the thin layer of hydrogel with phalloidin and DAPI, cellular morphology was monitored at different time points (Figure 6.14). The investigation revealed that L929 cells were able to interact with the matrix and showed a spread morphology as that of the control. Fluorescence images showed the cells on nanofibrillar cellulose and conjugate hydrogel with co-assembled peptide [NFC + (NapFFGKO + NapFFGDO)] were spread and had a larger area ( $405\pm 32$  and  $426\pm 34 \mu\text{m}^2$ , respectively). Conversely, conjugate hydrogel containing the positively charged peptide (NFC + NapFFGKO) showed cells with less spread area ( $302\pm 28 \mu\text{m}^2$ ) (Table 6.4). The CSI plot indicated that there had been no significant difference between all the samples as compared to the control (Figure 6.15). Whereas, less spread area was observed in NFC + NapFFGKO, correlating with the 2D culture results of differential surface topology led to the differential adhesion and proliferation. Further, the calculated CSI value represents the measure of cell shape and size parameters. The CSI value close to 1 represents the circular shape, while a CSI value close to 0 suggests a linear elongated morphology.

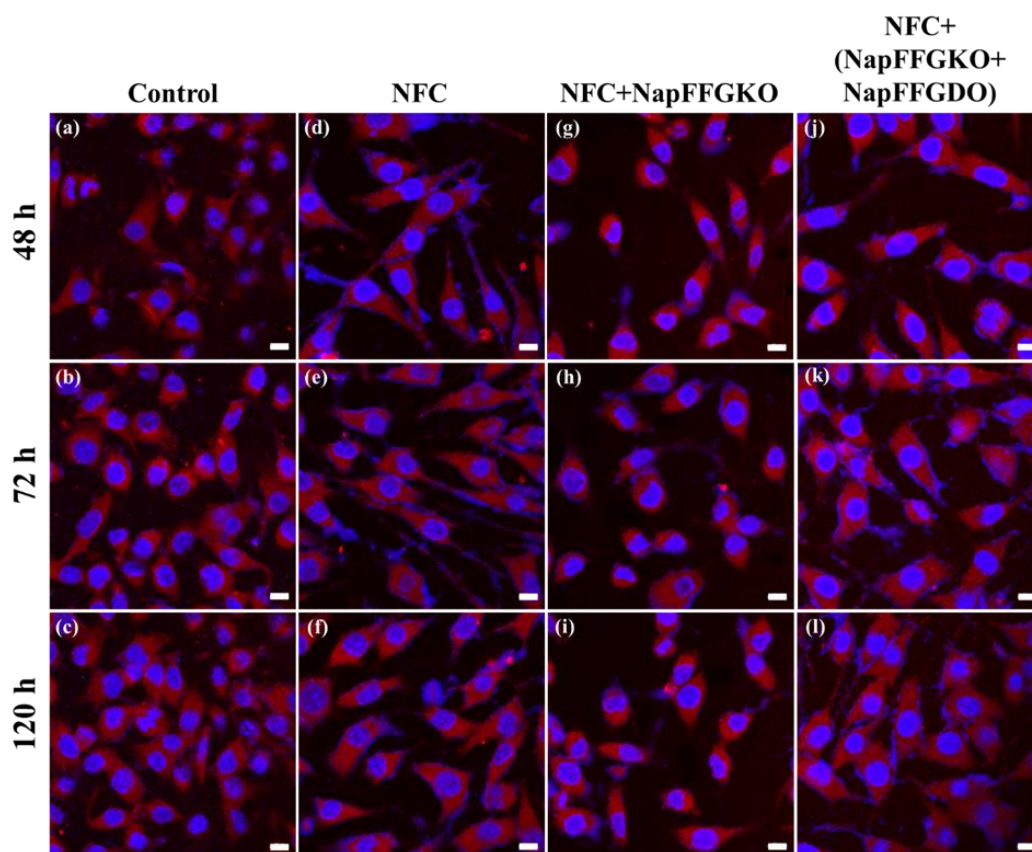


**Figure 6.14** Cytoskeletal analysis in L929 cells in 2D cell culture on NFC and peptide conjugated NFC. Staining of F-actin microfilaments with Rhodamine Phalloidin in L929 cells cultured on control coverslips (a-c), (d-f) Nanofibrillar cellulose, (g-i) NFC + NapFFGKO, and (j-l) NFC + (NapFFGKO+NapFFGDO) at different time point 48 hrs, 72 hrs, and 120 hrs of cell culture, respectively. Scale bar is 10 $\mu$ m.

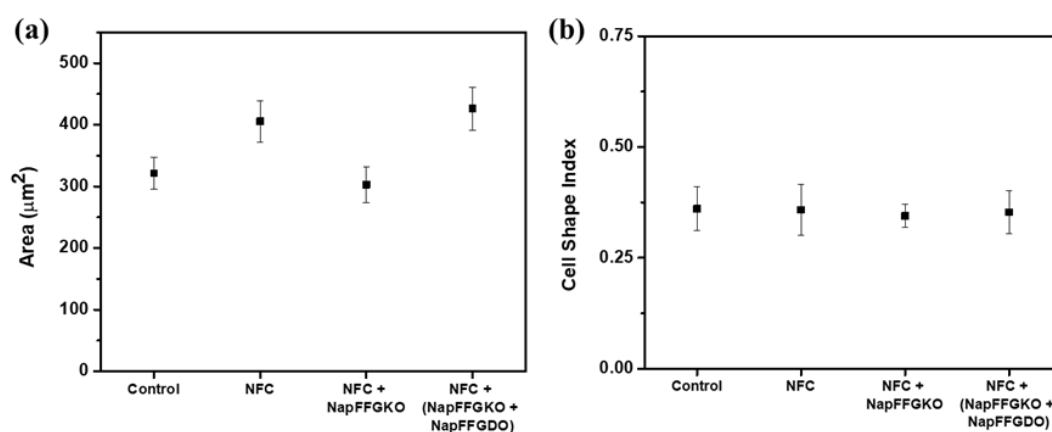


**Figure 6.15** Quantification of (a) cell spreading area and (b) cell shape index of fibroblast (L929) cells on uncoated control and hydrogel coated coverslips.

**Table 6.4** Table on CSI plot and area covered by fibroblast cells in F-actin staining.

Sample	CSI values	Area covered ( $\mu\text{m}^2$ )
Control	$0.3605 \pm 0.04901$	$321 \pm 26$
NFC	$0.35867 \pm 0.05698$	$405 \pm 32$
NFC+NapFFGKO	$0.3445 \pm 0.02622$	$302 \pm 28$
NFC+(NapFFGKO+NapFFGDO)	$0.35325 \pm 0.04884$	$426 \pm 34$

The CSI value of cells on control, nanofibrillar cellulose, and [NFC + (NapFFGKO + NapFFGDO)] conjugate hydrogel showed no significant differences. NFC showed a CSI value of ( $0.35 \pm 0.05$ ), and NFC + (NapFFGKO + NapFFGDO) showed a value of ( $0.35 \pm 0.04$ ), which were similar to that of the control sample ( $0.36 \pm 0.04$ ) (Figure 6.15). Whereas, NFC + NapFFGKO showed a value of ( $0.34 \pm 0.02$ ), suggesting a less spread cell morphology.

**6.2.10 Immunostaining.** Differentiation-dependent neural expression of class III  $\beta$ -tubulin in the central and peripheral nervous system can also be reproduced in neuronal or neuroblastic tumors. Class III  $\beta$ -tubulin is highly and consistently expressed both in neuroblastomas and neuronal neoplasms, but its distribution is more widespread in the subpopulation of tumor cells, demonstrating neuronal differentiation.<sup>69-71</sup> Differential expression of  $\beta$ -III tubulin leads to the differential organization of the actin cytoskeleton, which may drive the morphological changes in the neural cells.<sup>72</sup> To examine the morphological changes in SH-SY5Y cells at different time points on the nanofibrillar cellulose and peptide conjugated cellulose hydrogels, the microtubules of the cells were visualized using immunofluorescence labeling via confocal microscopy. SH-SY5Y cells were seeded on the hydrogel-coated coverslip and were observed for the  $\beta$ -III tubulin expression. The cells were visualized for different time points, i.e., 48 hrs, 72 hrs, 120 hrs (Figure 6.16). The cells on control coverslip and peptide conjugated cellulose hydrogel coverslip demonstrated positive staining with marginal difference in the cell morphology and cell spreading area. Cell spreading area and cell shape index (CSI) were examined to further quantify the change in cellular morphology of the adhered cells.

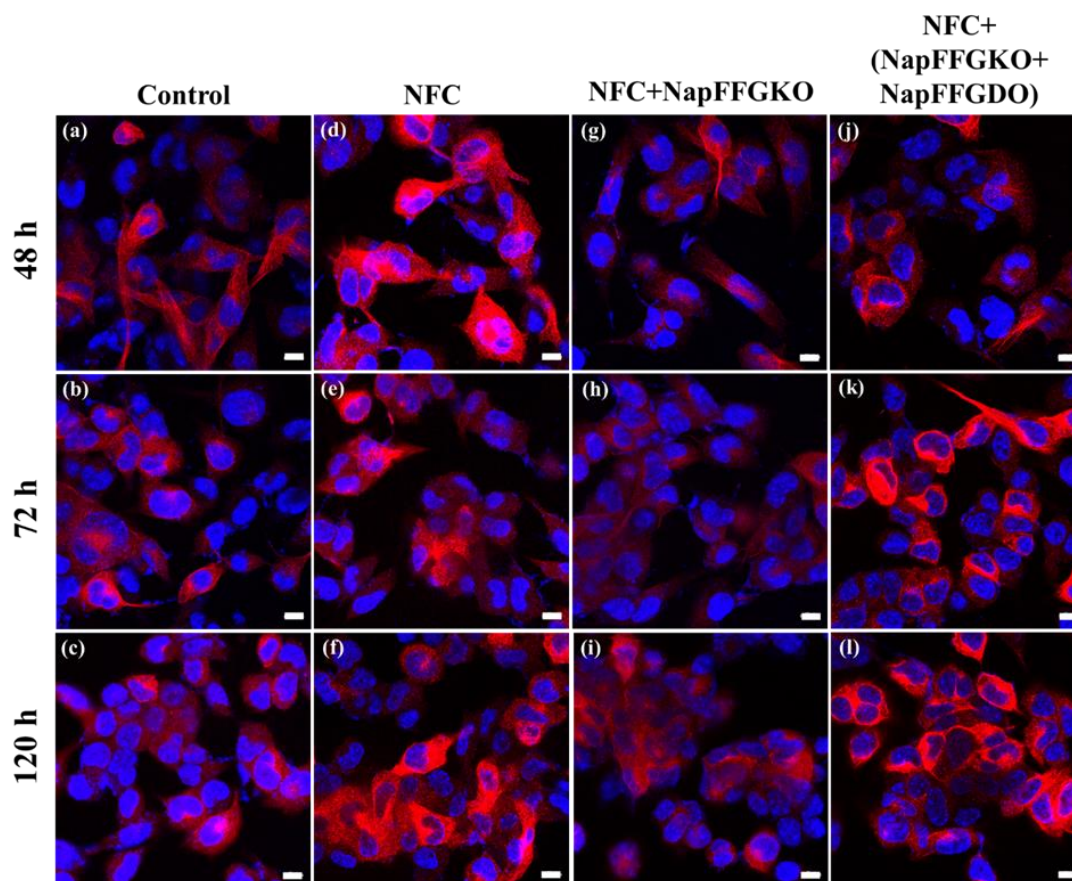


**Figure 6.16** Expression of neural marker  $\beta$ -III tubulin in SH-SY5Y cells in 2D cell culture. Immunofluorescent staining of  $\beta$ -III tubulin in SH-SY5Y cells cultured on control coverslips (a-c), (d-f) Nanofibrillar cellulose, (g-i) NFC + NapFFGKO, and (j-l) NFC + (NapFFGKO+NapFFGDO) at different time point 48 hrs, 72 hrs, and 120 hrs of cell culture, respectively. Scale bar is 10 $\mu$ m.

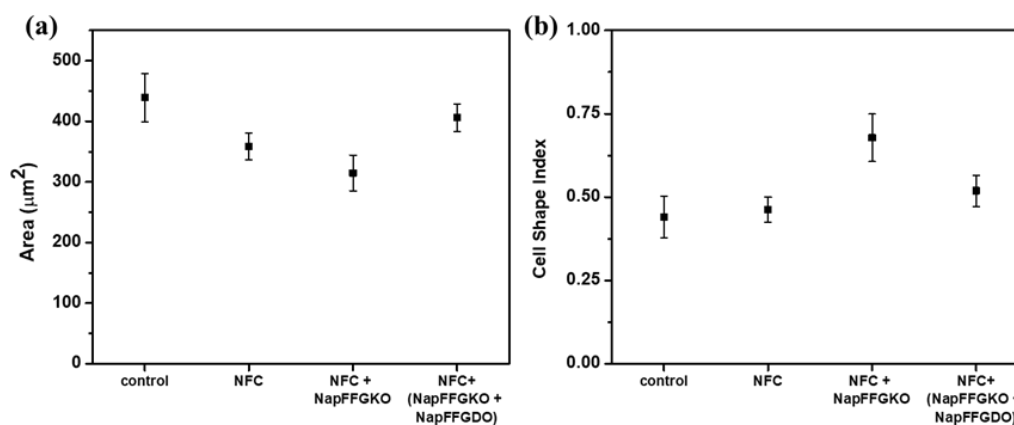


**Figure 6.17** Quantification of (a) cell spreading area and (b) cell shape index of neural (SH-SY5Y) cells on uncoated control and hydrogel coated coverslips.

The spreading area of the cells on peptide conjugate cellulose hydrogel [NFC + (NapFFGKO + NapFFGDO)] was found to be similar to the NFC ( $410 \pm 22$  and  $398 \pm 31 \mu\text{m}^2$ , respectively) (Table 6.5). While the conjugate hydrogel with positively charged peptide (NFC + NapFFGKO) showed ( $315 \pm 29 \mu\text{m}^2$ ) showed a decrease in the spread area (Figure 6.17), as the conjugate hydrogel with positively charged peptide showed less cellular compatibility. Further, the calculated CSI value represents the measure of cell shape and size parameters. The CSI value close to 1 represents the circular shape, while a CSI value close to 0 suggests a linear elongated morphology. The CSI value of cells on control, nanofibrillar cellulose, and [NFC + (NapFFGKO + NapFFGDO)] conjugate hydrogel showed no significant differences. NFC showed a CSI value of ( $0.46 \pm 0.03$ ), and NFC + (NapFFGKO + NapFFGDO) showed a value of ( $0.51 \pm 0.04$ ), which were similar to that of the control sample ( $0.44 \pm 0.06$ ) (Figure 6.17). Whereas, NFC + NapFFGKO showed a value of ( $0.67 \pm 0.07$ ), suggesting a less spread cell morphology.

**Table 6.5** Table on CSI plot and area covered by neuronal cells in  $\beta$ -III tubulin staining.

Sample	CSI values	Area covered ( $\mu\text{m}^2$ )
Control	$0.4405 \pm 0.06255$	$439.29067 \pm 39.83127$
NFC	$0.46167 \pm 0.03789$	$358.643 \pm 21.74971$
NFC+NapFFGKO	$0.67783 \pm 0.07132$	$314.74317 \pm 29.41307$
NFC+(NapFFGKO+NapFFGDO)	$0.5193 \pm 0.0467$	$406.2453 \pm 22.43296$

**6.2.11 Cellular migration assay.** Cell migration is a crucial process involved in many biological processes, as cells should display the potential ability to reach to wound site for its closure. Cell migration is an important procedure that governs the suitability of any new biomaterial for the development of the next-generation synthetic matrix. The cell's ability to interact with the matrix is a critical component that promotes cellular adhesion and proliferation. For wound closure, the synthetic matrix should contain bioactive motifs, which promote cellular adhesion, survival, and growth. In this direction, collagen, known to be the most abundant protein in ECM, plays a crucial role in cell adhesion and migration. As a result, the potential of our minimalistic peptide

design coupled with nanofibrillar cellulose in regulating cell migration can be investigated. Hence, our minimalistic peptide design conjugated with nanofibrillar cellulose can also be explored to reveal their potential in regulating cell migration.

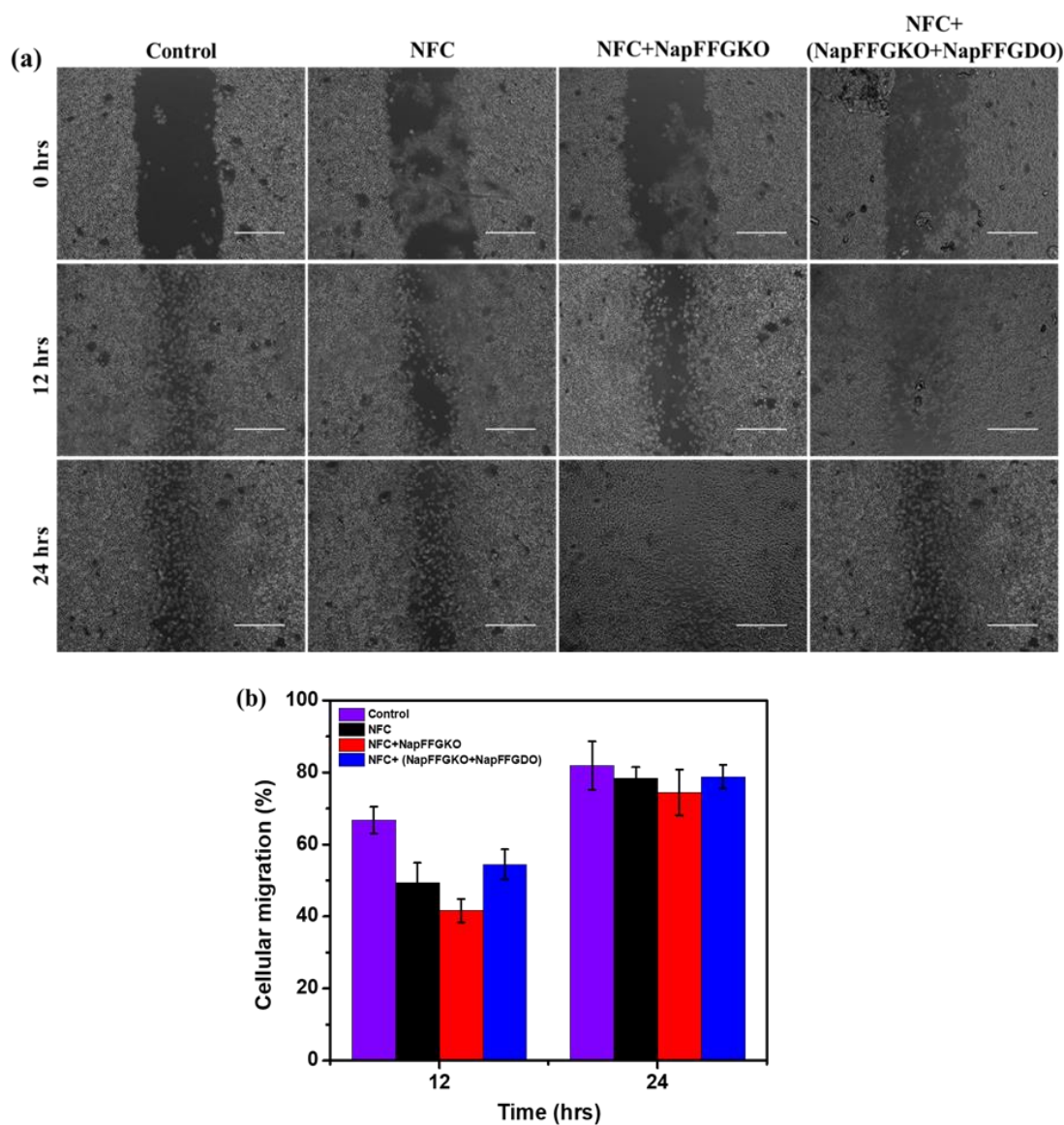


**Figure 6.18** Scratch assay to analyze the cellular migration of L929 cells in presence of nanofibrillar cellulose and peptide conjugated cellulose. (a) Scratch closure with the treatment of all the hydrogels as well as the untreated control at different time point; 0 hrs, 12 hrs, and 24 hrs. Scale bar is 400  $\mu$ m. (b) Quantification of the wound closure with time i.e., after 12 hrs and 24 hrs.

We applied a traditionally used method known as scratch wound assay<sup>72, 73</sup> to assess the cell migration ability of the nanofibrillar cellulose and peptide conjugated cellulose hydrogels. The migration of both fibroblast and neural cells was monitored under a

microscope at different time points up to 24 hours with the treatments. No significant difference was observed in the migration of L929 cells between nanofibrillar cellulose and peptide conjugated cellulose (Figure 6.18). However, a differential response was evident in the case of SH-SY5Y cells.

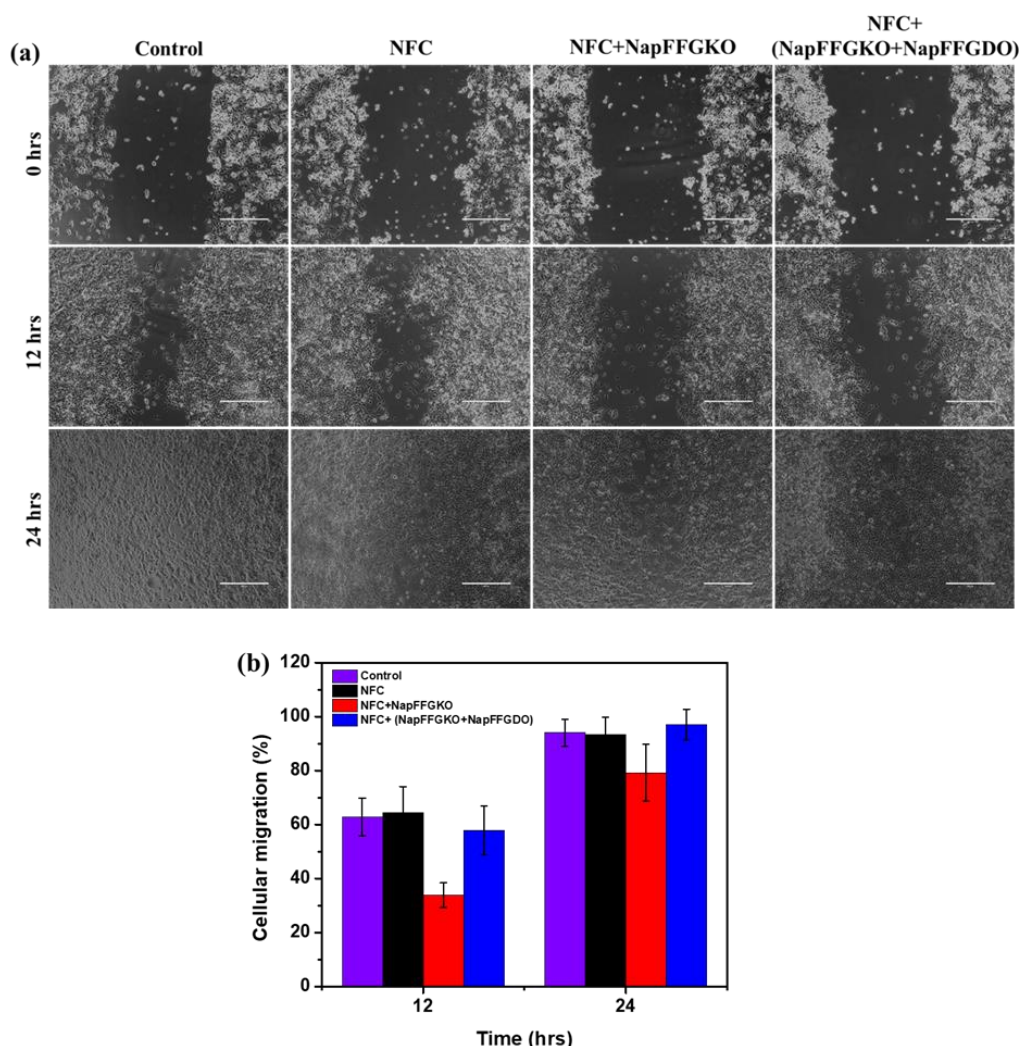


**Figure 6.19** Scratch assay to analyze the cellular migration of SH-SY5Y cells in presence of nanofibrillar cellulose and peptide conjugated cellulose. (a) Scratch closure with the treatment of all the hydrogels as well as the untreated control at different time point; 0 hrs, 12 hrs, and 24 hrs. Scale bar is 400  $\mu$ m. (b) Quantification of the wound closure with time i.e., after 12 hrs and 24 hrs.

In SH-SY5Y cells, a delayed migration was observed in the case of positively charged NapFFGKO conjugated with NFC hydrogel. In contrast, the conjugate system containing co-assembled peptides showed higher migration, similar to that of the control (Figure 6.19). Such observation again correlated that differential surface

topology led to differential bioactivity of the matrix. Thus, the cellular migration study again strengthens the virtue of these conjugate hydrogels scaffold.

**6.2.12 Quantitative analysis of cellular interaction via FACS.** To further support the 2D culture studies and proliferation results, both fibroblast and neural cells were subjected to quantitative live/dead assay using fluorescence-activated cell sorting (FACS). Whole population of treated and control cells were stained with live-dead stain (FDA/PI). Q1 region corresponds to the live cells, while Q3 region corresponds to dead cells (Figure 6.20). Live cell population of fibroblast cells in the nanofibrillar cellulose and peptide conjugate cellulose [NFC + (NapFFGKO + NapFFGDO)] showed similar percentage as that of the control. 95.2% cell population of control sample falls in Q1 region, while cell population in nanofibrillar cellulose and peptide conjugate cellulose [NFC + (NapFFGKO + NapFFGDO)] sample showed 92.7% and 96.1% live population. Interestingly, NFC + NapFFGKO showed 88.4% population in the Q1 region, hence corroborating with the results obtained from 2D and proliferation assays.

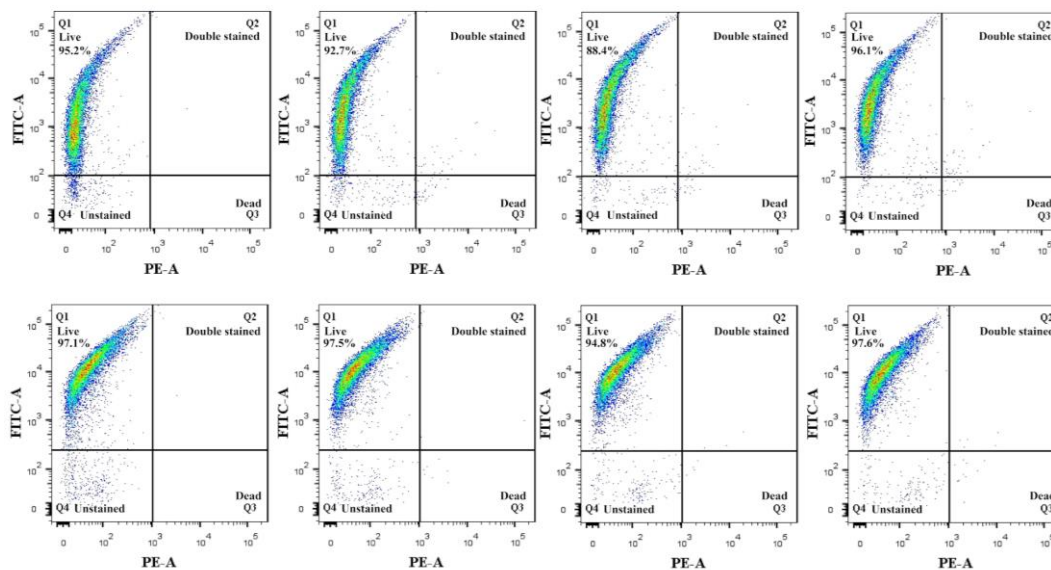


**Figure 6.20** FACS analysis of L929 (a-d) and SH-SY5Y (e-h) cell lines. Live-dead population were identified by staining the cells with FDA and PI. Quadrant Q1 and Q3 indicates the percentage of live and dead cells respectively.

A similar pattern of the live dead population was observed with neural (SH-SY5Y) cells as well. 97.1% control, 97.5% NFC, 94.8% NFC + NapFFGKO, and 97.6% [NFC + (NapFFGKO + NapFFGDO)] live population were observed. The results depicted the

differential role of surface topology that may control cellular adhesion and proliferation.

### **6.3 Conclusions**

In conclusion, we explored for the first time the conjugation of nanofibrillar cellulose with collagen inspired peptides via non-covalent interactions. The interesting class of biomaterial was fabricated by a simple mixing strategy, which offers dual advantages by combining biochemical cues offered by peptide segments coupled with structural stability and mechanical integrity induced by cellulose nanofibril. Our study demonstrated that the TEMPO-oxidized anionic cellulose nanofiber matrix was highly tunable. The incorporation of positively charged bioinspired peptide triggered the physical cross linking of cellulose with peptide motifs through charge pair interaction leading to pore closure in the multi-component assembly. Such reduced porous structure turns the surface smooth and may interfere with cellular adhesion. Such limitations can be overcome when two complementary ionic peptides were used. The preferable salt-bridge formation within the two complementary ionic peptides backbones further drives the assembly with cellulose through CH/ $\pi$  and H bonding interactions leading to fabrication of more porous and rough hydrogel surface to promote cellular adhesion. Our study demonstrated that the CIP conjugated NFC hydrogels can successfully promote cell adhesion, proliferation, and migration. These multi-component biomolecular hydrogel platform combines the biological world with the synthetic world through fabrication of a next-generation biomaterial using simplistic strategy of exploring non-covalent physical cross-linking and thus offering an enhanced scope for designing novel biomaterial, which may otherwise be inaccessible via covalent synthetic routes. This attempt further opens up a new avenue for bottom-up fabrication in minimalistic biomolecular nanotechnology to enhance complexity in multiscale assembly.

#### **Note:**

The permission has been granted by authors and corresponding author of the published paper prior to its adoption in the present thesis. The publication associated with this work is:

Vijay Kumar Pal, Rashmi Jain, Sourav Sen, Kamalakannan Kailasam, and Sangita Roy, Designing nanofibrillar cellulose peptide conjugated polymeric hydrogel scaffold for controlling cellular behaviour. *Cellulose*, **2021**, 28, 10335-10357.

## 6.4 References

1. Courtenay, J. C.; Johns, M. A.; Galembeck, F.; Deneke, C.; Lanzoni, E. M.; Costa, C. A.; Scott, J. L.; Sharma, R. I., Surface modified cellulose scaffolds for tissue engineering. *Cellulose* **2017**, 24 (1), 253-267.
2. Du, H.; Liu, W.; Zhang, M.; Si, C.; Zhang, X.; Li, B., Cellulose nanocrystals and cellulose nanofibrils based hydrogels for biomedical applications. *Carbohydr. Polym.* **2019**, 209, 130-144.
3. Dufresne, A., Nanocellulose: a new ageless bionanomaterial. *Mater. Today* **2013**, 16 (6), 220-227.
4. Habibi, Y.; Lucia, L. A.; Rojas, O. J., Cellulose Nanocrystals: Chemistry, Self-Assembly, and Applications. *Chem. Rev.* **2010**, 110 (6), 3479-3500.
5. Ferreira, F. V.; Souza, L. P.; Martins, T. M. M.; Lopes, J. H.; Mattos, B. D.; Mariano, M.; Pinheiro, I. F.; Valverde, T. M.; Livi, S.; Camilli, J. A.; Goes, A. M.; Gouveia, R. F.; Lona, L. M. F.; Rojas, O. J., Nanocellulose/bioactive glass cryogels as scaffolds for bone regeneration. *Nanoscale* **2019**, 11 (42), 19842-19849.
6. Ko, E.; Park, K. S.; Kim, S.; Kim, T.; Kim, H., Morphological study of cellulosic hydrogel nanofiber for biomedical application. *Cellulose* **2019**, 26 (17), 9107-9118.
7. Liu, J.; Cheng, F.; Grénman, H.; Spoljaric, S.; Seppälä, J.; Eriksson, J.; Willför, S.; Xu, C., Development of nanocellulose scaffolds with tunable structures to support 3D cell culture. *Carbohydr. Polym.* **2016**, 148, 259-271.
8. Syverud, K.; Pettersen, S. R.; Draget, K.; Chinga-Carrasco, G., Controlling the elastic modulus of cellulose nanofibril hydrogels—scaffolds with potential in tissue engineering. *Cellulose* **2015**, 22 (1), 473-481.
9. Xue, Y.; Mou, Z.; Xiao, H., Nanocellulose as a sustainable biomass material: structure, properties, present status and future prospects in biomedical applications. *Nanoscale* **2017**, 9 (39), 14758-14781.
10. Seddiqi, H.; Oliaei, E.; Honarkar, H.; Jin, J.; Geonzon, L. C.; Bacabac, R. G.; Klein-Nulend, J., Cellulose and its derivatives: towards biomedical applications. *Cellulose* **2021**, 28 (4), 1893-1931.
11. Nikolova, M. P.; Chavali, M. S., Recent advances in biomaterials for 3D scaffolds: A review. *Bioact. Mater.* **2019**, 4, 271-292.
12. Chau, M.; De France, K. J.; Kopera, B.; Machado, V. R.; Rosenfeldt, S.; Reyes, L.; Chan, K. J. W.; Förster, S.; Cranston, E. D.; Hoare, T.; Kumacheva, E., Composite Hydrogels with Tunable Anisotropic Morphologies and Mechanical Properties. *Chem. Mater.* **2016**, 28 (10), 3406-3415.
13. De France, K. J.; Hoare, T.; Cranston, E. D., Review of Hydrogels and Aerogels Containing Nanocellulose. *Chem. Mater.* **2017**, 29 (11), 4609-4631.
14. Lohrasbi, S.; Mirzaei, E.; Karimizade, A.; Takallu, S.; Rezaei, A., Collagen/cellulose nanofiber hydrogel scaffold: physical, mechanical and cell biocompatibility properties. *Cellulose* **2020**, 27 (2), 927-940.
15. Moon, R. J.; Martini, A.; Nairn, J.; Simonsen, J.; Youngblood, J., Cellulose nanomaterials review: structure, properties and nanocomposites. *Chem. Soc. Rev.* **2011**, 40 (7), 3941-3994.
16. Phogat, K.; Bandyopadhyay-Ghosh, S., Nanocellulose mediated injectable bio-nanocomposite hydrogel scaffold-microstructure and rheological properties. *Cellulose* **2018**, 25 (10), 5821-5830.

17. Courtenay, J. C.; Deneke, C.; Lanzoni, E. M.; Costa, C. A.; Bae, Y.; Scott, J. L.; Sharma, R. I., Modulating cell response on cellulose surfaces; tunable attachment and scaffold mechanics. *Cellulose* **2018**, *25* (2), 925-940.
18. Dai, L.; Nan, J.; Tu, X.; He, L.; Wei, B.; Xu, C.; Xu, Y.; Li, S.; Wang, H.; Zhang, J., Improved thermostability and cytocompatibility of bacterial cellulose/collagen composite by collagen fibrillogenesis. *Cellulose* **2019**, *26* (11), 6713-6724.
19. Khine, Y. Y.; Stenzel, M. H., Surface modified cellulose nanomaterials: a source of non-spherical nanoparticles for drug delivery. *Materials Horizons* **2020**, *7* (7), 1727-1758.
20. Saito, T.; Kimura, S.; Nishiyama, Y.; Isogai, A., Cellulose Nanofibers Prepared by TEMPO-Mediated Oxidation of Native Cellulose. *Biomacromolecules* **2007**, *8* (8), 2485-2491.
21. Chen, H.; Jiang, J.; Zhang, S.; Yu, J.; Liu, L.; Fan, Y., Surface modification of cellulose originated from different plant sources through TEMPO/Laccase/O<sub>2</sub> oxidation. *Industrial Crops and Products* **2022**, *176*, 114295.
22. Ruiz-Palomero, C.; Kennedy, S. R.; Soriano, M. L.; Jones, C. D.; Valcárcel, M.; Steed, J. W., Pharmaceutical crystallization with nanocellulose organogels. *Chem. Commun.* **2016**, *52* (50), 7782-7785.
23. Basu, A.; Kunduru, K. R.; Abtey, E.; Domb, A. J., Polysaccharide-Based Conjugates for Biomedical Applications. *Bioconjug Chem.* **2015**, *26* (8), 1396-1412.
24. Torres-Rendon, J. G.; Femmer, T.; De Laporte, L.; Tigges, T.; Rahimi, K.; Gremse, F.; Zafarnia, S.; Lederle, W.; Ifuku, S.; Wessling, M.; Hardy, J. G.; Walther, A., Bioactive Gyroid Scaffolds Formed by Sacrificial Templating of Nanocellulose and Nanochitin Hydrogels as Instructive Platforms for Biomimetic Tissue Engineering. *Adv. Mater.* **2015**, *27* (19), 2989-2995.
25. Bodin, A.; Ahrenstedt, L.; Fink, H.; Brumer, H.; Risberg, B.; Gatenholm, P., Modification of Nanocellulose with a Xyloglucan–RGD Conjugate Enhances Adhesion and Proliferation of Endothelial Cells: Implications for Tissue Engineering. *Biomacromolecules* **2007**, *8* (12), 3697-3704.
26. Torgbo, S.; Sukyai, P., Bacterial cellulose-based scaffold materials for bone tissue engineering. *Appl. Mater. Today* **2018**, *11*, 34-49.
27. Kummala, R.; Soto Véliz, D.; Fang, Z.; Xu, W.; Abitbol, T.; Xu, C.; Toivakka, M., Human Dermal Fibroblast Viability and Adhesion on Cellulose Nanomaterial Coatings: Influence of Surface Characteristics. *Biomacromolecules* **2020**, *21* (4), 1560-1567.
28. Skogberg, A.; Maki, A. J.; Mettanan, M.; Lahtinen, P.; Kallio, P., Cellulose Nanofiber Alignment Using Evaporation-Induced Droplet-Casting, and Cell Alignment on Aligned Nanocellulose Surfaces. *Biomacromolecules* **2017**, *18* (12), 3936-3953.
29. Mathew, A. P.; Oksman, K.; Pierron, D.; Harmand, M.-F., Fibrous cellulose nanocomposite scaffolds prepared by partial dissolution for potential use as ligament or tendon substitutes. *Carbohydr. Polym.* **2012**, *87* (3), 2291-2298.
30. Borges, A. C.; Eyholzer, C.; Duc, F.; Bourban, P.-E.; Tingaut, P.; Zimmermann, T.; Pioletti, D. P.; Månson, J.-A. E., Nanofibrillated cellulose composite hydrogel for the replacement of the nucleus pulposus. *Acta biomater.* **2011**, *7* (9), 3412-3421.
31. Zhong, J.; Chau, Y., Synthesis, characterization, and thermodynamic study of a polyvalent lytic peptide-polymer conjugate as novel anticancer agent. *Bioconjug Chem* **2010**, *21* (11), 2055-64.
32. Carlmark, A.; Malmström, E., Atom Transfer Radical Polymerization from Cellulose Fibers at Ambient Temperature. *J. Am. Chem. Soc.* **2002**, *124* (6), 900-901.
33. Roeder, R. D.; Garcia-Valdez, O.; Whitney, R. A.; Champagne, P.; Cunningham, M. F., Graft modification of cellulose nanocrystals via nitroxide-mediated polymerisation. *Polymer Chemistry* **2016**, *7* (41), 6383-6390.
34. Semsarilar, M.; Perrier, S., 'Green' reversible addition-fragmentation chain-transfer (RAFT) polymerization. *Nat. Chem.* **2010**, *2* (10), 811-820.
35. Guo, J.; Catchmark, J. M.; Mohamed, M. N. A.; Benesi, A. J.; Tien, M.; Kao, T.-h.; Watts, H. D.; Kubicki, J. D., Identification and Characterization of a Cellulose Binding Heptapeptide Revealed by Phage Display. *Biomacromolecules* **2013**, *14* (6), 1795-1805.

36. Lu, P.; Takai, K.; Weaver, V. M.; Werb, Z., Extracellular matrix degradation and remodeling in development and disease. *Cold Spring Harb Perspect Biol* **2011**, *3* (12), a005058.
37. He, L.; Theato, P., Collagen and collagen mimetic peptide conjugates in polymer science. *Eur. Polym. J.* **2013**, *49* (10), 2986-2997.
38. Hu, Y.; Wang, H.; Wang, J.; Wang, S.; Liao, W.; Yang, Y.; Zhang, Y.; Kong, D.; Yang, Z., Supramolecular hydrogels inspired by collagen for tissue engineering. *Org Biomol Chem* **2010**, *8* (14), 3267-71.
39. Kotch, F. W.; Raines, R. T., Self-assembly of synthetic collagen triple helices. *Proc Natl Acad Sci U S A* **2006**, *103* (9), 3028-33.
40. O'Leary, L. E. R.; Fallas, J. A.; Bakota, E. L.; Kang, M. K.; Hartgerink, J. D., Multi-hierarchical self-assembly of a collagen mimetic peptide from triple helix to nanofibre and hydrogel. *Nat. Chem.* **2011**, *3* (10), 821-828.
41. Pal, V. K.; Jain, R.; Roy, S., Tuning the Supramolecular Structure and Function of Collagen Mimetic Ionic Complementary Peptides via Electrostatic Interactions. *Langmuir* **2020**, *36* (4), 1003-1013.
42. Yue, B., Biology of the extracellular matrix: an overview. *J Glaucoma* **2014**, *23* (8 Suppl 1), S20-S23.
43. Amabilino, D. B.; Smith, D. K.; Steed, J. W., Supramolecular materials. *Chem. Soc. Rev.* **2017**, *46* (9), 2404-2420.
44. Chakraborty, P.; Ghosh, M.; Schnaider, L.; Adadi, N.; Ji, W.; Bychenko, D.; Dvir, T.; Adler-Abramovich, L.; Gazit, E., Composite of Peptide-Supramolecular Polymer and Covalent Polymer Comprises a New Multifunctional, Bio-Inspired Soft Material. **2019**, *40* (18), 1900175.
45. Du, X.; Zhou, J.; Shi, J.; Xu, B., Supramolecular Hydrogelators and Hydrogels: From Soft Matter to Molecular Biomaterials. *Chem. Rev.* **2015**, *115* (24), 13165-13307.
46. Ghosh, M.; Halperin-Sternfeld, M.; Grigoriants, I.; Lee, J.; Nam, K. T.; Adler-Abramovich, L., Arginine-Presenting Peptide Hydrogels Decorated with Hydroxyapatite as Biomimetic Scaffolds for Bone Regeneration. *Biomacromolecules* **2017**, *18* (11), 3541-3550.
47. Li, J.; Xing, R.; Bai, S.; Yan, X., Recent advances of self-assembling peptide-based hydrogels for biomedical applications. *Soft Matter* **2019**, *15* (8), 1704-1715.
48. Song, S.; Wang, J.; Cheng, Z.; Yang, Z.; Shi, L.; Yu, Z., Directional molecular sliding movement in peptide hydrogels accelerates cell proliferation. *Chem. Sci.* **2020**, *11* (5), 1383-1393.
49. Steed, J. W., Supramolecular gel chemistry: developments over the last decade. *Chem. Commun.* **2011**, *47* (5), 1379-1383.
50. Zhou, J.; Li, J.; Du, X.; Xu, B., Supramolecular biofunctional materials. *Biomaterials* **2017**, *129*, 1-27.
51. Isogai, A.; Saito, T.; Fukuzumi, H., TEMPO-oxidized cellulose nanofibers. *Nanoscale* **2011**, *3* (1), 71-85.
52. Saito, T.; Isogai, A., TEMPO-Mediated Oxidation of Native Cellulose. The Effect of Oxidation Conditions on Chemical and Crystal Structures of the Water-Insoluble Fractions. *Biomacromolecules* **2004**, *5* (5), 1983-1989.
53. Wan, Z.; Wang, L.; Ma, L.; Sun, Y.; Yang, X., Controlled Hydrophobic Biosurface of Bacterial Cellulose Nanofibers through Self-Assembly of Natural Zein Protein. *ACS Biomater. Sci. Eng.* **2017**, *3* (8), 1595-1604.
54. Jain, R.; Roy, S., Tuning the gelation behavior of short laminin derived peptides via solvent mediated self-assembly. *Materials Science and Engineering: C* **2020**, *108*, 110483.
55. Debye, P., Molecular-weight Determination by Light Scattering. *The Journal of Physical and Colloid Chemistry* **1947**, *51* (1), 18-32.
56. Zarzar, J.; Shatz, W.; Peer, N.; Taing, R.; McGarry, B.; Liu, Y.; Greene, D. G.; Zarraga, I. E., Impact of polymer geometry on the interactions of protein-PEG conjugates. *Biophys. Chem.* **2018**, *236*, 22-30.
57. Svergun, D. I.; Koch, M. H. J., Small-angle scattering studies of biological macromolecules in solution. *Rep. Prog. Phys.* **2003**, *66* (10), 1735-1782.

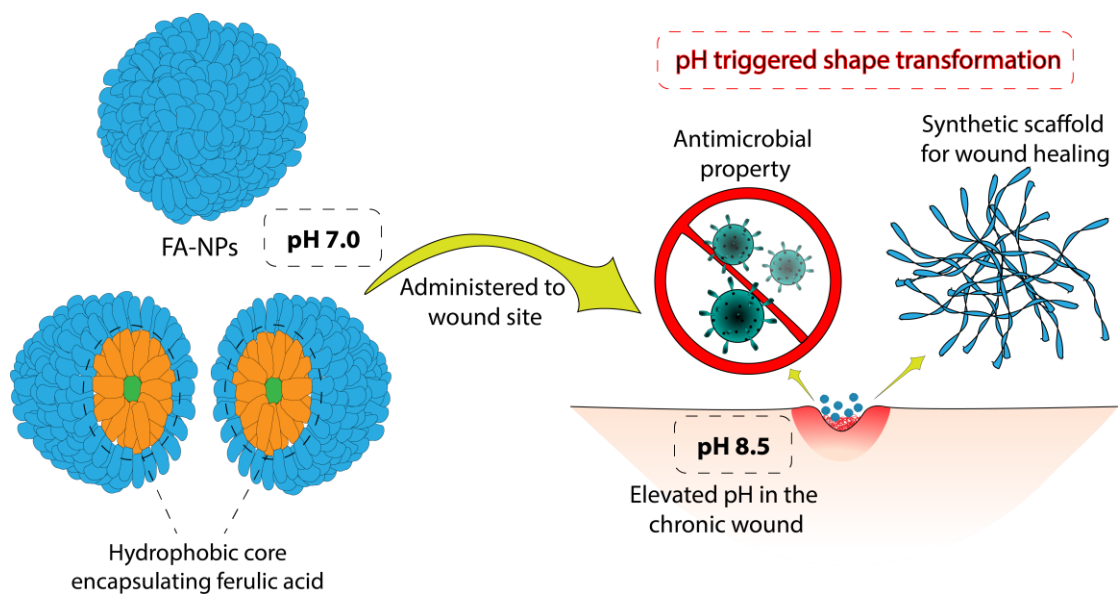
58. Jacques, D. A.; Trewthella, J., Small-angle scattering for structural biology--expanding the frontier while avoiding the pitfalls. *Protein Sci.* **2010**, *19* (4), 642-57.
59. Valentini, E.; Kikhney, A. G.; Previtali, G.; Jeffries, C. M.; Svergun, D. I., SASBDB, a repository for biological small-angle scattering data. *Nucleic Acids Res.* **2015**, *43* (Database issue), D357-D363.
60. Putnam, C. D.; Hammel, M.; Hura, G. L.; Tainer, J. A., X-ray solution scattering (SAXS) combined with crystallography and computation: defining accurate macromolecular structures, conformations and assemblies in solution. *Quarterly reviews of biophysics* **2007**, *40* (3), 191-285.
61. Glatter, O., A New Method for the Evaluation of Small-Angle Scattering Data. *J. Appl. Crystallogr.* **1977**, *10*, 415-421.
62. Hansen, S., BayesApp: a web site for indirect transformation of small-angle scattering data. *J. Appl. Crystallogr.* **2012**, *45* (3), 566-567.
63. Mertens, H. D.; Svergun, D. I., Structural characterization of proteins and complexes using small-angle X-ray solution scattering. *J Struct Biol* **2010**, *172* (1), 128-41.
64. Wade, R. J.; Burdick, J. A., Engineering ECM signals into biomaterials. *Mater. Today* **2012**, *15* (10), 454-459.
65. Jain, R.; Roy, S., Controlling Neuronal Cell Growth through Composite Laminin Supramolecular Hydrogels. *ACS Biomater. Sci. Eng.* **2020**, *6* (5), 2832-2846.
66. Yan, X.; Mohwald, H., Organized Peptidic Nanostructures as Functional Materials. *Biomacromolecules* **2017**, *18* (11), 3469-3470.
67. Zhang, C.; Shang, Y.; Chen, X.; Midgley, A. C.; Wang, Z.; Zhu, D.; Wu, J.; Chen, P.; Wu, L.; Wang, X.; Zhang, K.; Wang, H.; Kong, D.; Yang, Z.; Li, Z.; Chen, X., Supramolecular Nanofibers Containing Arginine-Glycine-Aspartate (RGD) Peptides Boost Therapeutic Efficacy of Extracellular Vesicles in Kidney Repair. *ACS Nano* **2020**, *14* (9), 12133-12147.
68. Sharma, P.; Kaur, H.; Roy, S., Designing Tenascin-C inspired short bioactive peptide scaffold to direct and control cellular behaviour. *ACS Biomater. Sci. Eng.* **2019**, *5* (12), 6497-6510.
69. Katsetos, C. D.; Del Valle, L.; Legido, A.; de Chadarévian, J. P.; Perentes, E.; Mörk, S. J., On the neuronal/neuroblastic nature of medulloblastomas: a tribute to Pio del Rio Hortega and Moises Polak. *Acta neuropathologica* **2003**, *105* (1), 1-13.
70. Katsetos, C. D.; Herman, M. M.; Mörk, S. J., Class III beta-tubulin in human development and cancer. *Cell motility and the cytoskeleton* **2003**, *55* (2), 77-96.
71. Katsetos, C. D.; Legido, A.; Perentes, E.; Mörk, S. J., Class III beta-tubulin isotype: a key cytoskeletal protein at the crossroads of developmental neurobiology and tumor neuropathology. *Journal of child neurology* **2003**, *18* (12), 851-66; discussion 867.
72. Kaur, H.; Roy, S., Designing aromatic N-cadherin mimetic short peptide based bioactive scaffolds for controlling cellular behaviour. *J. Mater. Chem. B* **2021**.
73. Pijuan, J.; Barceló, C.; Moreno, D. F.; Maiques, O.; Sisó, P.; Marti, R. M.; Macià, A.; Panosa, A., In vitro Cell Migration, Invasion, and Adhesion Assays: From Cell Imaging to Data Analysis. **2019**, *7* (107).



# Chapter 7

Designing pH responsive smart shape transformable dynamic nano-vehicle based on bioactive peptide nano-assemblies for antibacterial therapy and wound healing





**Dual functionality and environmental tunability of a new class of dynamic peptide-based bio-nano assemblies inspired from native collagen protein offers advancement towards development of nano-vehicle for the antimicrobial therapy and wound healing applications.**



## 7.1 Introduction

Recent advancement in the field of peptide self-assembly have revealed that the short peptide amphiphiles possess the unique tendency to self-assemble into differential nano-assemblies in response to their surrounding environment. These adaptive nano-assemblies have accomplished several advancements in the field of diagnostics, therapeutics, bioengineering, energy, and healthcare.<sup>1-6</sup> Over the past few years, developing new functional nanomaterial has become one of the utmost focuses of the research community, which may offer several solutions to the social problems.<sup>7</sup> In this direction, supramolecular self-assembly of short peptide subunits has gained immense attention as a bottom-up methodology to fabricate several materials at the nano dimension.<sup>8</sup> Novel nanostructures can be developed by harnessing the advantages of dynamic self-assembly and adaptability of the peptide-based biomolecules to the changes in the microenvironment of the designer nanostructures.<sup>9-12</sup> Furthermore, peptide/protein based self-assembled systems have been widely used in developing antimicrobial agents because of their structural versatility and functional benefits.<sup>9, 13-19</sup> Several peptides exhibit stimuli-responsive assembly behaviour, and their ability to achieve diverse nanoscale structures is highly dependent on the surrounding environmental conditions.<sup>20-23</sup> Such intrinsic transmorphic properties of peptide nanostructures facilitate the development of stimuli-responsive nanomaterials displaying efficient antimicrobial properties.<sup>24-28</sup> Hence, the emerging paradigm has witnessed a shift towards constructing an array of well-defined versatile biomolecular nanostructures with diverse antimicrobial functions and several other biomedical applications.<sup>29, 30</sup>

In this direction, peptide/protein-based nanoparticles have gained immense significance as a carrier for drug delivery because of their facile encapsulation ability of hydrophobic molecules in the hydrophobic core of the nano-assemblies and on-demand release potency upon external stimuli.<sup>30</sup> Furthermore, it was interesting to note that over the years, one of the hydroxycinnamic acid derivative i.e., ferulic acid (2E)-3-(4-hydroxy-3-methoxyphenyl) prop-2-enoic acid has been recognized as an abundant phenolic acid, which commonly exists in the plant cell wall.<sup>31</sup> Despite its abundance in natural sources and clinical benefits, the use of ferulic acid is limited due to its strong hydrophobic

nature, which leads to its decreased bioavailability.<sup>32, 33</sup> Ferulic acid has been reported to exhibit antibacterial activity against several pathogenic bacterial species like *A. baumannii*, *C. sakazakii* etc., via superoxide ion generation, ROS generation, and membrane disruption.<sup>34, 35</sup> In a study, Borges et al. reported the antibacterial activity of ferulic acid against pathogenic bacteria, which leads to irreversible changes in the bacterial membrane via local rupture and pore formation.<sup>36</sup> Another useful study by Pernin et al. demonstrated the inhibitory property of ferulic acid against *L. monocytogenes* in an emulsified system.<sup>37</sup> All these reports indicated that ferulic acid exhibits its antimicrobial activity at quite high concentration of this antimicrobial agent, which is evident in its minimum inhibitory concentration value i.e., 10-30mM. Such high concentration requirement for bacterial cell killing might have been originated from the less bioavailability of the ferulic acid in the aqueous environment. Such limitations of a potential antimicrobial agent enhance the demand for the development of a strategy to improve the availability and bio activity of such hydrophobic drug molecules. In this direction, the nanoprecipitation technique may offer a more simple, less complex, more feasible, and widely applicable method to encapsulate the hydrophobic drug without the help of any additive for particle stabilization.<sup>38</sup>

Furthermore, several polymeric nanoparticles have been used for encapsulating hydrophobic drugs via the nanoprecipitation method.<sup>39</sup> Solvent-based precipitation was first used to develop a nanocapsule of poly- (D, L-lactide) encapsulating indomethacin as a model drug.<sup>40</sup> This facile and simple technique of synthesizing polymeric nanoparticles was adapted with several other polymers, indicating the abundant use of polylactic-co-glycolic acid (PLGA) as one of the most popular candidates for nanoprecipitation.<sup>41</sup> In this direction, Reisch et al. reported an ultrasmall polymeric nanoparticles in the sub-20-nm range using nanoprecipitation technique.<sup>42</sup> The presence of differentially charged moieties (carboxylate, sulfonate, and trimethylammonium) to the polymeric chain (PLGA) affected the size of the nanoparticles formed via nanoprecipitation. The study demonstrated that by reducing the concentration of the polymer, the particle size could be reduced further to 15 nm without affecting the encapsulation efficiency of the nanoparticles.<sup>42</sup> In a study by the Mainardes group, it was evident that the bioavailability of the drug curcumin has been enhanced by incorporating a PLGA-PEG blend to stabilize the nanoparticles.<sup>43</sup> This classical study further demonstrated that using a single polymer and polymer blend improved the

pharmacokinetics of curcumin. A nanoparticle of <200 nm size showed enhanced release of curcumin from the polymer blend as compared to the single polymer. Another report by the Karnik group showed that the bigger cargos like insulin and other proteins could be encapsulated inside polymeric nanoparticles via nanoprecipitation.<sup>44</sup> Encapsulation of the relatively larger moieties inside the polymeric (PLGA-PEG) nanoparticles depends on the ionic chelation, buffer condition, and preparation method. To this direction, Tarhini et al. demonstrated the development of protein-based (BSA) nanoparticles via nanoprecipitation, and the effect of buffer solution, pH, and cross-linking was monitored to obtain a homogenous population of nanoparticles.<sup>45</sup> Hence, it has been evident that there is a growing interest in developing a strategy to encapsulate the hydrophobic drugs within in these protein/peptide based nanoparticles which may enhance their bioavailability. In this context, we have designed and developed a peptide amphiphile adapted from the smallest repetitive domain of collagen protein, which can mimic the structural and the functional attributes of the native collagen molecule, which we have reported in our earlier chapter. In this work, we have explored another attribute of this peptide to tune its nanoscale structure using different chemical stimuli. In particular, we have utilized this peptide amphiphile to synthesize spherical nanoparticles via nanoprecipitation, which allows the otherwise insoluble hydrophobic drug to get encapsulated in the hydrophobic core and renders the construct stable in the aqueous environment. Interestingly, this collagen-inspired peptide amphiphile has the propensity to self-assemble at basic pH to form peptide nanofibers.<sup>46</sup>

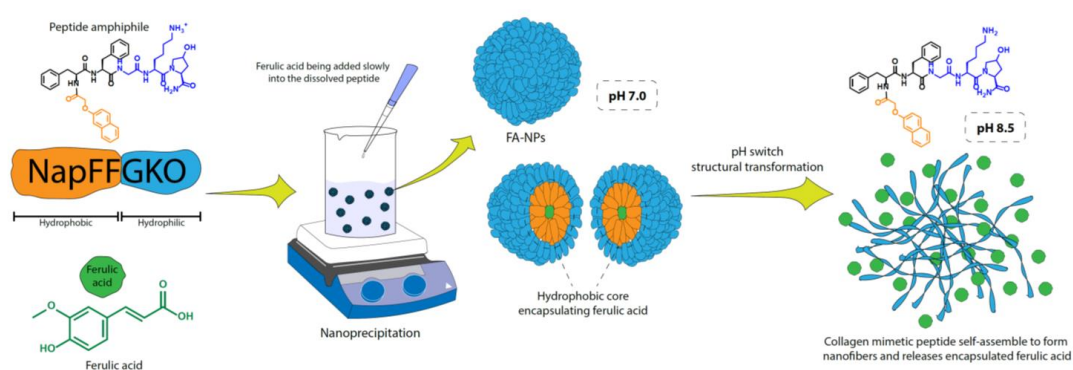


**Figure 7.1** Schematic representation of the encapsulated peptide nanoparticle synthesis via nanoprecipitation and structural transition of the peptide nanoparticles via pH switch from pH 7.0 to 8.5, leading to the transformation of nanosphere to nanofibers, releasing the FA.

This unique spontaneous self-assembling capability of this peptide amphiphile into a diverse nanoscale structure on pH switch was quite intriguing to utilize this dynamic shape transformation towards developing nanocarriers for drug delivery application (Figure 7.1). In particular, in order to trigger the release of encapsulated drug molecules from the nanoparticles, a small change in pH of the medium will be necessary, which will turn the medium weakly basic. Hence, keeping in mind several preclinical advantages of ferulic acid, we have attempted to explore the encapsulation and release of ferulic acid towards fabricating a novel nanocarrier based on collagen-inspired peptide nanoparticles. In particular, we were interested in the antimicrobial property of the ferulic acid at the wound site. In a condition of wounded skin, the acidic milieu and the surrounding pH (7.0) of neighboring tissues were disrupted. This exposed wound site provides a facile site for several microbial infections, which leads to the shift in the pH (7.5 - 8.9) of the wound site and makes it chronic.<sup>47</sup> Hence, we developed this unique strategy that utilizes the weakly basic pH of the wound site to trigger the structural transition of the peptide nanoparticles, which induces the self-assembly of the peptide to form peptide nanofibers and thus releasing the encapsulated ferulic acid from the nanosphere. When administered to these chronic wound sites, the proposed novel fabricated nanoparticles help to combat microbial infection, and the peptide nanofibers formed due to the pH switch will serve as a synthetic scaffold for promoting the cellular growth leading to wound closure. As the peptide nanoparticles were synthesized using a collagen-derived amphiphile, it serves dual functions i.e. (a) self-assembled system developed can be utilized as the carrier for the hydrophobic drug, and (b) due to its tendency to mimic the native collagen-based ECM derived protein, it provides bioactive scaffold for wound repair. To the best of our knowledge, this is the first study to fabricate a bio-nano construct with dual functionality and environmental tunability, which offer multiple advantages in wound healing. Specifically, the ferulic acid has been judiciously incorporated in the short peptide nanoparticles via nanoprecipitation technique, which not only acts as an antimicrobial agent but can simultaneously offer the beneficial effect of collagen inspired peptide to provide a stable scaffold at the wound site to recover faster. Such an approach for constructing peptide nanoparticles for entrapping hydrophobic drug moiety overcomes the limitations of the solubility of the drug and helps in constructing innovative peptide nanomaterials.

## 7.2 Results and discussions

**7.2.1 Synthesis and characterization of nanoparticles.** Peptide based nanomaterials possess diverse structural and functional properties, providing huge potential in the arena of biomedical and material technology.<sup>48</sup> Nanostructures developed from naturally derived peptide amphiphiles have emerged as a multifaceted potential candidate with wide range of applications in biomedicines.<sup>49</sup> Herein, we have designed and synthesized a positively charged collagen inspired pentapeptide (NapFFGKO) through solid phase peptide synthesis using a protocol mentioned in chapter 2.<sup>46</sup> The hydrophobic moiety of the amphiphilic peptide is composed of naphthoxy acetic acid attached to a dipeptide sequence comprising of the classical diphenylalanine motif, which is further linked to the short hydrophilic moiety inspired from native tripeptide unit of collagen protein i.e., (G-X-O). In particular, the proline residue of the native collagen sequence has been rationally modified with the basic amino acid residue, lysine to induce differential pH responsive self-assembly behaviour. We have already mentioned the biocompatible attributes of this peptide in chapter 3. The pentapeptide sequence, NapFFGKO with log P value of 1.03 ionizes at physiological pH and remains in the monomeric state at sub-micromolar concentration. The dissolved peptide has the tendency to self-assemble slowly into nanofiber in the presence of a weekly basic environment otherwise it formed sheet-like structures at physiological pH when it was allowed to settle for longer period of time (Figure 7.2).

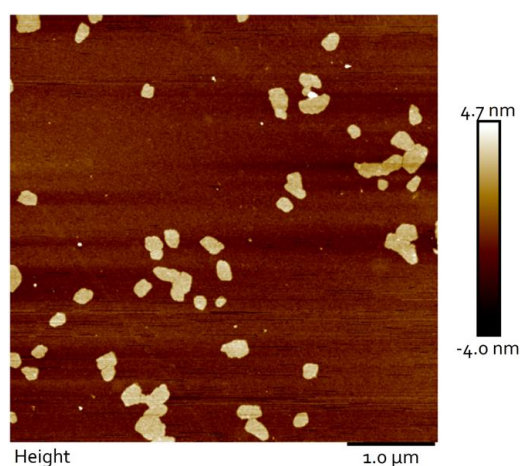


**Figure 7.2** Collagen inspired peptide, NapFFGKO at physiological pH showed the formation of sheet like structure at sub micromolar concentration (200 μM) as depicted by AFM studies.

To this direction, we were curious to explore the ability of this short peptide amphiphile to encapsulate the highly hydrophobic drug/therapeutic agent via nanoprecipitation. In this direction, we employed ferulic acid (4-hydroxy-3-methoxy cinnamic acid), a phenolic acid, which is well known for its wide range of applications as antioxidant, anti-inflammatory agents, and in several other areas of biomedicine, like in atherosclerosis treatment, as anti-cancerous, and anti-bacterial agents etc.<sup>50</sup> Although ferulic acid show several important applications, the hydroxycinnamic acid showed poor water solubility, which diminishes the scope of its usage in biomedical field.<sup>51</sup> In recent years, nanoprecipitation have gained immense importance as mode for facile encapsulation and release of the small hydrophobic molecules up on activation through external stimuli.<sup>52</sup> Nanoprecipitation is a simplistic and facile approach for nanoparticle formation, which enables dissolving the hydrophobic cargo in a water miscible solvent followed by its slow addition into the amphiphilic polymer or peptide solution.<sup>42, 53</sup> In the present study, we utilized this elegant approach of nanoprecipitation for preparing peptide nanoparticles to encapsulate ferulic acid (Figure 7.3).

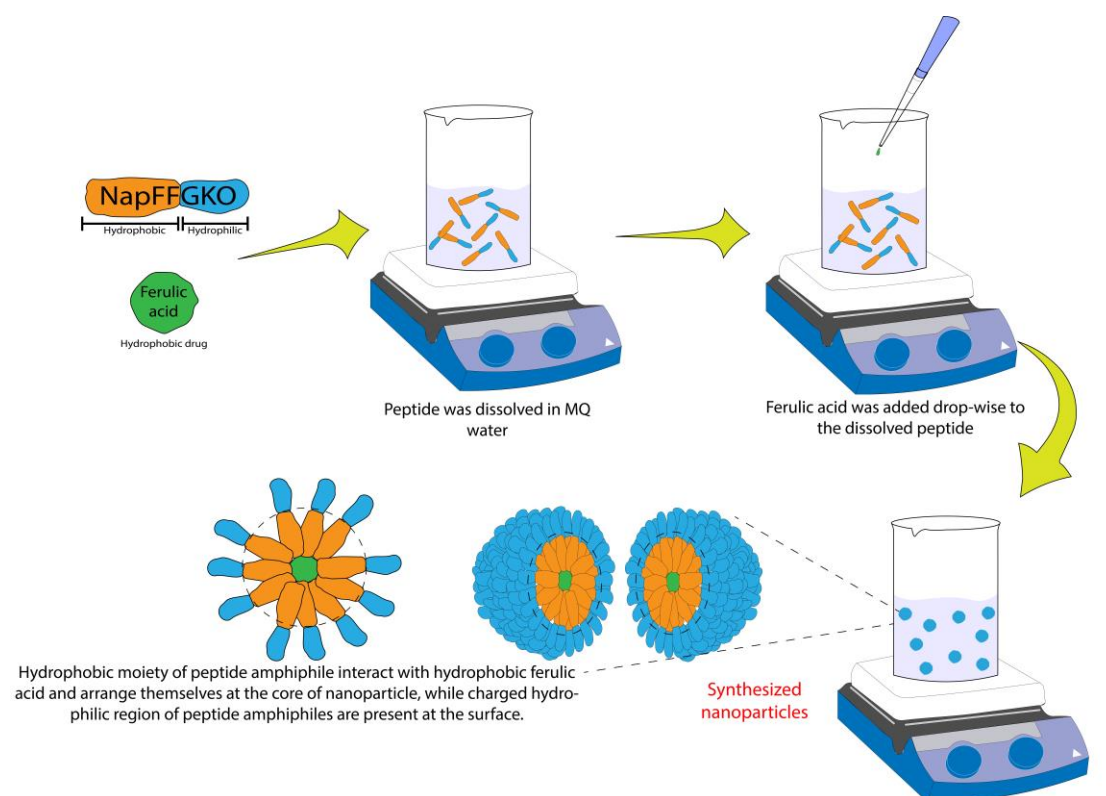


**Figure 7.3** Schematic representation of the synthesis methodology of peptide-based nanoparticle via nanoprecipitation for the encapsulation of hydrophobic drug molecules (ferulic acid).

The synthesized nanoparticles were subjected to dynamic light scattering (DLS) to determine the size of the nanoparticles. DLS study revealed that the hydrodynamic radii of the synthesized nanoparticles remain in the range of 40-45 nm with a polydispersity index (PDI) of 0.235 (Figure 7.4a). The synthesized nanoparticles were incubated for 36 hours in the aqueous medium at physiological pH. There were no significant changes in the size and PDI of the nanoparticles after incubation, which further confirmed that the nanoparticles are stable at physiological pH (Figure 7.4b). Moreover, the stability of the nanoparticles in nutrient broth and Dulbecco's modified eagle medium (DMEM) containing 10% fetal bovine serum (FBS) were investigated at physiological pH for a time period of 36 hours (Figure 7.4 c&d), since the biological assays were carried out in the media. DLS and PDI also showed no significant variation in size in the growth medium, suggesting the stable nature of the nanoparticles.

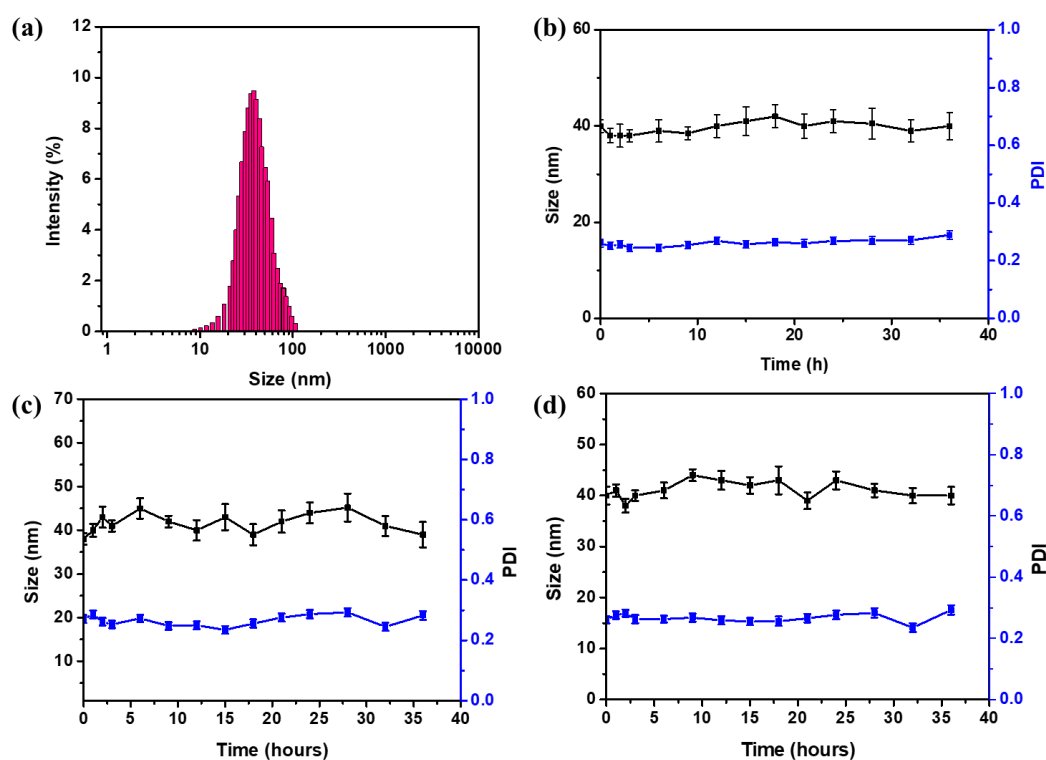


**Figure 7.4** Characterization of the ferulic acid encapsulated peptide nanoparticles (FANPs): (a) DLS study of the nanoparticles at physiological pH, (b) Hydrodynamic radii and polydispersity index of the synthesized nanoparticles confirmed the stability over a time period of 36 hours. Stability assessment of nanoparticles in presence of culture medium (c) nutrient broth for bacterial culture, (d) DMEM for mammalian cell culture studies.

We further investigated the surface charge of the nanoparticles to confirm the encapsulation of the hydrophobic drug moiety. The zeta potential ( $\zeta$ ) of nanoparticles displayed a surface charge of +20.8 mV suggesting the exposed surface of the particles bearing array of positively charged lysine (Figure 7.5a). The hydrophilic region of the peptide containing lysine tends to face the exterior of the spherical nanoparticles, hence giving an overall positive surface charge to the nanoparticles. Trans-ferulic acid showed a surface charge of -35 mV in its dissolved state, while collagen inspired peptide showed +45 mV in its monomeric state at physiological pH. The absence of the additional signature peaks of ferulic acid in the zeta potential study further suggested the complete encapsulation of the hydrophobic drug moiety inside the nanoparticles (Figure 7.5a). The synthesized nanoparticles were analyzed using atomic force microscopy to determine the morphological aspect of the nanoparticles. Morphological analysis of the synthesized nanoparticle revealed the formation of spherical nanoparticles in the range of 40-50 nm (Figure 7.5b).

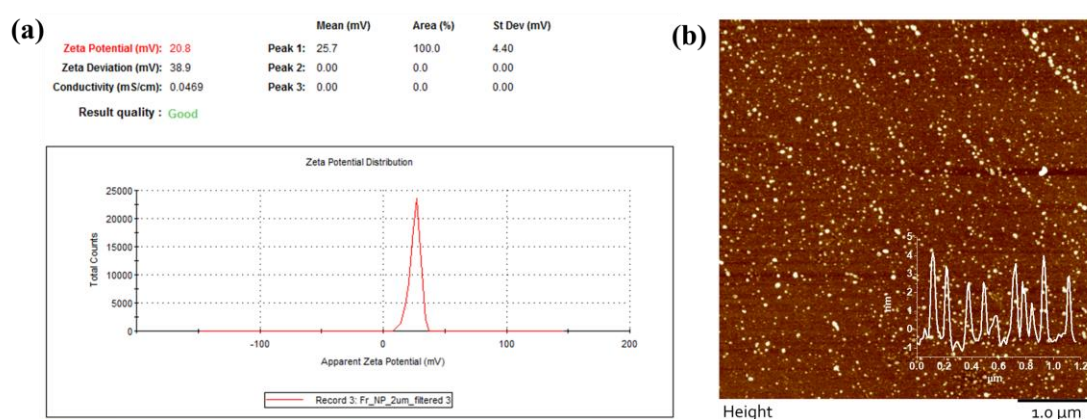


**Figure 7.5** (a) Surface charge of the peptide nanoparticles via zeta potential ( $\zeta$ ) measurement showing the positive charge on the surface of the nanoparticles at physiological pH. (b) AFM image of the nanoparticles showing the particle size in the range of 40-50 nm. Scale bar 1.0  $\mu$ m

It was evident from the earlier studies that the size and structure of the nanoparticles prepared via non-solvent-based precipitation, which is followed by the nucleation and growth leading to the generation of superstructure. The methodology is dependent on several parameters that are involved in the processing. More importantly, the generation of nanoparticles with the encapsulation of hydrophobic molecule within the core can be affected by the alteration in any of these steps, which may lead to the formation of

heterogeneous particles.<sup>45</sup> Hence an optimized protocol was adopted that includes continuous stirring and a steady and controlled addition of the non-solvent containing hydrophobic moiety was designed so that it can result in the formation of monodisperse nanoparticles of dimension in the range of 40-50 nm.

**7.2.2 Transmorphic behaviour of nanoparticles.** At this point, we were curious to study the mode of release of the encapsulated ferulic acid. It would be extremely interesting to get the insights into the physical or chemical stimuli that may assist in the release of the hydrophobic drug.

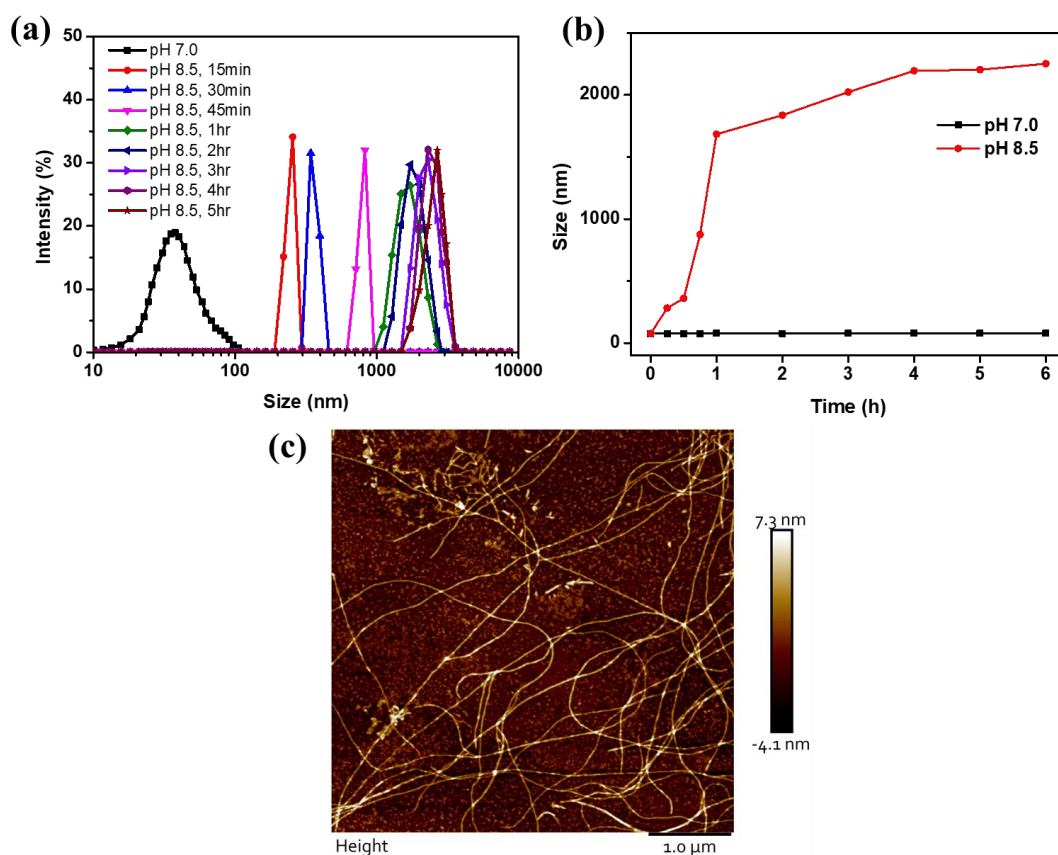


**Figure 7.6** Structural transition of the nanoparticles: (a) nanoparticle size distribution at physiological pH 7.0 and at slightly basic pH, 8.5, showed the drastic change in the size of the nanoparticles, (b) time dependent size analysis at a due course of 6 hours, (c) AFM of the peptide nanofibers as converted from spherical nanoparticles under pH stimuli (at pH 8.5) after 6 hours. Scale bar 1.0 μm.

As the earlier study indicated that the positively charged peptide display a pH responsive dynamic shape transition, particularly it has the tendency to self-assemble into higher order structure at slightly basic pH, hence we have checked the pH response

of these nanoparticles by exposing them to a weakly basic pH 8.5 in the aqueous medium. Structural transformation was observed immediately after changing the pH of the medium. This was evident in the change of the hydrodynamic radii of the nanoparticles, which was increased over time at basic pH and reached up to micron size (Figure 7.6 a&b). As shown in (Figure 7.6a, b) particle size was found to increase from the 40 nm to submicron level (2-3 micron) over the time period of 6 hours while exposed at pH 8.5. The major transformation in particle size was observed in the first hour of pH switch (Figure 7.6a), which further showed marginal shift in the enhancement of the size of the particle with time owing to the transformation of the nano particles to nanofibers. To this direction, we performed atomic force microscopy to understand the change in the morphology of the nanoparticles after pH switch. Interestingly, the nanoparticles incubated for 6 hours at basic pH (8.5) were found to demonstrate a structural transition from nanosphere to nanofibers (Figure 7.6c).

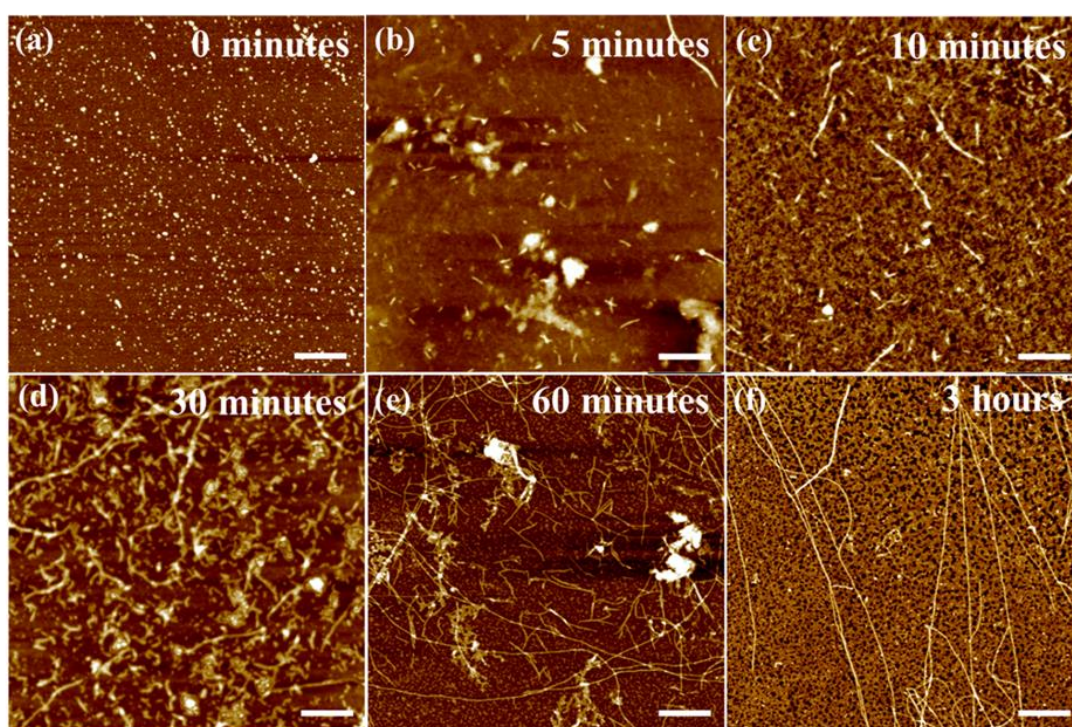


**Figure 7.7** Time dependent structural transition of the nanoparticles upon switching the pH of the aqueous medium from neutral (7.0) to basic (pH 8.5) via AFM studies. Scale bar 500 nm

To understand the multi-scale assembly of peptide governed via thermodynamic and kinetic variables, we performed time dependent AFM study to understand the dynamics of the nucleation and growth of the nanofiber formation from nanosphere upon

changing the pH.<sup>54, 55</sup> The time dependent AFM showed the structural transformation at the time periods of 5 minutes, 10 minutes, 30 minutes, 60 minutes, and 3 hours. After the pH switch, nucleation of the short fibers can be observed at a time point of 5 minutes, which was further followed by the growth over the time and formed long nanofibers were generated leading to higher order network of nanostructure (Figure 7.7). Since the peptide moiety containing the lysine residue has a high propensity to self-assemble at basic pH, we observed the spontaneous self-assembly of the collagen inspired peptide monomer as soon as the pH of the medium adjusted to basic pH owing to the minimization of the charge repulsion resulting from positively charged lysine residues at physiological pH. This slow nucleation at weakly basic pH leads to the growth of long fiber of peptide molecules and thus releasing the encapsulated ferulic acid into the medium.

**7.2.3 Equivalence point and H-bonding.** The ability of the nanoparticles to show the structural transformation at different pH values can be understood by the protonation and deprotonation of the amine group of the lysine residue in the peptide amphiphile. To understand the differential protonation state of the peptide at the physiological pH and the weakly basic pH, we performed acid-base titration of these peptide. This investigation would be beneficial as the differential ionization of the peptide is expected to dictate the differential self-assembly pattern of the peptide monomer and thus leading to the structural transformation of the peptide nanoparticles. In this context, the detailed understanding of the molecular mechanism is highly essential to fabricate the nanocarrier, which may release the cargo on demand. The titration curve showed the peptide stayed in the ionized form ( $\text{NH}_3^+$ ) at physiological pH and as the pH reaches close to 9, it gets deprotonated ( $\text{NH}_2$ ) (Figure 7.8a). The  $\text{pK}_a$  of 3.65 and equivalence point of 9.12 were observed for the positively charged lysine residue of collagen inspired peptide. Based on the titration analysis, we can predict that the peptide amphiphiles exist in the ionized ( $\text{NH}_3^+$ ) form at the neutral pH and up on increasing the pH to 8.5, a major fraction of the peptide monomer gets deprotonated and hence, the charge repulsion was found to decrease. Such changes in the ionization further could result in the increased affinity of the monomer to interact among themselves via hydrogen bonding,  $\pi$ - $\pi$  stacking, van der Waal interactions, and hydrophobic interactions. Such enhancement in the intermolecular interactions has led to the formation of self-assembled structures of peptide nanofibers, showing a structural

transition at slightly basic pH. The instant change in the hydrogen bonding interactions among the peptide on pH switch leading to the structural transition can be further confirmed by Fourier transform infrared spectroscopy (FTIR). A broad transmittance signal around 3300-3500  $\text{cm}^{-1}$  in the self-assembled state of the peptide nanostructure showed the presence of H-bond among the peptide amphiphile, which arises upon interaction between -NH and the -CO due to pH change. Furthermore, the appearance of the peak at around 1640  $\text{cm}^{-1}$  confirmed the formation of nanofibrillar structure formation (Figure 7.8b).<sup>46</sup>

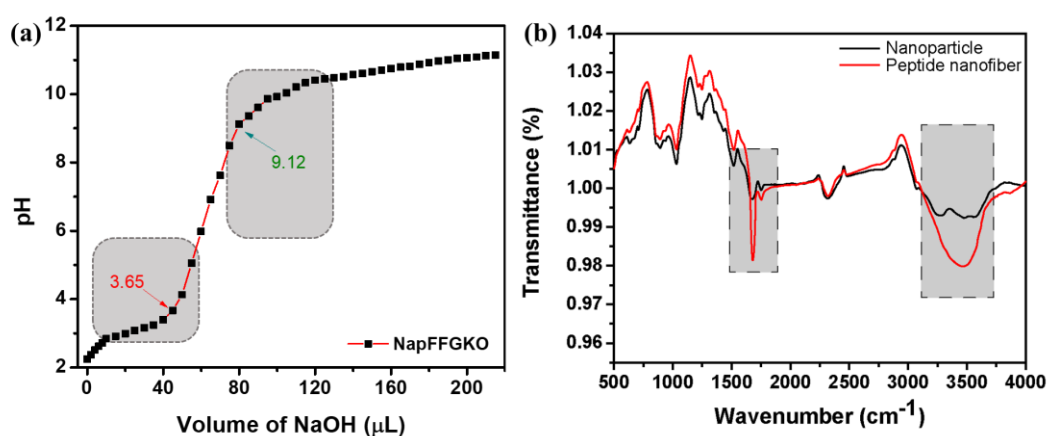


**Figure 7.8** (a) Acid-base titration curve to determine the equivalence point and the pKa value of the positively charged collagen inspired peptide, (b) FTIR spectra of the nanoparticles and peptide nanofibers.

The peptide in its monomeric state undergoes assembly via non-solvent-based precipitation to form spherical nanoparticles, owing to the lacking of the sufficient of H-bonding interactions among the peptide monomers. Whereas, upon pH shift, the peptide self-assemble to form peptide nanofibers and an increased peak intensity of N-H bending at 1640  $\text{cm}^{-1}$  suggested the formation of  $\beta$ -sheet like structures in these nanofibers.<sup>56</sup> Thus, spectroscopic studies provided the detailed insights into interaction mechanism among the peptide amphiphiles at molecular level, which remarkably helps in understanding the differential modes of self-assembly towards constructing smart peptide nanomaterials.

**7.2.4 Drug encapsulation efficiency.** In order to explore this unique shape transition behaviour of this collagen inspired peptide towards fabrication of a smart delivery vehicle for the therapeutic agent, it is essential to assess their encapsulation efficiency.

First of all, the encapsulation yield of the hydrophobic drug would ideally depend on factors like solvent miscibility, precipitation speed and drug solubility into the peptide amphiphile solution used for encapsulation.<sup>57</sup> In order to check the drug loading capacity of the synthesized nanoparticles, we further calculated the amount of ferulic acid encapsulated and released from the peptide nanoparticles via UV-Vis spectroscopy (UV-2600 Shimadzu).

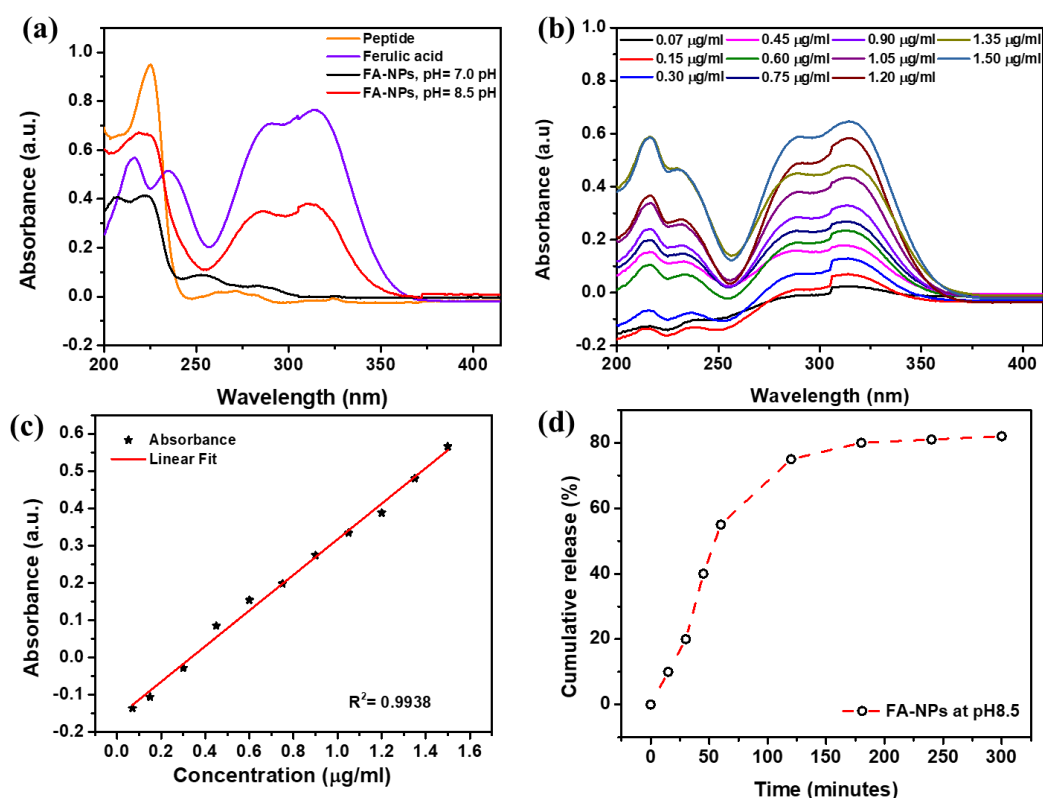


**Figure 7.9** Absorbance of nanoparticles: (a) UV-Vis spectra of the nanoparticles at pH 7.0 (black) and at pH 8.5 (red), respectively. The spectra at pH8.5 shows the presence of the characteristic peaks of ferulic acid, indicating the release of the encapsulated ferulic acid at pH 8.5. (b) UV-Vis spectra of the ferulic acid at different concentrations to make standard curve for the determination of the encapsulation efficiency. (c) Standard curve drawn from the respective absorbance obtained at 215 nm for determining the loading capacity of the peptide nanoparticles. (d) Cumulative release percentage of ferulic acid from the nanoparticles at weakly basic pH (8.5).

The UV spectra of the peptide itself exhibit a prominent absorption at 224 nm while ferulic acid showed its characteristic peaks at around 215 nm, 287 nm and 312 nm, respectively (Figure 7.9a). UV spectra of nanoparticles at physiological pH displayed

only the absorption peak of the peptide amphiphile, suggesting the exposure of the peptide monomers at the surface of the nanoparticles and also indicated the complete encapsulation of the hydrophobic drug. The standard curve has been made with a set of differential concentrations of ferulic acid to estimate the encapsulation efficiency. UV spectra of peptide nanoparticles after every 30 minutes up to 6 hours at pH 8.5 were used to calculate the total loading capacity of the nanoparticles. The encapsulation efficiency was calculated via the below formula: Encapsulation efficiency = (concentration of drug obtained in the nanoparticle / concentration of drug added)  $\times$  100. To calculate the encapsulation capacity and release of the ferulic acid, we obtained the UV-Vis spectra of the ferulic acid at different concentrations (Figure 7.9b). Complete disappearance of the signature peaks of ferulic acid from the nanoparticle solution suggested the maximum loading of the ferulic acid (Figure 7.9a). A standard curve has been drawn from the extent of differential absorption of ferulic acid at different concentrations (Figure 7.9c). The calibration curve was further utilized to evaluate the released amount of ferulic acid after 6 hours. The encapsulation efficiency of ferulic acid obtained after the release was  $82 \pm 3\%$  (Figure 7.9d).

**7.2.5 Exploration of this peptide based novel nanomaterial as an advanced biomaterial for application in antibacterial therapy.** We further explored the unique intrinsic stimuli responsive differential self-assembling property of the collagen inspired peptide to encapsulate and on-demand release of a hydrophobic drug. In particular, the drug encapsulated peptide nanoparticles when administered to the wound site, can easily release the entrapped drug as the pH of the chronic wounds are slightly basic 8.0 - 9.0. The novel nanomaterial will play a dual beneficial role; (a) it will act as carrier to deliver an antimicrobial drug to the chronic wound site, which will protect the wound from microbial infection while (b) the peptide nanofibers will act as synthetic scaffold for the wound repair. Thus, pH responsive structural transition will not only lead to an effective way of antimicrobial drug transportation at the wound site, simultaneously it will display a dual advantage by delivering the therapeutic agent for efficacious antibacterial therapy and providing effective scaffold for tissue engineering and regeneration.

**7.2.5.1 Determination of antimicrobial property.** In order to assess the antimicrobial potential of ferulic acid while released on-demand from the peptide nanoparticles both Gram-positive and Gram-negative bacterial strains were utilized. Bacterial strains,

*Escherichia coli* and *Staphylococcus aureus* were used to determine the antimicrobial property of the FA-NPs. Single colony was inoculated and incubated for 6 hours up to achieve 0.4 OD to prepare the primary culture, which was further used for determining minimum inhibitory concentrations (MIC) and for other assays. To determine the minimum inhibitory concentration of the nanoparticles, bacterial cells of 0.4 OD were incubated with nanoparticles at a concentration range of 0 to 1000  $\mu\text{g mL}^{-1}$  for 6 hours. To confirm the complete release of the ferulic acid from the nanoparticles and to obtain more compelling results, we have modified the growth medium, wherein, the pH of the medium was maintained to 8.5 to carry out all the antibacterial assays. After incubation, treated bacterial cells were again checked for the change in the bacterial population in comparison to control. Figure 7.8a depicts that at concentration of FA-NPs (900  $\mu\text{g mL}^{-1}$  or 4.63 mM) at which both the bacterial cell populations were adversely affected and showed complete death of the bacterial population. To further confirm the cell death, 100  $\mu\text{L}$  of the sample was plated on the LB agar medium and incubated overnight to check the growth of the bacterial cells on agar plate.

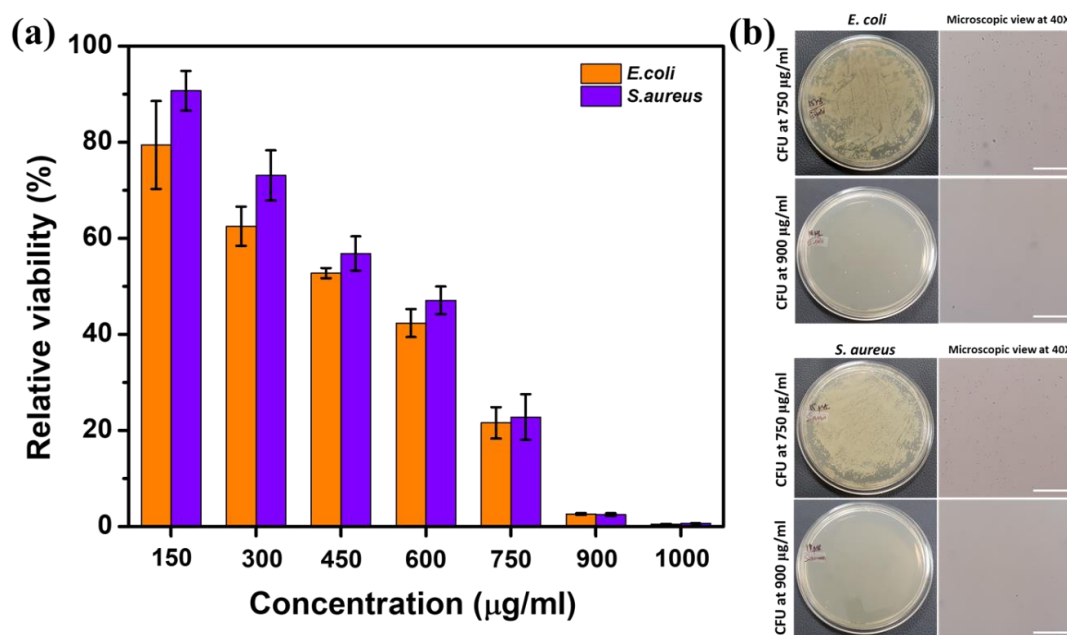


**Figure 7.10** Antimicrobial assay: (a) Determination of minimum inhibition concentration (MIC) against *E. coli* (Gram -ve) and *S. aureus* (Gram +ve) strains and (b) the respective colony forming unit (cfu) of both bacterial strains and their microscopic views at different concentrations of released FA, i.e., 750  $\mu\text{g/mL}$  and 900  $\mu\text{g/mL}$ . Scale bar 50  $\mu\text{m}$

Agar plates with two different concentrations 750 and 900  $\mu\text{g mL}^{-1}$  showed a clear difference in the cfu counts (Figure 7.10b), which can also be observed in the microscopic images taken at 40X. Bright field images showed negligible number of bacterial cells at 900  $\mu\text{g mL}^{-1}$  concentration, suggesting complete inhibition of the bacterial populations. The minimum inhibitory concentration reported in the present study showed an advancement in the bactericidal efficacy of the ferulic acid and a reduced MIC in comparison to the prior studies<sup>36, 37</sup> To this direction, both the cells were further stained with LIVE/DEAD Backlight Viability Kit to quantitate the bacterial population with damaged membrane via confocal laser scanning microscopy (CLSM). The viability kit contains two different dyes; SYTO 9 (green fluorescent),<sup>36</sup> which stains the nucleic acid irrespective of the live and dead populations, and propidium iodide (red fluorescent),<sup>36</sup> which only stains the bacterial population with damaged cell membrane.<sup>36</sup> Presence of green fluorescence in both the control bacterial samples (Figure 7.11) suggested the presence of live cells, while at concentration of 750  $\mu\text{g mL}^{-1}$  of the ferulic acid, it was evident from the respective images that a small fraction of bacterial population are displaying merged fluorescence of red and green.

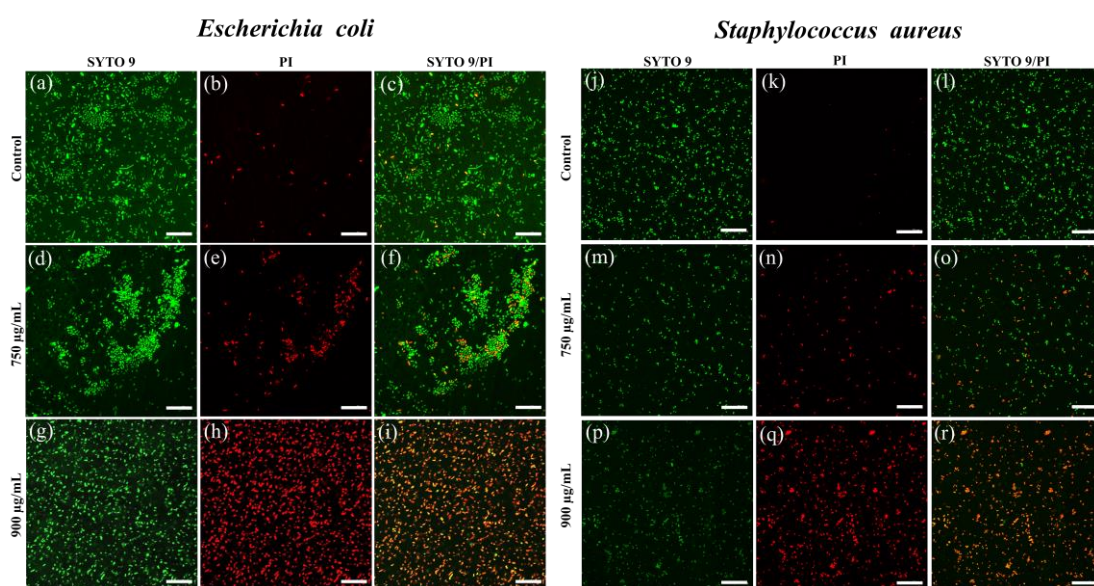


**Figure 7.11** Live-Dead assay via CLSM, panel 1: live cells (stained with SYTO 9), panel 2: dead cells (stained with PI). Panel 3: merged population (stained with SYTO 9/PI). (a-c) control *E. coli* cells (untreated), (d-f) cells exposed to FA-NPs at 750  $\mu\text{g/mL}$ , (g-i) cells exposed to FA-NPs at 900  $\mu\text{g/mL}$ . (j-l) control *S. aureus* cells (untreated), (m-o) cells exposed to FA-NPs at 750  $\mu\text{g/mL}$ , (p-r) cells exposed to FA-NPs at 900  $\mu\text{g/mL}$ . Scale bar 10  $\mu\text{m}$

Bacterial population at  $900 \mu\text{g mL}^{-1}$  showed red fluorescence, which indicated maximum number of dead cells, suggesting the killing of bacterial population. At this concentration, it was evident that the dead populations were stained with PI, which displayed red fluorescence while the green fluorescence was found to be significantly reduced, as it merged with the red fluorescence and the cells appeared orange in color. Further quantification of live and dead population was carried out using fluorescence assisted cell sorting (FACS). Flow cytometry allows fluorescent labelling at single-cell level and can differentiate a heterogenous subpopulation present in a sample treated with an antibacterial material.<sup>58</sup>

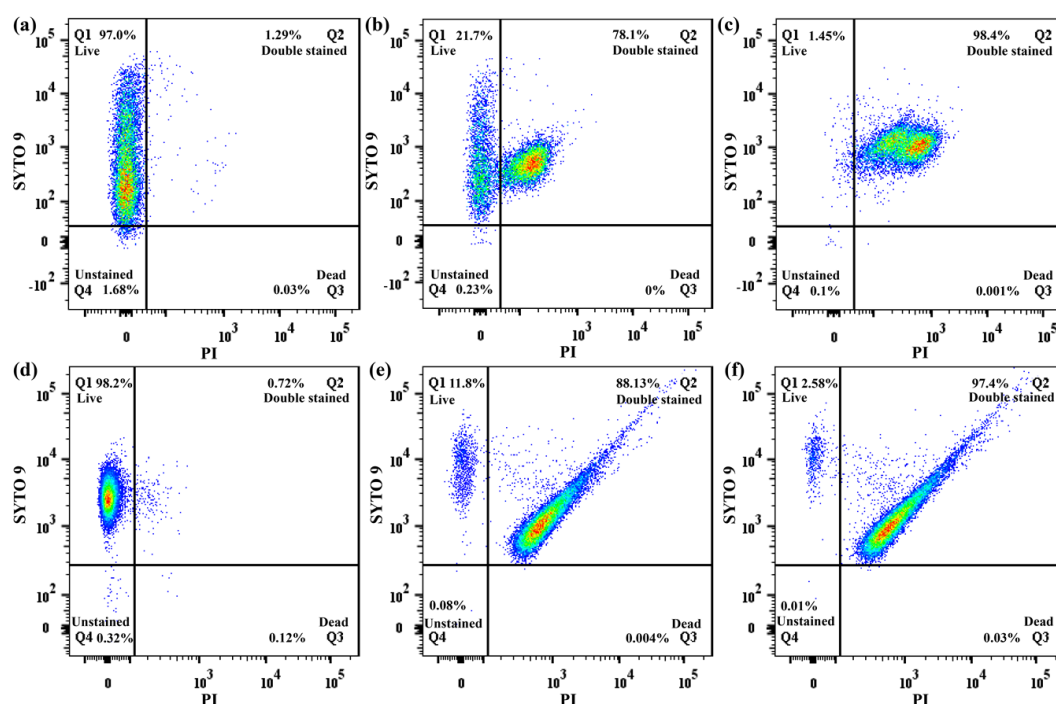


**Figure 7.12** Live-Dead assay via FACS (Quadrant 1: live cells, Quadrant 2: doubled stained cells, Quadrant 3: dead cells, Quadrant 4: unstained cells): (a-c) *E. coli* cells exposed to the different concentrations of nanoparticles with control cells. (d-f) *S. aureus* cells exposed to the different concentrations of the nanoparticles with control cells i.e.,  $750 \mu\text{g/mL}$  and  $900 \mu\text{g/mL}$ .

It was clearly observed that the cell population from quadrant 1 (Syto9+) shifted to quadrant 2 (Syto9+/PI+) with an increase in the concentration of the nanoparticles to  $900 \mu\text{g mL}^{-1}$  (Figure 7.12 b,c & e,f). The control sample showed higher cell population in the Q1 region (97.0%) and only a negligible amount of about 3% population in the Q2, Q3 and Q4 region. Whereas, upon treatment with the nanoparticles at different

concentration of 750 and 900  $\mu\text{g mL}^{-1}$ , the maximum cell population were drifted to the Q2 region (78.1% and 98.4% respectively), suggesting the quantitative assessment of the cell death at the respective nanoparticle concentrations (Figure 7.12a-c). Similar pattern of antimicrobial behaviour was observed with Gram positive strain as well. Control sample of *S. aureus* showed maximum population of 98.2% in Q1 region and rest in the unstained region. Whereas upon treatment with the nanoparticles at 750 and 900  $\mu\text{g mL}^{-1}$ , the cell population shifted to quadrant 2 with 88.12% and 97.4%, respectively suggesting bactericidal effect of released ferulic acid (Figure 7.12d-f). These observations concluded the pronounced antibacterial effect of FA-NPs at 900  $\mu\text{g mL}^{-1}$  concentration on bacterial cells, leading to the death of maximum cell population.

**7.2.5.2 Assays for antimicrobial mechanism.** At this point, it is crucial to understand the mechanism behind the antimicrobial property of the FA-NPs exposed to the bacterial cells, which can be attributed to the damage in the cell membrane causing the ion leakages and proton influx.<sup>59</sup> Disturbance in the cell membrane up on action by ferulic acid may lead to the change in intracellular ATP concentration, membrane potential and pH shift of the bacterial cells.<sup>35</sup> The generation of reactive oxygen species (ROS) above a cell's normal threshold is the most important factor in bacterial cell death<sup>34</sup>. In this direction, it was crucial to estimate the amount of free radicals generated in the treated bacterial cells.

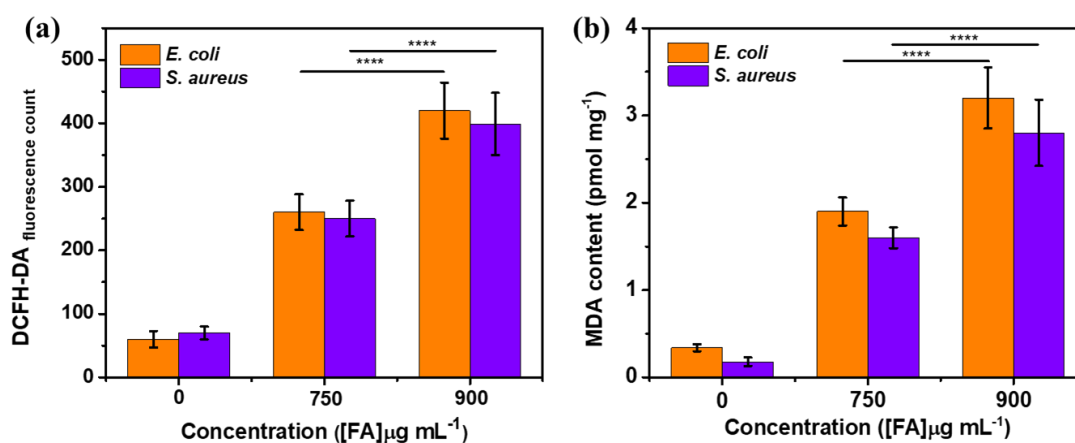


**Figure 7.13** Mechanism of antimicrobial property: (a) DCFH-DA assay to determine the ROS production via relative fluorescence intensity. (b) Malondialdehyde assay to determine the lipid peroxidation leading to the cell membrane disruption.

To quantify the level of ROS generation, we have used 2',7'-dichlorofluorescein diacetate (DCFH-DA), a non-fluorescent molecule, which shows fluorescence emission only after reacting to the intracellularly generated ROS.<sup>34</sup> A clear difference in the fluorescence count of the nanoparticle treated samples were observed in comparison to the untreated control cells (Figure 7.13). The extent of ROS generation was more prominent at 900  $\mu\text{g mL}^{-1}$  in both the bacterial strains. The enhanced ROS level observed at 900  $\mu\text{g mL}^{-1}$  as compared to the control cells depicts the detrimental activity of the ferulic acid to the bacterial cells and thus acting as an antimicrobial agent (Figure 7.13a). The pronounced level of ROS within the treated cells further suggested the internalization and release of the ferulic acid within the target cells. It can be realized that the gradual increase in the oxidative stress due to the membrane damage is the major outcome of the ROS generation and its accumulation in the bacterial cells. Moreover, ferulic acid was also known to damage the cellular membrane of the bacterial population.<sup>60</sup> To this direction, we have also performed malondialdehyde (MDA) assay to estimate the extent of damaged cellular membrane via lipid peroxidation.<sup>61</sup> A remarkable difference in the lipid peroxidation was observed in the nanoparticles treated bacterial samples as compared to the control untreated cells. A significantly higher level of MDA content was evident at 900  $\mu\text{g mL}^{-1}$  as compared to the concentration 750  $\mu\text{g mL}^{-1}$  in both the bacterial strains (Figure 7.13b). These observations clearly suggested the mode of action of ferulic acid towards displaying the detrimental effect against pathogenic bacterial strains. Both assays demonstrated the inhibitory mechanism of the ferulic acid towards bacterial population. It can be inferred that an increased level of reactive oxygen species (ROS), along with the morphological changes and the disintegration of the bacterial cell membrane due to lipid peroxidation are the probable reasons for the inhibition of the growth as well as survival of the bacterial populations.

**7.2.5.3 Microscopic examination of damaged cell membrane.** It has been already documented through DCFH-DA and MDA assays that the bacterial cell death took place due to the compromised cell membrane of the treated bacterial cell populations. A chain of oxidative degradation leads to the removal of electron from the lipid, which results in the damaged cell membrane.<sup>62</sup> Disruption in the cell membrane integrity and its structure was further visualized by FE-SEM in the FA-NPs treated bacterial cells (Figure 7.14). The typical rod shape of *E. coli* (2-3  $\mu\text{m}$  long and 0.4-0.5  $\mu\text{m}$  wide) and

cocci shape of *S. aureus* (0.5-0.8  $\mu\text{m}$  diameter) with even cell boundary and intact cell membrane without any damaged section were observed in the untreated cells (Figure 7.14 a,d). The FA-NPs treatment at  $750 \mu\text{g mL}^{-1}$  showed mixed bacterial population with reasonably distorted cell morphologies, which corroborates with the prior results of 75-80% cell death (Figure 7.14 b,e). However, bacterial cells treated with  $900 \mu\text{g mL}^{-1}$  FA-NPs led to the loss of structural integrity, loss of cytoplasmic content, deformed cell shape, referring to the cell death in both types of bacterial populations (Figure 7.14 c,f).

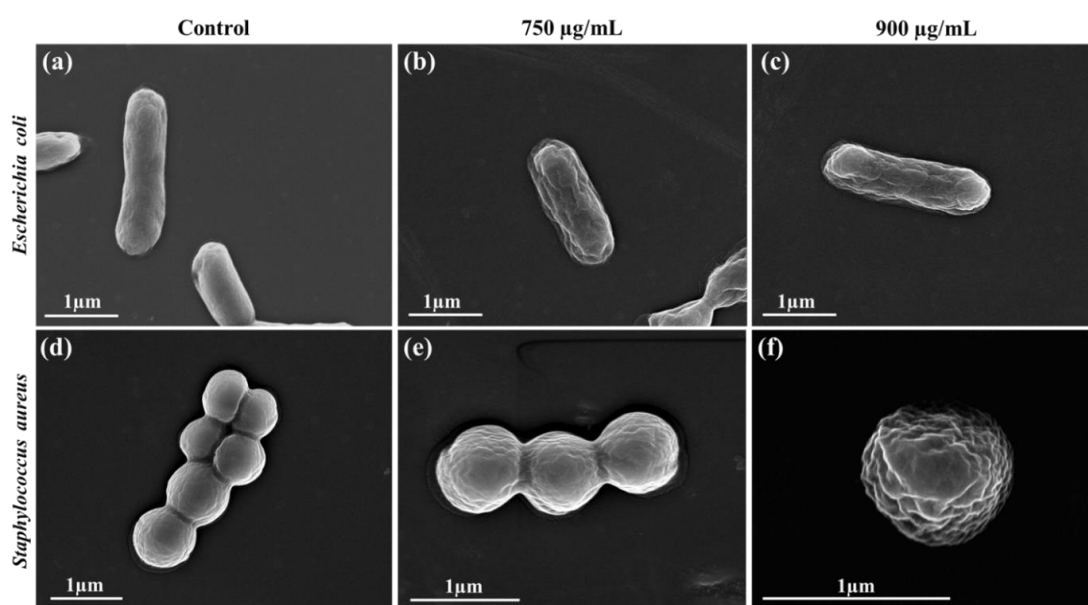


**Figure 7.14** Field Emission Scanning Electron Microscopic (FE-SEM) images of the control bacteria cells (a, d) showing intact cellular membrane. Bacterial cells at  $750 \mu\text{g mL}^{-1}$  treatment showed stressed population (b, e) and at  $900 \mu\text{g mL}^{-1}$  FA-NPs showed damaged cell membrane (c, f). Scale bar  $1 \mu\text{m}$

#### 7.2.5.4 Biocompatibility of these nanostructures to the mammalian cells.

Furthermore, the assessment of the biocompatibility of these dynamic nanostructures is highly desirable in order to design a next-generation nanocarrier for antimicrobial therapy. The cytocompatibility of these novel fabricated nanoparticles with fibroblast cells were carried out using MTT reduction assay. As indicated in chapter 3, our earlier report established that the collagen inspired peptide (NapFFGKO) were highly biocompatible, which was evident from their cellular viability against fibroblast cells, of around 85-100% at different concentrations of peptide.<sup>46</sup> To this direction, it was essential to monitor the effect of the spherical nanoparticles formed by the peptide

monomer towards mammalian cells. We speculate that the change in surface topology of the peptide nanoparticles and ferulic acid released at pH 8.5 might show an adverse effect on the mammalian cells. Therefore, we were curious to check the behaviour of the mammalian cells after exposure to the intact spherical nanoparticles and the peptide nanofibers with the released ferulic acid. We have chosen fibroblast cells (L929) to study the biocompatibility of the synthesized nanoparticles as the peptide construct was inspired from collagen molecule, which is the major protein associated in the wound healing process.<sup>63</sup> The cell viability was assessed after 24 hours for both types of peptide nanostructures, i.e., nanosphere with encapsulated with encapsulated drug and the nanofibers with the released drug. The FA-NPs and the peptide nanofibers with released drug showed biocompatible behaviour up to concentration 900  $\mu\text{g mL}^{-1}$  with the cell line, which can be observed from the bright field images (Figure 7.15). It is very crucial to assess whether there is any differential effect of the bactericidal agent, exists between the bacterial cells and the mammalian cells before considering it to be used as a therapeutic agent.

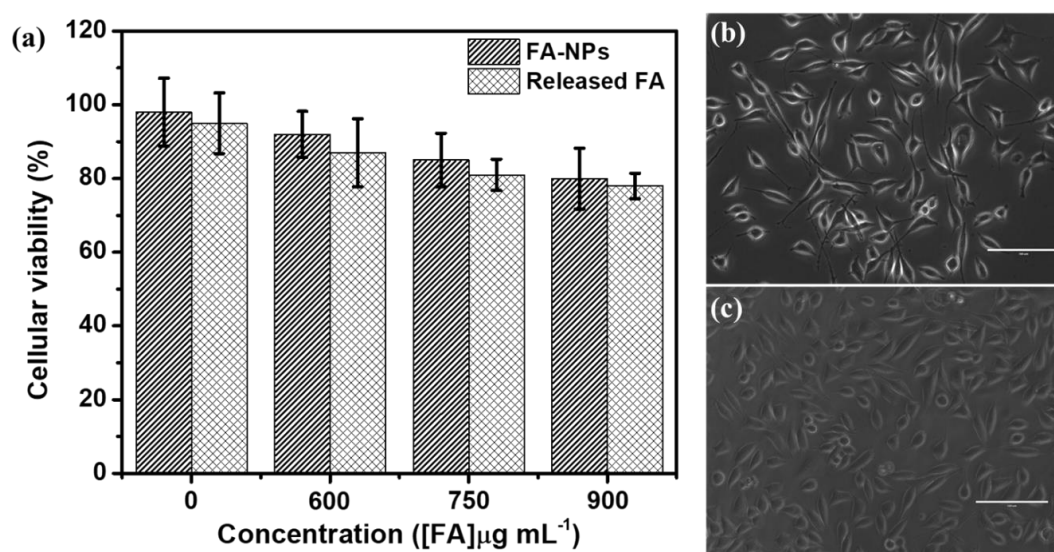


**Figure 7.15** Cellular viability of the nanoparticles with fibroblast cells; (a) Biocompatibility studies to compare the effect of FA-NPs and released ferulic acid. (b) Bright field images of L929 cells with FA-NPs and (c) Bright field images of L929 cells with released ferulic acid at 900  $\mu\text{g/mL}$ . Scale bar 100  $\mu\text{m}$

Ideally, it can be envisioned that the concentration that triggered the toxicity to the bacterial cells, should not induce any toxic effect to the mammalian cells. It was very

interesting to note that the drug encapsulated peptide nanoparticles at the 900  $\mu\text{g/mL}$  concentration was highly biocompatible to the fibroblast cells, which was revealed by the MTT assay, although at this concentration, these nanoparticles show toxicity to the bacterial cells. Thus, the biocompatible nature of the synthesized nanoparticles enhances the scope of these dynamic nanostructures for the futuristic applications.

#### 7.2.5.5 Cellular migration assay (Wound closure)

Cell migration is an important component in many biological processes as this gives the ability to reach to the wound site for its closure.

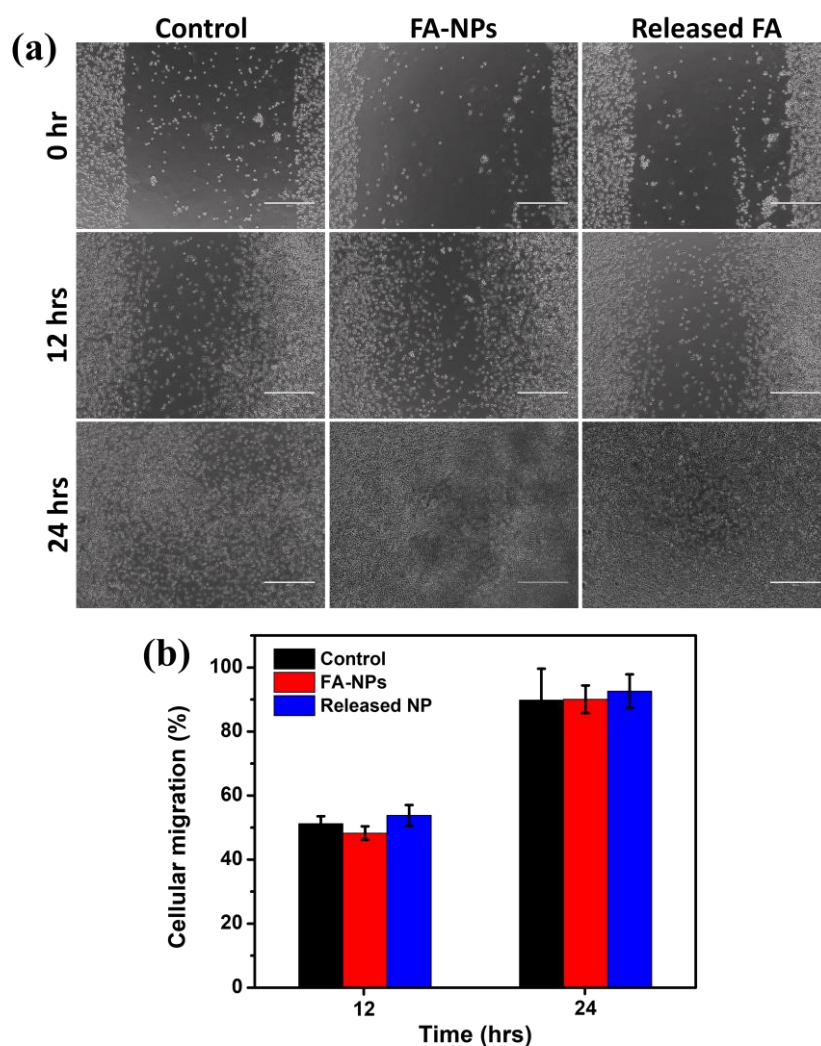


**Figure 7.16** Scratch wound assay to analyze the migration ability of the fibroblast cells in presence of peptide nanofibers; (a) Scratch closure with the treatment at different time points. Scale bar 400  $\mu\text{m}$ . (b) Quantification of the wound closure with time i.e., after 12 hours and 24 hours.

In order to function as a synthetic matrix for wound healing application the peptide nanofibers should be able to interact to the cells and improve the process of cellular migration.<sup>64</sup> The synthetic matrix contains bioactive motifs as discussed in the previous chapters, which promote the cellular adhesion, survival and growth. In this direction, the pH responsive dynamic nanofiber network evolved from our minimalistic peptide design was further explored to assess its potential in regulating cellular migration. We applied a well-known technique of scratch wound assay<sup>65, 66</sup> to assess the cellular migration ability of the nanofibrillar peptides. The migration of fibroblast cells was monitored under a microscope at different time points up to 24 hours with the peptide nanofibers as treatment. An increased migration rate was observed in the peptide treated samples, suggesting the supportive nature of the peptide nanofibers towards function as material for wound healing (Figure 7.16). Thus, the cellular migration study strengthens the virtue of these peptide nanofibers working as synthetic scaffold.

### **7.3 Conclusions**

In conclusion, we present for the first time the fabrication of a bio-nano construct based on bioactive peptide domain of a native ECM protein which offers dual functionality and environmental tunability, and thus displayed numerous advantages in wound healing applications. Specifically, we have explored the unique intrinsic stimuli responsive differential self-assembling property of the collagen inspired peptide to encapsulate and release the hydrophobic drug molecule and thus enhancing its therapeutic efficacy. A novel nano-formulation was fabricated in the form of spherical nanoparticles using the peptide amphiphile to encapsulate the hydrophobic drug ferulic acid, which renders the construct stable in aqueous environment. Interestingly, the peptide amphiphile has a propensity to show a dynamic behaviour up on pH switch, which is evident from its structural transition from nanosphere to nanofibers at weekly basic pH of 8.5 to release the antimicrobial drug at the wound site that displays a surrounding pH of 7.5-8.9. Hence, we developed this unique strategy that utilizes the weakly basic pH of the wound site to trigger the structural transition of the peptide nanoparticles, which induces the self-assembly of the peptide to form peptide nanofibers and thus releasing the encapsulated ferulic acid from the nanosphere. The proposed novel fabricated nanoparticles showed an enhanced efficacy of ferulic acid, which was evident in a lower value of MIC as reported earlier for ferulic acid ferulic acid in aqueous medium.<sup>36</sup> We envisage that these novel nano-constructs will offer a

dual advantage. In particular, the released drug from the nanosphere will help to combat microbial infection, and the peptide nanofibers formed due to the pH switch will serve as a synthetic scaffold for wound regeneration. Such pH responsive structural transition will lead to an efficient way of drug transportation to show the antimicrobial activity. The present study provides the insights into designing of transformable peptide-based nanostructure and demonstrate their application in antimicrobial therapy to construct next-generation biomaterial.

## 7.4 References

1. Dai, B.; Li, D.; Xi, W.; Luo, F.; Zhang, X.; Zou, M.; Cao, M.; Hu, J.; Wang, W.; Wei, G.; Zhang, Y.; Liu, C., Tunable assembly of amyloid-forming peptides into nanosheets as a retrovirus carrier. *Proc Natl Acad Sci U S A* **2015**, *112* (10), 2996-3001.
2. Hubbell, J. A.; Chilkoti, A., Nanomaterials for Drug Delivery. *Science* **2012**, *337* (6092), 303-305.
3. Lombardi, L.; Shi, Y.; Falanga, A.; Galdiero, E.; de Alteriis, E.; Franci, G.; Chourpa, I.; Azevedo, H. S.; Galdiero, S., Enhancing the Potency of Antimicrobial Peptides through Molecular Engineering and Self-Assembly. *Biomacromolecules* **2019**, *20* (3), 1362-1374.
4. Mitchell, M. J.; Billingsley, M. M.; Haley, R. M.; Wechsler, M. E.; Peppas, N. A.; Langer, R., Engineering precision nanoparticles for drug delivery. *Nat. Rev. Drug Discov.* **2021**, *20* (2), 101-124.
5. Sharma, P.; Pal, V. K.; Roy, S., An overview of latest advances in exploring bioactive peptide hydrogels for neural tissue engineering. *Biomater. Sci.* **2021**, *9* (11), 3911-3938.
6. Yang, Z.; Xu, B., Supramolecular hydrogels based on biofunctional nanofibers of self-assembled small molecules. *J. Mater. Chem.* **2007**, *17* (23), 2385-2393.
7. Kumar, A.; Chen, F.; Mozhi, A.; Zhang, X.; Zhao, Y.; Xue, X.; Hao, Y.; Zhang, X.; Wang, P. C.; Liang, X.-J., Innovative pharmaceutical development based on unique properties of nanoscale delivery formulation. *Nanoscale* **2013**, *5* (18), 8307-8325.
8. Singh, N.; Kumar, M.; Miravet, J. F.; Ulijn, R. V.; Escuder, B., Peptide-Based Molecular Hydrogels as Supramolecular Protein Mimics. *Chem. Rev.* **2017**, *23* (5), 981-993.
9. Guo, Z.; Wang, Y.; Tan, T.; Ji, Y.; Hu, J.; Zhang, Y., Antimicrobial d-Peptide Hydrogels. *ACS Biomater. Sci. Eng.* **2021**, *7* (4), 1703-1712.
10. Levin, A.; Hakala, T. A.; Schnaider, L.; Bernardes, G. J. L.; Gazit, E.; Knowles, T. P. J., Biomimetic peptide self-assembly for functional materials. *Nat. Rev. Chem.* **2020**, *4* (11), 615-634.
11. Qi, G.-B.; Gao, Y.-J.; Wang, L.; Wang, H., Self-Assembled Peptide-Based Nanomaterials for Biomedical Imaging and Therapy. *Adv. Mater.* **2018**, *30* (22), 1703444.
12. Williams, R. M.; Chen, S.; Langenbacher, R. E.; Galassi, T. V.; Harvey, J. D.; Jena, P. V.; Budhathoki-Uprety, J.; Luo, M.; Heller, D. A., Harnessing nanotechnology to expand the toolbox of chemical biology. *Nat. Che. Bio.* **2021**, *17* (2), 129-137.
13. Hendrikse, S. I. S.; Contreras-Montoya, R.; Ellis, A. V.; Thordarson, P.; Steed, J. W., Biofunctionality with a twist: the importance of molecular organisation, handedness and configuration in synthetic biomaterial design. *Chem. Soc. Rev.* **2022**, *51* (1), 28-42.
14. Li, S.; Xing, R.; Chang, R.; Zou, Q.; Yan, X., Nanodrugs based on peptide-modulated self-assembly: Design, delivery and tumor therapy. *Curr. Opin. Colloid Interface Sci.* **2018**, *35*, 17-25.
15. Loh, X. J., Latest Advances in Antibacterial Materials. *J. Mol. Eng. Mater.* **2017**, *05* (01), 1740001.

16. Schnaider, L.; Brahmachari, S.; Schmidt, N. W.; Mensa, B.; Shaham-Niv, S.; Bychenko, D.; Adler-Abramovich, L.; Shimon, L. J. W.; Kolusheva, S.; DeGrado, W. F.; Gazit, E., Self-assembling dipeptide antibacterial nanostructures with membrane disrupting activity. *Nat. Commun.* **2017**, *8* (1), 1365.
17. Shen, Z.; Guo, Z.; Zhou, L.; Wang, Y.; Zhang, J.; Hu, J.; Zhang, Y., Biomembrane induced in situ self-assembly of peptide with enhanced antimicrobial activity. *Biomater. Sci.* **2020**, *8* (7), 2031-2039.
18. Shi, Y.; Wareham, D. W.; Phee, L. M.; Azevedo, H. S., CHAPTER 12 Self-assembled Peptide Nanostructures for Antibacterial Applications. In *Peptide-based Biomaterials*, The Royal Society of Chemistry: 2021; pp 395-428.
19. Sinha, N. J.; Langenstein, M. G.; Pochan, D. J.; Kloxin, C. J.; Saven, J. G., Peptide Design and Self-assembly into Targeted Nanostructure and Functional Materials. *Chem. Rev.* **2021**, *121* (22), 13915-13935.
20. Du, X.; Zhou, J.; Shi, J.; Xu, B., Supramolecular Hydrogelators and Hydrogels: From Soft Matter to Molecular Biomaterials. *Chem. Rev.* **2015**, *115* (24), 13165-13307.
21. Fleming, S.; Ulijn, R. V., Design of nanostructures based on aromatic peptide amphiphiles. *Chem. Soc. Rev.* **2014**, *43* (23), 8150-8177.
22. Sheehan, F.; Sementa, D.; Jain, A.; Kumar, M.; Tayarani-Najjaran, M.; Kroiss, D.; Ulijn, R. V., Peptide-Based Supramolecular Systems Chemistry. *Chem. Rev.* **2021**, *121* (22), 13869-13914.
23. Zhao, F.; Ma, M. L.; Xu, B., Molecular hydrogels of therapeutic agents. *Chem. Soc. Rev.* **2009**, *38* (4), 883-891.
24. Jia, W.; Wang, Y.; Liu, R.; Yu, X.; Gao, H. J. A. F. M., Shape Transformable Strategies for Drug Delivery. *Adv. Funct. Mater.* **2021**, *31* (18), 2009765.
25. Li, R. S.; Liu, J.; Shi, H.; Hu, P. P.; Wang, Y.; Gao, P. F.; Wang, J.; Jia, M.; Li, H.; Li, Y. F.; Mao, C.; Li, N.; Huang, C. Z., Transformable Helical Self-Assembly for Cancerous Golgi Apparatus Disruption. *Nano Lett.* **2021**, *21* (19), 8455-8465.
26. Sun, B.; Chang, R.; Cao, S.; Yuan, C.; Zhao, L.; Yang, H.; Li, J.; Yan, X.; van Hest, J. C. M., Acid-Activatable Transmorphic Peptide-Based Nanomaterials for Photodynamic Therapy. *Angew. Chem. Int. Ed.* **2020**, *59* (46), 20582-20588.
27. Zhang, L.; Jing, D.; Jiang, N.; Rojalín, T.; Baehr, C. M.; Zhang, D.; Xiao, W.; Wu, Y.; Cong, Z.; Li, J. J.; Li, Y.; Wang, L.; Lam, K. S., Transformable peptide nanoparticles arrest HER2 signalling and cause cancer cell death in vivo. *Nat. Nanotechnol.* **2020**, *15* (2), 145-153.
28. Zhang, X.; Chen, X.; Song, J.; Zhang, J.; Ren, X.; Zhao, Y. J. A. M., Size-Transformable Nanostructures: From Design to Biomedical Applications. *Adv. Mater.* **2020**, *32* (48), 2003752.
29. Sis, M. J.; Webber, M. J., Drug Delivery with Designed Peptide Assemblies. *Trends in Pharmacological Sciences* **2019**, *40* (10), 747-762.
30. Yang, J.; An, H.-W.; Wang, H., Self-Assembled Peptide Drug Delivery Systems. *ACS Appl. Bio Mater.* **2021**, *4* (1), 24-46.
31. Ranjith, R.; Balraj, S.; Ganesh, J.; John Milton, M. C., Therapeutic agents loaded chitosan-based nanofibrous mats as potential wound dressings: A review. *Materials Today Chemistry* **2019**, *12*, 386-395.
32. Mateo Anson, N.; van den Berg, R.; Havenaar, R.; Bast, A.; Haenen, G. R. M. M., Bioavailability of ferulic acid is determined by its bioaccessibility. *J. Cereal Sci.* **2009**, *49* (2), 296-300.
33. Zhu, J.; Zhang, Z.; Wang, R.; Zhong, K.; Zhang, K.; Zhang, N.; Liu, W.; Feng, F.; Qu, W., Review of Natural Phytochemical-Based Self-Assembled Nanostructures for Applications in Medicine. *ACS Appl. Nano Mater.* **2022**.
34. Ibitoye, O. B.; Ajiboye, T. O., Ferulic acid potentiates the antibacterial activity of quinolone-based antibiotics against *Acinetobacter baumannii*. *Microbial pathogenesis* **2019**, *126*, 393-398.
35. Shi, C.; Zhang, X.; Sun, Y.; Yang, M.; Song, K.; Zheng, Z.; Chen, Y.; Liu, X.; Jia, Z.; Dong, R.; Cui, L.; Xia, X., Antimicrobial Activity of Ferulic Acid Against *Cronobacter*

sakazakii and Possible Mechanism of Action. *Foodborne pathogens and disease* **2016**, *13* (4), 196-204.

36. Borges, A.; Ferreira, C.; Saavedra, M. J.; Simões, M., Antibacterial activity and mode of action of ferulic and gallic acids against pathogenic bacteria. *Microbial drug resistance (Larchmont, N.Y.)* **2013**, *19* (4), 256-65.

37. Pernin, A.; Bosc, V.; Maillard, M.-N.; Dubois-Brissonnet, F., Ferulic Acid and Eugenol Have Different Abilities to Maintain Their Inhibitory Activity Against *Listeria monocytogenes* in Emulsified Systems. *Front. microbiol.* **2019**, *10* (137).

38. Silva, C. G.; Yudice, E. D. C.; Campini, P. A. L.; Rosa, D. S., The performance evaluation of Eugenol and Linalool microencapsulated by PLA on their activities against pathogenic bacteria. *Materials Today Chemistry* **2021**, *21*, 100493.

39. Tan, Y.; Xu, K.; Li, L.; Liu, C.; Song, C.; Wang, P., Fabrication of Size-Controlled Starch-Based Nanospheres by Nanoprecipitation. *ACS Appl. Mater. Interfaces* **2009**, *1* (4), 956-959.

40. Liu, H.; Finn, N.; Yates, M. Z., Encapsulation and Sustained Release of a Model Drug, Indomethacin, Using CO<sub>2</sub>-Based Microencapsulation. *Langmuir* **2005**, *21* (1), 379-385.

41. Hernández-Giottonini, K. Y.; Rodríguez-Córdova, R. J.; Gutiérrez-Valenzuela, C. A.; Peñuñuri-Miranda, O.; Zavala-Rivera, P.; Guerrero-Germán, P.; Lucero-Acuña, A., PLGA nanoparticle preparations by emulsification and nanoprecipitation techniques: effects of formulation parameters. *RSC Adv.* **2020**, *10* (8), 4218-4231.

42. Reisch, A.; Runser, A.; Arntz, Y.; Mély, Y.; Klymchenko, A. S., Charge-Controlled Nanoprecipitation as a Modular Approach to Ultrasmall Polymer Nanocarriers: Making Bright and Stable Nanoparticles. *ACS Nano* **2015**, *9* (5), 5104-5116.

43. Khalil, N. M.; do Nascimento, T. C.; Casa, D. M.; Dalmolin, L. F.; de Mattos, A. C.; Hoss, I.; Romano, M. A.; Mainardes, R. M., Pharmacokinetics of curcumin-loaded PLGA and PLGA-PEG blend nanoparticles after oral administration in rats. *Colloids and surfaces. B, Biointerfaces* **2013**, *101*, 353-60.

44. Chopra, S.; Bertrand, N.; Lim, J.-M.; Wang, A.; Farokhzad, O. C.; Karnik, R., Design of Insulin-Loaded Nanoparticles Enabled by Multistep Control of Nanoprecipitation and Zinc Chelation. *ACS Appl. Mater. Interfaces* **2017**, *9* (13), 11440-11450.

45. Tarhini, M.; Benlyamani, I.; Hamdani, S.; Agusti, G.; Fessi, H.; Greige-Gerges, H.; Bentaher, A.; Elaissari, A., Protein-Based Nanoparticle Preparation via Nanoprecipitation Method. *Materials (Basel)* **2018**, *11* (3), 394.

46. Pal, V. K.; Jain, R.; Roy, S., Tuning the Supramolecular Structure and Function of Collagen Mimetic Ionic Complementary Peptides via Electrostatic Interactions. *Langmuir* **2020**, *36* (4), 1003-1013.

47. Jones, E. M.; Cochrane, C. A.; Percival, S. L., The Effect of pH on the Extracellular Matrix and Biofilms. *Adv Wound Care (New Rochelle)* **2015**, *4* (7), 431-439.

48. Li, T.; Lu, X.-M.; Zhang, M.-R.; Hu, K.; Li, Z., Peptide-based nanomaterials: Self-assembly, properties and applications. *Bioact. Mater.* **2021**.

49. Jeong, W.-J.; Bu, J.; Kubiawicz, L. J.; Chen, S. S.; Kim, Y.; Hong, S., Peptide-nanoparticle conjugates: a next generation of diagnostic and therapeutic platforms? *Nano Converg* **2018**, *5* (1), 38-38.

50. Gan, X.; Wang, Z.; Hu, D., Synthesis of Novel Antiviral Ferulic Acid–Eugenol and Isoeugenol Hybrids Using Various Link Reactions. *J. Agric. Food. Chem.* **2021**.

51. Contardi, M.; Lenzuni, M.; Fiorentini, F.; Summa, M.; Bertorelli, R.; Suarato, G.; Athanassiou, A., Hydroxycinnamic Acids and Derivatives Formulations for Skin Damages and Disorders: A Review. *Pharmaceutics* **2021**, *13* (7), 999.

52. Panyam, J.; Labhasetwar, V., Biodegradable nanoparticles for drug and gene delivery to cells and tissue. *Adv Drug Deliv Rev* **2003**, *55* (3), 329-47.

53. Hornig, S.; Heinze, T.; Becer, C. R.; Schubert, U. S., Synthetic polymeric nanoparticles by nanoprecipitation. *J. Mater. Chem.* **2009**, *19* (23), 3838-3840.

54. Yuan, C.; Ji, W.; Xing, R.; Li, J.; Gazit, E.; Yan, X., Hierarchically oriented organization in supramolecular peptide crystals. *Nat. Rev. Chem.* **2019**, *3* (10), 567-588.

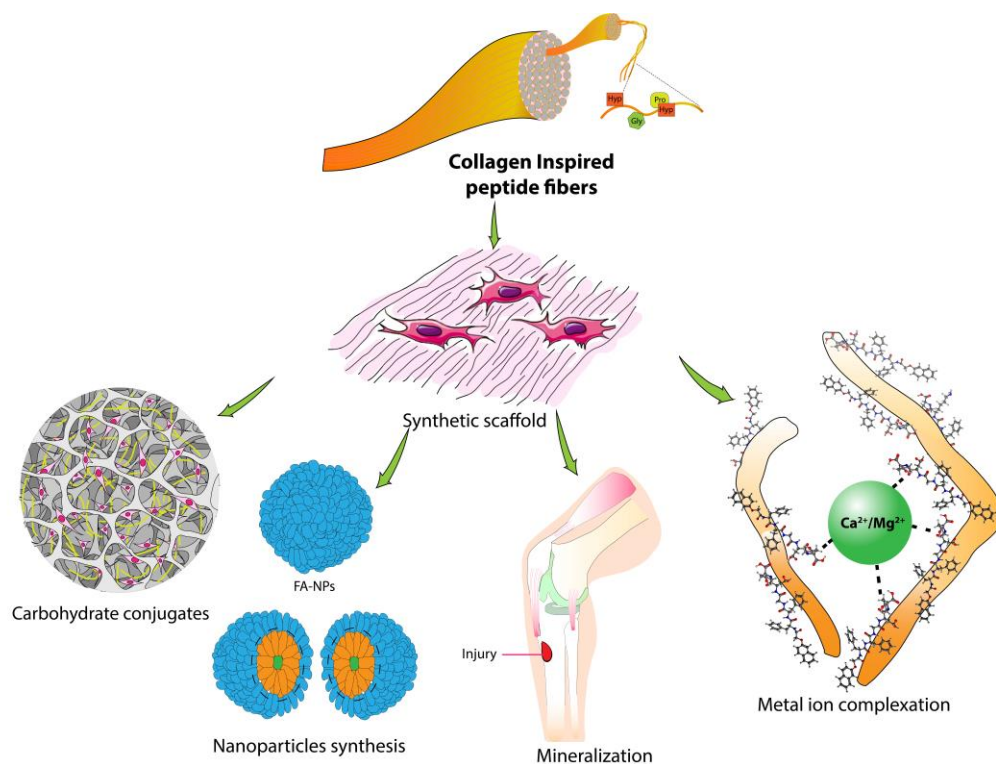
55. Yuan, C.; Levin, A.; Chen, W.; Xing, R.; Zou, Q.; Herling, T. W.; Challa, P. K.; Knowles, T. P. J.; Yan, X., Nucleation and Growth of Amino Acid and Peptide Supramolecular Polymers through Liquid–Liquid Phase Separation. *Angew. Chem. Int. Ed.* **2019**, *58* (50), 18116-18123.
56. Kaur, H.; Sharma, P.; Patel, N.; Pal, V. K.; Roy, S., Accessing Highly Tunable Nanostructured Hydrogels in a Short Ionic Complementary Peptide Sequence via pH Trigger. *Langmuir* **2020**, *36* (41), 12107-12120.
57. Romeo, A.; Musumeci, T.; Carbone, C.; Bonaccorso, A.; Corvo, S.; Lupo, G.; Anfuso, C. D.; Puglisi, G.; Pignatello, R., Ferulic Acid-Loaded Polymeric Nanoparticles for Potential Ocular Delivery. *Pharmaceutics* **2021**, *13* (5), 687.
58. Ambriz-Aviña, V.; Contreras-Garduño, J. A.; Pedraza-Reyes, M., Applications of flow cytometry to characterize bacterial physiological responses. *BioMed research international* **2014**, *2014*, 461941.
59. Campos, F. M.; Couto, J. A.; Figueiredo, A. R.; Tóth, I. V.; Rangel, A. O.; Hogg, T. A., Cell membrane damage induced by phenolic acids on wine lactic acid bacteria. *Int J Food Microbiol* **2009**, *135* (2), 144-51.
60. de Oliveira, E. F.; Yang, X.; Basnayake, N.; Huu, C. N.; Wang, L.; Tikekar, R.; Nitin, N., Screening of antimicrobial synergism between phenolic acids derivatives and UV-A light radiation. *Journal of Photochemistry and Photobiology B: Biology* **2021**, *214*, 112081.
61. Buege, J. A.; Aust, S. D., Microsomal lipid peroxidation. *Methods Enzymol.* **1978**, *52*, 302-10.
62. Wang, T.-Y.; Libardo, M. D. J.; Angeles-Boza, A. M.; Pellois, J.-P., Membrane Oxidation in Cell Delivery and Cell Killing Applications. *ACS Chem Biol* **2017**, *12* (5), 1170-1182.
63. Mayandi, V.; Wen Choong, A. C.; Dhand, C.; Lim, F. P.; Aung, T. T.; Sriram, H.; Dwivedi, N.; Periyah, M. H.; Sridhar, S.; Fazil, M. H. U. T.; Goh, E. T. L.; Orive, G.; W. Beuerman, R.; Barkham, T. M. S.; Loh, X. J.; Liang, Z.-X.; Barathi, V. A.; Ramakrishna, S.; Chong, S. J.; Verma, N. K.; Lakshminarayanan, R., Multifunctional Antimicrobial Nanofiber Dressings Containing  $\epsilon$ -Polylysine for the Eradication of Bacterial Bioburden and Promotion of Wound Healing in Critically Colonized Wounds. *ACS Appl. Mater. Interfaces* **2020**, *12* (14), 15989-16005.
64. Pal, V. K.; Roy, S., Cooperative Metal Ion Coordination to the Short Self-Assembling Peptide Promotes Hydrogelation and Cellular Proliferation. *Macromolecular Bioscience n/a* (n/a), 2100462.
65. Kaur, H.; Roy, S., Designing aromatic N-cadherin mimetic short-peptide-based bioactive scaffolds for controlling cellular behaviour. *J. Mater. Chem. B* **2021**, *9* (29), 5898-5913.
66. Pijuan, J.; Barceló, C.; Moreno, D. F.; Maiques, O.; Sisó, P.; Marti, R. M.; Macià, A.; Panosa, A., In vitro Cell Migration, Invasion, and Adhesion Assays: From Cell Imaging to Data Analysis. **2019**, *7* (107).



# **Chapter 8**

## **Conclusions and Future perspective**





**Schematic representation depicting the fabrication of the diverse nanostructure accessed in the single gelator domain derived from short collagen inspired peptide, which offer significant potential in diverse regime of biomedical nanotechnology-based applications.**



## 8.1 Summary

Focusing on the notion of utilizing the classical and elegant strategy of molecular self-assembly through exclusively choosing a minimalistic approach and emulating the bioactivity of natural design, we have tried to overcome the challenges involved in the design and synthesis of peptide-based biomaterials. Advanced tissue scaffolds developed from these short peptide amphiphiles are intended to govern the cellular behaviour by actively engaging with the cells and regulating the cellular proliferation rather than just functioning as sessile scaffold that provide structural support to hold the cells at the target region. We concentrated on building bioactive scaffolds based on the short/truncated bio-functional sequences of proteins found in the natural ECM. The rationale for targeting the ECM derived proteins relies on mimicking the similar microenvironments of the cells of choice to provide a more suitable habitat for the cells to achieve better adaptability. Furthermore, the constructed scaffolds allowed for a better understanding of the necessary parameters for controlling and regulating the physiochemical characteristics of the native ECM. For designing these biomolecular hydrogel scaffolds, we have utilized a well-known bioinspired bottom-up strategy i.e., molecular self-assembly. Molecular self-assembly offers a better control over the interactions, which allows achieving of the higher level of complexity, and thus creating a network very similar to that of the natural systems. This strategy was used in this thesis to design two ionic complementary collagen inspired peptide amphiphiles and tune their self-assembly behaviour through utilization of different external stimuli to achieve differential molecular organization. Such non-conventional approach of molecular self-assembly leads to fabrication of diverse nanostructures, which demonstrated different biological applications. Moreover, the peptides and proteins only represent a single component of biomacromolecules present in the native ECM. Thus, development of biomaterial solely using peptides to achieve the similar level of structural and functional complexity of the native ECM would not be a rational approach. In this direction, our smart approach was focused to design and develop a conjugate system containing the benefits of bioactive motifs of peptide for favorable cellular interactions and the biological polymer, which can provide the structural stability as well as mechanical rigidity to the scaffold. Further, we have demonstrated the fabrication of a new class of peptide-based bio-nano construct, which provides dual

functionality and environmental tunability offering the advancement in the microbial therapy and wound healing application.

The thesis begins with an overview of the current state of the art strategies that are developed in the advancement of bioinspired synthetic scaffolds, which is followed by a discussion on the importance of peptide-based bioactive materials in tissue engineering and regenerative medicine. Further we attempted to provide a thorough details of the advanced molecular-self-assembly strategies, which are frequently used in the fabrication of peptide-based biomaterials. This section is further followed by the various non-covalent interactions that guide peptide self-assembly and the specific gelation routes that are used to construct different scaffolds out of peptide-based building blocks. We've also discussed the relevance of biopolymer-peptide interactions in constructing a biomimetic advanced scaffold for tissue engineering applications in subsequent sections. Finally, we discussed the uses of peptide-based hydrogels in a variety of biological sectors. In summary, this chapter explores peptide-based supramolecular structures to offer an overview of the recent advancements in the field of biomaterial science. The materials and technique used for the synthesis, characterization, and assessment of the biological activity of the designer peptide hydrogels were discussed in the second chapter. The development of bioactive peptide hydrogels to attain structural and functional complexity in a gradual way, starting with peptide molecular assembly and progressing to multi-component co-assembly to construct next-generation biomaterials, was illustrated in the following chapters.

The main findings of the research work presented in thesis can be summarized as:

1. In chapter 3, we report the crucial molecular design of oppositely charged collagen inspired shortest bioactive pentapeptide sequences, as a minimalistic building block for the development of next-generation biomaterials. The peptide features the repeating unit of collagen molecule (Gly-Pro-Hyp), where proline has been replaced with two oppositely charged amino acids, lysine and aspartate in two ionic complementary sequences. The designed sequences showed effective self-assembly either at acidic/basic pH depending up on their overall surface charge. However, such phenomenon limits their bio-applications. Surprisingly, simple mixing of the two peptides were found to induce the co-assembly of these designed peptide, which drives the formation of self-

supporting hydrogel at physiological pH and thus enhanced the potential of exploring these peptides for biomedical purposes. Initiation of the electrostatic interaction was found to have profound effect on gelation behavior of the short bioactive peptides. The minimum gelation concentration of the individual peptides has been reduced with an increase in their mechanical strength at physiological pH for their co-assembled state. Such interesting feature enhanced the scope of these designed gels to be explored as smart biomaterial to support their biological functions. Interestingly, these bioinspired peptide sequences showed excellent biocompatibility with the fibroblast cells, which provides the evidence for developing such functional materials for biomedical applications.

2. In chapter 4, we present the cooperative effect of biologically relevant metal ion coordination in a minimalist bioactive peptide molecular domain to promote hydrogelation at physiological pH. By simply adding metal ions, the detrimental effect of surface charge of the peptide can be minimized, which has direct implication in promoting cellular proliferation to develop next-generation biomaterial for tissue engineering applications. We have explored the previously designed native collagen triple helical peptide sequence (Gly-Asp-Hyp) that display negatively charged surface at physiological pH and thus self-assemble at pH 5.0. Since, the peptide monomer failed to self-assemble at an ambient condition, hence its application in biomedicine is limited. Interestingly, the negatively charged peptide shifted its equilibrium point of self-assembly and showed conversion from sol to gel in the presence of divalent metal ions ( $\text{Ca}^{2+}/\text{Mg}^{2+}$ ) at physiological pH. Moreover, highly tunable hydrogels with diverse mechanical strength can be developed by simply tuning specific metal ions of biological relevance and their relative concentrations in the solution. Thus, this simple methodology can be utilized as a powerful approach that can overcome the limitations of charged peptide construct. In this regard, we achieved diverse gels with higher mechanical strength at a much lower concentration, as reported earlier. The changes in physical properties were found to bring in a difference in biological activities. The differential cellular response was observed in the new designer construct i.e., metal coordinated hydrogels. Cellular viability, adhesion, and proliferation demonstrated the importance of metal ions in modulating the collagen inspired peptide assembly

as a next-generation biomaterial. Furthermore, the new constructs with metal ions promoted cellular functions, as evident from the F-actin and  $\beta$ -III tubulin staining studies. Interestingly, significant enhancement in cellular viability, adhesion, and proliferation was evident in peptide hydrogels prepared with magnesium coordination compared to calcium ions, which may be attributed to their differential spatiotemporal arrangement in the self-assembled state. This may generate differential physical cues to the specific cell types. Such interesting cooperative self-assembly enhances the scope of these biomaterials, which can be applied in developing extracellular matrix mimics for futuristic applications.

3. In chapter 5, we demonstrated the cooperative deposition of calcium phosphate on the collagen fiber with preliminary growth of hydroxyapatite crystals. The overall mechanism involves the mutual and combined interaction of all the four components (peptide fiber, calcium chloride, disodium phosphate, and glutamic acid) to nucleate the mineralization. The glutamic acid adsorbed onto the peptide fiber surface interact through the electrostatic interaction between the positively charged lysine moieties present on the fiber surface. It was evident that the area of calcium deposits, which were considered as the site of nucleation further grows to cover the entire peptide nanofiber. Microscopic and spectroscopic characterization revealed that the presence of hydroxyapatite crystal on the peptide fiber. These mineralized fibers were also found to be biocompatible with the osteoblast and found to promote cellular proliferation of both the cell lines 7F2 and Saos-2. Furthermore, the mineralized peptide showed increased production of alkaline phosphatase (ALP) after 7 days of incubation and the similar phenomenon was observed in Alizarin Red S staining. Thus, this novel approach demonstrated that the mineralized collagen peptide is capable of promoting osteogenesis and enhances mineralization ability of the collagen fibers. This strategy further reinforced the potential application of the mineralized collagen fibers towards effectively fabricating the grafts for bone tissue engineering.
4. In chapter 6, we explored for the first time the conjugation of nanofibrillar cellulose with collagen inspired peptides via non-covalent interactions. The interesting class of biomaterial was fabricated by a simple mixing strategy,

which offers dual advantages by combining biochemical cues offered by peptide segments coupled with structural stability and mechanical integrity induced by cellulose nanofibril. Our study demonstrated that the TEMPO-oxidized anionic cellulose nanofiber matrix was highly tunable. The incorporation of positively charged bioinspired peptide triggered the physical cross linking of cellulose with peptide motifs through charge pair interaction leading to pore closure in the multi-component assembly. Such reduced porous structure turns the surface smooth and may interfere with cellular adhesion. Such limitations can be overcome when two complementary ionic peptides were used. The preferable salt-bridge formation within the two complementary ionic peptides backbones further drives the assembly with cellulose through CH/ $\pi$  and H bonding interactions leading to fabrication of more porous and rough hydrogel surface to promote cellular adhesion. Our study demonstrated that the CIP conjugated NFC hydrogels can successfully promote cell adhesion, proliferation, and migration. This multi-component biomolecular hydrogel platform combines the specificity and biochemical functionality of the biological world with the synthetic world through fabrication of a next-generation biomaterial using simplistic strategy of exploring non-covalent physical cross-linking. Thus, this simple mixing strategy has been offering an enhanced scope for designing novel biomaterial, which may otherwise be inaccessible via covalent synthetic routes. This attempt further opens up a new avenue for bottom-up fabrication in minimalistic biomolecular nanotechnology to enhance complexity in multiscale assembly.

5. In chapter 7, we present for the first time the fabrication of a bio-nano construct with dual functionality and environmental tunability, which offers numerous advantages in wound healing applications. Specifically, we have explored the unique intrinsic stimuli responsive self-assembling property of the collagen inspired peptide to encapsulate and release the hydrophobic drug molecule. A novel nano-formulation was fabricated in the form of spherical nanoparticles using the peptide amphiphile to encapsulate the hydrophobic drug ferulic acid, which renders the construct stable in aqueous environment. Interestingly, the peptide amphiphile display the propensity to show a dynamic behaviour under pH switch, which is evident from its structural transition from nanosphere to

nanofibers at weekly basic pH of 8.5. At this pH, it tends to release the antimicrobial drug at the wound site that displays a surrounding pH of 7.5-8.9. Hence, we developed this unique strategy that utilizes the weakly basic pH of the wound site to trigger the structural transition of the peptide nanoparticles, which induces the self-assembly of the peptide to form peptide nanofibers and thus releasing the encapsulated ferulic acid from the nanosphere. The proposed novel fabricated nanoparticles showed an enhanced efficacy of ferulic acid, which was evident in a lower value of MIC as reported earlier for ferulic acid ferulic acid in aqueous medium. We envisage that these novel nano-constructs will offer a dual advantage. In particular, the released drug from the nanosphere will help to combat microbial infection, and the collagen derived peptide nanofibers formed due to the pH switch will serve as a synthetic scaffold for wound regeneration. Such pH responsive structural transition will lead to an efficient way of drug transportation to show the antimicrobial activity. This unique study provided the insights into designing of transformable peptide-based nanostructure and demonstrated their applications in antimicrobial and biomaterial generation.

## **8.2 Future perspectives**

In the coming years, researchers will continue to be fascinated by the extraordinarily complicated and advanced functions performed by peptides, proteins, and sugars derived from the native ECM. Such unique advantages offered by the biomolecules will help the researchers to design biomimetic systems that govern cellular activity *in vitro*. Hydrogels made from short self-assembling peptides are an advanced class of biomaterials with a lot of potential for tissue engineering applications. The core structure of the basic building blocks may be easily changed to attain desired biological function due to their simple design flexibility. The self-assembly of peptides is primarily driven by non-covalent interactions, which constructs the final hydrogel material with specific structural and functional tunability. In comparison to previous synthetic systems investigated for tissue engineering applications, the physical characteristics, nano-topography, morphological traits, etc. can easily be modified in these macromolecular ensembles owing to the molecular association resulting from weak non-covalent interactions. Their advantageous attributes, including biocompatibility, optimal degradation rates, and simplicity of ligand presentation, make

them a great choice for further exploration. Furthermore, for the development of sophisticated tissue mimics, the combinatorial strategy exploiting the benefits of including diverse components of natural ECM such as peptides, sugars, vitamins, and growth factors inside a single scaffold is likely to gather enormous attention in the future. Furthermore, the tunability of peptide-based biomaterials to control physicochemical properties makes them an ideal candidate to be explored for other futuristic applications such as the development of environmentally friendly energy harvesting systems, wearable electronics by exploring peptide piezoelectric response, stimuli-responsive on-demand drug delivery vehicles for various diseases, biocompatible scaffolds for catalytic reactions, and probes for bioimaging purposes. We anticipate that present understanding and fundamental knowledge acquired in peptide self-assembly, as well as future advances in the area, will considerably contribute in overcoming the current clinical challenges in tissue engineering and regenerative medicine.



# Appendix I



## List of publications

### *Included in Thesis*

1. Vijay Kumar Pal, Rashmi Jain, and Sangita Roy, Tuning the supramolecular structure and function of collagen mimetic ionic complementary peptides via electrostatic interactions. *Langmuir*, **2019**, *36(4)*, 1003-1013.
2. Vijay Kumar Pal, Rashmi Jain, Sourav Sen, Kamalakannan Kailasam, and Sangita Roy, Designing nanofibrillar cellulose peptide conjugated polymeric hydrogel scaffold for controlling cellular behaviour. *Cellulose*, **2021**, *28*, 10335-10357.
3. Vijay Kumar Pal and Sangita Roy, Cooperative metal ion coordination to the short self-assembling peptide promotes hydrogelation and cellular proliferation. *Macromol. Biosci.*, **2022**, 2100462.
4. Vijay Kumar Pal and Sangita Roy, Bioactive peptide nano-assemblies with pH triggered shape transformation for antibacterial therapy. *ACS Appl. Nano Mater.* **2022**, *5(8)*, 12014-12039.
5. Vijay Kumar Pal and Sangita Roy, Cooperative calcium phosphate deposition on collagen-based peptide nanofibers for application in bone tissue engineering. (Manuscript under review).

### *Not included in Thesis*

1. Rashmi Jain, Vijay Kumar Pal, and Sangita Roy, Triggering supramolecular hydrogelation using a protein-peptide co-assembly approach. *Biomacromolecules*, **2020**, *21(10)*, 4180-4193.
2. Harsimran Kaur, Pooja Sharma, Nidhi Patel, Vijay Kumar Pal, and Sangita Roy, Accessing highly tunable nanostructured hydrogels in a short ionic complementary peptide sequence via pH trigger. *Langmuir*, **2020**, *36(41)*, 12107-12120.
3. Pooja Sharma, Vijay Kumar Pal, and Sangita Roy, An overview of latest advances in exploring bioactive peptide hydrogels for neural tissue engineering. *Biomater. Sci.* **2021**, *9*, 3911-3938.
4. Pooja Sharma, Harsimran Kaur, Vijay Kumar Pal, and Sangita Roy, Exploring co-assembly of TEMPO-Oxidized nanofibrillar cellulose and short peptide amphiphile to fabricate bio-functional cellular scaffold. *Biomacromolecules*, **2022**. (Just Accepted)

## **Conference Presentations**

1. INST-IISERM Bilateral Meeting 14-15th March 2022

Vijay Kumar Pal, and Sangita Roy

Poster: Developing Collagen Mimetic Ionic Complementary Peptide Hydrogels for Biomedical Applications

2. International e-Conference on Nanomaterials & Nanoengineering, (APA NANOFORUM) 24-26th February 2022 on Virtual Platform.

Vijay Kumar Pal, and Sangita Roy

Poster: Developing Collagen Mimetic Ionic Complementary Peptide Hydrogels for Biomedical Applications

3. International Conference Chemistry for Next-Gen Application (ICCNA'21) 24-26th September, 2021 (Oral presentation)

Vijay Kumar Pal, and Sangita Roy

Title: Designing collagen mimetic ionic complementary peptide hydrogels for biomedical applications. (Third prize)

4. 1st Annual Meeting of the Chemical Biology Unit, (AMCBU) Nano@Chembio 2021 (24-25 September 2021) at INST.

Vijay Kumar Pal, and Sangita Roy

Poster: Designing Collagen Mimetic Ionic Complementary Peptide Hydrogels for Biomedical Applications.

5. National Conference on Recent Trends in Materials Science and Technology (NCMST-2021)' (29-31 December 2021) on Virtual Platform.

Vijay Kumar Pal, and Sangita Roy

Poster: Designing Collagen Mimetic Ionic Complementary Peptide Hydrogels for Biomedical Applications.

6. NanoDay@INST 31st December 2021

Vijay Kumar Pal, and Sangita Roy

Poster: Developing Collagen Mimetic Ionic Complementary Peptide Hydrogels for Biomedical Applications

7. National Conference on Surfactant Emulsion and Biocolloids (NATCOSEB-XX) 9-11th December 2021

Vijay Kumar Pal, and Sangita Roy

Poster: Developing Collagen Mimetic Ionic Complementary Peptide Hydrogels for Biomedical Applications

8. International Conference on Nanotechnology for Better Living (ICNBL-2021) 7-11th September 2021 (Virtual Mode)

Vijay Kumar Pal, and Sangita Roy

Poster: Developing Collagen Mimetic Ionic Complementary Peptide Hydrogels for Biomedical Applications

9. Virtual Symposium: Systems Chemistry 2020, May 18-20, 2020 (*only participated*)

10. ICONSAT, Kolkata 5-7th March' 2020

Vijay Kumar Pal, Rashmi Jain, Sangita Roy

Poster title: Designing collagen mimetic ionic complementary peptide hydrogel for biomedical application. (Best Poster Prize)

11. CRIKC Chemistry Symposium 2019, IISER Mohali, 02-03rd November' 2019

Poster title: Designing collagen mimetic ionic complementary peptide hydrogel for biomedical application.

Vijay Kumar Pal, Rashmi Jain, Sangita Roy

12. International Conference on Life Science Research & its Interface with Engineering and Allied Science. (LSRIEAS-2018)

Poster Title: Designing collagen mimetic ionic complementary peptide hydrogel for biomedical application

Vijay Kumar Pal, Rashmi Jain, Sangita Roy

13. Indo-German Meeting 2018

Designing collagen mimetic ionic complementary peptide hydrogel for biomedical application

Vijay Kumar Pal, Rashmi Jain, Sangita Roy